



**HAL**  
open science

# Light emission from a Scanning Tunneling Microscope : Study of the electronic and optical properties of a hybrid metal-TMD system

Estefania Alves Alves

► **To cite this version:**

Estefania Alves Alves. Light emission from a Scanning Tunneling Microscope : Study of the electronic and optical properties of a hybrid metal-TMD system. Electronics. Université Paul Sabatier - Toulouse III, 2023. English. NNT : 2023TOU30351 . tel-04592705

**HAL Id: tel-04592705**

**<https://theses.hal.science/tel-04592705>**

Submitted on 29 May 2024

**HAL** is a multi-disciplinary open access archive for the deposit and dissemination of scientific research documents, whether they are published or not. The documents may come from teaching and research institutions in France or abroad, or from public or private research centers.

L'archive ouverte pluridisciplinaire **HAL**, est destinée au dépôt et à la diffusion de documents scientifiques de niveau recherche, publiés ou non, émanant des établissements d'enseignement et de recherche français ou étrangers, des laboratoires publics ou privés.



# THÈSE

En vue de l'obtention du  
**DOCTORAT DE L'UNIVERSITÉ DE TOULOUSE**  
Délivré par l'Université Toulouse 3 - Paul Sabatier

---

Présentée et soutenue par  
**Estefania ALVES ALVES**

Le 18 décembre 2023

**Émission de photons dans un microscope à effet tunnel:  
Application à l'étude des propriétés optiques et électroniques de  
systèmes hybrides métal/semi-conducteur**

---

Ecole doctorale : **SDM - SCIENCES DE LA MATIERE - Toulouse**

Spécialité : **Nanophysique**

Unité de recherche :  
**CEMES - Centre d'Elaboration de Matériaux et d'Etudes Structurales**

Thèse dirigée par  
**Roland CORATGER et Renaud PECHOU**

Jury

Mme Elizabeth BOER-DUCHEMIN, Rapporteure  
M. Nicolas LARGE, Rapporteur  
M. Nordin FELIDJ, Examineur  
M. Roland CORATGER, Directeur de thèse  
M. Renaud PECHOU, Co-directeur de thèse  
M. David GUERY-ODELIN, Président



## ACKNOWLEDGEMENTS

I would like to express my genuine gratitude to everyone who played a role in making the completion of this thesis possible, both on a professional and personal level.

I am deeply grateful to my thesis supervisors, Roland and Renaud, for their mentorship, patience, and expertise. Special thanks are also extended to Adnen, who generously shared his knowledge and offered valuable insights. I am grateful for the opportunities Roland, Renaud and Adnen provided me to grow as a scientist. Their guidance and encouragement have not only shaped my research but have also left an indelible mark on me.

I would like to express my gratitude to the referees of my work, Elizabeth Boer-Duchemin and Nicolas Large, for reading the manuscript and providing insightful comments. I also wish to thank the other jury members, Nordin Felidj and David Guéry-Odelin, for their helpful discussions.

I would like to acknowledge my colleagues, especially those from picolab, who have provided me with a supportive work environment. In particular, I would like to thank Grégory Seine and Olivier Guillermet for their help.

A big thank you to the PhD students and post-docs at CEMES for the awesome moments and friendly lunches. Special thanks to Kedar, Elio, Eloïse, Liz, Intan, and Akshay. You guys made my days easier and much more colorful.

Quiero agradecer de corazón a mis padres por educarme con amor y guiarme hasta este punto. También quiero expresar mi agradecimiento al resto de mi familia, incluyendo a mis hermanos, cuñadas y la familia de mi pareja, por su constante apoyo.

Quiero expresar mi gratitud hacia Anna, Hager, Nadia, Aida, Kritiy y demás amigas que componen mi red de apoyo. Aunque no he podido compartir mucho tiempo con ellas durante estos tres años, siempre han estado a mi lado.

Finalmente, quiero expresar mi profundo agradecimiento a Pepe, mi compañero de vida. Gracias por brindarme un apoyo incondicional, tu paciencia inquebrantable y por regalarme risas y sonrisas en cualquier situación. Has sido la persona que más ha estado allí para respaldarme en los momentos complicados. Te estaré agradecida eternamente.



# Table of Contents

<b>Introduction</b>	<b>8</b>
<b>1 State of the art</b>	<b>12</b>
1.1 Light emission induced by a Scanning Tunneling Microscope (STM-LE) . . . . .	12
1.1.1 Principles of the Scanning Tunneling Microscope (STM) . . . . .	13
1.1.2 Light emission from metallic junctions . . . . .	20
1.1.3 Light emission from semiconductor samples . . . . .	32
1.2 Transition-metal dichalcogenide (TMD) monolayers . . . . .	34
1.2.1 Crystal structure and physical properties . . . . .	35
1.2.2 Opto-electronic properties of TMD monolayers . . . . .	36
1.2.3 TMD/plasmonic nanostructures hybrid systems . . . . .	42
<b>2 Experimental tools and simulation methods</b>	<b>56</b>
2.1 Experimental setup . . . . .	56
2.1.1 The STM setup . . . . .	57
2.1.2 Light detection system . . . . .	59
2.1.3 Gold tip preparation . . . . .	63
2.2 TMD monolayer preparation and characterization . . . . .	64
2.2.1 Synthesis and transfer of TMD monolayers . . . . .	64
2.2.2 Characterization of TMD monolayers . . . . .	65
2.3 Simulation methods . . . . .	68
2.3.1 Discrete Dipole Approximation (DDA) . . . . .	69
2.3.2 Quantum-Corrected Model (QCM) . . . . .	71

<b>3</b>	<b>Experimental STM-induced light emission</b>	<b>77</b>
3.1	Light emission from plasmonic substrates . . . . .	78
3.1.1	Gold sample with granular surface . . . . .	78
3.1.2	Gold nanowires on non-plasmonic substrates . . . . .	82
3.2	Light emission from $MoSe_2$ monolayer on non-plasmonic substrates . . . . .	85
3.2.1	$MoSe_2$ on Graphene . . . . .	85
3.2.2	$MoSe_2$ on ITO . . . . .	87
3.3	Light emission from $MoSe_2$ monolayer on plasmonic substrates . . . . .	94
3.4	Light emission from $Au/MoSe_2/Au$ tunneling junction: role of the substrate morphology . . . . .	102
3.4.1	Nanostructured gold substrate: example of pyramidal cavities . . . . .	103
3.4.2	Nanostructured gold substrate: example of circular cavities . . . . .	107
3.5	Conclusion . . . . .	113
<b>4</b>	<b>Optical response of a hybrid <math>Au/MoSe_2/Au</math> tunneling junction</b>	<b>118</b>
4.1	Modeling of the STM junction . . . . .	119
4.1.1	Geometry and composition of the modeled tunneling junction . . . . .	120
4.1.2	Incident optical excitation . . . . .	122
4.2	Electromagnetic interaction between the $MoSe_2$ monolayer and the plasmonic junction . . . . .	124
4.2.1	Optical response of a purely metallic $Au/Au$ tunneling junction . . . . .	124
4.2.2	Optical response of a hybrid $Au/MoSe_2/Au$ tunneling junction . . . . .	127
4.2.3	Plasmon-exciton interaction . . . . .	134
4.3	Simulation of the electron tunneling using the Quantum- Corrected Model (QCM)	139
4.3.1	Implementation of the QCM in the numerical simulations . . . . .	139
4.3.2	Effect of the simulated STM electron tunneling on the optical response .	143
4.4	Tuning of the optical response of the hybrid $Au/MoSe_2/Au$ tunneling junction .	144
4.4.1	Dependence of the optical response on the main tunneling parameters .	145
4.4.2	Dependence of the optical response in terms of incidence angle . . . . .	149
4.4.3	Dependence of the optical response on the tip length and substrate dimensions . . . . .	153

4.5	Role of the substrate roughness . . . . .	156
4.5.1	Introduction of a rough substrate in the simulated junction . . . . .	156
4.5.2	Role of the substrate roughness in the optical response . . . . .	158
4.6	Conclusion . . . . .	166
<b>5</b>	<b>Theoretical model of light emission from a hybrid <math>Au/MoSe_2/Au</math> tunneling junction</b>	<b>171</b>
5.1	Light emission from inelastic tunneling in the junction: Plasmonic Emission . .	172
5.1.1	Model Description . . . . .	172
5.1.2	Formalism: modified version of the Johansson-Aizpurua model . . . . .	174
5.1.3	Spectral analysis of the plasmonic light emission . . . . .	183
5.2	Light emission from exciton radiative recombination: Excitonic Emission. . . . .	192
5.2.1	Model Description . . . . .	193
5.2.2	Formalism . . . . .	195
5.2.3	Spectral analysis of the excitonic light emission . . . . .	200
5.3	Analysis of plasmonic and excitonic light emission . . . . .	204
5.3.1	Comparison between plasmonic and excitonic light emission . . . . .	205
5.3.2	Role of the substrate roughness . . . . .	208
5.3.3	Comparison with experimental results . . . . .	214
5.4	Conclusion . . . . .	222
	<b>Conclusion</b>	<b>227</b>
	<b>Abstract - English</b>	<b>230</b>
	<b>Abstract - Français</b>	<b>232</b>
	<b>Résumé en Français</b>	<b>234</b>

# Introduction

Nano-optics is a fast-growing field of research dedicated to understanding, controlling, and manipulating light-matter interaction at the nanometer scale [1]. Conventional optical systems are constrained by the diffraction limit, hindering precise manipulation of light in this sub-wavelength scale. To transcend this barrier, innovative instruments and methods capable of surpassing the diffraction limit have been developed. Central to these innovations are the development and exploitation of plasmonic and excitonic systems [2, 3]. Plasmonics harnesses the collective electron oscillations in metal nanostructures to confine light into volumes far smaller than the wavelength of light. Similarly, excitonics involves the study of excitons, bound electron-hole pairs that play a major role in the dynamics of light-matter interactions in semiconductors. The progress in plasmonics and excitonics has been essential for developing highly efficient and compact nanoscale optical devices, revolutionizing various applications in science and technology, including optical nano-antennas [4], light harvesting systems [5], sensing [6] and catalysis [7] technologies, among others.

A valuable experimental technique for exploring nano-optical phenomena and probing the optical properties of metal and semiconductor nanostructures is the Scanning Tunneling Microscope (STM). Traditionally used for imaging conductive surfaces at atomic level, the STM has proven to be a useful tool to induce light emission by local electrical excitation [8]. The fundamental mechanism behind the STM-induced Light Emission (STM-LE) relies on the highly localized character of the tunnel current. The STM junction formed by the close proximity between tip and sample surface behaves as a plasmonic nanocavity when the materials involved are plasmonic metals. In this case, inelastic tunneling electrons trigger the excitation of plasmonic modes within the tip-sample gap, resulting in the emission of light. Furthermore, the local charge carriers injection provided by the STM can be used to induce light emission from semiconducting quantum emitters through the formation of excitons. Tunneling electrons in an STM junction possess low energy ( $< 4$  eV) and thus, a very shallow penetration depth. This characteristic enables effective interaction between tunneling electrons and ultra-thin samples, making the STM an ideal technique for investigating the properties of 2D materials at the nanoscale. In recent decades, 2D materials have attracted considerable attention owing to their importance in miniaturization and their outstanding features, including remarkable optical properties [9] that can be characterized using the STM-LE technique [10, 11].

This thesis focuses on the investigation of the light-emission induced by STM from transition-metal dichalcogenides (TMDs) monolayers, a two-dimensional semiconductor with exceptional optical and

excitonic properties [12]. By local injection of charge carriers into the monolayers via STM electron tunneling, excitons are created within the semiconductor. These excitons decay radiatively emitting photons whose energy corresponds to the TMD monolayer direct optical bandgap. In particular, hybrid TMD/plasmonic-metal STM junctions are addressed, combining the excitonic character of the TMD with the plasmonic properties of the STM junction. This hybridization results in a plasmon-exciton system whose STM-induced luminescence characteristics are thoroughly analyzed through both experimental and theoretical approaches. The insights derived from this analysis aim to characterize the opto-electrical properties of such hybrid TMD/metal system, offering valuable insights for the design and development of future nano-optics devices.

In this thesis, the exploration of STM-induced light emission from hybrid TMD/metal systems unfolds across five distinct chapters: the first two chapters primarily focus on providing the necessary context and detailing the methods employed, while the remaining three chapters delve into the experimental and theoretical investigation of this phenomenon.

The first chapter constitutes the state of the art and is structured into two parts. The first part provides a brief theoretical introduction of the working principle of STM, followed by a description of the mechanism responsible for STM-induced light emission from metallic junctions and semiconductor samples. A review of the current research work on TMD monolayers is offered in the second part, focusing on their outstanding electronic and optical properties.

In the second chapter, the experimental techniques used in this thesis are introduced, including a description of the setup for STM-LE measurements and the preparation and characterization of TMD monolayers. Additionally, the numerical methods used for electrodynamic simulations are presented. The experimental analysis of STM-induced light emission from different junctions is the main topic of the third chapter. The discussion focuses on the luminescence obtained from purely plasmonic junctions, STM junctions where the sample comprises a TMD monolayer on a non-plasmonic substrate, and hybrid TMD/plasmonic-metal junctions. This study emphasizes on the role of the substrate nature on the characteristics of the light emission generated by TMD monolayers. Moreover, using various nanostructured plasmonic substrates, the influence of their morphology is also explored.

In the fourth chapter, the light-matter interaction of a hybrid TMD/plasmonic-metal junction is investigated by numerical electrodynamic simulations where electron tunneling is taken into account. By simulating the optical response of the junction to an incident excitation wave, the electromagnetic properties of the junction and their behavior in terms of tunneling parameters and substrate roughness are addressed. The study delves into the plasmonic modes supported by the junction and their electromagnetic interaction with the excitons confined within the TMD monolayer.

The last chapter presents a model developed to compute theoretical light emission spectra for a hybrid TMD/plasmonic-metal STM junction. This model takes into account the opto-electronic properties of the TMD monolayer, and the electron tunneling as the excitation source for the light emission process. In addition, the effect of the substrate morphology on the light emission is studied theoretically.

The obtained results are compared with the experimental observations in order to validate the model presented.

Finally, in the last part, conclusions drawn from our work are presented, along with insights into future perspectives.

## Bibliography

- [1] L. Novotny and B. Hecht. *Principles of Nano-Optics*. Cambridge University Press, 2012.
- [2] S. A. Maier, M. L. Brongersma, P. G. Kik, S. Meltzer, A. A. G. Requicha, and H. A. Atwater. Plasmonics — a route to nanoscale optical devices. *Adv. Mater.*, 13(19):1501–1505, 2001.
- [3] G. D. Scholes and G. Rumbles. Excitons in nanoscale systems. *Nat. Mater.*, 5(9):683–696, 2006.
- [4] V. Giannini, A. I. Fernández-Domínguez, S. C. Heck, and S. A. Maier. Plasmonic nanoantennas: fundamentals and their use in controlling the radiative properties of nanoemitters. *Chem. Rev.*, 111(6):3888–3912, 2011.
- [5] A. O. Govorov and I. Carmeli. Hybrid structures composed of photosynthetic system and metal nanoparticles: plasmon enhancement effect. *Nano Lett.*, 7(3):620–625, 2007.
- [6] S. Lal, S. Link, and N. J. Halas. Nano-optics from sensing to waveguiding. *Nat. Photonics*, 1(11):641–648, 2007.
- [7] E. Cortés and P. H. C. Camargo. *Plasmonic Catalysis: From Fundamentals to Applications*. John Wiley & Sons, 2021.
- [8] J. H. Coombs, J. K. Gimzewski, B. Reihl, J. K. Sass, and R. R. Schlittler. Photon emission experiments with the scanning tunnelling microscope. *J. Microsc.*, 152(2):325–336, 1988.
- [9] H. Zhang. Ultrathin two-dimensional nanomaterials. *ACS Nano*, 9(10):9451–9469, 2015.
- [10] R. Beams, P. Bharadwaj, and L. Novotny. Electroluminescence from graphene excited by electron tunneling. *Nanotechnology*, 25(5):055206, 2014.
- [11] R. Péchou, S. Jia, J. Rigor, O. Guillermet, G. Seine, J. Lou, N. Large, A. Mlayah, and R. Coratger. Plasmonic-Induced Luminescence of MoSe<sub>2</sub> Monolayers in a Scanning Tunneling Microscope. *ACS Photonics*, 7(11):3061–3070, 2020.
- [12] G. Wang, A. Chernikov, M. M. Glazov, T. F. Heinz, X. Marie, T. Amand, and B. Urbaszek. Colloquium: Excitons in atomically thin transition metal dichalcogenides. *Rev. Mod. Phys.*, 90(2):021001, 2018.

# Chapter 1

## State of the art

This chapter lays on the theoretical foundations and experimental background of the main elements involved in the light emission process from hybrid TMD/metal systems in a Scanning Tunneling Microscope (STM). In the first section, a brief introduction to the STM working principle is provided and theoretical models describing electron tunneling are discussed. The next part of the section is dedicated to light emission from metallic junctions and semiconductor samples in an STM. The mechanism responsible for the light emission process is presented for each case and details on the key components involved are provided. This part includes as well an overview of the experimental and theoretical studies carried out on the STM-induced light emission phenomenon. A review of the current research work on TMD monolayers, a family of 2D semiconductors, is provided in the second section of this chapter. Particularly, their remarkable electronic and optical properties are highlighted. This part is followed by a discussion of the characteristics of hybrid systems in which TMDs are combined with plasmonic nanostructures.

### **1.1 Light emission induced by a Scanning Tunneling Microscope (STM-LE)**

A brief overview of the theory and the working principle of the Scanning Tunneling Microscope STM is provided in the first part of this section. The next part is focused on STM-induced light emission (STM-LE) from metallic junctions where the key factors governing light emission, inelastic electron tunneling and localized surface plasmon modes, are presented. In addition, a summary of the most relevant experimental studies and the main theoretical models carried out in this field is addressed. Finally, in the third part, the radiative process behind light emission from semiconductor samples in an STM is discussed in detail by reviewing the main experimental works describing this phenomenon.

### 1.1.1 Principles of the Scanning Tunneling Microscope (STM)

Quantum tunneling, whereby subatomic particles such as electrons can penetrate and even cross a potential barrier due to their dual wave-particle nature, is one of the most fascinating discoveries in quantum physics. This phenomenon has led to the development of modern electronic technologies, notably the Scanning Tunneling Microscope (STM). The latter was invented by Binnig and Rohrer at the IBM Research Laboratory in 1981 [1, 2], for which they were awarded the Nobel Prize in Physics in 1986 [3]. In spite of its straightforward operation principle, which consists of using electron tunneling to probe a surface, STM is a versatile technique that offers a wide range of applications. It was originally developed to image the topography of conductive surfaces with more detail than any previous microscope [4]. Over the following decades, topographic images with sub-nanometer resolution have been achieved by moving an extremely sharp conductive tip over conducting or semiconducting surfaces at the nanometer scale. This high resolution makes it possible to identify the atomic surface structure and its defects [5]. STM can as well be used to probe electronic properties such as the Local Density Of States (LDOS) and thus, the band gap for semiconductor samples by measuring the tunneling current as a function of the tip-sample bias voltage [6, 7]. This extension of STM is called Scanning Tunneling Spectroscopy (STS). In addition, STM can be used as a nanotool to manipulate atoms or absorbates to build artificial structures and investigate their quantum properties [8, 9]. This variety of functions and its ability to operate in different environments, including ultra-high vacuum, air, or liquid solutions, at different temperatures have made the STM a very powerful technique used in a wide range of fields, from biology to microelectronics.

Before describing the operating modes of an STM in detail, the quantum electron tunneling will be discussed.

#### a) Electron tunneling

In order to understand the working principle of STM, a brief description of electron tunneling is needed. When the conductive surfaces of two electrodes are brought in close proximity to one another (few angstroms), an electron with an energy  $E$  has a non-zero probability of tunneling through the potential barrier  $U(\mathbf{r})$  between both electrodes even if  $E < U(\mathbf{r})$ . In quantum mechanics, electrons can be treated as waves and be described by their wavefunction  $\psi(\mathbf{r})$  determined from the Schrödinger equation:

$$-\frac{\hbar^2}{2m_e}\nabla^2\psi(\mathbf{r}) + (U(\mathbf{r}) - E)\psi(\mathbf{r}) = 0 \quad (1.1)$$

with  $m_e$  the electron mass and  $U(\mathbf{r})$  the position dependent potential. In the simple case of a one-dimensional square potential barrier along  $z$  ( $U(z) = U$  for  $0 \leq z \leq d$  with  $d$  the tunneling barrier thickness), the solution of the equation (1.1), denoted as  $\psi(z)$ , consists of plane waves for the regions outside the barrier ( $z < 0$  and  $z > d$ ). However, within the barrier, the solution is non-oscillatory and

can be written as a superposition of two exponential decay terms:

$$\psi(z) = Ae^{+\kappa z} + Be^{-\kappa z} \quad (1.2)$$

with  $\kappa$  the decay constant:

$$\kappa = \sqrt{\frac{2m_e(U - E)}{\hbar^2}} \quad (1.3)$$

In Figure 1.1-A, the wavefunctions  $\psi(z)_+$  and  $\psi(z)_-$  representing electron tunneling from the left electrode to the right electrode and vice versa, are depicted. They exhibit an oscillatory behavior outside the barrier whereas in the barrier region,  $\psi(z)_+$  decays exponential in the  $+z$  direction, and  $\psi(z)_-$  decays in the  $-z$  direction.

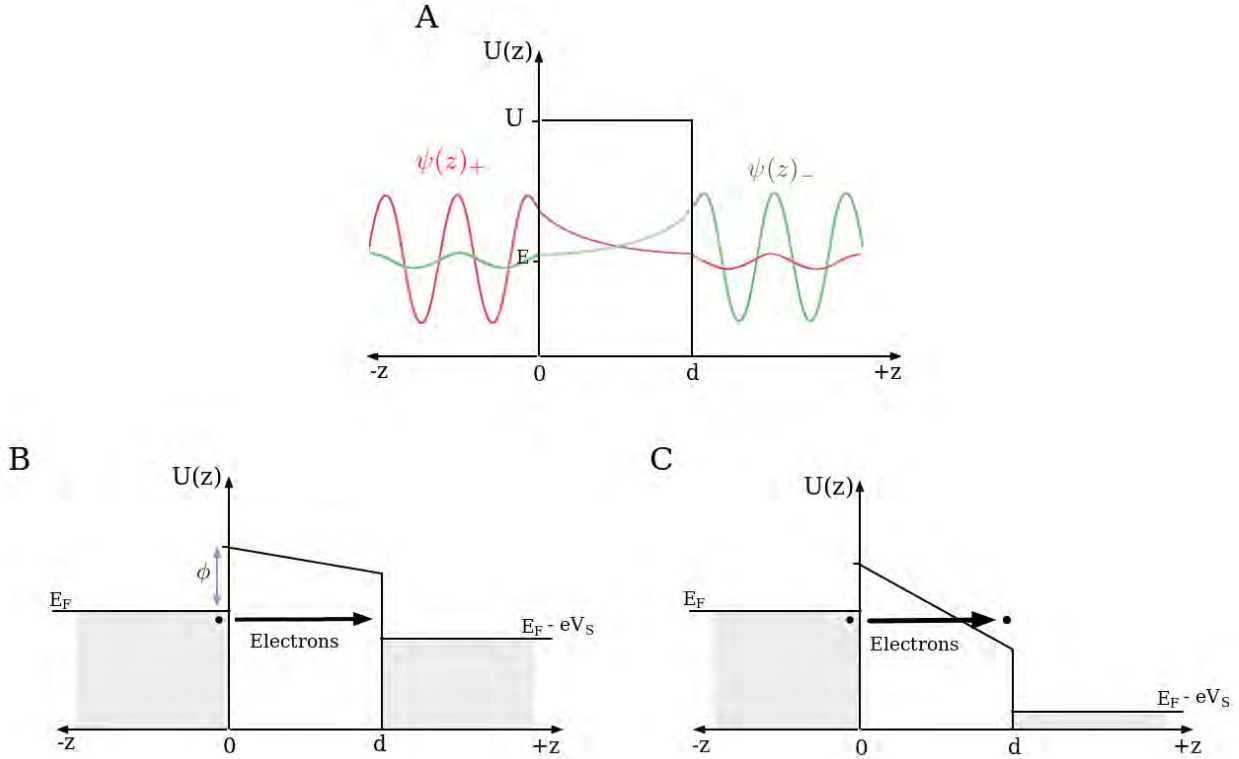


**Figure 1.1:** Schematic representation of 1D electron tunneling between two electrodes. (A) No bias voltage is applied, which leads to a square potential barrier. (B) At low bias voltage  $V_s$ , the potential barrier height is no longer constant and a net tunneling current appears. (C) At high bias voltage  $V_s$ , the potential barrier is triangular, and the junction is in the field emission regime.

The tunneling current  $I$  in a given direction is proportional to  $T$ , the transmission probability of electrons through the potential barrier which decays exponentially as:

$$I \propto T \sim e^{-2\kappa d} \quad (1.4)$$

The potential barrier height for metal-vacuum-metal tunneling is given by the work function  $\phi$  of the metals for electrons at the Fermi level. When both electrodes have the same work function and no bias voltage is applied between them, the potential barrier is square allowing electrons to tunnel in both directions with the same transmission probability  $T$ . Thus, the total tunneling current is zero. When a bias voltage  $V_s$  is applied, the Fermi levels  $E_F$  of both electrodes shift with respect to each other leading to a potential barrier height  $U(z)$  no longer constant across the gap. In such a case, a net tunneling current takes place in only one direction. The latter is determined by the sign of the bias voltage. For example, in Figure 1.1-B, the right electrode is positively biased leading to the tunneling of electrons from the left to the right electrode. The Wentzel-Kramers-Brillouin (WKB) approximation is often used to solve the Schrödinger equation for general potential barriers [10]. The transmission probability obtained with WKB is:

$$T = \exp\left(-2 \int_0^d \kappa(z) dz\right) \quad (1.5)$$

with

$$\kappa(z) = \sqrt{\frac{2m_e(U(z) - E)}{\hbar^2}} \quad (1.6)$$

In this approximation, the tunneling current is proportional to the bias voltage  $V_s$  and to the exponent of the distance  $d$ :

$$I \propto V_s \exp\left(-2\sqrt{\frac{2m_e(\bar{U} - E)}{\hbar^2}} d\right) \quad (1.7)$$

where  $\bar{U}$  is the average potential barrier height between  $z = 0$  and  $z = d$ . The tunneling current is then very sensitive to the tunneling parameters, i.e., the applied bias voltage  $V_s$  and the distance  $d$  between both electrodes. For example, a slight reduction in the inter-electrode distance of 0.1 nm results in a tenfold increase in the tunneling current. This expression is only valid for low voltages ( $\bar{U} - E > eV_s$ ) where electrons tunnel through an approximately rectangular potential barrier. For high-voltages ( $eV_s > \bar{U} - E$ ), a strong electric field lowers the potential barrier height leading to a triangular barrier (Figure 1.1-C). In this regime, known as field emission regime [11], electrons tunnel through the potential barrier in only a part of the insulating layer. When the electrons energy  $E$  becomes superior to the potential barrier height  $U(z)$ , electrons can move to the second electrode under the influence of the high electric field.

Analytical expressions for the tunneling current in a metal-vacuum-metal junction more accurate than equation (1.7) have been developed. The first theory of tunneling has been introduced by Bardeen [12] in 1961 using the transfer Hamiltonian method. In the Bardeen approach, the tunneling current

calculation is based on the overlap of the electron state wavefunctions of both electrodes. Using the Fermi golden rule and the time-dependent Schrödinger equation, the probability of electron transition from the initial state  $|i\rangle$  to the final state  $|f\rangle$  is calculated as follows:

$$\Gamma_{i \rightarrow f} = \frac{2\pi}{\hbar} |M_{i,f}|^2 \delta(E_i - E_f) \quad (1.8)$$

where  $E_i$  and  $E_f$  are the energies of the initial and final state, respectively. The delta function takes into account the elastic character of the tunneling: no energy loss from electrons is considered. The transition matrix element  $M_{i,f}$  is defined by Bardeen as:

$$M_{i,f} = \frac{\hbar^2}{2m_e} \int_{\Sigma} d\mathbf{S} \left( \psi_i^*(\mathbf{r}) \vec{\nabla} \psi_f(\mathbf{r}) - \psi_f(\mathbf{r}) \vec{\nabla} \psi_i^*(\mathbf{r}) \right) \quad (1.9)$$

The integration is considered over the separation surface  $\Sigma$  between the volumes defining the two electrodes.  $\psi_i(\mathbf{r})$  and  $\psi_f(\mathbf{r})$  are the wavefunctions of the initial and final state of the electron tunneling transition across the junction. The Bardeen model takes into account the fact that electrons are fermions. Hence, the electron occupation probability of the initial and final quantum states is given by the Fermi-Dirac distribution  $f(E)$ . The tunneling current is expressed as:

$$I = \frac{2\pi e}{\hbar} \sum_{i,f} f(E_i) [1 - f(E_f + eV_s)] |M_{i,f}|^2 \delta(E_i - E_f) \quad (1.10)$$

At low temperatures and for small voltages, the Fermi-Dirac distribution can be described by a Heaviside function. The tunneling current expression in this case can be written as:

$$I = \frac{2\pi e^2}{\hbar} V_s \sum_{i,f} |M_{i,f}|^2 \delta(E_f - E_F) \delta(E_i - E_F) \quad (1.11)$$

where  $E_F$  stands for the Fermi level energy. In this model, several assumptions have been considered: the electron-electron interaction is neglected and the formation of coupled electronic states in the barrier region is not taken into account. Later in this chapter (section 1.1.2), a modified version of the Bardeen model in which the formation of these coupled states is taken into account will be introduced to address the light emission from tunnel junctions.

The Bardeen description of the tunneling current is based on a planar tunnel junction. Tersoff and Hamann have adapted the Bardeen model to the geometry of the STM junction [13, 14]. The junction of an STM consists of a sharp metal tip brought into close proximity to a conductive sample. The tip apex, located at a distance  $d$  from the sample, is considered as a local spherical potential well centred at  $\mathbf{r}_0$  with a radius of curvature  $R$ :

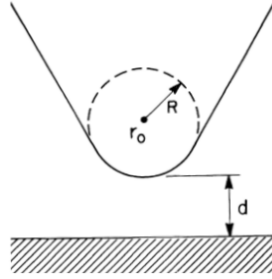


**Figure 1.2:** Tip-sample configuration considered in the Tersoff and Hamann model with  $d$  the shortest distance between the tip and the sample surface,  $R$  the radius of the spherical approximation of the tip and  $\mathbf{r}_0$  its center of curvature [13]

The tip quantum states are assumed to be pure s-like states with no angular dependency. The tip wavefunction  $\psi_t(\mathbf{r})$  used in the calculation is:

$$\psi_t(\mathbf{r}) = \frac{\mathcal{C}_t}{\Omega_t^{1/2}} \kappa R \exp(\kappa R) \frac{\exp(-\kappa |\mathbf{r} - \mathbf{r}_0|)}{\kappa |\mathbf{r} - \mathbf{r}_0|} \quad (1.12)$$

where  $\Omega_t$  is the tip volume and  $\mathcal{C}_t$  a constant determined by the tip sharpness and its electronic structure.  $\kappa$  is the decay constant of the tip wavefunction defined in equation (1.6). There are two different approaches to calculate the tunneling matrix (eq. (1.9)) from this tip wavefunction expression: the two-dimensional Fourier transform method as in the Tersoff-Hamann theory, or the C. J. Chen approach based on Green functions [15, 16]. In the following part, the second approach is described.

For large  $|\mathbf{r} - \mathbf{r}_0|$ , the tip wavefunction  $\psi_t(\mathbf{r})$  satisfies the Schrödinger equation in vacuum:

$$(\Delta - \kappa^2) \psi_t(\mathbf{r}) = 0 \quad (1.13)$$

Since the tunneling matrix is calculated from wavefunctions within the junction ( $|\mathbf{r} - \mathbf{r}_0| > R$ ), equation (1.13) is respected. The Green's function, denoted  $G(\mathbf{r} - \mathbf{r}_0)$ , that satisfies the following Schrödinger equation:

$$(\Delta - \kappa^2) G(\mathbf{r} - \mathbf{r}_0) = -\delta(\mathbf{r} - \mathbf{r}_0) \quad (1.14)$$

has an expression equal to that of the tip wavefunction (eq. (1.12)) up to a constant [16]:

$$G(\mathbf{r} - \mathbf{r}_0) = \frac{\exp(-\kappa |\mathbf{r} - \mathbf{r}_0|)}{4\pi |\mathbf{r} - \mathbf{r}_0|} \quad (1.15)$$

Considering that electrons tunnel from the tip (initial state defined by  $\psi_t(\mathbf{r})$ ) to the sample (final state defined by  $\psi_s(\mathbf{r})$ ), the tunneling matrix element can be written as:

$$M_{t,s} = \frac{\hbar^2}{2m_e} \int_{\Sigma} d\mathbf{S} \left( \psi_t^*(\mathbf{r}) \vec{\nabla} \psi_s(\mathbf{r}) - \psi_s(\mathbf{r}) \vec{\nabla} \psi_t^*(\mathbf{r}) \right) \quad (1.16)$$

$$= \frac{2\pi\hbar^2\mathcal{C}_t}{m_e\kappa\Omega_t^{1/2}} \kappa R \exp(\kappa R) \int_{\Sigma} d\mathbf{S} \left( G(\mathbf{r} - \mathbf{r}_0) \vec{\nabla} \psi_s(\mathbf{r}) - \psi_s(\mathbf{r}) \vec{\nabla} G(\mathbf{r} - \mathbf{r}_0) \right) \quad (1.17)$$

Using the divergence theorem, the surface integral of the tunneling matrix element can be converted into an integral over a volume. In particular, this integration is performed over the tip volume.

$$M_{t,s} = \frac{2\pi\hbar^2\mathcal{C}_t}{m_e\kappa\Omega_t^{1/2}} \kappa R \exp(\kappa R) \int_{\Omega_t} d^3\mathbf{r} [G(\mathbf{r} - \mathbf{r}_0)\Delta\psi_s(\mathbf{r}) - \psi_s(\mathbf{r})\Delta G(\mathbf{r} - \mathbf{r}_0)] \quad (1.18)$$

$$= \frac{2\pi\hbar^2\mathcal{C}_t}{m_e\kappa\Omega_t^{1/2}} \kappa R \exp(\kappa R) \int_{\Omega_t} d^3\mathbf{r} \left[ G(\mathbf{r} - \mathbf{r}_0)\kappa^2\psi_s(\mathbf{r}) - \psi_s(\mathbf{r})(-\delta(\mathbf{r} - \mathbf{r}_0) + \kappa^2 G(\mathbf{r} - \mathbf{r}_0)) \right] \quad (1.19)$$

$$= \frac{2\pi\hbar^2\mathcal{C}_t}{m_e\kappa\Omega_t^{1/2}} \kappa R \exp(\kappa R) \psi_s(\mathbf{r}_0) \quad (1.20)$$

The same tunneling matrix element expression is obtained in the Tersoff-Hamann theory. Thus, for small voltages, the tunneling current of equation (1.11) can be written as:

$$I = \frac{2\pi e^2}{\hbar} \frac{4\pi^2\hbar^4\mathcal{C}_t^2 R^2}{m_e^2\Omega_t} \exp(2\kappa R) V_s \sum_{t,s} |\psi_s(\mathbf{r}_0)|^2 \delta(E_s - E_F) \delta(E_t - E_F) \quad (1.21)$$

$$= \frac{32\pi^3\hbar^3 e^2 \mathcal{C}_t^2 R^2}{(2m_e)^2} \exp(2\kappa R) V_s \rho_t(E_F) \rho_s(\mathbf{r}_0, E_F) \quad (1.22)$$

In equation (1.22),  $\rho_s(\mathbf{r}_0, E_F) = \sum_s |\psi_s(\mathbf{r}_0)|^2 \delta(E_s - E_F)$  is the Local Density Of States (LDOS) of the sample at the Fermi level energy, and  $\rho_t(E_F) = (\sum_t \delta(E_t - E_F)) / \Omega_t$  is the tip Density Of States (DOS) at the Fermi level.

The derivative of the tunneling current with respect to the bias voltage  $V_s$  is then:

$$\frac{dI}{dV_s} \propto \rho_s(\mathbf{r}_0, E_F) \quad (1.23)$$

This approach shows that the conductance of an STM junction at low temperatures and small voltages is proportional to the sample LDOS at the center of the tip and at the Fermi level energy. In tunneling spectroscopy (STS) experiments, measurements of the tunneling conductance are carried out to probe the sample LDOS. More details on this technique will be given below.

In the Tersoff-Hamann approach described here, the tip wavefunction is assumed to be pure s-like and all other tip wavefunctions are neglected. This model is reliable for interpreting images of surface topography, but for atomic-resolution features, a more detailed description of the STM tip wavefunction is needed. In the Tersoff-Hamann theory, the two-dimensional Fourier transform method is used, which

restricts the incorporation of complex wavefunctions involving p- and d-states to describe the tip. However, the approach developed by C. J. Chen based on the Green's function called derivative rule, can be expanded to consider generalized tip wavefunctions [16, 17].

### b) Description of the STM working principle

The operating principle of the Scanning Tunneling Microscope is based on the strong distance dependence of the tunneling current (see equation (1.7)). The STM junction consists of a very sharp conductive tip, whose apex consists of only one or a few atoms, brought within the tunneling distance, typically within the sub-nanometer range, from a conductive sample. When a bias voltage  $V_s$  of a few volts is applied to the tip-sample junction, electrons will tunnel through the potential barrier resulting in a tunneling current typically in the nanoampere range. The tunneling process only takes place when both the sample and the tip are conductors or semiconductors. As discussed above (eq. (1.7)), the tunneling current is extremely sensitive to the distance  $d$  between the tip apex and the nearest atom of the sample. Thus, a variation of the tunneling current is detected when the tip moves from being directly above one atom of the sample to being positioned between two adjacent atoms.

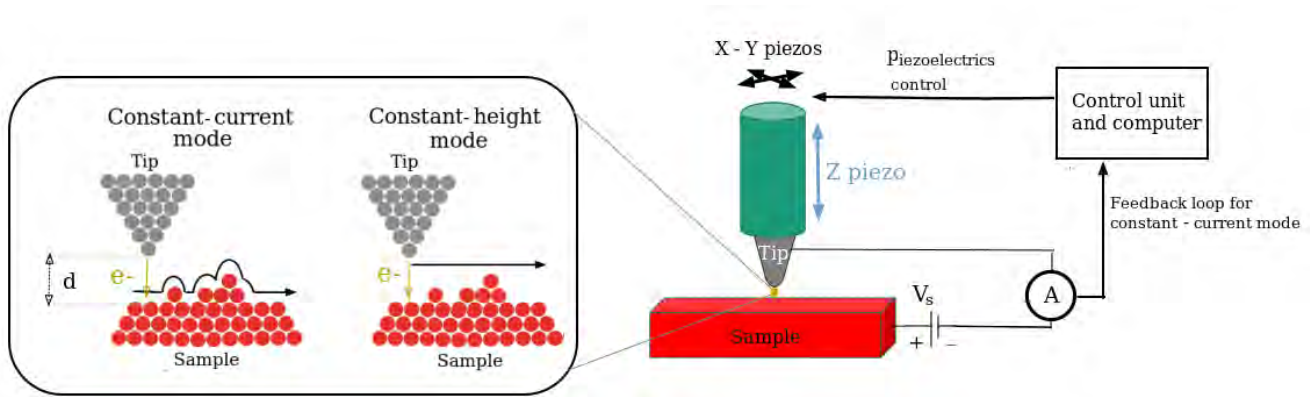


**Figure 1.3:** STM working principle. On the left: Enlarged view of the tunneling process showing the two STM imaging modes. On the right: Schematic configuration of an STM

This sensitivity is exploited to image the sample surface with atomic resolution. Three-dimensional images of the surface topography are obtained from the displacement of the tip with respect to the sample. For precise positioning and displacement of the tip and/or sample, piezoelectric crystals are employed (Figure 1.3). These crystals can expand or contract with the application of a bias voltage across them. The STM atomic resolution and the tunneling stability are only obtained when the microscope is isolated from external vibrational noise. In Chapter 2, the technical characteristics of the STM used to perform all the measurements in this thesis will be discussed.

Generally, an STM presents two operating modes to reveal the surface topography: the constant-current mode and the constant-height mode (see Figure 1.3). The constant-current mode is the most often used and it consists of maintaining constant the tunneling current by adjusting the tip-sample distance during the surface scanning. Thus, an electronic feedback loop is needed to control the tip-sample

distance. When the tip scans over the investigated surface, the feedback loop compares the measured tunneling current with a user-defined setpoint current. If both values do not coincide, the feedback loop modifies the vertical position of the tip until the setpoint current is reached. The vertical position of the tip  $z$  is recorded as a function of the lateral tip displacement  $(x, y)$  to produce topographic images. The constant-current mode is generally used for rough surfaces since high resolution and stability can be achieved due to the feedback loop. In order to obtain high-resolution images of the surface topography, the feedback loop requires a slow scan since its precision is related to the time it takes to correct the tunneling current with respect to the scan speed.

In the constant-height mode, the tip scans the surface while keeping constant the vertical position of the tip. The tunneling current then varies throughout the scan since it is very sensitive to the tip-sample distance. The tunneling current fluctuations as a function of the tip lateral position  $(x, y)$  result in a topographic image of the surface. This mode is only used for flat surfaces (roughness less than a few angstroms) to avoid tip damage during the scan. Since no feedback loop is necessary, the scan can be performed at high speed. This mode is useful for studying surface dynamic processes such as film growth or adsorbates diffusion.

The STM not only has the ability to image surfaces at the atomic scale but can also perform electronic spectroscopy. Indeed, there is a third STM operating mode, called spectroscopic mode, which is used to have direct access to the sample electronic properties [6, 7]. This mode is based on the dependence of the tunneling current on the bias voltage  $V_s$  (see equation (1.11)). At a specific point of the sample, the tip is held at a constant distance from the sample. Fluctuations of the tunneling current are then measured by varying the bias voltage, resulting in current-voltage  $I(V_s)$  curves. From numerical derivation or using a lock-in amplification technique, tunnel conductance  $dI/dV_s(V_s)$  spectra can also be obtained. As mentioned before, according to the equation (1.23), the tunnel conductance provides information about the local electronic properties of the sample, mainly the local density of states. Measuring the tunnel conductance at each point of the surface during a scan gives rise to conductance maps. These latter can be correlated with topographic images to study the spatial variation of the sample LDOS as a function of the surface topography.

## 1.1.2 Light emission from metallic junctions

### a) Introduction

As mentioned above, STM is a versatile technique that provides a broad spectrum of applications. One of its possible applications is to probe the optical properties of a surface by analyzing the light emitted during STM tunneling. Light emission mediated by tunneling electrons was first reported even before the invention of the STM. In 1976, Lambe and McCarthy [18] observed light emission from a biased planar metal-insulator-metal junction. Presenting a high-energy cutoff, the process was interpreted in terms of inelastic electron tunneling (IET) excitation. Luminescence induced in an STM junction has been detected for the first time in 1988 in two different experiments, each highlighting a

different mechanism for tunneling current to produce photon emission. Gimzewski *et al.* [19] recorded light emission from polycrystalline tantalum and silicon (111) 7x7 surfaces using high voltages ( $V_s \geq 9.5$  V). Electrons in the field emission regime, cross the junction and decay radiatively once they reach the sample. This mechanism responsible for photon emission is known as hot electron injection. Using small voltages ( $V_s$  between 1 and 4 volts), Coombs *et al.* [20] have observed light emission from silver films in an STM junction in the low-bias tunneling regime. In this case, the radiative process was triggered by IET. This mechanism predominates in metal-metal junctions with typical STM tunneling bias voltages ( $V_s < 4$  V). In the following paragraphs, the light emission process from metallic STM junctions induced by IET is discussed.

In the tunneling process (see previous section 1.1.1), most of the electrons will tunnel elastically through the potential barrier from one electrode to another, i.e., without energy loss. However, a tiny fraction of electrons crossing the junction (less than 1% [21]) will tunnel the potential barrier inelastically, i.e., losing all or part of their energy. This energy, given by the bias voltage applied between both electrodes  $V_s$ , is released in the barrier region and can trigger different excitations such as light emission (Figure 1.4-A). The tunneling process takes place for tip-sample distances  $d$  of a few angstroms. When the junction consists of a plasmonic tip and sample, this close tip-sample proximity forms a plasmonic nanocavity that hosts localized surface plasmon modes (LSP). These latter are collective oscillations of surface electrons localized on both sides of the junction that are coupled by electromagnetic interaction. These modes can then be excited by inelastic tunneling and may decay radiatively (Figure 1.4-B). A detailed description of the properties of surface plasmon modes is presented below.

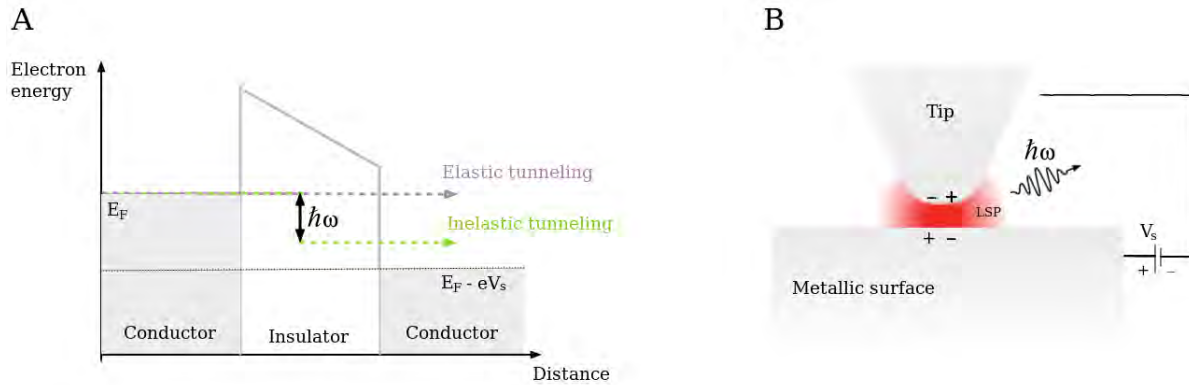


**Figure 1.4:** (A) Energy band diagram illustrating the elastic (violet) and inelastic (green) electron tunneling processes through a potential barrier. Inelastic electrons lose all or part of their energy ( $\hbar\omega$ ) exciting surface plasmons LSP modes (B) localized in the gap which can decay into photons.

Since the first observations of light emission induced by IET in an STM [20, 22], the potential of this technique has been highlighted as it allows one to study the optical properties of metallic surfaces with the high spatial resolution of the STM. Coombs *et al.* [20] reported in 1988 the first photonic maps making it possible to correlate the surface topography with the number of emitted photons at each point of the scan. The authors also recorded the first spectra of light emission in an STM induced by IET, from which they obtained an experimental light emission efficiency of  $\sim 10^{-4}$  photons per

tunneling electron. In the following years, a large number of experimental works on STM-induced light emission from metal tips and noble metal substrates have been reported [23–28]. The measurements were performed in vacuum or in an ambient environment. The development of this technique gives rise to photonic maps with ultra-high resolution at the atomic scale [29, 30]. In 1995, Berndt *et al.* [30] were able to identify the atoms of an  $Au(110)$  surface in a photonic map and matched it to the surface topography (Figure 1.5-A). The energy of the emitted photons can be determined by doing a spectral analysis of the emitted light. Generally, light emission spectra from an STM plasmonic junction are very broad with several peaks and present a high-energy cutoff (see Figure 1.5-B).

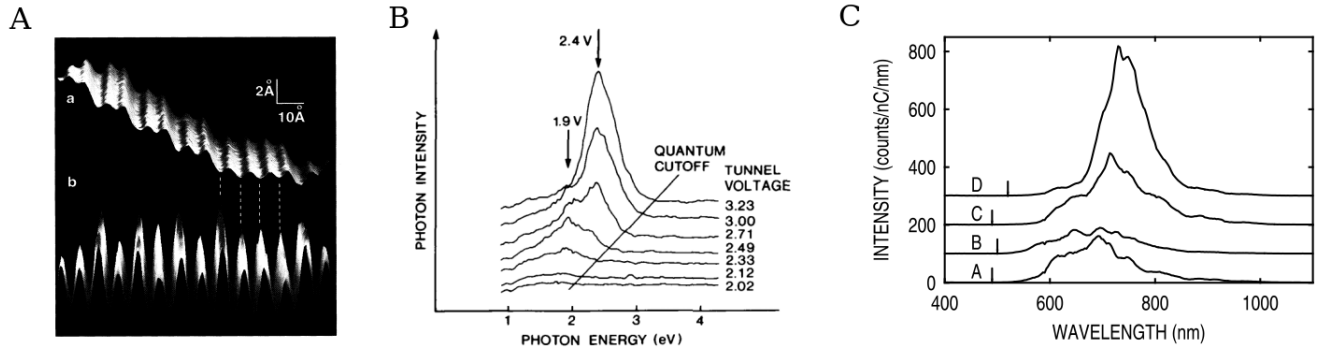


**Figure 1.5:** (A) Topographic image (a) and photonic map (b) of an  $Au(110)$  ( $1 \times 2$ ) surface measured simultaneously by Berndt *et al.* [30]. The topographic image displays the surface terraces with gold rows and monoatomic steps. The same atomic periodicity is observed in the photonic map. (B) Luminescence spectra obtained from silver films by Coombs *et al.* [20]. The bias voltage and the quantum cutoff for each spectrum are indicated. (C) Light emission spectra taken from the same sample location with different tips. These spectra were recorded by Hoffmann *et al.* [31].

Indeed, the energy released by inelastic electrons goes from zero to  $eV_s$  with  $V_s$  the applied bias voltage. Therefore, LSP modes excited by IET decay radiatively giving rise to light emission spectra with a high-energy quantum cutoff linked to the bias voltage according to the quantum law [32]:

$$\hbar\omega = eV_s \quad (1.24)$$

Thus, no radiation from IET is detected at an energy higher than  $eV_s$ . LSP modes and therefore, the light emission process (including its spectral distribution and efficiency) depend on the tunneling parameters as the applied bias voltage  $V_s$  and the tip-surface distance  $d$ . Their characteristics are also closely related to the properties of the materials involved in the junction and to the junction geometry. To illustrate this point, Hoffmann *et al.* [31] studied the influence of the tip geometry on the light emission process. They recorded light emission from exactly the same sample location using tips of different geometries. The resulting spectra, depicted in Figure 1.5-C, exhibit different lineshapes, showing that the spectral distribution of photon emission can strongly change when the tip geometry is modified.

Surface plasmon modes are a key element of light emission induced by IET since their properties

drive the characteristics of the light emission process. Therefore, before presenting the theoretical descriptions of this process, it is important to review the main surface plasmon modes properties.

### b) Surface plasmons polaritons (SPPs)

Plasmons are coherent oscillations of delocalized conduction-band electrons. They can be excited by both photons, via an incident electromagnetic field, or electrons, via electron beams or tunneling currents. When this excitation occurs at an interface formed by a conductor and a dielectric, an electromagnetic field is induced by the charge motion at the conductor surface. The electron oscillations coupled to the induced electromagnetic field are called surface plasmons polaritons SPPs (called in this thesis surface plasmons) [33]. The associated field can propagate in the case of extended structures whereas, for small particles, it is highly confined and non-propagating. Thus, SPPs can be divided into two categories: propagating surface plasmons (PSPs) which propagate along the interface, and localized surface plasmons (LSPs) corresponding to localized oscillations of surface electrons [34].

Propagating surface plasmons are characterized by an electromagnetic field propagating in the direction parallel to the interface with a parallel wavevector  $\mathbf{k}_{PSP}$ .

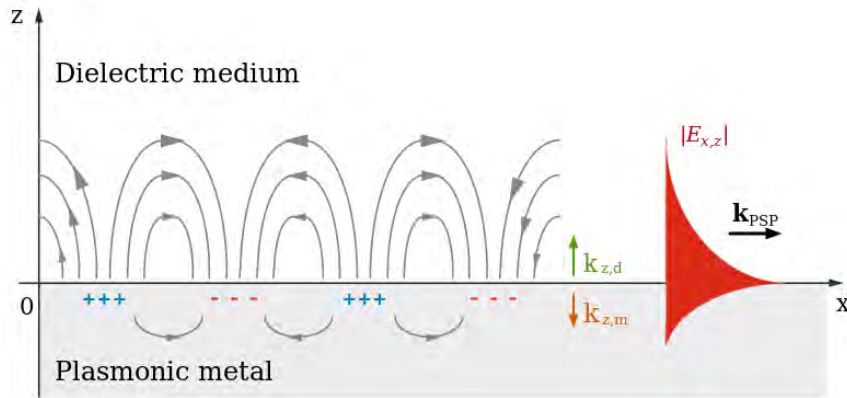


**Figure 1.6:** Schematic representation of the electric field for propagating surface plasmons supported by a dielectric-metal interface (adapted from [35]).

In the direction perpendicular to the interface, the electromagnetic field decreases exponentially into both metal ( $z < 0$ ) and dielectric ( $z > 0$ ). In Figure 1.6, the electric field  $\mathbf{E}=(E_x, 0, E_z)$  oscillates along the x-direction and its components can be defined as:

$$E_{x,z} = \mathcal{A}_{x,z} \exp(-k_{z,d} z) \exp(ik_{PSP}x) \quad \text{for } z > 0 \quad (1.25)$$

$$E_{x,z} = \mathcal{A}_{x,z} \exp(+k_{z,m} z) \exp(ik_{PSP}x) \quad \text{for } z < 0 \quad (1.26)$$

$k_{z,d}$  and  $k_{z,m}$  are the components perpendicular to the interface of the electromagnetic field wavevector for the dielectric and the metal, respectively. Such electromagnetic wave satisfies Maxwell's equations

only when the field continuity at the interface is respected. Then, the following equations have to be satisfied:

$$\frac{k_{z,m}(\omega)}{\epsilon_m(\omega)} = -\frac{k_{z,d}(\omega)}{\epsilon_d(\omega)} \quad k_{PSP}^2 - k_{z,n}^2 = \epsilon_n \left(\frac{\omega}{c}\right)^2 \quad n = m, d \quad (1.27)$$

where  $m$  and  $d$  stand for metal and dielectric respectively. Solving both equations, the dispersion relation  $k_{PSP}(\omega)$  of PSPs can be derived, on one hand, from the metal and dielectric permittivities  $\epsilon_m$  and  $\epsilon_d$ , and, on the other hand, from the excitation source frequency  $\omega$ :

$$k_{PSP}(\omega) = \frac{\omega}{c} \sqrt{\frac{\epsilon_m(\omega)\epsilon_d(\omega)}{\epsilon_m(\omega) + \epsilon_d(\omega)}} \quad (1.28)$$

The expressions of  $k_{z,m}(\omega)$  and  $k_{z,d}(\omega)$  can thus be defined by:

$$k_{z,m}(\omega) = \frac{\omega}{c} \sqrt{-\frac{\epsilon_m^2(\omega)}{\epsilon_m(\omega) + \epsilon_d(\omega)}} \quad k_{z,d}(\omega) = \frac{\omega}{c} \sqrt{-\frac{\epsilon_d^2(\omega)}{\epsilon_m(\omega) + \epsilon_d(\omega)}} \quad (1.29)$$

In order to have evanescent waves that decay exponentially away from the surface, the real parts of  $k_{z,m}$  and  $k_{z,d}$  must be positive ( $> 0$ ). In the simplest case where the permittivities are real, the system can support surface plasmons only if  $\epsilon_m(\omega) + \epsilon_d(\omega) < 0$ . Moreover, equations (1.27) are satisfied for frequencies lower than the plasma frequency of the metal  $\omega_p$  [36], when the real part of the dielectric function of the metal is negative [33, 37].

The dispersion relation  $k_{PSP}(\omega)$  is plotted in black in Figure 1.7. The blue line represents the vacuum light line  $\omega = k \times c$ . The plotting shows that the PSPs dispersion curve lies on the right of the vacuum light line and therefore, there is no momentum match for any frequency.

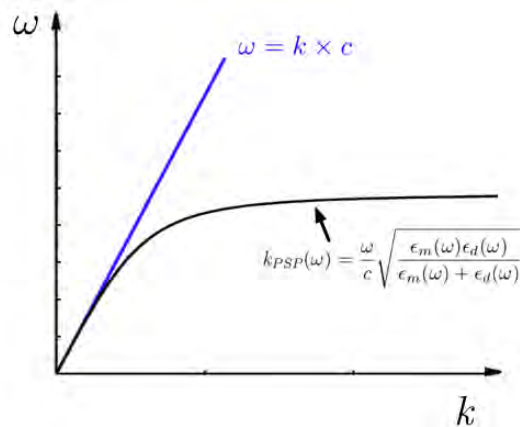


**Figure 1.7:** Dispersion curves for propagating surface plasmons supported by the dielectric-metal interface (black line) and for light in vacuum (blue line).

To optically excite PSPs in this case, optical components are thus required in order to match the incident electromagnetic field wavevector to the momentum associated with the plasmon wave. This

matching condition is as well necessary for PSPs to decay into photons. Optical components such as grating couplers [38, 39] and prism coupling [40, 41] have been developed to overcome this problem.

Plasmonic nanostructures such as nanoparticles or nanocavities can support localized surface plasmon modes [33, 35]. When LSPs are excited, charge oscillations in a confined volume take place leading to the enhancement of the electric field inside and in the near-field zone outside the particle (Figure 1.8).

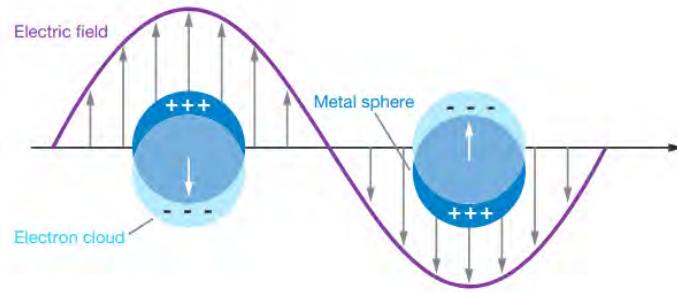


**Figure 1.8:** Schematic representation of localized surface plasmon modes. Electron oscillations (illustrated by white arrows) in a plasmonic metallic nanoparticle are induced by an incident electric field [35]

Thus, LSPs can be used to manipulate and confine light at the nanometer scale. In contrast to PSPs, localized surface plasmons can be easily excited by direct irradiation of light when its frequency matches the intrinsic plasmon resonance frequency of the nanoparticle [33]. This resonance is called localized surface plasmon resonance LSPR. Its frequency and intensity strongly depend on the nanoparticle shape and composition as well as on the surrounding medium refractive index [42]. Using Maxwell's equations, the electromagnetic field around the nanostructure and LSPR frequency can be calculated.

For simple structures such as spherical particles, Maxwell's equations can be solved analytically. For example, consider a spherical nanoparticle of sub-wavelength diameter  $a$ , having a dielectric permittivity  $\epsilon_m$ . This particle is placed in an isotropic dielectric medium with the permittivity  $\epsilon_d$  and exposed to a uniform electric field  $\mathbf{E}_0$ . The electric field inside the particle  $\mathbf{E}_{in}$  is uniform:

$$\mathbf{E}_{in} = \frac{3\epsilon_d}{\epsilon_m + 2\epsilon_d} \mathbf{E}_0 \quad (1.30)$$

while the electric field surrounding the particle  $\mathbf{E}_{out}$  is a superposition of the incident electric field and the field of an electric dipole noted  $\mathbf{E}_{Dip}(\mathbf{r})$ .

$$\mathbf{E}_{out}(\mathbf{r}) = \mathbf{E}_0 + \mathbf{E}_{Dip}(\mathbf{r}) = \mathbf{E}_0 + \frac{3\mathbf{n}(\mathbf{n} \cdot \mathbf{p}) - \mathbf{p}}{4\pi\epsilon_0\epsilon_m r^3} \quad (1.31)$$

with  $\mathbf{n}$  the unit vector in the direction  $\mathbf{r}$  and  $\mathbf{p}$  is the induced dipole moment proportional to the external electromagnetic wave:

$$\mathbf{p} = \epsilon_0 \epsilon_d \alpha \mathbf{E}_0 \quad (1.32)$$

The nanoparticle polarizability  $\alpha$  is determined in the electrostatic approximation [43]. Its frequency dependence is given by the nanoparticle dielectric function  $\epsilon_m(\omega)$  since the dielectric permittivity of the surrounding medium  $\epsilon_d$  is considered real and constant:

$$\alpha(\omega) = 4\pi\epsilon_0 \left(\frac{a}{2}\right)^3 \frac{\epsilon_m(\omega) - \epsilon_d}{\epsilon_m(\omega) + 2\epsilon_d} \quad (1.33)$$

The resonance frequency is obtained for a maximum of polarizability  $|\alpha|$ , i.e., when  $|\epsilon_m(\omega) + 2\epsilon_d|$  reaches a minimum. This is known as the Fröhlich condition [33]. Therefore, maximum of  $\alpha(\omega)$  is obtained when:

$$\epsilon_m(\omega) + 2\epsilon_d \rightarrow 0 \quad (1.34)$$

If the contribution from metal interband transitions is negligible and the metallic particle is considered as a lossless Drude metal, the LSPR frequency can be written as follows:

$$\omega_{LSPR} = \frac{\omega_p}{\sqrt{1 + 2\epsilon_d}} \quad (1.35)$$

with  $\omega_p$  the nanoparticle bulk plasma frequency.

The permittivity of the plasmonic nanoparticle is considered to be the same as the bulk one. However, it is worth noting that when the nanoparticle size is comparable to the mean path of free electrons ( $\sim 10$  nm), an additional term size-dependent  $\gamma(a)$  is included in the nanoparticle permittivity. This term, added to the bulk damping factor, is the surface plasmon damping due to the strong confinement [44]:  $\gamma(a) = \frac{2Av_f}{a}$  with  $A$  a phenomenological parameter,  $v_f$  the Fermi velocity of electrons and  $a$  the nanoparticle diameter.

Once the expression of the spherical nanoparticle polarizability  $\alpha$  is determined, the scattering and absorption cross sections can be calculated using the following expressions [45, 46]:

$$C_{sca} = \frac{k^4}{6\pi} |\alpha|^2 \propto \frac{a^6}{\lambda^4} \quad (1.36)$$

$$C_{abs} = k \text{Im}[\alpha] \propto \frac{a^3}{\lambda} \quad (1.37)$$

At the resonance frequency,  $\alpha$  reaches its maximum. Therefore,  $C_{sca}$  and  $C_{abs}$  are resonantly enhanced at the LSPR frequency. From their dependence on the nanoparticle size  $a$ , we deduce that the scattering

process is dominant for larger nanoparticles while the absorption is the most efficient process for smaller ones.

There is no analytical solution of Maxwell's equations for nanostructures with complex geometry. For this reason, numerical calculation methods have been developed to study the optical properties of nanoparticles with arbitrary geometries. There are two main numerical methods: finite-difference time domain (FDTD) method and discrete dipole approximation (DDA) method. The latter will be presented in section 2.3.1 of Chapter 2.

Localized surface plasmon LSP modes excited in an STM, sometimes referred to as tip-induced plasmon modes [47], are plasmon modes responsible for light emission in a plasmonic STM junction. After being excited by low-energy inelastic tunneling electrons, they can couple to extended propagating SPP modes of the metallic sample or to free-space photons. LSP modes created in the tip-sample nanocavity are inherently radiative due to the breaking of the surface translational symmetry by the tip. After addressing the specifics of LSP modes, the discussion can proceed to the theoretical models reported in the literature that aim to describe the STM-induced light emission from metallic junctions.

### c) Theoretical description of light emission process

Several theoretical models have been developed to understand and interpret the spectral distribution and intensity of light emission from STM plasmonic junctions. Different tips (with spherical or hyperbolic geometries) and sample shapes were considered in order to identify the impact of the junction geometry on the LSP modes frequency, and thus on the energy of the emitted photons. The properties of the materials involved in the junction were as well taken into account, as they play an important role in the light emission phenomenon.

Persson and Baratoff [48] have developed a theory for light emission from an STM junction in 1992. They have considered tunneling from an *s*-like orbital at the tip apex to a granular substrate modeled by a metallic sphere composed of free electrons. The radiative and non-radiative probabilities of two competing processes have been estimated and compared: inelastic electron tunneling (IET) on the one hand and hot electron injection on the other. Both processes have been presented at the beginning of this section. The radiative probability of IET is about  $\sim 10^{-3}$ , and it reaches about  $\sim 10^{-5}$  for hot electron injection. Despite the fact that this model does not describe the spectral distribution and intensity of light emission spectra, the calculated photon emission efficiencies are in good agreement with the experimental photon emission yield of silver granular films [20].

The energy of surface plasmon modes excited in a tunnel junction by IET has been studied analytically by Rendell and Scalapino [49, 50]. In their model, the tunnel junction consists of a metallic sphere of radius  $a$  placed in front of a completely flat metal surface at a distance  $d$ :

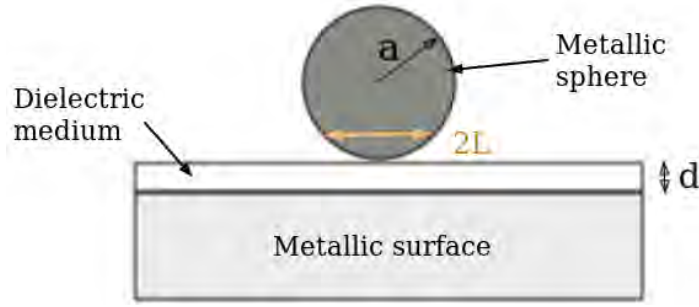


**Figure 1.9:** Geometric representation of the tunneling junction modeled by Rendell and Scalapino [49, 50]

Tersoff et Hamann [13, 14] have used this configuration for their tunneling current calculations which was discussed in section 1.1.1. For a geometry such as  $d \ll a$ , the lateral size of the cavity is defined by the distance from the bottom of the particle to the point where it has curved up to the distance  $d$ , so that  $L \sim \sqrt{2ad}$ . In such a confined cavity, the surface plasmon modes correspond to LSP modes and their frequency can then be written as:

$$\omega_{LSPR} \approx \frac{\omega_p}{\sqrt{\epsilon_d}} \left( \frac{d}{8a} \right)^{\frac{1}{4}} \quad (1.38)$$

where  $\omega_p$  is the average bulk plasma frequency of the involved metals and  $\epsilon_d$  is the gap dielectric function.

Based on Rendell and Scalapino's model, Johansson *et al.* [51, 52] described the light emission phenomenon from the tunneling current fluctuations in the junction and taking into account the electromagnetic coupling in the tip-surface gap. Theoretical light emission spectra have been computed from the calculation of the total radiated power (intensity of photon emission) per unit of solid angle and unit of photon energy:

$$\frac{d^2 P}{d\Omega d(\hbar\omega)} = 2c\epsilon_0 \sum_{i,f} r^2 |\mathbf{E}_{if}(\theta, \mathbf{r}, \omega)|^2 \delta(E_i - E_f - \hbar\omega) \quad (1.39)$$

The total radiated power is expressed as a function of the radiated electric field  $\mathbf{E}_{if}(\theta, \mathbf{r}, \omega)$  at the position  $\mathbf{r}$  and at a detection angle  $\theta$  with respect to the tip axis (see Figure 1.10-A). This electric field considered far away from the junction is derived from the electronic tunneling transition from an initial state  $|i\rangle$  to a final state  $|f\rangle$ . The  $\delta$ -function includes  $\hbar\omega$ , the electron energy loss during the inelastic tunneling.

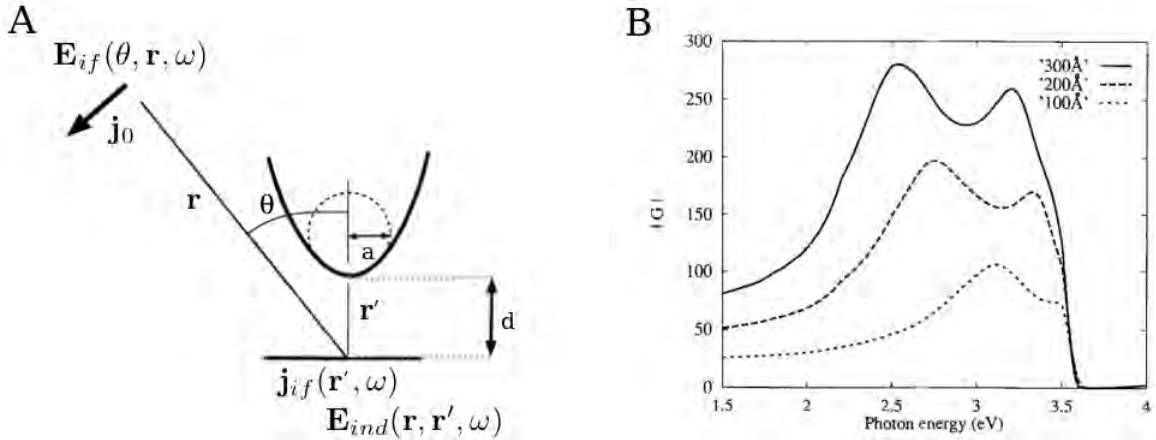


**Figure 1.10:** (A) Geometric representation of the STM tunneling junction modeled by Johansson *et al.* [51, 52]. The tunneling current  $\mathbf{j}_{i,f}$  causes the field  $\mathbf{E}_{i,f}$  far away from the gap, and  $\mathbf{j}_0$  is the source for the field induced in the gap  $\mathbf{E}_{ind}$ . (B) Spectra of the absolute value of the enhancement factor  $G$  below the sphere calculated for three different sphere radii  $a = 100, 200$  and  $300 \text{ \AA}$  with  $d = 5 \text{ \AA}$  and  $\theta = 45^\circ$  [52].

The reciprocity theorem of electrodynamics [53] is used to calculate the radiated electric field. This theorem links the radiated electric field induced by the tunneling current density fluctuations to the electric field induced in a cavity by an external current source by the following expression:

$$\mathbf{E}_{i,f}(\mathbf{r}, \omega) = (\mathbf{j}_0)^{-1} \int d^3r' \mathbf{E}_{ind}(\mathbf{r}, \mathbf{r}', \omega) \mathbf{j}_{i,f}(\mathbf{r}', \omega) \quad (1.40)$$

where  $\mathbf{j}_{i,f}(\mathbf{r}', \omega)$  is the tunneling current density at a point  $\mathbf{r}'$  of the gap and  $\mathbf{E}_{ind}(\mathbf{r}, \mathbf{r}', \omega)$  is the electric field at  $\mathbf{r}$  induced by an external delta-shaped current density  $\delta(\mathbf{r} - \mathbf{r}') \mathbf{j}_0$  located at  $\mathbf{r}$ .  $\mathbf{E}_{ind}(\mathbf{r}, \mathbf{r}', \omega)$  is the product of the plane wave generated by the external source and the optical response function at  $\mathbf{r}'$  noted  $G(\theta, \mathbf{r}', \omega)$  [54] (see Figure 1.10-A). This latter takes into account the junction's geometry and the properties of the materials involved.  $\mathbf{E}_{ind}(\mathbf{r}, \mathbf{r}', \omega)$  is then given by:

$$\mathbf{E}_{ind}(\mathbf{r}, \mathbf{r}', \omega) = \frac{i\omega}{4\pi\epsilon_0 c^2} \frac{e^{ikr}}{r} G(\theta, \mathbf{r}', \omega) \mathbf{j}_0 \quad (1.41)$$

By combining equations (1.40) and (1.41), the radiated electric field can be expressed as:

$$\mathbf{E}_{i,f}(\theta, \mathbf{r}, \omega) = \frac{i\omega}{4\pi\epsilon_0 c^2} \frac{e^{ikr}}{r} \int d^3r' G(\theta, \mathbf{r}', \omega) \mathbf{j}_{i,f}(\mathbf{r}', \omega) \quad (1.42)$$

Therefore, the radiated power per unit of solid angle and per unit of photon energy becomes:

$$\frac{d^2P}{d\Omega d(\hbar\omega)} = \frac{\omega^2}{8\pi^2\epsilon_0 c^3} \sum_{i,f} \left| \int d^3r' G(\theta, \mathbf{r}', \omega) \mathbf{j}_{i,f}(\mathbf{r}', \omega) \right|^2 \times \delta(E_i - E_f - \hbar\omega) \quad (1.43)$$

The light emission process is governed by two factors: the local density of electromagnetic modes in the gap and the tunneling current. Thus, the radiated power expression is derived from the product of two

contributions:

(i) the tunneling current density  $\mathbf{j}_{if}(\mathbf{r}', \omega)$ , determined from the transfer Hamiltonian method, and given by the Bardeen model [12] (see section 1.1.1). Its expression in the  $z$ -direction is:

$$\mathbf{z} \cdot \mathbf{j}_{if}(\mathbf{r}', \omega) = -i \frac{e\hbar}{2m} \left( \frac{\partial \psi_f^*}{\partial z'} \psi_i - \psi_f^* \frac{\partial \psi_i}{\partial z'} \right) (\mathbf{r}') \quad (1.44)$$

with  $\psi_i(r')$  and  $\psi_f(r')$  the wave functions of the initial and final states in the tip and sample respectively.  $\mathbf{z}$  is the unit vector in the  $z$ -direction (perpendicular to the sample surface).

(ii) the field enhancement factor  $G(\theta, \mathbf{r}', \omega)$  which describes the electrodynamic properties of the STM tunneling junction, i.e., the electromagnetic coupling of surface plasmons in the gap. Johansson *et al.* obtained  $G(\theta, \mathbf{r}', \omega)$  by computing the electrostatic potentials induced at the tip apex and sample surface. For that, they solved Laplace's equation analytically using the required boundary conditions. This approach leads to an electron-to-photon conversion modulated by the local electric field in the junction, which is characterized by the enhancement factor  $G$ . The configuration presented is the same as the one used by Rendell and Scalapino with a tip modeled by a sphere with a radius  $a$  at a distance  $d$  from the flat surface (Figure 1.10-A). They noticed that, for a given tip-sample distance, a larger sphere results in an increase of the enhancement factor  $G$  (see Figure 1.10-B). According to Johansson *et al.*, this trend is due to a larger cavity as the ratio  $a/d$  increases, leading to an increase of the cavity polarizability. In addition, a sphere with a larger radius leads to a decrease in the frequency corresponding to the maximum of  $G$ , i.e., a decrease of the LSPR frequency (Figure 1.10-B). This trend has been predicted by Rendell and Scalapino according to equation (1.38). Besides, the sudden decrease in  $G$  at approximately 3.55 eV is attributed to an electromagnetic decoupling between the sphere and the sample. They estimated a photon emission efficiency of  $\sim 10^{-4}$  photons per tunneling electron. The model presented by Johansson *et al.* follows a non-retarded approach which allows the production of light emission spectra in qualitative agreement with the experimental results. In 1998, Johansson improved this model by considering the effects of retardation [21]. These effects give rise to some quantitative changes in the theoretical light emission spectra improving the agreement with the experiments.

In 2000, Aizpurua *et al.* [55] introduced a model inspired by the work of Johansson *et al.*. The tip is modeled by a hyperboloid instead of a sphere leading to an additional degree of freedom. They compared light emission spectra calculated for different tip shapes by changing both aperture and curvature of the tip apex, separately (Figure 1.11-A). Then, the electromagnetic coupling in the gap is computed using the boundary charge method. In addition, they introduced a more accurate description of the tunneling current based on the Tersoff and Hamann approach [13, 14] and the Bardeen model [12] (see section 1.1.1).

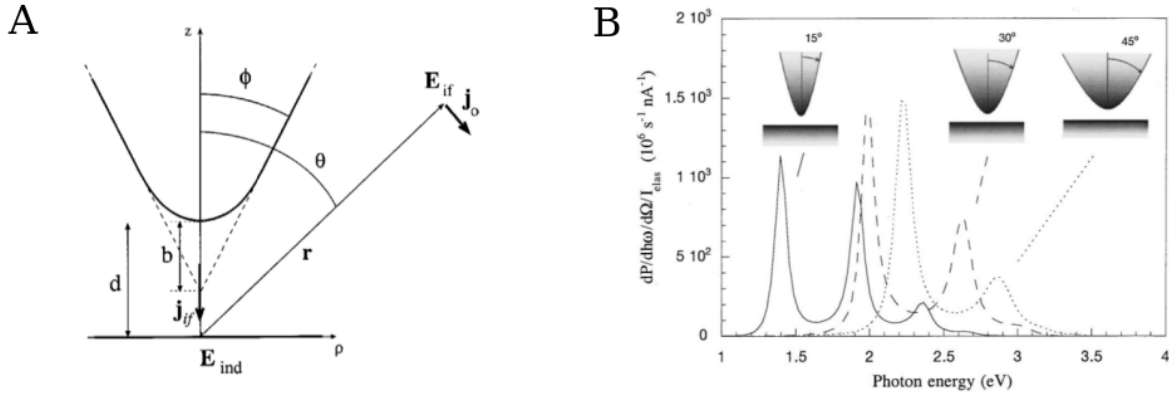


**Figure 1.11:** (A) Geometric representation of the STM tunneling junction modeled by Aizpurua *et al.* [55]. The tip shape is described by its aperture given by the angle  $\phi$  and the curvature of its apex given by the ratio  $b/d$ . (B) Differential radiated power spectra obtained for different tip apertures ( $\phi=15^\circ$ ,  $30^\circ$ , and  $45^\circ$ ) [55].

The tunneling current density expression in the  $z$ -direction proposed by Aizpurua *et al.* is:

$$\mathbf{z} \cdot \mathbf{j}_{if}(\mathbf{r}', \omega) = \frac{e}{i\hbar} \left[ \frac{\hbar^2}{2m} \left( \frac{\partial \psi_f^*}{\partial z'} \psi_i - \psi_f^* \frac{\partial \psi_i}{\partial z'} \right) (\mathbf{r}') + E_{fi} \int_0^d dz \Theta(z' - z) \psi_f^* \psi_i(\mathbf{r}) \right] \quad (1.45)$$

where  $d$  is the tip-sample distance,  $E_{fi} = E_f - E_i = -\hbar\omega$  is the energy difference between the initial and final states of the electronic tunneling transition. Heaviside step function  $\Theta(z' - z)$  takes into account that the inelastic process occurs at the point  $z'$  in the gap.

According to this model, the tip apex aperture has a significant impact on the overall shape of the light emission spectra, especially on the position of the peaks, while the tip apex curvature affects their relative intensities. Similar to the results of Johansson *et al.*, Aizpurua *et al.* found that, for a given tip-sample distance, when the tip aperture gets larger, the field enhancement  $G$  increases because there is a larger area of interaction between the tip and the sample. This gives rise to a higher luminescence intensity (Figure 1.11-B). Their results, concluding that light emission characteristics are very sensitive to the local tip geometry, align with the experimental findings reported by Hoffmann *et al.* [31] (see Fig. 1.5-C). In addition, the authors highlighted that a more realistic description of the tip shape leads to a better prediction of the experimental results. Indeed, this theoretical work, along with the other models discussed earlier, provides a better understanding of the observed experimental light emission behavior.

In Chapter 5 of this thesis, a theoretical model of light emission from a hybrid metal-semiconductor tunnel junction is presented. This model is developed based on the work of Aizpurua *et al.* and aims to interpret the experimental results presented in Chapter 3 for metallic and hybrid semiconductor-metal tunneling junctions. It includes the electromagnetic properties of these junctions, which have been studied by numerical simulation in Chapter 4. In particular, the field enhancement factor  $G$ , describing the electromagnetic coupling of the modeled tunneling junctions, is determined using the Discrete Dipole Approximation (DDA), a numerical method employed to compute the optical properties of arbitrary targets.

### 1.1.3 Light emission from semiconductor samples

Luminescence induced by scanning tunneling microscopy (STM-LE) has been observed in junctions formed by a semiconductor sample. In such junctions, the process of light emission is triggered by the injection of charges during STM tunneling. These charges undergo interband electronic transitions, losing energy within the semiconductor and leading to the emission of light. A similar process occurs with STM-LE from molecules. Indeed, in junctions composed of a molecular system positioned between the STM electrodes, light emission is initiated by the charge carriers injected into the molecules, which undergo transitions involving molecular energy levels [56, 57]. Unlike metallic junctions where the radiative process occurs in the gap involving surface plasmon modes, the light emission process highlighted here takes place within the bandgap sample itself. Consequently, the tip has a much less significant impact on photon emission and only acts as a charge injector.

This thesis focuses on STM-LE resulting from electron-hole pair recombinations in a 2D semiconductor. Therefore, it is decided to present in this section a brief overview of the most relevant experiments related to STM-LE from semiconductor samples. Indeed, the STM-LE technique appears to be a valuable spectroscopy tool for studying electronic transitions and excitonic recombination in semiconductor samples at the atomic scale. Sub-nanometric lateral resolution can be achieved through the extremely localized injection of low-energy electrons (or holes) provided by the STM.

STM-induced luminescence has been observed in a wide range of semiconductors, from surfaces [19, 58, 59] to low-dimensional structures, including quantum wells [60–63], quantum wires [64, 65], and even quantum dots [66–68]. In the following paragraphs, the luminescence from different semiconductor surfaces and quantum wells is discussed, along with the mechanism responsible for light emission, which depends on the bias voltage polarity and the doping level of the semiconductor.

In the first experiments of light emission from an STM junction, Gimzewski *et al.* [19] have reported photon emission from Si(111) 7x7 surfaces in the field emission regime using high voltages ( $V_s \geq 9.5$  V). The injection of high-energy charges can generate secondary electrons and trigger a complex cascade of small electronic transitions. Furthermore, the fact that silicon is an indirect bandgap semiconductor results in a very low quantum efficiency (number of emitted photons per tunneling electron) and in photonic maps with limited resolution. Direct bandgap semiconductors have been shown to produce photon emission more efficiently. In 1990, Abraham *et al.* [60] provided the first experimental proof of luminescence from direct bandgap semiconductor, precisely from *GaAs* quantum wells in a *GaAs/Al<sub>x</sub>Ga<sub>1-x</sub>As* heterostructure. Alvarado *et al.* [61] have investigated luminescence from the same heterostructure. From photonic maps, the authors have detected a strong luminescence intensity when tunneling into p-type *GaAs* quantum wells occurs (Figure 1.12-A). This luminescence arises from the injection of electrons with an energy above the *GaAs* conduction band (CB). By applying a positive bias voltage to the semiconductor, tunneling electrons cross the junction from the tip Fermi level to the *GaAs* CB. Once in the semiconductor, the injected electrons recombine radiatively with

the existing holes in the valence band (VB), given that the semiconductor is p-doped, giving rise to emitted photons with the *GaAs* bandgap energy (Figure 1.12-B).

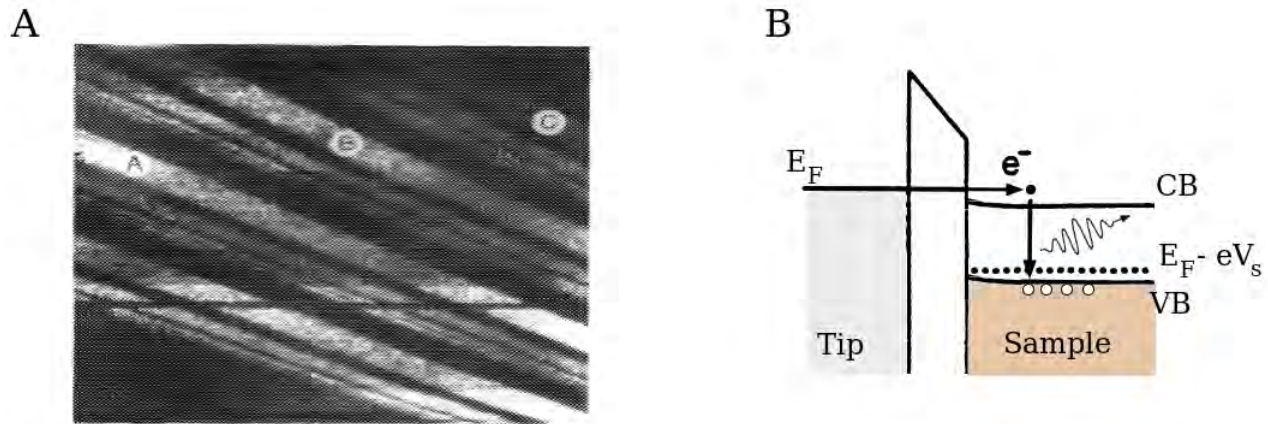


**Figure 1.12:** (A) Photonic map showing luminescent bands corresponding to *GaAs* layers [61]. (B) Energy band diagram showing the mechanism for tunneling-induced photon emission in the case of a p-doped semiconductor positively biased (adapted from [62]).  $V_s$  represents the bias voltage applied to the sample.

In 1992, Berndt *et al.* [58] have studied the luminescence from *CdS* (11 $\bar{2}$ 0) surfaces, a II-VI semiconductor. As the *CdS* samples were strongly n-doped, in order to trigger light emission, holes have been injected into the *CdS* valence band. The luminescence spectra obtained exhibit two characteristic peaks. The high-energy peak corresponds to the radiative recombination of electrons from the CB edge with the injected holes in the vicinity of the VB edge, while the low-energy one is attributed to the radiative recombination of electron-hole pairs originating from defects levels at the bandgap. STM-LE spectra can be used to probe the energy of defect states, which may be observed in photonic maps and/or topographic images.

When the bias voltage applied to the semiconductor is negative, holes are then created in the VB, allowing electron-hole pairs recombination (Figure 1.13-A).

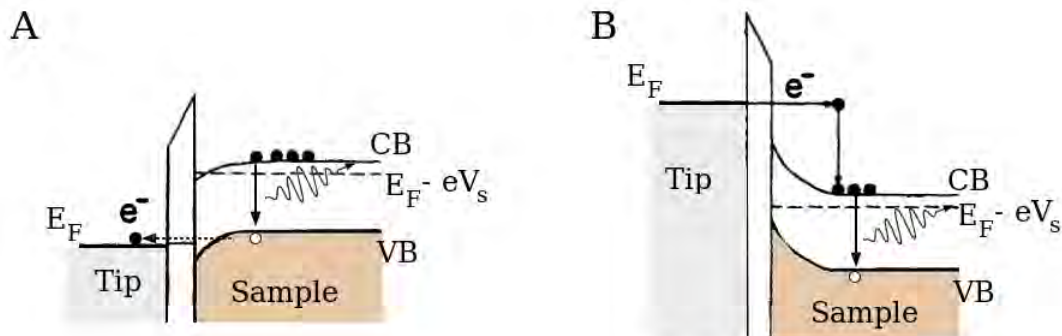


**Figure 1.13:** Energy band diagram showing the mechanism for tunneling-induced photon emission in the case of an n-doped semiconductor negatively (A) and positively (B) biased (adapted from [58]).  $V_s$  represents the bias voltage applied to the sample.

However, in the case of an n-doped positively biased semiconductor, the light emission mechanism consists of a two-step process: hot electrons tunnel from the tip to the semiconductor and are then

thermalized to the bottom of the CB. The electron population in the conduction band increases making the electron-hole recombination process only possible if the creation of holes by impact ionization takes place (see Figure 1.13-B).

Montelius *et al.* [59] have reported luminescence from p-doped *InP* samples using a low-temperature STM. The light emission is stimulated by the injection of minority-carrier: high-energy tunneling electrons are injected from the tip into the positively biased semiconductor. Then, they thermalize to the bottom of the CB and recombine with the VB holes (see Figure 1.14-A). When the semiconductor is negatively biased, the hole population in the vicinity of the VB increases and electron-hole pair recombinations are very unlikely (see Figure 1.14-B).

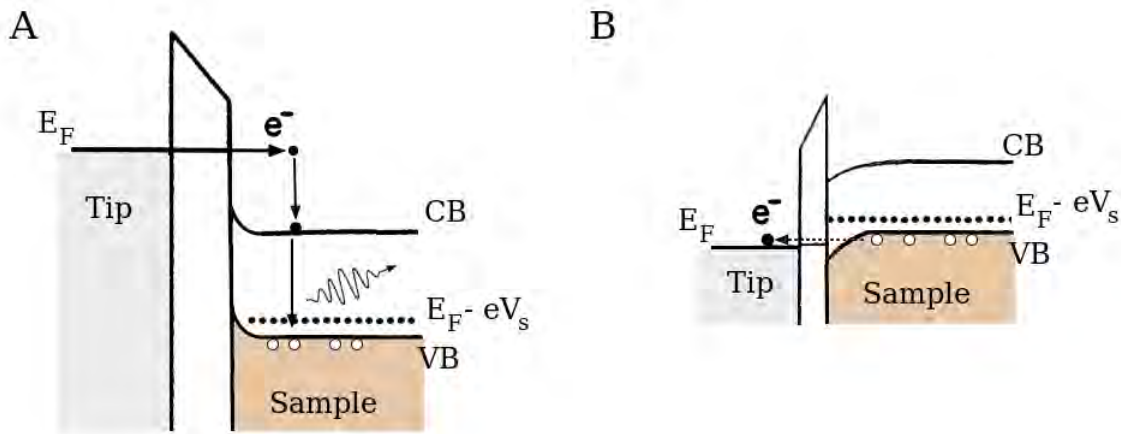


**Figure 1.14:** Energy band diagram showing the mechanism for tunneling-induced photon emission in the case of a p-doped semiconductor positively (A) and negatively (B) biased.  $V_s$  represents the bias voltage applied to the sample.

The mechanisms described above play an important role in the experimental luminescence observed in this thesis from a transition-metal dichalcogenide (TMD) monolayer, and presented in Chapter 3. In contrast to metallic STM junctions, to our knowledge, no theoretical model of light emission from semiconductor samples has been reported in the literature. In Chapter 5, we aim to fill this lack by developing a theoretical model to describe the STM-induced light emission from TMD monolayers. This model addresses the luminescence induced by minority-carrier injection that is discussed above.

## 1.2 Transition-metal dichalcogenide (TMD) monolayers

The discovery of the remarkable physical properties of ultrathin two-dimensional (2D) materials has brought a scientific revolution in fundamental research and in industrial applications. In fact, due to their exceptional geometry, characterized by a thickness of only one or a few atoms, they possess fascinating properties that differ significantly from their bulk counterparts. In 2004, Geim and Novoselov [69] isolated a graphite monoatomic layer known as graphene using mechanical exfoliation. This pioneering work on 2D materials was recognized with the Nobel Prize in Physics in 2010. Graphene

is a zero-bandgap semimetal with unusual electronic properties such as extremely high electron mobility at room temperature with a resistivity of  $\sim 10^{-6} \Omega\cdot\text{cm}$ . It presents as well exceptional mechanical, thermal and optical properties [70]. Since the graphene discovery, a wide variety of synthesis methods and characterization techniques have been developed allowing the production of high-quality ultrathin materials. As a result, many new 2D materials have emerged including superconductors ( $NbSe_2$ ), conductors ( $VS_2$ , graphene), semiconductors (TMD, black phosphorus), and insulators (h- $BN$ ). The family of 2D materials is very large and covers an extremely wide range of properties. Furthermore, these materials can be combined in vertical stacks leading to the formation of so-called van der Waals (vdW) heterostructures, which exhibit novel hybrid properties [71]. Both heterostructures and atomically thin 2D materials hold significant potential for a wide range of applications, especially in the development of electronic and opto-electronics devices such as field-effect transistors, light-emitting diodes, photodetectors and photovoltaics.

Among the above-mentioned 2D materials, transition-metal dichalcogenides (TMDs) have attracted considerable attention because their bandgap and optical properties can be tuned by varying the number of layers. The crystal structure and physical properties of TMDs are presented in the first part of this section. The next part focuses on the optical and electronic properties of TMD monolayers (ML). In particular, those of the  $MoSe_2$  monolayer are highlighted. Finally, the characteristics of hybrid systems composed of TMDs and plasmonic nanostructures are analyzed.

### 1.2.1 Crystal structure and physical properties

TMDs are a large family of about 60 crystals, most of them having a layered structure. In particular, group VI of semiconducting TMDs with general chemical formula  $MX_2$  with M a transition metal ( $Mo$ ,  $W$ ) and X a chalcogen ( $S$ ,  $Se$ ,  $Te$ ) has gained an enormous research interest. A single layer of  $MX_2$  is composed of three covalently bonded atomic planes that consist of a honeycomb sheet of metal atoms (M) sandwiched by two honeycomb sheets of chalcogen atoms (X) [72, 73] (see Figure 1.15-(A,B)). In their bulk form, single layers are held together by a weak van der Waals interaction between each layer. TMD bulk crystals can display different polymorphs such as 1T (trigonal), 2H (hexagonal) and 3R (rhombohedral) [72, 74, 75]. The TMDs used in this thesis present a 2H-phase in their bulk form where adjacent layers are rotated by 180 degrees and stacked directly on top of each other (Figure 1.15-C). They belong to point group symmetry  $D_{6h}$  and their inversion symmetry is broken when the number of layers is odd. In the monolayer form, the inversion symmetry is broken and the layer presents the lower symmetry  $D_{3h}$  point group.

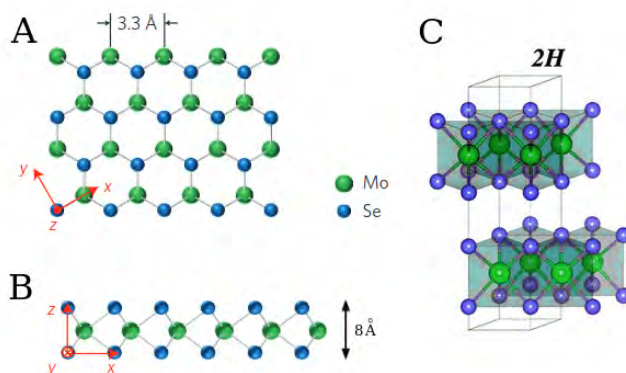


**Figure 1.15:** Crystal structure of  $MoSe_2$  monolayer with  $Mo$  atoms in green and  $Se$  atoms in blue: (A) Top view and (B) side view of the  $MoSe_2$  monolayer structure [76]. (C) Structural representation of the 2H polytype of  $MoSe_2$  [75].

The combination of transition metal atoms  $Mo$  or  $W$  and chalcogen atoms  $S$  or  $Se$  has led to a wide range of semiconductors whose band structure, including their bandgap, can be tuned by the number of layers. Indeed, these TMD crystals exhibit an indirect bandgap in their bulk form which turns into a direct bandgap when their thickness is reduced to a single layer [76, 77]. TMD monolayers are three-atoms-thick. In the case of  $MoSe_2$ , a single ML has a thickness of between 0.7 and 0.9 nm [78–80]. TMD-MLs are produced by micromechanical exfoliation or by synthesis methods (see section 2.2.1 Chapter 2). They are usually stable enough in ambient conditions to perform optical and electrical characterization [81].

## 1.2.2 Opto-electronic properties of TMD monolayers

The indirect-to-direct bandgap transition has made the TMD monolayers an ideal platform to investigate the light-matter interaction. Indeed, they exhibit a larger photoluminescence (PL) signal and more efficient light absorption compared to their bulk counterparts with indirect bandgap [82–85] (see Figure 1.16-A). Optical measurements performed on a TMD monolayer reveal electronic band structure features such as the bandgap energy. Depending on the choice of the metal and chalcogen atoms, TMD monolayers exhibit different bandgap energies, giving rise to absorption and optical emission spectra ranging from visible to near-infrared (Figure 1.16-B). The fascinating electronic and optical properties of TMDs, especially those of the  $MoSe_2$  monolayer, are addressed in the following paragraphs.

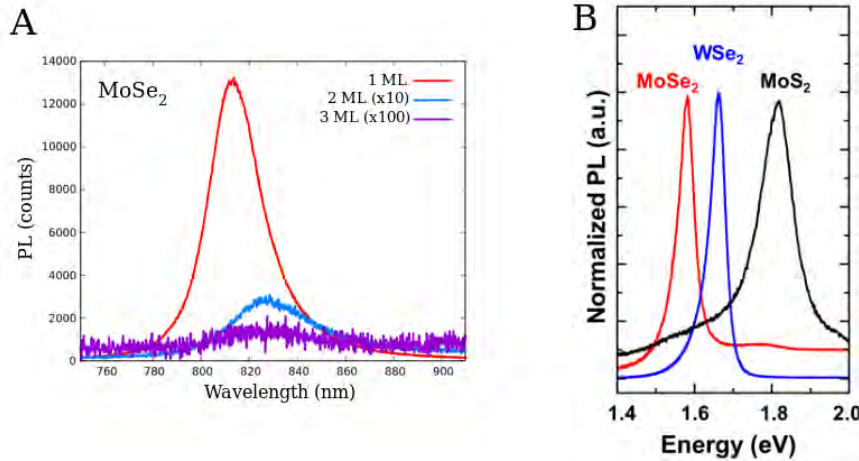


**Figure 1.16:** (A) Photoluminescence spectra of  $MoSe_2$  monolayer (red), bilayer (blue) and trilayer (violet) [85]. Increasing the number of layers leads to a significant reduction of the photoluminescence intensity. (B) Normalized PL spectra of  $MoSe_2$  (red),  $WSe_2$  (blue) and  $MoS_2$  (black) monolayers. PL measurements were performed at room temperature by Tongay *et al.* [86]

### a) Band structure

The electronic band structure of TMD monolayers is different from that of their bulk counterparts, as shown in Figure 1.17-A, due to quantum confinement effects and the lack of interlayer orbital interactions. TMD bulk or multilayer has an indirect band structure with a valence band maximum (VBM) at  $\Gamma$  (the center of the 1st Brillouin Zone) and a conduction band minimum (CBM) nearly halfway along the  $\Gamma$ - $K$  direction. Orbitals composing these states are extending out of the plane and spatial overlap between those of different layers takes place. When the number of layers is reduced, the energy of valence band states at  $\Gamma$  decreases causing the states at the  $K$  point to become the VBM. For the conduction band, the energy of the states along the  $\Gamma - K$  direction increases giving rise to a CBM at the  $K$  point. In fact, the CB and VB states at  $K$  do not change much when the number of layers decreases since their corresponding orbitals are mainly d-orbitals from the metal atoms. To be more precise, on the one hand, the valence band states at  $K$  are composed of transition metal atom  $d_{x^2-y^2} \pm id_{xy}$  states. On the other hand, those composing the conduction band states at  $K$  are  $d_{z^2}$  states. Both are slightly mixed with the  $p_x \pm ip_y$  orbitals of chalcogen atoms [87]. The VBM and CBM for TMD-ML are located at  $K$ , i.e., at the corners of the 1st Brillouin Zone leading to direct bandgap (Figure 1.17-B) [88, 89].

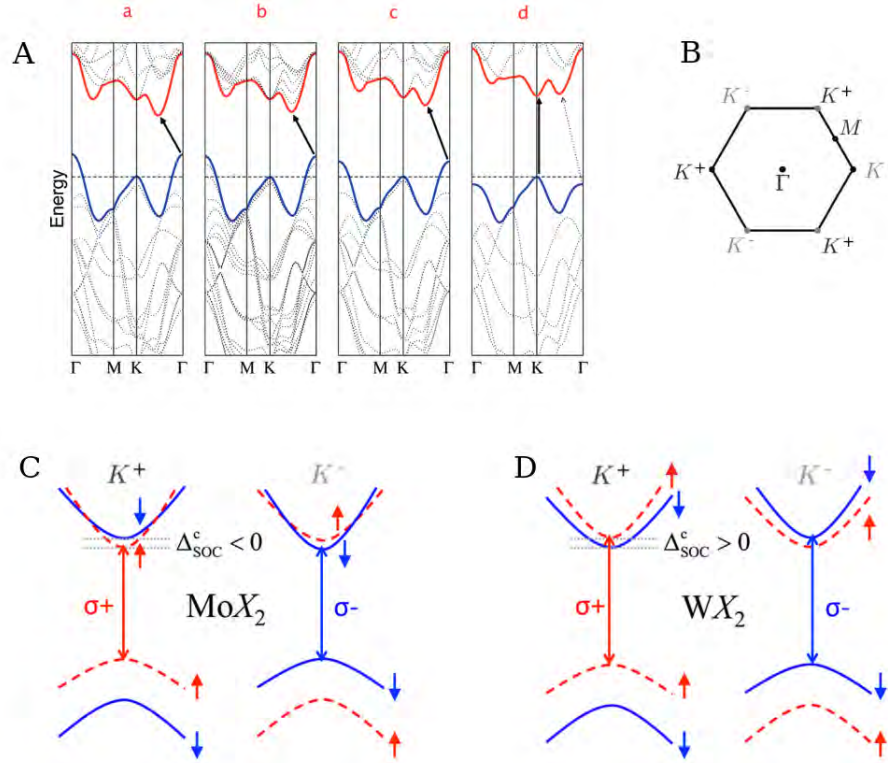


**Figure 1.17:** (A) Band structure of (a) bulk (b) quadrilayer, (c) bilayer and (d) monolayer  $MoS_2$  calculated by Splendiani *et al.* [83] (B) First Brillouin zone of a TMD monolayer [89]. (C-D) Schematic representation showing the spin-orbit splitting of the valence and conduction bands in  $K^+$  and  $K^-$  valleys for TMD monolayers with  $Mo$  as transition metal atom (C) and with  $W$  as transition metal atom (D) [90]

Due to the absence of inversion symmetry, the TMD-MLs band structure presents six  $K$  points divided into two inequivalent groups:  $K^+$  and  $K^-$  points, as depicted in Figure 1.17-B. The energy states close to these points are typically referred to as  $K^+$  and  $K^-$  valleys. In addition, a strong spin-orbit coupling (SOC) is induced by the broken inversion symmetry and the relatively heavy metal atoms composing the monolayer. This coupling gives rise to a spin splitting in the VB and CB at the inequivalent  $K^+$  and  $K^-$  valleys [90]. For the  $MoSe_2$  monolayer, the valence band splitting is close to 200 meV while the conduction band splitting is only a few meV [91]. Due to the time-reversal symmetry, this splitting at the  $K^+$  and  $K^-$  valleys must be opposite [92]. The VBM is defined as the valence sub-band with upper energy. At  $K^+$  valleys, it corresponds to spin-up states, while at  $K^-$  valleys, the VBM states are spin-down states. The states of the VBM and the CBM (defined as the conduction sub-band with lower energy) have the same spin for TMDs with  $Mo$  as transition metal, while for TMD-MLs with  $W$  as transition metal, these states have opposite spin. This is illustrated in Figure 1.17-(C,D). Hence, charge carriers have both spin and valley degrees of freedom, making the TMD-ML an interesting candidate for spintronics and valleytronics research.

## b) Exciton

In TMD-MLs, each electron excited from the VB to the CB leaves a hole in the VB. These electrons

and holes are strongly attracted by the Coulomb interaction giving rise to the formation of bound states called excitons (Figure 1.18-A). The bound electron-hole pair forming an exciton can belong to the same  $K$  valley (intravalley exciton) or to different  $K$  valleys (intervalley exciton). The strong Coulomb interaction is attributed to the low dielectric screening and quantum confinement effects characteristic of the monolayer due to its reduced dimensionality [90]. These excitons, which are considered as neutral quasiparticles, have a binding energy of several hundred of meV and a ground-state Bohr radius of a few nm. In addition, their wavefunction extends over several lattice sites. They are considered confined within the monolayer but are free to move through it (Figure 1.18-A). These particular features place the TMD-ML exciton in an intermediate position between two well-defined types of excitons: Wannier-Mott exciton, delocalized over several lattice sites, and Frenkel exciton, characterized by a small Bohr radius [93]. TMD-ML exciton states can be described by a quantum number  $n$  similarly to Rydberg series, with a ground state ( $n = 1$ ) and excited states ( $n > 1$ ) (Figure 1.18-B) [94, 95]. These states have a lower energy than the ground state of free electron-hole excitation. Hence, as exciton excitation requires less energy, light absorption and emission from a TMD-ML come from excitonic states.

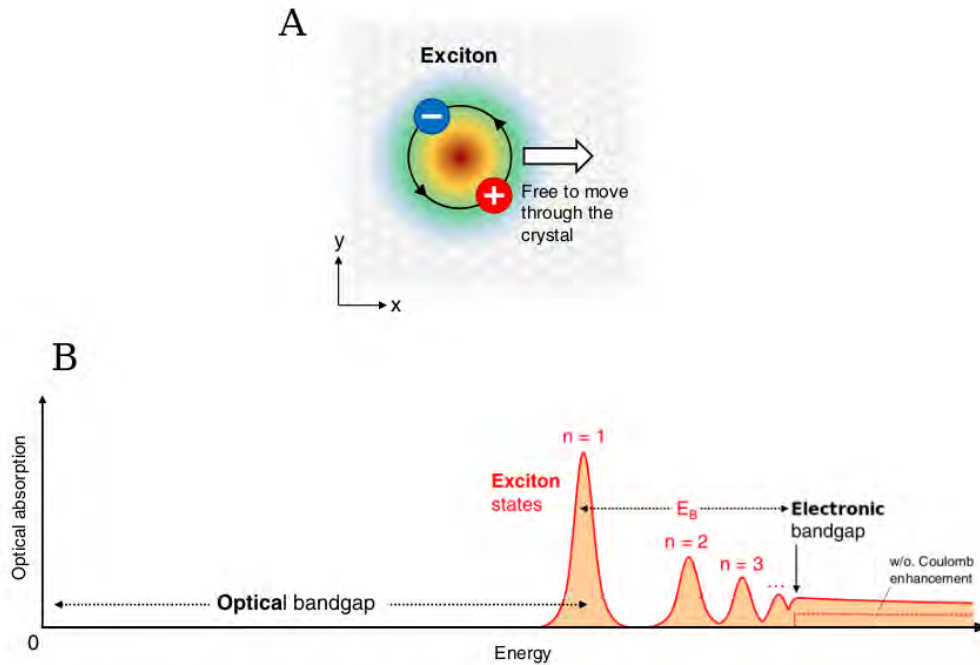


**Figure 1.18:** (A) Schematic representation of an exciton in real space (B) Schematic illustration showing the optical absorption of exciton resonances in an ideal 2D semiconductor. The series of exciton states defined by the quantum number  $n$  is depicted. The optical and electronic bandgap of the 2D semiconductor are represented as well as the exciton binding energy  $E_B$ . Both figures are taken from Wang *et al.* [90]

The TMD-ML optical bandgap is defined with respect to the ground-state exciton and it is obtained from optical measurements such as photoluminescence (see section 2.2.2 Chapter 2). It differs from the energy of an unbound electron-hole pair, which corresponds to the electronic bandgap, by the exciton binding energy  $E_B$  (Figure 1.18-B). Since the electronic bandgap of a TMD-ML can be obtained by electronic spectroscopy STS (see section 1.1.1 Chapter 1), the exciton binding energy can be calculated. Ugeda *et al.* [96] conducted this analysis for a  $MoSe_2$  ML grown on a bilayer graphene/ $SiC$  substrate.

Their findings revealed an electronic bandgap of about 2.18 eV and an optical bandgap of approximately 1.63 eV, resulting in an exciton binding energy of  $E_B \sim 0.55$  eV.

In the case of strongly doped TMD-MLs [90, 97], charged excitons and trions (formed by two electrons and one hole or vice-versa) are also generated and their signatures can be observed in optical measurements [98–100]. Since TMD-MLs are often n-doped [101] (as the  $MoSe_2$  monolayers studied in this thesis), these charged excitons are negative [102]. They have lower absorption and emission transition energies than neutral excitons because their binding energies  $E_B$  are greater than those of neutral excitons.

Depending on the synthesis method used (see section 2.2.1 Chapter 2), structure defects may be present in TMD-MLs. These defects modify the band structure of the monolayer and can become localized traps for excitons that generally propagate in the monolayer [86, 103–105].

The valence band splitting at  $K^+$  and  $K^-$  valleys mentioned before leads to two valence sub-bands. Two types of exciton arise from this valence band splitting: A-exciton and B-exciton. The holes involved in A-excitons are from the upper valence sub-band (VBM). This makes the A-exciton the less energetic and thus, the most favorable for photon absorption and emission. The holes involved in B-excitons are from the lower valence sub-band (Figure 1.19-(A,B)) [106, 107]. Therefore, the difference of energy between A-exciton and B-exciton corresponds approximately to the valence band splitting since the conduction band splitting is almost negligible [108]. According to photoluminescence measurements performed by Iberi *et al.* [109] at room temperature, the A- and B-excitons of a supported  $MoSe_2$  ML have an energy of 1.55 eV and 1.77 eV, respectively. Moreover, because of the spin splitting in the CB and the VB, A- and B- excitons can be spin-allowed excitons (electron and hole with the same spin) or spin-forbidden excitons (electron and hole with different spin). Spin-allowed excitons can be optically active, i.e., they can be excited by resonant photon absorption and decay radiatively. Thus, they are called bright excitons, while spin-forbidden excitons are optically inactive and are therefore called dark excitons (Figure 1.19-B) [110, 111]. In fact, dark excitons are not able to recombine radiatively, despite the fact that they can be excited by non-resonant optical excitation or electrical injection [90]. The difference of energy between a bright and a dark exciton is given by the CB spin splitting. Bright excitons have an electric dipole moment in the monolayer plane, whereas dark excitons have an electric dipole moment out of the monolayer plane [112–115]. In Figure 1.19-B, bright and dark excitons with A and B character are shown. A- and B-exciton optical properties defined by the spin-valley coupling of the monolayer band structure are discussed below. The TMD-MLs band structure exhibits parallel CB and VB along the  $\Gamma$ -M direction. This singularity called “band nesting” gives rise to C-excitons. They have an energy of about 2.6 eV for  $MoSe_2$  monolayers [116] (see Figure 1.19-A).

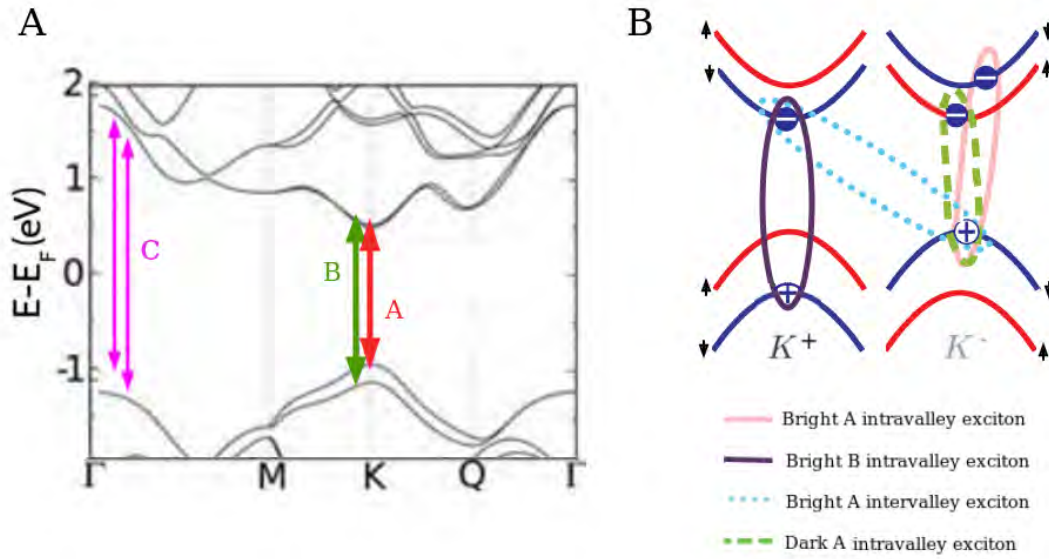


**Figure 1.19:** (A) Band structure of the  $MoSe_2$  monolayer showing A, B and C excitons. This figure is taken from [117]. (B) Scheme showing the variety of excitons: bright and dark, A and B, and intra and intervalley excitons. This figure is adapted from reference [111] showing the excitons of  $WSe_2$  monolayer

### c) Optical properties

Light-matter interaction in TMD-MLs obeys chiral optical rules established by energy, momentum, and spin conservation [90, 114]. Energy and momentum conservation are respected when the exciton energy ( $E_{exc}$ ) and momentum ( $\mathbf{K}_{exc} = \mathbf{k}_e + \mathbf{k}_h$ ) are equal to the photon energy ( $\hbar\omega$ ) and momentum ( $\mathbf{q}$ ), respectively. As previously mentioned, all optical interband transitions correspond to spin-conserved bright excitonic transitions. In some cases, these conditions are not fulfilled directly, and phonons, defects, exciton-exciton interactions, or exciton-electron interactions are required in the optical process for energy and momentum conservation, or even to induce spin flipping to obtain the spin conservation. In TMD-MLs, it is possible to address the optical excitation of bright excitons, formed by parallel-spin electron-hole pairs, in  $K^+$  or  $K^-$  valleys by using  $\sigma^+$  or  $\sigma^-$  circularly polarized light, respectively (Figure 1.17-(C,D)) [118–123]. This is called spin/valley pumping. Similarly, excitation with linearly polarized light can lead to a coherent superposition of  $K^+$  and  $K^-$  valleys states, known as valley coherence [124]. After their excitation, bright excitons can relax into different pathways involving different spin/valley depolarization mechanisms [125].

TMD-MLs present exceptional optical, electronic, valleytronic and spintronic properties. These properties are highly sensitive to the dielectric environment surrounding the monolayer [126–130]. Indeed, the dielectric screening of the surrounding environment can modify the Coulomb interaction between electrons and holes that form excitons [131]. Furthermore, the exciton radiative recombination itself depends on the density of available optical modes of the optical environment. Hence, depending on the media surrounding the monolayer, its light-matter interaction can be different. The properties

of TMD-MLs can therefore be externally tuned by the surrounding media. In the following section, the main properties of hybrid systems composed of TMD-MLs and plasmonic nanostructures are addressed.

### 1.2.3 TMD/plasmonic nanostructures hybrid systems

Plasmonic nanostructures display very interesting properties, including the control of light-matter interaction at the nanoscale. Their main characteristic is their ability to confine strong electric fields via localized surface plasmon (LSP) modes as it was previously described (section 1.1.2 Chapter 1). By combining plasmonic nanostructures with TMD-MLs, quantum-confined excitons can interact with plasmonic-enhanced electric fields, which results in electromagnetic coupling between LSP modes and TMD-ML excitons. Hybridized energy states can be generated from this plasmon-exciton coupling. Hybrid TMD/plasmonic nanostructures systems have been developed in order to study and exploit the novel properties resulting from this hybridization [132–138]. If the excitonic and plasmonic resonances match, this plasmon-exciton coupling can result in energy transfer, enhancing the optical properties of TMD-ML. The plasmonic resonances and thus, the plasmon-exciton coupling, are modulated by the geometry and configuration of the TMD/plasmonic nanostructure. In addition, the electrical and optical properties of these hybrid systems are significantly influenced by the contact interface between the TMD and the plasmonic metal.

The hybrid TMD/plasmonic nanostructure properties can be investigated by photoluminescence (PL technique is described in section 2.2.2 Chapter 2). Due to an energy transfer between plasmonic modes and excitons, the optical absorption of a TMD-ML can be strongly enhanced if the surface plasmon resonance matches the excitonic transitions of the monolayer. This absorption enhancement leads to an increase in photo-generated charge carriers, excitons and free-charges, in the monolayer. These photo-generated charges can relax through two possible pathways: transfer to the plasmonic metal, or radiative decay giving rise to an enhancement of photon emission. One or the other will be the dominant process depending on the TMD/metal interface. When the relative alignment of energy bands between the TMD and the metal leads to a small Schottky barrier at the TMD/metal interface, the charge transfer process is most favorable. In this case, the photo-generated charges are transported from the monolayer to the plasmonic metal before they can radiatively decay (Figure 1.20-A). As a result, the population of excitons in the monolayer decreases, as does the probability of photon emission by exciton radiative decay. Thus, a diminution of the photoluminescence intensity known as quenching is obtained (Figure 1.20-B). In some cases, the quenching of the PL is due to the transfer of hot charges from plasmonic nanoparticles to the TMD-ML. Indeed, the increase of high-energetic charges in the monolayer can lead to a modification of its band structure and thus of its opto-electronic properties. PL quenching has been observed in several hybrid systems composed of plasmonic nanoparticles deposited on a TMD-ML [139–142]. If a dielectric medium is placed at the TMD/plasmonic metal interface, the charge transfer will be blocked. In this case, the probability of radiative decay from photo-generated charge carriers increases giving rise to an enhancement of the photon emission [143, 144]. In fact, when the exciton population is not reduced by charge transfer, the energy transfer between plasmonic modes

and excitons leads to an enhancement of the optical absorption as well as of the photoluminescence intensity. [134, 145–148]. As mentioned before, the photon emission enhancement can be modulated by the geometry of the TMD/plasmonic nanostructure system, as shown in Figure 1.20-(C,D). In addition to affecting the intensity of the photon emission, the plasmonic environment surrounding the monolayer can induce a modification of the energy of the excitons leading to a shift in the PL spectra. [140, 141].

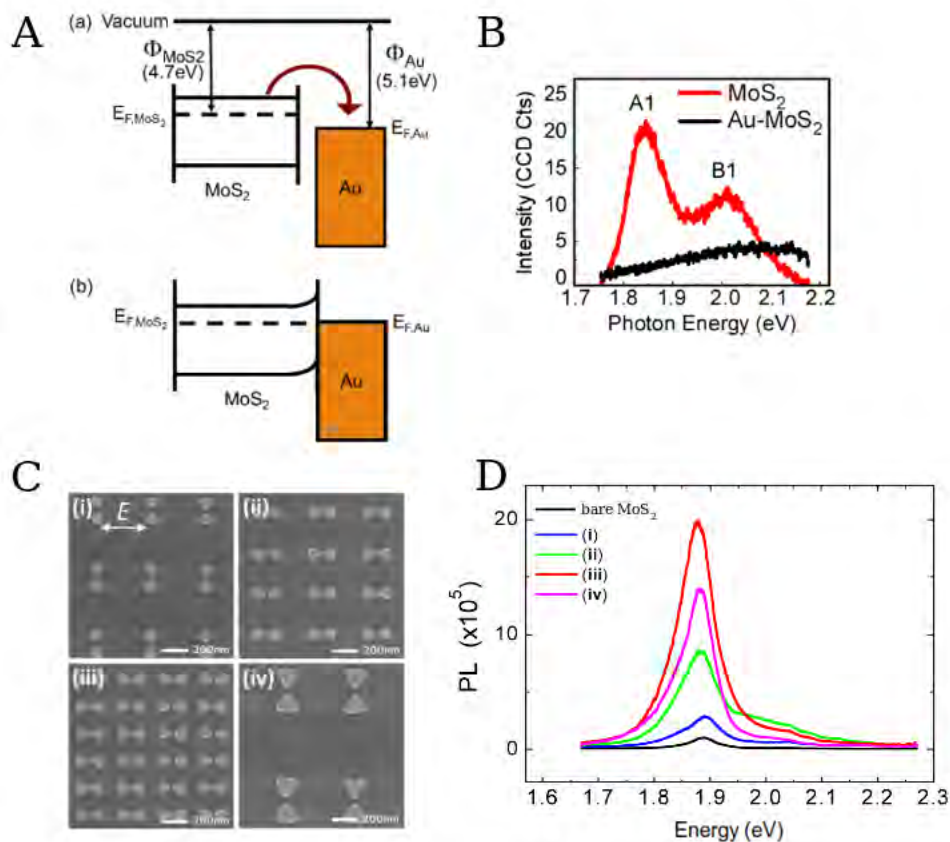


**Figure 1.20:** (A) Energy band diagram showing the Fermi level alignment before and after the establishment of the  $MoS_2/Au$  contact. The arrow represents the electrons transfer from the monolayer to gold [139]. (B) PL spectra of 2 layers of  $MoS_2$  flake before (red) and after (black) the deposition of 2 nm of  $Au$ . The charges transfer presented in (A) leads to a PL quenching [139]. (C) Hybrid TMD/plasmonic nanostructure system composed of a silver-bowtie nanoantenna array deposited on a  $MoS_2$  monolayer [145]. Four patterns of this hybrid system with different geometrical factors of the bowtie array are evaluated. (D) PL spectra obtained for each of the four patterns presented in (C) and for bare  $MoS_2$  monolayer [145]

In Chapter 3 of this thesis, the optical properties of a TMD/plasmonic nanostructure hybrid system are experimentally investigated using primarily electrical excitation. This hybrid system consists of an STM tunneling junction where a  $MoSe_2$  monolayer lays on a gold substrate which forms a plasmonic cavity with a gold tip. Both of the phenomena discussed here, photon emission enhancement by plasmon-exciton coupling and photon emission quenching due to charge transfer, will be addressed in Chapter 3. Furthermore, the plasmon-exciton coupling of a hybrid TMD/metal tunneling junction is studied in detail by numerical simulation in Chapter 4.

## Bibliography

- [1] G. Binnig, H. Rohrer, Ch. Gerber, and E. Weibel. Tunneling through a controllable vacuum gap. *Appl. Phys. Lett.*, 40(2):178–180, 1982.
- [2] G. Binnig, H. Rohrer, Ch. Gerber, and E. Weibel. Surface studies by scanning tunneling microscopy. *Phys. Rev. Lett.*, 49(1):57–61, 1982.
- [3] G. Binnig and H. Rohrer. Scanning tunneling microscopy—from birth to adolescence. *Rev. Mod. Phys.*, 59(3):615–625, 1987.
- [4] G. Binnig, H. Rohrer, Ch. Gerber, and E. Weibel.  $7 \times 7$  Reconstruction on Si(111) Resolved in Real Space. *Phys. Rev. Lett.*, 50(2):120–123, 1983.
- [5] J. V. Barth, H. Brune, G. Ertl, and R. J. Behm. Scanning tunneling microscopy observations on the reconstructed Au(111) surface: Atomic structure, long-range superstructure, rotational domains, and surface defects. *Phys. Rev. B*, 42(15):9307–9318, 1990.
- [6] R. Wiesendanger. *Scanning probe microscopy and spectroscopy: methods and applications*. Cambridge University Press, 1994.
- [7] R. J. Hamers and D. F. Padowitz. Methods of tunneling spectroscopy with the STM. *Scanning Probe Microscopy and Spectroscopy: Theory, Techniques, and Applications*, 2, 2001.
- [8] N. Nilius, T. M. Wallis, and W. Ho. Development of one-dimensional band structure in artificial gold chains. *Science*, 297(5588):1853–1856, 2002.
- [9] M. F. Crommie, C. P. Lutz, and D. M. Eigler. Confinement of Electrons to Quantum Corrals on a Metal Surface. *Science*, 262(5131):218–220, 1993.
- [10] L. D. Landau and E. M. Lifshitz. *Quantum mechanics: non-relativistic theory*, volume 3. Elsevier, 2013.
- [11] R. H. Fowler and L. Nordheim. Electron emission in intense electric fields. *Proc. R. Soc. London A.*, 119(781):173–181, 1928.
- [12] J. Bardeen. Tunnelling from a many-particle point of view. *Phys. Rev. Lett.*, 6(2):57–59, 1961.
- [13] J. Tersoff and D. R. Hamann. Theory and application for the scanning tunneling microscope. *Phys. Rev. Lett.*, 50(25):1998–2001, 1983.
- [14] J. Tersoff and D. R. Hamann. Theory of the scanning tunneling microscope. *Phys. Rev. B*, 31(2):805–813, 1985.
- [15] C. J. Chen. Tunneling matrix elements in three-dimensional space: The derivative rule and the sum rule. *Phys. Rev. B*, 42(14):8841–8857, 1990.

- 
- [16] C. J. Chen. *Introduction to Scanning Tunneling Microscopy Third Edition*, volume 69. Oxford University Press, USA, 2021.
- [17] C. J. Chen. Origin of atomic resolution on metal surfaces in scanning tunneling microscopy. *Phys. Rev. Lett.*, 65(4):448–451, 1990.
- [18] J. Lambe and S. L. McCarthy. Light Emission from Inelastic Electron Tunneling. *Phys. Rev. Lett.*, 37(14):923–925, 1976.
- [19] J. K. Gimzewski, B. Reihl, J. H. Coombs, and R. R. Schlittler. Photon emission with the scanning tunneling microscope. *Zeitschrift für Physik B Condensed Matter*, 72(4):497–501, 1988.
- [20] J. H. Coombs, J. K. Gimzewski, B. Reihl, J. K. Sass, and R. R. Schlittler. Photon emission experiments with the scanning tunnelling microscope. *J. Microsc.*, 152(2):325–336, 1988.
- [21] P. Johansson. Light emission from a scanning tunneling microscope: Fully retarded calculation. *Phys. Rev. B*, 58(16):10823–10834, 1998.
- [22] J. K. Gimzewski, J. K. Sass, R. R. Schlitter, and J. Schott. Enhanced Photon Emission in Scanning Tunnelling Microscopy. *Europhys. Lett.*, 8(5):435–440, 1989.
- [23] I. I. Smolyaninov, V. S. Edelman, and V. V. Zavyalov. Spectroscopic measurements of light emitted by the scanning tunneling microscope. *Phys. Lett. A*, 158(6-7):337–340, 1991.
- [24] R. Berndt and J. K. Gimzewski. The role of proximity plasmon modes on noble metal surfaces in scanning tunneling microscopy. *Surf. Sci.*, 269–270:556–559, 1992.
- [25] K. Ito, S. Ohyama, Y. Uehara, and S. Ushioda. STM light emission spectroscopy of surface micro-structures on granular Au films. *Surf. Sci.*, 324(2-3):282–288, 1995.
- [26] A. W. McKinnon, M. E. Welland, T. M. H. Wong, and J. K. Gimzewski. Photon-emission scanning tunneling microscopy of silver films in ultrahigh vacuum: A spectroscopic method. *Phys. Rev. B*, 48(20):15250–15255, 1993.
- [27] V. Sivel, R. Coratger, F. Ajustron, and J. Beauvillain. Photon emission stimulated by scanning tunneling microscopy in air. *Phys. Rev. B*, 45(15):8634–8637, 1992.
- [28] R. Péchou, R. Coratger, C. Girardin, F. Ajustron, and J. Beauvillain. Spectroscopy of Light Emission from a Scanning Tunneling Microscope in Air. *J. Phys. III*, 6(11):1441–1450, 1996.
- [29] R. Berndt, J. K. Gimzewski, and R. R. Schlittler. Photon emission from small particles in an STM. *Zeitschrift für Physik D Atoms, Molecules and Clusters*, 26:87–88, 1993.
- [30] R. Berndt, R. Gaisch, W. D. Schneider, J. K. Gimzewski, B. Reihl, R. R. Schlittler, and M. Tschudy. Atomic resolution in photon emission induced by a scanning tunneling microscope. *Phys. Rev. Lett.*, 74(1):102–105, 1995.

- [31] G. Hoffmann, J. Aizpurua, P. Apell, and R. Berndt. Influence of tip geometry in light emission from the scanning tunnelling microscope. *Surf. Sci.*, 482–485:1159–1162, 2001.
- [32] D. Hone, B. Mühlischlegel, and D. J. Scalapino. Theory of light emission from small particle tunnel junctions. *Appl. Phys. Lett.*, 33(2):203–204, 1978.
- [33] S. A. Maier. *Plasmonics: Fundamentals and Applications*, volume 1. Springer, 2007.
- [34] A. V. Zayats and I. I. Smolyaninov. Near-field photonics: surface plasmon polaritons and localized surface plasmons. *J. Opt. A: Pure Appl. Opt.*, 5(4):S16–S50, 2003.
- [35] K. A. Willets and R. P. Van Duyne. Localized surface plasmon resonance spectroscopy and sensing. *Annu. Rev. Phys. Chem.*, 58(1):267–297, 2007.
- [36] E. Hecht. *Optics*. Pearson education. Addison-Wesley, 2002.
- [37] L. Novotny and B. Hecht. *Principles of Nano-Optics*. Cambridge University Press, 2012.
- [38] R. H. Ritchie, E. T. Arakawa, J. J. Cowan, and R. N. Hamm. Surface-Plasmon Resonance Effect in Grating Diffraction. *Phys. Rev. Lett.*, 21(22):1530–1533, 1968.
- [39] H. Raether. Surface plasmons on smooth surfaces. *Surface plasmons on smooth and rough surfaces and on gratings*, pages 4–39, 2006.
- [40] E. Kretschmann and H. Raether. Radiative decay of non radiative surface plasmons excited by light. *Zeitschrift für Naturforschung A*, 23(12):2135–2136, 1968.
- [41] A Otto. Excitation of nonradiative surface plasma waves in silver by the method of frustrated total reflection. *Zeitschrift für Physik A Hadrons and nuclei*, 216(4):398–410, 1968.
- [42] K. L. Kelly, E. Coronado, L. L. Zhao, and G. C. Schatz. The Optical Properties of Metal Nanoparticles: The Influence of Size, Shape, and Dielectric Environment. *J. Phys. Chem. B*, 107(3):668–677, 2003.
- [43] U. Kreibig and M. Vollmer. *Optical Properties of Metal Clusters*, volume 25. Springer Science & Business Media, 2013.
- [44] A. Kawabata and R. Kubo. Electronic properties of fine metallic particles. II. Plasma resonance absorption. *J. Phys. Soc. Jpn.*, 21(9):1765–1772, 1966.
- [45] D. L. Fedlheim and C. A. Foss. *Metal nanoparticles: synthesis, characterization, and applications*. CRC press, 2001.
- [46] C. F. Bohren and D. R. Huffman. *Absorption and scattering of light by small particles*. John Wiley & Sons, 2008.

- [47] R. Berndt, J. K. Gimzewski, and P. Johansson. Inelastic tunneling excitation of tip-induced plasmon modes on noble-metal surfaces. *Phys. Rev. Lett.*, 67(27):3796–3799, 1991.
- [48] B. N. J. Persson and A. Baratoff. Theory of photon emission in electron tunneling to metallic particles. *Phys. Rev. Lett.*, 68(21):3224–3227, 1992.
- [49] R. W. Rendell, D. J. Scalapino, and B. Mühlischlegel. Role of local plasmon modes in light emission from small-particle tunnel junctions. *Phys. Rev. Lett.*, 41(25):1746–1750, 1978.
- [50] R. W. Rendell and D. J. Scalapino. Surface plasmons confined by microstructures on tunnel junctions. *Phys. Rev. B*, 24(6):3276–3294, 1981.
- [51] P. Johansson, R. Monreal, and P. Apell. Theory for light emission from a scanning tunneling microscope. *Phys. Rev. B*, 42(14):9210–9213, 1990.
- [52] P. Johansson and R. Monreal. Theory for photon emission from a scanning tunneling microscope. *Zeitschrift für Physik B Condensed Matter*, 84(2):269–275, 1991.
- [53] L. D. Landau, E. M. Lifshitz, and L. P. Pitaevskii. *Electrodynamics of Continuous Media*. Pergamon Press, 1984.
- [54] J. D. Jackson. *Classical electrodynamics*. New York :Wiley, 1999.
- [55] J. Aizpurua, S. P. Apell, and R. Berndt. Role of tip shape in light emission from the scanning tunneling microscope. *Phys. Rev. B*, 62(3):2065–2073, 2000.
- [56] S.-E. Zhu, Y.-M. Kuang, F. Geng, J.-Z. Zhu, C.-Z. Wang, Y.-J. Yu, Y. Luo, Y. Xiao, K.-Q. Liu, Q.-S. Meng, L. Zhang, S. Jiang, Y. Zhang, G.-W. Wang, Z.-C. Dong, and J. G. Hou. Self-decoupled porphyrin with a tripodal anchor for molecular-scale electroluminescence. *J. Am. Chem. Soc.*, 135(42):15794–15800, 2013.
- [57] B. Doppagne, M. C. Chong, E. Lorchat, S. Berciaud, M. Romeo, H. Bulou, A. Boeglin, F. Scheurer, and G. Schull. Vibronic spectroscopy with submolecular resolution from STM-induced electroluminescence. *Phys. Rev. Lett.*, 118(12):127401, 2017.
- [58] R. Berndt and J. K. Gimzewski. Injection luminescence from CdS (112<sup>-</sup> 0) studied with scanning tunneling microscopy. *Phys. Rev. B*, 45(24):14095–14099, 1992.
- [59] L. Montelius, M.-E. Pistol, and L. Samuelson. Low-temperature luminescence due to minority carrier injection from the scanning tunneling microscope tip. *Ultramicroscopy*, 42–44:210–214, 1992.
- [60] D. L. Abraham, A. Veider, Ch. Schönenberger, H. P. Meier, D. J. Arent, and S. F. Alvarado. Nanometer resolution in luminescence microscopy of III-V heterostructures. *Appl. Phys. Lett.*, 56(16):1564–1566, 1990.

- [61] S. F. Alvarado, Ph. Renaud, D. L. Abraham, Ch. Schönenberger, D. J. Arent, and H. P. Meier. Luminescence in scanning tunneling microscopy on III–V nanostructures. *J. Vac. Sci. Technol. B: Microelectron. Nanometer Struct. Process. Meas. Phenom.*, 9(2):409–413, 1991.
- [62] Ph. Renaud and S. F. Alvarado. Mapping quantum-well energy profiles of III-V heterostructures by scanning-tunneling-microscope-excited luminescence. *Phys. Rev. B*, 44(12):6340–6343, 1991.
- [63] S. Ushioda. Scanning tunneling microscope (STM) light emission spectroscopy of surface nanostructures. *J. Electron Spectrosc. Relat. Phenom.*, 109(1-2):169–181, 2000.
- [64] M. Pfister, M. B. Johnson, S. F. Alvarado, H. W. M. Salemink, U. Marti, D. Martin, F. Morier-Genoud, and F. K. Reinhart. Atomic structure and luminescence excitation of GaAs/(AlAs)<sub>n</sub>(GaAs)<sub>m</sub> quantum wires with the scanning tunneling microscope. *Appl. Phys. Lett.*, 65(9):1168–1170, 1994.
- [65] L. Samuelson, A. Gustafsson, J. Lindahl, L. Montelius, M.-E. Pistol, J.-O. Malm, G. Vermeire, and P. Demeester. Scanning tunneling microscope and electron beam induced luminescence in quantum wires. *J. Vac. Sci. Technol. B: Microelectron. Nanometer Struct. Process. Meas. Phenom.*, 12(4):2521–2526, 1994.
- [66] J. Lindahl, M.-E. Pistol, L. Montelius, and L. Samuelson. Stark effect in individual luminescent centers observed by tunneling luminescence. *Appl. Phys. Lett.*, 68(1):60–62, 1996.
- [67] K. Yamanaka, K. Suzuki, S. Ishida, and Y. Arakawa. Light emission from individual self-assembled InAs/GaAs quantum dots excited by tunneling current injection. *Appl. Phys. Lett.*, 73(11):1460–1462, 1998.
- [68] U. Håkanson, M. K.-J. Johansson, M. Holm, C. Pryor, L. Samuelson, W. Seifert, and M.-E. Pistol. Photon mapping of quantum dots using a scanning tunneling microscope. *Appl. Phys. Lett.*, 81(23):4443–4445, 2002.
- [69] K. S. Novoselov, A. K. Geim, S. V. Morozov, D. Jiang, Y. Zhang, S. V. Dubonos, I. V. Grigorieva, and A. A. Firsov. Electric field effect in atomically thin carbon films. *Science*, 306(5696):666–669, 2004.
- [70] A. K. Geim and K. S. Novoselov. The rise of graphene. *Nat. Mater.*, 6(3):183–191, 2007.
- [71] Yujing Ma. *Two Dimensional Layered Materials and Heterostructures, a Surface Science Investigation and Characterization*. PhD thesis, University of South Florida, 2017.
- [72] M. Chhowalla, H. S. Shin, G. Eda, L.-J. Li, K. P. Loh, and H. Zhang. The chemistry of two-dimensional layered transition metal dichalcogenide nanosheets. *Nat. Chem.*, 5(4):263–275, 2013.

- [73] C. Ataca, H. Sahin, and S. Ciraci. Stable, single-layer  $\text{MX}_2$  transition-metal oxides and dichalcogenides in a honeycomb-like structure. *J. Phys. Chem. C*, 116(16):8983–8999, 2012.
- [74] J. A. Wilson and A. D. Yoffe. The transition metal dichalcogenides discussion and interpretation of the observed optical, electrical and structural properties. *Adv. Phys.*, 18(73):193–335, 1969.
- [75] A. Kuc and T. Heine. The electronic structure calculations of two-dimensional transition-metal dichalcogenides in the presence of external electric and magnetic fields. *Chem. Soc. Rev.*, 44(9):2603–2614, 2015.
- [76] Y. Zhang, T.-R. Chang, B. Zhou, Y.-T. Cui, H. Yan, Z. Liu, F. Schmitt, J. Lee, R. Moore, Y. Chen, H. Lin, H.-T. Jeng, S.-K. Mo, Z. Hussain, A. Bansil, and Z.-X. Shen. Direct observation of the transition from indirect to direct bandgap in atomically thin epitaxial  $\text{MoSe}_2$ . *Nat. Nanotechnol.*, 9(2):111–115, 2014.
- [77] J. Kang, L. Zhang, and S.-H. Wei. A unified understanding of the thickness-dependent bandgap transition in hexagonal two-dimensional semiconductors. *J. Phys. Chem. Lett.*, 7(4):597–602, 2016.
- [78] J. C. Shaw, H. Zhou, Y. Chen, N. O. Weiss, Y. Liu, Y. Huang, and X. Duan. Chemical vapor deposition growth of monolayer  $\text{MoSe}_2$  nanosheets. *Nano Res.*, 7(4):511–517, 2014.
- [79] H.-L. Liu, C.-C. Shen, S.-H. Su, C.-L. Hsu, M.-Y. Li, and L.-J. Li. Optical properties of monolayer transition metal dichalcogenides probed by spectroscopic ellipsometry. *Appl. Phys. Lett.*, 105(20):201905, 2014.
- [80] X. Wang, Y. Gong, G. Shi, W. L. Chow, K. Keyshar, G. Ye, R. Vajtai, J. Lou, Z. Liu, E. Ringe, B. K. Tay, and P. M. Ajayan. Chemical vapor deposition growth of crystalline monolayer  $\text{MoSe}_2$ . *ACS Nano*, 8(5):5125–5131, 2014.
- [81] W. Zhang, K. Matsuda, and Y. Miyauchi. Photostability of monolayer transition-metal dichalcogenides in ambient air and acidic/basic aqueous solutions. *ACS Omega*, 4(6):10322–10327, 2019.
- [82] K. F. Mak, C. Lee, J. Hone, J. Shan, and T. F. Heinz. Atomically thin  $\text{MoS}_2$ : a new direct-gap semiconductor. *Phys. Rev. Lett.*, 105(13):136805, 2010.
- [83] A. Splendiani, L. Sun, Y. Zhang, T. Li, J. Kim, C.-Y. Chim, G. Galli, and F. Wang. Emerging photoluminescence in monolayer  $\text{MoS}_2$ . *Nano Lett.*, 10(4):1271–1275, 2010.
- [84] E. M. Alexeev, A. Catanzaro, O. V. Skrypka, P. K. Nayak, S. Ahn, S. Pak, J. Lee, J. I. Sohn, K. S. Novoselov, H. S. Shin, and A. I. Tartakovskii. Imaging of interlayer coupling in van der Waals heterostructures using a bright-field optical microscope. *Nano Lett.*, 17(9):5342–5349, 2017.

- [85] R. Péchou, S. Jia, J. Rigor, O. Guillermet, G. Seine, J. Lou, N. Large, A. Mlayah, and R. Coratger. Plasmonic-Induced Luminescence of MoSe<sub>2</sub> Monolayers in a Scanning Tunneling Microscope. *ACS Photonics*, 7(11):3061–3070, 2020.
- [86] S. Tongay, J. Suh, C. Ataca, W. Fan, A. Luce, J. S. Kang, J. Liu, C. Ko, R. Raghunathanan, J. Zhou, F. Ogletree, J. Li, J. C. Grossman, and J. Wu. Defects activated photoluminescence in two-dimensional semiconductors: interplay between bound, charged and free excitons. *Sci. Rep.*, 3(1):2657, 2013.
- [87] G.-B. Liu, W.-Y. Shan, Y. Yao, W. Yao, and D. Xiao. Three-band tight-binding model for monolayers of group-VIB transition metal dichalcogenides. *Phys. Rev. B*, 88(8):085433, 2013.
- [88] R. Roldán, J. A. Silva-Guillén, M. P. López-Sancho, F. Guinea, E. Cappelluti, and P. Ordejón. Electronic properties of single-layer and multilayer transition metal dichalcogenides MX<sub>2</sub> (M= Mo, W and X= S, Se). *Ann. Phys.*, 526(9-10):347–357, 2014.
- [89] G.-B. Liu, D. Xiao, Y. Yao, X. Xu, and W. Yao. Electronic structures and theoretical modelling of two-dimensional group-VIB transition metal dichalcogenides. *Chem. Soc. Rev.*, 44(9):2643–2663, 2015.
- [90] G. Wang, A. Chernikov, M. M. Glazov, T. F. Heinz, X. Marie, T. Amand, and B. Urbaszek. Colloquium: Excitons in atomically thin transition metal dichalcogenides. *Rev. Mod. Phys.*, 90(2):021001, 2018.
- [91] J. A. Reyes-Retana and F. Cervantes-Sodi. Spin-orbital effects in metal-dichalcogenide semiconducting monolayers. *Sci. Rep.*, 6(1):24093, 2016.
- [92] D. Xiao, G.-B. Liu, W. Feng, X. Xu, and W. Yao. Coupled spin and valley physics in monolayers of MoS<sub>2</sub> and other group-VI dichalcogenides. *Phys. Rev. Lett.*, 108(19):196802, 2012.
- [93] M. Fox. *Optical properties of solids*, 2002.
- [94] D. Y. Qiu, F. H. Da Jornada, and S. G. Louie. Optical spectrum of MoS<sub>2</sub>: many-body effects and diversity of exciton states. *Phys. Rev. Lett.*, 111(21):216805, 2013.
- [95] A. Chernikov, T. C. Berkelbach, H. M. Hill, A. Rigosi, Y. Li, B. Aslan, D. R. Reichman, M. S. Hybertsen, and T. F. Heinz. Exciton binding energy and nonhydrogenic Rydberg series in monolayer WS<sub>2</sub>. *Phys. Rev. Lett.*, 113(7):076802, 2014.
- [96] M. M. Ugeda, A. J. Bradley, S.-F. Shi, F. H. Da Jornada, Y. Zhang, D. Y. Qiu, W. Ruan, S.-K. Mo, Z. Hussain, Z.-X. Shen, F. Wang, S. G. Louie, and M. F. Crommie. Giant bandgap renormalization and excitonic effects in a monolayer transition metal dichalcogenide semiconductor. *Nat. Mater.*, 13(12):1091–1095, 2014.

- [97] J. Jadcak, J. Kutrowska-Girzycka, P. Kapuściński, Y. S. Huang, A. Wójs, and L. Bryja. Probing of free and localized excitons and trions in atomically thin  $\text{WSe}_2$ ,  $\text{WS}_2$ ,  $\text{MoSe}_2$  and  $\text{MoS}_2$  in photoluminescence and reflectivity experiments. *Nanotechnology*, 28(39):395702, 2017.
- [98] K. F. Mak, K. He, C. Lee, G. H. Lee, J. Hone, T. F. Heinz, and J. Shan. Tightly bound trions in monolayer  $\text{MoS}_2$ . *Nat. Mater.*, 12(3):207–211, 2013.
- [99] Y. You, X.-X. Zhang, T. C. Berkelbach, M. S. Hybertsen, D. R. Reichman, and T. F. Heinz. Observation of biexcitons in monolayer  $\text{WSe}_2$ . *Nat. Phys.*, 11(6):477–481, 2015.
- [100] E. Courtade, M. Semina, M. Manca, M. M. Glazov, C. Robert, F. Cadiz, G. Wang, T. Taniguchi, K. Watanabe, M. Pierre, W. Escoffier, E. L. Ivchenko, P. Renucci, X. Marie, T. Amand, and B. Urbaszek. Charged excitons in monolayer  $\text{WSe}_2$ : Experiment and theory. *Phys. Rev. B*, 96(8):085302, 2017.
- [101] A. Ayari, E. Cobas, O. Ogundadegbe, and M. S. Fuhrer. Realization and electrical characterization of ultrathin crystals of layered transition-metal dichalcogenides. *J. Appl. Phys.*, 101(1):014507, 2007.
- [102] J. S. Ross, S. Wu, H. Yu, N. J. Ghimire, A. M. Jones, G. Aivazian, J. Yan, D. G. Mandrus, D. Xiao, W. Yao, and X Xu. Electrical control of neutral and charged excitons in a monolayer semiconductor. *Nat. Commun.*, 4(1):1474, 2013.
- [103] A. Srivastava, M. Sidler, A. V. Allain, D. S. Lembke, A. Kis, and A. Imamoglu. Optically active quantum dots in monolayer  $\text{WSe}_2$ . *Nat. Nanotechnol.*, 10(6):491–496, 2015.
- [104] C. Chakraborty, K. M. Goodfellow, and A. N. Vamivakas. Localized emission from defects in  $\text{MoSe}_2$  layers. *Opt. Mater. Express*, 6(6):2081–2087, 2016.
- [105] B. Schuler, K. A. Cochrane, C. Kastl, E. S. Barnard, E. Wong, N. J. Borys, A. M. Schwartzberg, D. F. Ogletree, F. J. G. de Abajo, and A. Weber-Bargioni. Electrically driven photon emission from individual atomic defects in monolayer  $\text{WS}_2$ . *Sci. Adv.*, 6(38):eabb5988, 2020.
- [106] A. Ramasubramaniam. Large excitonic effects in monolayers of molybdenum and tungsten dichalcogenides. *Phys. Rev. B*, 86(11):115409, 2012.
- [107] T. Cheiwchanamngij and W. R. L. Lambrecht. Quasiparticle band structure calculation of monolayer, bilayer, and bulk  $\text{MoS}_2$ . *Phys. Rev. B*, 85(20):205302, 2012.
- [108] K Kośmider, J. W. González, and J. Fernández-Rossier. Large spin splitting in the conduction band of transition metal dichalcogenide monolayers. *Phys. Rev. B*, 88(24):245436, 2013.
- [109] V. Iberi, L. Liang, A. V. Ievlev, M. G. Stanford, M.-W. Lin, X. Li, M. Mahjouri-Samani, S. Jesse, B. G. Sumpter, S. V. Kalinin, D. C. Joy, K. Xiao, A. Belianinov, and O. S. Ovchinnikova.

- Nanoforging single layer MoSe<sub>2</sub> through defect engineering with focused helium ion beams. *Sci. Rep.*, 6(1):30481, 2016.
- [110] X.-X. Zhang, Y. You, S. Y. F. Zhao, and T. F. Heinz. Experimental evidence for dark excitons in monolayer WSe<sub>2</sub>. *Phys. Rev. Lett.*, 115(25):257403, 2015.
- [111] S.-Y. Chen, M. Pieczarka, M. Wurdack, E. Estrecho, T. Taniguchi, K. Watanabe, J. Yan, E. A. Ostrovskaia, and M. S. Fuhrer. Long-lived populations of momentum-and spin-indirect excitons in monolayer WSe<sub>2</sub>. *arXiv preprint arXiv:2009.09602*, 2020.
- [112] M. M. Glazov, T. Amand, X. Marie, D. Lagarde, L. Bouet, and B. Urbaszek. Exciton fine structure and spin decoherence in monolayers of transition metal dichalcogenides. *Phys. Rev. B*, 89(20):201302, 2014.
- [113] A. O. Slobodeniuk and D. M. Basko. Spin-flip processes and radiative decay of dark intravalley excitons in transition metal dichalcogenide monolayers. *2D Mater.*, 3(3):035009, 2016.
- [114] G. Wang, C. Robert, M. M. Glazov, F. Cadiz, E. Courtade, T. Amand, D. Lagarde, T. Taniguchi, K. Watanabe, B. Urbaszek, and X. Marie. In-plane propagation of light in transition metal dichalcogenide monolayers: optical selection rules. *Phys. Rev. Lett.*, 119(4):047401, 2017.
- [115] Y. Zhou, G. Scuri, D. S. Wild, A. A. High, A. Dibos, L. A. Jauregui, C. Shu, K. De Greve, K. Pistunova, A. Y. Joe, T. Taniguchi, K. Watanabe, P. Kim, M. D. Lukin, and H. Park. Probing dark excitons in atomically thin semiconductors via near-field coupling to surface plasmon polaritons. *Nat. Nanotechnol.*, 12(9):856–860, 2017.
- [116] D. Kozawa, R. Kumar, A. Carvalho, K. Kumar Amara, W. Zhao, S. Wang, M. Toh, R. M. Ribeiro, A. H. Castro Neto, K. Matsuda, and G. Eda. Photocarrier relaxation pathway in two-dimensional semiconducting transition metal dichalcogenides. *Nat. Commun.*, 5(1):4543, 2014.
- [117] Ines Abid. *Plasmonique hybride : Propriétés optiques de nanostructures Au-TMD, couplage plasmon-exciton*. PhD thesis, Université Paul Sabatier, 2017.
- [118] W. Yao, D. Xiao, and Q. Niu. Valley-dependent optoelectronics from inversion symmetry breaking. *Phys. Rev. B*, 77(23):235406, 2008.
- [119] T. Cao, G. Wang, W. Han, H. Ye, C. Zhu, J. Shi, Q. Niu, P. Tan, E. Wang, B. Liu, and J. Feng. Valley-selective circular dichroism of monolayer molybdenum disulphide. *Nat. Commun.*, 3(1):887, 2012.
- [120] K. F. Mak, K. He, J. Shan, and T. F. Heinz. Control of valley polarization in monolayer MoS<sub>2</sub> by optical helicity. *Nat. Nanotechnol.*, 7(8):494–498, 2012.

- [121] G. Sallen, L. Bouet, X. Marie, G. Wang, C. R. Zhu, W. P. Han, Y. Lu, P. H. Tan, T. Amand, B. L. Liu, and B. Urbaszek. Robust optical emission polarization in MoS<sub>2</sub> monolayers through selective valley excitation. *Phys. Rev. B*, 86(8):081301, 2012.
- [122] H. Zeng, J. Dai, W. Yao, D. Xiao, and X. Cui. Valley polarization in MoS<sub>2</sub> monolayers by optical pumping. *Nat. Nanotechnol.*, 7(8):490–493, 2012.
- [123] M. M. Glazov, E. L. Ivchenko, G. Wang, T. Amand, X. Marie, B. Urbaszek, and B. L. Liu. Spin and valley dynamics of excitons in transition metal dichalcogenide monolayers. *Phys. Status Solidi B*, 252(11):2349–2362, 2015.
- [124] A. M. Jones, H. Yu, N. J. Ghimire, S. Wu, G. Aivazian, J. S. Ross, B. Zhao, J. Yan, D. G. Mandrus, D. Xiao, W. Yao, and X. Xu. Optical generation of excitonic valley coherence in monolayer WSe<sub>2</sub>. *Nat. Nanotechnol.*, 8(9):634–638, 2013.
- [125] T. Yu and M. W. Wu. Valley depolarization due to intervalley and intravalley electron-hole exchange interactions in monolayer MoS<sub>2</sub>. *Phys. Rev. B*, 89(20):205303, 2014.
- [126] I. Kylänpää and H.-P. Komsa. Binding energies of exciton complexes in transition metal dichalcogenide monolayers and effect of dielectric environment. *Phys. Rev. B*, 92(20):205418, 2015.
- [127] A. V. Stier, N. P. Wilson, G. Clark, X. Xu, and S. A. Crooker. Probing the influence of dielectric environment on excitons in monolayer WSe<sub>2</sub>: insight from high magnetic fields. *Nano Lett.*, 16(11):7054–7060, 2016.
- [128] M. L. Trolle, T. G. Pedersen, and V. Véniard. Model dielectric function for 2D semiconductors including substrate screening. *Sci. Rep.*, 7(1):1–9, 2017.
- [129] M. Cotrufo, L. Sun, J. Choi, A. Alù, and X. Li. Enhancing functionalities of atomically thin semiconductors with plasmonic nanostructures. *Nanophotonics*, 8(4):577–598, 2019.
- [130] M. Grzeszczyk, M. R. Molas, K. Nogajewski, M. Bartoš, A. Bogucki, C. Faugeras, P. Kossacki, A. Babiński, and M. Potemski. The effect of metallic substrates on the optical properties of monolayer MoSe<sub>2</sub>. *Sci. Rep.*, 10(1):4981, 2020.
- [131] A. Raja, A. Chaves, J. Yu, G. Arefe, H. M. Hill, A. F. Rigosi, T. C. Berkelbach, P. Nagler, C. Schüller, T. Korn, C. Nuckolls, J. Hone, L. E. Brus, T. F. Heinz, D. R. Reichman, and A. Chernikov. Coulomb engineering of the bandgap and excitons in two-dimensional materials. *Nat. Commun.*, 8(1):15251, 2017.
- [132] X. Li, J. Zhu, and B. Wei. Hybrid nanostructures of metal/two-dimensional nanomaterials for plasmon-enhanced applications. *Chem. Soc. Rev.*, 45(11):3145–3187, 2016.

- [133] I. Abid, A. Bohloul, S. Najmaei, C. Avendano, H.-L. Liu, R. P echou, A. Mlayah, and J. Lou. Resonant surface plasmon–exciton interaction in hybrid MoSe<sub>2</sub>@Au nanostructures. *Nanoscale*, 8(15):8151–8159, 2016.
- [134] I. Abid, W. Chen, J. Yuan, A. Bohloul, S. Najmaei, C. Avendano, R. P echou, A. Mlayah, and J. Lou. Temperature-dependent plasmon–exciton interactions in hybrid Au/MoSe<sub>2</sub> nanostructures. *ACS Photonics*, 4(7):1653–1660, 2017.
- [135] M.-E. Kleemann, R. Chikkaraddy, E. M. Alexeev, D. Kos, C. Carnegie, W. Deacon, A. C. De Pury, C. Gro e, B. De Nijs, J. Mertens, A. I. Tartakovskii, and J. J. Baumberg. Strong-coupling of WSe<sub>2</sub> in ultra-compact plasmonic nanocavities at room temperature. *Nat. Commun.*, 8(1):1296, 2017.
- [136] J. Cuadra, D. G. Baranov, M. Wersall, R. Verre, T. J. Antosiewicz, and T. Shegai. Observation of tunable charged exciton polaritons in hybrid monolayer WS<sub>2</sub>–plasmonic nanoantenna system. *Nano Lett.*, 18(3):1777–1785, 2018.
- [137] X. Han, K. Wang, X. Xing, M. Wang, and P. Lu. Rabi splitting in a plasmonic nanocavity coupled to a WS<sub>2</sub> monolayer at room temperature. *ACS Photonics*, 5(10):3970–3976, 2018.
- [138] S. Hou, L. Y. M. Tobing, X. Wang, Z. Xie, J. Yu, J. Zhou, D. Zhang, C. Dang, P. Coquet, B. K. Tay, M. D. Birowosuto, E. H. T. Teo, and H. Wang. Manipulating coherent light–matter interaction: continuous transition between strong coupling and weak coupling in MoS<sub>2</sub> monolayer coupled with plasmonic nanocavities. *Adv. Opt. Mater.*, 7(22):1900857, 2019.
- [139] U. Bhanu, M. R. Islam, L. Tetard, and S. I. Khondaker. Photoluminescence quenching in gold-MoS<sub>2</sub> hybrid nanoflakes. *Sci. Rep.*, 4(1):5575, 2014.
- [140] Y. Kang, S. Najmaei, Z. Liu, Y. Bao, Y. Wang, X. Zhu, N. J. Halas, P. Nordlander, P. M. Ajayan, J. Lou, and Z. Fang. Plasmonic hot electron induced structural phase transition in a MoS<sub>2</sub> monolayer. *Adv. Mater.*, 26(37):6467–6471, 2014.
- [141] Z. Li, Y. Xiao, Y. Gong, Z. Wang, Y. Kang, S. Zu, P. M. Ajayan, P. Nordlander, and Z. Fang. Active light control of the MoS<sub>2</sub> monolayer exciton binding energy. *ACS Nano*, 9(10):10158–10164, 2015.
- [142] I. Abid, P. Benzo, B. P ecassou, S. Jia, J. Zhang, J. Yuan, J. B. Dory, O. G. Lafaye, R. P echou, and A. Mlayah. Plasmon damping and charge transfer pathways in Au@MoSe<sub>2</sub> nanostructures. *Mater. Today Nano*, 15:100131, 2021.
- [143] A. Sobhani, A. Lauchner, S. Najmaei, C. Ayala-Orozco, F. Wen, J. Lou, and N. J. Halas. Enhancing the photocurrent and photoluminescence of single crystal monolayer MoS<sub>2</sub> with resonant plasmonic nanoshells. *Appl. Phys. Lett.*, 104(3):031112, 2014.

- 
- [144] G. M. Akselrod, T. Ming, C. Argyropoulos, T. B. Hoang, Y. Lin, X. Ling, D. R. Smith, J. Kong, and M. H. Mikkelsen. Leveraging nanocavity harmonics for control of optical processes in 2D semiconductors. *Nano Lett.*, 15(5):3578–3584, 2015.
- [145] B. Lee, J. Park, G. H. Han, H.-S. Ee, C. H. Naylor, W. Liu, A. T. C. Johnson, and R. Agarwal. Fano resonance and spectrally modified photoluminescence enhancement in monolayer MoS<sub>2</sub> integrated with plasmonic nanoantenna array. *Nano Lett.*, 15(5):3646–3653, 2015.
- [146] Z. Wang, Z. Dong, Y. Gu, Y.-H. Chang, L. Zhang, L.-J. Li, W. Zhao, G. Eda, W. Zhang, G. Grinblat, S. A. Maier, J. K. W. Yang, C.-W. Qiu, and A. T. S. Wee. Giant photoluminescence enhancement in tungsten-diselenide–gold plasmonic hybrid structures. *Nat. Commun.*, 7(1):11283, 2016.
- [147] S. Butun, S. Tongay, and K. Aydin. Enhanced light emission from large-area monolayer MoS<sub>2</sub> using plasmonic nanodisc arrays. *Nano Lett.*, 15(4):2700–2704, 2015.
- [148] E. Palacios, S. Park, S. Butun, L. Lauhon, and K. Aydin. Enhanced radiative emission from monolayer MoS<sub>2</sub> films using a single plasmonic dimer nanoantenna. *Appl. Phys. Lett.*, 111(3):031101, 2017.

## Chapter 2

# Experimental tools and simulation methods

This chapter deals with the description of the experimental techniques and numerical methods used in this thesis. The first part of this chapter focuses on the experimental setup used to conduct STM-induced light emission measurements. Details of the customized STM and light detection system to which it is coupled are presented. This section is followed by a discussion on the preparation of the  $MoSe_2$  monolayers studied in Chapter 3. In addition to Scanning Tunneling Microscopy, the samples were characterized by Photoluminescence Spectroscopy and Atomic Force Microscopy, in order to improve our understanding of their optical and mechanical properties. Both techniques are introduced in the second section of this chapter. The numerical electrodynamic simulations performed in Chapter 4 are based on the Dipole Discrete Approximation method. The latter and the Quantum-Corrected model, used to account for the STM tunneling effect in the simulations, are presented in the last section.

### 2.1 Experimental setup

The STM-LE experimental setup used in this work has been described in [1]. It consists of two main parts: the Scanning Tunneling Microscope (STM) itself and the light detection system. Both are associated in order to observe and characterize the light emission stimulated by the localized STM tunneling current. The STM setup and each component of the optical detection system are described in the first and second parts of this section. The preparation of gold tips used in our experiments is addressed in the last part of this section. The experimental setup introduced here is installed in a clean room and the experiments are conducted in ambient conditions at room temperature.

### 2.1.1 The STM setup

The experiments are carried out using a customized hybrid instrument based on a Bruker Veeco Dimension D3100 setup. It can operate either as a Scanning Tunneling Microscope (STM) or as an Atomic Force Microscope (AFM). All STM-induced light emission experiments presented in Chapter 3 were performed using the STM configuration in constant-current mode. As already explained in section 1.1.1 of Chapter 1, a feedback loop is used to adjust the z-position of the tip, and thus the relative tip-sample distance in order to maintain the tunneling current constant during the sample surface scan. The STM head consists of a customized tip-holder placed at the end of a cylindrical piezoelectric tube. The tunneling tip is inserted into a tip-holding tube, which is mounted on the STM tip-holder. In Figure 2.1-(A,B), the orientation of the tip-holder is depicted within a reference frame. The axis along the tip-holding tube lies in the xz plane at a  $30^\circ$  angle from the z-axis, the vertical with respect to tip-holder base. The optical fiber, used to collect the emitted light, is positioned at a  $45^\circ$  angle relative to the +z axis, +x axis, and -y axis. This fiber is placed on the STM tip-holder so that its end is about 1 mm from the tip apex. Figure 2.1-C shows the tip-holder and piezoelectric tube with its electrode configuration. The voltage applied to the Z electrode controls the tip-sample distance, while the bias voltages applied to the  $\pm X$  and  $\pm Y$  electrodes deflect the piezoelectric tube horizontally to produce a precise scan over the sample surface. The tunneling tip is connected to ground and the positive or negative bias voltage  $V_s$  is applied to the conductive sample. The tunneling current from the high-impedance tunnel junction, which is typically in the pA to nA range for  $V_s$  in the mV to V range, is converted into a manageable voltage signal by a preamplifier mounted close to the STM head.

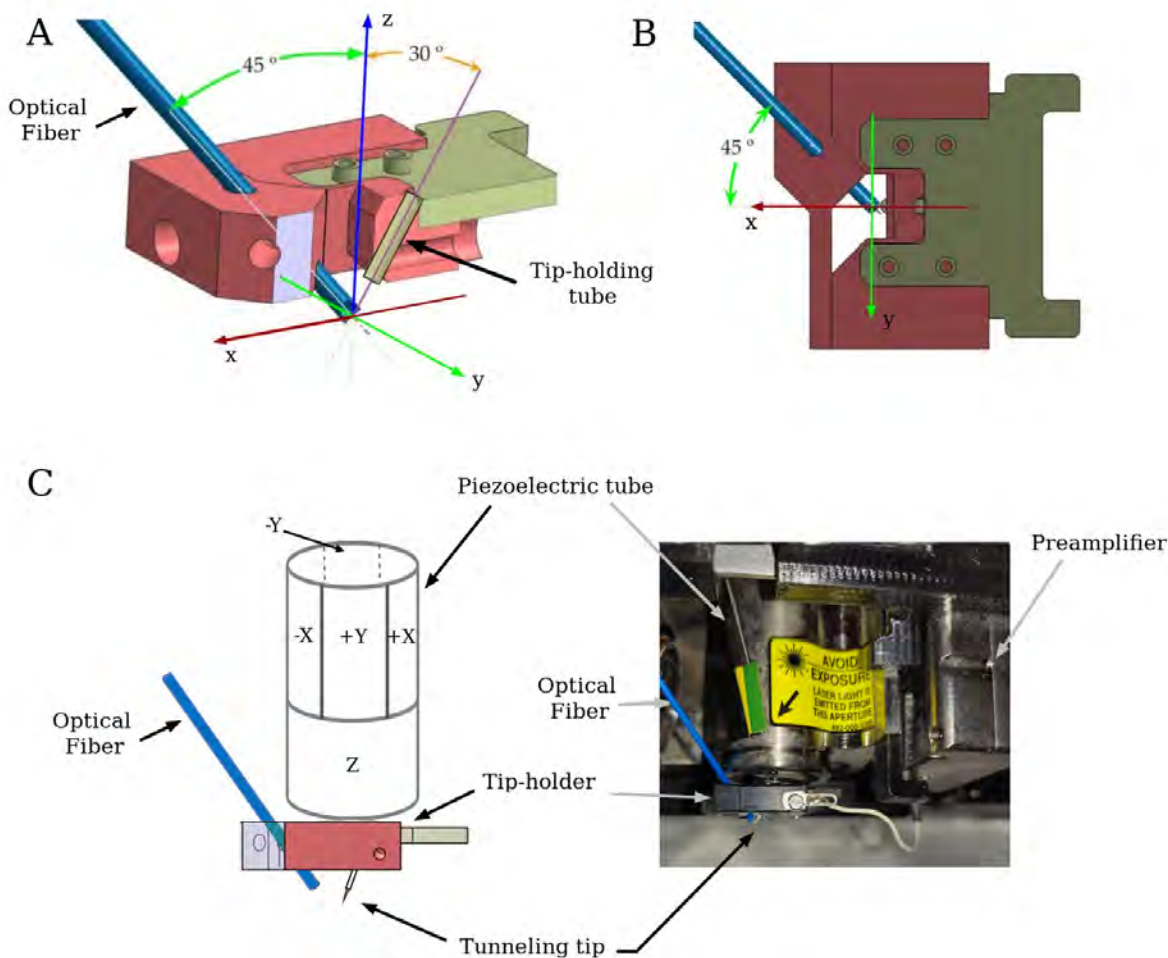


**Figure 2.1:** (A-B) Schematic representation of the tip-holder indicating the position of the optical fiber and the tip-holding tube. In the image (A), only half of the tip-holder is depicted. (C) Scheme (left) and picture (right) of the STM head.

The preamplifier employed has a sensitivity of a few nanoamperes per volt. The electrical feedback loop compares the voltage signal generated by the preamplifier with a reference voltage that reflects the user-defined setpoint current  $I_t$ . From this comparison, the feedback loop adjusts the tip-sample distance. The variation of the tip  $z$ -position is recorded at each lateral tip position  $(x, y)$ . This variation is encoded in color forming topographic images with a resolution in the nanometer range. The STM images recorded are formed by  $256 \times 256$  pixels and the pixel size depends on the user-defined scan size (Figure 2.6-A).

The sample is placed on a motorized X-Y stage that allows positioning the sample under the tip at the micron-scale. In addition, a motorized Z stage provides a precise approach (and withdraw) of the STM tip with respect to the sample surface until a tunnel distance is reached (see Figure 2.2). This configuration makes it possible to image different areas of a sample. Nanoscope III 5.13R1 software (Digital Instruments) allows the control of both stages as well as all the scanning tunneling parameters mentioned above. Topographic images are obtained from the data acquired in a line-by-line manner by the Nanoscope software and are analyzed using the WSxM software [2].

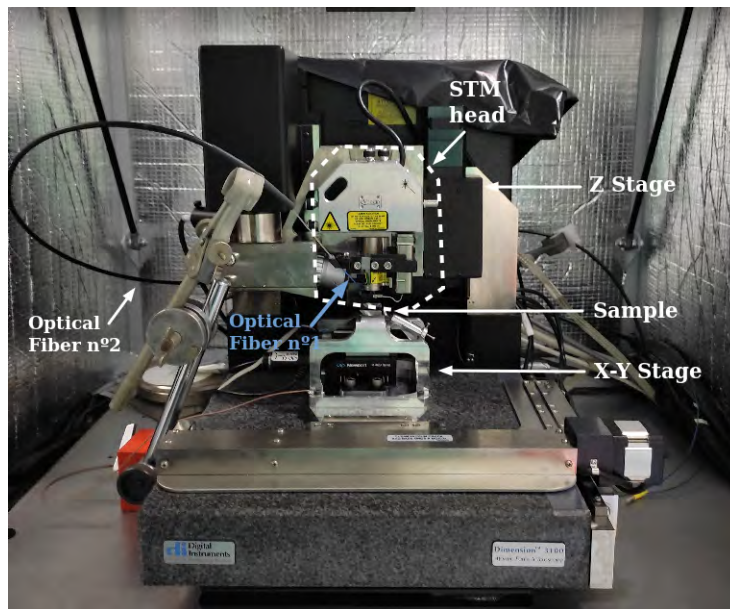


**Figure 2.2:** Picture of the STM inside the chamber.

Operating an STM in ambient conditions at room temperature makes sample and tip preparation easier. However, the resolution of STM images can be degraded by different factors. Temperature gradients may occur leading to thermal dilatation or shrinkage of STM components. In fact, the tip and the sample surface constantly shift with respect to each other, resulting in measurements of lower quality and topographic images with reduced resolution. The thermalization of the components is slow, which makes thermal drift more visible in the case of slow scanning. However, there are some methods to correct or compensate this effect [3–5]. In addition, using an STM in ambient conditions leads to adsorption of contaminants. This may affect the STM-induced light emission process and STM measurements and, in some cases, these contaminants can even damage the tunneling tip. Air currents can also disturb imaging with atomic resolution. To avoid these problems, it is necessary to protect the microscope. For this, the STM is placed in a chamber that blocks any air currents and acts as well as a Faraday cage to protect the STM from electromagnetic radiation (Figure 2.2). The chamber is located on a vibration-isolating table with air suspension to avoid acoustic and mechanical noise, since the resolution and stability of the STM tunneling are very sensitive to external vibrations. This setup is located in a clean room situated in the laboratory’s basement. Its open architecture allows not only an easy access to the sample and tip, but also an easy detection of the light emitted using the light detection system described below.

### 2.1.2 Light detection system

As mentioned above, the light emitted during STM tunneling is collected using an optical fiber (shown in blue in Figure 2.1). It is positioned at a distance of about 1 mm from the tip apex and its axis is tilted by an angle of  $45^\circ$  with respect to the base of the tip-holder. To maximize light-collecting efficiency, an optical fiber from ThorLabs with a core diameter of  $D=600\ \mu\text{m}$  and a large numerical

aperture (NA) of 0.48 has been chosen. In this configuration, light collection takes place in a particular direction and the effective solid angle  $\Omega$  is estimated to be  $\Omega = \frac{\pi D^2}{4a^2} = \frac{9\pi}{100} \sim 0.28$  sr (steradians). The collected light is transmitted outside of the STM chamber for optical analysis and detection. The fiber used to collect the light emitted by the tunnel junction is quite short to facilitate its placement as close as possible to the STM tip-surface gap. Hence, the light collected by this first fiber is delivered to a second optical fiber measuring 2.5 m in length and having a core diameter of 1.1 mm (see Figure 2.2). The latter is held in place by clamps and it is connected to either a spectrometer or to the optical window of a photomultiplier tube (PMT). It is worth noting that STM-LE measurements are performed under dark conditions, so the STM chamber is equipped to avoid any light leakage from outside.

### a) Spectrometer

The collected light can be transferred to a spectrometer for spectral analysis of the emitted photons. The spectrometer used (Princeton Instrument Acton SpectraPro-150) consists of a grating dispersion device coupled to a liquid-nitrogen cooled CCD detector (LN/CCD-1340/400-EB1, Princeton Instruments Roper Scientific). A grating with 150 grooves/mm blazed at 800 nm is used, providing a broad spectral region from 200 nm to 1400 nm. Weak STM-LE signals are often obtained in STM-LE experiments. For this reason, the spectrometer entrance slit is set to its maximum to improve the amount of light transmitted through the spectrometer. Even if this leads to a reduced spectral resolution, STM-LE spectra obtained with this spectrometer configuration have a typical resolution of about 1 nm. The CCD detector has a 1340 x 400 pixels matrix (each pixel has a size of  $20 \mu\text{m} \times 20 \mu\text{m}$ ) and its spectral response ranges from 400 nm to 1100 nm with a quantum yield maximum ( $\sim 50\%$ ) achieved at 700 nm (Figure 2.3). This detector has a low dark current on the order of 1 electron per hour and per pixel at the operating temperature of  $-100 \text{ }^\circ\text{C}$ . In our experiments, the operating temperature is approximately  $-120 \text{ }^\circ\text{C}$  and the acquisition time varies from 30 to 600 seconds, depending on the light-emission efficiency of the junction considered. WinSpec software is used for data acquisition and processing. It is as well employed for the wavelength calibration of the spectrometer which is performed with a mercury-vapor lamp and a neon lamp.

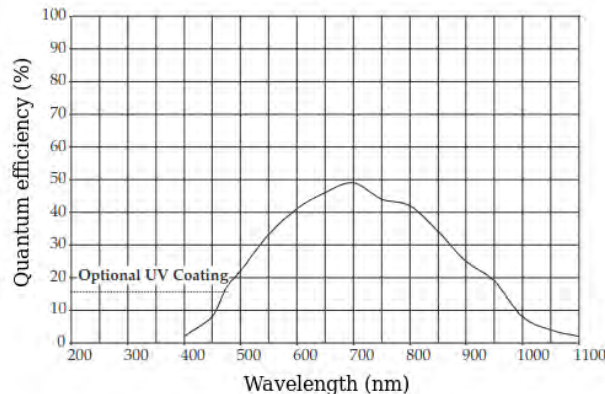


**Figure 2.3:** Quantum efficiency curve of the CCD detector (from [6]).

Due to the optical absorption of  $OH$  impurities present in the optical fibers employed, especially in the long optical fiber where the concentration of these impurities is higher (Figure 2.4-A), all STM-LE spectra obtained show an absorption dip around 940 nm (see Figure 2.4-B). It is important to note that all spectral measurements reported in this thesis are raw data, i.e., they are not corrected for the absorption of the optical fibers and for the spectral response of the measurement system.

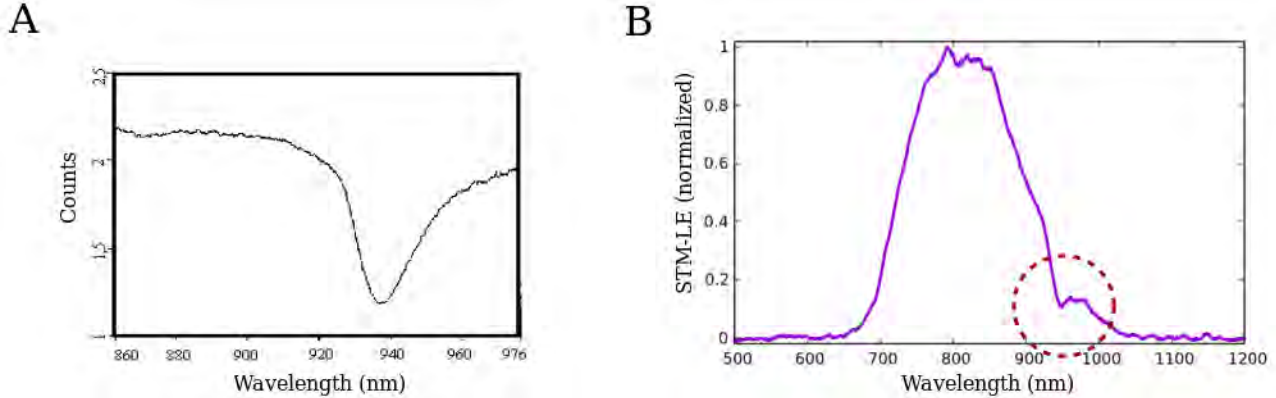


**Figure 2.4:** (A) Optical transmission spectrum of the long optical fiber (adapted from [7]) with an absorption dip at approximately 940 nm owing to  $OH$  impurities. (B) Typical STM-LE spectrum (normalized) obtained from an  $Au/MoSe_2/Au$  tunneling junction ( $V_s = -1.8$  V;  $I_t = 20$  nA and acquisition time: 90 s). The absorption dip is as well present (circled in red).

The quantum efficiency of the STM-induced light emission, defined as the number of emitted photons per injected charge carrier, can be deduced from an experimental spectrum. Indeed, by integrating the acquired spectrum and dividing it by the accumulation time, the number of photons emitted per second for a given tunneling current can be calculated. The photon emission efficiency is then obtained by dividing it by the number of electrons per second participating in the tunneling current. In this calculation, the solid angle of the collecting fiber and the quantum efficiency of the spectrometer must be taken into account. Typically, a quantum efficiency ranging from approximately  $10^{-8}$  to about  $10^{-6}$  photons per tunneling electron is obtained in our STM-LE experiments.

## b) Photomultiplier

A photomultiplier tube PMT (Hamamatsu Photonics, R943-02) is used for detection and quantification of the collected light. It consists of a  $GaAs$  photocathode followed by an electron multiplier. When a photon reaches the PMT photocathode, an electron is ejected. This electron is then accelerated in the PMT and ends up colliding with a dynode generating the release of several electrons. Finally, the number of electrons generated is counted, which is proportional to the number of photons at the detector input. The spectral window of the PMT ranges from 160 nm to 930 nm. In Figure 2.5, the photocathode sensitivity (photocurrent produced by the photocathode divided by the incident light power at a given wavelength) and the PMT quantum efficiency are plotted. Since the photocathode can produce a large amount of dark current at room temperature, the PMT is thermo-cooled to reach

an operating temperature of approximately  $-20$  °C. At this temperature, the dark current is about 20 counts per second.

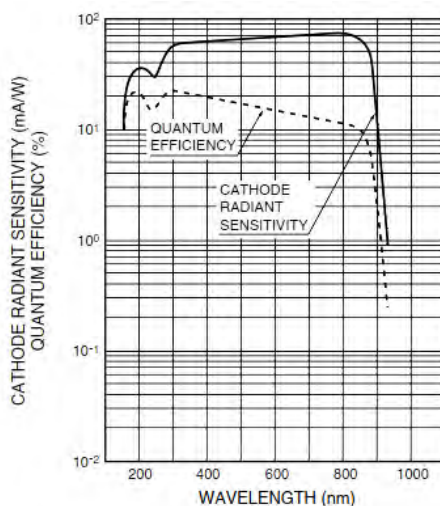


**Figure 2.5:** Spectral response (photocathode radiant sensitivity and quantum efficiency curves) of the R943-02 photomultiplier tube (from [8]).

The PMT is synchronized with the STM controller, enabling the simultaneous acquisition of the number of emitted photons and the STM topographic image during scanning. A LabVIEW code is used to perform the synchronized acquisition of both signals. The number of photons counted by the PMT is integrated over the time between two pixels of the STM image. This process generates photonic maps that represent the number of photons (encoded in color) counted at each pixel of the STM image. It is therefore possible to simultaneously produce a topographic STM image and a photonic map of the same area, as shown in Figure 2.6. Photonic maps have the same number of pixels ( $256 \times 256$ ) as the STM images. Their resolution is thus given by the chosen scan size. Photonic maps presented in this thesis are not corrected for the absorption of the optical fibers and for the response function of the PMT.

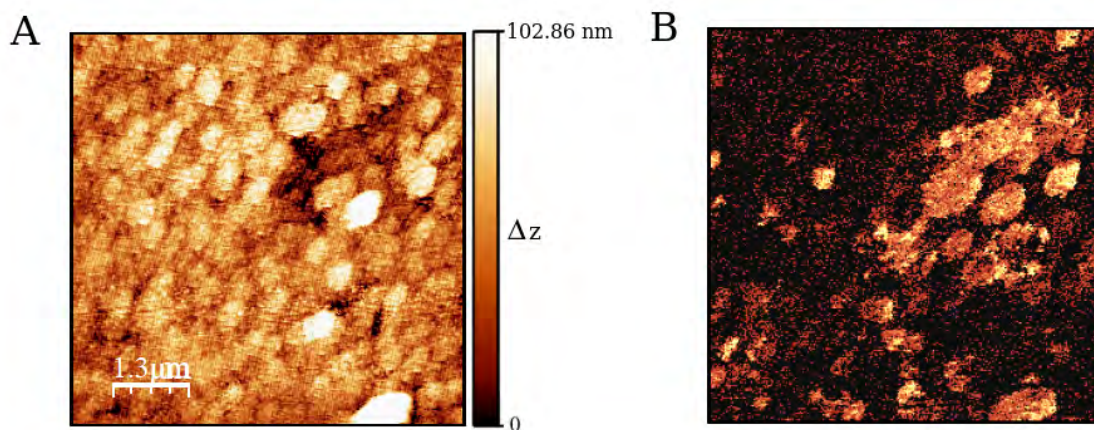


**Figure 2.6:** (A) STM topographic image and (B) corresponding photonic map recorded simultaneously on a  $6.5 \mu\text{m} \times 6.5 \mu\text{m}$  area. Each image consists of  $256 \times 256$  pixels. During the acquisition of the photonic map, an average of 275 counts per second is obtained. The sample is a  $\text{MoSe}_2$  monolayer deposited on a polycrystalline gold substrate ( $V_s = +1.8$  V;  $I_t = 15$  nA).

These measurements allow the correlation of the topography of the scanned surface with the photon emission. In Figure 2.6, this correlation is visible at the scale of a single gold grain (typical grain size of sub-100 nm). One can observe in the top right part of these images that an anomaly at the sample surface (a tear in the  $MoSe_2$  monolayer) leads to a more efficient light emission. The STM-LE quantum efficiency can be deduced from the number of photons per second counted by the PMT and taking into account the solid angle of the collecting fiber and the quantum efficiency of the PMT.

### 2.1.3 Gold tip preparation

The STM tips used in the experiments presented in Chapter 3 are gold tips fabricated from a 0.25 mm diameter  $Au$  wire (GoodFellow) by electrochemical etching. In fact, gold is a good candidate for STM-LE measurements as it provides a convenient plasmonic response in the visible range. Moreover, among other plasmonic metals, gold is more resistant to air oxidation and is therefore more stable under ambient conditions. However, due to its high ductility and high surface diffusion velocity, the shape of a gold tip apex can change during STM scanning and tunneling if high voltages  $V_s$  are applied. As mentioned in section 1.1.2 of Chapter 1, the tip geometry plays an important role in the light emission characteristics [9]. Hence, when analyzing the experimental STM-induced light emission, possible variations in the tip geometry during scanning must be taken into account for an accurate interpretation of the experimental observations.

The electrochemical etching process employed in this thesis has been described in detail in reference [10]. An electrolyte solution of concentrated hydrochloric acid ( $HCl$ ) and ethanol in a proportion of 1:1 is used. A gold ring, which is connected as the cathode, is placed on the surface of this solution so that 1/4 of the ring height is immersed in the solution. A gold wire as the anode is immersed in the center of the ring with an immersion length of a few mm (see Figure 2.7-A).

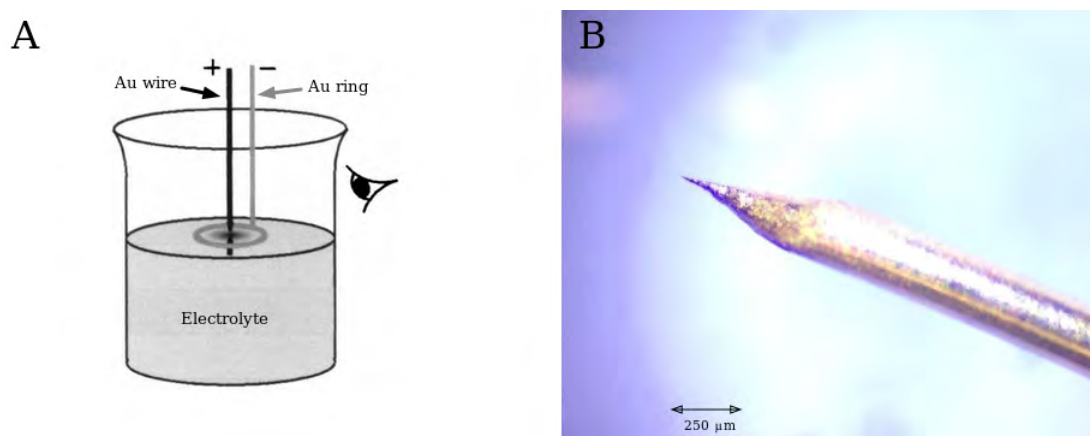


**Figure 2.7:** (A) Schematic diagram of the electrochemical etching setup used to fabricate gold tips (adapted from [10]). (B) Typical gold tip after etching imaged using an optical microscope.

It takes about 7 minutes to produce an  $Au$  tip using a direct current of about 8 mA with an etching voltage between 1.5 V and 2.5 V. After the etching process, the tip is rinsed with deionized water and

then cleaned with isopropanol to remove residual contaminants. The last step consists of examining the tip with an optical microscope to ensure that the tip is mesoscopically sharp (Figure 2.7-B). Gold tips with ultra-fine apexes giving rise to high-resolution STM images can be prepared by this method in a reproducible way. The obtained tips have a radius of curvature of a few tens of nm [10] which can be adjusted by playing with the etching parameters. However, this radius remains relatively large compared to the tip apex region where surface plasmon modes are localized (typically on the order of angstroms to a few nanometers).

## 2.2 TMD monolayer preparation and characterization

Chapter 3 of this thesis mainly focuses on the experimental STM-induced light emission from  $MoSe_2$  monolayers. The synthesis and transfer of  $MoSe_2$  monolayer flakes are presented in the first part of this section. The second part describes the operating principle of two characterization techniques, Photoluminescence (PL) Spectroscopy and Atomic Force Microscopy (AFM). Both techniques were used (see Chapter 3) to provide a better insight into the properties of the  $MoSe_2$  samples studied and a better understanding of the results from STM-LE experiments.

### 2.2.1 Synthesis and transfer of TMD monolayers

#### a) Synthesis

The TMD flakes studied in the thesis are grown by chemical vapor deposition (CVD). This synthesis process was carried out by the team of Pr. Jun Lou at Rice University. CVD is a popular bottom-up synthesis method for the controllable growth of high-quality, large-sized TMD-MLs, even up to the wafer scale, at a low cost [11, 12]. Although nanosheets grown by CVD present more defects compared to those synthesized by mechanical cleavage, in our case, CVD method is the best choice for the synthesis of  $MoSe_2$  monolayers to obtain large flakes, which facilitates their observation using STM microscopy. The growth of  $MoSe_2$  MLs takes place in a quartz tube where the substrate, in this case a  $SiO_2/Si$  film,  $MoO_3$  powder and selenium powder are placed (Figure 2.8-A). The tube is maintained at room temperature (25°C) for 20 minutes. During this period, the carrier gas (argon) flows along the tube to evacuate the water molecules contained in the air. The tube temperature is then increased to 765°C leading to the chalcogen and molybdenum evaporation which are subsequently deposited on the heated substrate. The vapor phase reaction results in the nucleation and growth of multi-layered and single-layered flakes of essentially triangular shape. The sides of these flakes have approximately the same length which varies from a few  $\mu\text{m}$  to a few hundred of  $\mu\text{m}$ . Very often, the monolayer flakes are not uniform and exhibit a multilayer area in the center (see Figure 2.8-B). In some cases, molybdenum oxides and sub-oxides are present at the crystalline edges of CVD grown flakes [13].

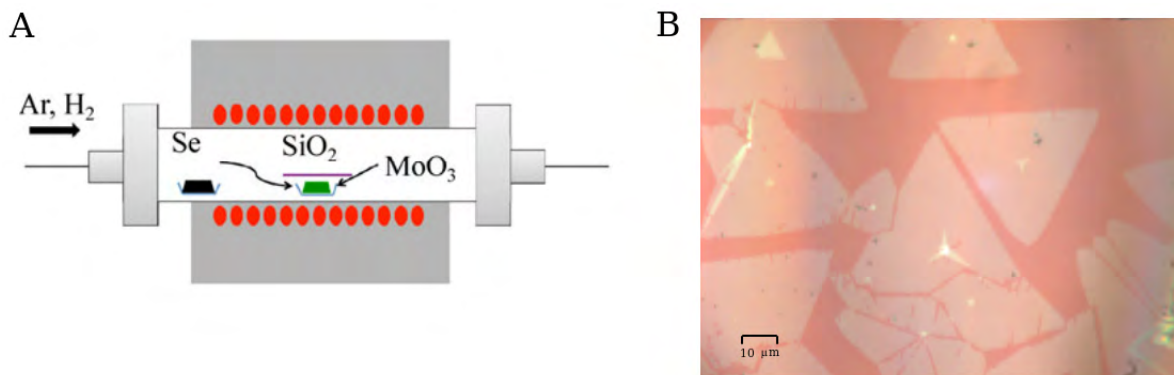


**Figure 2.8:** (A) Schematic representation of the CVD growth of  $MoSe_2$  flakes (from [12]). (B) Optical microscope image (x100) of CVD grown  $MoSe_2$  flakes transferred onto an indium tin oxide (ITO) substrate.

### b) Transfer

Once the  $MoSe_2$  flakes are synthesized, they are coated with a uniform-thick polymethylmetacrylate (PMMA) layer by spin coating. The coated sample is then immersed for hours into an aqueous potassium hydroxide ( $KOH$ ) solution to etch away the  $SiO_2/Si$  substrate. After several cleaning steps with deionized water to remove  $KOH$  residues, the PMMA/ $MoSe_2$  film floating in the solution is “fished” using a substrate of interest. The PMMA layer is then dissolved in acetone and the sample is finally washed with isopropanol and dried under nitrogen flow. In this thesis,  $MoSe_2$  flakes were transferred onto several different substrates such as gold, indium tin oxide (ITO) and graphite (see Chapter 3). All of these samples were deposited on a large and thick silica plate for better handling.

## 2.2.2 Characterization of TMD monolayers

### a) Photoluminescence spectroscopy

Photoluminescence (PL) spectroscopy is a rapid and non-invasive optical far-field technique that consists of exciting the sample with a laser beam and analyzing the light emitted by the sample. In our case, it is an interesting technique to induce light emission from  $MoSe_2$  monolayers using an optical source of excitation. For this, the laser wavelength must be selected according to the direct bandgap of the  $MoSe_2$  monolayer in order to induce the optical excitation and subsequently, the radiative decay of excitonic states. In fact, as seen in section 1.2.2 of Chapter 1,  $MoSe_2$  MLs exhibit exceptional optical properties, including strong photon absorption leading to the formation of excitons, bound electron-hole pairs. These excitons undergo relaxation processes, including radiative decay giving rise to photoluminescence spectra dominated by excitonic transitions [1, 14]. In addition to these transitions, light emission may be related to impurities or defects whose energy states lie within the forbidden gap [15]. Therefore, light emission spectra obtained by PL measurements can provide information on the bandgap, excitonic and defect states of  $MoSe_2$  MLs as well as on the competitive interplay between

radiative and non-radiative energy relaxation pathways. It is also worth mentioning that emission dynamics such as exciton radiative lifetime can be investigated from time-resolved PL experiments [16]. In this thesis, stationary photoluminescence measurements were performed on  $MoSe_2$  flakes obtained by CVD and transferred onto different substrates. These measurements, presented in Chapter 3, allow a fast quantitative characterization of the opto-electronic properties of these flakes. They were carried out at room temperature using Horiba Jobin Yvon Xplora MV2000 spectrometer (Figure 2.9-A). In all PL measurements, a laser wavelength of 532 nm is used, corresponding to an energy of 2.33 eV, higher than the  $MoSe_2$  ML electronic bandgap energy. The laser beam with a spot diameter of  $\sim 500$  nm is focused onto the sample by a X100 magnification objective with a numerical aperture NA of 0.90. The light emitted from the sample is collected by the microscope objective and then dispersed by a monochromator that can accommodate four different gratings (300 gr/mm, 600 gr/mm, 1800 gr/mm, and 2400 gr/mm). Finally, the signal is detected by a cooled-CCD detector. Acquisitions were made using typically 10 % of the maximum laser power ( $\sim 15.2$  mW). In addition, the spectrometer slit is set at  $200 \mu\text{m}$  and a dispersive grating of 600 gr/mm is employed, leading to a spectral resolution of  $\sim 0.2$  nm. For our measurements, a spectral range spanning from 700 nm to 900 nm and centred around the absorption wavelength of the  $MoSe_2$  monolayer exciton A (approximately 800 nm) is typically used (see Figure 2.9-B). Photoluminescence maps can also be obtained by scanning the sample and recording the PL signal at each scan pixel. This technique is called micro-photoluminescence because the resulting maps can achieve a spatial resolution slightly better than  $1 \mu\text{m}$ . All data were acquired and processed using the LabSpec Spectroscopy Software.

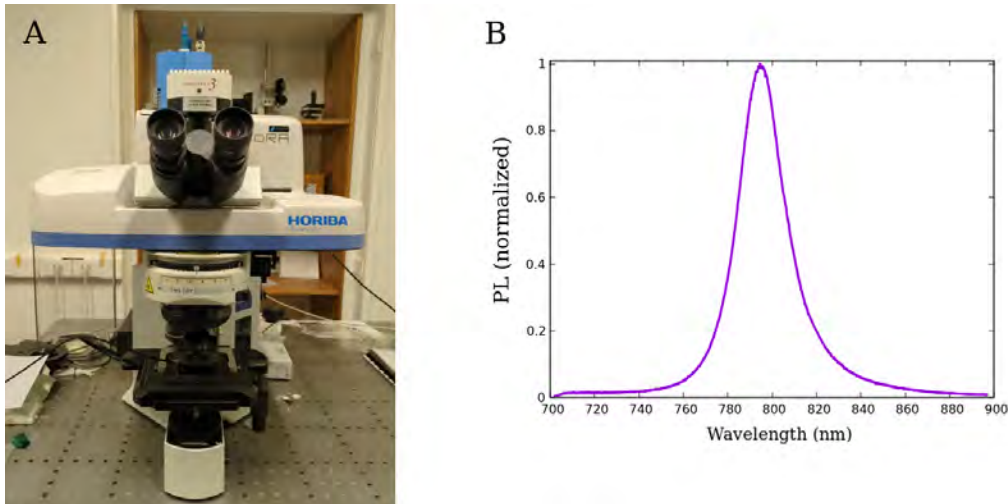


**Figure 2.9:** (A) Picture of the photoluminescence spectrometer. (B) Typical PL spectrum (normalized) obtained from a  $MoSe_2$  flake deposited on a gold substrate.

Compared to STM-LE experiments, PL spectroscopy is less time-consuming and provides a faster analysis of the optical properties of the  $MoSe_2$  flakes. Hence, before studying these samples by near-field STM-LE spectroscopy, far-field PL measurements were performed to obtain a first characterization of the luminescence properties. From PL spectra, the quality of the flakes related to the presence of defects as well as the role of the dielectric environment on the light emission (see section 1.2.3

Chapter 1) can be deduced. Furthermore, as mentioned above, multi-layered and single-layered flakes are synthesized by CVD. Since the PL signal from multilayer TMDs is extremely low compared to their monolayer counterparts [1, 14], the PL technique is used to identify and select monolayer flakes from the multilayer ones for further STM-LE analysis. Moreover, PL and STM-LE spectra and maps of the same sample allow the comparison of the luminescence of  $MoSe_2$  MLs induced by two different excitation sources. Indeed, STM tunneling is a very localized excitation source compared to the laser beam of PL spectroscopy. Hence, this comparison highlights the role of excitation source localization on the luminescence from  $MoSe_2$ .

### b) Atomic Force Microscopy

An Atomic Force Microscope (AFM) has been used to probe the mechanical properties of the studied samples, especially those of  $MoSe_2$  monolayers. AFM is a technique invented in 1985 by Binnig *et al.* [17] which belongs to the family of scanning probe microscopes, together with the STM. Instead of using tunneling current as the feedback signal, AFM uses the forces between the tip and the sample to probe the sample surface. Since electrical conductivity of the sample is not required, this microscope is commonly used to probe insulating surfaces. It consists of a sharp tip attached to the free end of a flexible cantilever. When the tip is brought close to the sample, it is subjected to forces leading to a deflection of the cantilever. Depending on the tip-sample distance, the tip-sample interaction is dominated by either attractive forces (as Van Der Waals forces for example) or repulsive forces (related to Pauli exclusion principle). The cantilever deflection is detected using a laser beam that illuminates the back of the cantilever and is reflected to a photodetector divided into four quadrants and mounted on the AFM. From the movement of the laser spot incident on the photodetector, the cantilever deflection is measured and is then sent to the feedback controller which corrects the tip-sample distance (see Figure 2.10).

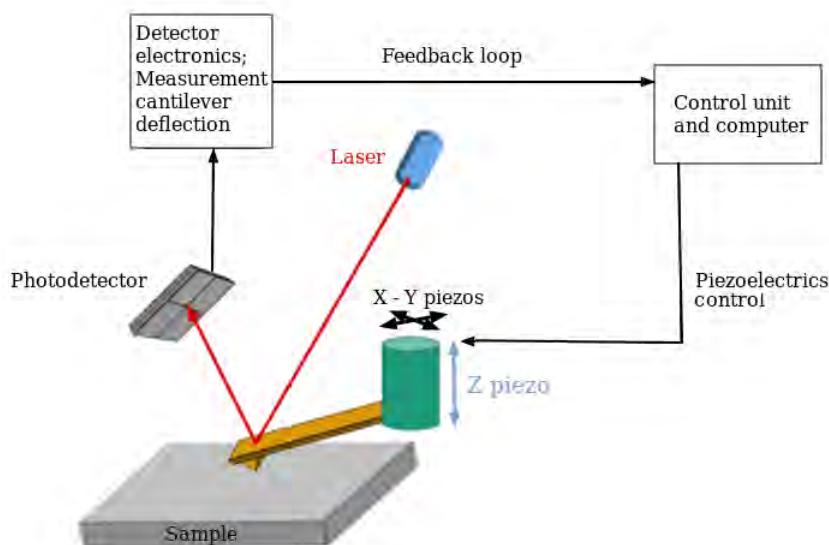


**Figure 2.10:** Schematic configuration of an AFM

AFM is a versatile tool capable of imaging surface topography at high resolution, and can be equipped with multiple measuring modes to probe mechanical, electrical and even magnetic properties of the sample. Among the multitude of working modes offered by the AFM, the choice of the one to use depends on the nature of the studied sample and on the surface property of interest.

The customized hybrid instrument (Bruker Veeco Dimension D3100) used for STM-LE measurements and described in section 2.1.1 can be operated as an AFM by changing the tip-holder. The rest of the setup remains unchanged, including the piezoelectric tube used to control the tip-sample distance and to move the tip over the sample surface with high precision. The AFM experiments presented in Chapter 3 were conducted in either contact or tapping mode. In contact mode, the user defines a cantilever deflection setpoint. The feedback loop adjusts the tip-sample distance during scanning to maintain the cantilever deflection constant at the setpoint. In this mode, the tip is very close to the sample, so that the main forces sensed by the tip are short range repulsive forces. On the other hand, in tapping mode, the cantilever is excited close to its resonance frequency, which causes the cantilever to oscillate with an amplitude of a few tens of nm. When the tip-sample distance varies, the resonance frequency of the cantilever shifts and the amplitude of its oscillation changes. In this mode, the user defines an oscillation amplitude to be maintained by the feedback loop. Compared to the contact mode, the tapping mode probes a large variety of forces, not only repulsive ones, and is less invasive. Depending on the measurement mode, a different cantilever and thus a different AFM tip made of silicon nitride are used. All probes employed in AFM measurements were commercial tips (Bruker OTESPA-R3).

Due to the extremely thinness of the  $MoSe_2$  monolayer, STM tunneling may not offer significant contrast between the flake and the bare substrate when imaging their surfaces, occasionally making it challenging to distinguish between them in STM images. On the other hand, AFM measures the interaction forces between the tip and the sample surface. This includes not only electronic properties but also mechanical properties. Since the monolayer and its underlying substrate exhibit different mechanical properties, a more significant contrast in AFM images is generally obtained. AFM images in tapping mode of some samples are presented in Chapter 3. In addition, mechanical properties of  $MoSe_2$  flakes that may play a role in the light emission process were studied using the AFM. This investigation involved analyzing force-distance curves, where the force between the AFM tip and the flake surface is measured at various distances during approach and retraction. These curves were obtained using both contact and tapping modes.

## 2.3 Simulation methods

The main scope of Chapter 4 is to study the electromagnetic modes of a hybrid tunneling STM junction which consists of a  $MoSe_2$  monolayer placed between a gold tip and a gold substrate. For this purpose,

numerical electrodynamic simulations based on the Discrete Dipole Approximation (DDA) method, which is discussed in the first part of this section, were carried out. The simulation results are expected to provide a better understanding of the experimental STM-LE results presented in Chapter 3. To this end, in order to achieve an accurate modeling of the experimental junction, electron tunneling is taken into account in the simulations using the Quantum-Corrected Model (QCM). The latter is introduced in the second part of this section.

### 2.3.1 Discrete Dipole Approximation (DDA)

Discrete Dipole Approximation is a numerical method widely used for modeling the optical properties of particles of any geometry. It is a well-known technique for calculating scattering and absorption of electromagnetic waves by isolated targets of finite size, or by 1D or 2D periodic structures of unit cells. The DDA theory was introduced in 1973 by Purcell and Pennypacker [18] and was greatly improved by Draine and Flatau [19, 20] with the development of its extension to periodic structures [21] and the introduction of near-field calculations [22]. The DDA model and its extensions are implemented in the software package DDSCAT. All DDA calculations performed in this thesis were conducted using the version 7.3 of this software. The DDSCAT code, developed by Draine and Flatau, is written in FORTRAN 90 and is publicly available.

The basic idea behind DDA consists in discretizing the volume of the target of interest in a 3D-array of  $N$  equidistant polarizable point dipoles. This principle is depicted in Figure 2.11 for a sphere.

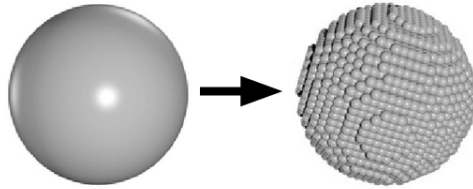


**Figure 2.11:** On the left, schematic representation of a sphere; on the right, its approximation by a 3D-array of discrete point dipoles (adapted from [23]).

Each of these dipoles acquires a polarization induced by the incident electric field and the fields at location  $\mathbf{r}_i$  due to all the other  $N - 1$  induced dipoles. The polarization of the  $i^{th}$  point dipole is written as:

$$\mathbf{P}_i = \alpha_i (\mathbf{E}_{inc,i} - \sum_{i \neq j}^N \mathbf{A}_{i,j} \mathbf{P}_j) \quad (2.1)$$

Where the term  $-\mathbf{A}_{i,j} \mathbf{P}_j$  corresponds to the electric field at  $\mathbf{r}_i$  generated by the dipole polarization  $\mathbf{P}_j$  located at  $\mathbf{r}_j$  with  $\mathbf{A}_{i,j}$  the dipole interaction tensor that represents the interaction between the dipole at  $\mathbf{r}_i$  and the one at  $\mathbf{r}_j$ . Then,  $\alpha_i$  is the polarizability of the point at  $\mathbf{r}_i$ . The calculation of  $\alpha_i$  is based on the Clausius-Mossotti polarizability relation:

$$\alpha_i = \frac{3d^3 \epsilon_i - 1}{4\pi \epsilon_i + 2} \quad (2.2)$$

where  $d$  is the inter-dipole distance. The polarizability of the  $i$ th dipole is related to the dielectric function  $\epsilon_i$  which provides the properties of the material being modeled at the point  $\mathbf{r}_i$ . It is important to select the appropriate dielectric function for correctly describing the optical properties of the target. Once  $\alpha_i$  is specified, Maxwell's equations can be solved accurately for the dipole array. Indeed, the polarization of each point dipole can be determined by solving, using an iterative algorithm, a system of complex linear equations given by equation (2.1). Far-field extinction  $C_{ext}$ , absorption  $C_{abs}$  and subsequently, scattering cross-sections  $C_{sca}$  can be computed from the solution of the system of equations [20]:

$$C_{ext} = \frac{4\pi k}{|\mathbf{E}_{inc}|^2} \sum_{j=1}^N \text{Im}(\mathbf{E}_{inc,j}^* \cdot \mathbf{P}_j) \quad (2.3)$$

$$C_{abs} = \frac{4\pi k}{|\mathbf{E}_{inc}|^2} \sum_{j=1}^N \left\{ \text{Im}(\mathbf{P}_j \cdot (\alpha_j^{-1})^* \mathbf{P}_j^*) - \frac{2}{3} k^3 |\mathbf{P}_j|^2 \right\} \quad (2.4)$$

$$C_{sca} = C_{ext} - C_{abs} \quad (2.5)$$

with  $k$  the wavevector magnitude of the incident field. This latter is characterized by a wavelength, a polarization, and a direction relative to the target defined by the user. Solving the system of linear equations provides the scattered field coefficients from which near-field quantities are computed [22]. Hence, the complex electric  $\mathbf{E}$  and magnetic  $\mathbf{B}$  fields at any point outside and inside the target can be calculated, as well as the Poynting vector. These fields are the sum of the incident and scattered fields:  $\mathbf{E} = \mathbf{E}_{inc} + \mathbf{E}_{sca}$  and  $\mathbf{B} = \mathbf{B}_{inc} + \mathbf{B}_{sca}$ .

The DDA method allows the calculation of the optical response of complex systems for which no analytical solutions exist. In Chapter 4, DDA calculations were carried out to study the electromagnetic modes and optical properties of a hybrid  $Au/MoSe_2/Au$  tunneling junction in STM configuration. For this purpose, far-field extinction cross-section spectra, as well as electric near-field spectra and maps were computed and analyzed. As discussed in Chapter 1 (section 1.1.2), the electric near-field enhancement factor  $G$  is a key element to model the light emission process. This factor, which describes the electromagnetic properties of the junction, is calculated in Chapter 4 for the hybrid junction from DDA simulations.

One of the main advantages of DDA is its capacity to simulate not only objects of complex geometries, but also of complex composition. This makes it possible to obtain an accurate modeling of the experimental junction. The optical anisotropy of the  $MoSe_2$  monolayer and other properties of the materials composing the junction are easily introduced into DDA calculations by means of their dielectric function provided in an input file. However, the DDA method has several limitations. When the

incident wavelength is close to the inter-dipole distance, errors start to appear in the calculated results. In addition, the accuracy of DDA is limited when simulating materials with a high refractive index. According to Draine and Flatau [20], the DDA approach provides reasonably good accuracy if the criterion  $kd|m| < 1$  is fulfilled with  $k$  the magnitude of the incident field wavevector,  $d$  the inter-dipole distance and  $m$  the complex refractive index of the material of interest. Due to slower convergence as the number of dipoles rises, more computing time is needed as the target size increases. Indeed, in DDA, computational resources not only in time but also in memory increase quickly when the target size increases. For this reason, DDA calculations which require large memory capacities were performed using HPC resources from the computing facility center CALMIP of the University of Toulouse (grant P22030).

### 2.3.2 Quantum-Corrected Model (QCM)

The optical response of the simulated junction obtained from DDA calculations is given in a classical electrodynamics framework. In this approach, the boundaries of a metallic target are perfectly defined and thus, quantum effects due to the spill-out of the electron wavefunctions or non-local screening are not addressed. Consequently, this formalism is unable to accurately reproduce the physics of the experimental hybrid tunneling junction studied in Chapter 3 because the STM tunneling, resulting from the spill-out of electrons across the gap, can not be taken into account. To overcome this situation, Esteban *et al.* [24, 25] proposed in 2012 a semi-classical approach called Quantum-Corrected Model (QCM) which consists in incorporating quantum-mechanical effects into classical electrodynamics simulations. In Chapter 4, this approach is used in order to account for the electron tunneling effects on the optical response of the simulated  $Au/MoSe_2/Au$  tunneling junction.

QCM was developed to address non-local effects and electron tunneling across sub-nanometer gaps between plasmonic nanoparticles. Indeed, at the gap thickness  $d < 0.5$  nm, quantum effects related to the quantum nature of electrons in the metal become relevant. By performing full-quantum mechanical calculations using for example Time Dependent Density Functional Theory (TDDFT), these effects can be captured. However, these computation quantum models are only capable to model relatively small and/or simple systems because of the huge computing resource load. QCM makes it possible to properly study the optical response of systems with a sub-nanometric gap without a high computational cost. While there are several approaches that deal with non-locality, QCM is the first model to account for the charge transfer between two metallic particles. It consists in introducing an effective conductive medium into the gap region to take into account the tunneling conductivity. A Drude-like effective dielectric function,  $\epsilon_g(\omega, d)$ , describes this effective medium and is derived from the conductivity of the gap  $\sigma_g(d)$ .

$$\epsilon_g(\omega, d) = 1 + i \frac{\sigma_g(d)}{\epsilon_0 \omega} \quad (2.6)$$

The conductivity  $\sigma_g(d)$  is considered static, meaning it is not dependent on  $\omega$ , based on the adiabatic assumption. It depends on the gap thickness  $d$ , as does the effective dielectric function. Thus, for no-planar tunneling gaps, the effective medium is modeled by a set of onion-like cylindrical shells. Each shell is defined by its own dielectric function (see Figure 2.12).

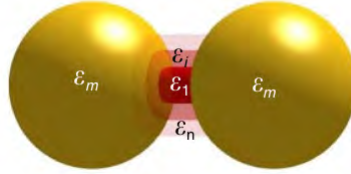


**Figure 2.12:** Schematic representation of the Quantum-Corrected Model (QCM) (from [24]). The set of homogeneous shells ( $i = 1, \dots, n$ ) of the effective medium that accounts for the tunneling current is shown.  $\epsilon_m$  is the dielectric constant of the metal.

The QCM model can be easily implemented in several classical frameworks of Maxwell's equation, including DDA. By computing the tunneling conductivity from quantum mechanical calculations, Esteban *et al.* applied this model for Drude metal dimers surrounded by vacuum [24, 25]. They obtained an excellent quantitative agreement between the results obtained with QCM and those obtained from full quantum mechanical calculations, validating this approach.

In our case, the tunneling gap studied is formed between a gold tip and a  $MoSe_2$  monolayer supported by a gold substrate. In addition to the tip-sample distance  $d$ , the gap conductivity depends on the bias voltage applied to the junction. Quantum calculations of the tunneling conductivity of the studied junction are beyond the scope of this thesis. Hence, empirical data for the conductivity of an  $Au/MoSe_2/Au$  stacked junction found in the literature were used [26]. Based on the exponential dependence of the tunneling current on the gap thickness (see section 1.1.1 of Chapter 1), a static conductivity is defined as follows:

$$\sigma_g(d, V) = \sigma_0(V) \exp\left(-\frac{2d}{l_c}\right) \quad (2.7)$$

with  $l_c$  the penetration depth of the conduction electron wavefunction into vacuum and  $\sigma_0(V)$  the conductivity of the  $MoSe_2$  monolayer stacked between two gold electrodes. Using this approach, the boundary conditions are respected. At zero gap thickness ( $d = 0$ ), the conductivity of the effective medium at the gap is equal to the empirical conductivity of the stacked  $Au/MoSe_2/Au$  junction, and for a large gap thickness ( $d \rightarrow \infty$ ), the permittivity of the effective medium  $\epsilon_g(\omega, d)$  is equal to 1, the surrounding dielectric function (vacuum). All the details concerning the tunneling conductivity calculations are given in section 4.3 of Chapter 4.

Non-locality can be integrated into QCM model by using non-local dielectric functions according to the nonlocal hydrodynamical description [27]. However, in this thesis, QCM is implemented in DDA

---

simulations which do not accept nonlocal dielectric functions. Therefore, all QCM-DDA calculations performed in Chapter 4 were carried out using local QCM ignoring the non-local effects.

## Bibliography

- [1] R. Péchou, S. Jia, J. Rigor, O. Guillermet, G. Seine, J. Lou, N. Large, A. Mlayah, and R. Coratger. Plasmonic-Induced Luminescence of MoSe<sub>2</sub> Monolayers in a Scanning Tunneling Microscope. *ACS Photonics*, 7(11):3061–3070, 2020.
- [2] I. Horcas, R. Fernández, J. M. Gomez-Rodriguez, J. Colchero, J. Gómez-Herrero, and A. M. Baro. WSXM: A software for scanning probe microscopy and a tool for nanotechnology. *Rev. Sci. Instrum.*, 78(1):013705, 2007.
- [3] R. M. Feenstra. Scanning tunneling microscopy and spectroscopy of gold on the GaAs (110) surface. *J. Vac. Sci. Technol. B: Microelectron. Process. Phenom.*, 7(4):925–930, 1989.
- [4] J. F. Jørgensen, L. L. Madsen, J. Garnæs, K. Carneiro, and K. Schaumburg. Calibration, drift elimination, and molecular structure analysis. *J. Vac. Sci. Technol. B: Microelectron. Nanometer Struct. Process. Meas. Phenom.*, 12(3):1698–1701, 1994.
- [5] M. P. Yothers, A. E. Browder, and L. A. Bumm. Real-space post-processing correction of thermal drift and piezoelectric actuator nonlinearities in scanning tunneling microscope images. *Rev. Sci. Instrum.*, 88(1):013708, 2017.
- [6] Acton Research Roper Scientific. SPECTRUMM SYSTEM - SpectruMM:400. <http://ridl.cis.rit.edu/products/IDTL%20products/Manuals/Acton%20manuals/CATALOG/SM400.pdf>.
- [7] Valérie Sivel. *Émission photonique en microscopie à effet tunnel dans l'air*. PhD thesis, Université Paul Sabatier, 1994.
- [8] Hamamatsu Photonics K.K. Photomultiplier Tube R943-02. [https://www.hamamatsu.com/content/dam/hamamatsu-photonics/sites/documents/99\\_SALES\\_LIBRARY/etd/R943-02\\_TPMH1115E.pdf](https://www.hamamatsu.com/content/dam/hamamatsu-photonics/sites/documents/99_SALES_LIBRARY/etd/R943-02_TPMH1115E.pdf), 2010.
- [9] G. Hoffmann, J. Aizpurua, P. Apell, and R. Berndt. Influence of tip geometry in light emission from the scanning tunnelling microscope. *Surf. Sci.*, 482-485:1159–1162, 2001.
- [10] B. Ren, G. Picardi, and B. Pettinger. Preparation of gold tips suitable for tip-enhanced Raman spectroscopy and light emission by electrochemical etching. *Rev. Sci. Instrum.*, 75(4):837–841, 2004.
- [11] S. Najmaei, Z. Liu, W. Zhou, X. Zou, G. Shi, S. Lei, B. I. Yakobson, J.-C. Idrobo, P. M. Ajayan, and J. Lou. Vapour phase growth and grain boundary structure of molybdenum disulphide atomic layers. *Nat. Mater.*, 12(8):754–759, 2013.
- [12] J. C. Shaw, H. Zhou, Y. Chen, N. O. Weiss, Y. Liu, Y. Huang, and X. Duan. Chemical vapor deposition growth of monolayer MoSe<sub>2</sub> nanosheets. *Nano Res.*, 7(4):511–517, 2014.

- [13] B. Li, Y. Gong, Z. Hu, G. Brunetto, Y. Yang, G. Ye, Z. Zhang, S. Lei, Z. Jin, E. Bianco, X. Zhang, W. Wang, J. Lou, D. S. Galvão, M. Tang, B. I. Yakobson, R. Vajtai, and P. M. Ajayan. Solid–vapor reaction growth of transition-metal dichalcogenide monolayers. *Angew. Chem.*, 128(36):10814–10819, 2016.
- [14] E. M. Alexeev, A. Catanzaro, O. V. Skrypka, P. K. Nayak, S. Ahn, S. Pak, J. Lee, J. I. Sohn, K. S. Novoselov, H. S. Shin, and A. I. Tartakovskii. Imaging of interlayer coupling in van der Waals heterostructures using a bright-field optical microscope. *Nano Lett.*, 17(9):5342–5349, 2017.
- [15] S. Tongay, J. Suh, C. Ataca, W. Fan, A. Luce, J. S. Kang, J. Liu, C. Ko, R. Raghunathanan, J. Zhou, F. Ogletree, J. Li, J. C. Grossman, and J. Wu. Defects activated photoluminescence in two-dimensional semiconductors: interplay between bound, charged and free excitons. *Sci. Rep.*, 3(1):2657, 2013.
- [16] C. Robert, D. Lagarde, F. Cadiz, G. Wang, B. Lassagne, T. Amand, A. Balocchi, P. Renucci, S. Tongay, B. Urbaszek, and X. Marie. Exciton radiative lifetime in transition metal dichalcogenide monolayers. *Phys. Rev. B*, 93(20):205423, 2016.
- [17] G. Binnig, C. F. Quate, and C. Gerber. Atomic force microscope. *Phys. Rev. Lett.*, 56(9):930–933, 1986.
- [18] E. M. Purcell and C. R. Pennypacker. Scattering and absorption of light by nonspherical dielectric grains. *Astrophys. J.*, 186:705–714, 1973.
- [19] B. T. Draine. The discrete-dipole approximation and its application to interstellar graphite grains. *Astrophys. J., Part 1*, 333:848–872, 1988.
- [20] B. T. Draine and P. J. Flatau. Discrete-dipole approximation for scattering calculations. *J. Opt. Soc. Am. A*, 11(4):1491–1499, 1994.
- [21] B. T. Draine and P. J. Flatau. Discrete-dipole approximation for periodic targets: theory and tests. *J. Opt. Soc. Am. A*, 25(11):2693–2703, 2008.
- [22] P. J. Flatau and B. T. Draine. Fast near field calculations in the discrete dipole approximation for regular rectilinear grids. *Opt. Express*, 20(2):1247–1252, 2012.
- [23] S. Kieß, M. Z. Shaikh, M. Grégoire, T. Bringewat, S. Simon, A. Tausendfreund, M. Zimmermann, and G. Goch. In-process optical characterization method for sub-100-nm nanostructures. In *2011 IEEE International Instrumentation and Measurement Technology Conference*, pages 1–4, 2011.
- [24] R. Esteban, A. G. Borisov, P. Nordlander, and J. Aizpurua. Bridging quantum and classical plasmonics with a quantum-corrected model. *Nat. Commun.*, 3(1):825, 2012.

- 
- [25] R. Esteban, A. Zugarramurdi, P. Zhang, P. Nordlander, F. J. García-Vidal, A. G. Borisov, and J. Aizpurua. A classical treatment of optical tunneling in plasmonic gaps: extending the quantum corrected model to practical situations. *Faraday Discuss.*, 178:151–183, 2015.
- [26] R. Ge, X. Wu, L. Liang, S. M. Hus, Y. Gu, E. Okogbue, H. Chou, J. Shi, Y. Zhang, S. K. Banerjee, Y. Jung, J. C. Lee, and D. Akinwande. A library of atomically thin 2D materials featuring the conductive-point resistive switching phenomenon. *Adv. Mater.*, 33(7):2007792, 2021.
- [27] C. Ciraci, J. B. Pendry, and D. R. Smith. Hydrodynamic model for plasmonics: a macroscopic approach to a microscopic problem. *ChemPhysChem*, 14(6):1109–1116, 2013.

# Chapter 3

## Experimental STM-induced light emission

In this chapter, the intensity, spectral features, and spatial localization of STM-induced luminescence from different tunnel junctions involving  $MoSe_2$  monolayers and/or other materials are experimentally explored. The dependence of STM-LE characteristics on tunneling parameters (tunneling current  $I_t$  and bias voltage  $V_s$ ) is also addressed. As discussed in section 1.1 of Chapter 1, the mechanism responsible for light emission varies considerably depending on whether the junction consists of plasmonic metals or semiconductors. In purely metallic junctions, light originates from the radiative decay of surface plasmon modes hosted in the tip-surface cavity while for junctions involving semiconductors, luminescence comes from the intrinsic electronic interband transition triggered by charge injection. The initial section focuses on light emission from purely plasmonic metal junctions. Two different samples have been investigated: a granular gold film and gold nanowires supported by a non-plasmonic substrate. The second section deals with the excitonic luminescence of  $MoSe_2$  monolayers, a two-dimensional semiconductor whose properties are described in section 1.2 of Chapter 1. These monolayers are deposited on a non-plasmonic substrate, such as graphene or ITO, to avoid any contribution from plasmon modes in the STM-LE signal. This part is followed by the study of the luminescence from a hybrid  $MoSe_2/Au$  tunneling junction. In this case, plasmon modes excited in the tip-surface gap will interact with the excitons confined in the monolayer and may have an impact on the monolayer luminescence as reported on other hybrid systems (see section 1.2.3 of Chapter 1). The influence of the plasmonic nature of the substrate on the light emission from the monolayer is then evaluated. In the final part of this chapter, the role of substrate morphology in STM-LE from the monolayer is investigated by using two different nanostructured gold substrates. The surface morphology of the latter allows the modulation of surface plasmon modes properties, leading to a different interaction between them and the excitons within the monolayer. Some results presented in the last section have been addressed in a published article [1]

In addition to STM-LE measurements, this chapter includes photoluminescence spectroscopy and AFM measurements (work principle of each technique is discussed in section 2.2.2 of Chapter 2) to

complement the STM-LE results and provide additional information about the studied samples. It is important to note that all the STM-LE measurements presented in this chapter were performed using plasmonic gold tips (see section 2.1.3 of Chapter 2 where their preparation is described).

## 3.1 Light emission from plasmonic substrates

The first part of this chapter focuses on the light emission induced by STM from plasmonic substrates. The mechanism behind light emission from such samples has been explained in section 1.1.2 of Chapter 1. Plasmonic modes known as localized surface plasmon (LSP) modes are excited by inelastic electron tunneling (IET), i.e., by electrons that tunnel through the potential barrier between electrodes losing all or part of their energy. Two different plasmonic substrates are investigated in this study: a granular gold film and gold nanowires deposited on non-plasmonic substrates.

### 3.1.1 Gold sample with granular surface

The initial part of this chapter is dedicated to the analysis of STM-induced light emission (STM-LE) from a granular gold substrate. It will serve as a valuable foundation for the last two sections, which focus on STM-induced luminescence from  $MoSe_2$  monolayers deposited on granular gold substrates. Thus, in this current section, the discussion will center on the role of the granular structure of the gold sample surface on light emission, as well as the spectral properties and the quantum yield of luminescence from such a plasmonic substrate.

Since the initial observation of STM-LE from noble metals in the 1980s, numerous experimental studies have been performed on the characteristics of light emission from granular gold substrates [2–4]. Polycrystalline gold samples demonstrate a higher light emission efficiency compared to their monocrystalline counterparts, owing to their roughness. Indeed, the granular structure can facilitate the electromagnetic coupling between the surface plasmon modes and photons [2, 3]. As surface roughness increases, there is a corresponding rise in photon emission. However, according to Laks and Mills [5, 6], beyond a certain amplitude of roughness, the intensity of emitted light saturates. The substrate studied in this section is a polycrystalline gold film composed of grains with a typical diameter below 100 nm.

In Figure 3.1, both the STM topographic image and its corresponding photonic map recorded simultaneously are shown. The STM topography reveals the presence of gold grains with sub-100 nm size as expected for an evaporated polycrystalline gold film. However, their contours are not well defined due to a weak spatial STM resolution. In order to observe the substrate grains, a small scan size should be considered. However, because of the open architecture of our STM setup and the fact that it operates in ambient conditions, achieving high resolution is inherently limited mainly due to contamination and thermal drift. Despite this, it is still possible to clearly identify individual grains in the STM topographic image (Figure 3.1-A).

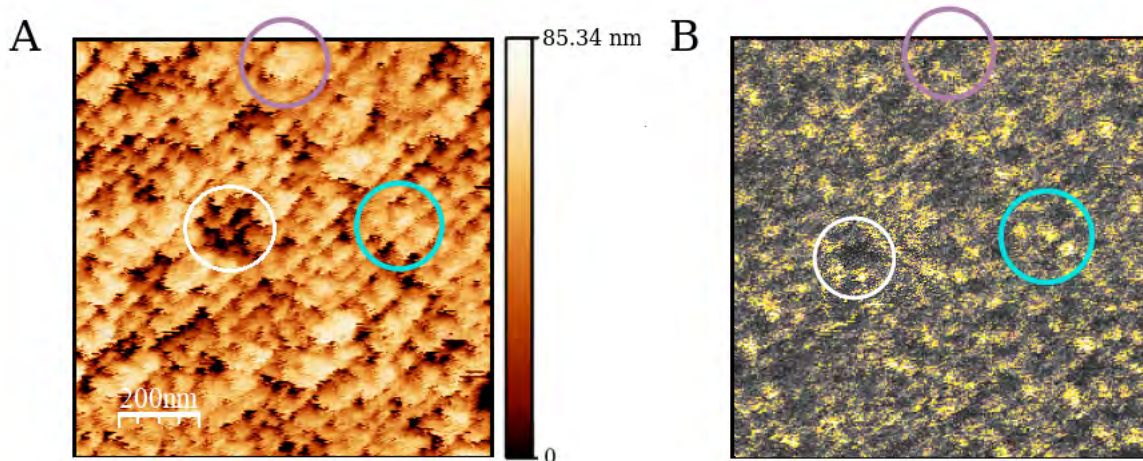


**Figure 3.1:** (A) STM topographic image and (B) corresponding photonic map of a granular gold sample. Both images were recorded simultaneously on a  $1 \mu\text{m} \times 1 \mu\text{m}$  area ( $V_s = +1.8 \text{ V}$ ;  $I_t = 10 \text{ nA}$ ). During the acquisition of the photonic map, an average of 650 counts per second is obtained. The white, blue and purple circles indicate three distinct surface areas exhibiting gold grains of different sizes.

The photonic map (Fig. 3.1-B) shows a non-uniform photon emission indicating the crucial role of the surface roughness in the light emission process. Indeed, during surface scanning, due to the granular structure, the geometry of the tip-surface cavity changes. This gives rise to localized surface plasmon LSP modes hosted by the cavity with different local properties and consequently, to variations in the light emission intensity. In this case, the granular structure of the sample surface can be observed in the photonic map and its correlation with the STM topographic image of the scanned surface can be deduced. The darker zones in the STM image correspond to areas on the surface where the gold grains are notably smaller (a few nanometers in diameter), forming a sort of cavity surrounded by larger grains (tens of nanometers in diameter) as in the zone circled in white. In these zones, the excitation of LSP modes by tunneling electrons is less efficient due to the tip geometry (the STM tip does not reach the bottom), resulting in low luminescence intensity. Moreover, individual grains can be identified in the photonic map where a more intense luminescence is observed when the tip is over the grain rather than at the grain boundaries (blue circled area). So, depending on the gold grain geometry, the light emission intensity will be different. However, it is important to note that intense luminescence does not always occur when the STM tip is positioned over a gold grain, as shown in the purple circled zone. In fact, apart from the surface geometry, a large number of other parameters are involved in light emission process, such as the morphology of the tip apex or the presence of contaminants on the surface since experiments are conducted in ambient conditions. It should be noted that a photonic map is a representation of the number of photons collected while the tip is over a particular location. Therefore, the precise spatial localization of the light emission process itself remains unknown. In addition, the collected light corresponds to light emitted in a specific direction (selected by the optical fiber), which may be shadowed by the surface roughness.

STM-induced luminescence spectra were acquired at different locations of the granular surface of

the gold substrate using the same tunneling parameters (see Figure 3.2-A). It is important to mention that these spectra were obtained using a “fixed tip position” (no-scanning mode during acquisition). The acquired spectra exhibit distinct lineshapes. Indeed, the number of peaks as well as their position and relative intensity fluctuate greatly from one spectrum to another. Hence, the spectral distribution of the emitted light is influenced by the surface geometry of the location where the spectrum was acquired but it is not solely determined by it. Every spectrum was captured using a unique tunnel junction characterized by the local surface and tip apex geometry, as well as the presence of contaminants between the tip and the surface. These factors which affect the electronic properties of both the tip and surface, as well as the potential tunnel barrier, can vary considerably between two consecutive acquisitions conducted within nanometer proximity or even during a single acquisition due to thermal drift, even with a short acquisition time (60 s). Consequently, the energy distribution of the electrons involved in the light emission process may differ between two spectral acquisitions at different locations even if the tunneling parameters (tunneling current  $I_t$  and bias voltage  $V_s$ ) are the same. Furthermore, these factors have also an impact on the properties of the LSP modes excited by inelastic electron tunneling located within the cavity formed by the tip and sample surface. Hence, at each acquisition, the energy distribution of tunnel electrons and the LSP modes responsible for the light emission process were different leading to distinct spectral distributions of the light emitted. A shared characteristic among these spectra is the presence of multiple peaks. This is attributed to the excitation of multiple LSP modes during acquisition. In fact, given the granular structure, it is very likely that the tip apex interacts with multiple grains, engaging several surface plasmon modes. Moreover, certain peaks at specific wavelengths are common in two or all spectra as, for example, the peaks at 750 nm and 910 nm (see Figure 3.2-A). These peaks can be attributed to the excitation of the same LSP modes.

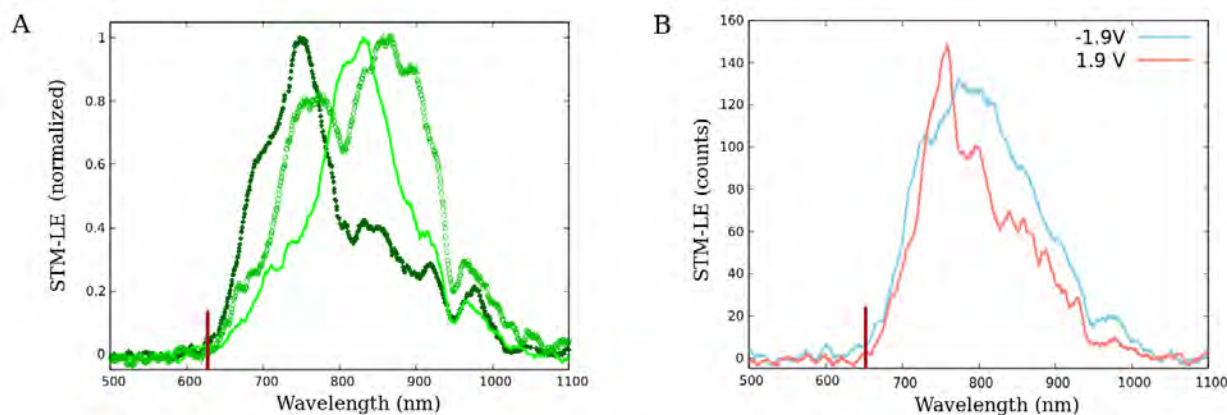


**Figure 3.2:** STM-induced luminescence spectra of a granular gold sample acquired: (A) at different locations of the surface using the same tunneling parameters:  $V_s = +2$  V;  $I_t = 15$  nA and (B) at the same location varying the sign of the bias voltage  $V_s$  ( $I_t = 20$  nA). All spectra were obtained with an acquisition time of 60 s and with the tip held in a fixed position (no scanning during spectra acquisition). The red bars indicate the high-energy quantum cutoff.

Figure 3.2-B displays two spectra obtained at the same location on the gold film surface using a positive (pink line) and a negative (light blue line) bias voltage  $V_s$ . Light emission occurs regardless of the sign

of the bias voltage, i.e., regardless of the direction of the electron tunneling. The differences between both spectra are primarily attributed to the asymmetry of the tunnel junction. It is worth noting, though, that they could also be influenced by tip or surface displacement between the two acquisitions due to thermal drift.

The spectral characteristics of the STM-induced luminescence of a granular gold substrate have also been investigated as a function of the tunneling parameters (bias voltage  $V_s$  and tunneling current  $I_t$ ). Figure 3.3-A shows STM-LE spectra acquired for different voltages applied to the junction. All spectra exhibit a high-energy threshold which is in agreement with the quantum cutoff ( $\hbar\omega = eV_s$ ) described in section 1.1.2 of Chapter 1 [7]. For clarity, this threshold is indicated in each spectrum by a vertical red bar. Several peaks at specific wavelengths can be identified in the presented series of spectra: at 710, 795 and 860 nm. As the bias voltage  $V_s$  increases, these and other peaks appear one after the other in the spectra, as higher energy electrons can participate in the light emission process. The emergence of new peaks and the increase in peak intensity suggest that the light emission efficiency increases with the bias voltage  $V_s$ . The intensity enhancement is more apparent in higher energy peaks. Indeed, above a certain value of  $V_s$ , the low-energy components of the spectra remain almost constant and only the contribution of high-energy electrons is observed. This behavior can be understood by considering equations 1.5 and 1.6 of section 1.1.1 of Chapter 1 which demonstrate that higher electron energies correspond to a more significant electron transmission coefficient. Hence, high-energy electrons are more probable to participate in the tunneling current and then, in the light emission process.

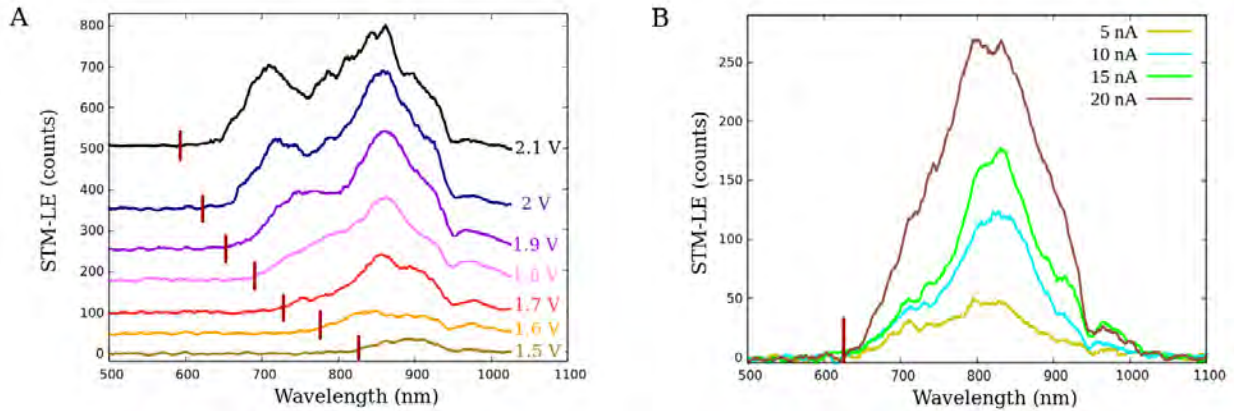


**Figure 3.3:** STM-induced luminescence spectra of a granular gold sample: (A) versus bias voltage  $V_s$  at the tunneling current  $I_t = 20$  nA (spectra are vertically offset for clarity) and (B) versus tunneling current  $I_t$  at the sample bias voltage of  $V_s = +2$  V. All spectra were obtained with an acquisition time of 60 s and with the tip held in a fixed position (no scanning during spectra acquisition). The red bars indicate the high-energy quantum cutoff.

Using a constant bias voltage  $V_s$ , a series of spectra was acquired at the same surface location by varying the tunneling current  $I_t$  (see Figure 3.3-B). It is observed that as the tunneling current  $I_t$  increases, the intensity of the peaks also increases, indicating a proportional relationship between the number of emitted photons and the number of electrons in the tunneling current. Some peaks

at specific wavelengths are present in all spectra (at 710, 795 and 830 nm). Each of these peaks is attributed to the excitation of a specific LSP mode whose energy does not depend on the tunneling current. For a constant bias voltage  $V_s$ , a change in the tunneling current induces a variation in the tip-surface distance  $d$ . Therefore, this series of experimental spectra contradicts Rendell and Scalapino's model [8, 9] discussed in section 1.1.2 of Chapter 1 since the energy of the excited LSP modes shows no dependence on the tip-surface distance  $d$ . Both series of spectra shown in Figure 3.3 were captured at distinct locations, resulting in entirely different spectra for each set. It is noteworthy that regardless of the specific location on the sample surface where measurements were taken, the spectral distribution behavior in response to changes in bias voltage ( $V_s$ ) or tunneling current ( $I_t$ ) is the same as in the series of spectra in Figure 3.3.

STM-LE spectra obtained from a granular gold sample exhibit a quantum cutoff, and their characteristics are mainly governed by the properties of the LSP modes, determined by the tip-surface cavity geometry. Thus, the resulting spectral lineshape is highly influenced by the surface location from which the spectrum is acquired. Furthermore, the number of photons emitted by this sample is proportional to the number of tunneling electrons.

### 3.1.2 Gold nanowires on non-plasmonic substrates

Extended plasmonic structures, such as nanorods or strips, can exhibit STM-induced luminescence. These structures could be interesting candidates to couple with TMD monolayers in order to create novel hybrid systems and study their optical properties by electronic excitation. In this section, the STM-induced luminescence of ultra-thin gold nanowires is presented. These one-dimensional structures are deposited on non-plasmonic substrates such as indium tin oxide (ITO) and graphite. The synthesis of the gold nanowires (NWs) studied has been carried out by the team of Lise-Marie Lacroix at LPCNO laboratory (Toulouse).

The nanowire synthesis method consists of gold chloride ( $HAuCl_4$ ) reduction in oleylamine solution in hexane using triisopropylsilane (TIPS) as reducing agents [12–14]. The gold nanowires obtained have a mean diameter ranging from 1.5 to 2 nm and a length of few micrometers (see Figure 3.4). They self-assemble in a parallel manner into hexagonal superlattices, as shown in the inset of Figure 3.4-A. These self-assembled NWs are separated by a double layer of ligands composed of oleylamine and oleylammonium chloride. A 3  $\mu$ L drop of an hexane solution containing gold nanowires is extracted and then deposited onto either a bare ITO surface or a freshly mechanically exfoliated graphite surface. The main advantage of using these two substrates is that they do not exhibit STM-LE in the energy range of interest. Thus, any light emission detected can be attributed to gold NWs. Furthermore, these substrates possess distinct electronic properties, with one being a highly doped semiconductor usually treated like a metal (ITO) and the other a semimetal (graphite), as well as different surface geometries: ITO has a granular surface, while graphite has a monocrystalline surface composed of large terraces separated by characteristic steps. By using both substrates, it becomes possible to determine which conditions are more favorable for achieving STM-LE from gold nanowires.

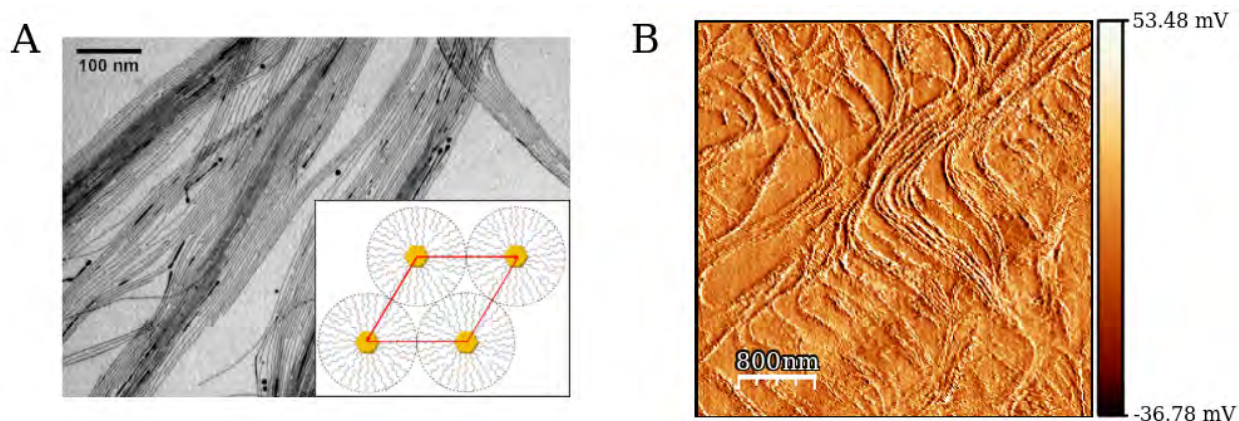


**Figure 3.4:** (A) Transmission electron microscopy image of gold nanowires (NWs) taken from Loubat *et al.* [12]. Inset: Scheme of the hexagonal unit cell of the self-assembled gold NWs (adapted from [12]). (B) Tapping mode AFM amplitude image ( $4 \mu\text{m} \times 4 \mu\text{m}$ ) of gold NWs deposited on a graphite substrate.

Figure 3.4-B is an AFM image of gold NWs deposited on the graphite substrate. The image reveals bundles of self-assembled gold NWs of different thicknesses, positioned randomly on the substrate. The terraced surface of graphite makes it easy to localize and identify the gold NWs. In the case of the ITO substrate, on the other hand, the observation of NWs in both AFM and STM was challenging. It is assumed that during the hexane evaporation after the deposition, the bundles of gold NWs are positioned at the grain boundaries of the ITO substrate surface.

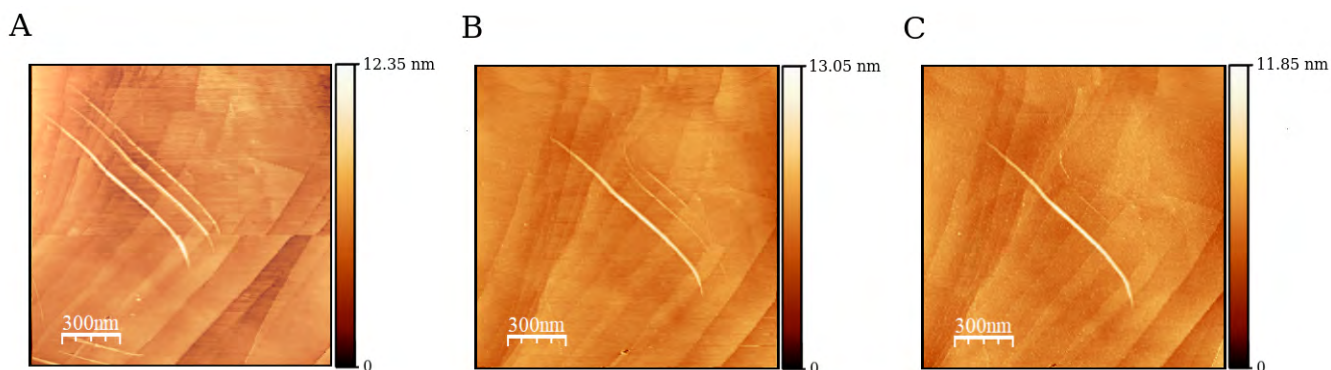


**Figure 3.5:** Sequence of STM topographic images of the same area ( $1.5 \mu\text{m} \times 1.5 \mu\text{m}$ ) showing the evolution of several bundles of self-assembled gold NWs deposited on a graphite substrate after one (A), three (B) and five (C) STM scans. These STM images were acquired with the same tunneling parameters:  $V_s = +0.5 \text{ V}$ ;  $I_t = 3 \text{ nA}$ .

Due to their small diameter, gold nanowires are very fragile [12] and can easily fragment. They remain fragile even when they are self-assembled as the ligand molecules between NWs can be easily moved. This delicate nature of gold NWs has been observed, especially during their characterization using STM. This instability is revealed in Figure 3.5. Even with very low bias voltage and tunneling current ( $V_s = +0.5 \text{ V}$ ;  $I_t = 3 \text{ nA}$ ), a noticeable deterioration of the gold NWs is observed after several STM scans. Three gold NWs bundles positioned perpendicularly to the substrate steps are observed in

the first STM scan (Fig. 3.5-A). After three subsequent STM scans of the same area, the length and thickness of two NWs bundles have significantly decreased (Fig. 3.5-B). Finally, in the fifth scan, only one self-assembled gold NWs bundle remains, while the other two are completely fragmented, as shown in the STM topographic image of Figure 3.5-C. This deterioration is attributed to the tip which, while scanning, breaks the ligands between NWs and causes the fragmentation of the latter. It is possible that the fragmented nanowires attach themselves to the tip and are subsequently transported during the scan. This instability makes it very difficult to obtain light emission from the nanowires.

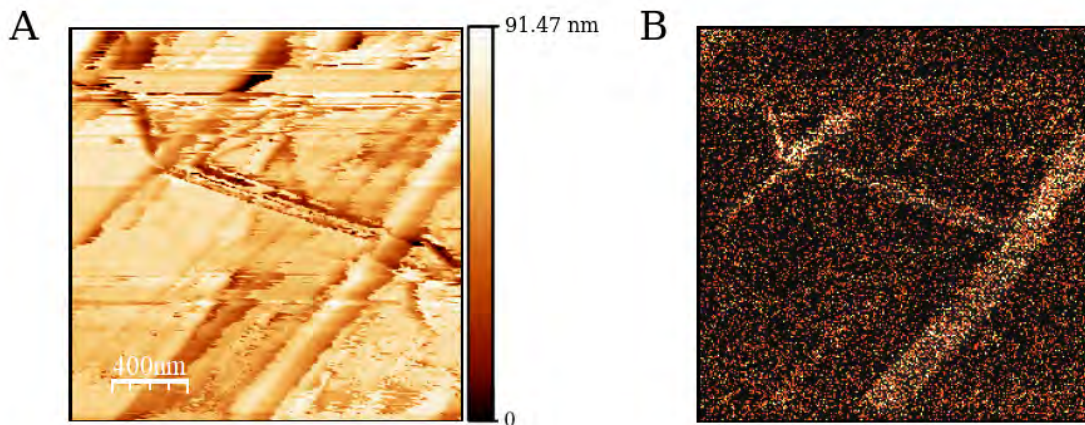


**Figure 3.6:** (A) STM topographic image and (B) corresponding photonic map of self-assembled gold NWs deposited on a graphite substrate. Both images were recorded simultaneously on a  $2 \mu\text{m} \times 2 \mu\text{m}$  area ( $V_s = +1.8 \text{ V}$ ;  $I_t = 15 \text{ nA}$ ). An average of 20 counts per second was obtained during the acquisition of the photonic map.

Light emission induced by STM from gold NWs on graphite has been detected as it is shown in the photonic map of Figure 3.6-B. The top part of the photonic map shows a sudden variation in the light emission signal. This is attributed to a tip-jump probably induced by the attachment of NWs to the tip during the scan. Reproducibility of STM-LE from gold nanowires has been challenging. Despite multiple STM-LE measurements, only a few photonic maps displaying an average of 10 to 20 counts per second have been obtained. Consequently, spectral measurements have not been achievable in these experiments due to such weak signals, and no further investigations have been pursued on these nanowires. The lack of reproducibility is mainly attributed to the inherent instability and fragility of gold NWs mentioned above. Indeed, excitation of plasmonic modes by the tunneling current is impossible if NWs fragment or attach themselves to the tip. Moreover, it is possible that only nanowires bundles with particular dimensions, similar to those depicted in Figure 3.6-A, might allow for STM-LE within the detection range of our light detection system. An additional hypothesis explaining the weak STM-LE signal obtained from these particular objects is the presence of ligands surrounding the nanowires, which may disturb the excitation of plasmon modes or the coupling between plasmons and photons.

After discussing the luminescence induced by STM from plasmonic samples, the focus now shifts to a distinct light emission process: STM-induced light emission from a semiconductor. In section 1.1.3 of Chapter 1, the discussion centers on this luminescence phenomenon, which is attributed to intrinsic electronic transitions involving interband or excitonic recombinations within the semiconductor. These transitions are triggered by the local injection of charges via STM electron tunneling. The investigation of excitonic light emission produced by a TMD monolayer, a direct bandgap semiconductor, in an STM is currently a dynamic and very active field of research [1, 15–19]. As highlighted in section 1.2.2 of Chapter 1, the  $MoSe_2$  monolayer possesses exceptional excitonic and optical properties, rendering it an ideal semiconductor for investigating STM-LE. In the following sections, STM-LE from  $MoSe_2$  monolayers deposited on substrates of different natures (non-plasmonic and plasmonic) will be discussed.

## 3.2 Light emission from $MoSe_2$ monolayer on non-plasmonic substrates

Luminescence from  $MoSe_2$  monolayers in a non-plasmonic STM junction is here addressed. Indeed, in order to prevent plasmon modes from being involved in the  $MoSe_2$  light emission, the monolayer is transferred onto substrates that are non-plasmonic in the investigated energy range: graphene or indium tin oxide (ITO). These two different substrates have very distinct optical and electronic properties. Moreover, while graphene is characterized by a completely flat surface, ITO exhibits a granular surface structure. This comparison allows one to assess the impact of substrate properties on the monolayer STM-LE and determine which substrate is more favorable for the light emission phenomenon.

### 3.2.1 $MoSe_2$ on Graphene

The first sample studied consists of  $MoSe_2$  monolayers grown by CVD and transferred onto a commercial substrate composed of a monolayer of undoped graphene fully covering a 90 nm thick  $SiO_2/Si$  substrate. Graphene is a very interesting substrate with extraordinary electronic properties due to its semimetallic character. Indeed, the absence of bandgap results in high electron mobility and exceptional thermal conductivity [20]. However, the lack of optical bandgap limits its interaction with light, including both absorption and luminescence phenomena. Among all the samples studied in this thesis, the  $MoSe_2$ /Graphene substrate stands out as particularly interesting due to its perfectly flat nature. This characteristic makes it a promising candidate for further exploration under vacuum conditions.

The observation of  $MoSe_2$  flakes transferred onto graphene using an optical microscope (Fig. 3.7-A), reveals the presence of some contaminants on both the flakes and the graphene substrate. These contaminants are attributed to residual PMMA left behind from the transfer process conducted after the flakes synthesis (see section 2.2.1 of Chapter 2).

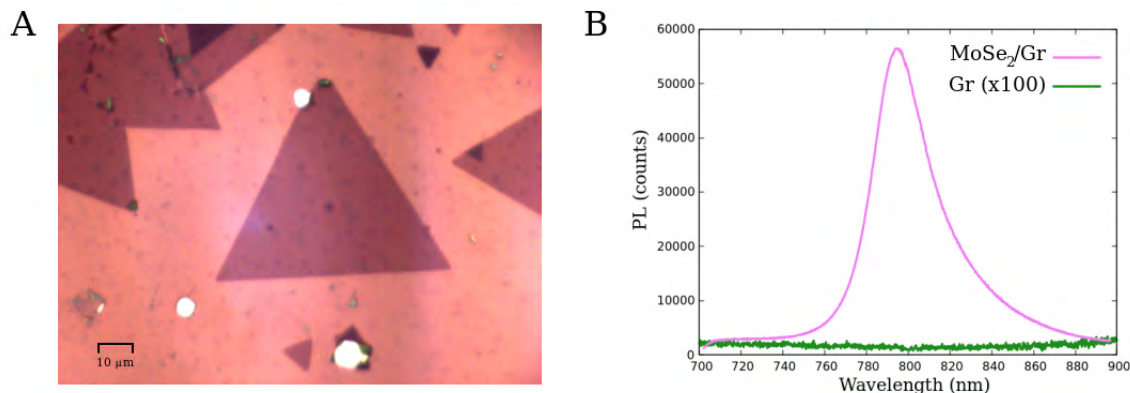


**Figure 3.7:** (A) Optical microscope image (x100) of CVD grown  $MoSe_2$  flakes transferred onto a substrate consisting of a graphene layer deposited on  $SiO_2/Si$ . (B) Far-field photoluminescence spectra recorded from a  $MoSe_2$  monolayer on graphene (pink line) and from the bare graphene substrate (dark green line). Both spectra were acquired under the same excitation (laser beam at 532 nm) and collection conditions.

Despite these contaminants, photoluminescence (PL) measurements were conducted on a  $MoSe_2$  monolayer flake as well as on the bare graphene substrate. As mentioned in Chapter 2 (section 2.2.2), the samples were first analyzed by PL before STM-LE measurements were performed. PL measurements provide a first characterization of TMD flakes luminescence, enabling  $MoSe_2$  monolayers to be identified and selected for further STM-LE analysis. The obtained PL spectra are depicted in Figure 3.7-B. The  $MoSe_2$ /Graphene spectrum (pink line) exhibits an emission peak at 795 nm (1.56 eV) with a full width at half maximum (FWHM) of about 70 meV. This intense peak, which is a clear signature of the luminescence from  $MoSe_2$  monolayers, corresponds to the radiative recombination of A-excitons. There is a slight shift in the peak maximum compared to PL measurements conducted by Iberi *et al.* [21] on a supported  $MoSe_2$  monolayer ( $\sim 1.55$  eV). This shift is attributed to the presence of the graphene substrate, which creates a different dielectric environment surrounding for the monolayer. The absence of photoluminescence signal from the bare graphene substrate (dark green line in Fig. 3.7-B) confirms its semimetallic character.

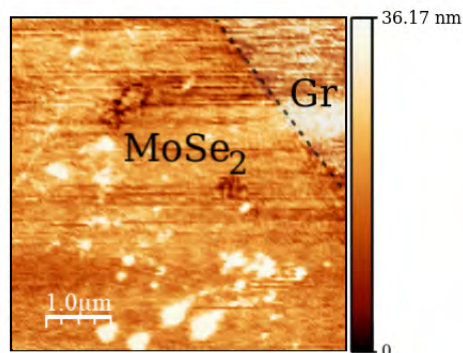


**Figure 3.8:**  $5\ \mu\text{m} \times 5\ \mu\text{m}$  STM topographic image ( $V_s = -1.8\ \text{V}$ ;  $I_t = 2\ \text{nA}$ ) of a  $MoSe_2$  monolayer deposited on the graphene substrate. The black dotted line outlines the boundary of the  $MoSe_2$  monolayer.

STM-LE measurements were carried out on  $MoSe_2$  monolayer flakes on graphene. Unfortunately, significant difficulties were encountered in achieving a stable tunneling current. Indeed, a noisy tunneling

current has been obtained in almost all STM acquisitions. This significantly affected the quality of the resulting STM images. Figure 3.8 displays the highest-quality STM image obtained from this sample, in which certain features of the sample surface can be distinguished. This image exhibits the presence of contaminants on both flake and bare graphene surfaces (bright contrasts in the image). These contaminants, residual PMMA remnants, were identified as responsible for the instability of the tunneling current during STM scanning. Further work is in progress regarding the transfer process of  $MoSe_2$  flakes, with a particular focus on optimizing surface cleaning to minimize the impact of chemical remnants. No STM-induced light emission was detected from this sample, neither during the acquisition of photonic maps using the photomultiplier nor through spectral measurements. Since STM-induced luminescence from such a sample has not yet been addressed in the literature to our knowledge, interpreting this absence of light emission is challenging. A possible explanation is the transfer of injected charges from the TMD to the graphene substrate. However, the intense PL signal obtained (Fig. 3.7-B) suggests that the transfer of photo-generated charges between the TMD and graphene layers does not occur. Therefore, achieving charge transfer using STM excitation seems unlikely. In fact, the PL signal leads us to think that the lack of STM-LE is more likely related to the electrical excitation source. Indeed, the presence of contaminants on the surface does not seem to affect the optical excitation or radiative decay of excitons. However, they could be an obstacle to the injection of charges into the monolayer via electron tunneling, hindering the formation of excitons.

### 3.2.2 $MoSe_2$ on ITO

The second non-plasmonic substrate onto which  $MoSe_2$  flakes have been transferred is an indium tin oxide (ITO) substrate. This latter has a thickness of a few hundred nanometers, and is deposited on a glass about 1 mm thick. The ITO substrate exhibits a unique combination of properties. It is a transparent oxide alloy that consists of indium oxide ( $In_2O_3$ ) and tin oxide ( $SnO_2$ ). It also has good electrical conductivity, making it an ideal candidate for opto-electronic devices. Furthermore, in the energy range of interest, ITO is not plasmonic as the real part of its permittivity remains positive [22]. Finally, unlike graphene, ITO has a granular surface. Photoluminescence and STM-induced luminescence of  $MoSe_2$  monolayers on ITO have recently been reported by Pommier *et al.* [15, 23]. It is important to note that in their measurements, they used a non-plasmonic tip ( $W$ ) and a different experimental setup where the emitted light is collected in transmission. A distinct mechanism underlying STM-induced light emission is emphasized by us, leading to experimental results that differ slightly from those of Pommier *et al.*. This aspect will be discussed further below.

The examination of the  $MoSe_2$ /ITO sample using an optical microscope reveals clean surfaces with few contaminants (Figure 3.9-A). Nevertheless, several flakes exhibit ripped areas and/or multilayered regions, generally located in the center of the flakes. A photoluminescence map was conducted on a small flake presenting a multilayered zone at its center (see Figure 3.9-B) with a filter centred at the A-exciton wavelength (800 nm) and a bandpass of  $\sim 20$  nm. As expected, the multilayered region does not exhibit any photoluminescence signal, which is in agreement with the discussion in section

1.2.2 of Chapter 1. Indeed, when a TMD flake is composed of more than one layer, its band structure presents an indirect bandgap and its interaction with light is very weak. Moreover, the PL map shows no light emission from the bare ITO substrate. Indeed, the latter does not exhibit any PL signal at 800 nm, as depicted in Figure 3.9-C. Within the monolayer region of the flake, variations in the PL signal are observed, with areas exhibiting higher intensity (depicted in white). This non-uniformity can be attributed to the presence of defects in the  $MoSe_2$  monolayer derived from the CVD synthesis method employed.

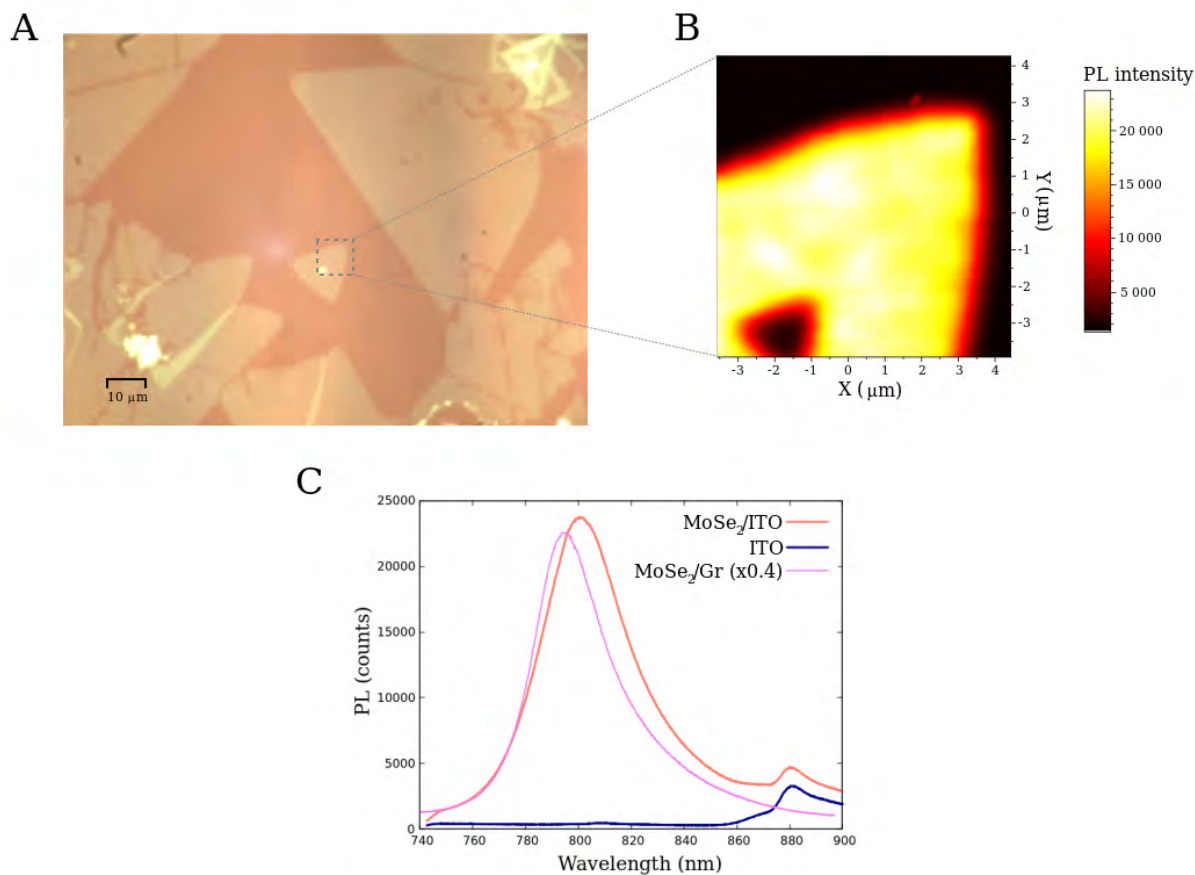


**Figure 3.9:** (A) Optical microscope image (x100) of CVD grown  $MoSe_2$  flakes transferred onto an ITO substrate. (B) Far-field photoluminescence intensity map of a  $MoSe_2$  monolayer flake (with a multilayer center) on ITO, acquired at the absorption wavelength of the A-exciton (800 nm). The acquisition area is indicated in panel (A) by a dashed gray rectangle. (C) Far-field photoluminescence spectra recorded from a  $MoSe_2$  monolayer on ITO (salmon color line) and from the bare ITO substrate (dark blue line). The photoluminescence spectrum recorded from a  $MoSe_2$  monolayer on graphene (pink line) is also plotted for comparison. These spectra along with the photoluminescence intensity map, were acquired under the same excitation conditions (laser beam at 532 nm) and collection parameters.

Photoluminescence spectra were acquired from both a  $MoSe_2$  monolayer on ITO and the bare ITO (see Figure 3.9-C). The PL spectrum of a  $MoSe_2$  flake on graphene is as well plotted for comparison. The  $MoSe_2/ITO$  spectrum exhibits a peak ascribed to A-exciton at 800 nm (1.55 eV) with a FWHM of  $\sim 84$  meV. Compared to  $MoSe_2/Graphene$ , this peak is approximately 2.5 times weaker. Additionally, it is redshifted and broader. These differences can be mainly attributed to the change of substrate,

which alters the dielectric environment of the  $MoSe_2$  ML and consequently affects its optical properties. The peak at 880 nm in the  $MoSe_2$ /ITO spectrum can be attributed to the ITO substrate, as it is also present in the spectrum of bare ITO. Indeed, the  $MoSe_2$ /ITO PL spectrum was acquired from a flake with ripped areas so the laser spot was exciting both the  $MoSe_2$  monolayer and a portion of the bare ITO substrate.

STM-induced luminescence measurements were performed on the  $MoSe_2$ /ITO sample. Photon emission has been detected from several  $MoSe_2$  flakes, allowing one to conduct photonic maps and spectral measurements. Light emission is detected only if a negative bias voltage  $V_s$  is applied to the sample. This contrasts with the results of Pommier *et al.* [15, 23]. In their case, light emission is detected only for a positively biased substrate. They reported that the use of a negative bias voltage applied to the substrate, leads to a deformation of the  $MoSe_2$ /ITO sample, which has not been observed in our case.

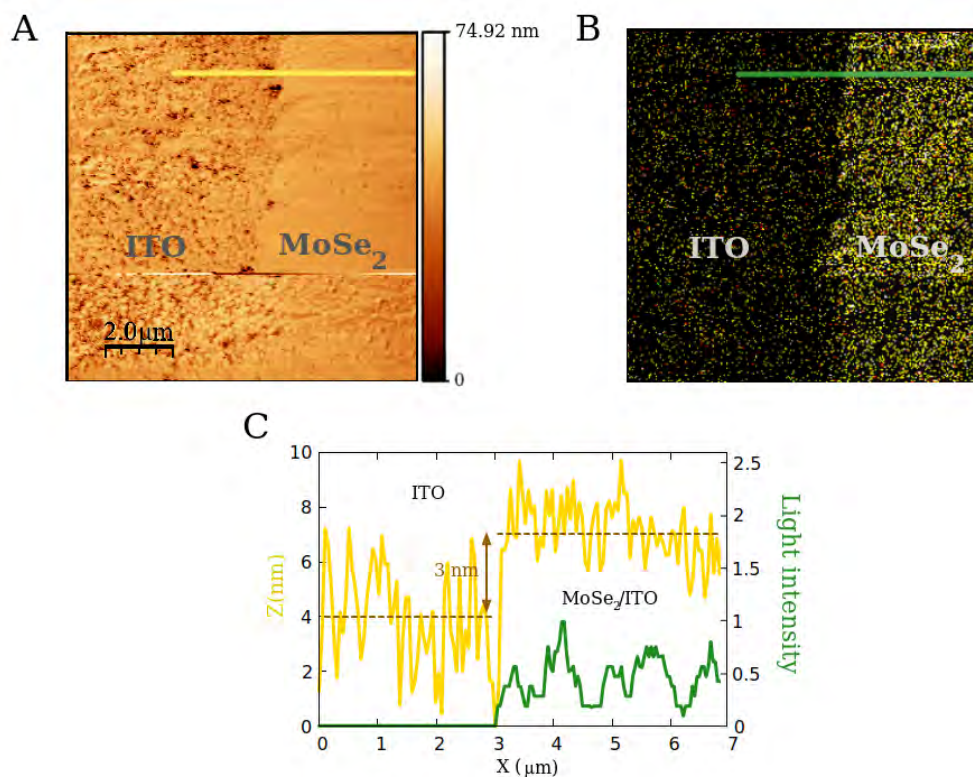


**Figure 3.10:** (A) STM topographic image and (B) corresponding photonic map of a  $MoSe_2$  monolayer on ITO. Both images were recorded simultaneously on a  $10\ \mu\text{m} \times 10\ \mu\text{m}$  area ( $V_s = -1.8\ \text{V}$ ;  $I_t = 15\ \text{nA}$ ). The boundary of the  $MoSe_2$  monolayer is clearly visible in both images. An average of 12 counts per second is obtained when the tip is scanning the  $MoSe_2$ /ITO area on the right of the panels (A) and (B). (C) Topographic and normalized light intensity profiles taken along the yellow and green lines in panels (A) and (B) respectively. The  $MoSe_2$  monolayer is unambiguously identified by a change in height ( $\Delta z = 3\ \text{nm}$ ) and an enhanced light emission intensity.

Figure 3.10 displays an STM topographic image and its corresponding photonic map. The bare ITO and the  $MoSe_2$  flake are clearly distinguished in both images: bare ITO on the left and  $MoSe_2$ /ITO

on the right. In the STM image, noticeable contrast differences can be observed between the two regions, with the bare ITO area exhibiting a more prominent surface roughness. The topographic profile along the yellow line (see Fig. 3.10-(A,C)) shows the granular structure of the ITO surface, even if a  $MoSe_2$  ML is deposited on it. An average height difference of 3 nm is obtained between the two regions. Considering that the thickness of the  $MoSe_2$  ML is approximately 0.8 nm, there is a separation of about 2.2 nm indicating that the  $MoSe_2$  ML and the substrate are decoupled. On the other hand, for the photonic map,  $MoSe_2$ /ITO is clearly identified as the only area exhibiting light emission. Indeed, as mentioned before, ITO does not present any STM-induced luminescence in the wavelength range of interest. This is as well confirmed by the light intensity profile taken along the green line (see Fig. 3.10-(B,C)). This photonic map is obtained using a negative bias voltage of  $V_s = -1.8$  V. It is worth noting that no light emission has been detected when a positive bias voltage was applied to the sample. A tip-jump at the bottom part of Figure 3.10-(A,B) can be observed. After the tip-jump (bottom part of both images recorded from an up-down scan), the tip apex geometry changes, resulting in a distinct STM topographic image and a photonic map with lower light emission intensity. An average of 12 counts per second was detected by the photomultiplier when the tip was scanning the  $MoSe_2$  flake with a tunneling current of  $I_t = 15$  nA. The measured light emission rate is thus around  $10^{-10}$  photons per tunneling electron. Considering the solid angle of the optical fiber used for photon collection ( $\Omega = \frac{9\pi}{100}$  sr) and the quantum efficiency of the photomultiplier at the wavelength of interest ( $\sim 10\%$ ), the estimated total light emission rate for this sample is  $\sim 3 \times 10^{-8}$  photons per tunneling electron. This value is slightly lower than the one obtained by Pommier *et al.* [15, 23] ( $10^{-7}$  photons per tunneling electron) using the transmission mode.

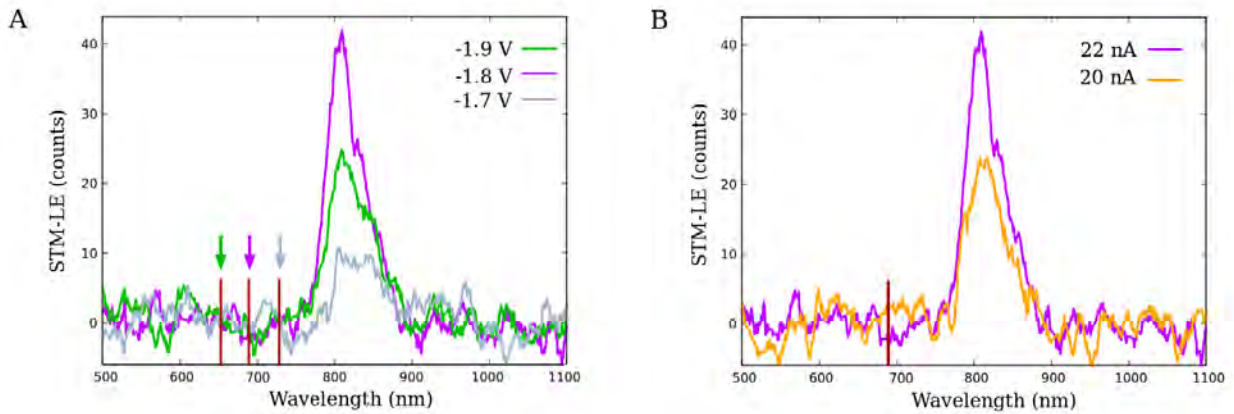


**Figure 3.11:** STM-induced luminescence spectra of a  $MoSe_2$  monolayer on ITO: (A) versus bias voltage  $V_s$  at the tunneling current  $I_t = 22$  nA and (B) versus tunneling current  $I_t$  at the sample bias voltage of  $V_s = -1.8$  V. All spectra were obtained with an acquisition time of 600 s. The arrows and red bars in panels (A) and (B) indicate the wavelength corresponding to the energy  $e|V_s|$ .

The  $MoSe_2$ /ITO sample exhibits a relatively low light emission efficiency. Thus, to analyze the spectral distribution of the emitted light, spectral measurements with an extended acquisition time (600 s) were conducted. The STM-LE spectral features are investigated as a function of the bias voltage  $V_s$  and tunneling current  $I_t$ , as shown in Figure 3.11. The spectra present a low signal-to-noise ratio

and a limited reproducibility. Indeed, the low light emission efficiency requires an extended acquisition time, which in turn introduces significant noise into the spectra. In order to minimize the noise, these spectra have been slightly smoothed. In Figure 3.11-A, three STM-LE spectra acquired at different bias voltages  $V_s$  are plotted. Unlike light emission from plasmonic substrates (see section 3.1.1), the spectra obtained do not have a high-energy threshold that follows the quantum law  $\hbar\omega = e|V_s|$ . Instead, regardless of the bias voltage  $V_s$ , the same asymmetric emission peak between approximately 740-910 nm, with a maximum intensity at around 805 nm (1.54 eV), is obtained. This peak corresponds to the radiative decay of A-excitons, formed from the injection of charges via the tunneling current. The peak intensity does not seem to follow a specific trend as  $|V_s|$  increases. The spectra of Figure 3.11-B exhibit the same peak of light emission regardless of the tunneling current  $I_t$  being considered. It is observed that a higher  $I_t$  results in a more intense emission peak. This can be explained by the fact that as the number of electrons participating in the tunneling current increases, a greater amount of charges are injected into the monolayer, leading to the formation of more excitons. Consequently, a higher light emission efficiency is achieved. Due to the aforementioned limitations, only a few spectra have been recorded. Therefore, the evolution of the emission peak intensity as a function of  $V_s$  and  $I_t$  observed in Figure 3.11 is not conclusive, since its reproducibility could not be confirmed. Given the long acquisition time, these spectra which were obtained using a “fixed tip position” (no-scanning mode), were actually acquired during a slow scanning process due to thermal drift, which causes the tip to gradually move relative to the surface. Thus, the same excitonic peak is obtained wherever the spectrum is acquired on the  $MoSe_2$  surface.

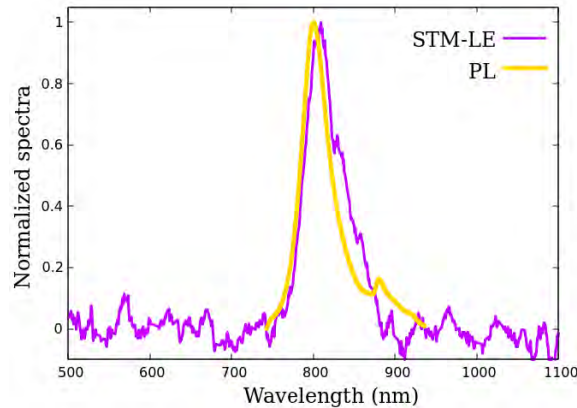


**Figure 3.12:** Normalized photoluminescence (yellow line) and STM-induced luminescence (violet line) spectra of a  $MoSe_2$  monolayer on ITO. The STM-LE spectrum was acquired using the tunneling parameters:  $V_s = -1.8$  V;  $I_t = 22$  nA and acquisition time of 600 s.

By comparing normalized STM-LE and PL spectra shown in Figure 3.12, both light emission processes can be unambiguously attributed to the same mechanism: the radiative decay of A-excitons within the  $MoSe_2$  monolayer. Indeed, both spectra exhibit the same spectral signature: a sharp emission peak at the A-exciton wavelength. Nevertheless, a few differences can be observed between the two spectra. With respect to the PL peak, the STM-LE peak maximum is slightly redshifted from 800 to 810 nm (from 1.55 to 1.53 eV) and broadened (from  $\sim 84$  meV to  $\sim 96$  meV). These spectral differences

can be attributed to various factors. The presence of the tip may modify the dielectric environment surrounding the  $MoSe_2$  monolayer, thereby altering its intrinsic optical properties. Additionally, the increase in sample temperature resulting from the local injection of charges could contribute to these differences. Furthermore, according to [18, 24], STM electron tunneling may broaden the excitonic peak by facilitating the formation of trions. Another notable difference between both spectra is the signal-to-noise ratio which is substantially lower for the STM-LE.

As previously stated, the STM-induced light emission from  $MoSe_2/ITO$  is only detected when a negative bias voltage is applied to the sample. In the range of tested bias voltages, varying from -0.5 V to -2 V, light emission is detected solely when  $V_s \leq -1.7$  V. To address this point, an excitation mechanism for the creation of excitons within the  $MoSe_2$  layer via the tunneling current is proposed, with the intention of offering an explanation for the excitonic STM-LE observed under these specific experimental conditions. An energy band diagram illustrating the creation mechanism of A-excitons within the TMD ML in the  $Au/MoSe_2/ITO$  tunneling junction is shown in Figure 3.13. The optical bandgap ( $E_{gap} = 1.55$  eV) of the monolayer is represented and for the sake of simplicity, the ground state of the A-exciton is considered the conduction band (CB) minimum. The  $MoSe_2$  flakes studied in this work are n-doped [25], i.e., electrons are the majority charge carriers in the monolayer. Considering the energy band diagram of a n-doped  $MoSe_2$  ML transferred onto a gold substrate determined by Chang *et al.* [26] using ultraviolet photoemission spectroscopy, and the similarity in work functions between gold and ITO ( $\phi_{ITO} = 5.2$  eV [27] and  $\phi_{Au} = 5.1$  eV), it is assumed that the Fermi level lies a few hundreds of meV below the CB minimum of the  $MoSe_2$  layer (see Fig. 3.13-A). The absence of a Schottky barrier is assumed between the monolayer and the substrate due to the extreme thinness of the  $MoSe_2$  layer. Furthermore, it is considered that the substrate acts as a reservoir of electrons, and that electrons can easily tunnel between the monolayer and the substrate [1]. When a negative bias voltage  $V_s$  is applied to the substrate (see Fig. 3.13-B), the energy levels of the monolayer and substrate shift up. When the bias voltage  $V_s$  exceeds a certain threshold ( $-eV_s > [E_{gap} - \text{a few hundred meV}]$ ), electron tunneling can take place from the valence band (VB) of the monolayer to the tip. This process leaves a hole in the TMD VB (around the  $K$ -valley) which can attract an electron either from the CB or from the substrate electronic states, resulting in the formation of an exciton. Subsequently, this exciton can recombine radiatively, giving rise to the observed light emission.

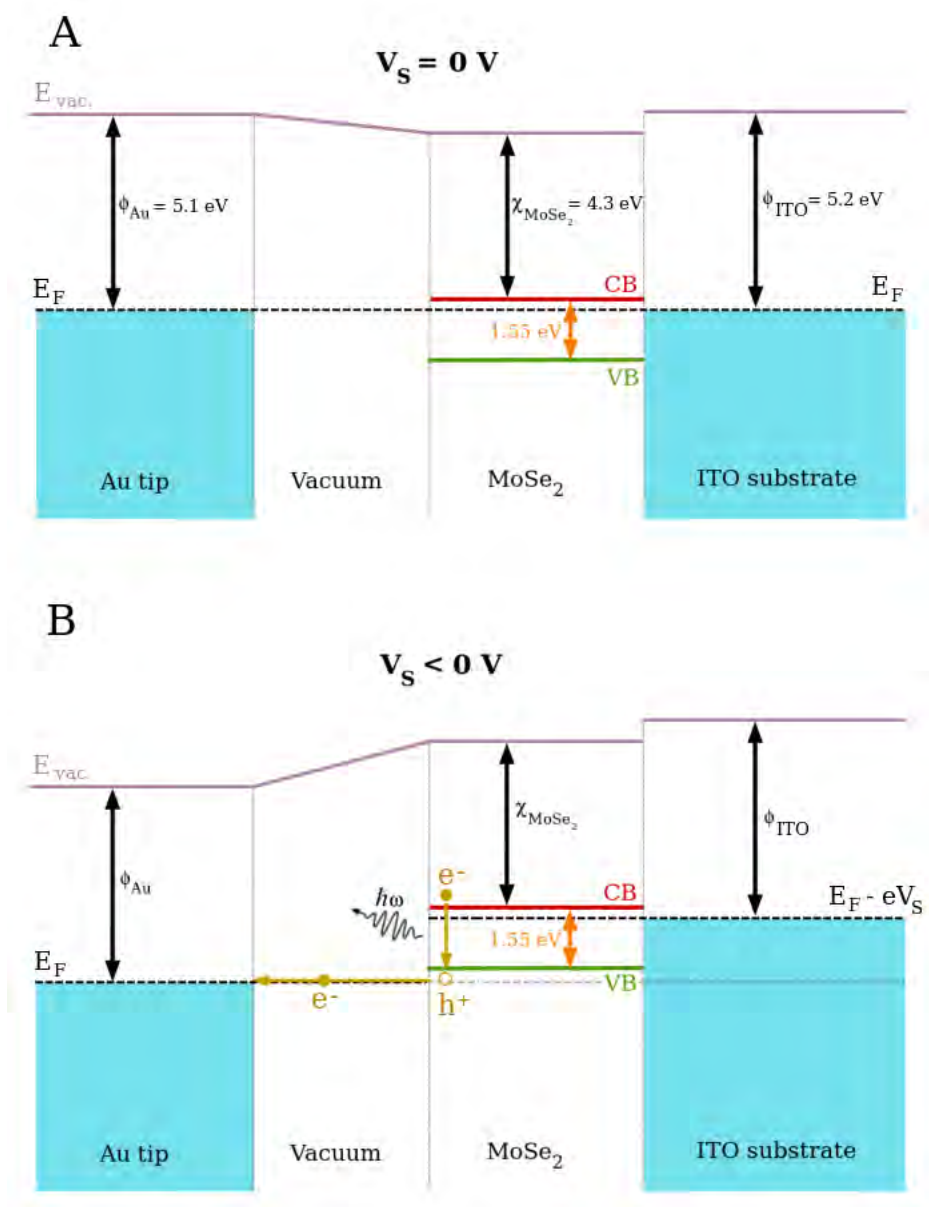


**Figure 3.13:** Energy band diagrams of the  $Au/MoSe_2/ITO$  tunneling junction when: (A) no bias voltage is applied to the sample ( $V_s = 0\text{ V}$ ) and (B) a negative bias voltage is applied to the sample ( $V_s < 0\text{ V}$ ). In the latter case, the application of a negative bias voltage induces electron tunneling from the  $MoSe_2$  monolayer to the gold tip, resulting in the generation of holes in the  $MoSe_2$  valence band. This process enables the recombination of electron-hole pairs.

As previously discussed, an analysis of the height profile along the boundary of a  $MoSe_2$  flake (see Fig. 3.10) reveals an average separation of approximately 2.2 nm between the monolayer and the substrate. Hence, there is no direct contact or tunneling distance between them, reducing the charge transfer probability between the two materials. This could explain the relatively low emission rate obtained. Moreover, it is possible that the energy difference between the CB minimum and the Fermi level has been overestimated. Indeed, the Fermi level could be situated only a few tens of meV below the CB minimum, providing an explanation for the STM-induced light emission being only observed

at bias voltages  $V_s \leq -1.7$  eV. Another possibility that can not be ruled out is a band bending of the TMD, which could result in a reduced difference of potential between the tip and the monolayer. When a positive bias voltage  $V_s$  is applied to the sample, electrons may tunnel from the tip to the monolayer CB. However, as the monolayer is n-doped, this leads to an increase in the electron population within the CB. Since there is a lack of available holes in the TMD VB, exciton formation is very unlikely to occur. This explains the absence of light emission when a positive bias voltage is used. In this case, the electron-hole recombination process is only possible through the creation of holes by impact ionization, i.e., by collision of hot inelastic electrons within the monolayer. This process can be amplified by the very high DC electric field applied to the tunnel junction. In their work, Pommier *et al.* [15, 23] attributed the light emission to a resonant energy transfer from the tunneling current to the excitons confined in the  $MoSe_2$  monolayer via near-field electromagnetic coupling. While this excitation mechanism can take place as well in our case, it cannot be the sole mechanism responsible for the observed light emission. The tunneling conditions necessary for light emission in our experiments differ from theirs, pointing to the involvement of a distinct mechanism: electron-hole pair recombination triggered by holes creation via charge injection.

### 3.3 Light emission from $MoSe_2$ monolayer on plasmonic substrates

In the first part of this chapter, the experimental results of STM-LE measurements carried out on purely plasmonic tunneling junctions, as well as on  $MoSe_2$  monolayers deposited on non-plasmonic substrates were addressed. The subsequent sections of this chapter deal with the light emission from hybrid junctions composed of  $MoSe_2$  monolayers transferred onto a plasmonic gold substrate. In a hybrid TMD/plasmonic-metal STM junction, both distinct radiative processes studied in the first part of this chapter can occur: the radiative decay of plasmon modes excited by inelastic electron tunneling, and the radiative recombination of excitons within the TMD monolayer created by charge injection. Spectral analysis of the obtained luminescence will provide details of the radiative mechanism underlying the STM-LE. As discussed in section 1.2.3 of Chapter 1, the interaction between plasmon modes and confined excitons can give rise to hybrid systems with novel properties. Studying the light emission from a hybrid  $Au/MoSe_2/Au$  junction offers then an interesting approach to explore the interplay between plasmon modes and excitons. Their respective role in the light emission process are analyzed by comparing the experimental STM-LE results obtained from this hybrid junction with those obtained from other samples studied in the earlier sections of this chapter. Similar results to those presented here were published by Péchou *et al.* [1], i.e., by our research team, prior to the start of my thesis.

The CVD grown  $MoSe_2$  monolayers were transferred onto a gold film similar to the one described in section 3.1.1, playing the role of plasmonic substrate. The latter presents a granular surface with

grains with a typical diameter of less than 100 nm. The optical microscope image of such a sample is shown in Figure 3.14-A. Most of the larger flakes exhibit a multilayered region at their center, such as the flake located at the top right corner of the image. Thus, to ensure light emission to occur, PL and STM-LE measurements were mainly conducted on small flakes to avoid multilayered areas. Light emission measurements were conducted on the cleanest parts of the sample to avoid residual chemical remnants.

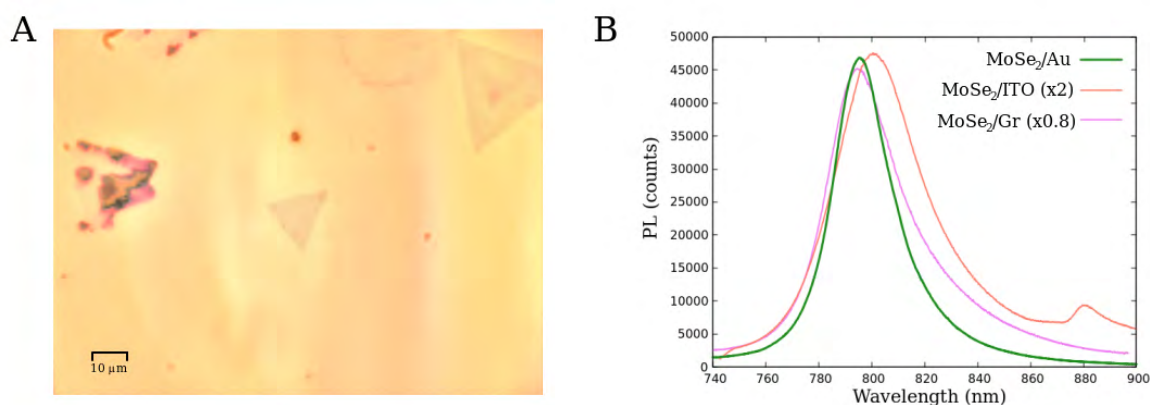


**Figure 3.14:** (A) Optical microscope image (x100) of CVD grown  $MoSe_2$  flakes transferred onto a granular gold substrate. (B) Far-field photoluminescence spectra recorded from a  $MoSe_2$  monolayer on gold (dark green line), on ITO (salmon color line) and on graphene (pink line). The spectra of  $MoSe_2$  monolayer on ITO and on graphene are plotted for comparison. All these spectra were acquired under the same excitation (laser beam at 532 nm) and collection conditions.

The typical photoluminescence spectrum recorded from a  $MoSe_2$  monolayer supported by the gold substrate is plotted in green in Figure 3.14-B. Additionally, the PL spectra of  $MoSe_2$ /ITO and  $MoSe_2$ /Graphene are also plotted for comparison. As in the case of non-plasmonic substrates, an intense peak at the A-exciton wavelength is observed. Since all PL spectra were acquired under the same excitation and collection conditions, they can be directly compared. Among the three PL spectra, the one corresponding to  $MoSe_2$ /Au exhibits the narrowest peak with a FWHM of  $\sim 52$  meV, and its intensity maximum at 797 nm (1.56 eV) lies between those of the PL spectra obtained with graphene and ITO substrates. Indeed, the use of different substrates leads to different PL signals. As discussed previously, varying the dielectric environment surrounding the monolayer results in slight variations in the optical properties of the latter. Indeed, the dielectric screening of the substrate can change the Coulomb interaction between electrons and holes, thereby affecting the formation and properties of excitons.

Figure 3.15 shows an STM topographic image and its corresponding photonic maps acquired at the boundary of a  $MoSe_2$  monolayer flake. The STM image (Fig. 3.15-A) and the photonic map acquired with a positive bias voltage  $V_s$  (Fig. 3.15-B) were simultaneously recorded. On the other hand, the photonic map obtained using a negative bias voltage (Fig. 3.15-C) was recorded in the same area immediately afterward in order to minimize any displacement of the tip or surface caused by thermal

drift. The boundary between the TMD monolayer and the bare substrate is clearly visible in all three images. In the STM image, due to the thinness of the monolayer, the granular structure of the gold substrate is observed even when the tip scans the monolayer since this latter follows the substrate topography. This makes it difficult to distinguish between the two regions based on a difference in corrugation. However, the boundary is identified by a disruption in the surface topography.

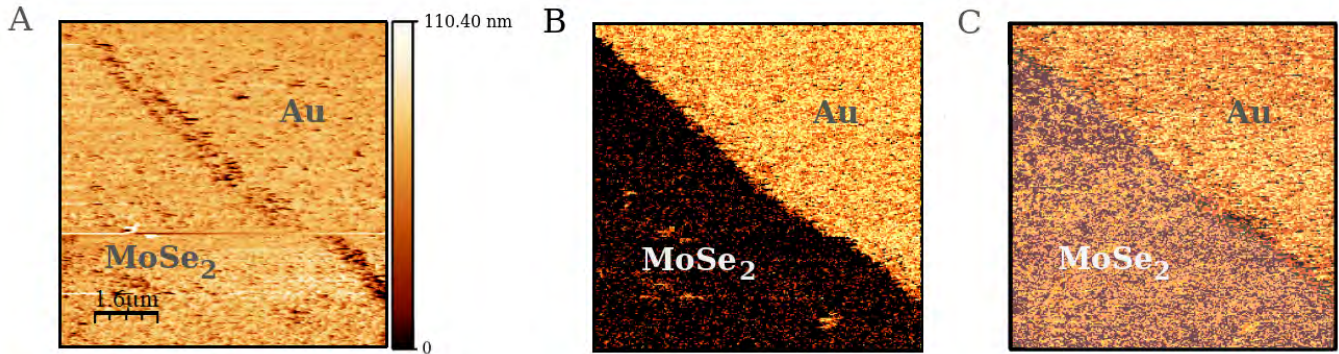


**Figure 3.15:** (A) STM topographic image and (B-C) corresponding photonic maps recorded on a  $8 \mu\text{m} \times 8 \mu\text{m}$  area with a (B) positive bias voltage  $V_s = +1.7 \text{ V}$  and a (C) negative bias voltage  $V_s = -1.7 \text{ V}$ . (A) and (B) were acquired simultaneously while (C) was recorded at the same location immediately afterward. The tunneling current used is  $I_t = 5 \text{ nA}$ . At a positive bias voltage (B), the scanning of the bare gold substrate and the  $\text{MoSe}_2$  flake yields to an average of 600 and 5 photon counts per second, respectively. At a negative bias voltage (C), the gold substrate displays an average photon count of 500 per second, while the  $\text{MoSe}_2$  flake shows an average of 150 photon counts per second.

In the photonic maps, both regions are distinguishable due to an evident difference in light emission intensity. For  $V_s > 0$ , a significant difference in STM-LE intensity is detected between the bare gold substrate, which presents an average of 600 photon counts per second, and the  $\text{MoSe}_2$  layer exhibiting only 5 photon counts per second. On the other hand, for  $V_s < 0$ , the difference in luminescence intensity significantly decreases with an average of 500 and 150 photon counts per second for the gold substrate and the TMD monolayer, respectively. As discussed in section 3.1.1 of this chapter, the gold substrate exhibits light emission regardless of the sign of the bias voltage  $V_s$  applied to the substrate. Indeed, plasmonic modes in the tip-surface cavity are excited regardless of the direction of the tunneling electron flow. However, a slight difference (about 100 photon counts per second) is observed in the light emission rate of the bare substrate when the sign of  $V_s$  is modified. This difference is attributed to the asymmetry of the STM junction, which leads to a distinct excitation of plasmon modes depending on the direction of electron flow. On the other hand, the  $\text{MoSe}_2$  monolayer exhibits a significantly different STM-LE rate depending on the  $V_s$  sign, as observed in the case of the  $\text{MoSe}_2/\text{ITO}$  sample studied in the previous section. Indeed, a yield about 30 times higher is obtained when the sample is negatively biased. It is worth noting that the luminescence from the monolayer detected when  $V_s > 0$  is localized mostly in some spots. This luminescence can be attributed to various factors such as light emission from the substrate caused by tearing, cracks, or other defects in the  $\text{MoSe}_2$  monolayer. Another possible explanation, less unlikely given the size of the luminescence spots, is the radiative decay of excitons

trapped in monolayer defects and formed by impact ionization [1]. The difference in the light emission rate between the gold substrate and the monolayer for  $V_s < 0$  is attributed to a distinct radiative process behind STM-LE. To investigate this further, a spectral analysis of  $MoSe_2$  luminescence is conducted (see below).

The quantum efficiency of the light emission from the  $MoSe_2/Au$  sample when a negative bias voltage is used can be estimated from the photonic map of Figure 3.15-C. An average of 150 photon counts per second using a tunneling current of  $I_t = 5$  nA corresponds to a total quantum yield of around  $1 \times 10^{-6}$  photons per tunneling electron (taking into account the solid angle of the fiber and the quantum efficiency of the photomultiplier). Since the STM-LE measurements carried out on  $MoSe_2/Au$  and  $MoSe_2/ITO$  were conducted using different gold tips and a different alignment between the tip apex and the optical fiber used for light collection, the comparison of emission quantum efficiency can only be done qualitatively. The light emission rate obtained using gold substrates is approximately two orders of magnitude superior to the one obtained with ITO ( $\sim 3 \times 10^{-8}$  photons per electron), a non-plasmonic substrate. This enhancement of the light emission rate is therefore attributed to the plasmonic character of the substrate. Consequently, it is reasonable to assume that plasmon modes play a significant role in the light emission generated by the monolayer. The quantum efficiency obtained is comparable to the value reported by P  chou *et al.* [1] ( $4 \times 10^{-6}$  photons per electron) obtained from the same kind of  $MoSe_2/Au$  sample and using the same experimental setup.

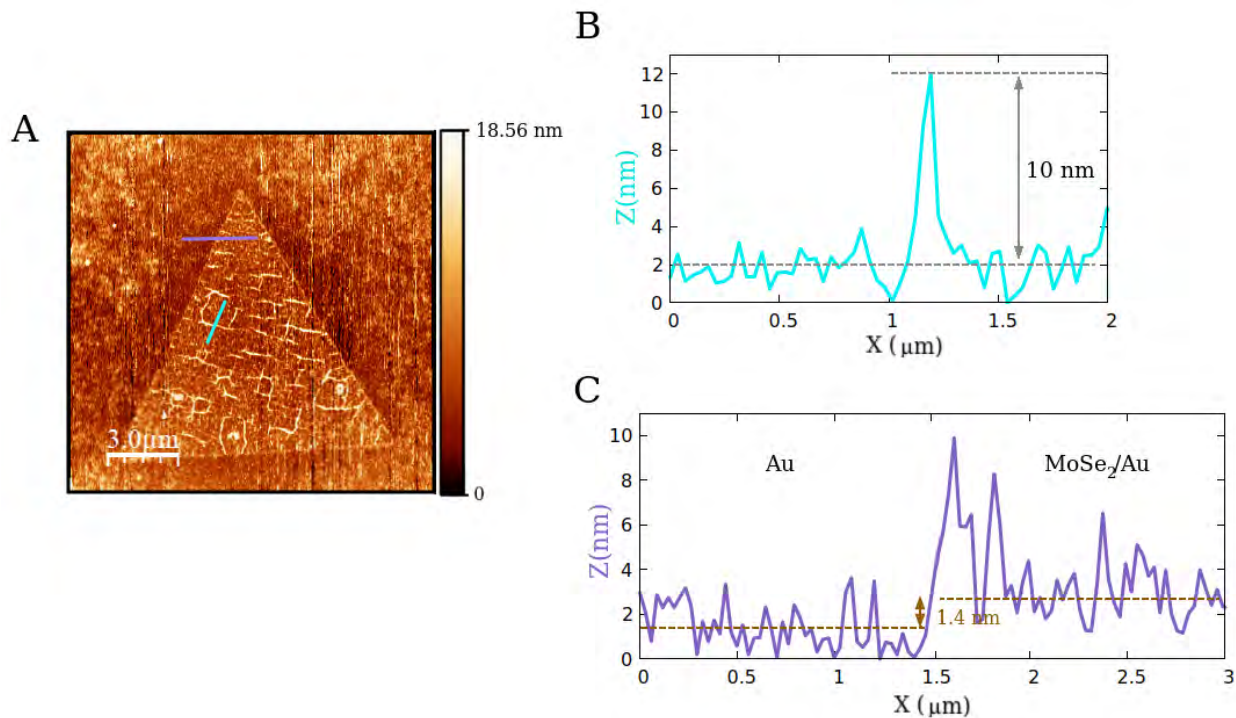


**Figure 3.16:** (A)  $15 \mu\text{m} \times 15 \mu\text{m}$  AFM height image of a  $MoSe_2$  monolayer flake deposited onto a granular gold substrate. (B) Topographic profile taken along the blue line in panel (A) showing a fold in the  $MoSe_2$  flake. (C) Topographic profile taken along the violet line in panel (A) indicating a step height of 1.4 nm at the boundary of the  $MoSe_2$  flake.

As luminescence spots from the  $MoSe_2/Au$  sample were observed in the photonic map recorded with a positive  $V_s$  (Figure 3.15-B), an AFM height image of the flake, shown in Figure 3.16-A, has been conducted in order to evaluate the quality of the ML. The AFM image reveals numerous folds originated from the transfer process of the flake onto the gold substrate. Some of these folds extend over several micrometers, and according to the topographic profile of Figure 3.16-B, these folds can reach a height of ten nanometers compared to the rest of the flake. Including those that are too small to be observed in the large-scale AFM image, the flake folds can serve as ideal traps for excitons. The presence of these folds leads us to question the quality of the flake transfer process and thus, to suspect the presence of other not visible defects (tearing, cracks, missing or impurity atoms) within the monolayer. These defects could explain the aforementioned spots of luminescence. Moreover, an average height difference of 1.4 nm is obtained between the  $MoSe_2$  flake observed in the AFM image and the bare substrate (see Fig. 3.16-C) indicating an average separation of 0.6 nm between them (a monolayer thickness of  $\sim 0.8$  nm is considered). This sub-nanometric distance suggests that the monolayer is coupled to the gold substrate, as electrons from the metallic substrate can easily tunnel to the  $MoSe_2$  monolayer.

Spectral analysis has been conducted on the STM-induced light emission obtained from the  $MoSe_2$  monolayer using a negative bias voltage. A series of spectra as a function of the bias voltage  $V_s$  and the tunneling current  $I_t$  acquired with a “fixed tip position” (no-scanning mode) are shown in Figure 3.17.

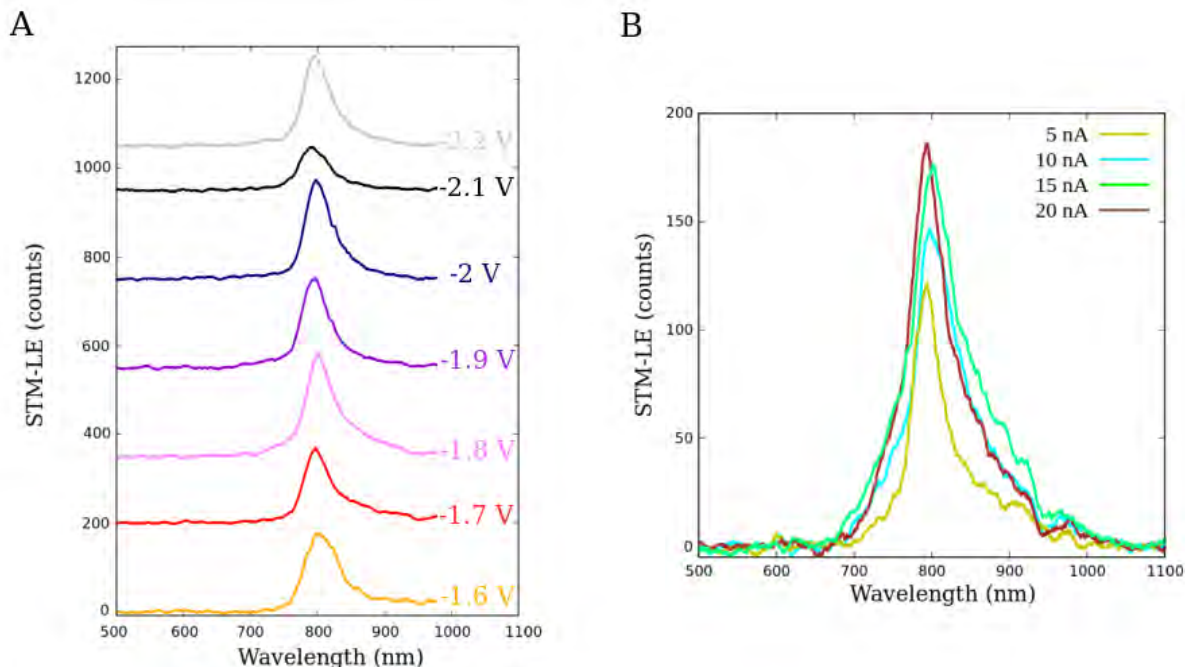


**Figure 3.17:** STM-induced luminescence spectra recorded from a  $MoSe_2$  monolayer on a granular gold sample: (A) versus bias voltage  $V_s$  at the tunneling current  $I_t = 20$  nA (spectra are vertically offset for clarity) and (B) versus tunneling current  $I_t$  at the sample bias voltage of  $V_s = -1.8$  V. All spectra were obtained with an acquisition time of 90 s.

A unique and relatively sharp peak with a maximum around the A-exciton wavelength (800 nm

corresponding to an energy of 1.55 eV) is obtained in all spectra regardless of the (negative) bias voltage and the tunneling current. These asymmetric peaks exhibit extended high-wavelength tails compared to those obtained in the case of  $MoSe_2/ITO$ . This difference can be attributed to the presence of high background noise in the  $MoSe_2/ITO$  STM-LE spectra, which conceals the small light emission contribution at the peak tails. Another possibility is that the photon emission observed at high wavelengths corresponds to plasmonic emission from the substrate. Spectral features such as the absence of a high-energy quantum cutoff in the series of spectra as a function of  $V_s$  (see Fig. 3.17-A) and the presence of a single emission peak, confirm that light emission originates from the radiative decay of excitons confined within the monolayer and not from the decay of plasmon modes. Even if the same spectrum is always obtained, some random-like variations in both the peak intensity and position (the peak maximum varies within a small range of energy from 1.55 to 1.564 eV) are observed as  $V_s$  increases. These variations are attributed to the fact that, due to thermal drift, each spectrum was acquired at slightly different locations (within nanometer proximity) on the  $MoSe_2$  monolayer surface. On the other hand, when the tunneling current  $I_t$  increases, the intensity of STM-LE increases as shown in Figure 3.17-B. This indicates that a large number of injected charges within the monolayer leads to an increase of the light emission.

The mechanism behind STM-LE from the  $MoSe_2/Au$  sample is very similar to the one proposed for the  $MoSe_2/ITO$  sample in section 3.2.2 of this chapter, since both light emissions have the same spectral signature and similar bias voltage-dependent behavior. Indeed, luminescence from  $MoSe_2/Au$  is only detected when a negative bias voltage  $V_s$  inferior or equal to -1.6 V ( $V_s \leq -1.6$  V) is used. When the substrate is negatively biased and a certain voltage threshold is exceeded, electrons can tunnel from the monolayer valence band to the tip, resulting in the creation of holes. These holes can attract electrons from the ML conduction band or from the substrate and form excitons, which may decay radiatively giving rise to the observed light emission. Since a relatively small separation between the monolayer and the gold substrate has been measured (an average of 0.6 nm), it is reasonable, in this scenario, to consider the metal substrate as a reservoir of electrons, and charge transfer can easily take place from the monolayer to the substrate and vice-versa. The difference in light emission rate obtained when using a gold or an ITO substrate can be partly attributed to the small separation between the monolayer and the gold substrate allowing a more efficient transfer of charges. However, the main reason for this difference is ascribed to the interaction between the excitons confined in the monolayer and the localized surface plasmon modes excited in the tip-surface gap region, both being induced by the tunneling current. It is worth noting that while excitons are created through the injection of charges into the monolayer, the excitation of plasmon modes comes from the energy loss of inelastic tunneling electrons. A near-field electromagnetic coupling takes place between plasmon modes and excitons resulting from their spatial and spectral overlap. This coupling leads to a highly efficient energy transfer, resulting in an increase in exciton creation within the monolayer and thus, an increment in the light emission rate. As for some TMD/plasmonic systems discussed in section 1.2.3 of Chapter 1, in

this hybrid junction, the interaction between plasmon modes excited in the gap and excitons, leads to an exaltation of the optical properties of the monolayer. The substrate plays thus a crucial role in the intensity of the excitonic light emission from  $MoSe_2$  monolayers. Chapter 4 of this manuscript is devoted to the theoretical description of the plasmon-exciton coupling taking place in this hybrid junction through electrodynamic simulations. The aim is to gain insights into the conditions and properties of the plasmon-exciton interaction. Based on the comparison of the light emission rates obtained for  $MoSe_2/Au$  and  $MoSe_2/ITO$  samples, it can be suggested that plasmon-exciton energy transfer is more efficient than the resonant energy transfer from the tunneling current to the excitons discussed in the  $MoSe_2/ITO$  section.

Figure 3.18 presents the linear and semilog scale plots of the normalized STM-LE and PL spectra recorded from the  $MoSe_2/Au$  sample. The interaction between plasmon modes and excitons enhances the excitonic light emission, leading to an STM-LE spectrum with a very high signal-to-noise ratio, comparable to that obtained by PL. This is a remarkable result, given that the tunneling current is a more localized source of excitation than the PL optical excitation. Both spectra exhibit the same light emission peak with a maximum at 797 nm (1.56 eV).

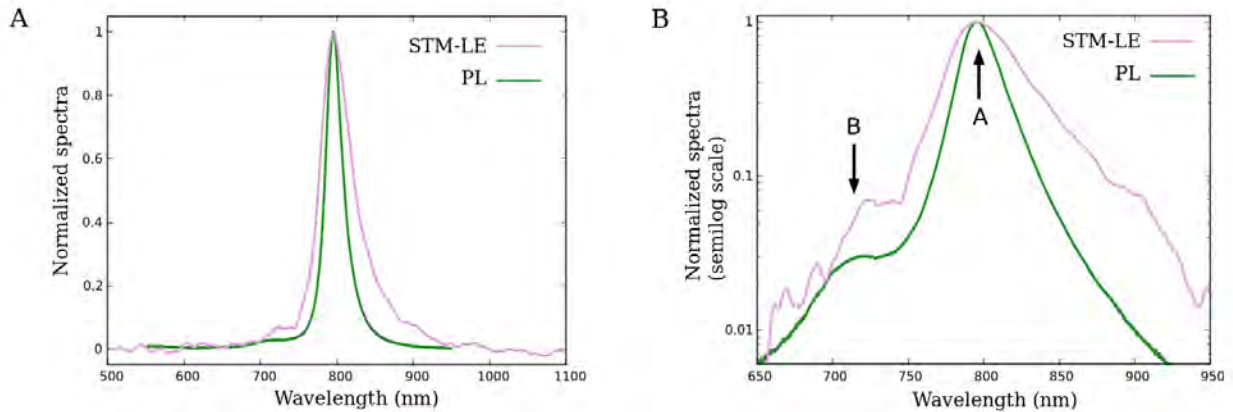


**Figure 3.18:** Normalized photoluminescence (dark green line) and STM-induced luminescence (pink line) spectra of a  $MoSe_2$  monolayer on a granular gold substrate using linear (A) and semilog scale (B). The STM-LE spectrum was acquired with the following tunneling parameters:  $V_s = -2$  V;  $I_t = 20$  nA and an acquisition time of 90 s. Both spectra exhibit a second peak visible in the semilog scale (B) at the B-exciton absorption wavelength.

However, the peak in the PL spectrum is narrower and exhibits greater symmetry than the STM-LE spectrum. A FWHM of  $\sim 52$  meV and  $\sim 94$  meV has been measured for the PL and STM-LE spectra, respectively. The presence of localized electronic states within the optical gap of the monolayer, induced by the gold substrate, as suggested by Péchou *et al.* [1], could account for these spectral variations. Indeed, these electronic states would lead to radiative recombinations at slightly lower energies than the optical bandgap, thus explaining the asymmetry and broadening of the STM-LE peak lineshape. By applying a semilog scale, a second emission peak around 720 nm (1.72 eV) is highlighted. This peak can be ascribed to the radiative decay of B-excitons. It is worth noting that this second peak

is redshifted ( $\sim 50$  meV) compared to the B-exciton peak reported by Iberi *et al.* [21] for suspended  $MoSe_2$  monolayers. This redshift can be assigned to the use of a different substrate, leading to a different dielectric environment around the monolayer.

The spectra acquired during STM scanning of some  $MoSe_2$  flakes can be classified into three categories, as shown in Figure 3.19-A. Excitonic-type light emission spectra, whose signature is highlighted and described above, can be obtained. They are characterized by a single narrow light emission peak at the A-exciton wavelength. On the other hand, it is also possible to obtain spectra with a typical plasmonic signature. Indeed, luminescence can be dominated by inelastic electron transitions between the tip and TMD states, while excitonic radiative recombination is quenched [28]. The plasmonic luminescence spectral distribution, as discussed in section 3.1.1, is characterized by its broad nature, multiple peaks, and a cutoff at high energy following the quantum law  $\hbar\omega = e|V_s|$ .

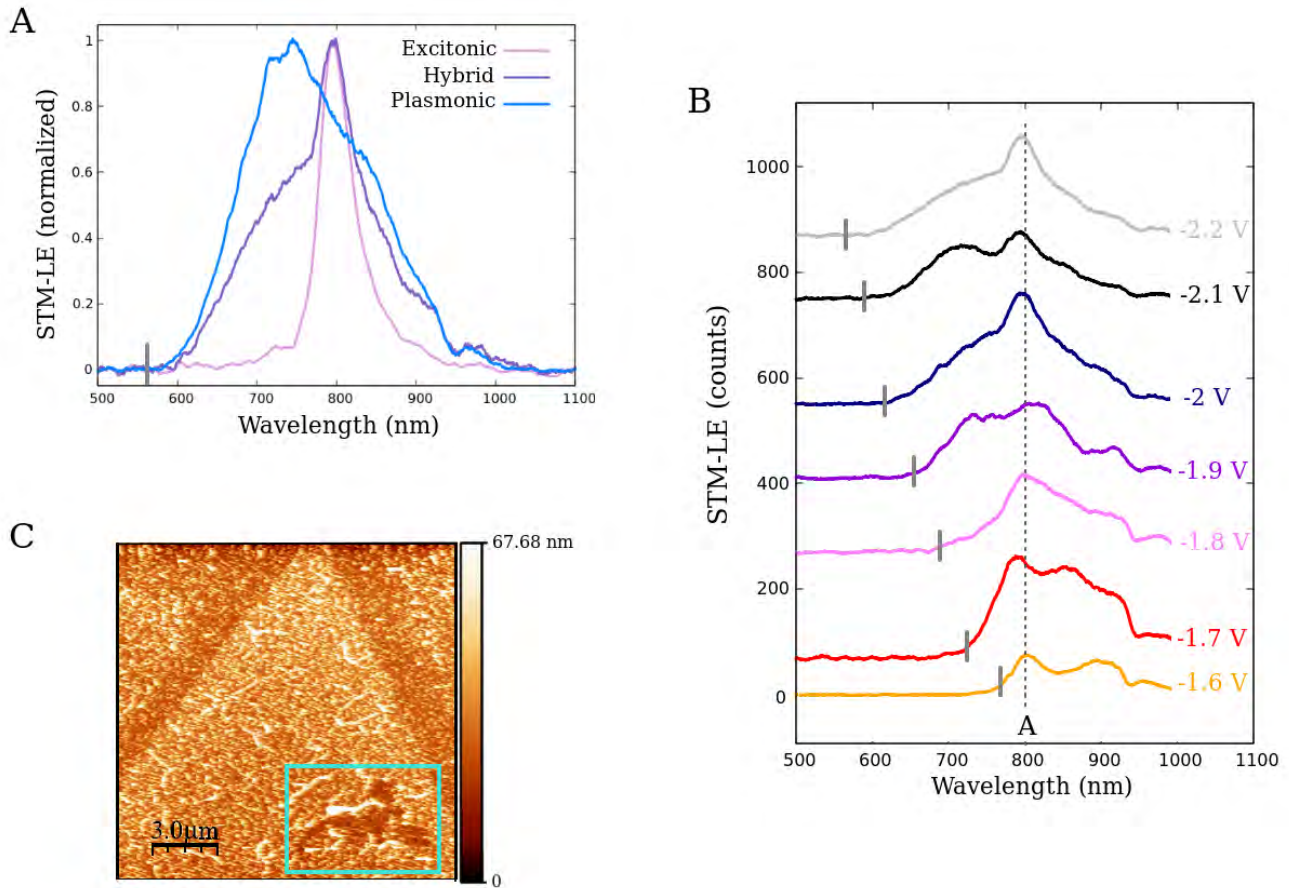


**Figure 3.19:** (A) Types of STM-induced luminescence spectra obtained when the tip is scanning  $MoSe_2$  flakes: excitonic, hybrid and plasmonic ( $V_s = -2.2$  V;  $I_t = 20$  nA and an acquisition time of 90 s). (B) Hybrid STM-induced luminescence spectra recorded from a damaged  $MoSe_2$  flake versus bias voltage  $V_s$  at the tunneling current  $I_t = 20$  nA and an acquisition time of 90 s (spectra are vertically offset for clarity). The dashed line indicates the A-exciton absorption wavelength. (C)  $15 \mu m \times 15 \mu m$  AFM height image of a  $MoSe_2$  monolayer flake deposited onto a granular gold substrate presenting an area damaged by the STM tip (blue rectangle).

A third type of spectrum has been obtained, referred to as hybrid, exhibiting characteristics of

both excitonic and plasmonic radiative processes. The spectral distribution of hybrid STM-LE is characterized by a plasmonic component with a broad peak presenting a high-energy quantum cutoff, and an excitonic component represented by a narrow peak at the wavelength of the A-exciton. In Figure 3.19-B, a series of hybrid spectra as a function of  $V_s$  is shown. The quantum cutoff at high energy related to the plasmonic component, and the peak maximum around 800 nm (peak maximum varies in a range of energy from 1.572 to 1.53 eV) corresponding to the excitonic component are clearly observed in all spectra. Hybrid and plasmonic STM-LE spectra were obtained using negative bias voltages while scanning areas of the  $MoSe_2$  monolayer exhibiting tears, cracks or tip-induced damage (such as the area highlighted in blue in the AFM image of Figure 3.19-C). Sometimes, these STM-LE spectra were acquired in regions of the monolayer that appear defect-free. Nonetheless, it is important to note that even in such cases, there may be defects at the atomic scale, such as impurities or missing atoms, which are not visible in our STM or AFM topographic images. The presence of these defects prevents or reduces the coupling between plasmon modes and excitons. Hence, instead of transferring energy to the excitons, the plasmon modes decay radiatively, resulting in a plasmonic luminescence. In addition, at some specific points of the TMD surface, due to the substrate roughness, this coupling is not efficient or does not take place at all, and light emission is dominated by the decay of LSP modes in the gap junction. During the scanning process, both excitonic emission from the monolayer and plasmonic emission from the tip-substrate tunneling junction can occur, leading to these three categories of spectra.

### 3.4 Light emission from $Au/MoSe_2/Au$ tunneling junction: role of the substrate morphology

It has been observed that a high excitonic STM-LE from  $MoSe_2$  monolayers can be achieved using a plasmonic substrate due to the plasmon-exciton coupling. This coupling can be adjusted using the surface morphology of the metallic substrate to tune/detune excitonic and plasmonic resonances. Thus, by selecting an appropriate substrate morphology, STM-LE can be further enhanced. In order to explore this point,  $MoSe_2$  flakes were transferred onto two different nanostructured gold substrates, consisting of geometric arrays of micrometric cavities drilled in a polycrystalline gold film. The cavities of each substrate display a distinct geometry, with one being pyramidal and the other circular. These cavities also differ in dimensions. These variations between the two gold nanostructured substrates provide an opportunity to study different plasmon modes supported by each substrate. Moreover, the arrangement of the  $MoSe_2$  flakes deposited on each substrate, such as how they are suspended over the cavities, will differ, due to the different substrate morphology. Consequently, for each substrate, the plasmon-exciton interaction will be different due to a distinct spatial and spectral overlap between specific surface plasmon modes and excitons.

### 3.4.1 Nanostructured gold substrate: example of pyramidal cavities

The first nanostructured substrate studied is characterized by a periodic pattern consisting of pyramidal cavities with a depth of  $1\ \mu\text{m}$  and an in-plane period of about  $2\ \mu\text{m}$  [1]. This substrate, initially designed for SERS measurements, was purchased from Renishaw Diagnostics. The AFM height image of the bare nanostructured substrate before the transfer of  $\text{MoSe}_2$  flakes is displayed in Figure 3.20-A. The periodic 2D array of cavities is depicted, and the geometry and dimensions of the pyramidal cavities are revealed by the topographic profile along the yellow line (Fig. 3.20-B).

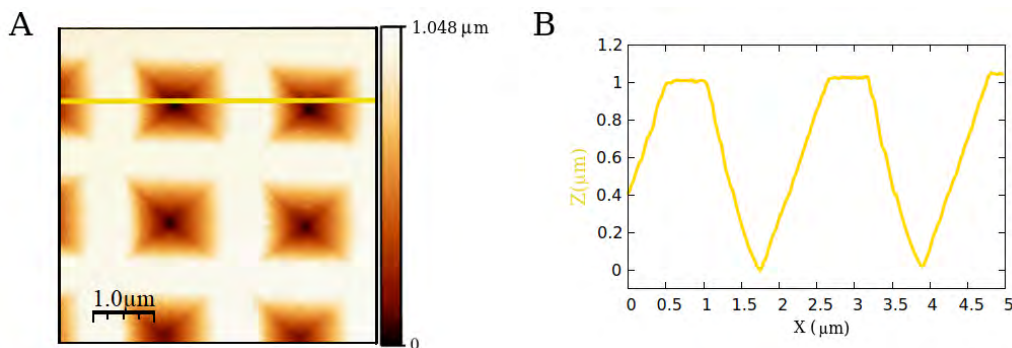


**Figure 3.20:** (A)  $5\ \mu\text{m} \times 5\ \mu\text{m}$  AFM height image displaying the nanostructured gold substrate patterns. (B) Topographic profile taken along the yellow line in panel (A) showing the geometry and depth of the pyramidal cavities.

Far-field micro-photoluminescence measurements were performed on a  $\text{MoSe}_2$  flake that covers the nanostructured area and a flat region outside the nanostructure area of the substrate. This flake is imaged by optical microscope and it is depicted in Figure 3.21-A. By performing photoluminescence measurements on this flake using identical excitation and collection conditions, it is possible to quantitatively compare and analyze the photoluminescence signal obtained from various areas of the flake. A photoluminescence map (see Fig. 3.21-B) was recorded on a small region of the flake covering the nanostructured area. This region, indicated in the optical microscope image by a dashed white rectangle, is large enough to include several cavities of the nanostructured sample. The acquisition of the PL map was performed without any filters. The  $\text{MoSe}_2$  layer is supposed to be free-standing, suspended over the pyramidal cavities. The PL signal obtained from the regions corresponding to the cavities is clearly higher than that recorded from the areas between adjacent cavities, which are flat bars. PL spectral measurements were conducted on three regions of the same flake: a flat region outside the nanostructured area (green line), a nanostructured region corresponding to a flat bar between adjacent cavities (orange line) and a nanostructured region corresponding to a cavity (pink line). The spectra obtained are plotted in Figure 3.21-C along with the PL spectrum of the bare nanostructured substrate (gray line). All spectra acquired from the flake, regardless of the region, exhibit the spectral signature of the  $\text{MoSe}_2$  photoluminescence with a peak at the A-exciton wavelength. The PL spectra obtained from the part of the flake covering the nanostructured area are clearly enhanced compared to the one acquired from the flake part on the flat gold substrate. Furthermore, in the nanostructured area, the PL signal acquired from the free-standing monolayer over a cavity is one order of magnitude higher in

intensity than that acquired from the monolayer on a flat bar region between adjacent cavities. This is in agreement with the findings of the photoluminescence map.

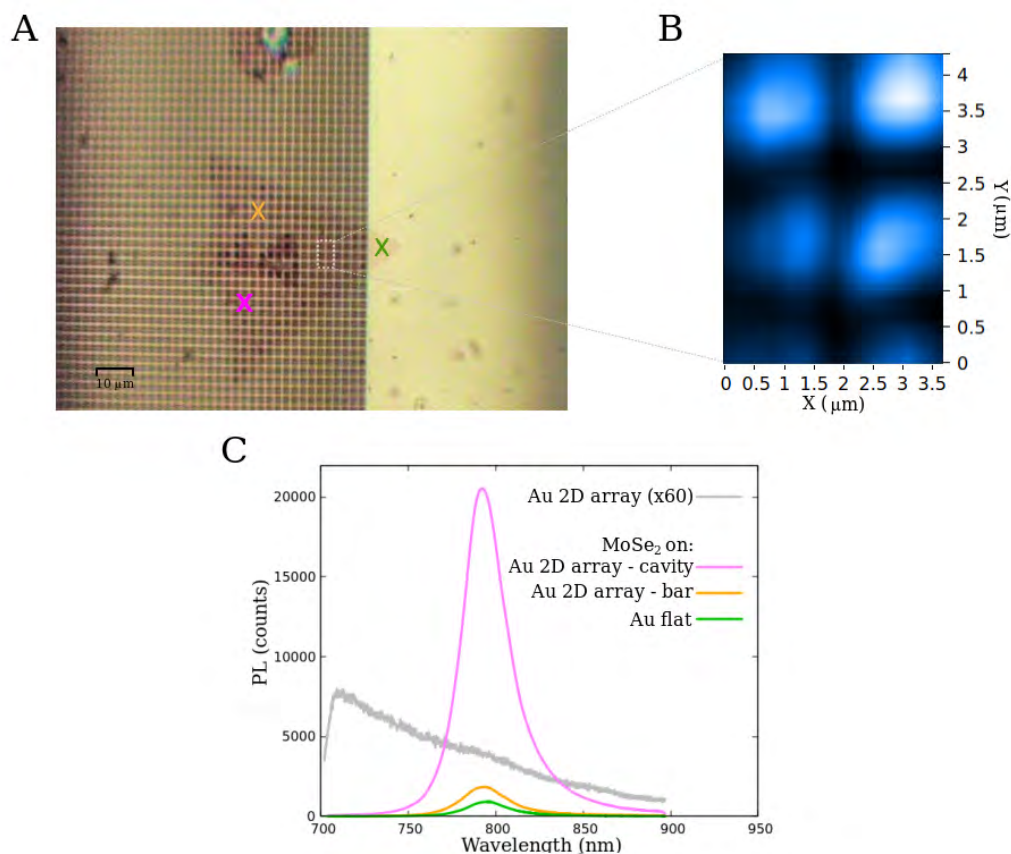


**Figure 3.21:** (A) Optical microscope image (x100) of a CVD grown  $MoSe_2$  flake transferred onto the nanostructured gold substrate with pyramidal cavities. The flake covers the nanostructured area (left part of the image) and the flat region (right part of the image) outside the nanostructured area. (B) Far-field photoluminescence intensity map of the  $MoSe_2$  monolayer on the nanostructured gold substrate. The acquisition area is indicated in panel (A) by a dashed white rectangle. (C) Far-field photoluminescence spectra recorded from the  $MoSe_2$  monolayer of panel (A) on three different regions of the gold substrate: the flat region outside the nanostructured area (green line), the nanostructured region corresponding to a flat bar between adjacent cavities (orange line) and the nanostructured region corresponding to a cavity (pink line). The locations where these spectra were acquired are denoted in panel (A) by crosses. The far-field photoluminescence spectrum recorded from the bare nanostructured substrate (gray line) is also plotted. These spectra were acquired under the same excitation conditions (laser beam at 532 nm) and collection parameters, along with the photoluminescence intensity map.

STM-LE measurements were performed on the same flake. Due to the thermal drift, it is challenging to perform STM-LE measurements at specific locations on the  $MoSe_2$  monolayer surface, particularly at positions corresponding to  $MoSe_2$  suspended over a single cavity or lying on a flat bar between cavities. In fact, determining the exact surface location where a specific STM-LE spectrum is acquired is impossible with our experimental setup since the tip is in constant displacement with respect to the sample during the data acquisition over tens of seconds or several minutes. On the other hand, it is perfectly possible to compare the STM-LE from the  $MoSe_2$  flake on the nanostructured area and on

the flat region outside the nanostructured area. Both STM-LE, acquired under the same tunneling conditions, are plotted in Figure 3.22.

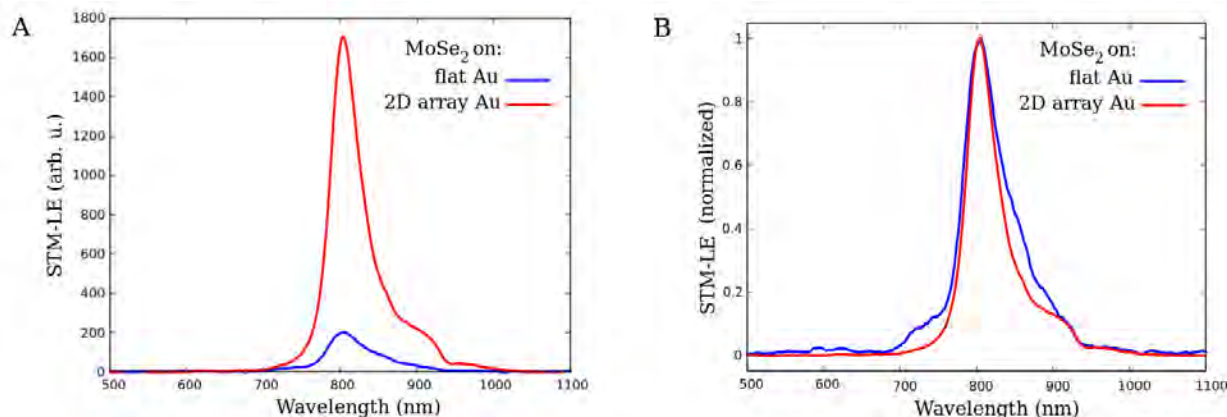


**Figure 3.22:** (A) STM-induced luminescence spectra of the  $MoSe_2$  monolayer on the flat region outside the nanostructured area (dark blue line) and on the nanostructured area (red line) of the nanostructured gold substrate with pyramidal cavities. Both spectra were acquired with the following tunneling parameters:  $V_s = -1.8$  V;  $I_t = 10$  nA and an acquisition time of 120 s. (B) Same spectra as in panel (A) after normalization.

A notable enhancement of the light emission is observed for the monolayer on the nanostructured area. In particular, the peak maximum around 800 nm exhibits an enhancement of approximately one order of magnitude. Moreover, the total number of photon counts integrated across the full spectrum (under the same tunneling current) is amplified by a factor of 6.5. For a more effective comparison of their spectral differences, these spectra are normalized in Figure 3.22-B. They are very similar with a sharp asymmetric peak at 805 nm (1.54 eV) and comparable FWHM ( $\sim 100$  meV). As both spectra exhibit identical spectral excitonic features, they can be both ascribed to the same STM-LE mechanism. The higher rate of excitonic light emission obtained in the case of the nanostructured substrate is then attributed to a more efficient plasmon-exciton coupling. This improved coupling arises from a more favorable spectral overlap between the excitonic transitions and the surface plasmon modes of the nanostructured substrate excited by inelastic electron tunneling.

Although a direct comparison of the spectral characteristics of STM-LE from specific locations on the  $MoSe_2$  surface corresponding to the monolayer suspended over a single cavity or laying on a flat bar between cavities is not possible, the variation in luminescence intensity across different areas of the sample can be investigated through a photonic map. Figure 3.23 shows an STM topographic image and its corresponding photonic map recorded on a region of the flake covering the nanostructured area. In the STM image and the topographic profile taken along the yellow line, the main characteristics of the 2D array of cavities are clearly visible, despite the strong distortions caused by the asymmetric STM tip and thermal drift (consecutive to an extended acquisition time). A strong correlation is observed between the photonic map and the STM topographic image. Notably, the photonic map clearly demonstrates that, despite local fluctuations, the light emission is enhanced when the tip is positioned on top of the free-standing monolayer suspended over a cavity, rather than on the ML laying

on a flat bar. This enhancement is confirmed by the topographic and light intensity profiles, shown in Fig. 3.23-C, measured along the yellow and green lines in the STM image and photonic map.

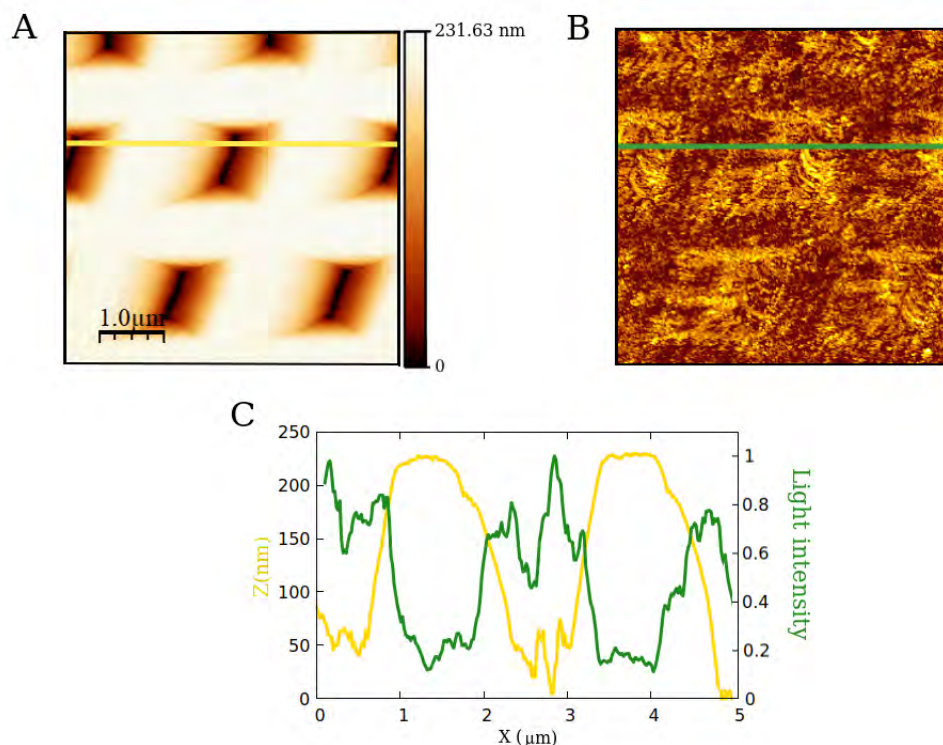


**Figure 3.23:** (A) STM topographic image and (B) corresponding photonic map of a  $MoSe_2$  monolayer on the nanostructured gold substrate. Both images were recorded simultaneously on a  $5 \mu\text{m} \times 5 \mu\text{m}$  area ( $V_s = -1.7 \text{ V}$ ;  $I_t = 2 \text{ nA}$ ). During the acquisition of the photonic map, an average of 2500 counts per second was obtained. (C) Topographic and normalized light intensity profiles taken along the yellow and green lines in panels (A) and (B) respectively. The STM tip is unable to reach the bottom of the cavities due to its highly asymmetric geometry.

It is worthy to mention that all STM-induced luminescence spectra acquired from  $MoSe_2$  on the nanostructured area, regardless of the position of the tip relative to the cavities, exhibit an excitonic signature. One might then speculate that the observed difference in light emission on the photonic map is due to a quenching effect of the luminescence when the monolayer is supported by the substrate due to charge transfer. However, this quenching effect can only be partial and rather weak, since the STM-LE detected from the monolayer laying on a flat bar is significantly higher compared to that obtained for a flat gold substrate. It is also worth mentioning that the STM-LE photonic map exhibits a strong correlation with the far-field photoluminescence map of Figure 3.21-B. On the other hand, the STM-LE technique offers considerably improved spatial resolution compared to photoluminescence. This highlights its clear advantage in the study of light emission processes localized at the nanoscale.

### 3.4.2 Nanostructured gold substrate: example of circular cavities

The second nanostructured gold substrate studied consists of a 2D array of circular cavities with a depth of about 230 nm and a diameter of  $\sim 850$  nm. The fabrication of these cavities was achieved by a lithography process. Figure 3.24-A shows an AFM image of the bare nanostructured substrate prior to the deposition of  $MoSe_2$  flakes. The periodic arrangement of circular cavities can be observed. The topographic profile along the yellow line (Fig. 3.24-B) provides insights into the geometrical characteristics of these circular cavities.

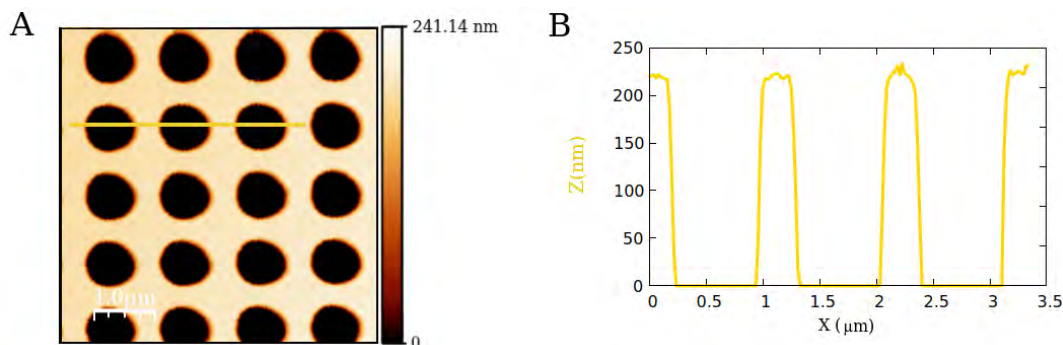


**Figure 3.24:** (A)  $5\ \mu\text{m} \times 5\ \mu\text{m}$  AFM height image displaying the nanostructured gold substrate patterns. (B) Topographic profile taken along the yellow line in panel (A) showing the diameter and depth of the circular cavities.

Figure 3.25-A presents an optical microscope image depicting a transferred  $MoSe_2$  flake onto this substrate. The presence of a multilayered region at the center is commonly observed in most of the transferred flakes, such as the one illustrated in the image. To ensure light emission, PL and STM-LE measurements were primarily conducted on the regions near the edges of the flakes, which are one monolayer thick. Figure 3.25-B displays a photoluminescence map recorded without the use of any filters, on a small region of the flake covering several circular cavities of the nanostructured substrate. The map reveals areas with a higher photoluminescence signal. Upon comparison with the substrate nanostructure pattern, it becomes evident that the intense signal areas correspond to the  $MoSe_2$  flake supposedly suspended over the substrate cavities. In contrast, the areas with weaker luminescence correspond to the  $MoSe_2$  monolayer laying on the bars separating adjacent cavities. PL spectral measurements were conducted on the  $MoSe_2$  monolayer suspended over a cavity (brown line) and laying on a bar between cavities (black line). In addition, the PL spectrum of a different flake located on a flat region outside the nanostructured area was recorded. These spectra, shown in Figure 3.25-C, exhibit the characteristic spectral signature of a  $MoSe_2$  monolayer, with a prominent peak around 790 nm (1.57 eV). The PL spectrum obtained from the TMD monolayer over a cavity is about 4 times more intense than the one acquired from the same monolayer laying on a bar. This aligns with the photoluminescence map of Figure 3.25-B. Moreover, the PL spectrum acquired from a  $MoSe_2$  flake on a flat region (blue line) is less intense than both spectra obtained from the flake on the nanostructured region. Thus, the nanostructured substrate exhibits plasmonic properties that enhance the photoluminescence of  $MoSe_2$  monolayers, with a more pronounced enhancement occurring when the monolayer is over the cavities.

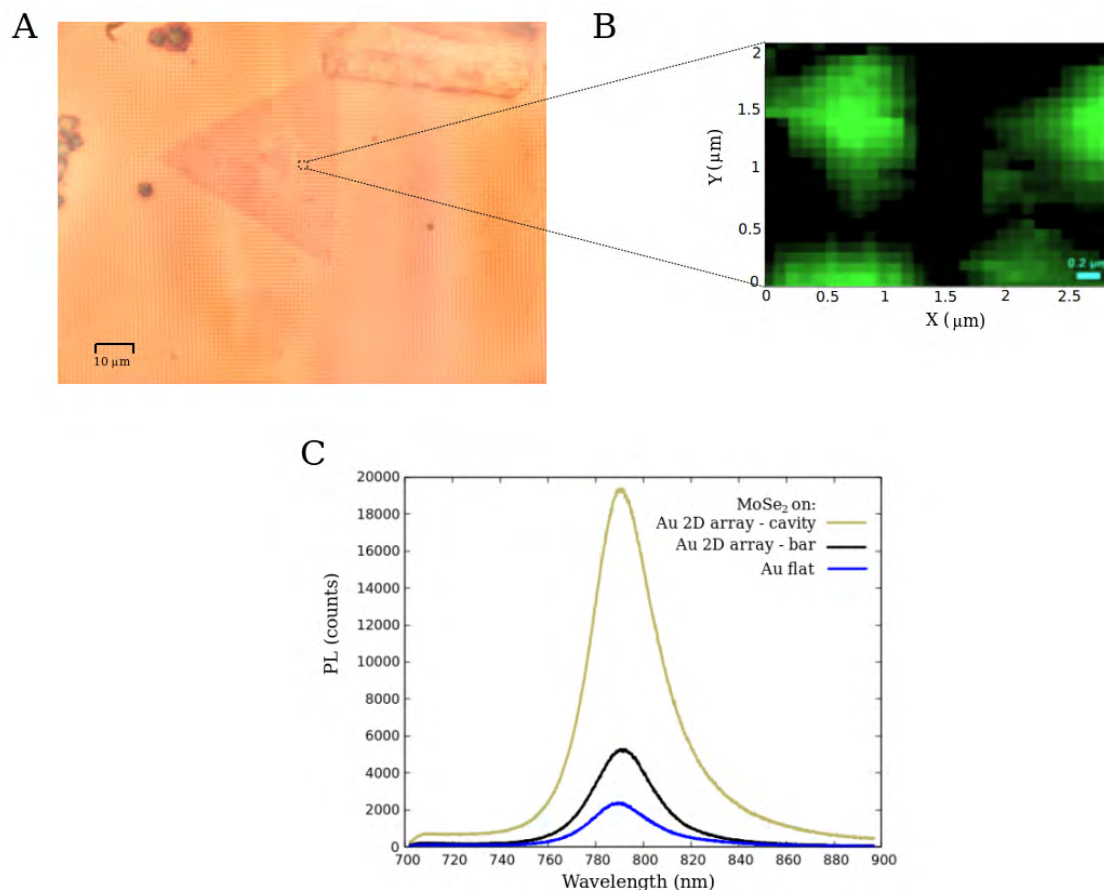


**Figure 3.25:** (A) Optical microscope image (x100) of a CVD grown  $MoSe_2$  flake transferred onto the nanostructured gold substrate with circular cavities. (B) Far-field photoluminescence intensity map of the  $MoSe_2$  monolayer on the nanostructured gold substrate. The acquisition area is indicated in panel (A) by a dashed black rectangle. (C) Far-field photoluminescence spectra recorded from the  $MoSe_2$  monolayer on the nanostructured substrate: one from the nanostructured region corresponding to a flat bar between adjacent cavities (black line) and another from the nanostructured region corresponding to a cavity (brown line). The far-field photoluminescence spectrum recorded from a  $MoSe_2$  monolayer on a flat region outside the nanostructured area is also plotted (blue line). These spectra were acquired under the same excitation conditions (laser beam at 532 nm) and collection parameters, along with the photoluminescence intensity map.

Similarly to the previously described sample, which features a nanostructured substrate with pyramidal cavities, a  $MoSe_2$  flake covering both the nanostructured area and a flat region outside the nanostructured area has been selected for STM-LE measurements. This allows for a quantitative comparison of the intensity and spectral characteristics of the STM-LE obtained from the  $MoSe_2$  ML on both nanostructured and flat regions of the substrate. The AFM height image of this flake is displayed in Figure 3.26-A. The  $MoSe_2$  monolayer's extreme thinness makes it challenging to discern the flake clearly in this AFM topographic image. Nevertheless, its presence is revealed by the characteristic folds (see Fig. 3.26-B) observed around the circular cavities, resulting from local deformations of the flake. The topographic profile taken along several folds, shown in Fig. 3.26-B, indicates that these folds have a height of a few tens of nanometers. These folds are also observed in the flake on the flat region with an in-plane extension of several  $\mu m$ . The absence of these features in the previous sample, which

comprises a nanostructured substrate with pyramidal cavities, suggests that the  $MoSe_2$  monolayer is suspended over the circular cavities in a distinct manner compared to its suspension over the pyramidal cavities. This distinction is further supported by the fact that the circular cavities are significantly shallower than the pyramidal cavities.

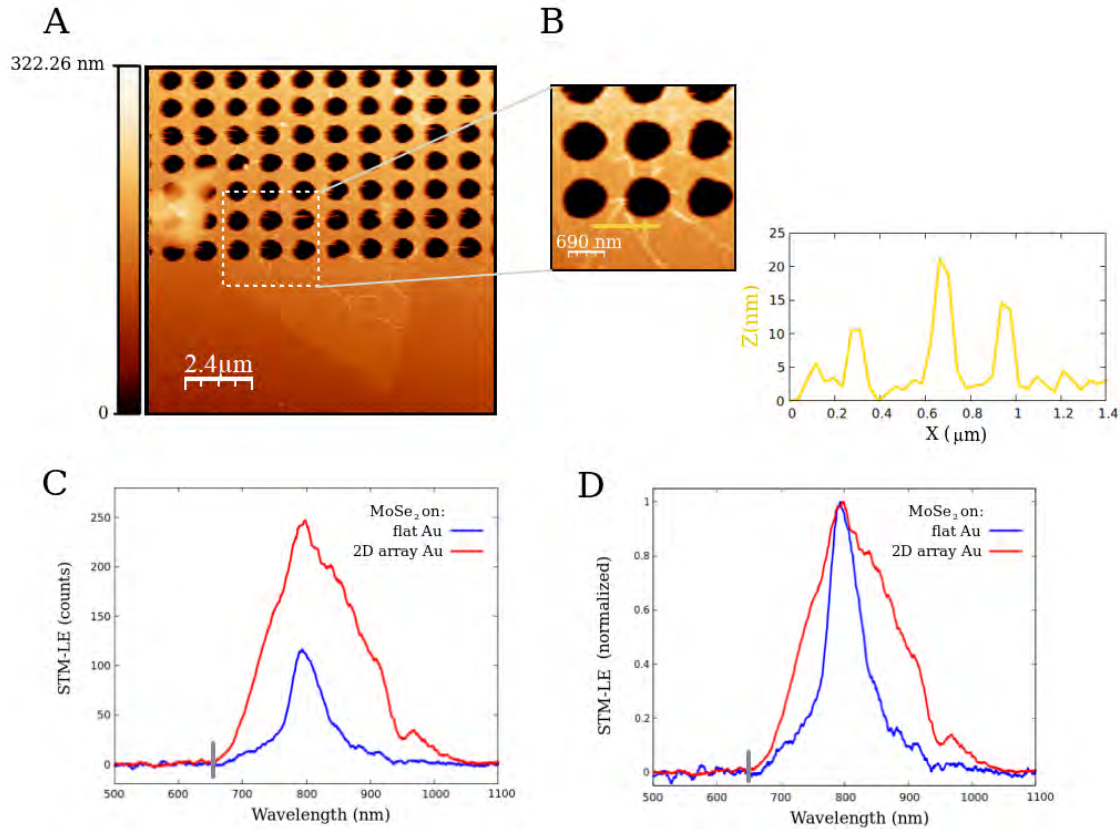


**Figure 3.26:** (A)  $12 \mu m \times 12 \mu m$  AFM height image of a  $MoSe_2$  flake covering the nanostructured area (top part of the image) and the flat region (bottom part of the image) outside the nanostructured area. (B) Zoomed AFM height image ( $3.45 \mu m \times 3.45 \mu m$ ) of the framed area (dashed white rectangle) in panel (A) showing several folds of the  $MoSe_2$  flake and topographic profile along the yellow line indicating the height of these folds. (C) STM-induced luminescence spectra of the  $MoSe_2$  monolayer on the flat region outside the nanostructured area (dark blue line) and on the nanostructured area (red line) of the nanostructured gold substrate with circular cavities. Both spectra were acquired with the following tunneling parameters:  $V_s = -1.9$  V;  $I_t = 20$  nA and an acquisition time of 90 s. (D) Same spectra as in panel (C) after normalization. The gray bars indicate the high-energy quantum cutoff.

STM-LE spectra obtained from the  $MoSe_2$  flake on the nanostructured area and on the flat region outside the nanostructured area are plotted in Figure 3.26-(C,D). The two spectra are considerably different, with the STM-LE from  $MoSe_2$  on the nanostructured area being approximately twice as intense, and its total number counts integrated across the full spectrum (under the same tunneling current) being around four times higher. Thus, a higher light emission rate is obtained for the flake placed on the nanostructured region. Moreover, while the STM-LE from the monolayer on the flat region (dark blue line) presents a single sharp peak (FWHM of 115 meV), the STM-LE from the monolayer on the nanostructured area (red line) exhibits multiple peaks and is much broader (FWHM around 300

meV). Nevertheless, there are certain similarities between the two spectra. Both exhibit a peak intensity maximum at 795 nm (corresponding to 1.55 eV) and a high-energy cutoff at 652 nm (1.9 eV), indicated in both graphs of Figure 3.26-(C,D) by a vertical gray bar. Both spectra are considered hybrid, with the STM-LE spectrum from the  $MoSe_2$  on the flat region displaying a more pronounced excitonic light emission component. Thus, since both spectra present a plasmonic component, it is suggested that plasmonic light emission occurs while the tip is over the flake, regardless of the region from which the spectrum was acquired. It is worthy to mention that both spectra were obtained using a “fixed tip position” (no-scanning mode). The occurrence of plasmonic light emission is attributed to defects in the  $MoSe_2$  monolayer, such as tears, folds, or cracks. Indeed, when the  $MoSe_2$  monolayer presents this kind of defects, the formation of excitons induced by STM tunneling is reduced. Consequently, plasmon modes excited by inelastic electron tunneling do not transfer energy to excitons; instead, they decay radiatively, leading to plasmonic emission. It is believed that the flakes on the nanostructured substrate with pyramidal cavities are of higher quality and/or have undergone a cleaner and more effective transfer process, resulting in a lack of defects and consequently, the absence of plasmonic light emission.

In Figure 3.27-A, an STM topographic image captured from a region of the flake covering the nanostructured area is shown. The two corresponding photonic maps recorded on the same region with opposite bias voltage are as well displayed (Fig. 3.27-(B,D)). The STM image and the photonic map obtained with a positively biased substrate were recorded simultaneously, while the photonic map taken with  $V_s < 0$  was recorded immediately afterward to minimize the impact of thermal drift. There is a strong correlation between the STM image and both photonic maps. In fact, the periodic arrangement of cavities, clearly visible in the STM image, is distinguished in both photonic maps by a notable increase in light emission intensity at the cavity locations. A topographic profile covering several cavities is measured along the yellow line in the STM image. Additionally, light intensity profiles were measured in both photonic maps (for positive and negative bias voltage) along the same line as the topographic profile of the sample surface. These profiles are displayed in Figure 3.27-(C,E). Despite local fluctuations, both photonic maps show an increase in light emission intensity when the tip scans the  $MoSe_2$  flake suspended over a cavity, compared to when it is positioned over the flake lying on a flat bar between cavities. This enhancement, confirmed by the topographic and light intensity profiles taken along several cavities, takes place regardless of the sign of  $V_s$ . As discussed in previous sections, excitonic STM-LE from the  $MoSe_2$  monolayer only occurs when a negative bias voltage  $V_s$  is used, while plasmonic light emission can be generated regardless of the sign of  $V_s$ . Therefore, the spatial localization of the light emission that is originated from the radiative decay of plasmon modes can be determined from the photonic map recorded with a positive  $V_s$  (see Fig. 3.27-D). Plasmonic STM-LE is detected in most of the cavities where the  $MoSe_2$  flake is probably damaged, presenting defects (tears or cracks) or absent due to mechanical constraints during its deposition. In some cavities, plasmonic luminescence is not detected for  $V_s > 0$  but light emission is observed for  $V_s < 0$ , such as

the third cavity (the one further to the right) in the topographic and light intensity profiles depicted in Figure 3.27-(C,E). In these cavities, the presence of an undamaged  $MoSe_2$  monolayer is assumed giving rise to excitonic STM-LE. In order to confirm this point, spectral STM-LE measurements were conducted (see below).

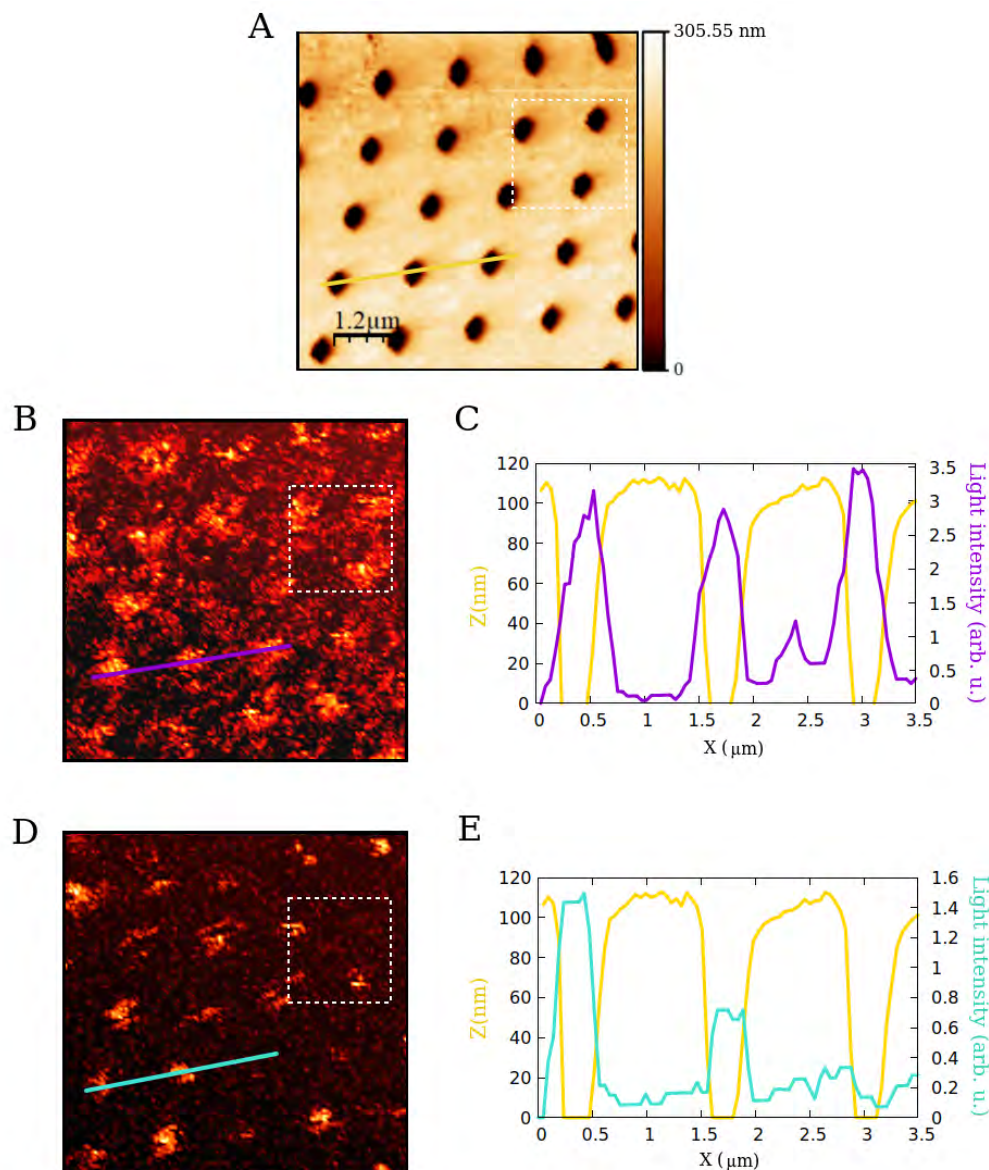


**Figure 3.27:** (A) STM topographic image and corresponding photonic maps recorded on a  $6 \mu\text{m} \times 6 \mu\text{m}$  area with a (B) negative bias voltage  $V_s = -1.8 \text{ V}$  and a (D) positive bias voltage  $V_s = +1.8 \text{ V}$ . (A) and (D) were recorded simultaneously while (B) was recorded on the same area immediately afterward. The tunneling current used is  $I_t = 5 \text{ nA}$ . The scanning of this sample with negative and positive  $V_s$  yields an average of 60 and 30 photon counts per second, respectively. (C) Topographic and light intensity profiles taken along the yellow and violet lines in panels (A) and (B) respectively. (E) Topographic and light intensity profiles taken along the yellow and blue lines in panels (A) and (D) respectively. The dashed white rectangle in panels (A), (B) and (D) corresponds to the area analyzed in Figure 3.28.

The enhancement of light emission rate obtained when the tip is over a cavity, rather than over the flat

bar between adjacent cavities may be attributed, depending on the cavity, to the occurrence of plasmonic emission or to a higher excitonic light emission rate resulting from a more efficient plasmon-exciton coupling. During the scanning process of a  $MoSe_2$  flake deposited on the nanostructured substrate, a twice higher average light emission rate is obtained when the sample is negatively biased, since both enhanced excitonic and plasmonic luminescence can take place. On the other hand, for a  $V_s > 0$ , only plasmonic light emission occurs.

Spectral STM-LE measurements were conducted on a small region of the  $MoSe_2$  flake on the nanostructured substrate. An STM topographic image of this region is shown in Figure 3.28-A. It corresponds approximately to the area of the sample surface enclosed by a dashed white rectangle in Figure 3.27-(A,B,D). Strong distortions caused by the asymmetric STM tip and thermal drift are observed. This area contains several cavities. The cavity on the top right of the STM image (Fig. 3.28-A) presents an intense light emission for a negative bias voltage and no luminescence for a positive  $V_s$ , according to the photonic maps in Figure 3.27-(B,D). On the other hand, the bottom cavity exhibits luminescence regardless of the sign of the bias voltage.

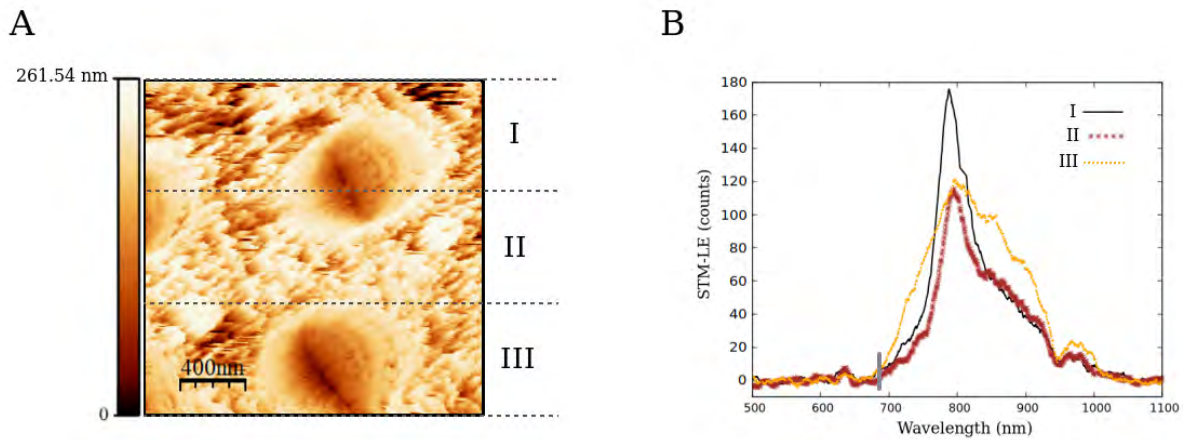


**Figure 3.28:** (A)  $2 \mu\text{m} \times 2 \mu\text{m}$  STM topographic image ( $V_s = -1.8 \text{ V}$ ;  $I_t = 20 \text{ nA}$ ) of the area enclosed by a dashed white rectangle in panels (A), (B) and (D) of Figure 3.27. The image is divided into three regions labeled as scan areas I, II and III. (B) STM-induced luminescence spectra obtained when the tip is scanning the area I, II and III. These spectra were acquired with the following tunneling parameters:  $V_s = -1.8 \text{ V}$ ;  $I_t = 20 \text{ nA}$  and an acquisition time of 90 s. The gray bar indicates the high-energy quantum cutoff.

Spectral STM-LE measurements on a single cavity can not be carried out due to thermal drift. However, it is possible to obtain an STM-LE spectrum from a restricted region of the surface where only a single cavity is present. Three STM-LE spectra were acquired while the tip was scanning the surface to produce the STM topographic image shown in Fig. 3.28-A. The spectra obtained when the tip scanned the three different areas (I, II and III) depicted in the STM image, are displayed in Figure 3.28-B. The spectra obtained are hybrid, exhibiting spectral features of both plasmonic and excitonic light emission. The spectra obtained when the top cavity was scanned (spectra I and II) have a more pronounced excitonic light emission component than the spectrum III acquired when scanning

the bottom cavity. These spectral measurements provide evidence that in the cavities where no light emission is observed for  $V_s > 0$  in the photonic map of Fig. 3.27-(D), the  $MoSe_2$  flake is present giving rise to excitonic light emission when  $V_s < 0$ . In contrast, the luminescence observed in the cavities presenting STM-LE in both photonic maps, i.e., regardless of the sign of  $V_s$ , is attributed to plasmonic light emission as it was expected.

In cavities presenting plasmonic light emission, the flake is assumed to be damaged or simply absent. Another possibility could be the presence of contaminants within these cavities between the monolayer and the substrate, hindering the injection of charges into the monolayer. To clarify this point, force-distance curves were measured in contact and tapping modes on these cavities. The same measurements were conducted on bare flat  $Au$  substrate and on a  $MoSe_2$  flake deposited on a flat gold substrate for comparison. The aim of these measurements is, by comparing the force-distance curves obtained, to determine whether the monolayer is present at the bottom of these cavities. Unfortunately, the curves obtained in the three cases do not present significant differences to reach a meaningful conclusion. Indeed, no significant differences have been observed when comparing the force-distance curves measured on a  $MoSe_2$  deposited on a flat gold substrate and on bare gold substrate. This may be attributed to the extreme thinness of the monolayer.

## 3.5 Conclusion

Throughout this chapter, the role of the nature and morphology of the materials involved in the tunnel junction on the STM-induced luminescence has been investigated. Our findings reveal substantial differences in luminescence characteristics, such as the spectral signature and the tunneling conditions required to trigger light emission, between STM-LE obtained from a purely plasmonic junction and from a junction with a  $MoSe_2$  monolayer where no plasmon modes are involved. These disparities can be explained by a distinct mechanism behind light emission in each case: on one hand, radiative decay of tip-induced surface plasmon modes, and on the other hand, radiative decay of bright excitons confined within the monolayer. The insertion of a  $MoSe_2$  monolayer in a plasmonic junction significantly enhances its excitonic luminescence. A remarkable increment of two orders of magnitude is obtained in the emission quantum efficiency when a plasmonic substrate (gold) is used instead of a non-plasmonic substrate (ITO). This enhancement is attributed to the electromagnetic coupling between plasmon modes and excitons. The plasmonic nature of the substrate plays thus an active role in the light emission. Moreover, our results demonstrate that the nanostructuring of the plasmonic substrate supporting the  $MoSe_2$  monolayer enables a more favorable spectral and spatial overlap between plasmon modes and excitons, resulting in a more efficient plasmon-exciton electromagnetic coupling. This improved coupling leads to an increment of the STM-LE signal by one order of magnitude.

Given its significant role in STM-LE, the plasmon-exciton coupling in a hybrid  $Au/MoSe_2/Au$  STM junction is investigated in Chapter 4 through electromagnetic simulations. This will constitute a crucial step for the theoretical investigation of STM-LE from this hybrid junction carried out in Chapter 5.

---

For future work, significant efforts are required to optimize the transfer and subsequent cleaning procedure in order to achieve STM junction components of higher quality. The presented work provides a good starting point for the design of plasmonic nanostructured substrates whose surface plasmon modes could be engineered, aiming to optimize their coupling with the excitons in terms of efficient spectral and spatial overlap, thus achieving an enhanced and controlled light emission process. With the possibility of achieving enhanced light emission rates, STM-LE becomes a powerful spectroscopy tool for exploring the properties of light emitters with atomic-scale resolution.

## Bibliography

- [1] R. P echou, S. Jia, J. Rigor, O. Guillermet, G. Seine, J. Lou, N. Large, A. Mlayah, and R. Coratger. Plasmonic-Induced Luminescence of MoSe<sub>2</sub> Monolayers in a Scanning Tunneling Microscope. *ACS Photonics*, 7(11):3061–3070, 2020.
- [2] Renaud P echou. * mission de photons dans un microscope   effet tunnel*. PhD thesis, Universit  Paul Sabatier, 1997.
- [3] M. M. J. Bischoff, M. C. M. M. van der Wielen, and H. van Kempen. STM-induced photon emission spectroscopy of granular gold surfaces in air. *Surf. Sci.*, 400(1):127–133, 1998.
- [4] C. Maurel, R. Coratger, F. Ajustron, G. Seine, R. P echou, and J. Beauvillain. Photon emission from STM of granular gold in UHV: Comparison with air and study of spectra shifting with tip position. *Eur. Phys. J. AP*, 21(2):121–126, 2003.
- [5] B. Laks and D. L. Mills. Photon emission from slightly roughened tunnel junctions. *Phys. Rev. B*, 20(12):4962–4980, 1979.
- [6] B. Laks and D. L. Mills. Roughness and the mean free path of surface polaritons in tunnel-junction structures. *Phys. Rev. B*, 21(11):5175–5184, 1980.
- [7] J. H. Coombs, J. K. Gimzewski, B. Reihl, J. K. Sass, and R. R. Schlittler. Photon emission experiments with the scanning tunnelling microscope. *J. Microsc.*, 152(2):325–336, 1988.
- [8] R. W. Rendell, D. J. Scalapino, and B. M uhlschlegel. Role of local plasmon modes in light emission from small-particle tunnel junctions. *Phys. Rev. Lett.*, 41(25):1746–1750, 1978.
- [9] R. W. Rendell and D. J. Scalapino. Surface plasmons confined by microstructures on tunnel junctions. *Phys. Rev. B*, 24(6):3276–3294, 1981.
- [10] P. Bharadwaj, A. Bouhelier, and L. Novotny. Electrical Excitation of Surface Plasmons. *Phys. Rev. Lett.*, 106(22):226802, 2011.
- [11] Y. Zhang, E. Boer-Duchemin, T. Wang, B. Rogez, G. Comtet, E. Le Moal, G. Dujardin, A. Hohenau, C. Gruber, and J. R. Krenn. Edge scattering of surface plasmons excited by scanning tunneling microscopy. *Opt. Express*, 21(12):13938–13948, 2013.
- [12] A. Loubat, M. Imperor-Clerc, B. Pansu, F. Meneau, B. Raquet, G. Viau, and L.-M. Lacroix. Growth and self-assembly of ultrathin Au nanowires into expanded hexagonal superlattice studied by in situ SAXS. *Langmuir*, 30(14):4005–4012, 2014.
- [13] R. K. Ramamoorthy, E. Yildirim, E. Barba, P. Roblin, J. A. Vargas, L.-M. Lacroix, I. Rodriguez-Ruiz, P. Decorse, V. Petkov, S. Teychen , and G. Viau. The role of pre-nucleation clusters in the crystallization of gold nanoparticles. *Nanoscale*, 12(30):16173–16188, 2020.

- [14] E. Yildirim, R. K. Ramamoorthy, R. Parmar, P. Roblin, J. A. Vargas, V. Petkov, A. Diaz, S. Checchia, I. Rodriguez Ruiz, S. Teychené, L.-M. Lacroix, and G. Viau. Simple Synthesis of Monodisperse Ultrasmall Au Icosahedral Nanoparticles. *J. Phys. Chem. C*, 127(6):3047–3058, 2023.
- [15] D. Pommier, R. Bretel, L. E. Parra López, F. Fabre, A. Mayne, E. Boer-Duchemin, G. Dujardin, G. Schull, S. Berciaud, and E. Le Moal. Scanning Tunneling Microscope-Induced Excitonic Luminescence of a Two-Dimensional Semiconductor. *Phys. Rev. Lett.*, 123(2):027402, 2019.
- [16] R. J. Peña Román, Y. Auad, L. Grasso, F. Alvarez, I. D. Barcelos, and L. F. Zagonel. Tunneling-current-induced local excitonic luminescence in p-doped WSe<sub>2</sub> monolayers. *Nanoscale*, 12(25):13460–13470, 2020.
- [17] Y. Ma, R. A. Kalt, and A. Stemmer. Local strain and tunneling current modulate excitonic luminescence in MoS<sub>2</sub> monolayers. *RSC Adv.*, 12(38):24922–24929, 2022.
- [18] R. J. Peña Román, D. Pommier, R. Bretel, L. E. Parra López, E. Lorchat, J. Chaste, A. Ouerghi, S. Le Moal, E. Boer-Duchemin, G. Dujardin, A. G. Borisov, L. F. Zagonel, G. Schull, S. Berciaud, and E. Le Moal. Electroluminescence of monolayer WS<sub>2</sub> in a scanning tunneling microscope: Effect of bias polarity on spectral and angular distribution of emitted light. *Phys. Rev. B*, 106(8):085419, 2022.
- [19] L. E. Parra López, A. Rosławska, F. Scheurer, S. Berciaud, and G. Schull. Tip-induced excitonic luminescence nanoscopy of an atomically resolved van der Waals heterostructure. *Nat. Mater.*, 22(4):482–488, 2023.
- [20] A. K. Geim and K. S. Novoselov. The rise of graphene. *Nat. Mater.*, 6(3):183–191, 2007.
- [21] V. Iberi, L. Liang, A. V. Ievlev, M. G. Stanford, M.-W. Lin, X. Li, M. Mahjouri-Samani, S. Jesse, B. G. Sumpter, S. V. Kalinin, D. C. Joy, K. Xiao, A. Belianinov, and O. S. Ovchinnikova. Nanoforging single layer MoSe<sub>2</sub> through defect engineering with focused helium ion beams. *Sci. Rep.*, 6(1):30481, 2016.
- [22] R. J. Moerland and J. P. Hoogenboom. Subnanometer-accuracy optical distance ruler based on fluorescence quenching by transparent conductors. *Optica*, 3(2):112–117, 2016.
- [23] Delphine Pommier. *Electrically excited nanosources of light*. PhD thesis, Université Paris-Saclay, 2021.
- [24] R. J. Peña Román, R. Bretel, D. Pommier, L. E. Parra López, E. Lorchat, E. Boer-Duchemin, G. Dujardin, A. G. Borisov, L. F. Zagonel, G. Schull, S. Berciaud, and E. Le Moal. Tip-induced and electrical control of the photoluminescence yield of monolayer WS<sub>2</sub>. *Nano Lett.*, 22(23):9244–9251, 2022.

- [25] X. Wang, Y. Gong, G. Shi, W. L. Chow, K. Keyshar, G. Ye, R. Vajtai, J. Lou, Z. Liu, E. Ringe, B. K. Tay, and P. M. Ajayan. Chemical vapor deposition growth of crystalline monolayer MoSe<sub>2</sub>. *ACS Nano*, 8(5):5125–5131, 2014.
- [26] Y.-H. Chang, W. Zhang, Y. Zhu, Y. Han, J. Pu, J.-K. Chang, W.-T. Hsu, J.-K. Huang, C.-L. Hsu, M.-H. Chiu, T. Takenobu, H. Li, C.-I. Wu, W.-H. Chang, A. T. S. Wee, and L.-J. Li. Monolayer MoSe<sub>2</sub> grown by chemical vapor deposition for fast photodetection. *ACS Nano*, 8(8):8582–8590, 2014.
- [27] J. Rittich, S. Jung, J. Siekmann, and M. Wuttig. Indium-Tin-Oxide (ITO) Work Function Tailoring by Covalently Bound Carboxylic Acid Self-Assembled Monolayers. *Phys. Status Solidi (B)*, 255(8):1800075, 2018.
- [28] N. Krane, C. Lotze, J. M. Läger, G. Reecht, and K. J. Franke. Electronic Structure and Luminescence of Quasi-Freestanding MoS<sub>2</sub> Nanopatches on Au(111). *Nano Lett.*, 16(8):5163–5168, 2016.

## Chapter 4

# Optical response of a hybrid *Au/MoSe<sub>2</sub>/Au* tunneling junction

In the previous chapter, the enhancement of the excitonic light emission of a *MoSe<sub>2</sub>* monolayer interacting with plasmonic modes localized in the tip-surface STM cavity has been pointed out. This enhancement depends on the characteristics of the plasmon modes excited in the junction defined in part by the substrate morphology. Thus, the electromagnetic modes present in the junction, particularly those interacting with the *MoSe<sub>2</sub>* excitons, play a very important role in the process of Scanning Tunneling Microscope induced Light Emission (STM-LE).

The aim of this chapter is to explore the main characteristics of these electromagnetic modes and their behavior with respect to various parameters, including the tunneling parameters and the substrate roughness. This study is undertaken through numerical electrodynamic simulations based on the Discrete Dipole Approximation (DDA) method (described in section 2.3.1 of Chapter 2), using an incident plane wave as excitation source.

After a brief description of the hybrid *Au/MoSe<sub>2</sub>/Au* tunneling junction modeling, its electromagnetic response to an optical excitation will be presented. As a starting point, the study is developed in the non-tunneling regime, i.e. for a tip-surface distance  $d > 0.5$  nm, following the terminology proposed by Esteban *et al.* [1, 2]. The frequency and strength of the electromagnetic modes resonance are investigated by analyzing the far- and near-field optical response of the junction. To better identify the electromagnetic modes supported by the junction and investigate their interaction with the monolayer, a study on a purely metallic *Au/Au* junction will be first addressed. The *MoSe<sub>2</sub>* layer will then be introduced and its anisotropic character will be taken into account and analyzed. As the tip-surface distance  $d$  decreases and becomes less than 0.5 nm, quantum tunneling effects on the electromagnetic modes can no longer be considered negligible and must be taken into account for an accurate description of the underlying physics governing the junction. In this so-called tunneling regime [1, 2], the optical characteristics of the junction can not be adequately captured by a classical electrodynamic framework. To overcome this situation, Quantum-Corrected Model (QCM) (presented in section 2.3.2. of Chapter

2) is introduced in the simulations. The incorporation of QCM into DDA simulations, as well as the influence of STM electron tunneling on the junction's optical response, are described in the third part of this chapter. This is followed by a discussion on the tuning of the electromagnetic characteristics of the junction by the main tunneling parameters, namely the tip-surface distance and the applied bias voltage. Furthermore, the dependence of these properties on the incident electric field polarization, and on the dimensions of the finite-size components of the modeled junction is presented. Finally, in the last section of this chapter, a further step to precisely model the experimental STM junction presented in section 3.3 of Chapter 3 is taken by considering a rough substrate. Then, the role of the substrate roughness on the optical properties of the junction is investigated. It is worth noting that a significant part of the results detailed in this chapter has been addressed in a published article [3].

## 4.1 Modeling of the STM junction

This section provides the details about how the STM junction, consisting of a plasmonic tip on top of a  $MoSe_2$  monolayer lying on a flat plasmonic substrate, is simulated using the Discrete Dipole Approximation (DDA) method. The latter, which is thoroughly described in section 2.3.1 of Chapter 2, is a well-known numerical approach for studying the optical properties of objects with complex geometries (such as an STM junction) composed of different materials. In DDA simulations, the simulated structure, called the target, is approximated by a 3D-array of point dipoles. The size of the target is then related to the number of dipoles and the inter-dipole distance. It is important to note that a significant number of dipoles leads to the requirement of huge amounts of memory and computing time. In an STM junction, tip and sample are separated by a tunneling distance of a few angstroms. To model such a system accurately, it is essential to ensure that the inter-dipole distance is smaller than the tip-surface distance. In our simulations, an inter-dipole distance of 0.1 nm is thus considered, corresponding to half of the minimum tip-surface distance set in this study at  $d = 0.2$  nm. This small inter-dipole distance forces us to reduce the global size of the elements composing the junction in order to maintain a reasonable number of dipoles in terms of computation time and memory requirements. The first part of this section addresses the geometry and composition of the simulated hybrid  $Au/MoSe_2/Au$  junction. This is followed by the characteristics of the incident optical excitation used in our simulations. It is worthy to mention that the junction described here features a flat substrate and a tip-surface distance in the non-tunneling regime ( $d \geq 0.5$  nm). This junction goes through modifications in sections 4.3, 4.4 and 4.5 of this chapter in order to incorporate the QCM in the simulations to take into account the electron tunneling for  $d < 0.5$  nm, and to introduce roughness in the substrate surface. These modifications are particularly reported in sections 4.3.1 and 4.5.1.

### 4.1.1 Geometry and composition of the modeled tunneling junction

#### a) Hyperboloid tip

A hyperboloid profile is selected to replicate the shape of the STM tip. Typically, an STM tip, such as those used in the STM-LE measurements described in Chapter 3, exhibits a conical structure at its end with a rounded apex. A revolution hyperboloid tip provides a more accurate description of these characteristics than a paraboloid or conical structure. The mathematical expression of the hyperboloid profile is as follows:

$$\frac{z^2}{c^2} = 1 + \frac{x^2}{a^2} + \frac{y^2}{a^2} \quad (4.1)$$

The parameters  $a$  and  $c$  are assigned specific values:  $a = \sqrt{\frac{1764}{6625}}$  nm and  $c = 2$  nm. These values are carefully chosen to better mimic the three-dimensional structure of a real STM tip with a sharp apex composed of only one or a few atoms. In addition, these values are selected while considering the need to keep the simulated tip small in size due to the limited number of discretized dipoles. Figure 4.1-A displays the two-dimensional plot of the hyperboloid profile obtained using these values. The tip is symmetric with respect to the  $z$ -axis.

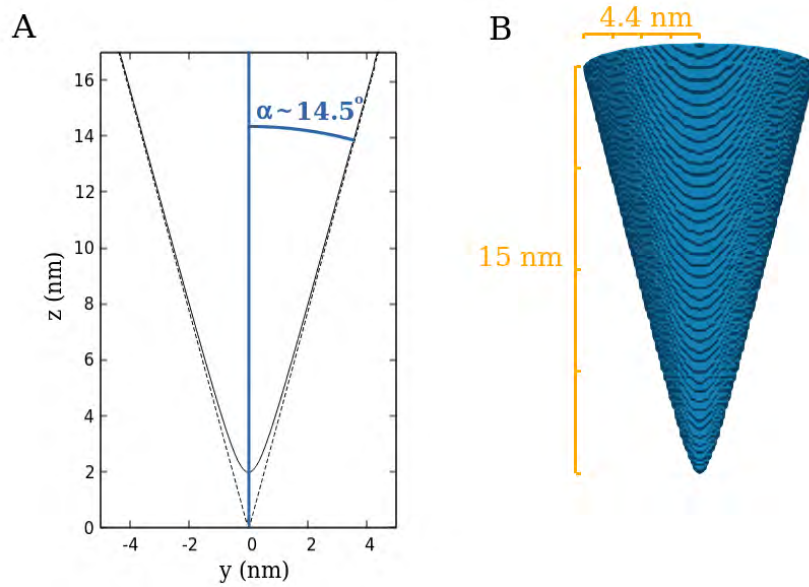


**Figure 4.1:** (A) Cross-section diagram of the hyperboloid tip and (B) schematic representation of its modeling by discrete point dipoles (DDA). Some parameters of the modeled tip are depicted such as its length, the radius of its base and its aperture given by the angle  $\alpha$ .

The curvature radius at the apex of the tip, i.e., at the point  $(x_0=0$  nm,  $y_0=0$  nm,  $z_0=2$  nm) is:

$$R = a^2 c^2 \left( \frac{x_0^2}{a^4} + \frac{y_0^2}{a^4} + \frac{z_0^2}{c^4} \right)^{\frac{3}{2}} = a^2 c^2 \left( \frac{z_0^2}{c^4} \right)^{\frac{3}{2}} \sim 0.133 \text{ nm} \quad (4.2)$$

This radius is comparable with the empirical ( $\sim 0.135$  nm) [4] and calculated ( $\sim 0.174$  nm) [5] radius of a gold atom. Besides the curvature radius, the sharpness of the tip is also determined by its aperture angle, denoted as  $\alpha$ . This angle is defined as a half angle between the asymptotes to the hyperboloid also plotted in Figure 4.1-A:  $\alpha = \tan^{-1}\left(\frac{a}{c}\right) \sim 14.5^\circ$ . Indeed, the chosen parameters result in a sharp tip, characterized by both a small curvature radius and a narrow aperture angle.

The size of the tip is deliberately kept “small” with a length of 15 nm and a radius at its base of approximately 4.4 nm. In the DDA simulations, this user-designed tip is discretized in almost 330 000 point dipoles, which is relatively small. This gives us room to simulate the sample of the STM junction with a fairly high number of dipoles. A scheme of the discretized tip is shown in Figure 4.1-B. The effect of the tip size on the optical response of the hybrid  $Au/MoSe_2/Au$  tunneling junction is investigated in the last part of section 4.4 of this chapter. The optical properties of the simulated gold tip are incorporated in DDA simulations through its dielectric permittivity, provided by Johnson and Christy [6].

#### b) $MoSe_2$ monolayer and gold substrate

The sample of the modeled STM hybrid junction consists of a  $MoSe_2$  monolayer supported by a gold substrate without any gap in between. It is worth recalling that in DDA simulations, the different materials are separated by sharp boundaries. The thickness of the TMD-ML is set to 0.8 nm [7]. Throughout this chapter, the gold substrate is assumed to be completely flat, except for the last section (section 4.5) where the optical properties of the  $Au/MoSe_2/Au$  junction are explored using two different user-designed rough substrates. The DDA method forces us to model the sample as a finite-size object, constrained in dimensions by the number of dipoles. Thus, both the monolayer and substrate are modeled as rectangular bricks whose length and width are set to 20 nm. The substrate thickness is selected to be 2.2 nm. The simulated sample, displayed in Figure 4.2-A a few nanometers from the tip apex, is discretized in DDA simulations by approximately 1 250 000 dipoles. With this choice of substrate dimensions, rapid convergence of the DDA calculations can be achieved, and a far-field spectrum, for example, can be calculated within a few days. Furthermore, since we are dealing with a finite-size substrate, its dimensions have been selected to establish a plasmon substrate resonance in the visible range, facilitating the study of the substrate role in the optical response of the hybrid junction. This aspect will be addressed later, particularly in section 4.4.3, where the tuning of the optical response of the hybrid junction is explored by varying the substrate dimensions.

As discussed in the second part of Chapter 1, a TMD monolayer exhibits an atomically layered structure. As a consequence, a TMD-ML possesses highly anisotropic optical properties [10]. This anisotropic character is taken into account in the simulations by considering in- and out-of-plane optical indices to describe the properties of the  $MoSe_2$  layer. The in-plane optical index used is the one measured by Liu *et al.* [8] by spectroscopic ellipsometry. Due to the high refractive index of  $MoSe_2$ , ellipsometry measurements are mainly sensitive, in the visible range, to the in-plane optical response. Thus, the refractive index obtained corresponds to the in-plane one. Experimental data for the  $MoSe_2$

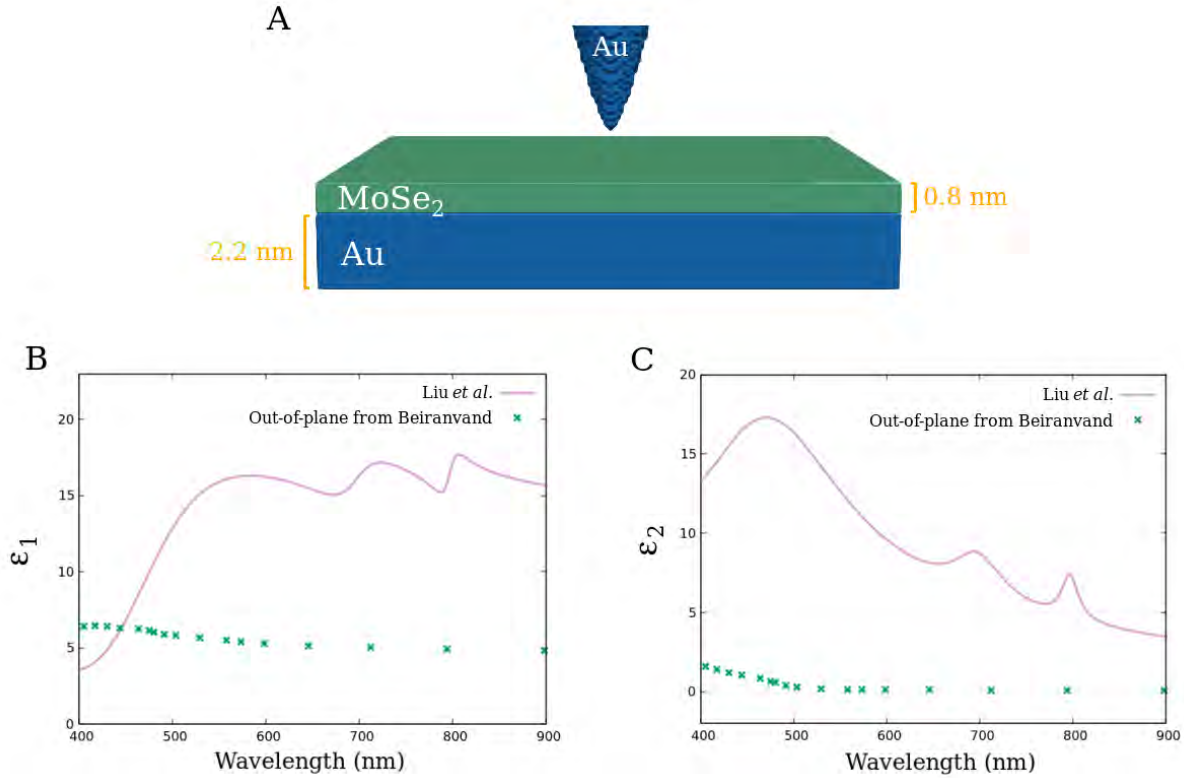


**Figure 4.2:** (A) Schematic representation of the sample which consists in a  $MoSe_2$  monolayer simulated by a 0.8 nm-thick rectangular brick supported by a gold substrate with no gap between them. A part of the tip, including its apex, is also shown, positioned a few angstroms away from the monolayer surface. Real (B) and imaginary (C) parts of the  $MoSe_2$  monolayer dielectric function measured by Liu *et al.* [8] (continuous purple lines) and calculated by Beiranvand [9] along the out-of-plane direction (green points).

monolayer out-of-plane optical index were not available at the time of the study. So instead, the out-of-plane dielectric function computed by Beiranvand [9] through DFT calculations is used. The real and imaginary parts of the in- and out-of-plane dielectric functions used in our DDA simulations are plotted in Figure 4.2-(B,C). Pronounced resonances are observed in the imaginary part of the in-plane permittivity at  $\sim 798$  nm (1.55 eV),  $\sim 695$  nm (1.78 eV) and  $\sim 470$  nm (2.64 eV) corresponding to A-, B- and C-excitons respectively. These values are in reasonable agreement with the A-, B- and C-excitons energies mentioned in Chapter 1 [11, 12]. The influence of the anisotropic character of the TMD-ML on the optical properties of the hybrid  $Au/MoSe_2/Au$  junction is discussed in section 4.2.2 by comparing the optical responses calculated considering both isotropic and anisotropic optical indices. The isotropic  $MoSe_2$  layer is described by the permittivity from Liu *et al.* [8].

### 4.1.2 Incident optical excitation

The modeled junction is excited by an incident electromagnetic field taken as a plane wave with an amplitude set to  $|E_{inc}|=1$ . Its characteristics, including wavelength, direction of propagation, and state of polarization are user-defined. The chosen wavelengths fall within the visible range, ranging from 400

nm to 900 nm.

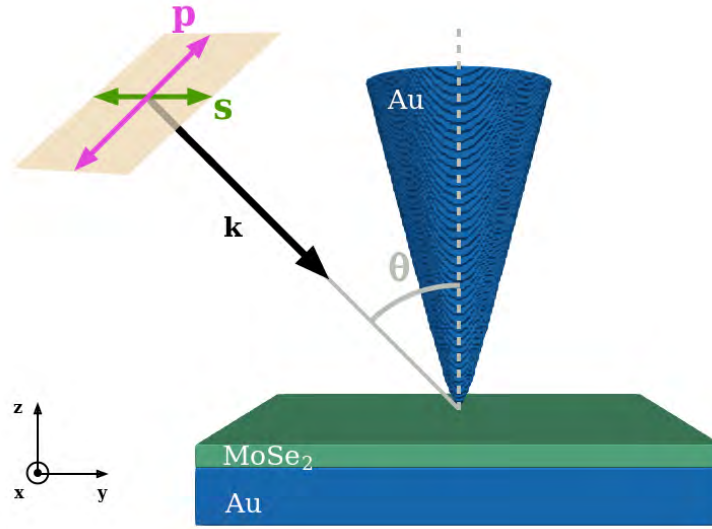


**Figure 4.3:** Schematic representation of the simulated hybrid  $Au/MoSe_2/Au$  tunneling junction. The structure is excited by an incident electromagnetic wave impinging on the monolayer at an angle  $\theta$  with respect to the tip axis. The incident optical excitation is linearly p- or s-polarized (pink and green arrows respectively).

The direction of the incident radiation, given by the wavevector  $\mathbf{k}$ , is defined by the angle  $\theta$  with respect to the tip axis. Despite the sample being square in the  $xy$  plane, it is assumed that the junction exhibits symmetry with respect to the  $z$ -axis and, therefore, that the properties of the junction remain unchanged under rotations around the  $z$ -axis. Figure 4.3 displays the simulated junction along with the incident wavevector  $\mathbf{k}$  impinging on the monolayer at an incidence angle  $\theta$ .

Given the asymmetry of the junction's geometry, the direction of the polarization of the incident field relative to the junction is a crucial parameter that significantly influences the junction optical response. The incident light used in our simulation is linearly p- or s-polarized, represented in Figure 4.3 by a pink and a green arrow, respectively. On the one hand, the p-polarization direction lies in the incidence plane. Thus, the p-polarized incident electric field has two components: one orthogonal and the other parallel to the tip-axis. On the other hand, the s-polarization direction is orthogonal to the incidence plane and the s-polarized incident electric field is then parallel to the  $MoSe_2$  layer surface. By using two different polarizations, distinct optical properties of the junction are expected to be highlighted. Furthermore, in section 4.4.2, the dependence of the optical response on the incident polarization is addressed by varying the incidence angle. Indeed, in the case of p-polarization, the relative contributions of the components of the incident electric field parallel and orthogonal to the tip axis will vary by changing  $\theta$ . However, for s-polarization, the incident electric field always oscillates parallel to the monolayer surface and  $\theta$  plays no particular role.

## 4.2 Electromagnetic interaction between the $MoSe_2$ monolayer and the plasmonic junction

This section deals with the optical response of the hybrid  $Au/MoSe_2/Au$  junction in the non-tunneling regime. Thus, a sufficiently large tip-surface distance  $d$  is considered ( $d= 0.5$  nm) so that electron tunneling and quantum corrections are negligible, as suggested by Esteban *et al.* [1, 2]. Therefore, QCM is not required in the simulations. As the electromagnetic interaction between the  $MoSe_2$  monolayer and the plasmonic junction is specially addressed, the optical response of a purely metallic  $Au/Au$  junction is first examined. Subsequently, the response obtained will be compared with that of the hybrid  $Au/MoSe_2/Au$  junction. The far-field extinction cross-section spectra, along with the electric near-field enhancement spectra and maps resulting from DDA simulations, are analyzed to investigate the spectral properties and spatial localization of the electromagnetic modes present in the junction. Additionally, the role of the anisotropic character of the TMD monolayer is also addressed. Finally, in the last part of this section, the interaction between the excitons confined in the  $MoSe_2$  monolayer and the surface plasmon modes localized within the hybrid tunnel junction is studied. For this, the far-field extinction spectra lineshape is analyzed using coupled-oscillators analytical models.

### 4.2.1 Optical response of a purely metallic $Au/Au$ tunneling junction

The simulated purely metallic  $Au/Au$  junction, depicted in the inset of Figure 4.4-A, is composed by the tip and the substrate described in section 4.1.1 with a distance between the tip apex and the upper substrate surface of  $d= 0.5$  nm. It is excited by the incident plane wave previously described with an incidence angle of  $\theta= 45^\circ$  (with respect to the tip axis). The DDA method enables the computation of far-field and near-field optical spectra, as well as of the spatial distribution of the electromagnetic field inside the simulated target and its surroundings. Compared to far-field measurements, the study of the electromagnetic field at the local scale offers an additional approach to explore and understand electromagnetic modes, especially those that are more localized because of the junction confinement, and their interaction [13].

In Figure 4.4-A, the far-field extinction spectra obtained for an incident p- and s-polarized electric field are shown. Both spectra exhibit an intense peak at 620 nm and the spectrum obtained for p-polarization shows an additional peak at 710 nm of lower intensity. As seen in the previous section, the p-polarized incident electric field comprises both vertical and horizontal components (p-polarization direction lies in the incidence plane), allowing it to excite both transverse and longitudinal (with respect to the tip axis) plasmon modes. In contrast, when using an s-polarized incident light, only transverse modes can be excited. This distinction enables us to differentiate between the transverse and longitudinal modes and discern their resonances within the observed spectral features. Hence, the peak at 620 nm, present in both spectra, is attributed to a transverse surface plasmon resonance, and the peak at 710 nm is, on the other side, attributed to a longitudinal surface plasmon resonance excited by the vertical component of the p-polarized electric field.

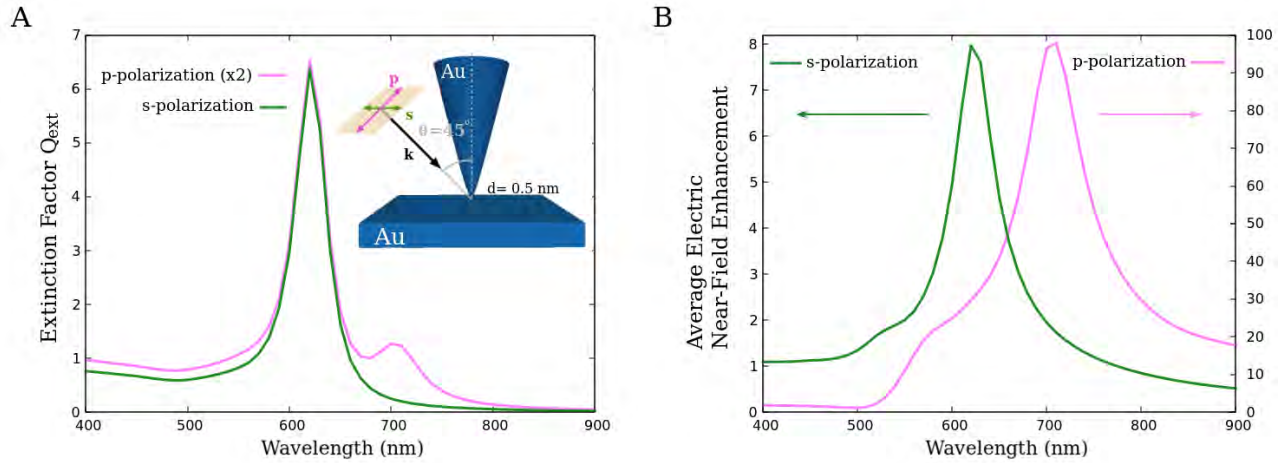


**Figure 4.4:** (A) Far-field optical extinction cross-section spectra (in units of  $\pi a^2$ ,  $a$  being the radius of the sphere of equivalent volume) and (B) average electric near-field enhancement spectra of the purely metallic  $Au/Au$  junction for p and s-incident polarizations (pink and green lines respectively). Inset in (A) shows the simulated junction along with the parameters considered: an incidence angle of  $\theta = 45^\circ$  and a tip-surface distance set to  $d = 0.5$  nm. The near-field enhancement (B) is averaged over a volume that includes the gap, the tip apex and part of the gold substrate for p-polarization, while for s-polarization, the averaging is performed over a finite plane perpendicular to the tip axis and located within the substrate at 0.4 nm from its upper surface.

To more accurately identify the electromagnetic modes corresponding to each peak, and potentially observe additional modes with a low far-field response, the near-field optical response of this metallic junction is investigated. For this purpose, the electric near-field enhancement, defined as the ratio of the calculated electric field over the incident electric field, is computed inside and around the junction. In addition to generating electric near-field enhancement maps, near-field optical spectra are computed by considering the averaged field enhancement. For an incident p-polarized electric field, which possesses both vertical and horizontal components, the field enhancement is averaged over a specific volume. This volume, represented in Fig. 4.5-A by a gray rectangle, includes the gap, the tip apex, and a part of the substrate, as the gap junction is aligned along the tip axis and may contribute to the observed peak at 710 nm. Conversely, for an incident s-polarized electric field oscillating parallel to the monolayer surface, the field enhancement is averaged over a plane perpendicular to the tip apex. This plane, depicted in gray in Figure 4.6-A, is positioned at 0.4 nm below the upper substrate surface. This specific positioning of the averaging plane is chosen in relation to the  $Au/MoSe_2/Au$  configuration, where the near-field optical response for s-polarization is evaluated over a plane located at the middle of the monolayer and thus at 0.4 nm from its upper surface (see section 4.2.2). These spectra are plotted in Figure 4.4-B. For p-polarization, the peak observed at 710 nm in far-field measurements is also clearly evident in the near-field spectrum with a strong intensity, confirming its gap plasmon character. However, the peak at 620 nm is not observed, and instead, a shoulder is present at 575 nm. For s-polarization, the peak at 620 nm observed in the far-field measurements is revealed again, suggesting that it corresponds to the transverse surface plasmon of the substrate. A weak shoulder is as well observed for s-polarization at 530 nm. Electric field enhancement maps are computed at  $\lambda = 710$  and 580 nm for p-polarization (displayed

in Figure 4.5) and at  $\lambda = 620$  and  $530$  nm for s-polarization (depicted in Figure 4.6) to spatially localize and identify the electromagnetic modes responsible for the observed spectral resonances. Finally, an important point to highlight is that the resonance obtained for p-polarization is about 10 times more intense than the one obtained with an incident s-polarized light (Figure 4.4-B).

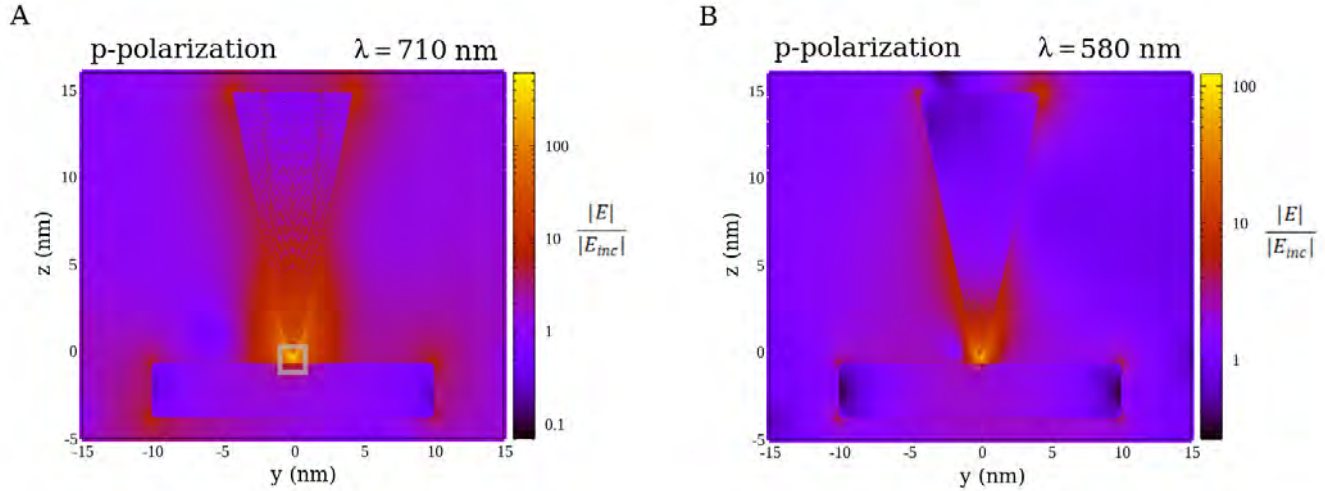


**Figure 4.5:** Electric near-field enhancement maps (in log scale) calculated in the  $yz$  plane. The purely metallic  $Au/Au$  junction is excited by a p-polarized light (A) at  $\lambda = 710$  nm and (B)  $\lambda = 580$  nm under  $45^\circ$  incidence with respect to the  $z$ -axis. The tip-surface distance is  $d = 0.5$  nm. The averaging volume considered to compute the near-field optical spectra for p-polarization is depicted in gray in (A).

According to the electric near-field enhancement map in Figure 4.5-A, the peak at 710 nm can be clearly assigned to the longitudinal tip-surface plasmon modes, referred to in the literature as dipolar gap plasmon modes [14, 15]. Indeed, a significant electric field is induced in the gap, attributed to the confinement of plasmonic oscillations in the gap excited by the vertical component of the p-polarized incident field [15, 16]. The primary region of the tip involved in the gap plasmonic field is the tip apex, which has a curvature radius of  $R \sim 0.133$  nm, comparable to the radius of a gold atom. Following the characterization provided by Benz *et al.* [17], such tip-surface junction can be defined as a plasmonic picocavity. The electromagnetic mode responsible for the shoulder at approximately 580 nm is challenging to identify directly from the field enhancement map shown in Figure 4.5-B. This difficulty arises because the electric field associated with the gap plasmon modes remains prominent at this wavelength. Nevertheless, the near-field optical response of the tip obtained by modeling exclusively the tip in DDA simulations, allows one to identify this shoulder as a plasmon mode originating from the tip itself and exhibiting both longitudinal and transverse (with respect to the tip axis) components. From now on, this mode will be referred to as the apex plasmon mode of the tip. The asymmetric electric field surrounding the tip is indeed associated with this mode. It is worthy to mention that at this tip-surface distance ( $d = 0.5$  nm), gap plasmon modes of higher order are not excited in the investigated spectral range using a plane wave as excitation source [1, 2].

In both electric field enhancement maps calculated for s-polarization, and shown in Figure 4.6, a

field enhancement in the substrate is evidenced, which is more intense at the edges. Additionally, at  $\lambda=530$  nm, a field enhancement is also observed at the upper surface of the tip. Based on these maps,

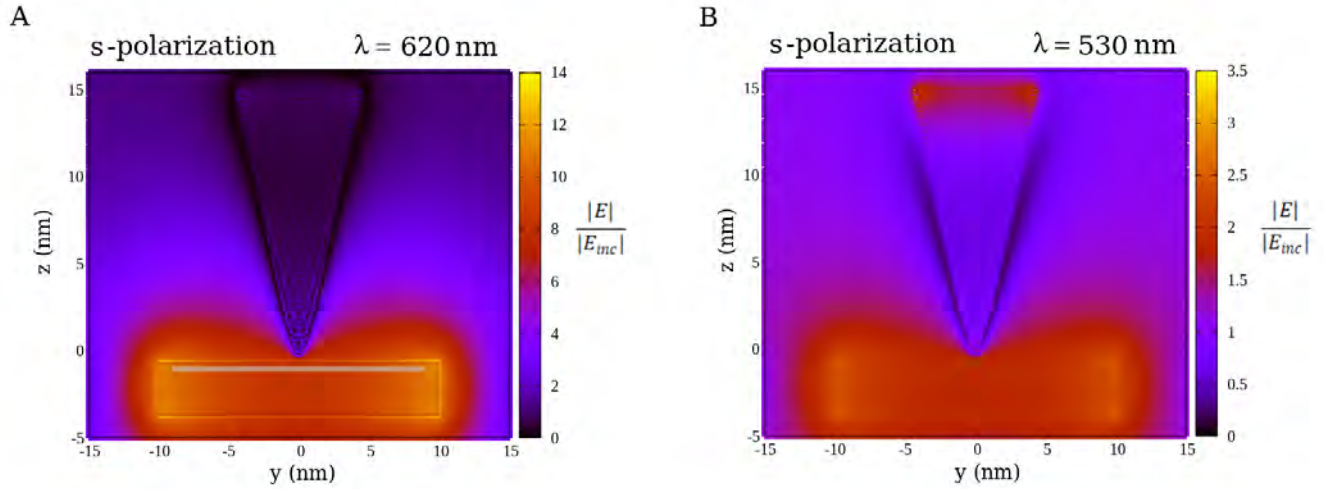


**Figure 4.6:** Electric near-field enhancement maps calculated in the  $yz$  plane. The purely metallic  $Au/Au$  junction is excited by an s-polarized light (A) at  $\lambda= 620$  nm and (B)  $\lambda= 530$  nm under  $45^\circ$  incidence with respect to the  $z$ -axis. The tip-surface distance is  $d= 0.5$  nm. The averaging plane considered to compute the near-field optical spectra for s-polarization is depicted in gray in (A).

it can be deduced that the peak at 620 nm corresponds to the dipolar transverse (with respect to the tip axis) localized surface plasmon resonance (LSPR) of the substrate, while the weak shoulder at 530 nm is attributed to the transverse LSPR of the tip and its interaction with the substrate. The latter assignment is supported by the near-field optical response of the tip, confirming the presence of the tip transverse LSPR at 530 nm. The comparison of the maximum intensity of the field enhancement maps computed for p and s-polarization reveals that the electric field associated with the gap plasmon resonance is more intense than the one associated with the transverse LSPR of the substrate, owing to a stronger localization of plasmonic modes in the gap. This observation is in agreement with the difference in intensity of the resonance peaks between the near-field optical spectra shown in Figure 4.4-B. However, this effect is not observed in the far-field results as strongly localized gap plasmon modes exhibit a weak far-field response (Figure 4.4-A).

#### 4.2.2 Optical response of a hybrid $Au/MoSe_2/Au$ tunneling junction

After studying the optical response of the purely metallic  $Au/Au$  junction, the focus now shifts to the optical response of the hybrid  $Au/MoSe_2/Au$  tunneling junction. The simulated hybrid junction under investigation corresponds to the one described in section 4.1.1, with a tip-surface distance of  $d= 0.5$  nm. It is excited by an incident p- or s-polarized light impinging the junction with an incidence angle of  $\theta= 45^\circ$ . Following the same approach as before, the electromagnetic modes of this junction are identified by analyzing the far- and near-field optical spectra and the near-field maps resulting from DDA simulations. Moreover, in order to study how the presence of the TMD monolayer in the gap

modifies the electromagnetic environment of the STM junction, these modes will be compared with those of the purely metallic junction. Simultaneously, the impact of the anisotropic character of the  $MoSe_2$  layer on the optical properties of the junction is explored by successively comparing the optical responses obtained using an isotropic (same in- and out-of-plane refractive indices) and an anisotropic (different in- and out-of-plane refractive indices)  $MoSe_2$  layer. The optical indices used in each case are presented in section 4.1.1.

### a) Incident p-polarized light

The inset of Figure 4.7-A presents a scheme of the investigated junction illuminated by a p-polarized light. The far-field extinction spectra obtained with an isotropic and an anisotropic  $MoSe_2$  layer are plotted in the same figure. It is observed that these far-field spectra differ significantly from those obtained for a purely metallic junction under the same incident polarization (Figure 4.4-A). Indeed, instead of a narrow resonance structure, an asymmetric broad peak is exhibited, showing spectral dips at  $\lambda \sim 720$  nm and  $\sim 800$  nm. The wavelength of the first dip is close to the B-exciton energy (1.77 eV), with a small shift of  $\sim 20$  nm, while the second dip's wavelength matches with the A-exciton energy (1.55 eV). These dips are thus attributed to an effective electromagnetic coupling between the plasmon modes and the excitons confined within the monolayer. More precisely, they arise from the interferences between plasmonic and excitonic resonances [18–22]. In the upcoming section, the interaction between plasmon modes and excitons will be examined by analyzing the lineshape of far-field spectra using a simple analytical model. This analysis will allow us to confirm the coupling regime and the strength of this coupling. Indeed, as will be shown in section 4.2.3, these interferences appear to be of Fano type, resulting from an intermediate plasmon-exciton coupling regime called the Fano regime [18–20]. Further investigations are required to determine which surface plasmon modes observed in the purely metallic junction (the gap plasmon modes, the transverse LSPR of the substrate, or both) are responsible for these interferences.

A small resonance is observed at  $\sim 550$  nm in Figure 4.7-A for both isotropic and anisotropic spectra. According to the analysis carried out on the optical response of the purely metallic junction, this resonance can be assigned to the apex plasmon mode of the tip.

Differences between the anisotropic and isotropic spectra are observed. In the case of the isotropic monolayer, the dip at  $\sim 800$  nm is more pronounced, while the dip at  $\sim 720$  nm is not observed; instead, it is replaced by a shoulder at 700 nm. Hence, it can be confirmed that the anisotropic character of the TMD monolayer plays a significant role, at least in the far-field optical response of this hybrid junction.

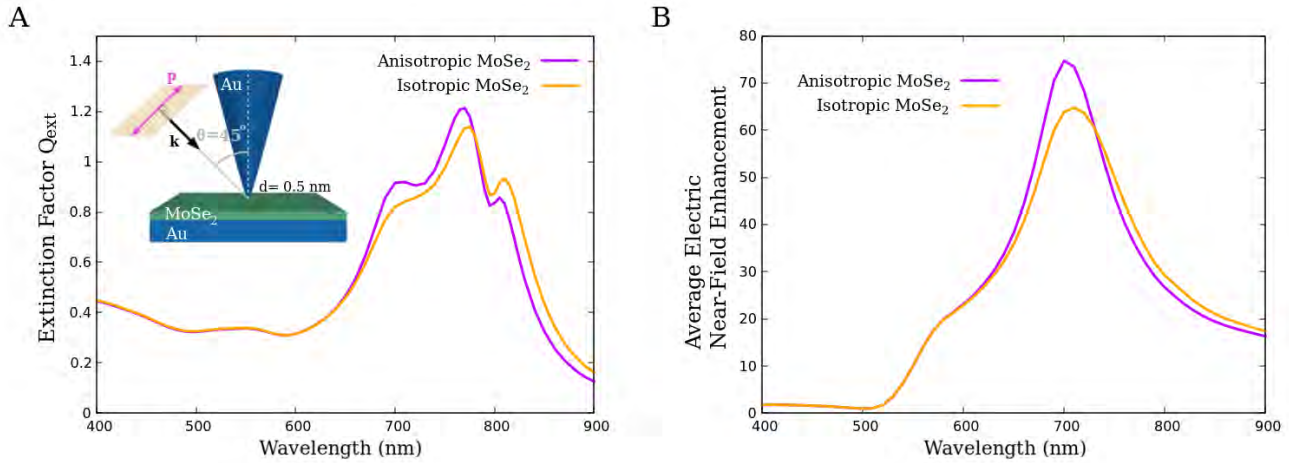


**Figure 4.7:** (A) Far-field optical extinction cross-section spectra (in units of  $\pi a^2$ ,  $a$  being the radius of the sphere of equivalent volume) and (B) average electric near-field enhancement spectra of the hybrid  $Au/MoSe_2/Au$  junction for p-incident polarization obtained using an anisotropic (violet line) and isotropic (orange line) refractive index for the  $MoSe_2$  layer. Inset in (A) shows the simulated junction along with the parameters considered: an incidence angle of  $\theta=45^\circ$  and a tip-surface distance set to  $d=0.5$  nm. The near-field enhancement (B) is averaged over a volume that includes the gap, the tip apex and part of the monolayer.

As already done for the purely metallic junction, electric near-field enhancement spectra are computed for an isotropic and an anisotropic  $MoSe_2$  layer. These spectra are plotted in Figure 4.7-B. The calculation and averaging of the field enhancement are performed over a volume that includes the gap, the tip apex and part of the monolayer. It is worthy to mention that the average volume considered in the near-field spectra calculation has the same size for both metallic and hybrid junctions. These near-field spectra are very similar to the one obtained for a purely metallic junction (see Fig. 4.4-B), exhibiting an intense resonance attributed to the gap plasmon modes. However, the intensity of the gap plasmon resonance is reduced (from  $\sim 100$  to less than 75), and its full width at half maximum (FWHM) slightly increases when a  $MoSe_2$  monolayer is introduced into the gap, regardless of whether the monolayer is isotropic or anisotropic. Moreover, Fig. 4.7-B shows that the gap plasmon resonance for the isotropic monolayer exhibits a lower intensity and a larger FWHM compared to its anisotropic counterpart. The introduction of the  $MoSe_2$  layer in the gap causes damping of the gap plasmon resonance, as the  $MoSe_2$  layer acts as an absorbing medium at the gap plasmon wavelength. This damping effect is more pronounced when an isotropic  $MoSe_2$  optical index is used, due to its larger damping factor compared to the out-of-plane anisotropic  $MoSe_2$  index (see Fig. 4.2-(B,C)). Similarly, the differences between the far-field spectra shown in Figure 4.7-A can be attributed to a stronger damping in the plasmon-exciton interaction, given by a more significant out-of-plane permittivity of the  $MoSe_2$  layer when this latter is supposed isotropic. Note that the interferences observed in the far-field spectra are absent in the near-field spectra because the field enhancement is computed over a volume that includes only a portion of the monolayer and where the electric field associated with the gap plasmon predominates over any other electric field.

The shoulder observed at 575 nm in the near-field spectra remains unaffected whether the TMD

monolayer is considered anisotropic or isotropic, and it remains identical to the one obtained for a purely metallic junction (Fig. 4.4-B). This observation confirms the attribution of this shoulder to the apex plasmon mode of the tip. A slight shift in energy is observed with respect to its resonance in the far-field spectra. The spatial distribution of this mode is investigated below through an electric-field enhancement map (Fig. 4.8-A).

The observation of the gap plasmon resonance in the near-field spectra suggests that the dip at  $\sim 715$  nm in the far-field spectrum for the anisotropic monolayer, which is slightly shifted with respect to the B-exciton energy, could be due to the appearance of the gap plasmon resonance at  $\lambda = 700$  nm. Similarly, the shoulder at 700 nm in the far-field spectrum for the isotropic monolayer could have the same origin. In section 4.4 of this chapter, a further investigation of the contribution of the gap plasmon resonance to the interferences observed in the far-field optical response of the hybrid junction will be addressed.

To provide an insight into the spatial characteristics of the mentioned modes, electric field enhancement maps of the hybrid junction are calculated at  $\lambda = 580$  nm and  $\lambda = 710$  nm and are presented in Figure 4.8. The choice of the wavelength  $\lambda = 710$  nm aims to offer additional information about the gap plasmon modes and their interaction with excitons.

The field enhancement map in Fig. 4.8-A is very similar to one obtained for a purely metallic junction (Fig. 4.5-B) exhibiting the electric field associated with the gap plasmon modes. Nevertheless, the electric field around the tip related to the apex plasmon mode of the tip is still discernible. The field enhancement maps obtained at  $\lambda = 710$  nm (Fig. 4.8-(B,C)) show as well the induced electric field related to gap plasmon modes and concentrated between the tip apex and the  $MoSe_2$ . Considering an anisotropic  $MoSe_2$  layer, the maximum local-field intensity enhancement, which is located under the tip apex, reaches a value of about 450. Fig. 4.8-C shows a field enhancement map computed over a smaller surface centred in the junction gap. This map shows that in addition to the strong electric field induced in the gap, a field enhancement is observed within the monolayer and at the interface between the  $MoSe_2$  layer and the gold substrate. This induced field corresponds to the hybrid plasmon-exciton mode involving the excitons within the monolayer, the gap plasmon modes and the transverse LSPR of the substrate. This also explains the interferences observed in the far-field spectra. For simplicity, this mode will be denoted as “gap plasmon-exciton” mode.

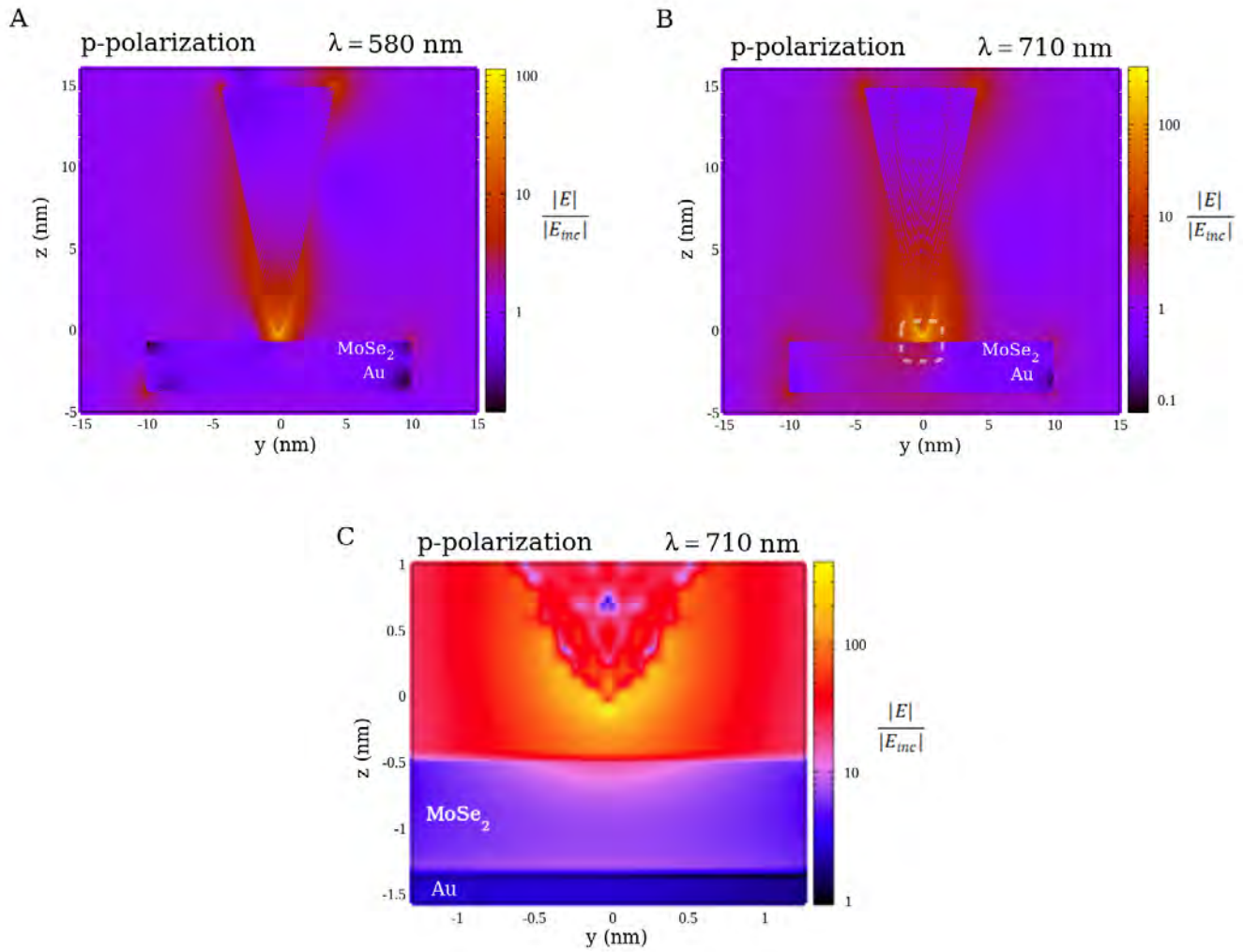


**Figure 4.8:** Electric near-field enhancement maps (in log scale) calculated in the  $yz$  plane. The hybrid  $Au/MoSe_2/Au$  junction is excited by a p-polarized light (A) at  $\lambda = 580$  nm and (B,C)  $\lambda = 710$  nm under  $45^\circ$  incidence with respect to the  $z$ -axis. The tip-surface distance is  $d = 0.5$  nm. The enhancement map in panel (C) represents the spatial electric field distribution within the dashed white rectangle in panel (B). To better visualize this distribution over this small area, a different color palette is employed. The  $MoSe_2$  layer is described by an anisotropic optical index.

### b) Incident s-polarized light

The same analysis conducted above is now presented for an incident s-polarized light. The simulated junction and the incident plane wave along with the direction of the s-polarization are depicted in the inset of Figure 4.9-A. Far-field extinction spectra calculated for an isotropic and an anisotropic monolayer are as well plotted in the same figure. These spectra exhibit a similar lineshape to the ones obtained for p-polarization (Fig. 4.7-A). Specifically, interferences with two dips are observed, one less pronounced at the B-exciton energy ( $\sim 700$  nm) and another more pronounced one at the A-exciton energy ( $\sim 800$  nm). As observed in section 4.2.1, for s-polarization, only transverse electromagnetic modes are excited, leading to the absence of gap plasmon modes. The sharp resonance assigned to

the transverse LSPR of the substrate detected in the far-field spectra of the purely metallic junction is here not observed. Indeed, due to the presence of the  $MoSe_2$  layer, this resonance, located at 620 nm for the purely metallic junction (Fig. 4.4-A), has redshifted by about 100 nm and now overlaps with the A and B excitonic resonances giving rise to these interferences. Thus, for s-polarization, an effective electromagnetic coupling takes place between the transverse LSPR of the substrate and the excitons of the TMD monolayer. Although the lineshape obtained is very similar to the one obtained for p-polarization, it is not identical. This confirms that the plasmon-exciton coupling observed for p-polarization involves not only the transverse LSPR of the substrate, but also the gap plasmon modes. The resonance corresponding to the transverse LSPR of the tip is as well observed at  $\sim 530$  nm. As expected, its energy remains unchanged with the introduction of the monolayer in the junction. The differences between the far-field spectra obtained using an isotropic and an anisotropic optical index to describe the TMD monolayer can be attributed to the damping factor of the out-of-plane component of the optical index, which is significantly larger in the case of the isotropic  $MoSe_2$ .

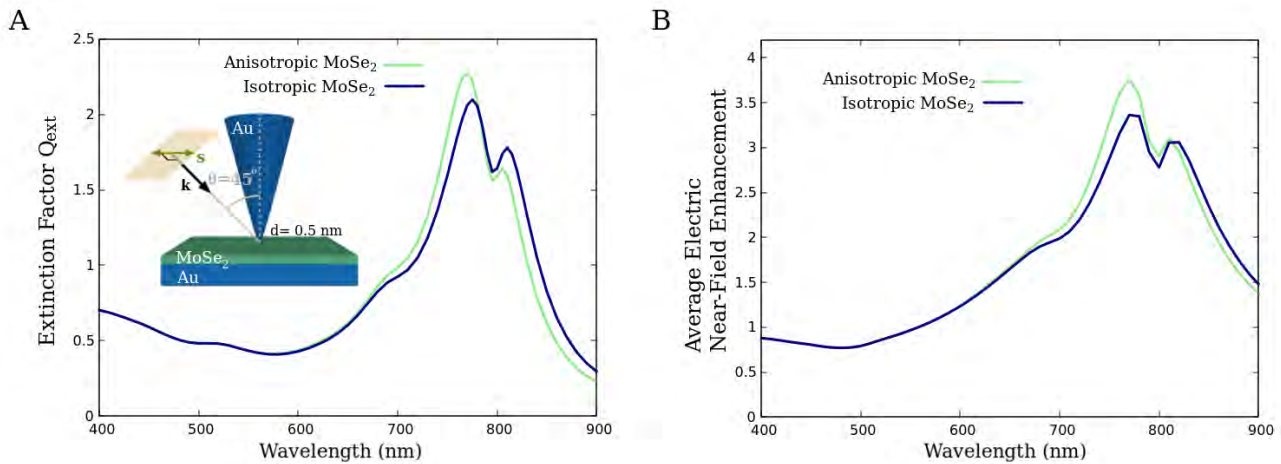


**Figure 4.9:** (A) Far-field optical extinction cross-section spectra (in units of  $\pi a^2$ ,  $a$  being the radius of the sphere of equivalent volume) and (B) average electric near-field enhancement spectra of the hybrid  $Au/MoSe_2/Au$  junction for s-incident polarization obtained using an anisotropic (light green line) and isotropic (dark blue line) refractive index for the  $MoSe_2$  layer. Inset in (A) shows the simulated junction along with the parameters considered: an incidence angle of  $\theta = 45^\circ$  and a tip-surface distance set to  $d = 0.5$  nm. The near-field enhancement (B) is averaged over a plane normal to the tip axis and located within the monolayer at 0.4 nm from its upper surface.

Near-field optical spectra are also computed (see Figure 4.9-B). The electric near-field enhancement is calculated and averaged over a plane perpendicular to the tip axis. This plane is strategically positioned in the middle of the  $MoSe_2$  layer, enabling us to explore the interaction between the monolayer and its surrounding electromagnetic environment. The obtained near-field spectra exhibit a close resemblance to the far-field spectra, indicating similar interferences arising from the plasmon-exciton coupling. Thus, since the average is taken within the TMD monolayer, it is deduced that the plasmon-exciton coupling takes place within the monolayer. A very small dip at  $\sim 470$  nm, which is almost unnoticeable in the far-field spectra due to the resonance at 530 nm, can be observed in the near-field. This dip is at

the C-exciton energy and it is attributed to the coupling between the plasmon modes and C-excitons. Electric near-field enhancement maps are computed to provide insight into the spatial localization of the observed plasmon-exciton coupling. These maps are shown in Figure 4.10.

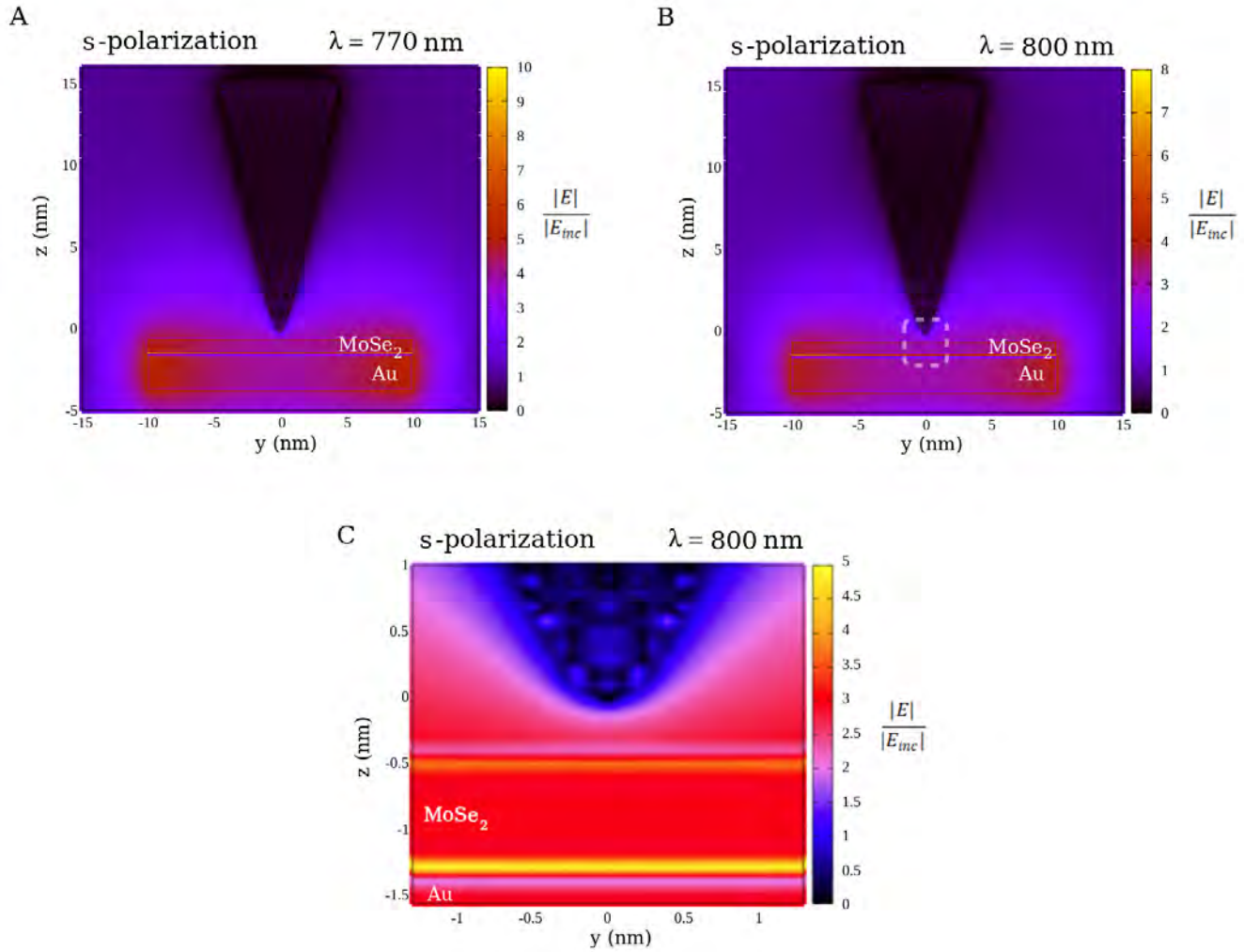


**Figure 4.10:** Electric near-field enhancement maps calculated in the  $yz$  plane. The hybrid  $Au/MoSe_2/Au$  junction is excited by an s-polarized light (A) at  $\lambda = 770$  nm and (B,C)  $\lambda = 800$  nm under  $45^\circ$  incidence with respect to the  $z$ -axis. The tip-surface distance is  $d = 0.5$  nm. The enhancement map in panel (C) represents the spatial electric field distribution within the dashed white rectangle in panel (B). To better visualize this distribution over this small area, a different color palette is employed. The  $MoSe_2$  layer is described by an anisotropic optical index.

Field enhancement maps are calculated at  $\lambda = 770$  nm and  $\lambda = 800$  nm, corresponding approximately to a local maximum and minimum of the plasmon-exciton coupling interferences observed in the far-field spectra of Fig. 4.9-A. The distribution of the electric field, which is associated with the transverse LSPR of the substrate, is the same in both maps with a higher maximum observed in the case of  $\lambda = 770$  nm. Furthermore, by computing a field enhancement map over a small surface centred on the gap, an electric field enhancement is observed at the  $MoSe_2/Au$  substrate interface. This field is

attributed to the hybrid mode resulting from the coupling between the substrate plasmonic resonance and the TMD monolayer excitons. The field enhancement map clearly shows that this mode presents an interface character [23].

A summary of all the spectral features discussed in this section along with their associated electromagnetic mode is given in Table 4.1. The calculations show that plasmon-exciton coupling takes place for both incident polarizations. For s-polarization, it occurs between the transverse LSPR of the substrate and the excitons confined within the  $MoSe_2$  monolayer. For p-polarization, the plasmon-exciton coupling involves not only the transverse LSPR of the substrate and the excitons of the monolayer but also the gap plasmon modes. In the next section, an analytical model is used to evaluate the strength of these electromagnetic couplings.

	Spectral feature	Associated electromagnetic mode
p-polarization	Interferences 600 - 900 nm	Fano-type interferences between plasmon modes and A- and B-excitons
	Peak 550 nm	Apex plasmon mode of the tip
	Peak 700 nm	Gap plasmon modes
	Shoulder 575 nm	Apex plasmon mode of the tip
s-polarization	Interferences 600 - 900 nm	Fano-type interferences between plasmon modes and A- and B-excitons
	Peak 530 nm	Transverse LSPR of the tip
	Interferences 600 - 900 nm	Fano-type interferences between plasmon modes and A- and B-excitons
	Dip 470 nm	Coupling between plasmon modes and C-excitons

**Table 4.1:** Summary of the spectral characteristics observed in the far-field (light gray-shaded rows in the table) and in the near-field (dark gray-shaded rows) optical spectra and their associated electromagnetic mode for both incident p- and s-polarized light.

The electric near-field enhancement results obtained in this section will be used in Chapter 5 to take into account the junction electromagnetic properties for the calculation of theoretical light emission spectra. Lastly, it is important to mention that, the use of an isotropic refractive index for the  $MoSe_2$  layer always results in a stronger damping of electromagnetic modes in the hybrid tunnel junction. Henceforth, the  $MoSe_2$  monolayer will be simulated using an anisotropic optical index.

### 4.2.3 Plasmon-exciton interaction

The aim of this section is to determine the coupling strength and identify the coupling regime of the plasmon-exciton interaction. For this purpose, the extinction far-field spectra calculated from DDA simulations are fitted using the phenomenological analytical coupled-oscillators model. In this model, the plasmonic and excitonic optical responses are described as damped harmonic oscillators that are coupled together through the electric near-field with a certain coupling strength.

### a) Plasmon–exciton multimode coupling

In a first step, the plasmon–exciton coupling obtained for both polarizations is considered as a multimode coupling. It is assumed that the A- and B-excitons are simultaneously coupled to the same plasmonic modes and thus, that their optical responses are not independent. Actually, A- and B-excitons are coupled to each other via the plasmon modes. For the sake of simplicity, the plasmonic modes that may interact with both excitons are described by only one oscillator. Thus, the hybrid system considered in this analysis is composed of three coupled oscillators: the surface plasmon mode, the A-exciton, and the B-exciton and consequently, the three coupled-oscillators model is employed. This model has already been used to study the plasmon–exciton coupling of hybrid systems similar to ours [22, 24, 25]. The motion equations for the three oscillators are written as follows [25, 26]:

$$\begin{aligned}
 \ddot{x}_{sp}(t) + \gamma_{sp}\dot{x}_{sp}(t) + \omega_{sp}^2 x_{sp}(t) + g_A \dot{x}_{ex_A}(t) + g_B \dot{x}_{ex_B}(t) &= F_{sp}(t) \\
 \ddot{x}_{ex_A}(t) + \gamma_{ex_A}\dot{x}_{ex_A}(t) + \omega_{ex_A}^2 x_{ex_A}(t) - g_A \dot{x}_{sp}(t) &= F_{ex_A}(t) \\
 \ddot{x}_{ex_B}(t) + \gamma_{ex_B}\dot{x}_{ex_B}(t) + \omega_{ex_B}^2 x_{ex_B}(t) - g_B \dot{x}_{sp}(t) &= F_{ex_B}(t)
 \end{aligned} \tag{4.3}$$

The plasmon, A-exciton, and B-exciton oscillators are represented by  $x_{sp}(t)$ ,  $x_{ex_A}(t)$ , and  $x_{ex_B}(t)$ , respectively. Then, the damping parameters for the plasmon, A-exciton, and B-exciton are denoted as  $\gamma_{sp}$ ,  $\gamma_{ex_A}$ , and  $\gamma_{ex_B}$ , respectively. Besides, the angular frequencies of the plasmon, A-exciton, and B-exciton are given by  $\omega_{sp}$ ,  $\omega_{ex_A}$ , and  $\omega_{ex_B}$ , respectively. Finally, the coupling rates between the plasmon and A-exciton, and between the plasmon and B-exciton, are represented by  $g_A$  and  $g_B$ . The forces driving the motion of the plasmonic and excitonic A and B resonators due to the electromagnetic field are denoted as  $F_{sp}(t)$ ,  $F_{ex_A}(t)$ , and  $F_{ex_B}(t)$ . It is assumed that the extinction cross-section of the A- and B-excitons are negligible compared to the plasmonic modes, as supported by experimental data reported in [27]. This results in  $F_{ex_A}(t)$  and  $F_{ex_B}(t)$  being approximately equal to zero. The extinction cross-section of this coupled system can be obtained by solving equations (4.3). Its expression is as follows:

$$C_{ext}(\omega) \propto \omega Im \left[ \frac{1}{(\omega_{sp}^2 - \omega^2 - i\omega\gamma_{sp}) - \frac{g_A^2 \omega^2}{\omega_{ex_A}^2 - \omega^2 - i\omega\gamma_{ex_A}} - \frac{g_B^2 \omega^2}{\omega_{ex_B}^2 - \omega^2 - i\omega\gamma_{ex_B}}} \right] \tag{4.4}$$

During the fitting procedure, some parameters of the extinction cross-section expression are held constant, such as the damping rates and the angular frequencies of A- and B-excitons. The plasmon–exciton coupling is evaluated as a function of the tip–surface distance, bias voltage, and incident polarization throughout this chapter. It is assumed that the properties of the excitons confined within the monolayer are independent of these parameters. The values used for the damping rates and angular frequencies of the A- and B-excitons are extracted from the energies and FWHM of A and B peaks of the photoluminescence spectrum of a  $MoSe_2$  monolayer transferred onto a  $SiO_2$  substrate, reported

in the literature. For the A-exciton, the values considered are:  $\hbar\omega_{ex_A}=1.56$  eV and  $\hbar\gamma_{ex_A}=42$  meV [19, 20], while for the B-exciton, they are:  $\hbar\omega_{ex_B}=1.77$  eV and  $\hbar\gamma_{ex_B}=112$  meV [11, 28]. Hence, in the fitting procedure,  $\hbar\omega_{sp}$ ,  $\hbar\gamma_{sp}$ ,  $\hbar g_A$  and  $\hbar g_B$  are adjustable parameters determined by fitting the resulting extinction cross-section spectrum to the one computed from DDA calculations. The optimized parameters of the model are obtained using the Levenberg-Marquardt nonlinear least squares algorithm, which is implemented in the Python routine “*scipy.optimize.curve\_fit*”. This algorithm is employed to determine the values of the adjustable parameters, ensuring an optimized fitting. These calculations are performed in the 600 to 900 nm wavelength range, corresponding to the spectral range of the interferences observed in the DDA far-field spectra.

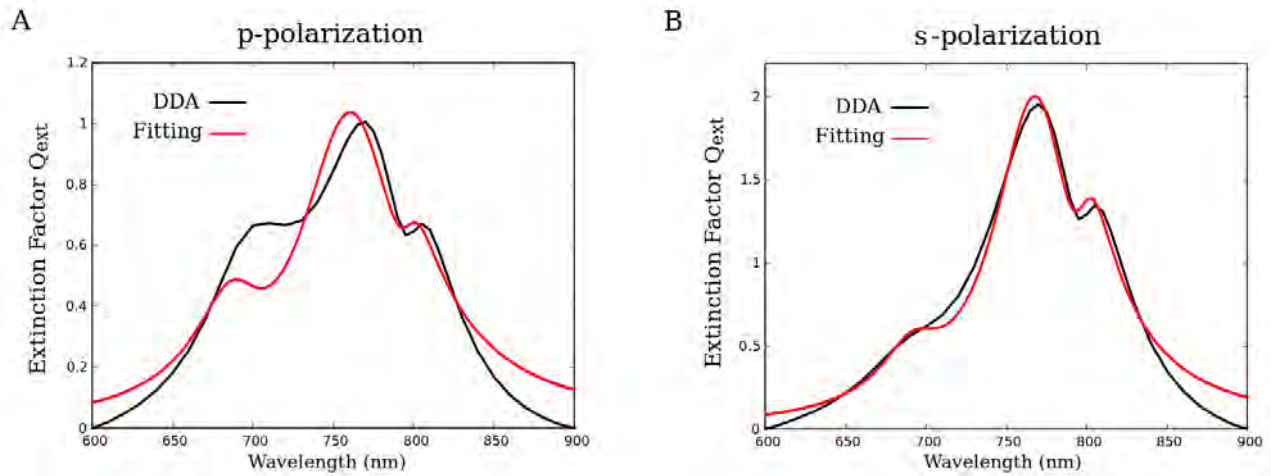


**Figure 4.11:** Far-field optical extinction cross-section spectra (in units of  $\pi a^2$ ,  $a$  being the radius of the sphere of equivalent volume) obtained from DDA simulations (black lines) with the baseline corrected for p- (A) and s- (B) incident polarizations, and spectra calculated using the three coupled-oscillators model and fitted to the DDA spectra (red lines).

In Figure 4.11, the extinction cross-section spectra obtained from DDA simulations for each incident polarization are plotted in black lines. These spectra correspond to the ones presented in the previous section with the baseline adjusted for a better fitting. The extinction cross-section spectra, obtained through calculations using the three coupled-oscillators model and then fitted to the DDA spectra, are also depicted as red lines. These spectra correspond to the better fit obtained after a complete optimization of the adjustable parameters. For the p-polarization, the adjustable parameters obtained are:  $\hbar\omega_{sp}=1.65$  eV,  $\hbar\gamma_{sp}=198$  meV,  $\hbar g_A=49.5$  meV and  $\hbar g_B=128$  meV. For s-polarization,  $\hbar\omega_{sp}=1.62$  eV,  $\hbar\gamma_{sp}=152$  meV,  $\hbar g_A=50.8$  meV and  $\hbar g_B=109$  meV have been obtained. For s-polarization, the fitted curve replicates the far-field spectrum satisfactorily (Figure 4.11-B). However, for p-polarization, discrepancies with the DDA spectrum are observed, particularly in the spectral region around the energy of the B-exciton (Fig. 4.11-A). For s-polarization, excitons are coupled solely with the substrate transverse LSPR, whereas for p-polarization, an additional plasmonic mode (gap plasmon modes) is assumed to be involved in the plasmon-exciton coupling. The three coupled-oscillators model may not fully capture the intricacies of this coupling obtained under p-polarization. Moreover,

the potential presence of the gap plasmon resonance in the far-field spectra at 700 nm could result in modifications in the coupling interferences that the model is unable to capture. Indeed, in Fig. 4.11-A, it is clear that the spectrum obtained using the three coupled-oscillators model achieves a better fit for the longer wavelengths but fails to accurately represent the region where the resonance of the gap plasmon is located.

Due to the discrepancies observed in the case of an incident p-polarized electric field, the decision was made to not use the analytical three coupled-oscillators model to evaluate the plasmon-exciton coupling taking place in the simulated junction. Nevertheless, the study of this coupling and its behavior as a function of tunneling parameters and incident polarization remains crucial to characterize the optical properties of the simulated junction. Consequently, it was decided to focus only on the coupling between plasmons and A-excitons. Indeed, the fit achieved using the three coupled-oscillators model suggested that it could be possible to obtain a satisfactory fitting for both incident polarizations by focusing solely on the spectral range around the dip at the A-exciton energy (750 - 830 nm).

### b) Coupling between A-excitons and plasmon modes

In the approach presented here, it is assumed that the plasmon-exciton coupling occurs only between the plasmon modes and A-excitons and there is no interaction between these modes and B-excitons. In this case, the plasmon-exciton coupling is evaluated using the two coupled-oscillators analytical model [19–21, 27]. The same methodology used for the three coupled-oscillators model is followed, wherein surface plasmon modes and A-excitons are described as damped harmonic oscillators. The extinction cross-section of this system can be written as follows [26]:

$$C_{ext}(\omega) \propto \omega \text{Im} \left[ \frac{\omega_{exA}^2 - \omega^2 - i\omega\gamma_{exA}}{(\omega_{exA}^2 - \omega^2 - i\omega\gamma_{exA})(\omega_{sp}^2 - \omega^2 - i\omega\gamma_{sp}) - g^2\omega^2} \right] \quad (4.5)$$

For the fitting procedure,  $\hbar\omega_{exA}=1.56$  eV and  $\hbar\gamma_{exA}=42$  meV [19, 20] are kept constant.  $\hbar g$  is defined as the interaction energy between the two oscillators.  $\hbar\omega_{sp}$ ,  $\hbar\gamma_{sp}$  and  $\hbar g$  are determined by fitting the resulting extinction cross-section spectrum obtained with equation (4.5) to DDA calculated spectra. The fitting procedure was performed in the 750 to 830 nm wavelength range and hence, the B-exciton contribution is not taken into account.

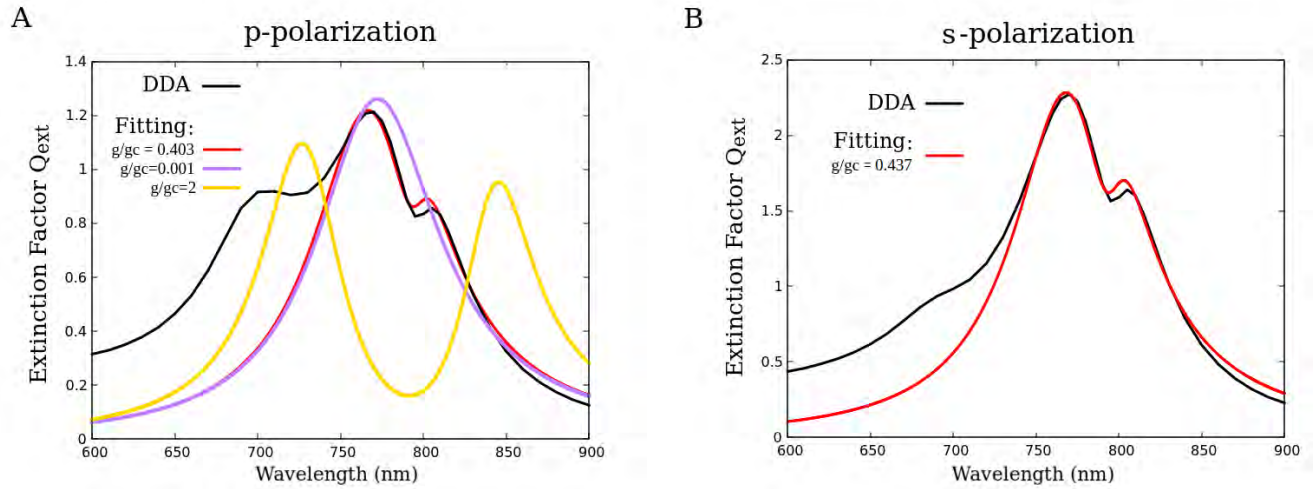


**Figure 4.12:** Far-field optical extinction cross-section spectra (in units of  $\pi a^2$ ,  $a$  being the radius of the sphere of equivalent volume) obtained from DDA simulations (black lines) for p- (A) and s- (B) incident polarizations and spectra calculated using the two-coupled oscillators model and fitted to the DDA spectra (red lines). For both incident polarizations, the obtained ratio  $g/g_c \sim 0.4$  indicates that the plasmon-exciton coupling is in the Fano regime. In (A), spectra calculated from the coupled oscillators model corresponding to the weak  $g/g_c = 0.001$  (purple line) and strong  $g/g_c = 2$  (yellow line) coupling regime are also plotted for comparison.

Figure 4.12 shows the far-field extinction spectra computed using DDA (black lines) and fitted using eq. (4.5) (red lines) for p and s-polarizations. Within the spectral range considered (between 750 and 830 nm), a satisfactory agreement is observed between the spectra obtained from DDA simulations and those calculated using the two coupled-oscillators model. For p-polarization, the adjustable parameters resulting from the fitting are:  $\hbar\omega_{sp} = 1.605$  eV,  $\hbar\gamma_{sp} = 188 \pm 0.650$  meV, and  $\hbar g = 46.4 \pm 1.55$  meV. On the other hand, for s-polarization, the fitting procedure provides the following parameters:  $\hbar\omega_{sp} = 1.600$  eV,  $\hbar\gamma_{sp} = 177 \pm 0.650$  meV, and  $\hbar g = 47.8 \pm 1.50$  meV. The red spectra of Figure 4.12 are calculated using these values. The error range of  $\hbar\gamma_{sp}$  and  $\hbar g$  is determined using a tolerance of 0.25 %. This implies that any fitted spectrum calculated with a value of  $\hbar\gamma_{sp}$  within its error interval has an area under the curve that deviates by less than 0.25 % from that of the DDA spectrum. The same applies to  $\hbar g$ .

The coupling regime relies on the interaction strength  $\hbar g$  and the critical value  $\hbar g_c$ . The latter is defined as  $\hbar g_c = (\hbar\gamma_{ex_A} + \hbar\gamma_{sp})/2$  [19, 20, 27, 29]. When  $g > g_c$ , the coupling regime is categorized as strong, wherein the interaction between the excitonic and plasmonic resonances gives rise to the formation of two hybrid states. As a result, the optical spectrum exhibits a characteristic Rabi splitting, manifesting in the appearance of two distinct peaks. This regime is often referred to as the Rabi regime. When  $g < g_c$ , but still close to  $g_c$ , the coupling regime is classified as intermediate, also known as the Fano regime. In this regime, interference occurs between the broad plasmonic resonance and the narrow excitonic transition, which can be destructive at certain wavelengths. This leads to the formation of an asymmetric lineshape in the extinction cross-section spectrum, exhibiting a transparency dip. Finally, when  $g \ll g_c$ , the coupling regime is categorized as weak. In this case, there is no hybridization or interference between the plasmonic and excitonic resonances. The decay of the excitonic transition into

the plasmonic mode is described by the Fermi golden rule.

Then, the ratio  $g/g_c$  is calculated to establish the coupling regime of the plasmon-exciton coupling under study. For p-polarization, the critical value  $\hbar g_c$  is 115 meV, and the ratio  $g/g_c$  obtained is:  $g/g_c = 0.403 \pm 0.0148$  while for s-polarization, we obtain  $\hbar g_c = 109.5$  meV and  $g/g_c = 0.437 \pm 0.0153$ . This sets the coupling between plasmon modes and A-excitons in the Fano coupling regime for both polarizations. Additionally, it is noteworthy to highlight that when employing s-polarized light, the electromagnetic coupling between plasmon modes and excitons is stronger than for p-polarized light. This is due to the larger spatial overlap of the plasmonic near-field with the  $MoSe_2$  layer for s-polarization as can be deduced by comparing the field enhancement maps of Fig. 4.8 and 4.10 of section 4.2.2. This will be discussed in more details in section 4.4. In Figure 4.12-A, the extinction spectra calculated with the same adjusted parameters and with three different coupling factors are plotted in order to compare the extinction spectra obtained for each regime. The yellow line, which corresponds to  $g = 2 g_c$ , exhibits two resonances clearly separated, demonstrating the Rabi regime. On the other hand, the purple line, with  $g$  set to  $g = 0.001 g_c$ , shows a single resonance characteristic of weak coupling.

### 4.3 Simulation of the electron tunneling using the Quantum-Corrected Model (QCM)

The Quantum-Corrected Model (QCM), developed by Esteban *et al.* [1, 2], is applied in our DDA simulations to account for electron tunneling when dealing with tip-surface distances in the tunneling regime ( $d < 0.5$  nm). Indeed, electron tunneling is a critical element of an STM junction. Therefore, its inclusion in our simulations will allow a more accurate description of the behavior and properties of the STM junction and provides a step forward for the understanding of the experimental results observed in Chapter 3. The QCM, described in section 2.3.2 of Chapter 2, is a semi-classical approach. The implementation of this model in our simulations is presented in the first part of this section. Then, the STM electron tunneling effects on the optical response of the hybrid  $Au/MoSe_2/Au$  junction are discussed in a second part.

#### 4.3.1 Implementation of the QCM in the numerical simulations

As discussed in section 2.3.2 of Chapter 2, the QCM is based on the introduction of an effective conductive medium into the gap region to take into account the tunneling conductivity. This medium is described by a Drude-like effective dielectric function  $\epsilon_g(\omega, d)$ , which expression is derived from the conductivity of the gap  $\sigma_g(d)$ , the latter being considered static:

$$\epsilon_g(\omega, d) = 1 + i \frac{\sigma_g(d)}{\epsilon_0 \omega} \quad (4.6)$$

While the QCM is typically used for Drude metal dimers surrounded by vacuum, our scenario

involves an STM junction formed by a plasmonic tip and a 2D semiconductor supported by a plasmonic substrate. The determination of the tunneling gap conductivity by complex quantum calculations is beyond the scope of this thesis. Instead, an alternative approach is proposed to compute this conductivity using the experimental conductivity of the stacked  $Au/MoSe_2/Au$  junction. In this approach, the composition of the junction and the dependence of gap conductivity on the applied bias voltage  $V$  and tip-surface distance  $d$  are considered. The proposed expression for tunneling conductivity is based on the exponential decay of the tunneling current with increasing the gap thickness  $d$  (see section 1.1.1 of Chapter 1) and is given by:

$$\sigma_g(d, V) = \sigma_0(V) \exp\left(-\frac{2d}{l_c}\right) \quad (4.7)$$

where  $\sigma_0(V)$  is the bias voltage-dependent conductivity of a  $MoSe_2$  monolayer, sandwiched between two gold electrodes, and  $l_c$  is the penetration depth of the conduction electron wavefunction into vacuum. By employing equation (4.7), the boundary conditions are satisfied. When the tip-surface distance  $d$  is zero, the conductivity of the effective medium at the gap corresponds to the empirical conductivity of the stacked  $Au/MoSe_2/Au$  junction. Then, as  $d$  tends towards infinity, the permittivity of the effective medium  $\epsilon_g$  converges to 1, which corresponds to the vacuum dielectric function. The approach described here is schematized in Figure 4.13.

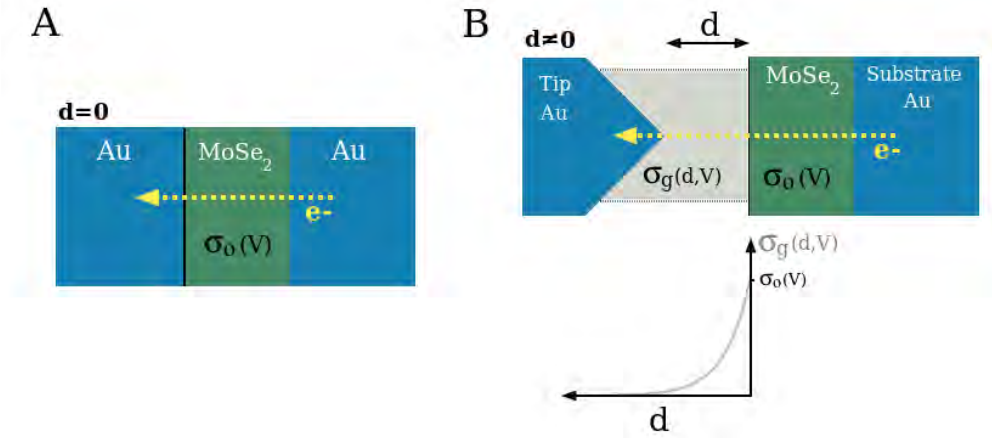


**Figure 4.13:** (A) Schematic representation of the  $Au/MoSe_2/Au$  stacked junction with a conductivity  $\sigma_0(V)$ . (B) Schematic representation of the  $Au/MoSe_2/Au$  tunneling junction with  $\sigma_g(d, V)$  denoting the calculated conductivity of the gap, dependent exponentially on the tip-surface distance  $d$ .

The permittivity of the effective medium that accounts for electron tunneling depends on the tip-surface distance  $d$  (eq. (4.6)). Due to the STM junction gap geometry, this gap is modeled by a set of  $n$  nested cylindrical homogeneous shells, as depicted in a schematic illustration in Fig. 4.14-A. Each shell is characterized by a gap thickness and bias voltage-dependent dielectric function  $\epsilon_i = \epsilon(\omega, d_i, V)$ , where  $d_i$  denotes the longitudinal length (along  $z$ ) of the  $i^{th}$  shell.

In our DDA simulations, an inter-dipole distance of 0.1 nm is used. Consequently, the smallest tip-surface distance that can be considered is  $d=0.2$  nm. An effective medium is introduced in the gap

for tip-surface distances ranging from  $d = 0.2$  nm to 0.4 nm. For larger distances, it is assumed that the junction is no longer in the tunneling regime, and quantum effects, including electron tunneling, become negligible [1, 2].

Figure 4.14-(B,C) provides a schematic representation of the effective media introduced in the simulated junction for a distance between the tip apex and the  $MoSe_2$  surface of 0.2 nm. Due to the tip geometry and its discretization, the gap is divided into three cylindrical shells with lengths of  $d_1 = 0.2$  nm (shell n°1 depicted in red),  $d_2 = 0.3$  nm (shell n°2 depicted in orange) and  $d_3 = 0.4$  nm (shell n°3 depicted in yellow). These shells are approximated by discrete point dipoles. As the distance between the tip apex and the  $MoSe_2$  surface increases, the number of shells decreases until reaching the non-tunneling regime ( $d \geq 0.5$  nm), where no shell remains.

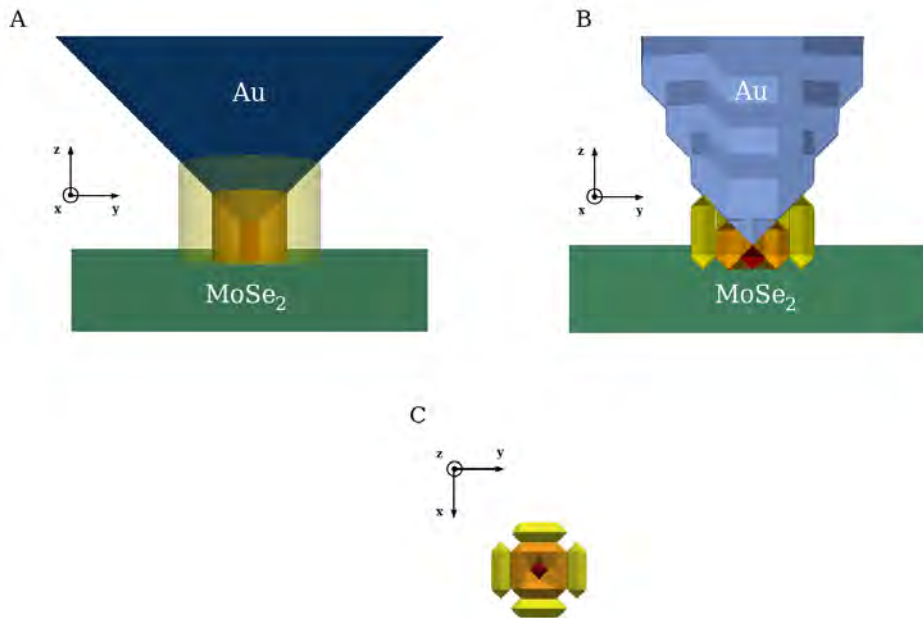


**Figure 4.14:** (A) Sketch of the Quantum-Corrected Model (QCM) implemented in the gap of the hybrid  $Au/MoSe_2/Au$  tunneling junction. The set of cylinders between the tip and the monolayer corresponds to the effective media that account for the quantum tunneling. The effective medium n°1 with a length of  $d_1 = 0.2$  nm is depicted in red, whereas the effective media n°2 and n°3 with a length of  $d_2 = 0.3$  nm and  $d_3 = 0.4$  nm are shown in orange and yellow respectively. (B-C) Schematic representation of the simulated effective media embedded in the modeled junction and approximated by discrete point dipoles, viewed from the  $yz$  (B) and  $xy$  (C) planes.

Unfortunately, no experimental data reporting the conductivity or electronic properties of an  $Au/MoSe_2/Au$  stacked junction have been found in the literature for the calculation of the gap tunneling conductivity  $\sigma_g(d, V)$ . However, electrical measurements on an  $Au/MoS_2/Au$  stacked junction have been reported by Ge *et al.* [30]. These authors performed transport measurements on a  $MoS_2$  monolayer supported by a flat gold substrate, with a gold STM tip in controlled physical contact with the  $MoS_2$  surface. The assumption was made that the  $Au/MoS_2/Au$  stacked junction has electronic transport properties similar to those of the  $Au/MoSe_2/Au$  sandwiched junction, considering the similarity in Schottky barrier heights at the  $MoSe_2/Au$  interface ( $\Phi_{B_{MoSe_2}} = 0.62$  eV [31]) and the  $MoS_2/Au$  interface

( $\Phi_{B_{MoS_2}} = 0.8$  eV [32]). Thus, the conductivity  $\sigma_0(V)$  used for computing the tunneling conductivity  $\sigma_g$  is calculated from the I-V curve of an  $Au/MoS_2/Au$  junction [30]. In Table 4.2, the conductivity  $\sigma_0(V)$  calculated for four bias voltages  $V$  are listed. It is worth mentioning that the selection of these four bias voltages in the 1.5 V - 2.25 V range was intended to closely mimic the experimental STM configuration described in Chapter 3. In addition, and for the same reason,  $\sigma_0(V)$  is calculated using the data considering electron transfer from the gold substrate to the STM tip in contact with the monolayer (see Fig. 4.13).

The tunneling conductivity  $\sigma_g(d, V)$  is then calculated for  $d = 0.2, 0.3$  and  $0.4$  nm and a bias voltage  $V$  ranging from  $V = 1.5$  V to  $V = 2.25$  V (see Table 4.2). In the tunneling conductivity calculation, the penetration depth of the conduction electron wavefunction into vacuum  $l_c$  is given by:

$$l_c = \frac{\hbar}{\sqrt{2m\Phi_{B_{MoSe_2}}}} \sim 0.25 \text{ nm} \quad (4.8)$$

where  $m$  is the free-electron mass.

Bias Voltage V (V)	$\sigma_0(V)$ (S.m <sup>-1</sup> )	d (nm)	$\sigma_g(d, V)$ (S.m <sup>-1</sup> )
1.5	0.842	0.2	0.168
		0.3	0.0749
		0.4	0.0334
1.75	2.72	0.2	0.542
		0.3	0.242
		0.4	0.108
2	13.8(6)	0.2	2.76
		0.3	1.23
		0.4	0.551
2.25	20.1	0.2	4.01
		0.3	1.79
		0.4	0.798

**Table 4.2:** QCM parameters used in the simulations:  $\sigma_0(V)$  is calculated from the I-V curve of a stacked  $Au/MoS_2/Au$  junction [30].  $\sigma_g(d, V)$  is computed using eq. (4.7).

For a bias voltage  $V$  ranging from 1.5 V to 2.25 V,  $\sigma_0(V)$  increases from 0.842 S.m<sup>-1</sup> to 20.1 S.m<sup>-1</sup>. The values of  $\sigma_g(d, V)$  obtained using the equation (4.7) range from 0.0334 S.m<sup>-1</sup> for  $d = 0.4$  nm and  $V = 1.5$  V, to 4.01 S.m<sup>-1</sup> for  $d = 0.2$  nm and  $V = 2.25$  V.  $\sigma_g(d, V)$  is significantly smaller than  $\epsilon_0\omega$  (eq. (4.6)) in the investigated spectral range, which is of the order of  $10^4$  S.m<sup>-1</sup>. In Figure 4.15, the ratio  $\sigma_g(d, V)/\epsilon_0\omega$  for  $d = 0.2, 0.3$  and  $0.4$  nm and  $V = 2$  V are plotted.

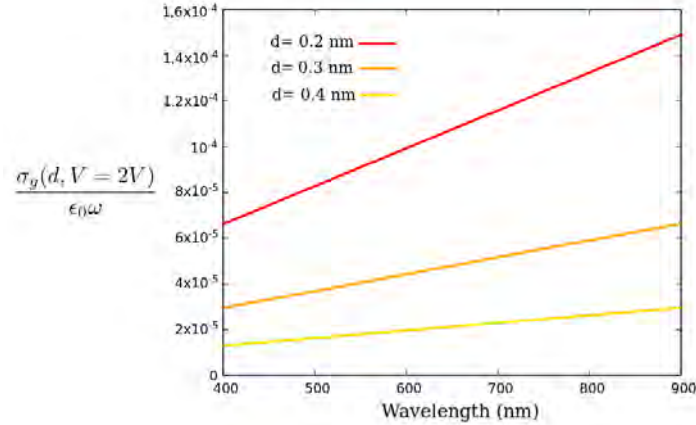


**Figure 4.15:** Imaginary part ( $\sigma_g(d, V)/\epsilon_0\omega$ ) of the effective medium permittivity  $\epsilon_g(\omega, d, V)$  calculated for  $d = 0.2, 0.3$  and  $0.4$  nm and  $V = 2$  V.

Since  $\sigma_g(d, V)$  is significantly lower than  $\epsilon_0\omega$ , the obtained ratio  $\sigma_g(d, V)/\epsilon_0\omega$  is extremely small. This ratio corresponds to the imaginary part of the dielectric function  $\epsilon_g(\omega, d, V)$  (see eq. (4.6)) used to describe the effective media accounting for electron tunneling in the QCM-DDA simulations. As a result, the simulated effective media exhibit a refractive index close to that of vacuum. Thus, it is expected that quantum corrections to the classical electrodynamic calculations will have a moderate impact on the optical response of the hybrid  $Au/MoSe_2/Au$  tunneling junction. However, it remains interesting to investigate their effect.

### 4.3.2 Effect of the simulated STM electron tunneling on the optical response

The effect of electron tunneling simulated using QCM on the optical response is examined by comparing the near-field optical response obtained in two scenarios: one with QCM implemented in the DDA simulations and the other without QCM. The tip-surface distance is set to  $d = 0.2$  nm (tunneling regime) and QCM is used with a bias voltage of  $V = 2$  V. As previously done in section 4.2.2 for p-polarization, the near-field spectrum is obtained by calculating and averaging the electric near-field enhancement over a volume that includes the tip apex, the gap, and part of the monolayer. This volume includes as well the effective media when QCM is added in the simulations. For s-polarization, the field enhancement is calculated and averaged over a plane perpendicular to the tip axis, located at  $0.4$  nm below the upper surface of the  $MoSe_2$  layer. The resulting near-field spectra are displayed in Figure 4.16.

For p-polarization (Fig. 4.16-A), when the QCM is applied, a redshift of the gap plasmon resonance at  $\lambda = 740$  nm is expected due to the introduction of three effective media in the gap (see Fig. 4.14). However, this redshift is negligible in the present case (a few nanometers). According to Esteban *et al.* [1, 2], electron transfer between the tip and the monolayer screens the polarization charges localized at the opposite sides of the junction resulting in a reduction of the electric field enhancement. This

reduction is however very weak and practically undetectable in the spectra. The weak effect of electron tunneling is attributed to the fact that the dielectric functions of the effective media introduced in the gap are nearly equal to 1. In the case of a purely metallic junction [1, 2], or with a smaller band gap semiconductor with higher electrical conductivity, the conductivity in the gap would have been greater, leading to more significant quantum corrections.

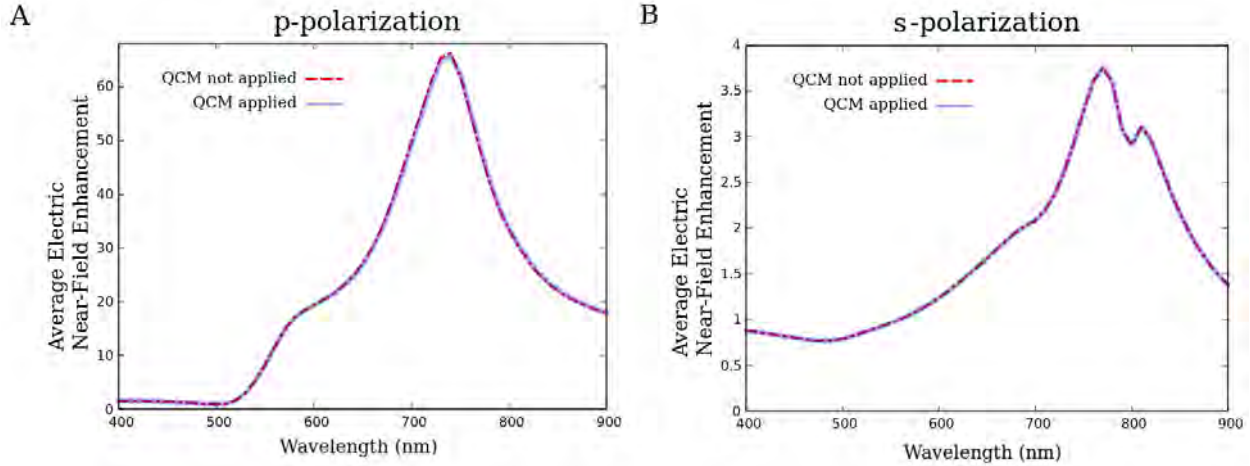


**Figure 4.16:** Average electric near-field enhancement spectra of the hybrid  $Au/MoSe_2/Au$  tunneling junction excited by (A) a p- and (B) s-polarized incident light calculated without (red dashed lines) and with (blue continuous lines) QCM correction. The tip-surface distance is  $d = 0.2$  nm and the bias voltage used in DDA-QCM simulations is  $V = 2$  V.

For s-polarization (Fig. 4.16-B), the Fano-lineshape interference resulting from the plasmon-exciton coupling remains unaffected by the presence of the effective media in the gap and the resulting quantum corrections. Indeed, as shown in Figure 4.10-C (section 4.2.2), the electric field associated with this coupling is localized mainly at the  $MoSe_2/Au$  interface, far from the effective media which account for tunneling in the STM junction.

## 4.4 Tuning of the optical response of the hybrid $Au/MoSe_2/Au$ tunneling junction

In section 4.2, the electromagnetic modes sustained by a hybrid  $Au/MoSe_2/Au$  tunneling junction as well as their spectral properties and spatial localization were identified and analyzed. In particular, gap plasmon modes and Fano-type plasmon-exciton coupling taking place at the  $MoSe_2/Au$  substrate interface were highlighted. The tuning of the optical properties of these modes as a function of several parameters is the central topic of the current section. In a first step, the junction's optical response is analyzed in relation with the main tunneling parameters: bias voltage  $V$  and tip-surface distance  $d$ . Indeed, by using QCM, quantum effects such as electron tunneling can be taken into account allowing the proper simulation of the hybrid junction for tip-surface distances  $d$  in the tunneling regime. Furthermore, the QCM enables us to numerically evaluate the optical response dependence on the bias

voltage. Following this discussion, the dependence of the junction's optical properties on the incidence angle is studied. Indeed, the role of the polarization direction of the incident plane wave on the optical response is analyzed by varying the angle  $\theta$ . Finally, the last part of this section is devoted to the study of the impact of the modeled tip and substrate size on the optical response of the junction, since these elements are necessarily of finite size in DDA simulations.

#### 4.4.1 Dependence of the optical response on the main tunneling parameters

##### a) Bias voltage

By means of QCM-DDA simulations, the dependence of the gap plasmon resonance and plasmon-exciton coupling is investigated in terms of bias voltage  $V$  applied to the junction, with a tip-surface distance set at  $d=0.2$  nm (tunneling regime). In order to excite gap plasmon modes, an incident p-polarized light is used. Electric near-field enhancement spectra are calculated for different bias voltages used in the QCM implemented in the simulations. The field enhancement is calculated and averaged over a volume that includes the tip apex, the gap, the effective media accounting for electron tunneling, and part of the  $MoSe_2$  monolayer. The spectra obtained are displayed in Figure 4.17-A. On the other side, the dependence of the plasmon-exciton coupling on the bias voltage  $V$  is investigated from the interaction energy  $\hbar g$  between plasmon modes and A-excitons. This latter is determined by analyzing the far-field spectra lineshape using the two coupled-oscillators model, as described in section 4.2.3. Figure 4.17-B shows the evolution of the coupling strength ratio  $g/g_c$  as a function of the bias voltage  $V$  for an incident p and s-polarized light.

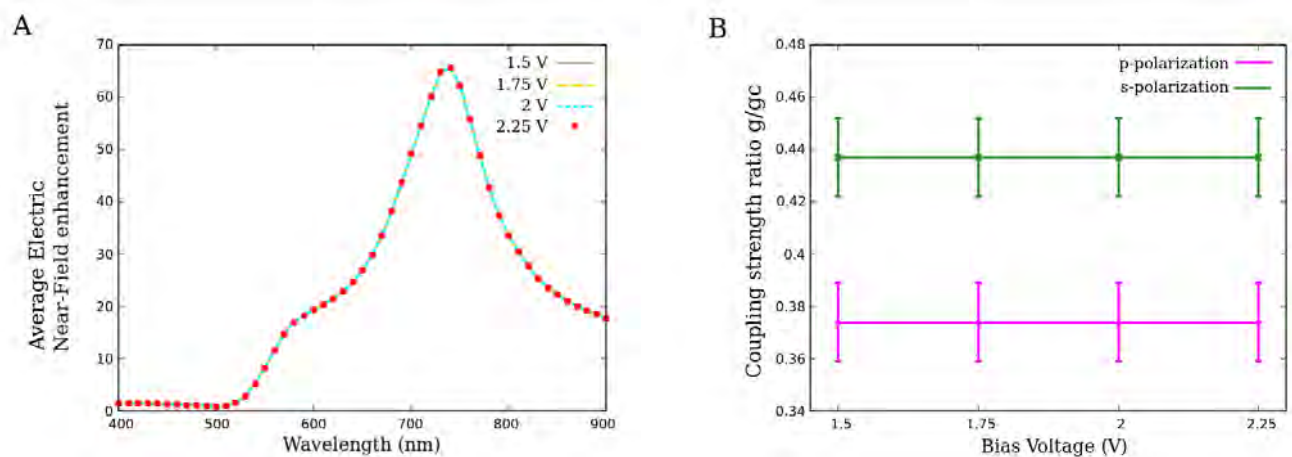


**Figure 4.17:** (A) Average electric near-field enhancement spectra calculated for different bias voltages  $V$  considered in the QCM-DDA simulations. The average is done over a volume that includes the gap, the tip apex, the effective media accounting for electron tunneling, and part of the  $MoSe_2$  monolayer. (B) Evolution of the ratio  $g/g_c$  of the coupling between plasmon modes and A-excitons as a function of the bias voltage  $V$  for both p- and s- polarized incident light. The incidence angle is  $\theta=45^\circ$  and the tip-surface distance is set to  $d=0.2$  nm (tunneling regime).

In Figure 4.17-A, no significant difference is observed among the calculated near-field spectra. As shown in Table 4.2 of the previous section, the tunneling conductivity  $\sigma_g(d, V)$  increases by nearly a factor of 24 for a bias voltage ranging from 1.5 V to 2.25 V for a given distance  $d$ . However, despite this increment, the conductivity in the gap remains very small compared to  $\epsilon_0\omega$  (see eq. (4.6)) resulting in a negligible impact of the quantum corrections on the junction's optical response. Therefore, the gap plasmon resonance does not depend on the bias voltage. As the near-field spectra of Figure 4.17-A, the far-field spectra obtained for each incident polarization present the same lineshape for  $V$  ranging from 1.5 V to 2.25 V. Thus, the same coupling strength ratio  $g/g_c$  is obtained, as shown in Fig. 4.17-B. As discussed earlier, the plasmon-exciton coupling primarily occurs at the  $MoSe_2/Au$  interface and, as a result, is independent of the conductivity of the effective media introduced in the junction gap. For p-polarization, the ratio  $g/g_c$  obtained is:  $g/g_c = 0.374 \pm 0.0147$  while for s-polarization, the value of  $g/g_c$  is  $g/g_c = 0.437 \pm 0.0153$ . In the s-polarization configuration, the ratio  $g/g_c$  is identical to the one obtained in section 4.2.3 for a hybrid junction in the non-tunneling regime ( $d = 0.5$  nm). This is consistent with the fact that the coupling takes place at the  $MoSe_2/Au$  interface, and thus, it remains unaffected by tunneling or variations in the tip-surface distance. However, in the p-polarization configuration, a slightly lower ratio is obtained. The findings presented in this section, along with those from the previous section, suggest that this ratio variation cannot be attributed to electron tunneling, which is accounted for in the tunneling regime, but rather to the tip-surface distance  $d$ . In the next subsection, the role of this distance on the plasmon-exciton coupling will be investigated, and an interpretation of the variation in the ratio  $g/g_c$  for p-polarization will be provided.

### b) Tip-surface distance

The following paragraphs focus on tuning of the optical response of the hybrid  $Au/MoSe_2/Au$  tunneling junction by modifying the tip-surface distance  $d$  from  $d = 0.2$  nm to  $d = 2$  nm. Both far-field and near-field optical spectra are calculated. For tip-surface distances in the tunneling regime ( $d < 0.5$  nm), the QCM is implemented in the DDA simulations with a bias voltage of  $V = 2$  V to take into account the electron tunneling occurring at sub-nanometer gaps.

In Figure 4.18-(A,C), the far-field spectra obtained for both incident polarizations and for different tip-surface distances  $d$  are depicted. In order to evaluate the dependence of the gap plasmon resonance on  $d$ , a maximum electric near-field enhancement spectrum is computed for each tip-surface distance using an incident p-polarized light. These spectra are plotted in Figure 4.18-B. Since the geometric volume of the tip-surface plasmonic cavity affects the electric field in the gap [15–17], the maximum electric field enhancement rather than its average over a specific volume has been computed. This maximum is calculated inside a volume which includes the gap, the tip apex and part of the  $MoSe_2$  layer. For  $d < 0.5$  nm, this volume also includes the effective media of the QCM. Finally, the coupling strength ratio  $g/g_c$  of the electromagnetic coupling between plasmon modes and A-excitons is determined for each tip-surface distance  $d$  and for both incident polarizations (the method to obtain this ratio has

been described in section 4.2.3). The obtained ratios are presented in Figure 4.18-D.

For p-polarization, the lineshape of far-field spectra exhibit significant variations as the tip-surface distance changes (see Fig. 4.18-A). These variations, observed in the 600 nm to 900 nm spectral range, are particularly pronounced at the wavelengths close to the B-exciton energy ( $\sim 700$  nm). Indeed, a dip around the B-exciton wavelength becomes more pronounced as  $d$  increases. This dip is particularly profound when  $d=2$  nm. A detailed discussion of its origin will be provided below. The dip at the A-exciton wavelength ( $\sim 800$  nm) is as well modified, but slightly when  $d$  increases.

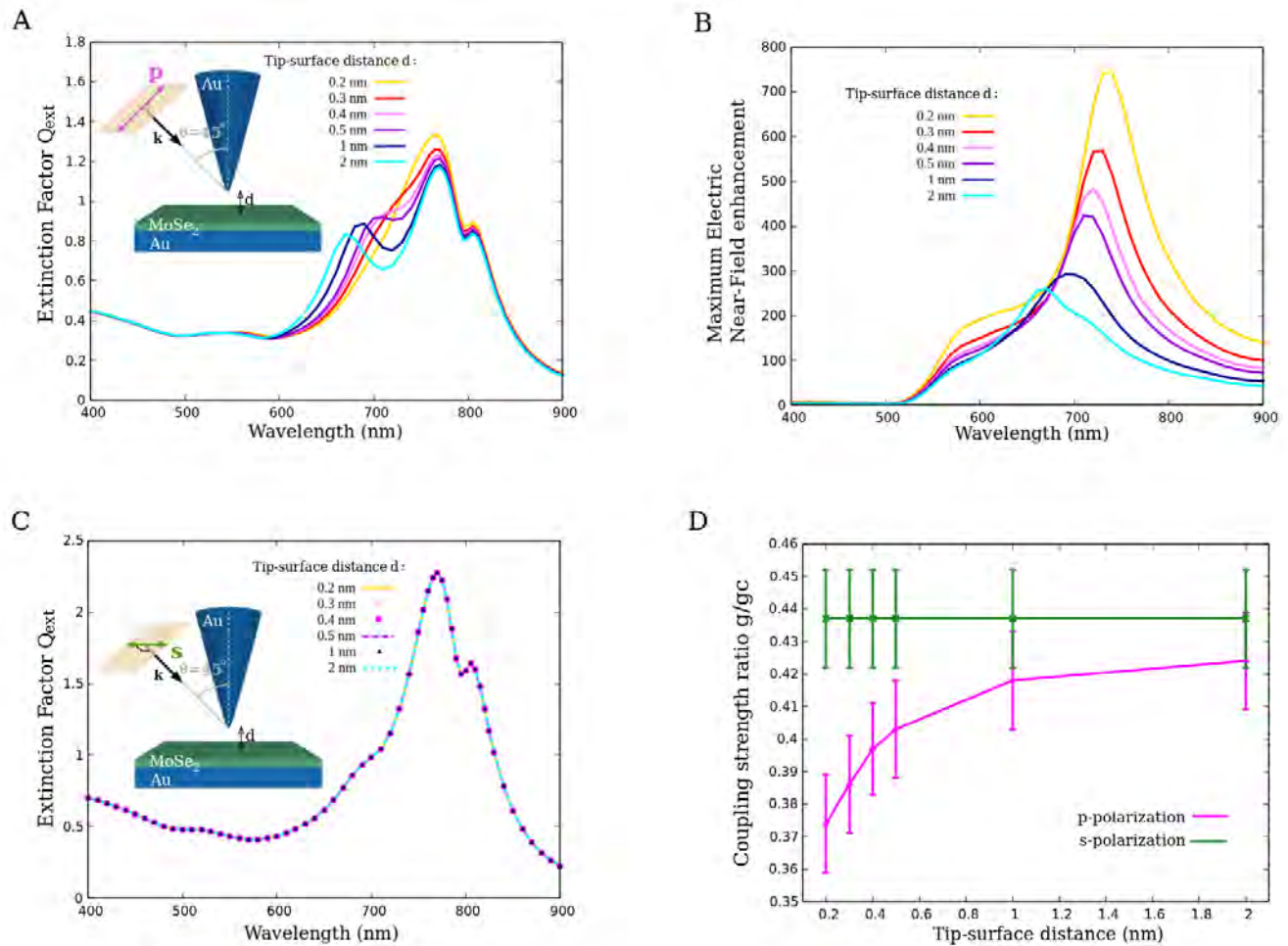


**Figure 4.18:** (A,C) Far-field optical extinction cross-section spectra (in units of  $\pi a^2$ ,  $a$  being the radius of the sphere of equivalent volume) obtained from DDA simulations for different tip-surface distances  $d$  ranging from  $d=0.2$  nm to  $d=2$  nm considering a p- (A) and s- (C) incident polarization. Insets in (A) and (C) show the simulated junction with the considered incidence angle of  $\theta=45^\circ$ . (B) Spectra of the maximum electric near-field enhancement calculated inside the gap region for different tip-surface distances  $d$ . (D) Evolution of the ratio  $g/g_c$  of the coupling between plasmon modes and A-excitons as a function of the tip-surface distance  $d$  for both p- and s- polarized incident light. QCM is applied with a bias voltage of  $V=2$  V for  $d < 0.5$  nm.

For s-polarization, the far-field spectra remain unchanged regardless of the tip-surface distance  $d$  (Fig. 4.18-C). As discussed in section 4.2.2, the far-field spectra for s-polarization exhibit Fano-type interferences, arising from the interaction between the transverse plasmon resonance of the substrate and

the monolayer's excitons, while for p-polarization, these interferences are modified by the contribution of gap plasmon modes that come into play in the plasmon-exciton coupling. Hence, the considerable variation in the far-field spectra when varying  $d$  for p-polarization can be ascribed to the excitation of gap plasmon modes.

In order to clarify this point, the resonance of the gap plasmon modes is studied as a function of the tip-surface distance  $d$  (Fig. 4.18-B). As the tip-surface distance decreases from  $d= 2$  nm to  $d= 0.2$  nm, this resonance strongly redshifts (from 670 nm to 740 nm), and its intensity increases from approximately 260 to around 750. This variation comes from the Coulomb interaction between the polarization charges that accumulate at the opposite sides of the gap, which increases as  $d$  decreases. In the tunneling regime, the redshift of the gap plasmon resonance could even be more pronounced due to the introduction of effective media within the gap region when using QCM. However, these media behave as vacuum (due to their weak conductivity) and their effect on the optical response is negligible as discussed in the previous section. This dependence of the gap plasmon resonance on the tip-surface distance explains the observed fluctuations in the far-field spectra for p-polarization. Indeed, the depth and wavelength of the dip around 700 nm appear to follow the same trend as the variations of the gap plasmon resonance as a function of  $d$ . With increasing  $d$ , the gap plasmon resonance experiences a blueshift, and consequently, its contribution in the far-field spectra becomes more significant since it is no longer hidden or overshadowed by the Fano-type interferences which exhibit a strong far-field signal around 770 nm. This leads to the variations observed in the 600 nm to 770 nm spectral range. Further investigation on this point will be explored in the following section.

Finally, Figure 4.18-D shows that, for p-polarization, the ratio  $g/g_c$  of the coupling between plasmon modes and A-excitons depends on the tip-surface distance  $d$  as it increases from  $g/g_c= 0.374 \pm 0.0147$  to  $g/g_c= 0.424 \pm 0.0152$  for  $d$  ranging from  $d= 0.2$  nm to  $d= 2$  nm. On the contrary, a constant  $g/g_c= 0.437 \pm 0.0153$  is obtained regardless of the tip-surface distance for s-polarization. To gain deeper insights, this ratio is also calculated for a junction modeled without a tip, simulating the scenario where  $d$  tends towards infinity. In this case, both polarizations yield an identical ratio  $g/g_c= 0.437 \pm 0.0153$ . Indeed, by comparing the ratios obtained for p and s-polarizations, it can be deduced that the excitation of gap plasmon modes when a p-polarization is used leads to a diminution of the plasmon-exciton interaction strength. This reduction is even more pronounced for a smaller tip-surface distance  $d$ . As  $d$  tends to infinity, the absence of gap prevents the excitation of gap plasmon modes, causing the ratio for p-polarization to converge towards the value obtained for an incident s-polarized light. Based on the near-field spectra in Fig. 4.18-B, one might expect a stronger plasmon-exciton coupling as the tip-surface distance decreases, due to a more favorable spectral match between the gap plasmon resonance and the A-exciton wavelength ( $\sim 800$  nm). However, this is not the observed behavior. To gain better insight into this result, field enhancement maps are computed at  $\lambda= 800$  nm for two different tip-surface distances:  $d= 0.2$  nm and  $d= 2$  nm.

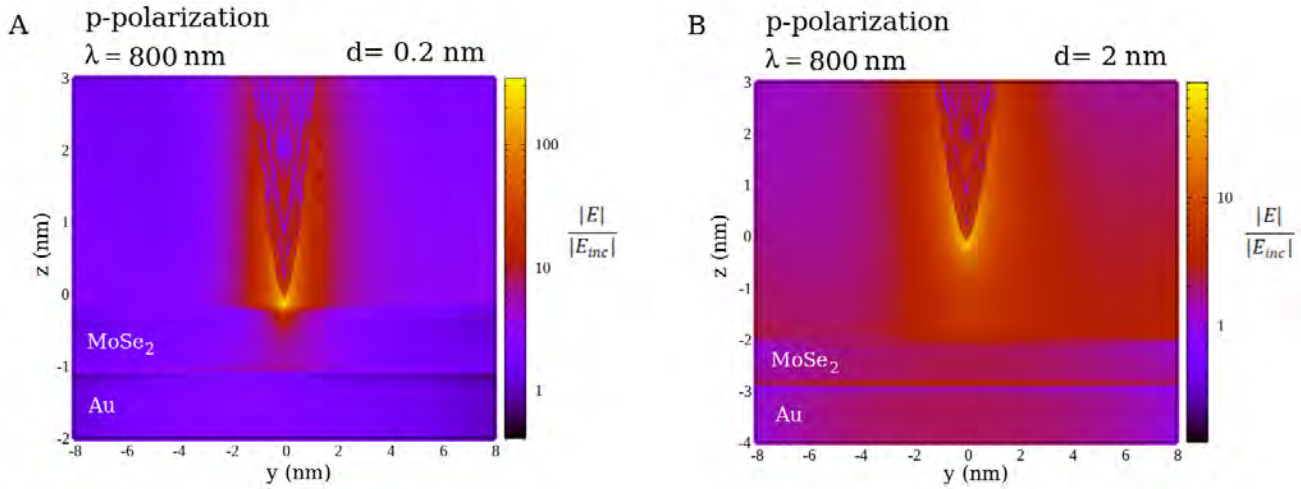


**Figure 4.19:** Electric near-field enhancement maps (in log scale) of the hybrid  $Au/MoSe_2/Au$  junction calculated in the  $yz$  plane for a tip-surface distance of (A)  $d=0.2$  nm and of (B)  $d=2$  nm. In both cases, the junction is excited by a p-polarized incident light at  $\lambda=800$  nm under  $45^\circ$  incidence with respect to the  $z$ -axis. For  $d=0.2$  nm, QCM is applied with a bias voltage of  $V=2$  V.

In Figure 4.19, it is observed that, as the tip-surface distance decreases, the field enhancement is more localized in the gap region and in the  $MoSe_2$  layer directly underneath the gap. As discussed in section 4.2.2, the induced electric field observed within the monolayer and at the  $MoSe_2/Au$  substrate interface is associated with the so-called gap plasmon-exciton mode. The latter arises from the intricate interplay between the tip-surface gap plasmon modes and the hybrid plasmon-exciton mode at the  $MoSe_2/Au$  substrate interface formed from the coupling between the substrate transverse LSPR and the monolayer's excitons. When  $d$  goes from  $d=0.2$  nm to  $d=2$  nm, the gap plasmon-exciton field becomes less localized and its overlap with the  $MoSe_2$  monolayer increases (Fig. 4.19-B). This phenomenon leads to an increase in the plasmon-exciton coupling ratio, as shown in Fig. 4.18-D. When  $d$  tends to infinity or when an s-polarized light is used, no gap plasmon modes are excited and thus, the gap plasmon-exciton field is not present. In this case, the excitons only interact with the plasmonic resonance of the substrate. This interaction is not sensitive to the tip-surface distance. The electric near-field associated with the transverse LSPR of the substrate substantially overlaps with the  $MoSe_2$  layer, as shown in Figure 4.10, leading to a stronger plasmon-exciton coupling (Fig. 4.18-D).

#### 4.4.2 Dependence of the optical response in terms of incidence angle

In the preceding sections, it was demonstrated that the optical properties of the hybrid  $Au/MoSe_2/Au$  junction considerably differ depending on whether the incident light is p- or s- polarized. The excitation of gap plasmon modes by the vertical component of the p-polarization configuration is at the origin of the observed differences. When these modes are excited, a hybrid gap plasmon-exciton mode emerges. In Figure 4.19, the spatial localization of this mode is observed within the monolayer and at the  $MoSe_2/Au$  substrate interface. In order to better understand the properties of this mode, an investigation into the dependence of the junction's optical response as a function of the incidence angle  $\theta$  is carried out.

The appearance of the hybrid gap plasmon-exciton mode occurs when the incident electric field possesses a vertical component in the z-direction (along the tip axis) which allows the excitation of the gap plasmon modes, along with a horizontal component (in the xy plane parallel to the  $MoSe_2$  surface) that triggers the excitation of the substrate transverse LSPR. In the previous sections, an incidence angle of  $\theta = 45^\circ$  was used in all calculations, resulting in a p-polarized electric field characterized by vertical and horizontal components of equivalent magnitude. Nonetheless, it would be interesting to study how this mode behaves when the magnitudes of the vertical and horizontal components of the incident p-polarized electric field are no longer equal. To address this issue, the optical response of the junction is studied by varying the angle of incidence from  $\theta = 15^\circ$  to  $\theta = 75^\circ$ . The p-polarization direction forms an angle equal to  $90^\circ - \theta$  with the tip axis. For example, at  $\theta = 15^\circ$ , the p-polarized electric field oscillates in a direction oriented  $75^\circ$  with respect to the tip axis, having a horizontal component greater than the vertical one. Conversely, at  $\theta = 75^\circ$ , its vertical component surpasses its horizontal one. It is worthy to note that, due to symmetry considerations, the previously described s-polarized optical excitation is equivalent to the p-polarization configuration with a normal incidence excitation ( $\theta = 0^\circ$ ). This angle will be taken into account to include in the present study the junction's optical response obtained under incident s-polarized light, extensively analyzed in previous sections. Thus, the far-field and near-field optical responses of the junction are investigated by considering an incident p-polarized light for  $\theta$  ranging from  $0^\circ$  to  $75^\circ$  and for two different tip-surface distances:  $d = 0.2$  nm and  $d = 2$  nm. For each angle  $\theta$ , the ratio  $g/g_c$  of the coupling between the plasmon modes excited in the junction and A-excitons is also determined.

Figure 4.20-A displays the far-field spectra obtained for different angles  $\theta$  and for a tip-surface distance of  $d = 0.2$  nm (tunneling regime). It is observed that as  $\theta$  increases, the Fano-type interferences resulting from the plasmon-exciton coupling gradually disappear. Indeed, the dips at the A- and B-exciton wavelengths are less and less pronounced. On the contrary, a resonance attributed to the gap plasmon modes at  $\lambda = 740$  nm emerges. This gap plasmon resonance as a function of  $\theta$  is examined by computing and averaging the electric near-field enhancement over a volume that includes the tip apex, the effective media in the gap since QCM is applied, and a part of the monolayer. The resulting spectra are plotted in Figure 4.20-B. At  $\theta = 0^\circ$ , there are no gap plasmon modes and the near-field spectrum obtained reveals the presence of Fano-type interferences (light blue line). On the other hand, for  $\theta > 0^\circ$ , gap plasmon modes are excited and their resonance intensity augments with increasing  $\theta$  due to the increment of the vertical component of the incident electric field along the z-axis. The wavelength of the gap plasmon resonance is not affected by  $\theta$ . Finally, the coupling ratio  $g/g_c$  decreases from  $g/g_c = 0.437 \pm 0.0153$  to  $g/g_c = 0.179 \pm 0.00564$  when  $\theta$  goes from  $\theta = 0^\circ$  (s-polarization) to  $\theta = 75^\circ$ .

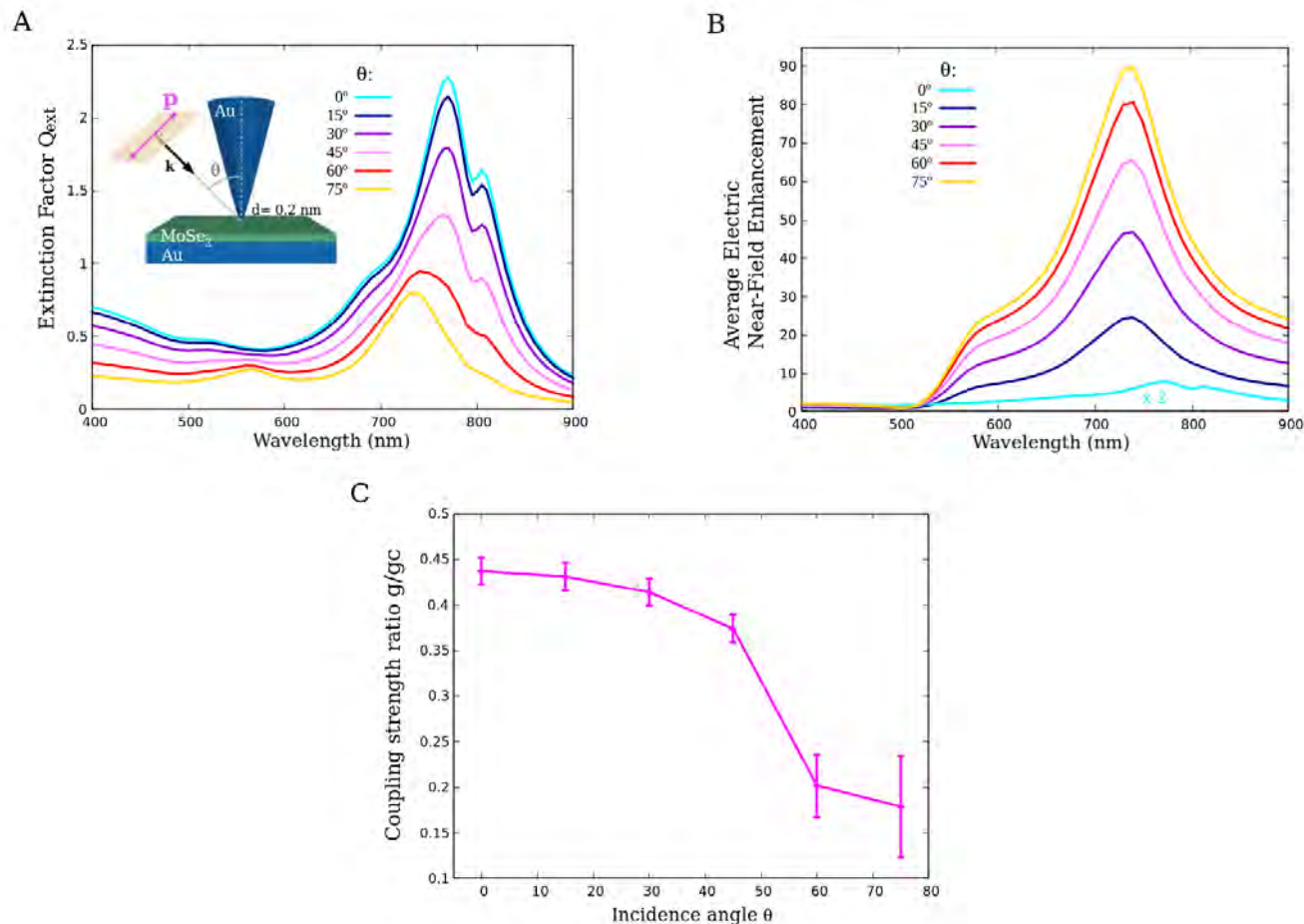


**Figure 4.20:** (A) Far-field optical extinction cross-section spectra (in units of  $\pi a^2$ ,  $a$  being the radius of the sphere of equivalent volume) obtained from DDA simulations for an incidence angle  $\theta$  ranging from  $\theta = 0^\circ$  to  $\theta = 75^\circ$ . Inset in (A) shows the simulated junction excited by a p-polarized incident light along with the considered tip-surface distance of  $d = 0.2$  nm. QCM is applied with a bias voltage of  $V = 2$  V. (B) Average electric near-field enhancement spectra for different incidence angles  $\theta$  calculated over a volume that includes the gap, the tip apex and a part of the monolayer. (C) Evolution of the ratio  $g/g_c$  of the coupling between plasmon modes and A-excitons as a function of the incidence angle  $\theta$  for a p-polarized incident light.

For  $\theta = 0^\circ$ , the plasmon modes involved in the plasmon-exciton coupling are only the substrate transverse LSPR. This configuration results in a high ratio  $g/g_c$  due to the large spatial overlap of the substrate plasmonic electric field with the excitons confined within the monolayer. For  $\theta > 0^\circ$ , gap plasmon modes come into play, leading to the emergence of the hybrid gap plasmon-exciton mode. As discussed previously, the electric field associated with this mode is strongly localized in the part of the  $MoSe_2$  layer underneath the gap, reducing its overlap with the monolayer. This explains the decrease of  $g/g_c$  when  $\theta$  is greater than  $0^\circ$ . Then, with increasing  $\theta$ , the vertical component of the incident electric field grows, and subsequently its horizontal component decreases. This results in the progressive “undressing” of the hybrid gap plasmon-exciton mode from its excitons to become a pure gap plasmon mode. This phenomenon leads to the gradual disappearing of Fano-type interferences and the emergence of the gap plasmon resonance at  $\lambda = 740$  nm observed in the far-field spectra (Fig. 4.20-A). Besides this “undressing” process, as  $\theta$  increases, the intensity of the electric field excited by

the horizontal component of the p-polarized optical wave decreases, resulting in a diminution of the plasmon-exciton coupling strength (Fig. 4.20-C).

An identical analysis is carried out for a hybrid  $Au/MoSe_2/Au$  junction with a tip-surface distance of  $d=2$  nm (non-tunneling regime). Indeed, far-field spectra were computed, along with the corresponding coupling strength ratios  $g/g_c$ . The obtained results are presented in Figure 4.21. This study allows for the investigation of how the behavior of the gap plasmon-exciton mode is influenced by the tip-surface distance as  $\theta$  increases.

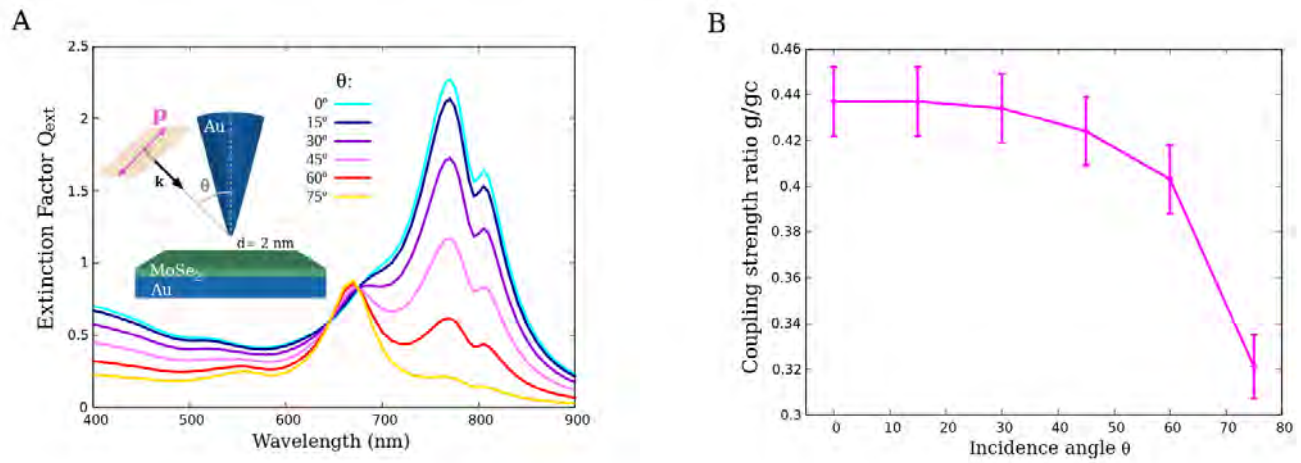


**Figure 4.21:** (A) Far-field optical extinction cross-section spectra (in units of  $\pi a^2$ ,  $a$  being the radius of the sphere of equivalent volume) obtained from DDA simulations for an incidence angle  $\theta$  ranging from  $\theta=0^\circ$  to  $\theta=75^\circ$ . Inset in (A) shows the simulated junction excited by a p-polarized incident light along with the considered tip-surface distance of  $d=2$  nm. (B) Evolution of the ratio  $g/g_c$  of the coupling between plasmon modes and A-excitons as a function of the incidence angle  $\theta$  for a p-polarized incident light.

In the far-field spectra obtained (Fig. 4.21-A), a similar observation to that at  $d=0.2$  nm can be made: with increasing the incidence angle, the dips of the Fano-type interference are less prominent, and simultaneously, the resonance of the gap plasmon modes at  $\lambda=670$  nm becomes more visible. Besides, the coupling strength ratio  $g/g_c$  follows a similar evolution as a function of  $\theta$  as the one obtained with  $d=0.2$  nm: it decreases as  $\theta$  increases. Again, with the increment of the incidence angle, the hybrid gap plasmon-exciton mode undergoes the same “undressing” process, transforming into a pure gap plasmon mode that no longer interacts with excitons. Hence, the gap plasmon-exciton mode behavior is the same regardless of the tip-surface distance. The coupling ratio  $g/g_c$  decreases from  $g/g_c=0.437 \pm 0.0153$  to  $g/g_c=0.321 \pm 0.0147$  as  $\theta$  increases. It is noteworthy that, for any given incidence angle, the ratio  $g/g_c$  achieved with  $d=2$  nm exceeds the ratio obtained for  $d=0.2$  nm, due to the larger spatial overlap of the gap plasmon-exciton field with the TMD monolayer, as discussed above.

It is interesting to note that, at  $d=2$  nm, the gap plasmon resonance is situated on the low wavelength edge of the Fano-interferences spectral range. This positioning allows for a better observation, in the far-field spectra, of the gradual variations of the Fano-type interferences and the gap plasmon resonance. In fact, it is clearly shown in Fig. 4.21-A, specially for high incidence angles, that the

overall or local maximum located around the B-exciton wavelength ( $\sim 700$  nm) corresponds to the gap plasmon resonance. Therefore, this confirms that the local maximum observed in Figure 4.18-A around the B-exciton wavelength of the far-field spectrum obtained for  $d=2$  nm and  $\theta=45^\circ$ , can be attributed to the emergence of the gap plasmon resonance. This interpretation rules out the possibility of a Rabi splitting arising from a strong coupling between plasmon modes and B-excitons, an assumption that has been considered due to the substantial depth of the dip around the B-exciton wavelength.

Using high incidence angles allows the clear observation of the pure gap plasmon resonance in far-field spectra. Thus, in order to have a better understanding of the behavior of this plasmon mode, the far-field optical response of the hybrid junction is computed by varying the tip-surface distance from  $d=0.2$  nm to  $d=2$  nm using an incidence angle of  $\theta=75^\circ$ . The obtained spectra are presented in Figure 4.22.

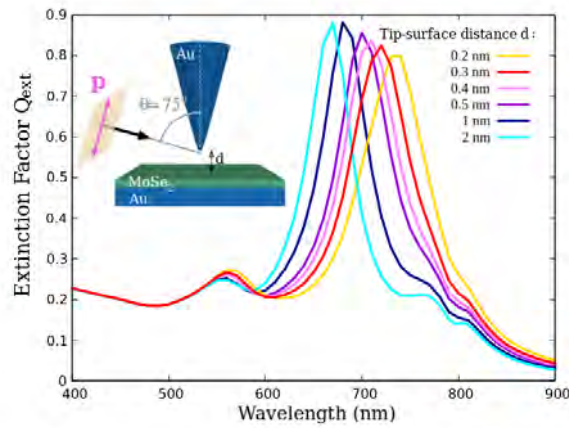


**Figure 4.22:** Far-field optical extinction cross-section spectra (in units of  $\pi a^2$ ,  $a$  being the radius of the sphere of equivalent volume) obtained from DDA simulations for a tip-surface distance  $d$  ranging from  $d=0.2$  nm to  $d=2$  nm. Inset shows the simulated junction excited by a p-polarized incident light along with the considered incidence angle of  $\theta=75^\circ$ . QCM is applied with a bias voltage of  $V=2$  V for  $d < 0.5$  nm.

The gap plasmon resonance for each tip-surface distance is depicted in Figure 4.22, clearly discernible due to the high incidence angle. Its wavelength shifts from 670 nm to 740 nm as  $d$  decreases, consistent with the shift observed in the near-field optical response shown in Figure 4.18-B for  $\theta=45^\circ$ . Based on these results, it can be concluded that the variations in the spectral lineshape observed around 700 nm in Figure 4.18-A arise from the emergence of the gap plasmon resonance in the far-field spectra, which moves away from the Fano-type interferences spectral range as the distance  $d$  increases.

### 4.4.3 Dependence of the optical response on the tip length and substrate dimensions

In DDA calculations, the simulated target is constrained to be modeled by a finite-size object. At the beginning of this chapter, the specific geometry and size of the finite-size tip and sample composing the hybrid junction have been presented. In this section, an analysis is conducted to assess how the

dimensions of the tip and substrate impact the optical response of the hybrid junction. To achieve this, the far-field optical response of hybrid  $Au/MoSe_2/Au$  junctions featuring tips of varying lengths and substrates with diverse dimensions is investigated.

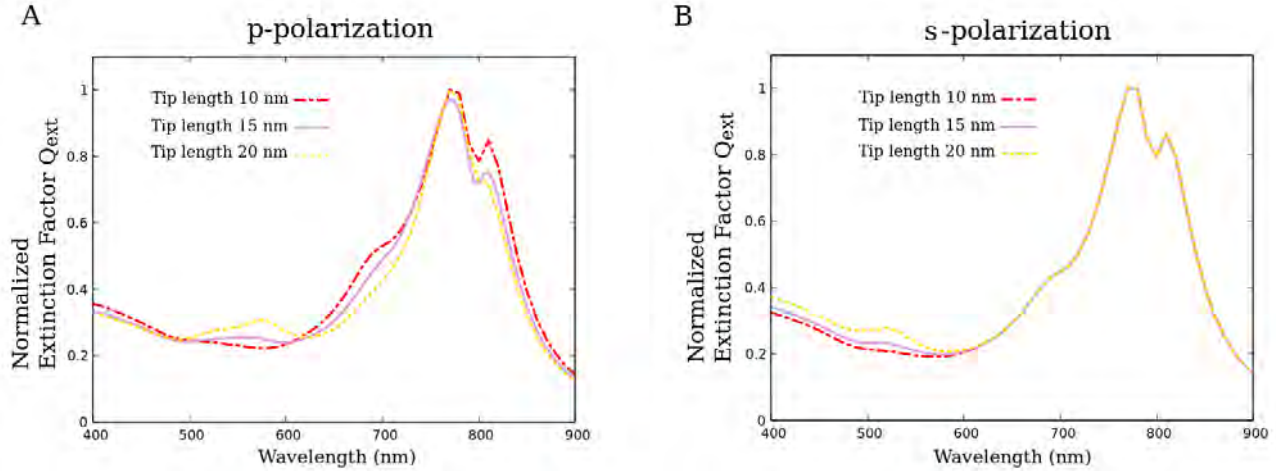


**Figure 4.23:** Normalized far-field optical extinction cross-section spectra obtained for three different tip lengths: 10, 15 and 20 nm. The hybrid junctions are excited by a (A) p- and (B) s-polarized incident light under  $45^\circ$  incidence with respect to the z-axis. The three tips considered have the same radius of curvature ( $R \sim 0.133$  nm) and aperture angle ( $\alpha \sim 14.5^\circ$ ). The gold substrate dimensions are  $20$  nm  $\times$   $20$  nm  $\times$   $2.2$  nm and the tip-surface distance is  $d = 0.2$  nm. QCM is used with a bias voltage  $V = 2V$ .

Figure 4.23 displays the far-field spectra acquired for three different tip lengths: 10, 15 and 20 nm. The dimensions of the gold substrate are the same as presented in section 4.1 ( $20$  nm  $\times$   $20$  nm  $\times$   $2.2$  nm) and the tip-surface distance and incidence angle considered are  $d = 0.2$  nm and  $\theta = 45^\circ$ , respectively. It is observed that the plasmon modes sustained solely by the tip, such as the tip apex plasmon mode around 550 nm excited by the incident p-polarized field and the tip transverse LSPR excited at approximately 530 nm by the s-polarized optical wave, depend on the tip length. Indeed, the wavelength and intensity of their resonance exhibit variations as the tip's length changes. Moreover, the tip length has an impact on the lineshape of the Fano-type interferences only when a p-polarization is used. Indeed, for this polarization, the gap plasmon modes are involved in the plasmon-exciton coupling, which gives rise to the observed interferences. A variation of the tip length modifies the properties of the gap plasmon modes, and thus these interferences. It is hypothesized that a longer tip may result in a more intense gap plasmon resonance due to an increased confinement within the junction wherein the overall size of the junction increases while the gap size remains constant. On the other hand, for s-polarization, the interferences arise from the coupling between the transverse LSPR of the substrate and excitons, and thus, they are not sensitive to the tip size (Fig. 4.23-B).

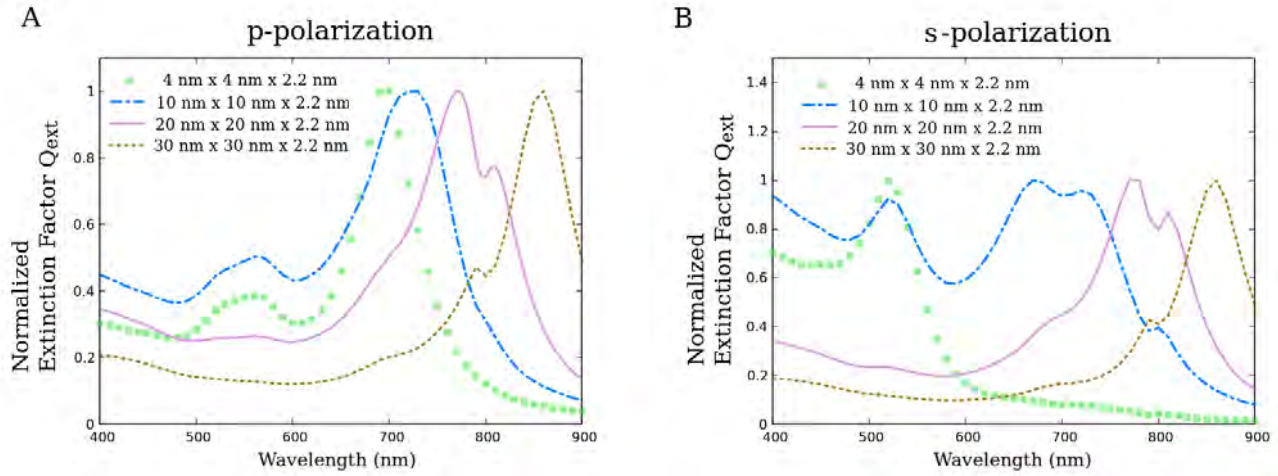


**Figure 4.24:** Normalized far-field optical extinction cross-section spectra obtained for different substrate dimensions. The hybrid junctions are excited by a (A) p- and (B) s-polarized incident light. The tip length is 15 nm and the tip-surface distance is  $d = 0.2$  nm. QCM is used with a bias voltage  $V = 2V$ .

Plasmonic resonances are sensitive to factors like the size, shape, and surrounding environment of the nanostructure [33]. By changing the substrate dimensions, the frequency of the substrate transverse LSPR shifts. As a result, its spectral overlap with excitonic resonances might change leading to Fano-type interferences with different features, as shown in Figure 4.24. For both incident polarizations, variations in the lineshape of the interferences are observed as the substrate size changes. When the spectral overlap is remarkably weak, these interferences vanish as shown in the spectra calculated with the smallest substrate ( $4 \text{ nm} \times 4 \text{ nm} \times 2.2 \text{ nm}$ ) depicted in Figure 4.24.

The optical response of the hybrid junction depends thus on the tip length and on the substrate dimensions, since they influence the optical properties of the electromagnetic modes supported by the junction, thereby affecting the tuning/detuning resonance conditions between the plasmonic modes and the  $MoSe_2$  exciton resonances.

The chosen dimensions for modeling the hybrid junction studied throughout this chapter have been carefully configured in such a way that the resonances of the plasmonic modes present in the junction do match the excitonic resonances. Indeed, a plasmonic-excitonic resonances match has been observed and pointed out in the experimental results, and therefore, it is crucial to consider it in the simulations for a more substantial correlation between the results obtained in this study and the experimental findings presented in Chapter 3. For further work, it would be interesting to explore the effect of the tip geometry (radius of curvature and angle of aperture) on the optical response of the hybrid junction. The presented model involves finite-size components, and as a result, artificial tip and substrate plasmonic resonances arising from their finite size are obtained. These plasmonic modes might differ from the modes involved in an actual STM experiment. Nevertheless, this model efficiently captures the underlying physics governing the emergence of gap plasmons, and their interaction with the  $MoSe_2$

monolayer without loss of generality.

In an experimental STM junction such as the one presented in section 3.3 of Chapter 3, the surface roughness of the polycrystalline gold substrate reduces the coherence length of plasmon-polaritons propagating along the surface due to disorder effects. Thus, rather than describing the plasmonic resonances as plasmon-polaritons reflected back and forth on the tip and the substrate boundaries, they should be considered as spectrally distributed local surface plasmon resonances which tend to hybridize to form local gap plasmon mode and local hybrid gap plasmon-exciton mode when their resonances are close to the excitonic ones.

A step toward a more realistic simulation of the experimental STM junction would be to include surface roughness to account for local surface plasmon resonances. This point is addressed in the following section.

## 4.5 Role of the substrate roughness

In the STM-LE experiments carried out in Chapter 3, the  $MoSe_2$  monolayer is deposited on a polycrystalline gold substrate, characterized by its granular surface. To achieve a simulated STM junction that closely mimics the experimental conditions, the substrate roughness is introduced in our simulations. As highlighted in Chapter 3, the roughness of the substrate plays a crucial role in the light emission induced by STM. In purely metallic tunneling junctions, diffraction of tip-induced plasmon modes by the surface roughness increases the light emission rate [34, 35]. This occurs by creating new plasmonic wavevector components, and thereby allowing the crossing of the plasmonic and photonic dispersion curves. Furthermore, when a semiconductor is present in the tunneling junction, surface roughness features act as traps for excitons, and therefore as light emission hot spots [23]. Hence, it becomes imperative to consider these disorder effects in the simulations to attain more accurate insights into the optical properties of the experimental STM junction. The first part of this section is dedicated to the introduction of the substrate roughness in our DDA simulations. Two hybrid junctions are simulated, each having a different rough substrate. They differ by the level of confinement given by the geometry of the cavity formed by the substrate and the tip. A higher level of confinement indicates a more restricted space within the cavity. The impact of the substrate roughness on the optical response of the hybrid  $Au/MoSe_2/Au$  tunneling junction is then analyzed.

### 4.5.1 Introduction of a rough substrate in the simulated junction

For the simulation of a rough substrate, a large and wide flat gold substrate with a thickness of 2.2 nm is first considered, similar to the one presented in section 4.1. Then, 16 semi-spheres are modeled and placed onto the flat substrate at random positions. The radii of these semi-spheres are also randomly set within a range of values from 0 to 5 nm. The tip considered in these simulations is the same as the one described in section 4.1. Once the gold rough substrate is modeled, an anisotropic  $MoSe_2$  monolayer with a thickness of 0.8 nm [7] is conformally placed on the substrate. When the tip scans

over a granular surface during STM-LE measurements, it experiences different levels of confinement. Indeed, the geometry of the junction, and consequently, the level of confinement within the tip-surface cavity, has a direct impact on the electromagnetic interaction between the tip and the sample surface, resulting in point-dependent light emission, as discussed in Chapter 3. For this reason, two distinct junction configurations are simulated, each presenting a different cavity geometry formed between the tip and the sample. These configurations exhibit varying levels of confinement, meaning the volume between the tip and the sample surface is more or less restricted. In the first configuration, the tip apex is positioned above one of the semi-spheres, close to its highest point, while in the second configuration, the tip apex is located between three semi-spheres. As a result, the level of confinement of the cavity is considered to be moderate in the first configuration and strong in the second one. Finally, the boundaries of the simulated samples are adjusted to achieve dimensions of 20 nm in both length and width, as the flat substrate described in section 4.1. Additionally, it is worthy to mention that the tip axis is always located at the center of the sample. Schematic representations of both configurations are depicted in Figure 4.25 with panel A representing the first configuration (labeled n°1) while the second configuration (labeled n°2) is shown in panel B.

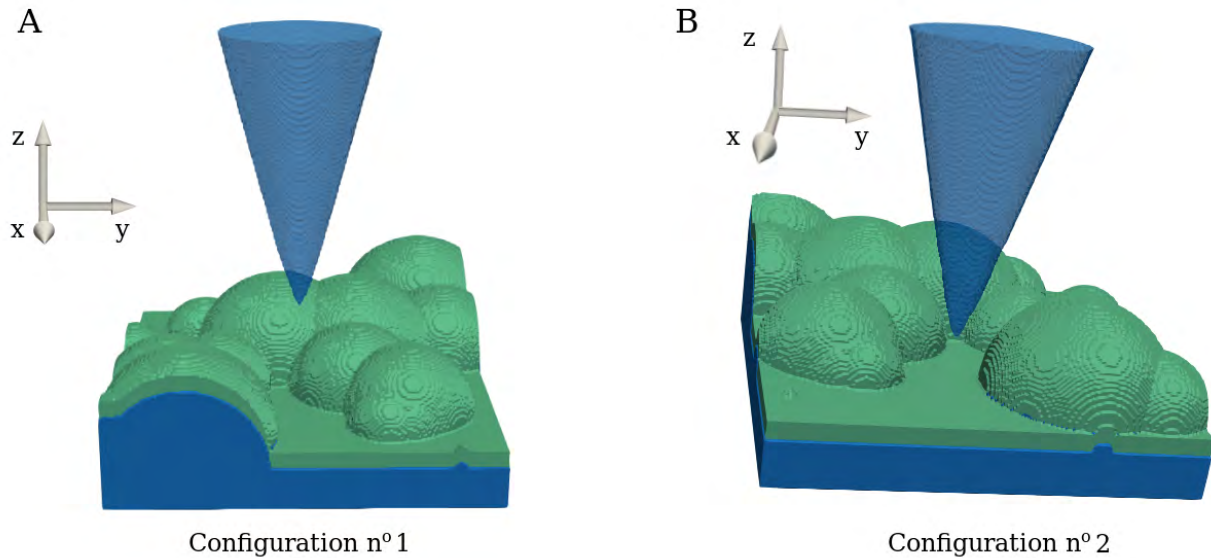


**Figure 4.25:** Schematic representation of the simulated  $Au/MoSe_2/Au$  junction with two different rough substrates. In the configuration n°1 (A), the tip apex is located in a less confined plasmonic cavity compared to the configuration n°2 (B).

For the configuration n°1, the tip is positioned in such a way that the minimum distance between the tip and the  $MoSe_2$  surface corresponds to the distance between the tip apex and the top surface of one semi-sphere. This distance is equal to  $d \sim 0.224$  nm. On the other hand, for the configuration n°2, the minimum tip-surface distance  $d$  is set to  $d = 0.2$  nm, corresponding to the distance between the lateral side of the tip and the surface of one semi-sphere. Both junctions are thus in the tunneling regime. However, as demonstrated in section 4.3.2, QCM corrections have a negligible impact on the junction's optical response. Therefore, to simplify, QCM is not integrated into the simulations. In

order to evaluate the role of the sample roughness in the optical response, a hybrid junction with a flat substrate is as well simulated with a tip-surface distance of  $d = 0.2$  nm. To properly compare the optical response obtained in each case, the thickness of the flat substrate is chosen to have a volume comparable to that of the rough substrates.

Contrary to the flat substrate, both rough substrates present no symmetry with respect to the  $z$ -axis. The direction of the incident plane wave is chosen to impinge on the monolayer at an angle of  $\theta = 45^\circ$  with respect to the tip axis, with the incidence plane aligned parallel to the  $xz$  plane (see Fig. 4.25). This incident electric field is linearly p- or s-polarized.

## 4.5.2 Role of the substrate roughness in the optical response

### a) Incident p-polarized light

The far-field and near-field optical responses of a hybrid  $Au/MoSe_2/Au$  junction with a flat substrate and with a rough substrate presenting either the first or the second configuration are analyzed. In this first part, the incident light is considered as p-polarized. The far-field and near-field optical responses obtained from DDA simulations are plotted in Figure 4.26. By using an incident p-polarized electric field, gap plasmon modes are expected to be excited. Thus, to assess these modes, near-field spectra are computed by calculating the electric near-field enhancement in a volume including the gap region. Since the cavity geometry is different in each case, the maximum electric near-field enhancement is considered. The latter is calculated within a large cubic volume (each side measuring 5 nm) centred at the tip apex. This volume includes the tip apex, the gap, and a part of the  $MoSe_2$  monolayer.

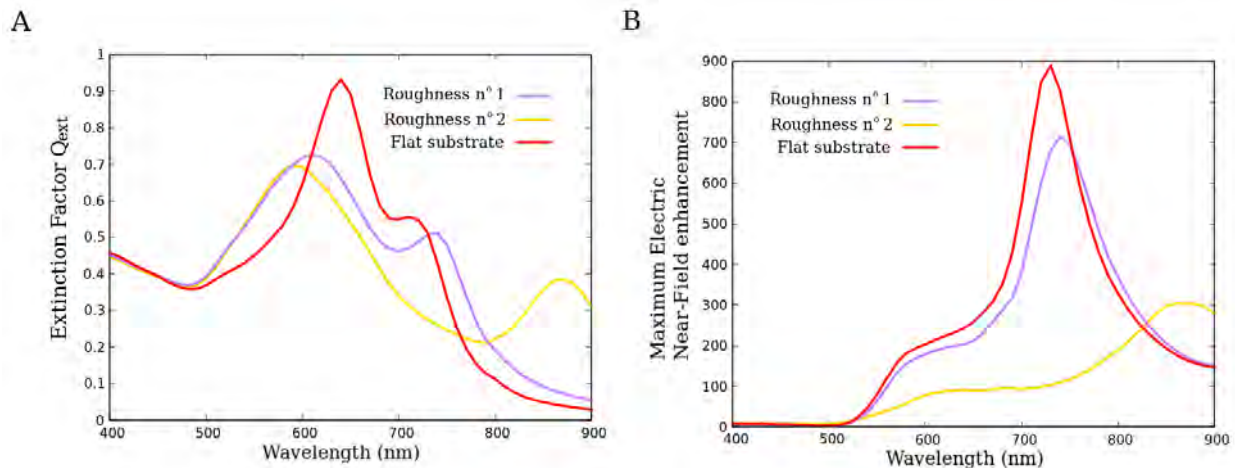


**Figure 4.26:** (A) Far-field optical extinction cross-section spectra (in units of  $\pi a^2$ ,  $a$  being the radius of the sphere of equivalent volume) and (B) maximum electric near-field enhancement spectra of the hybrid  $Au/MoSe_2/Au$  junction for p-incident polarization obtained using a flat substrate (red lines) and two different rough substrates. The violet lines are the optical responses obtained with the rough substrate n°1 (less confined plasmonic cavity) while the optical responses obtained with the rough substrate n°2 (more confined cavity) are shown in yellow lines. The tip-surface distance  $d$  is set to  $d = 0.2$  nm except for the rough substrate n°1, where is  $d \sim 0.224$  nm. The incidence angle is set to  $\theta = 45^\circ$ . The maximum near-field enhancement (B) is calculated inside a volume that includes the gap, the tip apex and a part of the monolayer.

The far-field spectra obtained for each substrate exhibit notable differences. Although all three spectra present two peaks, their wavelengths, intensities, and widths differ, as shown in Figure 4.26-A. The spectrum obtained for the flat substrate exhibits two peaks at 640 nm and 710 nm with a dip at 700 nm. This specific lineshape could in fact correspond to interferences arising from electromagnetic coupling between plasmon modes and B-excitons. A similar lineshape is observed for the rough substrate n°1 with peaks at 610 nm and 740 nm, and a dip aligned with the B-exciton wavelength. On the other hand, for the rough substrate n°2, the two peaks at 590 nm and 870 nm are widely separated. Each of these peaks is attributed to the resonance of an electromagnetic mode.

Near-field spectra are calculated to provide insights into the electromagnetic modes present within and around the gap region. Each near-field spectrum depicted in Figure 4.26-B exhibits a peak, which is attributed to the gap plasmon resonance, and a shoulder around 600 nm, assigned to the apex plasmon mode of the tip. Indeed, the near-field spectra obtained with the rough substrates have a similar lineshape to that obtained with a flat substrate, facilitating the identification of the electromagnetic modes related to each peak. The most evident difference observed is the gap plasmon resonance of the rough substrate n°2 which is located at 870 nm, far away from the gap plasmon resonances of the other two substrates. This significant redshift is attributed to the highly confined cavity in the case of the rough substrate n°2. Indeed, this cavity presents a substantially different geometry, and consequently, a distinct tip-surface gap shape compared to the other two junctions, resulting in the observed spectral disparity. An electric field enhancement map is computed for each substrate at its gap plasmon resonance (see Fig. 4.27) to better understand the observed differences.

Based on the near-field optical responses, some features of the far-field spectra can be identified. For instance, the peak at 870 nm observed for the rough substrate n°2 can be attributed to the gap plasmon resonance, and hence, the other peak at 590 nm can be assigned to the transverse LSPR of the substrate. Moreover, as discussed in previous sections, the local maximum around 700 nm observed for the flat and the rough substrate n°1 is likely ascribed to the emergence of the gap plasmon resonance, rather than to interferences resulting from a plasmon-exciton coupling. It is worth mentioning that the near-field spectra obtained for the flat and the rough substrate n°1 are very similar. However, their far-field optical responses exhibit more pronounced differences. This is attributed to the presence of local surface plasmon resonances that are excited in the case of rough substrates. These resonances give rise to far-field spectra exhibiting broader peaks. Indeed, the short-wavelength peak around 620 nm, which is attributed to the transverse LSPR of the substrate, becomes broader when the substrate is rough due to additional plasmonic transverse resonances brought about by the electromagnetic interaction between the semi-spheres of the rough surface. Figure 4.28 displays electric near-field enhancement maps computed in the xy plane to highlight these local surface plasmon modes.

Introducing substrate roughness results in broad peaks in the far-field optical response, each associated with specific electromagnetic modes. The properties of these modes change depending on the substrate roughness, leading to peaks with varying wavelengths, intensities, and widths. This fluctuation of peaks as a function of the substrate roughness has been observed in experimental STM-LE spectra obtained

from purely plasmonic junctions (see Fig. 3.2-A). Indeed, light emission from these junctions is governed by the electromagnetic modes within the gap. During scanning, the properties of these modes hosted by the tip-surface cavity change due to the sample roughness, leading to spectra exhibiting peaks with different wavelengths, intensities, and widths. Therefore, these simulations effectively replicate the influence of substrate roughness on the electromagnetic properties of the STM junction.

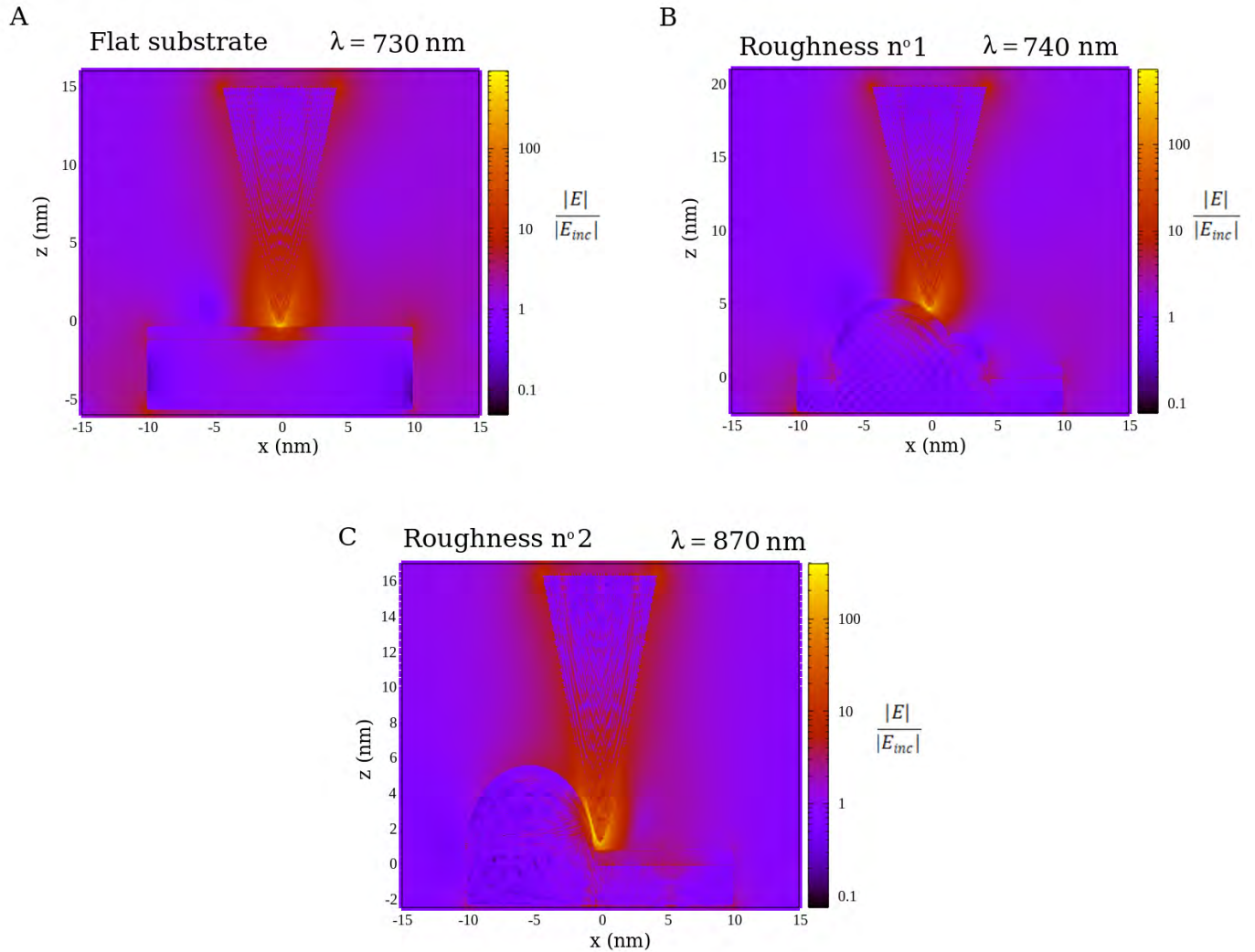


**Figure 4.27:** Electric near-field enhancement maps (in log scale) calculated in the  $xz$  plane for a hybrid  $Au/MoSe_2/Au$  junction with a flat substrate (A), with a rough substrate presenting the first configuration (B) and the second configuration (C). An incident p-polarized light is used with an incidence angle of  $\theta = 45^\circ$ . These maps are computed at the gap plasmon resonance of each junction: for the flat surface it corresponds to  $\lambda = 730$  nm (A); for the rough substrate n°1, the field enhancement map is computed at  $\lambda = 740$  nm (B) while for the rough substrate n°2, it is calculated at  $\lambda = 870$  nm (C). The tip-surface distance  $d$  is set to  $d = 0.2$  nm except for the rough substrate n°1, where is  $d \sim 0.224$  nm.

The electric field associated with gap plasmon modes is observed in the three field enhancement maps depicted in Figure 4.27. In the case of the flat surface and the rough substrate n°1, this induced field is strongly localized between the tip apex and the TMD monolayer with a maximum directly

located under the tip apex. However, for the rough substrate n°2, this field is less localized due to a larger area of interaction between the tip and the TMD monolayer.

Indeed, due to the sample surface roughness, the tip-surface cavity where gap plasmon modes are localized, undergoes a complete change in geometry. Specifically, for the rough substrate n°2, not only does the tip apex interact with the TMD surface, but also a portion of its side does. Indeed, variations in both the morphology of the sample surface and the tip [36], even at the atomic level [17], significantly impact the plasmonic field in the gap junction. For the flat and rough substrate n°1, only the tip apex is involved in the plasmonic field. In contrast, for the rough substrate n°2, a much larger surface area of the tip participates in the excitation of plasmon modes, resulting in an electric field associated with gap plasmons no longer confined solely beneath the tip apex but extends across a larger area including the tip sides and the surrounding semi-spheres. Hence, the observed strong redshift and low intensity of the gap plasmon resonance obtained for the rough substrate n°2 compared to the other two junctions in Figure 4.26-B can be ascribed to variations in the geometry of the tip-surface cavity, resulting in distinct tip and sample surface areas being involved in the excitation of gap plasmon modes. Similarly, the slight redshift and intensity reduction of the gap plasmon resonance of the rough substrate n°1 compared to the one obtained with the flat surface can be attributed to a slightly greater tip-surface interaction area in the case of the rough substrate. It should be pointed out that the fluctuations in electric field enhancement observed in the maps within significant portions of the substrate are a consequence of the convergence of the DDA method.

Field enhancement maps are also generated in the xy plane at the wavelength  $\lambda = 620$  nm, which is close to the substrate transverse LSPR wavelength, in order to compare the plasmonic modes supported by the sample (see Fig. 4.28). For the flat surface case, the map is computed within the  $MoSe_2$  monolayer at 0.4 nm from its upper surface. The transverse LSPR of the substrate with an electric field highly localized at the corner of the sample is observed. Towards the center, one can detect the slight presence of the electric field associated with the gap plasmon mode. On the other hand, for both rough substrates, the maps are calculated at a height of 0.2 nm above the lowest point of the sample upper surface. In addition to the transverse LSPR of the substrate, a field enhancement is observed around the semi-spherical components of the granular surface. Indeed, this field enhancement arises from the electromagnetic interaction occurring between the grains on the substrate's surface, resulting in the emergence of local surface plasmon modes. The intensity of these local plasmonic fields is enhanced when the semi-spheres are in close proximity to each other. The gap plasmon electric field is as well observed for the rough substrate n°2.

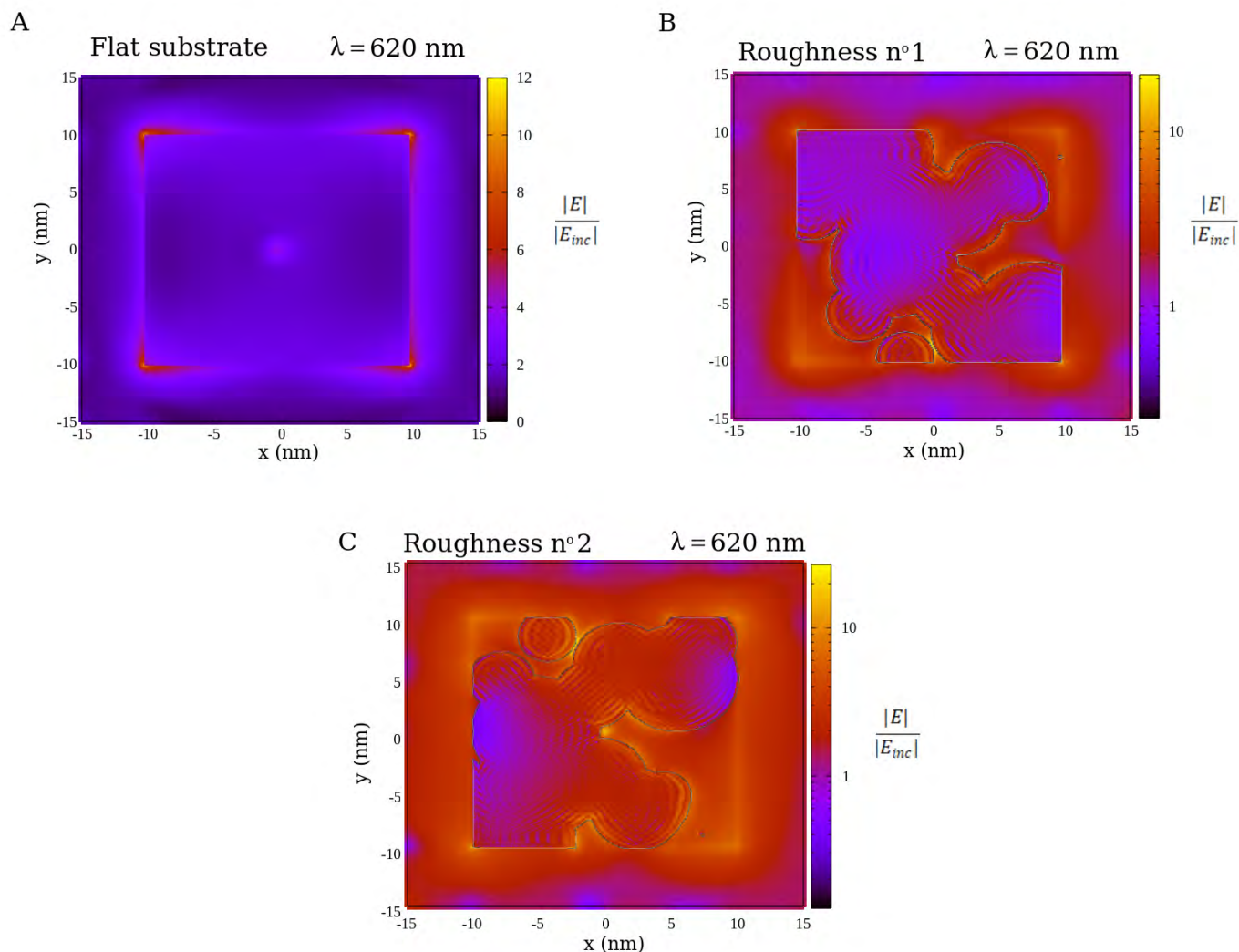


**Figure 4.28:** Electric near-field enhancement maps calculated in the  $xy$  plane for a hybrid  $Au/MoSe_2/Au$  junction with a flat substrate (A), with a rough substrate n°1 (B) and with a rough substrate n°2 (C). The spatial distribution of field enhancement in maps (B) and (C) is presented using a logarithmic scale. An incident p-polarized light is used with an incidence angle of  $\theta = 45^\circ$  and a wavelength of  $\lambda = 620$  nm. The tip-surface distance  $d$  is set to  $d = 0.2$  nm except for the rough substrate n°1, where is  $d \sim 0.224$  nm.

It will be interesting for future work to displace the tip while scanning the sample surface and calculate the near-field optical response to generate near-field intensity maps. This approach would provide a deeper understanding of the local effect of the substrate roughness on the optical properties of the STM junction.

### b) Incident s-polarized light

An identical analysis of both far-field and near-field optical responses, previously conducted for p-polarization, is now performed for an incident s-polarized light. In Figure 4.29-A, the far-field spectra obtained for each substrate are presented. The peak corresponding to the transverse LSPR of the substrate is discernible in all three cases. As for p-polarization, the width of this peak increases when the

roughness of the substrate is introduced in the calculations. This broadening is due to additional local surface plasmon resonances emerging from the interactions between the grains of the sample surface.

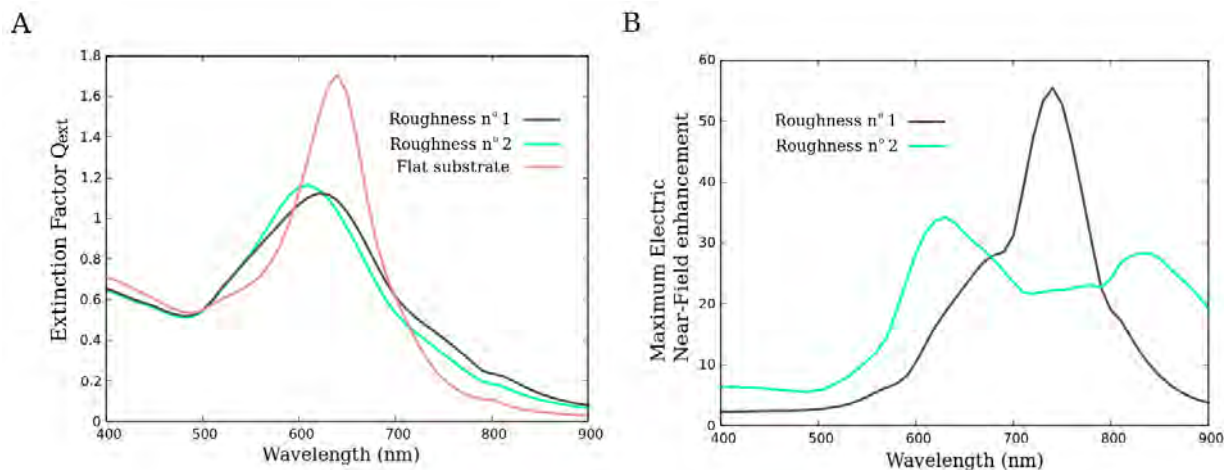


**Figure 4.29:** (A) Far-field optical extinction cross-section spectra (in units of  $\pi a^2$ ,  $a$  being the radius of the sphere of equivalent volume) and (B) maximum electric near-field enhancement spectra of the hybrid  $Au/MoSe_2/Au$  junction excited by an incident s-polarized light presenting a flat substrate (pink line) and two different rough substrates. The dark gray lines represent the optical responses obtained with the rough substrate  $n^\circ 1$  (less confined plasmonic cavity) while the optical responses obtained with the rough substrate  $n^\circ 2$  (more confined cavity) are shown in light green lines. The tip-surface distance  $d$  is set to  $d = 0.2$  nm except for the rough substrate  $n^\circ 1$ , where is  $d \sim 0.224$  nm. The incidence angle is set to  $\theta = 45^\circ$ . The maximum near-field enhancement (B) is calculated inside a volume that includes the gap, the tip apex and a part of the monolayer.

In previous sections dealing with a flat substrate surface, it was shown that for s-polarization, the excitation of gap plasmon modes does not occur at all. Indeed, there is no interaction between the tip and the surface when the incident electric field oscillates in the xy plane perpendicular to the tip axis. Nevertheless, in the case of rough substrates, it is possible for tip-surface interactions to occur along the direction perpendicular to the tip axis, depending on the tip position. Thus, in order to see if gap plasmon modes are excited in that direction, the maximum electric near-field enhancement inside a volume that includes the gap, the tip apex and a part of the monolayer, is calculated for both rough substrates. The near-field spectra obtained are plotted in Fig. 4.29-B. Since a part of the monolayer is included in the volume used in the calculations, the spectra exhibit the transverse LSPR of the substrate in the 600 - 700 nm range as a shoulder for the rough substrate  $n^\circ 1$ , and as a peak for the rough substrate  $n^\circ 2$ . Moreover, another distinct peak is discernible at 740 nm for the rough substrate  $n^\circ 1$  and at 830 nm for the rough substrate  $n^\circ 2$ . These peaks are attributed to gap plasmon modes arising from the electromagnetic interaction occurring between the tip and the TMD surface in the horizontal direction (within the xy plane). Compared to the gap plasmon resonances observed for p-polarization (Fig. 4.26-B), these gap plasmon resonances exhibit reduced intensity and a slight wavelength shift ( $\sim 40$  nm) in the case of the rough substrate  $n^\circ 2$ . These differences are attributed to the fact that, depending on the polarization of the incident electric field, the region of the tip and the area of the  $MoSe_2$  surface involved in the excitation of gap plasmon modes may vary, leading to distinct

gap plasmon resonances. By incorporating substrate roughness into the hybrid junction simulation, tip-surface gap plasmon modes can be excited even if the incident electric field has no component along the tip axis. As a consequence, the optical responses obtained using a p and s-polarized light are similar when a rough substrate is considered.

Field enhancement maps in the  $yz$  plane are computed for the flat and the rough substrates for an incident s-polarized electric field (see Fig. 4.30). It is worthy to recall that the incident s-polarized electric field oscillates in the  $y$ -axis direction since the incidence plane is parallel to the  $xz$  plane (see Fig. 4.25).

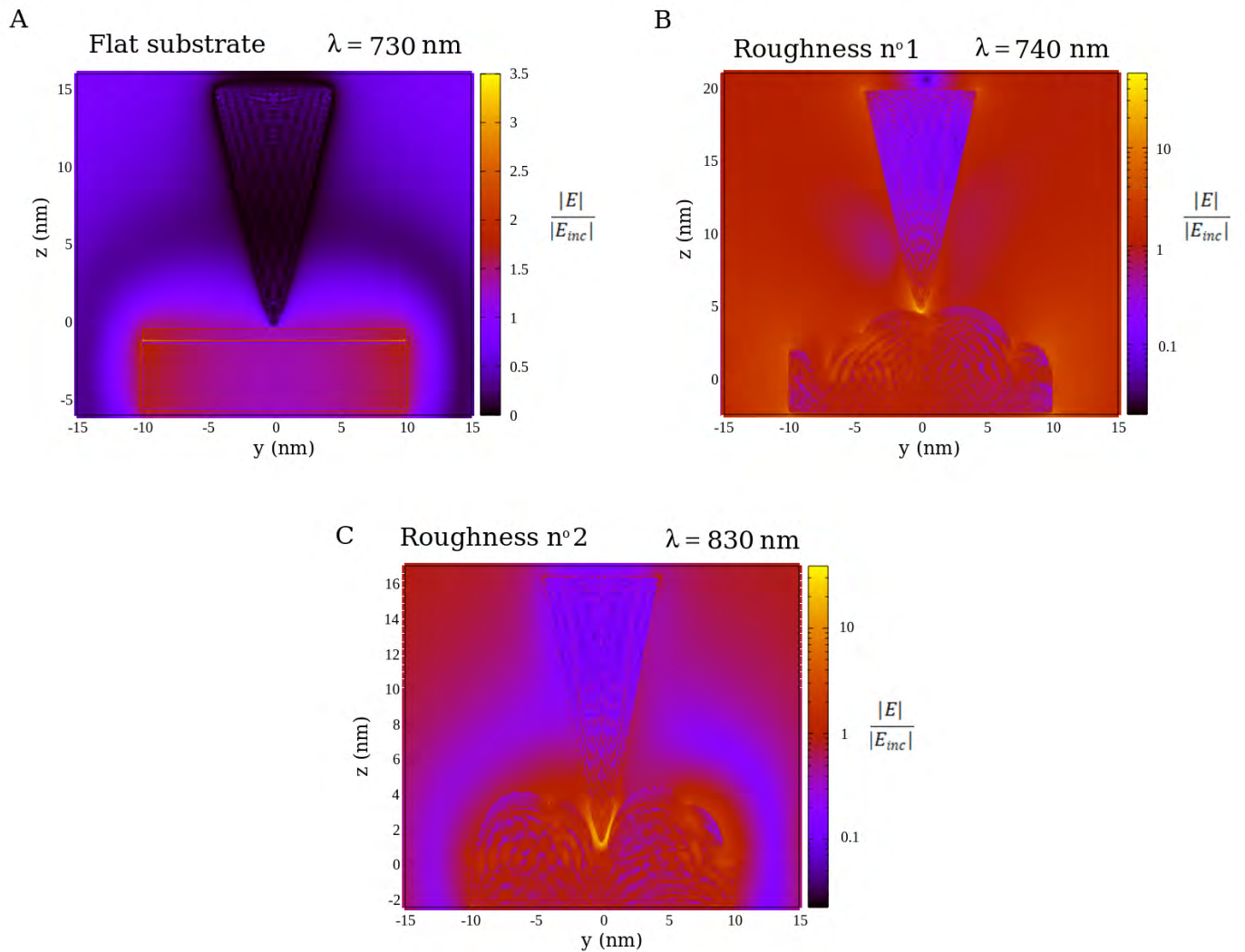


**Figure 4.30:** Electric near-field enhancement maps calculated in the  $yz$  plane for a hybrid  $Au/MoSe_2/Au$  junction with a flat substrate (A), with a rough substrate presenting the first configuration (B) and presenting the second configuration (C). An incident s-polarized light is used with an incidence angle of  $\theta = 45^\circ$ . For the flat surface, the map is computed at  $\lambda = 730$  nm (A). For the rough substrate n°1, the field enhancement map is computed at  $\lambda = 740$  nm (B) while for the rough substrate n°2, it is calculated at  $\lambda = 830$  nm (C). For the rough substrates, these maps (in log scale) are calculated at the gap plasmon resonance obtained for each configuration. The tip-surface distance  $d$  is set to  $d = 0.2$  nm except for the rough substrate n°1, where is  $d \sim 0.224$  nm.

As expected, it is observed that gap plasmon modes are not excited in the flat surface case. Under incident s-polarization, only the transverse plasmonic mode of the substrate is activated. However, for both rough substrates, an electric field enhancement is observed in the gap region between the tip and the TMD surface. This confirms that gap plasmon modes can be excited even if the incident electric field polarization is perpendicular to the tip axis when substrate roughness is introduced. In the  $yz$  plane, the highly confined tip-surface cavity of the junction with the rough substrate  $n^{\circ}2$  is clearly evident. As shown in Fig. 4.30, this confinement results in a large area of interaction between the tip and the sample, leading to a gap plasmon electric field less localized compared to the rough substrate  $n^{\circ}1$ .

Figure 4.31 displays the field enhancement maps computed in the  $xy$  plane.

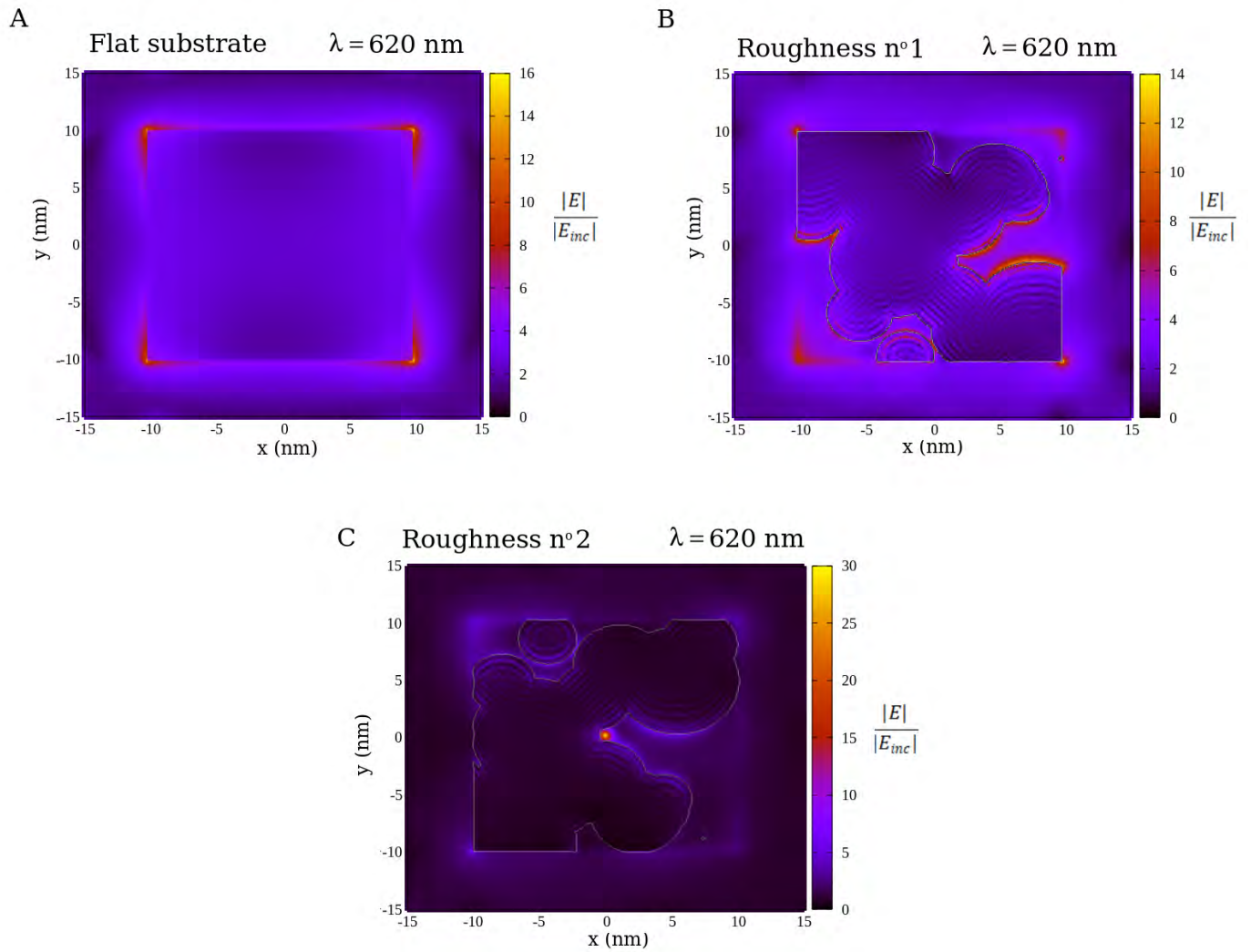


**Figure 4.31:** Electric near-field enhancement maps calculated in the  $xy$  plane for a hybrid  $Au/MoSe_2/Au$  junction with a flat substrate (A), with a rough substrate presenting the first configuration (B) and presenting the second configuration (C). An incident s-polarization light is used with an incidence angle of  $\theta = 45^\circ$  and a wavelength of  $\lambda = 620$  nm. The tip-surface distance  $d$  is set to  $d = 0.2$  nm except for the rough substrate  $n^{\circ}1$ , where is  $d \sim 0.224$  nm.

Similar to the maps obtained with p-polarization, an electric field enhancement at the surface grain boundaries is observed for both rough substrates. This field enhancement results from the local electromagnetic interaction between grains.

The introduction of a rough substrate into the simulation of a hybrid  $Au/MoSe_2/Au$  tunneling junction shows that the interaction between tip and surface, leading to the excitation of gap plasmon modes, can take place even if an incident polarization perpendicular to the tip axis is used; a possibility not achievable with a flat substrate. Hence, when a rough substrate is used, the optical response of the junction becomes less dependent on the polarization of the incident electric field. The geometry (size and shape) of the tip-surface gap depends on the tip location relative to the surface topography, resulting in gap plasmon modes with different properties. For instance, in the configuration of the rough substrate n°2, where the tip apex is situated between three grains, a highly confined cavity is formed. In this arrangement, not only does the tip apex interact with the sample surface, but a large portion of its lateral side also participates, resulting in a larger interaction area between the tip and the surface. This, in turn, gives rise to a gap plasmon resonance with a wavelength and intensity markedly different from those obtained with a flat surface. Another important point to be highlighted is the excitation of local surface plasmon resonances arising from the electromagnetic interaction between the surface grains of the rough substrates. The near-field optical responses calculated in this section will be used in Chapter 5 to take into account the electromagnetic environment of the hybrid junction with a rough substrate for the calculation of theoretical light emission spectra.

## 4.6 Conclusion

In this chapter, the properties of the electromagnetic modes of a hybrid  $Au/MoSe_2/Au$  tunneling junction are studied by means of numerical simulations. More precisely, a Fano-type plasmon-exciton coupling involving the substrate plasmonic mode, the excitons confined within the TMD monolayer and the gap plasmon modes is pointed out. This interaction gives rise to a hybrid gap plasmon-exciton mode localized within the monolayer and at the  $MoSe_2/Au$  substrate interface. The spectral behavior of the mentioned modes and their spatial distribution are studied as a function of the main tunneling parameters: bias voltage  $V$  and tip-surface distance  $d$ . This study is carried out using the Quantum-Corrected Model to take into account the effects of electron tunneling when the junction is in the tunneling regime ( $d < 0.5$  nm). However, due to the weak tunneling conductivity considered, these effects are negligible. When the tip-surface distance decreases, gap plasmon modes become more localized leading to a diminution of the gap plasmon-exciton coupling. The characteristics of the latter are also studied as a function of the incident field polarization. As the electric field component along the tip axis increases, the hybrid gap plasmon-exciton mode gets “undressed” of its excitonic character to gradually become a pure gap plasmon mode. Finally, introducing a rough substrate in the simulations induces modifications of the gap geometry, thereby reducing the extent to which the optical response of the hybrid junction relies on

the incident polarization. In addition, local surface plasmon modes resulting from the electromagnetic interaction between the protrusions of the rough substrate surface have been highlighted.

The findings outlined in this chapter provide insights into the complex light-matter interaction between localized surface plasmons and excitons in an STM configuration. This contributes to an improved understanding of the experimental STM-LE results obtained from a hybrid junction such as those presented in Chapter 3. Indeed, light emission depends on the radiative electromagnetic modes sustained by the junction. Furthermore, it has been observed that the excitonic luminescence can be enhanced when gap plasmon modes are involved. Therefore, careful examination of plasmonic modes and their interaction with excitons, as carried out in this study, is essential in the context of STM-LE. The results presented here constitute a fundamental element of the theoretical model developed in Chapter 5, aimed at incorporating the electromagnetic properties of the junction into the modeling of light emission process.

## Bibliography

- [1] R. Esteban, A. G. Borisov, P. Nordlander, and J. Aizpurua. Bridging quantum and classical plasmonics with a quantum-corrected model. *Nat. Commun.*, 3(1):825, 2012.
- [2] R. Esteban, A. Zugarramurdi, P. Zhang, P. Nordlander, F. J. García-Vidal, A. G. Borisov, and J. Aizpurua. A classical treatment of optical tunneling in plasmonic gaps: extending the quantum corrected model to practical situations. *Faraday Discuss.*, 178:151–183, 2015.
- [3] E. Alves, R. Péchou, R. Coratger, and A. Mlayah. Gap plasmon modes and plasmon-exciton coupling in a hybrid Au/MoSe<sub>2</sub>/Au tunneling junction. *Opt. Express*, 31(8):12549–12561, 2023.
- [4] J. C. Slater. Atomic radii in crystals. *J. Chem. Phys.*, 41(10):3199–3204, 1964.
- [5] E. Clementi, D. L. Raimondi, and W. P. Reinhardt. Atomic screening constants from SCF functions. II. Atoms with 37 to 86 electrons. *J. Chem. Phys.*, 47(4):1300–1307, 1967.
- [6] P. B. Johnson and R. W. Christy. Optical Constants of the Noble Metals. *Phys. Rev. B*, 6(12):4370–4379, 1972.
- [7] X. Wang, Y. Gong, G. Shi, W. L. Chow, K. Keyshar, G. Ye, R. Vajtai, J. Lou, Z. Liu, E. Ringe, B. K. Tay, and P. M. Ajayan. Chemical vapor deposition growth of crystalline monolayer MoSe<sub>2</sub>. *ACS Nano*, 8(5):5125–5131, 2014.
- [8] H.-L. Liu, C.-C. Shen, S.-H. Su, C.-L. Hsu, M.-Y. Li, and L.-J. Li. Optical properties of monolayer transition metal dichalcogenides probed by spectroscopic ellipsometry. *Appl. Phys. Lett.*, 105(20):201905, 2014.
- [9] R. Beiranvand. Theoretical investigation of electronic and optical properties of 2D transition metal dichalcogenides MoX<sub>2</sub> (X= S, Se, Te) from first-principles. *Physica E Low Dimens. Syst. Nanostruct.*, 126:114416, 2021.
- [10] W. Y. Liang. Optical anisotropy in layer compounds. *J. Phys. C: Solid State Phys.*, 6(3):551–565, 1973.
- [11] V. Iberi, L. Liang, A. V. Ievlev, M. G. Stanford, M.-W. Lin, X. Li, M. Mahjouri-Samani, S. Jesse, B. G. Sumpter, S. V. Kalinin, D. C. Joy, K. Xiao, A. Belianinov, and O. S. Ovchinnikova. Nanoforging single layer MoSe<sub>2</sub> through defect engineering with focused helium ion beams. *Sci. Rep.*, 6(1):30481, 2016.
- [12] D. Kozawa, R. Kumar, A. Carvalho, K. Kumar Amara, W. Zhao, S. Wang, M. Toh, R. M. Ribeiro, A. H. Castro Neto, K. Matsuda, and G. Eda. Photocarrier relaxation pathway in two-dimensional semiconducting transition metal dichalcogenides. *Nat. Commun.*, 5(1):4543, 2014.

- [13] B. M. Ross and L. P. Lee. Comparison of near-and far-field measures for plasmon resonance of metallic nanoparticles. *Opt. Lett.*, 34(7):896–898, 2009.
- [14] A. L. Tchebotareva, M. A. Van Dijk, P. V. Ruijgrok, V. Fokkema, M. H. S. Hesselberth, M. Lippitz, and M. Orrit. Acoustic and optical modes of single dumbbells of gold nanoparticles. *ChemPhysChem*, 10(1):111–114, 2009.
- [15] I Romero, J Aizpurua, G. W. Bryant, and F. J. García de Abajo. Plasmons in nearly touching metallic nanoparticles: singular response in the limit of touching dimers. *Opt. Express*, 14(21):9988–9999, 2006.
- [16] E. Hao and G. C. Schatz. Electromagnetic fields around silver nanoparticles and dimers. *J. Chem. Phys.*, 120(1):357–366, 2004.
- [17] F. Benz, M. K. Schmidt, A. Dreismann, R. Chikkaraddy, Y. Zhang, A. Demetriadou, C. Carnegie, H. Ohadi, B. De Nijs, R. Esteban, J. Aizpurua, and J. J. Baumberg. Single-molecule optomechanics in “picocavities”. *Science*, 354(6313):726–729, 2016.
- [18] B. Lee, J. Park, G. H. Han, H.-S. Ee, C. H. Naylor, W. Liu, A. T. C. Johnson, and R. Agarwal. Fano resonance and spectrally modified photoluminescence enhancement in monolayer MoS<sub>2</sub> integrated with plasmonic nanoantenna array. *Nano Lett.*, 15(5):3646–3653, 2015.
- [19] I. Abid, A. Bohloul, S. Najmaei, C. Avendano, H.-L. Liu, R. Péchou, A. Mlayah, and J. Lou. Resonant surface plasmon–exciton interaction in hybrid MoSe<sub>2</sub>@Au nanostructures. *Nanoscale*, 8(15):8151–8159, 2016.
- [20] I. Abid, W. Chen, J. Yuan, A. Bohloul, S. Najmaei, C. Avendano, R. Péchou, A. Mlayah, and J. Lou. Temperature-dependent plasmon–exciton interactions in hybrid Au/MoSe<sub>2</sub> nanostructures. *ACS Photonics*, 4(7):1653–1660, 2017.
- [21] J. Wen, H. Wang, W. Wang, Z. Deng, C. Zhuang, Y. Zhang, F. Liu, J. She, J. Chen, H. Chen, S. Deng, and N. Xu. Room-temperature strong light–matter interaction with active control in single plasmonic nanorod coupled with two-dimensional atomic crystals. *Nano Lett.*, 17(8):4689–4697, 2017.
- [22] J. Cuadra, D. G. Baranov, M. Wersall, R. Verre, T. J. Antosiewicz, and T. Shegai. Observation of tunable charged exciton polaritons in hybrid monolayer WS<sub>2</sub>-plasmonic nanoantenna system. *Nano Lett.*, 18(3):1777–1785, 2018.
- [23] R. Péchou, S. Jia, J. Rigor, O. Guillermet, G. Seine, J. Lou, N. Large, A. Mlayah, and R. Coratger. Plasmonic-Induced Luminescence of MoSe<sub>2</sub> Monolayers in a Scanning Tunneling Microscope. *ACS Photonics*, 7(11):3061–3070, 2020.

- [24] P. Jiang, G. Song, Y. Wang, C. Li, L. Wang, and L. Yu. Tunable strong exciton–plasmon–exciton coupling in WS<sub>2</sub>–J-aggregates–plasmonic nanocavity. *Opt. Express*, 27(12):16613–16623, 2019.
- [25] Z. He, C. Xu, W. He, J. He, Y. Zhou, and F. Li. Principle and applications of multimode strong coupling based on surface plasmons. *Nanomaterials*, 12(8):1242, 2022.
- [26] X. Wu, S. K. Gray, and M. Pelton. Quantum-dot-induced transparency in a nanoscale plasmonic resonator. *Opt. Express*, 18(23):23633–23645, 2010.
- [27] Ines Abid. *Plasmonique hybride : Propriétés optiques de nanostructures Au-TMD, couplage plasmon-exciton*. PhD thesis, Université Paul Sabatier, 2017.
- [28] C. T. Le, D. J. Clark, F. Ullah, V. Senthilkumar, J. I. Jang, Y. Sim, M.-J. Seong, K.-H. Chung, H. Park, and Y. S. Kim. Nonlinear optical characteristics of monolayer MoSe<sub>2</sub>. *Annalen der Physik*, 528(7-8):551–559, 2016.
- [29] M. M. Petrić, M. Kremser, M. Barbone, A. Nolinder, A. Lyamkina, A. V. Stier, M. Kaniber, K. Müller, and J. J. Finley. Tuning the optical properties of a MoSe<sub>2</sub> monolayer using nanoscale plasmonic antennas. *Nano Lett.*, 22(2):561–569, 2022.
- [30] R. Ge, X. Wu, L. Liang, S. M. Hus, Y. Gu, E. Okogbue, H. Chou, J. Shi, Y. Zhang, S. K. Banerjee, Y. Jung, J. C. Lee, and D. Akinwande. A library of atomically thin 2D materials featuring the conductive-point resistive switching phenomenon. *Adv. Mater.*, 33(7):2007792, 2021.
- [31] L. Huang, B. Li, M. Zhong, Z. Wei, and J. Li. Tunable Schottky barrier at MoSe<sub>2</sub>/Metal interfaces with a buffer layer. *J. Phys. Chem. C*, 121(17):9305–9311, 2017.
- [32] W. Mönch. Valence-band offsets and Schottky barrier heights of layered semiconductors explained by interface-induced gap states. *Appl. Phys. Lett.*, 72(15):1899–1901, 1998.
- [33] K. L. Kelly, E. Coronado, L. L. Zhao, and G. C. Schatz. The Optical Properties of Metal Nanoparticles: The Influence of Size, Shape, and Dielectric Environment. *J. Phys. Chem. B*, 107(3):668–677, 2003.
- [34] Renaud Péchou. *Émission de photons dans un microscope à effet tunnel*. PhD thesis, Université Paul Sabatier, 1997.
- [35] M. M. J. Bischoff, M. C. M. M. van der Wielen, and H. van Kempen. STM-induced photon emission spectroscopy of granular gold surfaces in air. *Surf. Sci.*, 400(1):127–133, 1998.
- [36] Garikoitz Aguirregabiria. *Theoretical study of the linear and nonlinear optical response of plasmonic tunneling gaps*. PhD thesis, Universidad del País Vasco, 2018.

## Chapter 5

# Theoretical model of light emission from a hybrid $Au/MoSe_2/Au$ tunneling junction

In STM-induced luminescence (STM-LE) experiments on a  $MoSe_2$  monolayer deposited on a granular gold substrate, two distinct light emission processes, namely plasmonic and excitonic, can take place, as previously observed in Chapter 3. Plasmonic light emission refers to the phenomenon of photon emission arising from the excitation of plasmon modes by inelastic electron tunneling within the STM junction gap. On the other hand, excitonic light emission involves the radiative recombination of excitons confined within the monolayer. This recombination is triggered by carriers injection into the semiconductor layer through electron tunneling. This chapter introduces theoretical models aimed at describing these light emission phenomena occurring in a hybrid  $Au/MoSe_2/Au$  tunneling junction. In the first part, a theoretical description of plasmonic emission is presented. This model is an adaptation of the approaches found in the literature and unveiled in Chapter 1 that describe the plasmonic emission taking place in purely metallic tunneling junctions. The calculations related to electron tunneling are based on the mathematical formalisms established in those earlier models. Besides electron tunneling, the local electromagnetic environment plays a crucial role in the plasmonic light emission process. This is implemented into our model through the electromagnetic properties of the gap given by the near-field optical response of the hybrid junction studied in Chapter 4. The second section of this chapter is dedicated to the excitonic light emission, which involves three distinct physical processes: electron tunneling, exciton creation, and exciton radiative recombination. A description of electron tunneling similar to the one developed for plasmonic emission is used in the calculations. For the excitons generation, it is postulated that each carrier injected through electron tunneling gives rise to an exciton. Then, the radiative recombination of excitons is described mathematically using the Fermi golden rule and taking into account the surrounding local electromagnetic field. Similar to the approach used to describe plasmonic emission, this field is determined from the optical response of the

hybrid tunneling junction investigated in Chapter 4 and incorporated into the model. In each section, a detailed description of the developed theoretical model, including all underlying assumptions, is provided. This is followed by the mathematical formalism used to compute the theoretical light emission spectra. Furthermore, an analysis of these calculated spectra and their behavior as a function of the main tunneling parameters, i.e. the bias voltage  $V_s$  and the tip-surface distance  $d$  is carried out. The substrate roughness is introduced in these models, enhancing their interest and marking a significant step forward in the theoretical framework of STM-LE. In the third section of this chapter, a detailed quantitative analysis of the role of the surface sample roughness on the theoretical plasmonic and excitonic spectra is presented. Finally, a comparison between the main characteristics of the theoretical light emission and the experimental results obtained in Chapter 3 is presented. This comparison focuses in particular on the spectral characteristics and the light emission rate.

## 5.1 Light emission from inelastic tunneling in the junction: Plasmonic Emission

This first section focuses on the light emission process resulting from inelastic electron tunneling taking place in the gap of a plasmonic STM junction. This phenomenon is referred to as the plasmonic light emission process. As detailed in section 1.1.2, the energy lost by tunneling electrons leads to the excitation of localized surface plasmon modes confined within the nanocavity formed by the tip and the sample surface. These plasmon modes may decay radiatively giving rise to the experimental plasmonic STM-LE spectra described in Chapter 3. A model is presented here in order to provide a theoretical framework for this light emission process originating within the gap of a hybrid  $Au/MoSe_2/Au$  tunneling junction. A description of this model is given in the first part of this section, followed by the mathematical formalism used to derive theoretical plasmonic light emission spectra. As mentioned before, both inelastic tunneling and electromagnetic properties of the gap play crucial roles in this light emission process. In the last part of this section, a detailed analysis of each of these elements is conducted. This analysis is important for gaining insights into the spectral characteristics of the resulting light emission spectra.

### 5.1.1 Model Description

The model being discussed in this section is adapted from the approaches developed by Johansson *et al.* [1, 2] and Aizpurua *et al.* [3] presented in section 1.1.2. However, while these earlier models considered a purely metallic junction, the junction studied here is composed by a gold tip and a sample consisting on a  $MoSe_2$  monolayer supported by a gold substrate. Inelastic tunneling transitions between the monolayer and the tip are thus considered, each of them leading to the emission of a photon with an energy  $\hbar\omega$ . The latter corresponds to the energy difference between the initial and final states of

the electronic transition. In addition, these transitions are assumed to occur exclusively along the  $z$ -direction. In line with the experimental STM-LE measurements presented in Chapter 3, a negatively biased substrate (with respect to the tip) is considered resulting in electronic transitions from the monolayer to the tip. In Figure 5.1, the energy band diagram of the described junction is presented. As shown in this diagram, the TMD monolayer surface is defined as the starting point for these transitions, and is represented by the coordinate  $z = 0$  while the tip apex is positioned at a tip-surface distance  $d$  from the monolayer. For the sake of simplicity, only three initial energy states for electron transitions are considered. The first one is the conduction band minimum, characterized by an energy denoted as  $E_C$  and represented by a red line in Fig. 5.1. Furthermore, given the strong spin splitting of the TMD valence band, two different energy levels are considered corresponding to the top of each sub-band, the one at higher energy has an energy denoted as  $E_{V_A}$  and the other as  $E_{V_B}$ . Both are depicted by a dark and light green line in Fig. 5.1. These two valence energy states are at the origin of the formation of A- and B-excitons in the TMD monolayer.

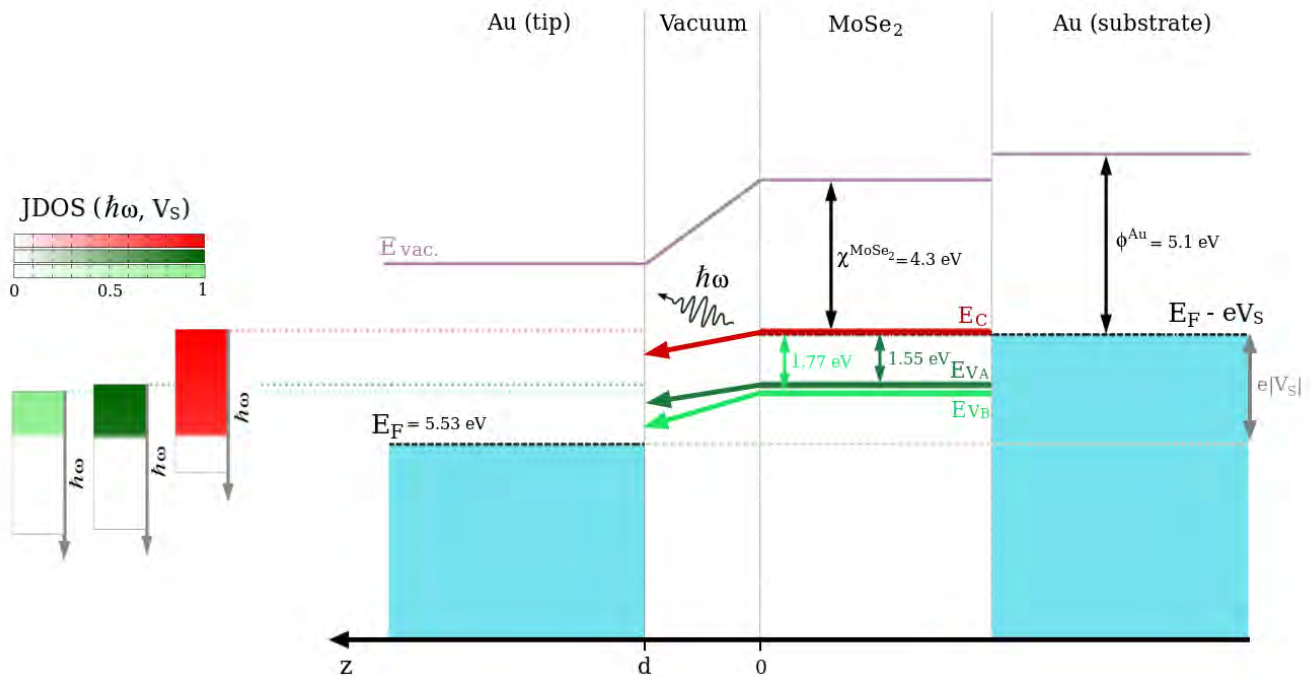


**Figure 5.1:** Energy band diagram of the hybrid  $Au/MoSe_2/Au$  tunneling junction with a negative bias voltage  $V_s$  applied to the gold substrate (with respect to the tip). Inelastic electron tunneling occurring from the  $MoSe_2$  monolayer at  $z = 0$  to the gold tip at  $z = d$  resulting in the emission of photons with an energy  $\hbar\omega$  within the gap is depicted. The tunneling process involves only three initial energy levels: the conduction band minimum with an energy  $E_C$  (depicted in red) and the maximum of each valence sub-band with energies  $E_{V_A}$  and  $E_{V_B}$  (shown in dark and light green) respectively. On the left side, the normalized joint density of states (JDOS) is displayed for each initial energy state under consideration. JDOS represents the density of accessible energy states in the tip and the probability of these states being occupied by an electron from an initial energy state.

The  $MoSe_2$  monolayers investigated in Chapter 3 are n-doped. According to Chang *et al.* [4], when these semiconductors are transferred onto a gold substrate, their Fermi level is typically positioned a few

hundred meV below the conduction band minimum (CBM). To simplify the model, it is assumed that the Fermi level coincides with the conduction band minimum. Consequently, given the applied bias, the CBM energy can be expressed as  $E_C = E_F - eV_s$ , where  $V_s$  is negative and thus,  $eV_s < 0$  with  $e$  the elementary charge. The Fermi energy used in the calculations corresponds to that of bulk gold, which is  $E_F = 5.53$  eV [5] (with 0 eV corresponding to the lowest occupied energy level). For any value of  $V_s < 0$ , the CBM of the TMD monolayer has a higher energy than the tip Fermi level allowing electron tunneling from this conduction state to the tip. The ground state of both A- and B-excitons is assumed to be the CBM. Indeed, the binding energy of the excitons is ignored to simplify the model. Hence, the energy difference between the valence sub-bands and the CBM is considered equivalent to the exciton energy (optical bandgap). These energy differences are expressed by the relations:  $E_C - E_{V_A} = \hbar\omega_{exA}$  and  $E_C - E_{V_B} = \hbar\omega_{exB}$ , with  $\hbar\omega_{exA} = 1.55$  eV and  $\hbar\omega_{exB} = 1.77$  eV being the energy of the A- and B-excitons, respectively [6]. Therefore, inelastic tunneling can occur from valence sub-band “A” (with the energy  $E_{V_A}$ ) only when the bias voltage satisfies  $-eV_s > 1.55$  eV, and similarly for valence sub-band “B”, inelastic tunneling takes place when the bias voltage fulfills  $-eV_s > 1.77$  eV. As the bias voltage  $V_s$  becomes more negative, the energy of the initial states under consideration becomes higher than the tip Fermi level enabling inelastic tunneling channels to open up from the TMD monolayer to the tip. Figure 5.1 illustrates these energy states, and also includes additional parameters, such as the gold work function  $\phi^{Au} = 5.1$  eV and the  $MoSe_2$  electron affinity  $\chi^{MoSe_2} = 4.3$  eV [7]. All these parameters are involved in the calculations of the theoretical light emission spectra, discussed below.

An additional important parameter to take into account is the occupancy of the states involved in the tunneling transitions. For that, the joint density of states (JDOS) accounting for the density of available energy states in the tip and the probability of these states being occupied by an electron originating from an initial state is included in the calculations. Its mathematical definition will be provided in the following section (eq. (5.14)), and it is illustrated on the left side of Figure 5.1. It is essential to underline that this model assumes the tunnel junction to be at room temperature.

The mathematical formalism developed below incorporates all the elements and assumptions mentioned here. In particular, tunneling transitions are described by a tunneling transition matrix. The latter is derived from Fermi golden rule given by using the first-order perturbation theory, considering the coupling between the tip and the sample as a small perturbation. Furthermore, it is important to note that the electromagnetic properties of the gap of the hybrid  $Au/MoSe_2/Au$  tunneling junction are also included in the formalism. These properties which have been extensively studied in the previous Chapter 4, are a key element in the light emission process.

### 5.1.2 Formalism: modified version of the Johansson-Aizpurua model

Calculations of the light emission efficiency are conducted in terms of radiated power. The mathematical formalism used is a modified version of the one developed by Johansson *et al.* [1, 2] and Aizpurua *et al.* [3], which is here adapted to the case of the hybrid tunneling junction described earlier.

### a) Radiated Power

To derive the expression of the radiated power arising from inelastic electron tunneling in an STM junction, let us begin with a simple scenario. For an oscillating electric dipole, the electric and magnetic far-fields are perpendicular to each other and to the radial direction  $\mathbf{r}$ . The Poynting vector, which represents the rate of energy transfer per unit area carried by an electromagnetic wave, can be expressed as follows:

$$\mathbf{S} = \frac{1}{\mu_0} \{\mathbf{E} \times \mathbf{B}\} = \epsilon_0 c |\mathbf{E}|^2 \mathbf{r} \quad (5.1)$$

with  $c$  the speed of light. The power radiated by the dipole per unit time passing through an infinitesimal spherical area of radius  $r$  is written as:

$$dP = \mathbf{S} \cdot \mathbf{r} r^2 d\Omega \quad (5.2)$$

The power radiated per unit solid angle becomes:

$$\frac{dP}{d\Omega} = \mathbf{S} \cdot \mathbf{r} r^2 = \epsilon_0 c r^2 |\mathbf{E}|^2 \quad (5.3)$$

In our case, the emission of light is caused by many different inelastic transitions taking place between the monolayer surface and the tip apex. These transitions are uncorrelated to each other and contribute to the light emission with a wide range of frequencies. The radiated power resulting from these transitions can be deduced by analogy with that obtained for a single electric dipole by considering the electromagnetic far field generated by each transition. To do so, the magnitude of the electric field in eq. (5.3) is replaced by an incoherent sum of the magnitudes  $|\mathbf{E}_{if}(\mathbf{r}, \omega)|^2$  of the individual radiated electric fields, each generated by the inelastic transition from an initial state  $|i\rangle$  to a final state  $|f\rangle$ . Furthermore, rather than considering the power radiated per unit solid angle, the power radiated per unit solid angle and per unit photon energy  $\hbar\omega$  should be computed [8, 9]. The expression of the latter is given by:

$$\frac{d^2 P}{d\Omega d(\hbar\omega)} = 2 \epsilon_0 c \sum_{i,f} r^2 |\mathbf{E}_{if}(\mathbf{r}, \omega)|^2 \delta(E_i - E_f - \hbar\omega) \quad (5.4)$$

where  $E_i$  and  $E_f$  are the energy of the initial and final states, respectively. The energy conservation for the inelastic tunneling transition is assured by the Dirac delta function. This expression is given in the Johansson and Aizpurua models presented in Chapter 1 (see eq. (1.39)).

In line with these models, in order to determine the expression of the radiated electric field  $\mathbf{E}_{if}(\mathbf{r}, \omega)$  at the position  $\mathbf{r}$  far from the gap, the reciprocity theorem of electrodynamics [10] is applied. The radiated electric far-field induced by the tunneling current is linked to the near electric field within the

gap induced by a source of plane waves situated far from the gap. After considering equations (1.40) to (1.42), the radiated power per unit solid angle and unit photon energy can be defined as follows:

$$\frac{d^2P}{d\Omega d(\hbar\omega)} = \frac{\omega^2}{8\pi^2\epsilon_0c^3} \sum_{i,f} \left| \int d^3r' G(\mathbf{r}', \omega) \mathbf{j}_{if}(\mathbf{r}', \omega) \right|^2 \times \delta(E_i - E_f - \hbar\omega) \quad (5.5)$$

where  $G(\mathbf{r}', \omega)$  is the local field enhancement within the gap. Unlike the approach followed in Johansson and Aizpurua models, this quantity is computed here from numerical electrodynamic simulations. In Chapter 4, the optical response of the hybrid  $Au/MoSe_2/Au$  tunneling junction has been studied by QCM-DDA simulations. Thus, the electric near field induced in and around the junction, including the gap region, has already been computed. This analysis has enabled the determination of  $G(\mathbf{r}', \omega)$ . It is important to note that  $G(\mathbf{r}', \omega)$  is used to integrate the electromagnetic properties of the junction into the model, which holds significance for the process of light emission. In the following section, a further investigation of the characteristics of this term is conducted.

The second main factor in the radiated power calculation is the tunnel current which is the source for radiation. This tunnel current arises from electron transitions from the monolayer to the tip and it is directed along  $\mathbf{z}$ , the unit vector in the z-direction perpendicular to the sample surface (see Figure 5.1). The current density expression in this direction is also defined in Aizpurua model:

$$\mathbf{z} \cdot \mathbf{j}_{if}(\mathbf{r}', \omega) = \frac{e}{i\hbar} \left[ \frac{\hbar^2}{2m_e} \left( \frac{\partial\psi_f^*}{\partial z'} \psi_i - \psi_f^* \frac{\partial\psi_i}{\partial z'} \right) (\mathbf{r}') + E_{fi} \int_0^d dz \Theta(z' - z) \psi_f^* \psi_i(\mathbf{r}) \right] \quad (5.6)$$

where  $d$  represents the tip-surface distance, while  $E_{fi} = E_f - E_i = -\hbar\omega$  is the energy difference between the initial and final states of the electronic tunneling transition. The Heaviside step function  $\Theta(z' - z)$  accounts for the occurrence of the inelastic process at the location  $z'$  within the gap. Then,  $\psi_i$  and  $\psi_f$  are the wave functions of the initial and final states, respectively. The first term is derived from the tunneling current expression provided by Bardeen [11] whose model is outlined in section 1.1.1 of Chapter 1. Bardeen's model describes elastic tunneling. Thus, in order to describe inelastic tunneling within the Bardeen approach, an additional term (second term of eq. (5.6)) is introduced into the tunneling density calculation [3] that accounts for tunneling transitions in which the energies of the involved states are not equal.

The tunneling matrix element  $M_{if}(z_o, \omega)$  is defined as the integration over the current density in the transverse direction. This integration implies the conservation of the transverse momentum of the tunneling electrons.  $M_{if}(z_o, \omega)$  is written as follows with  $z_o$  representing the specific location within the gap where the inelastic process occurs (see Fig. 5.2):

$$M_{if}(z_o, \omega) = \int d^2\mathbf{S}' \left[ \frac{\hbar^2}{2m_e} \left( \frac{\partial\psi_f^*}{\partial z'} \psi_i - \psi_f^* \frac{\partial\psi_i}{\partial z'} \right) (\mathbf{r}') \Big|_{z'=z_o} - \hbar\omega \int_0^d dz \Theta(z_o - z) \psi_f^* \psi_i(\mathbf{r}) \right] \quad (5.7)$$

The radiated power can then be written as:

$$\frac{d^2P}{d\Omega d(\hbar\omega)} = \frac{\alpha}{h} \left(\frac{\omega}{c}\right)^2 \sum_{i,f} \left| \int_0^d dz_o G(z_o, \omega) M_{if}(z_o, \omega) \right|^2 \times \delta(E_i - E_f - \hbar\omega) \quad (5.8)$$

with  $\alpha = \frac{e^2}{2\epsilon_0\hbar c}$ , the fine-structure constant. For the sake of simplicity and since the field-enhancement factor decays in the transverse direction slower than the tunneling current (exponential decay),  $G$  is integrated solely over  $z_o$ , i.e. in the direction perpendicular to the monolayer surface.

The calculation of  $G(\mathbf{r}', \omega)$  is not the sole aspect of the model presented here that differs from the Johansson and Aizpurua models. As previously discussed, our junction is not purely metallic and instead, it consists of a  $MoSe_2$  monolayer placed on a gold substrate, which is assumed to be negatively biased, and a gold tip. In addition, only three initial energy states are considered: the conduction band minimum and the maximum of each valence sub-band (Fig. 5.1). The strategy chosen here consists in evaluating the radiated power  $\frac{d^2P}{d\Omega d(\hbar\omega)}$  for each individual initial state and subsequently sum the results obtained.

When a single initial state is considered, the sum over the initial states in the expression of the radiated power of eq. (5.8) disappears. Moreover, in order to provide a more practical way to describe the tip states, it is decided to approximate the sum over discrete final states with a continuum by considering the density of states (DOS) of the tip, which will be denoted as  $\rho_t(E)$ . In addition, to model the STM-LE experiments of Chapter 3, electrons follow the Fermi-Dirac distribution at room temperature. Hence, occupation factors are incorporated into the radiated power calculations. The resulting expression of the radiated power is written as follows with  $V_s$ , the bias voltage applied to the sample:

$$\frac{d^2P}{d\Omega d(\hbar\omega)} = \frac{\alpha}{h} \left(\frac{\omega}{c}\right)^2 \int_0^\infty \rho_t(E_f) [f(E_i + eV_s) - f(E_f)] \left| \int_0^d dz_o G(z_o, \omega) M_{if}(z_o, V_s, \omega) \right|^2 \times \delta(E_i - E_f - \hbar\omega) dE_f \quad (5.9)$$

Certain elements of the preceding equation are illustrated in Figure 5.2, including the bias voltage  $V_s$  and the energies  $E_i$  and  $E_f$  of the states involved in the inelastic tunneling process occurring at the location  $z_o$ .

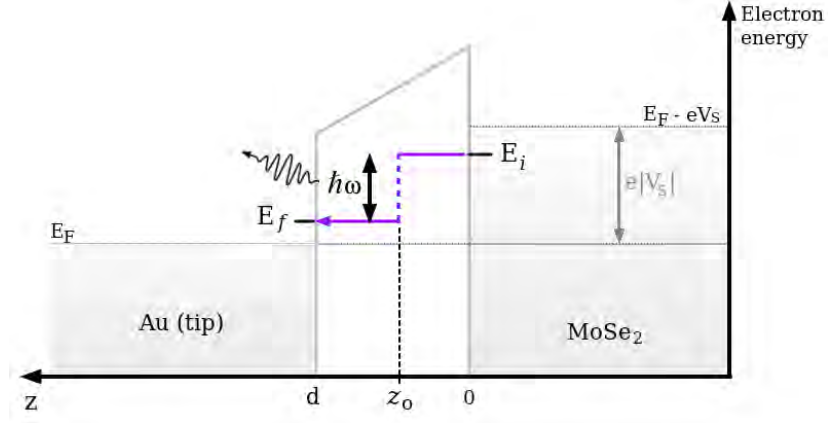


**Figure 5.2:** Energy band diagram showing the inelastic electron tunneling transition from the TMD monolayer initial state (with an energy  $E_i$ ) to the tip final state (with an energy  $E_f$ ) resulting in the emission of a photon with an energy  $\hbar\omega$ . The inelastic process occurs at the location  $z_o$  within the gap.

In section 1.1.1 of Chapter 1, the dependence of the tunneling current on the bias voltage applied to the junction was demonstrated. This dependence is present here through the tunneling matrix element  $M_{if}$  and the Fermi-Dirac occupation factors  $f$ . The local-field enhancement could as well be dependent on the bias voltage. However, as shown in section 4.4.1 of Chapter 4, the electric near-field enhancement calculated in the gap region by QCM-DDA simulations is barely affected by the bias voltage. Consequently, it has been opted not to consider the dependence of  $G$  on  $V_s$ . The index  $i$  is used to designate the initial state, which can be one of the three  $MoSe_2$  states previously described. By using the delta Dirac function, equation (5.9) becomes:

$$\frac{d^2P}{d\Omega d(\hbar\omega)} = \frac{\alpha}{h} \left(\frac{\omega}{c}\right)^2 \rho_t(E_i - \hbar\omega) [f(E_i + eV_s) - f(E_i - \hbar\omega)] \left| \int_0^d dz_o G(z_o, \omega) M_i(z_o, V_s, \omega) \right|^2 \quad (5.10)$$

The wavefunctions  $\psi_f$  of the final states are expressed in a manner where their dependence on the final state index  $f$  is solely based on the energy  $E_f$ . By using the delta Dirac function, the latter is expressed as a function of the initial state energy. Consequently, both the final state wavefunctions and the tunneling matrix element  $M_{if}$  no longer have a direct dependency on the specific index  $f$ . To simplify notation, the wavefunction of the tip states will be denoted  $\psi_t$  from now on. The expression of the density of state  $\rho_t(E_i - \hbar\omega)$  of the tip is given by:

$$\rho_t(E_i - \hbar\omega) = \frac{V_{tip}(E_i - \hbar\omega)^{\frac{1}{2}}(2m_t)^{\frac{3}{2}}}{2\pi^2\hbar^3} \quad (5.11)$$

with  $V_{tip}$  the volume of the metallic tip,  $m_t$  the effective mass of an electron in bulk gold tip assumed to be equal to the free-electron mass  $m_e$ , and a factor 2 accounting for the spin. This computation considers the tip a three-dimensional electrode. Indeed, both electrodes (tip and monolayer) are regarded as three-dimensional objects where tunneling occurs between them along the  $z$ -direction (potential change just along  $z$ ) with conservation of transverse momentum.

The expression of the occupation factors are:

$$f(E_i + eV_s) = \frac{1}{\exp[(E_i + eV_s - E_F)/k_B T] + 1} \quad (5.12)$$

$$f(E_i - \hbar\omega) = \frac{1}{\exp[(E_i - \hbar\omega - E_F)/k_B T] + 1} \quad (5.13)$$

Multiplying the DOS by the occupation factors yields a quantity representing both the density of available energy states and the probability of those states being occupied by electrons. This quantity is commonly denoted as the joint density of states (JDOS) [12] and it is depicted on the left side of Figure 5.1 for each initial state:

$$JDOS(\hbar\omega, V_s) = \rho_t(E_i - \hbar\omega) [f(E_i + eV_s) - f(E_i - \hbar\omega)] \quad (5.14)$$

The radiated power obtained for each initial state is normalized by its corresponding elastic current. This normalization provides a more meaningful and reliable comparison of the different radiated powers obtained. Following the same approach as in Chapter 3 where the experimental light emission process is investigated, in order to compare the light emission efficiency obtained for each examined configuration, the number of photons per tunneling electron is evaluated. In addition, this normalization allows one to get rid of the term  $V_{tip}$ , the actual volume of the tip, in the calculations. The expression of the elastic current considered is a modified version of the one defined in Bardeen's model [11] (see eq. (1.10)). The elastic current is assumed to be constant in the gap region and it is evaluated at the center of the gap  $z = \frac{d}{2}$ .

$$I_{elas} = \frac{4\pi e}{\hbar} \rho_t(E_i) [f(E_i + eV_s) - f(E_i)] \left| M_i \left( \frac{d}{2}, V_s \right) \right|^2 \quad (5.15)$$

With:

$$\rho_t(E_i) = \frac{V_{tip}(E_i)^{\frac{1}{2}}(2m_e)^{\frac{3}{2}}}{2\pi^2\hbar^3} \quad (5.16)$$

$$f(E_i + eV_s) = \frac{1}{\exp[(E_i + eV_s - E_F)/k_B T] + 1} \quad (5.17)$$

$$f(E_i) = \frac{1}{\exp[(E_i - E_F)/k_B T] + 1} \quad (5.18)$$

The detailed procedure for computing the tunneling term  $M_i$ , which appears in the expression for radiated power and for elastic current in equations (5.10) and (5.15), is described below.

### b) Tunneling term $M_i$

After applying the delta Dirac function, the tunneling matrix element, having the dimension of energy, can be expressed as:

$$M_i(z_o, V_s, \omega) = \int d^2\mathbf{S}' \left[ \frac{\hbar^2}{2m_e} \left( \frac{\partial \psi_t^*}{\partial z'} \psi_i - \psi_t^* \frac{\partial \psi_i}{\partial z'} \right) (\mathbf{r}') \Big|_{z'=z_o} - \hbar\omega \int_0^d dz \Theta(z_o - z) \psi_t^* \psi_i(\mathbf{r}) \right] \quad (5.19)$$

Since the tunneling is considered to take place along the z-direction, the potential barrier is then solely characterized by the spatial coordinate  $z$ . As in Johansson model, initial and final states are described by free-electron wavefunctions in the xy plane:

$$\text{TMD monolayer:} \quad \psi_i(\mathbf{r}) = \frac{\mathcal{C}_i}{\sqrt{V_{MoSe_2}}} e^{j\mathbf{k}_{\parallel i} \mathbf{r}_{\parallel i}} \phi_i(z) \quad (5.20)$$

$$\text{Tip:} \quad \psi_t(\mathbf{r}) = \frac{\mathcal{C}_t}{\sqrt{V_{tip}}} e^{j\mathbf{k}_{\parallel t} \mathbf{r}_{\parallel t}} \phi_t(z)$$

where  $\mathbf{k}_{\parallel i,t}$  and  $\mathbf{r}_{\parallel i,t}$  are the electron wavevector and the position vector in the xy plane parallel to the monolayer surface (perpendicular to the tunneling). As mentioned before, the transverse momentum of tunneling electrons is conserved, thus  $\mathbf{k}_{\parallel i} = \mathbf{k}_{\parallel t}$ .  $V_{MoSe_2}$  and  $V_{tip}$  are the  $MoSe_2$  and tip volumes and  $\mathcal{C}_i$  and  $\mathcal{C}_t$  are normalization constants. The functions  $\phi_i(z)$  and  $\phi_t(z)$  are calculated by solving the Schrödinger equation using Wentzel-Kramers-Brillouin (WKB) approximation [13]:

$$\text{TMD monolayer:} \quad \phi_i(z) = \frac{\sqrt{\kappa_i^*(z=0)}}{\sqrt{\kappa_i^*(z)}} e^{-\int_0^z \kappa_i^*(z') dz'} \quad (5.21)$$

$$\text{Tip:} \quad \phi_t(z) = \frac{\sqrt{\kappa_t^*(z=d)}}{\sqrt{\kappa_t^*(z)}} e^{-\int_z^d \kappa_t^*(z') dz'}$$

$\kappa_{i,t}^*(z)$  is the inverse decay length of the initial and tip states wavefunctions along  $z$  which expression is  $\kappa_{i,t}^*(z) = \sqrt{\kappa_{i,t}(z)^2 + k_{\parallel i,t}^2}$  with:

$$\kappa_i(z) = \frac{\sqrt{2m_e(E_F + \phi^{Au} + (\chi^{MoSe_2} - \phi^{Au} - eV_s) \left(\frac{d-z}{d}\right) - E_i)}}{\hbar} \quad (5.22)$$

$$\kappa_t(z) = \frac{\sqrt{2m_e(E_F + \phi^{Au} + (\chi^{MoSe_2} - \phi^{Au} - eV_s) \left(\frac{d-z}{d}\right) - (E_i - \hbar\omega))}}{\hbar} \quad (5.23)$$

where  $E_F$  is the Fermi energy,  $\phi^{Au}$  the gold tip work function and  $\chi^{MoSe_2}$  the electron affinity in  $MoSe_2$ . These quantities are depicted in Figure 5.1. The potential barrier in the junction is considered trapezoidal. As previously mentioned,  $E_i$  represents the energy of the initial state, while  $E_i - \hbar\omega$  corresponds to the energy of the final (tip) state.

It is worthy to mention that the electron mass  $m_e$  present in equations (5.22) and (5.23), as well as in eq. (5.19), corresponds to the free-electron mass since it is the mass of an electron tunneling in the junction. However, it has been determined that for  $\kappa_i^*(z=0)$  with  $z=0$  corresponding to the position of the initial state, the electron mass considered will be the effective electron mass of the initial  $MoSe_2$  state  $m_i^*$ :

$$\kappa_i(z=0) = \frac{\sqrt{2m_i^*(E_F + \phi^{Au} + \chi^{MoSe_2} - \phi^{Au} - eV_s - E_i)}}{\hbar} \quad (5.24)$$

Even though the initial states are described by the same simplified wavefunction, introducing  $m_i^*$  which is specific for each initial state, will provide a more refined description of the system and a more accurate comparison of the radiated power obtained for each case. Indeed, through the energy  $E_i$  and effective mass  $m_i^*$ , the tunneling term  $M_i$  computed for each initial state will be different. The values of  $m_i^*$  considered are extracted from the literature:  $m_{i=C}^*/m_e = 0.8$  for the conduction band state [14],  $m_{i=V_A}^*/m_e = 0.67$  and  $m_{i=V_B}^*/m_e = 0.75$  for both states at the valence band [15]. The same approach could be conducted for  $\kappa_i^*(z=d)$  with  $z=d$  corresponding to the position of the tip (final state) but as mentioned earlier, the effective mass of an electron in the bulk gold tip is assumed to be equal to the free-electron mass.

Using the wavefunctions described above, equation (5.19) becomes:

$$M_i(z_o, V_s, \omega) = \frac{C_i C_t A}{\sqrt{V_{MoSe_2} V_{tip}}} T_i(z_o, V_s, \omega) \delta_{\mathbf{k}_{\parallel i}, \mathbf{k}_{\parallel t}} \quad (5.25)$$

with  $A$  the tunneling effective cross-section area. The conservation of parallel momentum of tunneling electrons is given by the term  $\delta_{\mathbf{k}_{\parallel i}, \mathbf{k}_{\parallel t}}$ . In reality, the emitted photons carry away a certain parallel momentum [2]. The tunneling term  $T_i(z_o, V_s, \omega)$  is given by:

$$T_i(z_o, V_s, \omega) = \frac{\hbar^2}{2m_e} \left( \frac{d\phi_t^*}{dz'} \phi_i - \phi_t^* \frac{d\phi_i}{dz'} \right) (z') \Big|_{z'=z_o} - \hbar\omega \int_0^d dz \Theta(z_o - z) \phi_t^* \phi_i(z) \quad (5.26)$$

The wavefunction derivation is provided as follows:

$$\frac{d\phi_i(z)}{dz} = \frac{\sqrt{\kappa_i^*(z=0)}}{\sqrt{\kappa_i^*(z)}} e^{-\int_0^z \kappa_i^*(z') dz'} \left( -\frac{\kappa_i^*(z)'}{2\kappa_i^*(z)} - \kappa_i^*(z) \right) \quad (5.27)$$

$$\frac{d\phi_t(z)}{dz} = \frac{\sqrt{\kappa_t^*(z=d)}}{\sqrt{\kappa_t^*(z)}} e^{-\int_z^d \kappa_t^*(z') dz'} \left( -\frac{\kappa_t^*(z)'}{2\kappa_f(z)} + \kappa_t^*(z) \right) \quad (5.28)$$

Thus,  $T_i(z_o, V_s, \omega)$  becomes:

$$\begin{aligned} T_i(z_o, V_s, \omega) = & \frac{\hbar^2}{2m_e} \frac{\sqrt{\kappa_i^*(0)}}{\sqrt{\kappa_i^*(z_o)}} e^{-\int_0^{z_o} \kappa_i^*(z') dz'} \frac{\sqrt{\kappa_t^*(d)}}{\sqrt{\kappa_t^*(z_o)}} e^{-\int_{z_o}^d \kappa_t^*(z') dz'} \left( -\frac{\kappa_t^*(z_o)'}{2\kappa_t^*(z_o)} + \kappa_t^*(z_o) + \frac{\kappa_i^*(z_o)'}{2\kappa_i^*(z_o)} + \kappa_i^*(z_o) \right) \\ & - \hbar\omega \int_0^{z_o} dz \frac{\sqrt{\kappa_i^*(0)}}{\sqrt{\kappa_i^*(z)}} e^{-\int_0^z \kappa_i^*(z') dz'} \frac{\sqrt{\kappa_t^*(d)}}{\sqrt{\kappa_t^*(z)}} e^{-\int_z^d \kappa_t^*(z') dz'} \end{aligned} \quad (5.29)$$

In Aizpurua model [3], the tip wavefunction is described using Tersoff and Hamann theory (see equation (1.12) in section 1.1.1 of Chapter 1). In this approach, the tip is assumed to be locally spherical and the tip wavefunctions are approximated by s-wave solutions of a spherical potential well. However, in the gap along the z-direction, WKB solutions are employed resulting in a tunneling matrix element  $M_{fi}$  expression that involves a constant multiplied by  $T_{fi}(z_o, \omega)$ , similar to the expression of equation (5.25). In addition, the  $T_{fi}(z_o, \omega)$  expression derived by Aizpurua *et al.* aligns in form with the  $T_i(z_o, V_s, \omega)$  obtained by our model.

The constants present in the  $M_i$  expression of eq. (5.25) are removed from the radiated power expression when the latter is normalized by the elastic current. Indeed, the tunneling term  $M_i$  in the elastic current expression can be written as:

$$M_i\left(\frac{d}{2}, V_s\right) = \frac{C_i C_t A}{\sqrt{V_{MoSe_2} V_{tip}}} T_i\left(\frac{d}{2}, V_s\right) \delta_{\mathbf{k}_{\parallel i}, \mathbf{k}_{\parallel t}} \quad (5.30)$$

with

$$T_i\left(\frac{d}{2}, V_s\right) = \frac{\hbar^2}{2m_e} \frac{\sqrt{\kappa_i^*(0)}}{\sqrt{\kappa_i^*\left(\frac{d}{2}\right)}} e^{-\int_0^{\frac{d}{2}} \kappa_i^*(z') dz'} \frac{\sqrt{\kappa_t^*(d)}}{\sqrt{\kappa_t^*\left(\frac{d}{2}\right)}} e^{-\int_{\frac{d}{2}}^d \kappa_t^*(z') dz'} \left( -\frac{\kappa_t^*\left(\frac{d}{2}\right)'}{2\kappa_t^*\left(\frac{d}{2}\right)} + \kappa_t^*\left(\frac{d}{2}\right) + \frac{\kappa_i^*\left(\frac{d}{2}\right)'}{2\kappa_i^*\left(\frac{d}{2}\right)} + \kappa_i^*\left(\frac{d}{2}\right) \right) \quad (5.31)$$

In the elastic case,  $\kappa_i^*$  and  $\kappa_t^*$  differ only in the effective mass of the electrons when  $z=0$ , since the tip state energy is equal to the initial state energy. The expression of the radiated power normalized by the elastic current results in:

$$\frac{d^2 P}{d\Omega d(\hbar\omega)} / I_{elas} = \frac{\frac{\alpha}{\hbar} \left(\frac{\omega}{c}\right)^2 \overbrace{\rho_t(E_i - \hbar\omega) [f(E_i + eV_s) - f(E_i - \hbar\omega)]}^{JDOS(\omega, V_s)} \left| \int_0^d dz_o G(z_o, \omega) T_i(z_o, V_s, \omega) \right|^2}{\frac{4\pi e}{\hbar} \rho_t(E_i) [f(E_i + eV_s) - f(E_i)] \left| T_i\left(\frac{d}{2}, V_s\right) \right|^2} \quad (5.32)$$

In order to simplify the calculations, it is assumed that  $\kappa_{i,t}^*(z)$  does not depend on the parallel momentum and thus,  $\kappa_{i,t}^*(z) = \kappa_{i,t}(z)$ . In the next section, the characteristics of the tunneling quantity  $T_i$  computed for each initial state, are investigated.

As presented above, the tunneling matrix  $M$  is computed using a simple description of the final and initial states wavefunctions and in addition, several assumptions are made. This simplified representation of the complex tunneling process is as well considered in the excitonic emission process (see next section of this chapter) enabling a fair and consistent comparison between plasmonic and excitonic light emission processes. However, the comparison with the experimental light emission results of Chapter 3 can only be done in a qualitative manner due to the relative simplicity of our model. This comparative analysis is carried out in the last part of this chapter.

It is worthy to mention that for an accurate comparison, a more sophisticated model would be necessary, accounting for a three-dimensional potential barrier and taking into account the parallel momentum in the inverse decay length of the initial and tip states wavefunctions. In fact, the latter point is particularly crucial for the  $MoSe_2$  states as they are located at  $K$  points of the first Brillouin Zone, thereby exhibiting significant  $k_{\parallel}$ . Moreover, it will as well be interesting to describe the initial and final states wavefunctions by a linear combination of atomic orbitals, s-type orbitals for the gold tip states and mixed d and p orbitals for the  $MoSe_2$  states. This approach is specially compelling considering that, as discussed in section 1.2.2 of Chapter 1, the conduction and valence bands of the monolayer are composed of distinct orbital states. Adopting this approach could facilitate a more precise comparison of the radiated power acquired for each initial state. Incorporating all these elements in the  $M$  calculation could give rise to a more realistic description of the tunneling process. However, it is important to point out that the implementation of these elements demands a substantial investment of time, effort, and potentially resources. Given these challenges, a careful evaluation is required to determine whether the accuracy gained from this approach justifies the significant investment.

### 5.1.3 Spectral analysis of the plasmonic light emission

As mentioned before, the plasmonic light emission process is governed by inelastic electron tunneling and the electromagnetic properties of the gap. To gain a deeper understanding of these critical elements, the field enhancement  $G$  and the tunneling term  $T_i$  characteristics are investigated as a function of the main tunneling parameters: the tip-surface distance  $d$  and the bias voltage  $V_s$ . This analysis constitutes the initial part of this section and is expected to offer valuable insights into the spectral features of

the calculated radiated power spectra. The latter are studied in greater detail in the last part of this section.

### a) Field enhancement $G$ in the gap

The characteristics of the field enhancement  $G$ , defined as the modulus  $\left| \frac{\mathbf{E}}{\mathbf{E}_{inc}} \right|$  in the gap are here addressed. In particular, its spatial distribution as well as its spectral features with respect to the incident electric field polarization and the tip-surface distance  $d$  are investigated. It is important to note that since electron tunneling is crucial for light emission, tip-surface distances in the tunneling regime ( $d < 0.5$  nm) are considered. As mentioned before, the dependence of  $G$  on the bias voltage  $V_s$  is negligible, according to the discussion of section 4.4.1 of the previous chapter, and thus, it is not evaluated. The hybrid tunneling junction considered here involves a flat substrate such as the modeled junction presented in section 4.1 (Fig. 4.3).

In a first step, the spatial distribution of  $G$  in the gap along the  $z$ -direction is analyzed. It is calculated using an incident p- or s-polarized electric field impinging on the junction with an incidence angle of  $\theta = 45^\circ$  and a tip-surface distance set to  $d = 0.2$  nm. In Figure 5.3-(A,B), this distribution as a function of the energy of the incident electric field ranging from 1.38 eV (900 nm) to 3.1 eV (400 nm) for both polarizations is depicted. The enhancement maps obtained show that the electric field induced within the gap exhibits a non-uniform distribution, and in addition, its intensity depends on the incident electric field energy. Indeed, for p-polarization, a strong electric field localized at the middle of the gap is induced for  $\hbar\omega \sim 1.7$  eV. On the other hand, in the case of s-polarization, an electric field is generated at a lower energy, predominantly concentrated near the  $MoSe_2$  surface. The electromagnetic properties of the gap depend thus on the position  $z$  and the energy  $\hbar\omega$ . This means that, based on the precise location (within the gap) where the inelastic process occurs during tunneling, and on the energy lost during this process, the electromagnetic modes excited in the gap will be different leading to a more or less favorable electron-to-photon conversion.

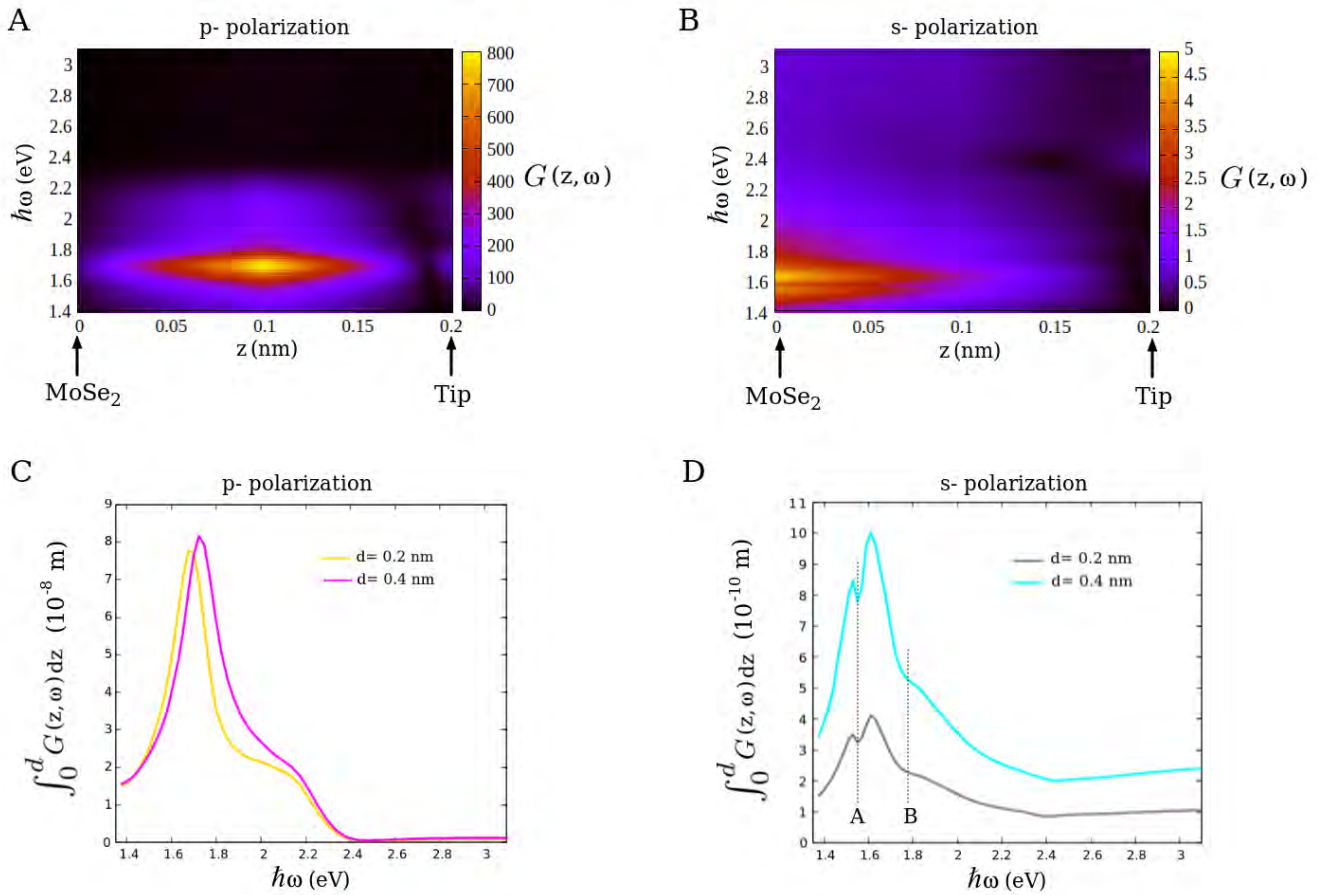


**Figure 5.3:** (A-B) Electric field enhancement  $G$  calculated in the gap along the  $z$ -direction (perpendicular to the monolayer surface) as a function of the energy of the incident p- (A) or s- (B) polarized electric field. The tip and the monolayer are separated by a distance of  $d = 0.2$  nm and their positions on each side of the gap are indicated by arrows. (C-D) Electric field enhancement  $G$  integrated over  $z$  for p- (C) and s- (D) incident polarizations. The integral is evaluated for two different tip-surface distances:  $d = 0.2$  nm and  $d = 0.4$  nm. In (D), the dips at the A- and B-exciton energies are indicated by dashed lines.

To examine the spectral characteristics of  $G$  and its relationship with the tip-surface distance  $d$ , the integral of  $G$  over  $z$  with  $z$  ranging from 0 ( $\text{MoSe}_2$  position) to  $d$  (tip position) is calculated. This choice is motivated by the fact that, in the expression of the radiated power in equation (5.32), the field enhancement  $G$  is integrated over the gap thickness along the  $z$ -direction. Figure 5.3-(C,D) presents the value of this integral as a function of  $\hbar\omega$ , computed for both polarizations of the incident electric field and two tip-surface distances. The resulting spectra are very similar to the near-field optical response of the junction evaluated in Chapter 4 (see section 4.2.2). Thus, the spectral characteristics can be easily identified. For p-polarization, the gap plasmon resonances at 1.67 eV (740 nm) for  $d = 0.2$  nm and at 1.72 eV (720 nm) for  $d = 0.4$  nm are observed. Moreover, a distinctive shoulder around 2.15 eV, attributed to the tip apex plasmon mode, is discernible. These resonances have been discussed in section 4.2.2 of the previous chapter. In the case of s-polarization, the Fano-type interferences are observed exhibiting dips at the A- and B-excitons energies (Figure 5.3-D). These interferences, exhaustively analyzed in the previous chapter, arise from the coupling between the substrate transverse

LSPR and excitons. The field associated with this coupling is mainly localized within the substrate and the TMD monolayer (see Fig. 4.10), and extends along the gap as shown in Figure 5.3-(B). Among the electromagnetic modes mentioned here, only the energy of the gap plasmon resonance is dependent on the tip-surface distance  $d$ . Indeed, as  $d$  decreases, the gap plasmon resonance redshifts. On the other side, the value of the integral of  $G$  over  $z$  increases in general with the tip-surface distance for both polarizations. This effect arises because the integration is performed over a broader range of  $z$  as  $d$  increases. Although the intensity of the gap plasmon resonance is stronger for  $d= 0.2$  nm than for  $d= 0.4$  nm due to a more confined gap (as depicted in Fig. 4.18-B), when considering the integral over  $z$ , this difference in intensity is compensated for, and is not obvious in Fig. 5.3-C. It is worthy to point out that the spectra of the integral of  $G$  computed for both incident polarizations exhibit a minimum around  $\sim 2.5$  eV. This minimum can be attributed to two different factors: either the interaction between the plasmonic modes with C-excitons leading to interferences with a dip at approximately 2.6 eV (C-excitons energy), or it could be due to a field enhancement node associated with the finite size of the tip, and localized under the tip apex at this energy. This node can be slightly distinguished in the enhancement map for s-polarization (Fig. 5.3-B), where the electric field enhancement is found to be close to zero at  $z \sim 0.13$  nm and at the incident energy of approximately 2.5 eV.

### b) Tunneling term $T_i$

In addition to the electromagnetic properties of the gap, an important element characterizing the plasmonic light emission process is the inelastic tunneling. In the radiated power expression of equation (5.32), the inelastic tunneling term  $T_i(z, V_s, \omega)$  relies on several parameters: the initial state  $i$  considered, the emitted photon energy  $\hbar\omega$  evaluated in the visible range (between 1.38 eV and 3.1 eV), the point in the gap  $z$  where it is calculated (denoted  $z_o$  in the radiated power expression) and the bias voltage  $V_s$ . An analysis is conducted to investigate how this term behaves with respect to these parameters in comparison to its elastic counterpart computed at the midpoint of the gap, denoted as

$$T_i\left(\frac{d}{2}, V_s\right).$$

Firstly, as done for the field enhancement  $G$ , the spatial distribution of the inelastic term  $T_i(z, V_s, \omega)$  in the gap along  $z$  is evaluated. This distribution, displayed in Figure 5.4-A, is computed as a function of the emitted photon energy considering the conduction band minimum as the initial state, a bias voltage of  $V_s= -4$  V and a tip-surface distance of  $d= 0.2$  nm. The inelastic tunneling term  $T_i$  exhibits a relatively uniform behavior within the gap along  $z$ . Indeed, it appears to have a weak dependence on the location  $z$  in the gap, except for the region close to the tip. In fact, for  $z$  exceeding 0.15 nm, the inelastic tunneling term is significantly reduced. This phenomenon can be explained by examining the expression of  $T_i(z, V_s, \omega)$ :

$$\begin{aligned}
T_i(z, V_s, \omega) = & \frac{\hbar^2}{2m_e} \frac{\sqrt{\kappa_i^*(0)}}{\sqrt{\kappa_i^*(z)}} e^{-\int_0^z \kappa_i^*(z') dz'} \frac{\sqrt{\kappa_t^*(d)}}{\sqrt{\kappa_t^*(z)}} e^{-\int_z^d \kappa_t^*(z') dz'} \left( -\frac{\kappa_t^*(z)'}{2\kappa_t^*(z)} + \kappa_t^*(z) + \frac{\kappa_i^*(z)'}{2\kappa_i^*(z)} + \kappa_i^*(z) \right) \\
& - \hbar\omega \int_0^z dz' \frac{\sqrt{\kappa_i^*(0)}}{\sqrt{\kappa_i^*(z')}} e^{-\int_0^{z'} \kappa_i^*(z'') dz''} \frac{\sqrt{\kappa_t^*(d)}}{\sqrt{\kappa_t^*(z')}} e^{-\int_{z'}^d \kappa_t^*(z'') dz''}
\end{aligned} \tag{5.33}$$

This expression consists of two terms: the first term does not depend directly on the photon energy, unlike the second one. The variation of  $T_i(z, V_s, \omega)$  with respect to  $z$  is mainly attributed to the second term. For large values of  $z$ , the integral of the second term is performed over a broader range and thus, its value increases. This increment leads to a decrease of the overall tunneling term  $T_i$  observed in the spatial distribution of Fig. 5.4-A. This behavior can be interpreted as a diminution of the probability for an electron to undergo an inelastic process (loss of energy) as it tunnels from the monolayer to the tip, i.e, as  $z$  increases. Another observed trend is the decrease of  $T_i(z, V_s, \omega)$  as the energy of the emitted photons  $\hbar\omega$  increases. This can also be attributed to the increasing contribution of the second term of the previous equation, which depends directly on the photon energy, as  $\hbar\omega$  increases. It is worthy to note that for the spatial distribution, the inelastic tunneling term  $T_i(z, V_s, \omega)$  is normalized by its elastic counterpart computed at the middle of the gap and not depending of  $z$ . For any values of  $z$  and  $\hbar\omega$ , the normalized tunneling term  $T_i(z, V_s, \omega)/T_i(\frac{d}{2}, V_s)$  remains below unity, indicating that inelastic tunneling processes are less likely to occur than elastic tunneling processes. Furthermore, when an inelastic tunneling process does occur, the smaller the energy lost by the electron, the higher the possibility of this phenomenon happening.

After the evaluation of its dependence on  $z$ , the evolution of the inelastic tunneling term  $T_i$  concerning the initial state  $i$  and the bias voltage  $V_s$  is investigated. As discussed above, three initial states for inelastic tunneling are considered: the conduction band minimum (CBM) and the maximum of each valence sub-band, labeled as “valence band A” and “valence band B”. For each of these initial states, the inelastic tunneling term  $T_i(z, V_s, \omega)$  is calculated for  $z = \frac{d}{2}$ ,  $d = 0.2$  nm and  $V_s = -4$  V. The resulting  $T_i$  as a function of the photon energy  $\hbar\omega$  are depicted in Figure 5.4-B. In addition, the inelastic tunneling term considering the CBM as the initial state for a bias voltage of  $V_s = -2$  V is as well computed and displayed in the same plotting in order to evaluate the impact of  $V_s$ . Each inelastic tunneling term is normalized by its respective elastic counterpart. Since the theoretical light emission spectra, which are analyzed later, involve the normalization of the radiated power with respect to the elastic current, the normalization process carried out here is essential for establishing a connection between the properties of the tunneling term under investigation and the characteristics of the resulting light emission spectra. No particular differences are observed among the normalized  $T_i(\frac{d}{2}, V_s, \omega)$  calculated for each initial state. They exhibit a similar decreasing trend as the energy  $\hbar\omega$  increases. Furthermore, as  $\hbar\omega$  tends to zero, the inelastic term converges toward its elastic counterpart, causing  $T_i(\frac{d}{2}, V_s, \omega)/T_i(\frac{d}{2}, V_s)$  to approach 1.

Both inelastic and elastic tunneling terms  $T_i$  depend on the initial state considered through the energy  $E_i$  and the effective mass  $m_i^*$  present in the expression of the inverse decay length of the initial and tip states  $\kappa_{i,t}^*$  (see equations (5.22), (5.23) and (5.24)). However, the way they depend on these quantities is different. Nonetheless, it is highlighted that, regardless of the specific initial state being considered, the relationship between the inelastic and elastic tunneling terms remains almost unchanged. In other words, while the absolute values of these terms may vary with different initial states, their relative ratios remain the same.

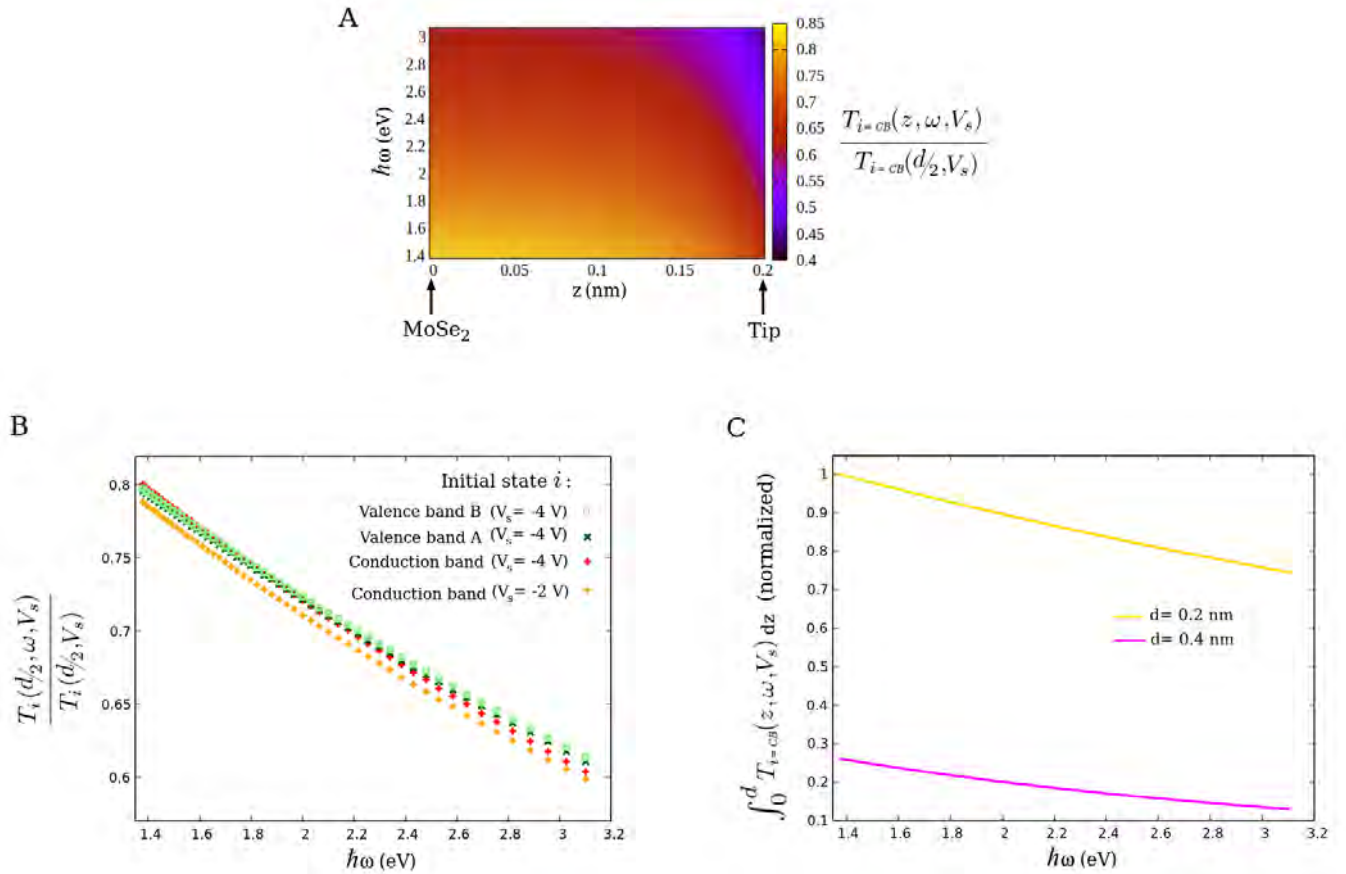


**Figure 5.4:** (A) Normalized tunneling term  $T_i(z, V_s, \omega)$  calculated in the gap along the  $z$ -direction as a function of the photon energy  $\hbar\omega$  considering the conduction band minimum as initial state. The normalization is performed with respect to the elastic  $T_i$  computed at  $z = d/2$ . The tip-surface distance is set to  $d = 0.2$  nm and the bias voltage used is  $V_s = -4$  V. (B) Inelastic tunneling term  $T_i$  computed at  $z = d/2$  and normalized with respect to its elastic counterpart for different initial states  $i$  with a tip-surface distance and bias voltage set to  $d = 0.2$  nm and  $V_s = -4$  V. Additionally, the normalized tunneling term computed considering the conduction band minimum as the initial state and a bias voltage of  $V_s = -2$  V is plotted (orange points) to assess the impact of  $V_s$ . (C) Inelastic tunneling term  $T_i$  integrated over  $z$  for two different tip-surface distances:  $d = 0.2$  nm and  $d = 0.4$  nm. The integrals are calculated for a bias voltage of  $V_s = -4$  V and considering the conduction band minimum as initial state. They are normalized by the maximum value of the integral obtained for  $d = 0.2$  nm.

When employing a bias voltage of  $V_s = -2$  V, a slightly reduced normalized inelastic tunneling term  $T_i$  is observed compared to when a bias voltage of  $V_s = -4$  V is applied. This implies that, as the

absolute value of the bias voltage decreases, the probability for electrons to undergo inelastic tunneling becomes smaller in comparison to the probability for them to undergo elastic tunneling. However, given the small difference in the obtained normalized  $T_i$  when varying the bias voltage by a factor 2, the role of  $V_s$  on the normalized tunneling term is considered as negligible.

Finally, the inelastic tunneling term  $T_i$  is evaluated as a function of the tip-surface distance  $d$ . For this, as done for the field enhancement  $G$ , an integration of  $T_i(z, V_s, \omega)$  over the  $z$  variable is performed for two distinct tip-surface distances. It is worth noting that in the radiated power expression (eq. (5.32)),  $T_i$  is subjected to the same integration. In order to evaluate the role of  $d$  on the inelastic tunneling term  $T_i$ , it is decided not to normalize it with respect to the elastic tunneling term. This choice is motivated by the subsequent investigation, where the radiated power itself is evaluated rather than its normalized value when examining the influence of  $d$  on the properties of the light emission spectra. This decision is based on the observation that, for a given bias voltage  $V_s$ , a change in  $d$  (by adjusting the tunneling current) primarily affects the number of electrons involved in the tunneling process. Indeed, as  $d$  varies, the overlap of electronic wavefunctions between the tip and the monolayer states also changes, leading to fluctuations in the probability of electron tunneling. Thus, in order to appropriately analyze the relation between the amount of tunneling electrons with the amount of emitted photons, the study of the radiated power not normalized by the elastic current as a function of  $d$  is carried out. This analysis will facilitate a more straightforward comparison with the experimental results, which will be conducted in the final part of this chapter. In Figure 5.4-C, the resulting integrals of  $T_i(z, V_s, \omega)$  over  $z$  for  $d= 0.2$  and  $0.4$  nm as a function of  $\hbar\omega$  are presented. These integrals are normalized by the maximum value obtained for  $d=0.2$  nm. As  $\hbar\omega$  increases, there is a corresponding decrease in the value of the integral for both tip-surface distances under consideration. This decrease can be attributed to the fact that, as discussed earlier, an increase in the energy lost during the inelastic tunneling process reduces the probability of this phenomenon to occur. Furthermore, when  $d$  increases from  $d= 0.2$  nm to  $d= 0.4$  nm, even though the integration range over  $z$  expands, the value of the obtained integral is smaller for all values of  $\hbar\omega$ . This indicates that, as  $d$  increases, the inelastic electron tunneling process becomes less probable, as expected, due to the weakening of the overlap between the initial and final states wavefunctions.

### c) Radiated Power

The spectral characteristics of the plasmonic light emission are here analyzed. Specially, the spectra dependence with respect to the bias voltage  $V_s$  and to the tip-surface distance  $d$  is studied. Moreover, a comparison is made between the light emission spectra obtained for each initial state under consideration.

Figure 5.5 displays the evolution of the radiated power (normalized by its corresponding elastic current) calculated for each initial state as a function of the bias voltage  $V_s$ . Furthermore, this figure also presents the total radiated power, which is determined by adding the normalized radiated power obtained for each initial state. This approach ensures that the contribution to the total radiated power from each

initial state is appropriately weighted by its corresponding elastic current.

The plasmonic light emission spectra present a high-energy quantum cutoff associated with the bias voltage. This energy threshold varies depending on the specific initial state considered. As described in the first part of this section (Fig. 5.1), the energies of the initial states are defined by the bias voltage  $V_s$  but differently for each state. When the conduction band minimum (CBM) is considered as the initial state, the quantum cutoff is observed at  $\hbar\omega = e|V_s|$ . Indeed, the energy of this state is determined by  $E_C = E_F - eV_s$  and thereby, the maximum energy that can be lost during an inelastic tunneling transition from this state to a tip state is equal to  $e|V_s|$ . On the other hand, when the initial state for inelastic tunneling is one of the two considered valence sub-band maxima, the maximum energy of an emitted photon is given by  $E_{V_{A,B}} - E_F = -\hbar\omega_{ex_{A,B}} - eV_s$  with  $\hbar\omega_{ex_A} = 1.55$  eV and  $\hbar\omega_{ex_B} = 1.77$  eV being the energies of the A- and B-excitons, respectively. For  $V_s = -2$  V, this maximum energy falls within the infrared region and thus, there is no light emission within the visible range (Fig. 5.5-A). For  $V_s = -3$  V, the maximum energy of an emitted photon according to the previous relationships, is 1.45 eV for the valence band A and 1.23 eV for the valence band B. However, the observed quantum cutoff in Figure 5.5-B are located at higher energies. This disparity is due to the occupation factor of these valence bands, which is equal to 1, allowing inelastic transitions from these states to tip states below the Fermi level (see equation (5.12) and (5.13)). This results in the emission of photons with energies exceeding  $E_{V_{A,B}} - E_F$ . It is worthy to note that, since the CBM is aligned with the sample Fermi level, its occupation factor is equal to 0.5 at room temperature. Therefore, there is no discrepancy between the observed quantum cutoff and the energy difference between this state and the tip Fermi level. Thus, one can say that the quantum cutoff for each initial state is determined by its joint density of state JDOS defined earlier. For  $V_s = -4$  V, the energy threshold for the CBM is not observed since it exceeds the range of photon energies under investigation. The same behavior described before is observed for both valence bands.

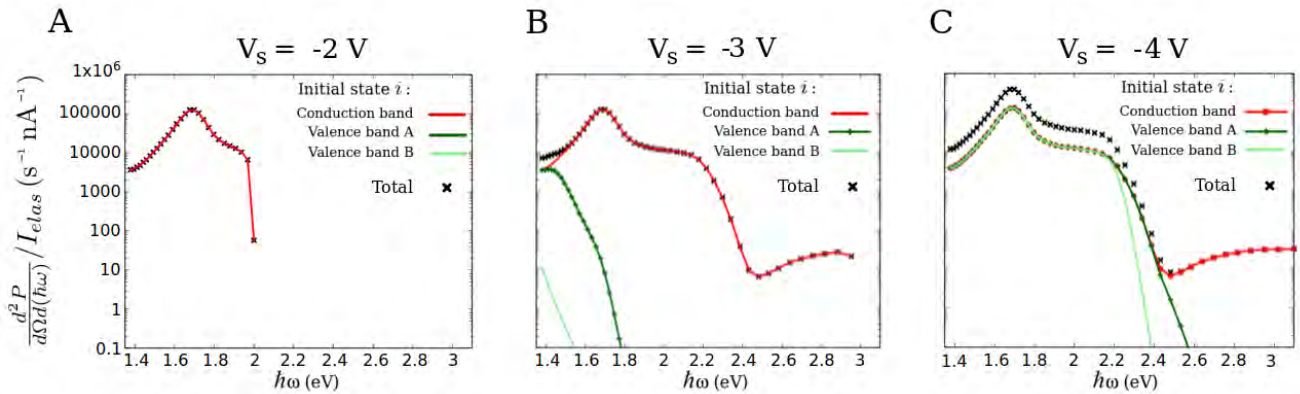


**Figure 5.5:** Radiated power normalized by the elastic current (in log scale) calculated for three bias voltages:  $V_s = -2$  V (A),  $V_s = -3$  V (B), and  $V_s = -4$  V (C). The conduction band minimum (shown in red) and the maximum of each valence sub-band (in dark and light green) are considered as initial state. The black crosses represent the total radiated power, obtained by summing the radiated power from each of these three initial states. The tip-surface distance is set to  $d = 0.2$  nm. These calculations account for the electric field enhancement in the gap, computed using an incident p-polarized electric field.

For each initial state, a quantum cutoff exists, which shifts to higher energies as the absolute value of  $V_s$  increases, resulting in the gradual emergence of emission peaks. Once these peaks appear in the spectra, their intensities increase slightly with  $|V_s|$ . Moreover, it is observed that for a sufficiently high value of  $|V_s|$  (see Fig. 5.5-C), the same spectral features are obtained for each initial state. A detailed analysis of this lineshape is provided below. It is further noted that for a bias voltage close to 0, the total radiated power is nearly identical to the radiated power obtained when considering the CBM as initial state, as the contribution of the other initial states is very low or absent in the visible range. Then, as  $|V_s|$  increases, the contribution of the radiated power obtained for both valence bands becomes more significant, leading to a more intense total radiated power.

Finally, the dependence of plasmonic light emission spectra on the tip-surface distance  $d$  is examined. As mentioned earlier, it has been decided to evaluate this dependence by analyzing the radiated power itself, rather than its normalized value. This approach is considered more suitable for studying the relation between the amount of emitted photons and the amount of tunneling electrons. Firstly, the spectral lineshape obtained for different  $d$  is analyzed. To do so, the total radiated power, computed by summing the radiated power of each initial state, is calculated considering two different tip-surface distances:  $d=0.2$  and  $0.4$  nm. The obtained total radiated powers are then normalized with respect to their respective maximum values and plotted in Figure 5.6. A bias voltage of  $V_s=-4$  V is used to avoid the presence in the resulting spectra of a quantum cutoff in the spectral range under investigation. The spectra are calculated for the two polarizations of the incident electric field used to compute the field enhancement in the gap.

The resulting spectra of Fig. 5.6 exhibit strong similarities with the spectra obtained when analyzing the integral over  $z$  of  $G$ , the field enhancement in the gap (see Fig. 5.3-(C,D)). For p-polarization, the gap plasmon modes resonance (at 1.67 eV and 1.72 eV for  $d=0.2$  and  $0.4$  nm, respectively) and the tip apex plasmon mode shoulder around 2.15 eV are observed. On the other hand, for s-polarization, the Fano-type interferences with dips at the A- and B-exciton energies are evident. Additionally, both insets, where these spectra are displayed in a semi-logarithmic scale, reveal the distinct presence of a dip at approximately 2.5 eV, which may be attributed to an interaction between plasmon modes and C-excitons or to a field enhancement node in the gap. All these spectral features, analyzed above, share the same energy as those observed in the integral of  $G$  spectra. Despite the presence of other terms in the radiated power expression (equation (5.32)) that depend on  $\hbar\omega$ , the spectral characteristics of the plasmonic light emission spectra are mainly governed by the field enhancement in the gap  $G$ . However, it is worth noting that the relative intensities of the observed spectral features may differ from those in Figure 5.3-(C,D). For example, the relative difference between the maximum of the gap plasmon resonance and the shoulder at higher energy is considerably larger than what is observed in the integral of  $G$ . This can primarily be attributed to the squaring of the integral of  $G$  weighted by the inelastic term  $T$  in the radiated power expression.

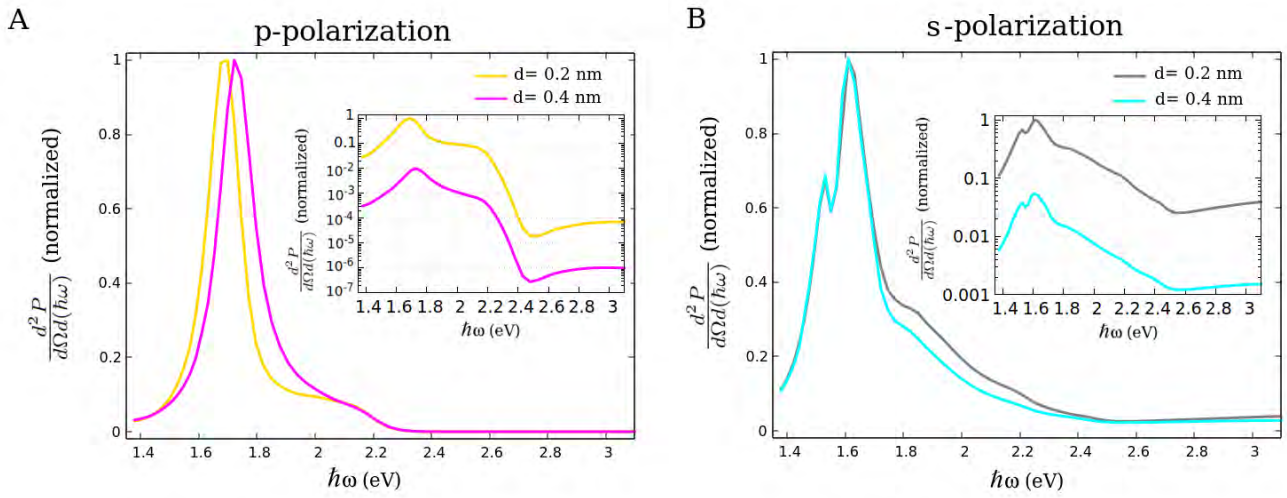


**Figure 5.6:** Total radiated power, normalized by its respective maximum, calculated for two tip-surface distances:  $d = 0.2$  and  $0.4$  nm. Inset: Total radiated power, normalized with respect to the maximum value obtained for  $d = 0.2$  nm. An incident p- (A) and s- (B) polarized electric field is used to compute the electric field enhancement in the gap included in the radiated power calculations. The bias voltage is set to  $V_s = -4$  V.

Thus, each emission peak observed in the plasmonic light emission spectra corresponds to an excited electromagnetic mode. Some of these modes may show energy dependence on the tip-surface distance  $d$ , as is the case of gap plasmon mode. Indeed, the resonance of the latter blueshifts when  $d$  changes from  $0.2$  nm to  $0.4$  nm, as evidenced by the spectra obtained for p-polarization (Fig. 5.6-A). The energy of the other observed spectral features does not appear to have a significant dependency on  $d$ .

In the insets of Fig. 5.6, the total radiated powers are plotted but this time, their normalization is performed with respect to the maximum value obtained for  $d = 0.2$  nm, allowing a comparison of the plasmonic light emission intensity as  $d$  varies. In fact, when  $d$  increases from  $d = 0.2$  to  $0.4$  nm, the plasmonic contribution decreases substantially. For p-polarization, the light emission spectrum obtained for  $d = 0.2$  nm is nearly 100 times more intense than that obtained for  $d = 0.4$  nm. For s-polarization, this difference is on the order of a few tens. This significant difference is mainly assigned to the substantial reduction in the inelastic tunneling term  $T_i$  observed in Fig. 5.4-C as  $d$  increases. Hence, a more effective light emission process takes place when  $d$  is small. As previously discussed, as  $d$  decreases, the probability of electron tunneling increases, and this leads to a greater number of emitted photons.

## 5.2 Light emission from exciton radiative recombination: Excitonic Emission.

This section deals with the light emission process arising from the radiative decay of excitons within the  $MoSe_2$  monolayer. As previously mentioned, experimental STM-LE measurements, as those described in Chapter 3, have been conducted on n-doped  $MoSe_2$  monolayers exhibiting an excess of electrons. Through STM electron tunneling, holes are injected in the valence band of the monolayer, which along with the conduction electrons already present, give rise to the formation of excitons. These excitons,

once generated, may decay radiatively leading to the emission of light observed. In this section, a theoretical model is introduced to provide a comprehensive understanding of this phenomenon. In fact, this model is specially designed to describe the excitonic radiative process taking place within the TMD monolayer of a hybrid  $Au/MoSe_2/Au$  tunneling junction. In the initial part, a description of this model will be presented, as well as the mathematical formalism proposed to explain this light emission process. Finally, the main spectral characteristics of the resulting light emission spectra are investigated.

### 5.2.1 Model Description

The model presented here aims to describe the radiative process resulting from the recombination of A- and B-excitons within a  $MoSe_2$  monolayer. The latter is considered to be supported by a gold substrate which along with a gold tip, forms an STM junction. The energy band diagram of this junction is displayed in Figure 5.7 showing a negatively biased sample ( $V_s < 0$ ) allowing hole injection into the monolayer. Moreover, the radiative electron-hole recombination of excitons giving rise the emission of photons with an energy  $\hbar\omega$  is represented by a brown arrow for A-excitons and a yellow arrow for B-excitons. It is considered that the energy levels involved in the decay of these excitons are: the conduction band minimum with an energy  $E_C$  (depicted by a red line), the state at the maximum of the valence sub-band with an energy  $E_{V_A}$  (dark green line) for A-excitons, and the valence sub-band state with an energy  $E_{V_B}$  (light green line) for B-excitons. In the previous section, the energies of these states with respect to the Fermi level have been defined, along with the following relations:  $E_C - E_{V_A} = 1.55$  eV and  $E_C - E_{V_B} = 1.77$  eV corresponding to the A- and B-excitons energy, respectively [6].

The formation of excitons and thus, their recombination, can only occur when holes are created within the valence band. These holes result from electron tunneling, involving both elastic and inelastic processes, occurring along the z-direction between the  $MoSe_2$  monolayer at  $z = 0$  and the gold tip at  $z = d$ . In particular, electron tunneling from the maxima of the valence sub-bands “A” and “B” of the TMD monolayer to the tip is considered, as indicated by the green arrows in the energy band diagram of Fig. 5.7. Elastic and inelastic tunneling, crucial for the excitonic radiative process, are taken into account in the theoretical light emission calculations presented below. However, it is worthy to note that the energy of the emitted photons generated by inelastic tunneling within the gap (denoted  $\hbar\omega'$ ) is not included in the total energy radiated by the junction arising from the excitonic light emission process, only the energy of the photons resulting from the excitons radiative decay is taken into account. Moreover, for holes to be created in the valence sub-bands, the energy of the latter must be higher than the tip Fermi level and thus, the condition  $-eV_s > 1.55$  eV is required for the radiative decay of A-excitons. Similarly, for the radiative decay of B-excitons to occur,  $-eV_s > 1.77$  eV must be satisfied. Furthermore, it is assumed that every created hole directly results in the formation of an exciton. However, in reality, injected holes in the valence band may not always form excitons. Indeed, they can take different pathways, including interactions with other carriers or phonons, or be captured by defects, before combining with an excess electron to generate an exciton. Thus, this assumption, also employed

to describe electroluminescence from devices based on 2D TMDs as reported in [16, 17], results in an overestimation of the number of excitons formed within the TMD monolayer.

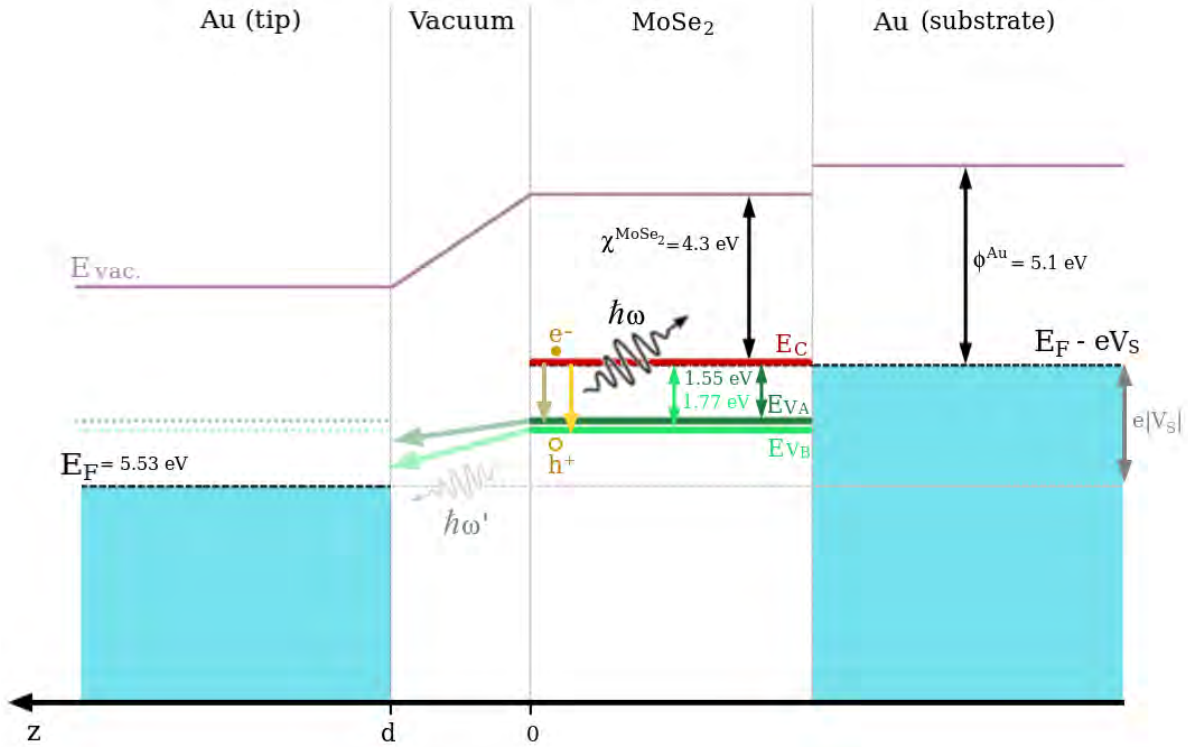


**Figure 5.7:** Energy band diagram of the hybrid  $Au/MoSe_2/Au$  tunneling junction with a negative bias voltage  $V_s$  applied to the gold substrate with respect to the tip. The radiative recombination of excitons (bound electron-hole pairs) within the monolayer is shown. The exciton decay process gives rise to the emission of photons characterized by the energy  $\hbar\omega$ . Particularly, the radiative decay of two distinct types of excitons (A- and B-excitons) is displayed. Their respective decays are visually represented by a brown and a yellow arrow. It is considered that the energy levels involved in the decay of A- and B-excitons are: the conduction band minimum with an energy  $E_C$  (depicted by a red line), the state at the maximum of the valence band with an energy  $E_{V_A}$  (dark green line) for A-excitons, and the valence band state with an energy  $E_{V_B}$  (light green line) for B-excitons. The radiative recombination of excitons is initiated by the creation of holes within the valence band. These holes are originating from elastic and inelastic electron tunneling occurring from the  $MoSe_2$  monolayer at  $z = 0$  to the gold tip at  $z = d$  (green arrows). The energy of the emitted photons resulting from inelastic electron tunneling is denoted  $\hbar\omega'$ .

The joint density of states, as defined in the previous section, is also incorporated into the presented model, particularly in the calculations of the probability of having holes in the monolayer valence band through electron tunneling.

In the formalism presented in the next part of this section, all the components involved in the excitonic light emission process, along with the assumptions made, are mathematically described. The radiative decay of excitons is calculated using Fermi golden rule considering a weak coupling between the excitons and the electromagnetic field. The model presented here takes into account the electromagnetic environment surrounding the exciton, utilizing the electromagnetic properties of the monolayer in this hybrid tunneling junction previously characterized (refer to Chapter 4). Moreover, electron tunneling is

described as discussed in the previous section and it is assumed that the junction is operating at room temperature.

### 5.2.2 Formalism

As was done in the previous section, the excitonic light emission process is evaluated in terms of radiated power. This power, denoted as  $P$ , is related to the rate of exciton radiative recombination (probability per unit time)  $\Gamma_{rad}$  as:

$$P(\omega) = \hbar\omega \Gamma_{rad}(\omega) \quad (5.34)$$

In order to trigger the radiative exciton recombination, the presence of a hole is required within one of the two considered valence states. This is taken into account in the calculation of the radiated power by incorporating the probability of a hole being present in the valence band (VB) generated by electron tunneling from the VB to the tip. The probability per unit time for an electron to tunnel from the VB to the tip is noted  $W_{tunnel}$ . Multiplying  $W_{tunnel}$  by the lifetime of the exciton  $\tau$ , results in  $W_{tunnel} \tau$  the number of tunneling transitions that would happen during the exciton lifetime. This latter can be separated into the non-radiative lifetime  $\tau_{nr}$  and the radiative lifetime  $\tau_r$  by the equation  $\frac{1}{\tau} = \frac{1}{\tau_{nr}} + \frac{1}{\tau_r}$ . For the A- and B-excitons of the  $MoSe_2$  monolayer,  $\tau_r$  significantly exceeds  $\tau_{nr}$  (see below). Thus, the exciton lifetime can be approximated by the non-radiative lifetime. This leads to the following expression for the radiated power:

$$P(\omega) = \hbar\omega \Gamma_{rad}(\omega) W_{tunnel} \tau_{nr} \quad (5.35)$$

According to this formulation, every created hole gives rise to an exciton. Nevertheless, as previously discussed, in reality, a created hole can take multiple distinct routes before ultimately combining with an electron to form an exciton. In a first step, all electronic transitions from the VB to the tip are supposed to be elastic.  $W_{tunnel}$  corresponds to the number of elastic tunneling electrons per unit of time and can be written as:

$$W_{tunnel} = \frac{dn_e}{dt} = \frac{I_{elas}}{e} \quad (5.36)$$

The expression of the elastic current  $I_{elas}$  has been developed in the previous section for the plasmonic emission formalism. Thus,  $W_{tunnel}$  can be expressed as follows:

$$W_{tunnel} = \frac{4\pi}{\hbar} \rho_t(E_i) [f(E_i + eV_s) - f(E_i)] \left| M_i \left( \frac{d}{2}, V_s \right) \right|^2 \quad (5.37)$$

Each term of this equation is elaborated upon in the preceding section, including the calculation of

the tunneling term  $M_i$ . The index  $i$  corresponds to the initial state of the elastic tunneling transition, which in the excitonic emission case corresponds to one of the two valence states under consideration.

By employing Fermi golden rule, it is possible to derive the rate of exciton radiative recombination [18]. The process of exciton decay can be interpreted as an electronic transition from a state at the conduction band  $|c\rangle$  to a state in the valence band  $|v\rangle$ . The probability per unit of time of this transition to occur is expressed as follows:

$$\Gamma_{rad}(\omega) = \frac{2\pi}{\hbar} |H_{vc}|^2 \delta(E_C - E_V - \hbar\omega) g(\hbar\omega) \quad (5.38)$$

where  $H_{vc} = \langle v | \hat{H}_{int} | c \rangle$  with  $\hat{H}_{int}$  the dipole interaction Hamiltonian which describes the coupling between the exciton and the local electric field of its environment. Using the electric dipole approximation, the Hamiltonian  $H_{vc}$  can be written as [18]:

$$H_{vc} = -\mathbf{d}_{cv} \cdot \mathbf{E} = -\mathbf{d}_{ex} \cdot \mathbf{E} \quad (5.39)$$

$\mathbf{d}_{cv}$  stands for the matrix element of the transition dipole moment, which in this instance corresponds to the electric dipole moment of the exciton  $\mathbf{d}_{ex} = d_{ex} \mathbf{e}_d$  with  $\mathbf{e}_d$  the dipole direction.  $\mathbf{E}$  is the local electric field in which the exciton is embedded. When an exciton undergoes radiative decay, it interacts with the electromagnetic modes associated with the local electromagnetic field. This interaction causes the release of exciton energy in the form of photons, which are transferred to the surrounding electromagnetic field. The local electric field is described by its quantized expression:

$$\mathbf{E}(\mathbf{r}, \omega) = \sqrt{\frac{\hbar\omega n}{2\epsilon_0 V}} \mathbf{G}(\mathbf{r}, \omega) \quad (5.40)$$

$V$  denotes the quantization volume and  $n$  is the refractive index of the medium where the electric field is located. Here, since the electric field is the one experienced by the exciton localized within the monolayer, the refractive index considered is that of the monolayer itself, denoted as  $n_{MoSe_2}$ . The vector field  $\mathbf{G}(\mathbf{r}, \omega)$  is a dimensionless quantity. Thus, the Hamiltonian of equation (5.38) becomes:

$$|H_{vc}|^2 = \frac{\hbar\omega n_{MoSe_2} d_{ex}^2}{2\epsilon_0 V} |\mathbf{e}_d \cdot \mathbf{G}(\mathbf{r}, \omega)|^2 \quad (5.41)$$

In its quantized form, a plane wave exhibits an amplitude equal to  $\sqrt{\frac{\hbar\omega n}{2\epsilon_0 V}}$  [18]. Thus, based on equation (5.40), the term  $|\mathbf{e}_d \cdot \mathbf{G}(\mathbf{r}, \omega)|$  can be interpreted as the electric near-field enhancement at  $\mathbf{r}$  and along  $\mathbf{e}_d$  when an incident plane wave is used as excitation source. Indeed,  $\mathbf{G}$  represents the field enhancement  $\frac{\mathbf{E}}{|\mathbf{E}_{inc}|}$  and can be determined from the near-field optical response of the hybrid  $Au/MoSe_2/Au$  junction investigated in Chapter 4 by QCM-DDA simulations. It is chosen to be

evaluated at the position of the exciton  $\mathbf{r}_{ex}$ . In the upcoming section, a thorough investigation of this term is conducted. It is noteworthy that through this term, the interaction between the exciton and its electromagnetic environment, including its coupling with plasmon modes, is introduced into our theoretical framework. The interaction between plasmon modes and excitons is a crucial factor, as emphasized in Chapter 3, for the excitonic light emission process.

The exciton radiative recombination rate can be expressed as:

$$\Gamma_{rad}(\omega) = \frac{2\pi}{\hbar} \frac{\hbar\omega}{2\epsilon_0 V} n_{MoSe_2} d_{ex}^2 |\mathbf{e}_d \cdot \mathbf{G}(\mathbf{r}_{ex}, \omega)|^2 \delta(E_C - E_V - \hbar\omega) g(\hbar\omega) \quad (5.42)$$

where  $g(\hbar\omega)$  is the density of photon states. It is defined as  $g(\hbar\omega) = \int dg(\hbar\omega)$  where  $dg(\hbar\omega)$  describes the number of photon states per photon energy interval  $d(\hbar\omega)$  in the solid angle element  $d\Omega$ . Thus, considering the emission of a photon into  $d\Omega$ , the density of allowed states  $dg(\hbar\omega)$  is given by [19]:

$$dg(\hbar\omega) = \frac{dN}{d(\hbar\omega)} = \frac{V k^2 dk d\Omega}{\pi^3 d(\hbar\omega)} \times 2 = \frac{V(\hbar\omega)^2 d\Omega}{\hbar^3 c^3 \pi^3} \times 2 \quad (5.43)$$

The factor 2 accounts for the two possible polarization states of the photon. The k-space volume taken up by each allowed state is  $\frac{\pi^3}{V}$ . To determine the density of states  $g(\hbar\omega)$ , the integral over  $d\Omega$  is conducted with the constraint  $k_x, k_y, k_z > 0$ , resulting in  $\int d\Omega = \frac{\pi}{2}$ . The transition probability per unit time into a solid angle element  $d\Omega$  can thus be written as:

$$\begin{aligned} d\Gamma_{rad}(\omega) &= \frac{2\pi}{\hbar} \frac{\hbar\omega}{2\epsilon_0 V} n_{MoSe_2} d_{ex}^2 |\mathbf{e}_d \cdot \mathbf{G}(\mathbf{r}_{ex}, \omega)|^2 \delta(E_C - E_V - \hbar\omega) \frac{V(\hbar\omega)^2 d\Omega}{\hbar^3 c^3 \pi^3} \times 2 \\ &= \frac{2(\hbar\omega)^3 n_{MoSe_2} d_{ex}^2 d\Omega}{\epsilon_0 c^3 \pi^2 \hbar^4} |\mathbf{e}_d \cdot \mathbf{G}(\mathbf{r}_{ex}, \omega)|^2 \delta(E_C - E_V - \hbar\omega) \end{aligned} \quad (5.44)$$

The energy gap between the conduction band state and the valence band state is considered to be equivalent to the exciton energy, resulting in  $E_C - E_V = \hbar\omega_{ex}$ . By applying the Dirac delta function, the preceding equation becomes:

$$d\Gamma_{rad} = \frac{2(\hbar\omega_{ex})^3 n_{MoSe_2} d_{ex}^2 d\Omega}{\epsilon_0 c^3 \pi^2 \hbar^4} |\mathbf{e}_d \cdot \mathbf{G}(\mathbf{r}_{ex}, \omega_{ex})|^2 \quad (5.45)$$

The dipole moment of the exciton  $d_{ex}$  is related to the exciton radiative lifetime through Einstein's relation [20, 21]:

$$\frac{1}{\tau_r} = \frac{d_{ex}^2 \omega_{ex}^3 n_{MoSe_2}}{3\pi \hbar \epsilon_0 c^3} \quad (5.46)$$

As a result, equation (5.45) can then be written as:

$$d\Gamma_{rad} = \frac{6}{\pi} \frac{d\Omega}{\tau_r} |\mathbf{e}_d \cdot \mathbf{G}(\mathbf{r}_{ex}, \omega_{ex})|^2 \quad (5.47)$$

which accounts for the radiative decay enhancement by the local electromagnetic field. After establishing the exciton radiative recombination rate  $d\Gamma_{rad}$ , the power radiated into a solid angle  $d\Omega$  can be expressed as follows:

$$dP(\hbar\omega) = \hbar\omega \frac{24\tau_{nr}}{\hbar\tau_r} |\mathbf{e}_d \cdot \mathbf{G}(\mathbf{r}_{ex}, \omega_{ex})|^2 \rho_t(E_i) [f(E_i + eV_s) - f(E_i)] \left| M_i \left( \frac{d}{2}, V_s \right) \right|^2 d\Omega \quad (5.48)$$

Hence, the radiated power per unit solid angle and per unit photon energy is given by:

$$\frac{d^2P}{d\Omega d(\hbar\omega)} = \frac{24\tau_{nr}}{\hbar\tau_r} |\mathbf{e}_d \cdot \mathbf{G}(\mathbf{r}_{ex}, \omega_{ex})|^2 \rho_t(E_i) [f(E_i + eV_s) - f(E_i)] \left| M_i \left( \frac{d}{2}, V_s \right) \right|^2 \quad (5.49)$$

The radiated power per unit solid angle and per unit photon energy arising from the radiative recombination of excitons is computed for both A- and B-excitons. For each type of exciton, a distinct initial state is chosen for the elastic tunneling process: for A-excitons, valence band state at energy  $E_{V_A}$  is considered, whereas for B-excitons, the initial state is at energy  $E_{V_B}$ . Consequently, since two different initial states are considered with different energies, a distinct tunneling term  $M_i$  is computed for each exciton. Additionally, distinct radiative lifetimes are assigned to each exciton, with  $\tau_r = 380$  ps for exciton A and  $\tau_r = 187$  ns for exciton B, as reported in [22]. The non-radiative lifetime, assumed to be identical for both A- and B-excitons, has been extracted from the literature with a value of  $\tau_{nr} = 114$  ps [23].

Experimental light emission spectra obtained from the radiative decay of excitons exhibit an energy distribution. Indeed, while the exciton energy itself may have a specific value based on the energy gap between the involved energy levels, the emission of photons resulting from exciton recombination can be influenced by various factors that broaden the observed energy distribution. These factors include exciton-exciton and exciton-phonons interactions, as well as the presence of localized defects and dopant levels. To account for the energy distribution observed in experimental measurements such as those presented in Chapter 3, the radiated power expression of equation (5.49) is modulated by a Lorentzian function [24, 25]. This procedure allows the exciton damping rate  $\hbar\gamma$  to be incorporated into the theoretical model presented here. The Lorentzian function used is defined as:

$$L(\hbar\omega - \hbar\omega_{ex}) = \frac{1}{\pi} \frac{\frac{\hbar\gamma}{2}}{(\hbar\omega - \hbar\omega_{ex})^2 + \left(\frac{\hbar\gamma}{2}\right)^2} \quad (5.50)$$

such that:

$$\int_{-\infty}^{\infty} L(\hbar\omega - \hbar\omega_{ex}) d(\hbar\omega) = 1 \quad (5.51)$$

The damping rates employed to compute the theoretical light emission spectra are sourced from the literature. Particularly, they are derived from the full width at half maximum of the A and B peaks of photoluminescence (PL) spectra, which were acquired through PL measurements of a  $MoSe_2$  monolayer transferred onto a  $SiO_2$  substrate at room temperature. For the A-exciton, the extracted damping rate is  $\hbar\gamma_{ex_A}=42$  meV [21, 26], while for the B-exciton, the extracted rate is  $\hbar\gamma_{ex_B}=112$  meV [25].

Finally, equation (5.49) is adjusted to accommodate the potential situation in which the radiative recombination of excitons can be triggered by inelastic electron tunneling between the VB and the tip. Under such conditions, the probability of having a hole in the VB is calculated by integrating the probability of having a tunneling transition over the energy lost by the electron during the tunneling process, denoted as  $\hbar\omega'$ . This latter goes from 0 to include the elastic tunneling, to the maximum of energy that an electron tunneling from the VB to the tip can lose:  $E_i - E_F$ . The energy of the photons emitted within the gap due to the tunneling process is not included in the amount of emitted energy calculated here. In fact, the following equation corresponds to the radiated power per unit solid angle and per unit photon energy originating exclusively from the radiative recombination of excitons. Thus, the radiated power of equation (5.35) finally becomes:

$$\begin{aligned} \frac{d^2 P}{d\Omega d(\hbar\omega)} &= \frac{24 \tau_{nr}}{\hbar \tau_r} |\mathbf{e}_d \cdot \mathbf{G}(\mathbf{r}_{ex}, \omega_{ex})|^2 L(\hbar\omega - \hbar\omega_{ex}) \\ &\int_0^{E_i - E_F} \rho_t(E_i - \hbar\omega') [f(E_i + eV_s) - f(E_i - \hbar\omega')] \left| M_i \left( \frac{d}{2}, V_s, \hbar\omega' \right) \right|^2 d(\hbar\omega') \end{aligned} \quad (5.52)$$

The tunneling term  $M_i$  is evaluated at the middle of the gap. As for the plasmonic emission, the radiated power obtained for each state  $E_i$  (initial state for the tunneling process) is normalized by its corresponding elastic current:

$$\begin{aligned} \frac{d^2 P}{d\Omega d(\hbar\omega)} / I_{elas} &= \frac{24 \tau_{nr}}{\hbar \tau_r} |\mathbf{e}_d \cdot \mathbf{G}(\mathbf{r}_{ex}, \omega_{ex})|^2 L(\hbar\omega - \hbar\omega_{ex}) \times \frac{\hbar}{4\pi e} \\ &\frac{\int_0^{E_i - E_F} \rho_t(E_i - \hbar\omega') [f(E_i + eV_s) - f(E_i - \hbar\omega')] \left| T_i \left( \frac{d}{2}, V_s, \hbar\omega' \right) \right|^2 d(\hbar\omega')}{\rho_t(E_i) [f(E_i + eV_s) - f(E_i)] \left| T_i \left( \frac{d}{2}, V_s \right) \right|^2} \end{aligned} \quad (5.53)$$

The expression of the term  $T_i$  is detailed in section 5.1.2 within this chapter.

### 5.2.3 Spectral analysis of the excitonic light emission

In this section, the spectral features of the excitonic light emission resulting from the calculations are investigated. Before delving into this investigation, the characteristics of the field enhancement vector  $\mathbf{G}$  at the exciton position are analyzed with the aim of providing information for further analysis of the light emission spectra.

#### a) Field enhancement $G$ at the exciton position within the TMD monolayer

The vector field enhancement  $\mathbf{G}$  is here obtained from the near-field optical response of the hybrid  $Au/MoSe_2/Au$  tunneling junction investigated in Chapter 4 by QCM-DDA simulations. For the computation of  $\mathbf{G}$ , a flat substrate is considered and an incident p- and s-polarized electric field is used with an incidence angle of  $\theta = 45^\circ$ . Moreover, a tip-surface distance in the tunneling regime is considered for electron tunneling to occur, essential for the excitonic light emission process.  $\mathbf{G}$  is calculated for incident electric field wavelengths corresponding to the A- and B-excitons energies, specifically at  $\lambda=800$  nm (1.55 eV) and 700 nm (1.77 eV). Moreover, the vector field  $\mathbf{G}$  is computed at the exciton position  $\mathbf{r}_{ex}$  where the interaction between the exciton and its electromagnetic environment, resulting in photon emission, is considered to occur. In the hybrid tunneling junction described in Fig. 5.7, it is assumed that the exciton generated through hole injection is formed at the center of the TMD monolayer and undergoes radiative decay before any displacement within the monolayer. Thus, the exciton coordinates are set as  $x=0$  nm,  $y=0$  nm, and  $z=-0.4$  nm. Thus, the exciton and the tunneling process occurring along  $z$  are aligned in the same position within the  $xy$ -plane.

In fact, the expression of the radiated power (eq. (5.52)) includes the field enhancement vector component along the direction of the exciton dipole:  $\mathbf{e}_d \cdot \mathbf{G}(\mathbf{r}_{ex}, \omega_{ex})$ . As explained in section 1.2.2 of Chapter 1, A- and B-excitons are bright excitons with electric dipoles parallel and within the monolayer plane [27]. Therefore, in the presented configuration of the junction,  $\mathbf{e}_d$  lies in the  $xy$  plane.

In Figure 5.8-A, the real part of the vector field  $\mathbf{G}$  in the  $xy$  plane centred at the exciton position is depicted. It is calculated for an incident p-polarized electric field at the A-exciton energy and a tip-surface distance of  $d=0.2$  nm. The vector field is primarily oriented along the  $+x$  axis. Nevertheless, in the proximity of the exciton position, both its orientation and intensity exhibit variations. These variations are attributed to the gap plasmon modes excited when an incident p-polarized field is used. The electric field associated with these modes is strongly localized in the gap region and in the TMD monolayer directly underneath the gap. This point has been discussed in section 4.2.2 of the previous chapter (see Fig. 4.8-C). Hence, by introducing  $\mathbf{G}$ , which is calculated within the monolayer underneath the gap, into the theoretical light emission calculations, the interaction between gap plasmon modes and excitons is taken into account. This interaction plays a crucial role in the experimental excitonic light emission observed in Chapter 3.

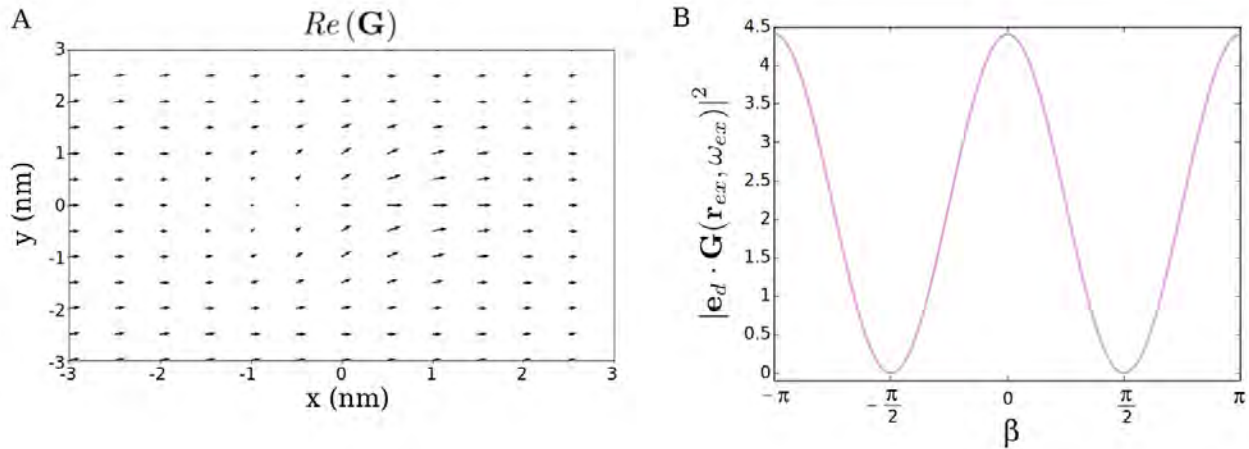


**Figure 5.8:** (A) Vector map of the real component of the field  $\mathbf{G}$  in the  $xy$  plane at  $z = -0.4$  nm and (B) evolution of the square modulus of the vector field  $\mathbf{G}$  at the exciton position  $\mathbf{r}_{ex}$  (situated at the monolayer center:  $x = 0$  nm,  $y = 0$  nm,  $z = -0.4$  nm) and along the direction  $\mathbf{e}_d = \cos(\beta)\mathbf{e}_x + \sin(\beta)\mathbf{e}_y$  as a function of the angle  $\beta$  (angle formed by the dipole vector and the unit vector along the  $x$ -axis). The vectorial field map (A) and the graph of (B) are computed for an incident p-polarized light with an energy corresponding to the A-exciton energy  $\hbar\omega_{exA} = 1.55$  eV ( $\lambda = 800$  nm) and a tip-surface distance of  $d = 0.2$  nm.

The electric dipole moment lies in the  $xy$  plane but its exact orientation in this plane remains unknown. To address this uncertainty, the dipole vector  $\mathbf{e}_d$  is defined as follows:  $\mathbf{e}_d = \cos(\beta)\mathbf{e}_x + \sin(\beta)\mathbf{e}_y$  with  $\beta$  representing the angle formed by the dipole vector and the unit vector along the  $x$ -axis. Since the specific value of this angle is uncertain, the square modulus of the vector field component along the dipole direction  $|\mathbf{e}_d \cdot \mathbf{G}(\mathbf{r}_{ex}, \omega_{ex})|^2$  is computed as a function of  $\beta$ , as shown in Figure 5.8-B. Following this, the average value over  $\beta$  is computed. In Table 5.1, the average  $|\mathbf{e}_d \cdot \mathbf{G}(\mathbf{r}_{ex}, \omega_{ex})|^2$  over all directions in the  $xy$  plane for both incident electric field polarizations, two different tip-surface distances  $d$  and both exciton energies are listed.

For both incident polarizations and both tip-surface distances considered, a larger value of  $|\mathbf{e}_d \cdot \mathbf{G}(\mathbf{r}_{ex}, \omega_{ex})|^2$  is obtained for A-excitons (1.55 eV) compared to B-excitons (1.77 eV), as shown in Table 5.1. According to the discussion of section 4.2.2 of Chapter 4, the electric near-field enhancement at the point  $r_{ex}$  within the monolayer is attributed to the hybrid gap plasmon-exciton mode arising from the interaction between gap plasmon mode, the substrate plasmonic resonance and the TMD monolayer excitons when an incident p-polarized light is used (Fig. 4.8-C). On the other hand, for an incident s-polarized electric field, the field enhancement within the TMD monolayer is assigned to the transverse LSPR of the substrate and its interaction with the excitons (Fig. 4.10-B). The electric fields at  $r_{ex}$  resulting from these interactions exhibit a larger component in the  $xy$  plane at the A-exciton energy than at the B-exciton energy. Indeed, the orientation of  $\mathbf{G}$  relative to the  $xy$  plane, where the exciton dipole moment lies, determines the intensity of  $|\mathbf{e}_d \cdot \mathbf{G}(\mathbf{r}_{ex}, \omega_{ex})|^2$ , leading to a more or less favorable coupling between the excitons and its electromagnetic environment for radiative decay. Moreover, the nearly twofold difference between the values obtained with p- and s-polarization is attributed to the excitation

p-polarization		
Tip-surface distance $d$ (nm)	$\hbar\omega_{ex}$ (eV)	$ \mathbf{e}_d \cdot \mathbf{G}(\mathbf{r}_{ex}, \omega_{ex}) ^2$
0.2	1.55	2.2026
	1.77	1.1495
0.4	1.55	2.2018
	1.77	1.1534
s-polarization		
Tip-surface distance $d$ (nm)	$\hbar\omega_{ex}$ (eV)	$ \mathbf{e}_d \cdot \mathbf{G}(\mathbf{r}_{ex}, \omega_{ex}) ^2$
0.2	1.55	4.3963
	1.77	2.2968
0.4	1.55	4.3963
	1.77	2.2968

**Table 5.1:** Numerical values of  $|\mathbf{e}_d \cdot \mathbf{G}(\mathbf{r}_{ex}, \omega_{ex})|^2$  computed for both incident polarizations, both tip-surface distances  $d= 0.2$  and  $0.4$  nm, and A- and B-exciton energy.

of gap plasmon modes when an incident p-polarized field is used. When excitons interact solely with the substrate plasmonic resonance, a substantial component of  $\mathbf{G}$  in the xy plane is observed. However, when gap plasmon modes are excited, as previously mentioned, the intensity of this vector field in the xy plane at the point  $r_{ex}$  is reduced. Finally, negligible differences are observed between the values of  $|\mathbf{e}_d \cdot \mathbf{G}(\mathbf{r}_{ex}, \omega_{ex})|^2$  obtained for  $d= 0.2$  and  $0.4$  nm for both incident polarizations.

### b) Radiated Power

After addressing the characteristics of  $G$ , the investigation now focuses on the spectral features of the excitonic light emission. To begin with, the evolution of these spectra resulting from the radiative decay of A- and B-excitons as a function of  $V_s$  is studied. In Figure 5.9, excitonic light emission spectra calculated for different bias voltages  $V_s = -2$  V,  $-3$  V, and  $-4$  V are depicted, considering an incident p-polarized electric field and a tip-surface distance of  $d = 0.2$  nm. The lineshapes of the obtained spectra are characterized by a single peak occurring at the energy of the exciton, more precisely at 1.55 eV for the A-exciton decay spectra and at 1.77 eV for the B-exciton decay spectra. These lineshapes result from the Lorentzian function of equation (5.50). In addition, the excitonic spectra from B-excitons radiative decay exhibit a broader peak compared to that of A-excitons, due to a larger damping rate. In contrast with the plasmonic light emission process, the excitonic spectra do not exhibit a high-energy quantum cutoff related to the bias voltage applied to the junction. In fact, as long as  $-eV_s > \hbar\omega_{ex}$  (refer to Fig. 5.7), the radiative decay of the exciton can occur, and the energy of the resulting peak emission remains independent of  $V_s$ . However, as shown Figure 5.9, the intensity of this peak increases with rising the absolute value of the bias voltage  $V_s$  for both A- and B-excitons radiative

decay spectra. By examining equation (5.53) and since the inelastic tunneling term  $T_i$  normalized by its elastic counterpart remains relatively constant as  $V_s$  varies (see section 5.1.3), the increase of the peak emission intensity can be assigned to the integral over the energy of the emitted photons in the gap  $\hbar\omega'$ . Indeed, as  $|V_s|$  increases, the energy of the valence band, the initial state for the tunneling process, increases. Consequently, the energy range of the integral of eq. (5.53) also expands leading to a higher integral value and, in turn, to an overall increase in the radiated power intensity. This behavior can be interpreted as an increase in the probability of hole creation in the valence band due to a greater number of channels for inelastic tunneling transitions as the energy of the valence band rises. Furthermore, it is worth pointing out that, for a given bias voltage, the light emission spectrum of A-excitons is several thousand times more intense than that of B-excitons. This intensity difference is mainly ascribed to the distinct exciton radiative lifetime and damping rate assigned to each exciton.

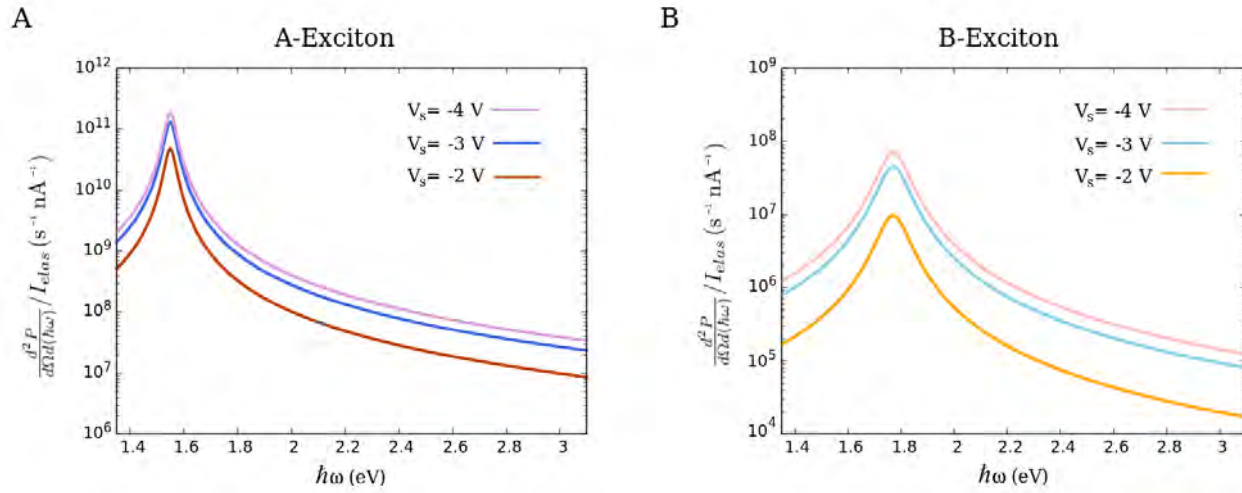


**Figure 5.9:** Radiated power normalized by the elastic current (in log scale) resulting from the radiative recombination of A-excitons (A) and B-excitons (B) and calculated for three bias voltages:  $V_s = -2$  V,  $-3$  V and  $-4$  V. The tip-surface distance is set to  $d = 0.2$  nm. These spectra are calculated considering an electric field enhancement within the monolayer computed using an incident p-polarized electric field.

In addition to the bias voltage  $V_s$ , the role of the tip-surface distance  $d$  on the excitonic light emission spectra is studied. As in the case of plasmonic emission, this dependency is examined by assessing the radiated power itself, without normalizing it with respect to the elastic current. Moreover, for this study, the total radiated power obtained by summing the radiated power obtained for each exciton is considered. It should be noted that no specific weights are applied to this summation. The total radiated power is calculated for two tip-surface distances  $d = 0.2$  and  $0.4$  nm and for both incident polarizations used to compute the electric field enhancement within the monolayer. The resulting spectra, normalized by the maximum total radiated power obtained for  $d = 0.2$  nm and for an incident s-polarized electric field, are displayed in Figure 5.10.

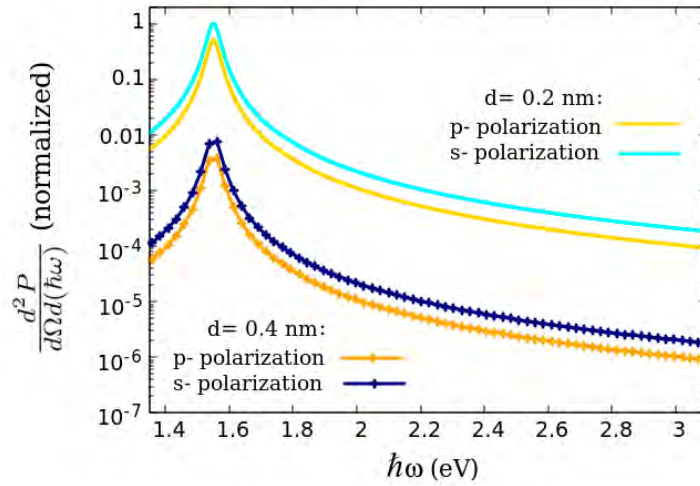


**Figure 5.10:** Total radiated power (in log scale) calculated for two tip-surface distances:  $d=0.2$  and  $0.4$  nm and for both incident polarizations used to compute the electric field enhancement within the monolayer. They are normalized by the maximum radiated power obtained for  $d=0.2$  nm and for an incident s-polarized electric field. The bias voltage is set to  $V_s = -4$  V.

All the total radiative power spectra obtained exhibit a peak emission at the A-exciton energy. Indeed, due to the substantial difference in intensity between the A- and B-exciton light emission spectra, the lineshape of the total radiated power is practically identical to that of the radiated power resulting from the radiative decay of A-excitons. For both incident polarizations, a more intense total radiated power is obtained for  $d=0.2$  nm than for  $d=0.4$  nm. By examining equation (5.53), this difference in intensity when varying  $d$  can be attributed to the tunneling term  $T_i$ . Indeed, as discussed in section 5.1.3, the probability of inelastic (and elastic) tunneling is reduced when the tip-surface distance increases. This, in turn, leads to a decrease in the likelihood of hole creation in the valence band. Consequently, the number of excitons and thus, the number of emitted photons by excitonic decay decreases. Finally, Figure 5.10 shows that, for a given tip-surface distance, there is a two-fold difference in the intensity of the total radiated power between incident s-polarization and p-polarization. This variation is a consequence of the disparity between the field enhancements within the monolayer obtained for each polarization, as detailed in Table 5.1.

### 5.3 Analysis of plasmonic and excitonic light emission

In the previous sections, the models describing the plasmonic and excitonic light emission processes in a hybrid  $Au/MoSe_2/Au$  tunneling junction were provided. Furthermore, the properties of the resulting light emission spectra and their dependence on the main tunneling parameters were analyzed. The surface roughness of the sample proves to be a crucial element in the experimental STM-induced light emission, as evidenced in Chapter 3. Therefore, its incorporation into our model represents an important advancement in our understanding of STM-LE. The impact of the substrate roughness on the studied light emission processes is addressed in this section by considering a rough substrate in the hybrid

*Au/MoSe<sub>2</sub>/Au* junction. Before going further into this analysis, a summary and comparison of the key characteristics of the plasmonic and excitonic light emission spectra obtained with a flat substrate will be presented. Moreover, the investigation of the quantum yield, which is defined as the number of emitted photons per tunneling electron, will be carried out for both flat and rough substrates. In the final part of this section, a comparison will be made between the primary theoretical results presented in this chapter and the experimental findings obtained in Chapter 3, with the aim of evaluating the alignment of the models with the experimental observations.

### 5.3.1 Comparison between plasmonic and excitonic light emission

The plasmonic and excitonic light emission spectra presented in the previous sections were calculated in the simple case of a flat substrate in the hybrid *Au/MoSe<sub>2</sub>/Au* tunneling junction. A comparison of the main characteristics of these spectra obtained for each process is presented here. In Figure 5.11, the plasmonic and excitonic total radiated powers, normalized by their respective elastic current, are plotted. They are calculated for the two polarizations of the incident electric field used to compute the electromagnetic properties of the junction, included in the light emission calculations. To ensure the absence of the quantum cutoff within the studied spectral range, a bias voltage of  $V_s = -4$  V is applied. Additionally, a tip-surface distance of  $d = 0.2$  nm is considered.

For both polarizations, the spectral profiles of the plasmonic and excitonic light emission spectra are completely different. In the case of plasmonic light emission, multiple peaks (and shoulders) are observed. These peaks are associated with the different electromagnetic modes supported by the gap. Thus, the spectral features of the plasmonic emission are mainly determined by the electromagnetic properties of the gap.

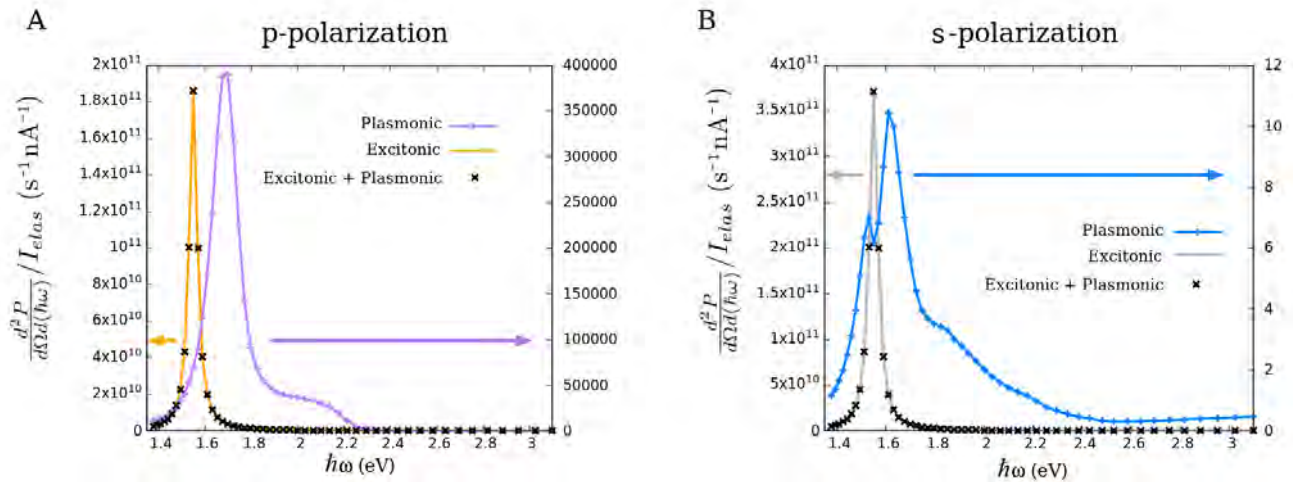


**Figure 5.11:** Total radiated power for plasmonic (purple and blue lines) and excitonic (orange and gray lines) light emission processes. An incident p- (A) and s- (B) polarized electric field is used to compute the electric field enhancement in the gap and within the monolayer included in the radiated power calculations. The spectra are normalized by the elastic current corresponding to each case. The sum of radiated power from both plasmonic and excitonic processes is also depicted by black crosses. The bias voltage is set to  $V_s = -4$  V and the tip-surface distance considered is  $d = 0.2$  nm. The sample is modeled with a flat surface.

On the other side, excitonic light emission arises from the radiative recombination of excitons, resulting in the emission of photons with specific energies. This emission process is notably more efficient for the A-exciton, rendering the contribution from B-excitons nearly negligible by comparison. As a result, only a single peak emission at the A-exciton energy is observed.

An examination of the spectral features obtained for each process with respect to the main tunneling parameters was carried out in the previous sections. While for the plasmonic light emission, the energy of emitted photons is constrained by the bias voltage  $V_s$  (Fig. 5.5), for the excitonic light emission process, the radiative recombination can occur for any value of  $V_s$ , as long  $e|V_s|$  exceeds the exciton energy (Fig. 5.9). In fact, in excitonic emission, the influence of the bias voltage  $V_s$  is primarily observed as an increase in intensity as  $|V_s|$  increases. This effect is also present in plasmonic emission but to a much lesser extent. On the other hand, both light emission processes exhibit a stronger signal when a small tip-surface distance  $d$  is considered (Figures 5.6 and 5.10). Indeed, as  $d$  decreases, the probability of electron tunneling increases, leading to a greater amount of emitted photons.

For both polarizations, there is a significant difference in the maximum light emission intensity achieved for each process as shown in Figure 5.11. To be more precise, for p-polarization, the excitonic spectrum is of the order of  $5 \times 10^5$  more intense than the plasmonic one, whereas for s-polarization, this difference is about  $3 \times 10^{10}$ . In fact, for p and s-polarizations, when the plasmonic and excitonic light emission spectra are combined, the resulting spectrum is identical to the excitonic one. In order to understand this disparity, it is important to keep in mind that a strong assumption is made in the excitonic process model, where it is assumed that each hole created in the valence band through electron tunneling results in the formation of an exciton. This point is discussed below from the theoretical quantum yield calculation.

Similarly to the approach used to compare the experimental light emission efficiency obtained for different configurations in Chapter 3, a theoretical light emission rate, denoted  $\eta$ , is calculated. This rate, defined as the number of emitted photons per elastic tunneling electron, is computed for both plasmonic and excitonic processes. To compute the theoretical quantum yield, the radiated power, which is calculated per unit of solid angle and per unit of photon energy, is integrated over both the emitted photon energy and the solid angle, while being normalized by the elastic current. As for the experimental quantum yields calculated in Chapter 3, the light emission is evaluated for a solid angle corresponding to the hemisphere of emission  $\Omega = 2\pi$ . This solid angle represents the hemisphere above the sample surface where the emitted photons are assumed to propagate into the ambient medium.

$$\frac{P}{I_{Elas}} = \int_0^{\Omega=2\pi} \left( \int \frac{d^2P}{d\Omega d(\hbar\omega)} / I_{elas} d(\hbar\omega) \right) d\Omega \quad (5.54)$$

For instance, considering the plasmonic light emission spectra depicted in Figure 5.11, calculated for  $V_s = -4$  V and  $d = 0.2$  nm, the estimated values of  $\frac{P}{I_{Elas}}$  are approximately  $10^{-4}$  W·A<sup>-1</sup> for p-polarization and  $\sim 10^{-9}$  W·A<sup>-1</sup> for s-polarization. Here,  $P$  represents the total energy radiated by the junction per unit time and over the hemisphere above the sample surface. To determine the number

of emitted photons per second, this radiated power is divided by the energy of a photon, which is taken as 2 eV. Additionally, an elastic tunneling current of 1 A corresponds to approximately  $6.24 \times 10^{18}$  electrons per second. The number of photons per elastic tunneling electron can then be obtained. The resulting quantum yields for the plasmonic and excitonic light emission spectra shown in Figure 5.11, are presented in the following table.

	p-polarization	s-polarization
Plasmonic quantum yield $\eta_{plas}$	$3.94 \times 10^{-5}$	$1.79 \times 10^{-9}$
Excitonic quantum yield $\eta_{exc}$	5.93	$1.18 \times 10^1$

**Table 5.2:** Quantum yield calculated for the plasmonic and excitonic light emission processes for both incident polarizations used to compute the field enhancement in the radiated power calculations. These values are calculated considering a bias voltage of  $V_s = -4$  V and a tip-surface distance of  $d = 0.2$  nm. The sample surface is modeled as flat.

A higher quantum yield  $\eta_{plas}$  is achieved when an incident p-polarized electric field is used for the field enhancement calculation than when it is s-polarized. This is due to the fact that for p-polarization, highly localized gap plasmon modes are excited within the gap, leading to a more favorable coupling with the inelastic tunneling electrons and, consequently, a higher light emission rate. On the contrary, for s-polarization, less favorable electromagnetic modes for electron-to-photon conversion are excited. As shown in Table 5.2, a more efficient excitonic light emission is achieved when the incident field used to compute the field enhancement within the monolayer is s-polarized. This is attributed to the orientation of the vector field enhancement  $\mathbf{G}$ , which, when s-polarization is employed, exhibits a large component within the plane where the exciton dipole moment lies. On the other hand, for p-polarization, this component is reduced due to the excitation of gap plasmon modes. Therefore, for s-polarization, a stronger interaction between excitons and the local electric field is achieved, leading to a more efficient exciton radiative decay.

When comparing  $\eta_{plas}$  and  $\eta_{exc}$ , the excitonic quantum yields significantly exceed the plasmonic ones, with a difference of approximately  $1.5 \times 10^5$  for p-polarization and around  $7 \times 10^9$  for s-polarization. This disparity, also observed when comparing the intensity of the light emission spectra of Figure 5.11, results primarily from the strong assumption made in the excitonic light emission model which causes an overestimation of the amount of excitons, and thus of the number of emitted photons, by created hole within the monolayer. This assumption also results in excitonic quantum yields greater than one. This outcome contradicts the actual physical light emission process since it is inherently impossible to generate more photons than the number of tunneling electrons involved. A further discussion about the excitonic quantum yield and the determination of this overestimation is provided in the latter part of this section, where the theoretical and experimental excitonic quantum yields are compared.

Once the characteristics of plasmonic and excitonic light emission processes considering a hybrid junction with a flat substrate are addressed, the next part will involve the exploration of these

characteristics for a hybrid tunneling junction with a rough substrate to investigate the impact of substrate corrugation.

### 5.3.2 Role of the substrate roughness

Plasmonic and excitonic light emission spectra are now calculated for a hybrid  $Au/MoSe_2/Au$  tunneling junction presenting a rough substrate. In particular, the hybrid junction with a rough substrate labeled n°2 in section 4.5 is considered. A schematic representation of this junction is provided in Figure 5.12-A. The tip is positioned between three semi-spheres representing the granular surface. The minimum tip-surface distance  $d$  corresponds to the distance between the lateral side of the tip and the surface of one of these semi-spheres, and is set to  $d= 0.2$  nm.

For the calculation of the radiated power, the electric field enhancement, computed in the gap for the plasmonic process and within the monolayer for the excitonic emission, is the only aspect that undergoes modification when a junction with a rough substrate is considered. As discussed in section 4.5.2, there is a notable difference in the size and shape of the gap of the junction with a rough substrate compared to that of the junction with a flat substrate. Nonetheless, the calculation of electron tunneling is unchanged when the substrate roughness is introduced in the theoretical models. More precisely, for the rough substrate considered, electron tunneling is regarded as occurring between a point on the surface of the TMD monolayer and a point on the lateral side of the tip, with a separation distance of  $d= 0.2$  nm. This tunneling process is represented in Figure 5.12-B by an orange arrow. A local reference frame specific to this gap is defined, with  $\mathbf{e}_{z'}$  the unit vector along the tunneling direction forming an orthonormal basis alongside  $\mathbf{e}_{x'}$  and  $\mathbf{e}_{y'}$ . Thus, the tunneling takes place from the monolayer at  $z'=0$  to the tip at  $z'=d$ . This local reference frame, shown in Fig. 5.12-B, can be defined with respect to the global reference frame  $(x, y, z)$ . The latter is the reference frame used throughout this thesis, including when describing the theoretical light emission process for a hybrid junction with a flat substrate. The relationship between the local and global reference frames is defined as follows:  $\mathbf{e}_{x'} = \sin(\alpha)\mathbf{e}_x - \cos(\alpha)\mathbf{e}_z$ ,  $\mathbf{e}_{y'} = \mathbf{e}_y$  and  $\mathbf{e}_{z'} = \cos(\alpha)\mathbf{e}_x + \sin(\alpha)\mathbf{e}_z$  with  $\alpha \sim 18.5^\circ$  for the tip-surface gap considered.

For both plasmonic and excitonic processes, when employing the local reference frame, the tunneling component of the radiated power equation and the expression of the elastic current remain the same as those derived previously (section 5.1.2.). It is important to note that if the tip were positioned at a different point on the rough substrate, a distinct gap would be obtained leading to a new local reference frame specific to that gap. Nevertheless, the expression of the tunneling components would remain unchanged.

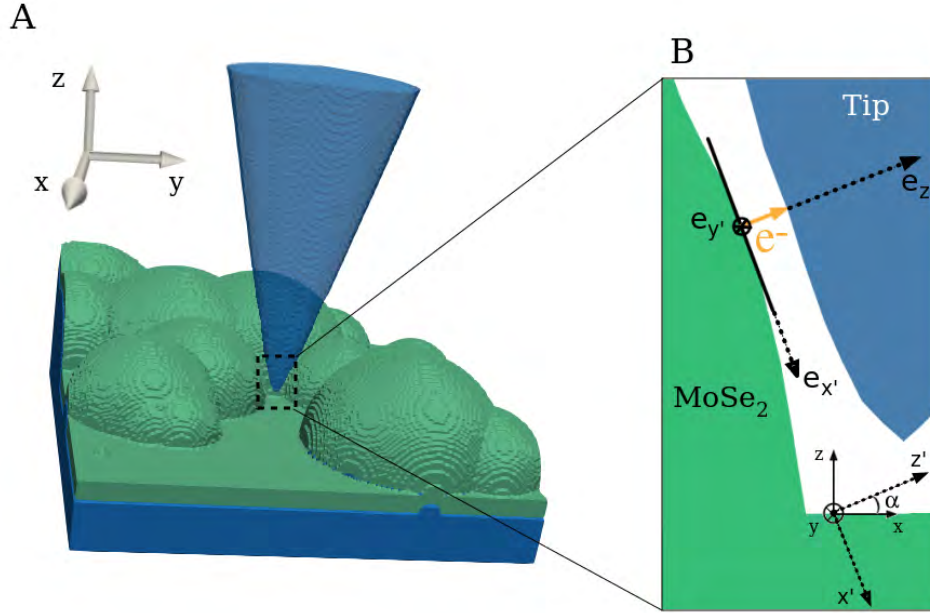


**Figure 5.12:** (A) Schematic representation of the simulated hybrid  $Au/MoSe_2/Au$  junction with a rough substrate. (B) Schematic representation of the gap formed by the lateral side of the tip and the  $MoSe_2$  monolayer surface (zoomed in on the framed area of (A)). The local reference frame  $(x', y', z')$  and the global reference frame  $(x, y, z)$  are depicted, with  $\alpha$  the angle between the x-axis and the  $z'$ -axis. Electron tunneling from the TMD monolayer to the tip along the  $z'$ -direction is illustrated by an orange arrow.

Since the electromagnetic properties of the junction change when the substrate roughness is introduced (see section 4.5.2), prior to analyzing the light emission spectra obtained for a junction with a rough substrate, the field enhancement in the gap and within the monolayer is investigated. For the plasmonic light emission spectra, as done for the junction with a flat surface, the field enhancement  $G$  in the gap along the tunneling direction is calculated. For this, an incident p and s-polarized electric field impinging on the junction with an incidence angle of  $\theta = 45^\circ$  is considered. The orientation and position of the incidence plane with respect to the geometry of the junction with a rough substrate are given in section 4.5.1. To investigate the electromagnetic properties of the junction's gap, the integral of  $G$  over  $z'$  is computed for both polarizations. The resulting spectra are depicted in Figure 5.13.

The spectral characteristics observed in Fig. 5.13 closely resemble those obtained in the analysis of the near-field optical response of the junction with the rough substrate  $n^{\circ}2$  discussed in section 4.5.2 (see Figures 4.26-B and 4.29-B). In particular, the gap plasmon resonance at approximately 1.45 eV and the LSPR of the rough substrate at around 2.05 eV are discernible for both polarizations.

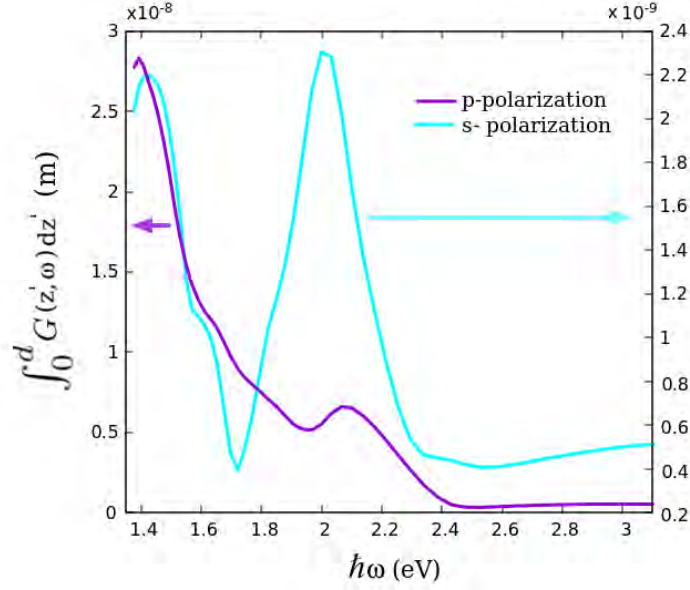


**Figure 5.13:** Electric field enhancement  $G$  integrated over  $z'$  for an incident p- (violet line) and s- (blue line) polarized electric field. The integral is evaluated for a tip-surface distance of  $d=0.2$  nm. The sample is modeled with a rough surface.

The spectra of Figure 5.13 are drastically different from those obtained for a flat substrate (Fig. 5.3-(C,D)). They exhibit distinct resonances associated with different electromagnetic modes. The only common resonance between the spectra obtained for a flat and a rough substrate is the gap plasmon resonance, albeit at a different energy and only for an incident p-polarization. Indeed, no gap plasmon modes are excited for s-polarization in the case of a flat substrate. Therefore, it is important to highlight that the introduction of substrate roughness in the hybrid  $Au/MoSe_2/Au$  junction leads to a different interaction between the tip and the surface, resulting in modifications in the electromagnetic properties of the gap.

To establish the values of  $\mathbf{r}_{ex}$  and  $\mathbf{e}_d$  of the term  $|\mathbf{e}_d \cdot \mathbf{G}(\mathbf{r}_{ex}, \omega_{ex})|^2$  calculated for the excitonic light emission process, the local reference frame defined above (see Fig. 5.12-B) is used. In this frame, the origin corresponds to the starting point for electron tunneling. The coordinates of the exciton are then specified within this reference frame as  $x'=0$  nm,  $y'=0$  nm, and  $z'=-0.4$  nm. This choice positions the exciton at the same location within the  $x'y'$ -plane where electron tunneling occurs, and at a distance of 0.4 nm, which corresponds to half of the thickness of the  $MoSe_2$  monolayer, relative to the starting point for electron tunneling located on the  $MoSe_2$  surface. Because of the sample roughness, the orientation of the TMD monolayer surface can vary from point to point. To account for this variability and evaluate  $\mathbf{e}_d$ , a local flat surface is considered parallel to the  $x'y'$ -plane and to which the starting point of electron tunneling  $z'=0$  belongs. It is assumed that the dipole vector  $\mathbf{e}_d$  lies within a plane parallel to this local surface and is expressed as  $\mathbf{e}_d = \cos(\beta)\mathbf{e}_{x'} + \sin(\beta)\mathbf{e}_{y'}$ . As done for the flat substrate,  $|\mathbf{e}_d \cdot \mathbf{G}(\mathbf{r}_{ex}, \omega_{ex})|^2$  is computed by taken its average value over  $\beta$ . The resulting values are presented in Table 5.3 for both polarizations of the incident electric field, and calculated at the A- and

B-exciton energy.

	$\hbar\omega_{ex}$ (eV)	$ \mathbf{e}_d \cdot \mathbf{G}(\mathbf{r}_{ex}, \omega_{ex}) ^2$
p-polarization	1.55	4.0405
	1.77	1.0124
s-polarization	1.55	0.2375
	1.77	0.1524

**Table 5.3:** Numerical values of  $|\mathbf{e}_d \cdot \mathbf{G}(\mathbf{r}_{ex}, \omega_{ex})|^2$  computed for both incident electric field polarizations and for A- and B-exciton energy. The sample is modeled with a rough surface.

For the rough substrate, the exciton at the position considered, interacts mainly with the electric field associated with the gap plasmon modes. Consequently, the differences between the values of  $|\mathbf{e}_d \cdot \mathbf{G}(\mathbf{r}_{ex}, \omega_{ex})|^2$  in Table 5.3 can be attributed to these electromagnetic modes, in particular to the intensity and orientation of their electric field with respect to the plane containing the exciton dipole moment. The energy of gap plasmon resonance is determined to be around 1.45 eV, as shown in Figure 5.13. Hence, at the A-exciton energy (1.55 eV), the intensity of the electric field related to these modes, including their component in the  $x'y'$ -plane at the point  $r_{ex}$ , exceeds that at the B-exciton energy (1.77 eV) for both polarizations. Similarly, when an incident p-polarized electric field is used, the gap plasmon electric field is more intense (more pronounced resonance) than in the case of s-polarisation. This, along with a more favorable orientation of the gap plasmon electric field, results in a higher value of  $|\mathbf{e}_d \cdot \mathbf{G}(\mathbf{r}_{ex}, \omega_{ex})|^2$  for p-polarization.

When examining the field enhancement within the monolayer for a junction with a flat surface (see section 5.2.3), it was also considered that the values of  $|\mathbf{e}_d \cdot \mathbf{G}(\mathbf{r}_{ex}, \omega_{ex})|^2$  obtained under incident p-polarization (see Table 5.1) were influenced by the gap plasmon modes. Upon comparing those values with the ones obtained in the current study (rough substrate) for the same tip-surface distance ( $d=0.2$  nm), significant differences are observed, especially for the values calculated at the A-exciton energy. Indeed, a higher value of  $|\mathbf{e}_d \cdot \mathbf{G}(\mathbf{r}_{ex}, \omega_{ex})|^2$  for the A-exciton and a slightly lower value for the B-exciton are obtained when considering a rough substrate. These differences can be attributed to several factors. First, the gap plasmon modes exhibit a different resonance energy in the rough substrate case compared to the flat surface case. This shift in resonance energy affects the interaction between the electric field associated with these modes and the excitons within the monolayer, leading to variations in the calculated values. Additionally, the spatial overlap of the gap plasmon electric field with the exciton within the monolayer ( $r_{ex}$ ) and its orientation with respect to the exciton dipole moment are not identical in both cases. This contributes to the observed differences in the calculated values. Indeed, by introducing a rough substrate, not only do the properties of gap plasmon modes undergo changes, but their interaction with excitons is also affected. It is important to note that whereas gap plasmon modes are excited for an incident s-polarization for a rough substrate, they are not for a flat surface. This explains the differences in the calculated values observed between flat and rough substrates when considering an incident s-polarized field.

After examining the field enhancement  $G$ , which is included in the calculation of plasmonic and excitonic light emission spectra, the analysis shifts to the investigation of the total radiated power computed for both processes while considering a rough substrate. Figure 5.14 presents these radiated powers, normalized by their respective elastic current, calculated for a tip-surface distance of  $d = 0.2$  nm and a bias voltage of  $V_s = -4$  V.

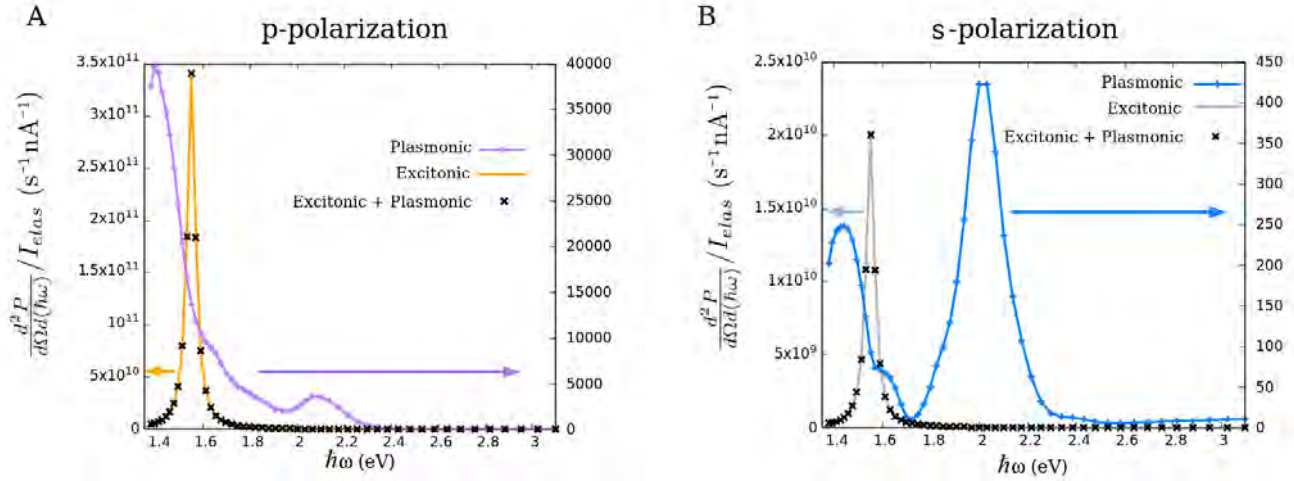


**Figure 5.14:** Total radiated power for plasmonic (purple and blue lines) and excitonic (orange and gray lines) light emission processes. An incident p- (A) and s- (B) polarized electric field is used to compute the electric field enhancement in the gap and within the monolayer included in the radiated power calculations. The spectra are normalized by the elastic current corresponding to each case. The sum of radiated power from both plasmonic and excitonic processes is also depicted by black crosses. The bias voltage is set to  $V_s = -4$  V and the tip-surface distance considered is  $d = 0.2$  nm. The sample is modeled with a rough surface.

As previously mentioned for the flat surface, the spectral features of the plasmonic light emission are primarily determined by the electromagnetic properties of the gap, resulting in spectra with multiple peaks. The peaks of the plasmonic spectra of Figure 5.14 obtained for both polarizations, differ in both energy and intensity compared to those obtained for the flat substrate (Fig. 5.11). This discrepancy is due to the introduction of the surface roughness, which alters the electromagnetic interaction between the tip and the sample and thus, the electromagnetic properties of the gap. Indeed, with surface roughness, completely different electromagnetic modes emerge within the gap. In addition, for modes such as the gap plasmon modes, which are present in both scenarios, their characteristics undergo modifications due to a different gap geometry.

The excitonic light emission spectra of Figure 5.14 present a single peak of emission at the A-exciton energy, such as the excitonic emission spectra calculated for a flat substrate displayed in Fig. 5.11. The introduction of substrate roughness does not affect the energy of this peak; however, it does impact its intensity which is related to the strength of the electric field enhancement within the TMD monolayer along the exciton dipole moment direction. The effect of substrate roughness on the intensity depends on the polarization of the incident electric field used to compute the field enhancement. Specifically, under p-polarization, the rough substrate yields a more intense peak compared to when a flat substrate is considered. This is due to a more efficient interaction between A-excitons and the electric field

associated with gap plasmon modes, resulting from a more favorable orientation of the latter with respect to the exciton dipole moment. Conversely, for s-polarization, a lower peak emission is observed in Fig. 5.14-B when comparing with the flat substrate case (Fig. 5.11-B). Indeed, for the flat substrate, since gap plasmon modes are not excited, excitons interact solely with the LSPR of the substrate which electric field presents a significant component in the plane containing the exciton dipole moment. However, for the rough substrate, excitons interact with the gap plasmon electric field, which exhibits a weaker component in the exciton dipole moment plane at the  $r_{ex}$ , leading then to a less intense emission. Finally, as for the flat substrate, the excitonic spectra exhibit significantly greater intensity compared to the plasmonic spectra for both polarizations. Consequently, when combining the plasmonic and excitonic light emissions, the resulting spectra are identical to the excitonic ones.

Besides these spectral features, the plasmonic and excitonic light emission rates are also evaluated for a rough substrate, using the same approach as for the flat sample. The calculated quantum yields are presented in the table below.

	p-polarization	s-polarization
Plasmonic quantum yield $\eta_{plas}$	$4.13 \times 10^{-6}$	$7.52 \times 10^{-8}$
Excitonic quantum yield $\eta_{exc}$	$1.09 \times 10^1$	$6.39 \times 10^{-1}$

**Table 5.4:** Quantum yield calculated for the plasmonic and excitonic light emission processes for both incident polarizations used to compute the field enhancement in the radiated power calculations. These values are calculated considering a bias voltage of  $V_s = -4$  V and a tip-surface distance of  $d = 0.2$  nm. The sample is modeled with a rough surface.

The electromagnetic properties of the junction gap play a crucial role in the amount of emitted photons. When an incident p-polarization is considered, the electromagnetic modes supported by the gap for a flat substrate exhibit a more intense resonance than those generated when a rough substrate is considered. This stronger resonance results in a more efficient photon emission process (almost 10 times more photons per elastic tunneling electron). This can be interpreted as more a favorable coupling between the electromagnetic modes of the gap and the inelastic tunneling electrons when the hybrid junction presents a flat substrate. However, it is worthy to point out that this difference is specific to the particular tip-surface gap formed by the considered rough substrate. If the tip were placed at a different location on the substrate, it would result in a different gap. Consequently, different electromagnetic modes within the gap would be excited, potentially leading to a more efficient photon emission process compared to the case of a flat substrate. On the other hand, for an incident s-polarized electric field, the situation is reversed. Indeed, in this case, a rough substrate becomes more advantageous for photon emission. This advantage is primarily due to the presence of specific gap plasmon modes within the gap, which can only be excited in the case of a rough substrate.

The orientation and intensity of the local electric field at the exciton position strongly influence the excitonic light emission rate. For an incident p-polarized electric field, gap plasmon modes are excited

for both rough and flat substrate scenarios. Compared to the case of a flat substrate, the electric field associated with these modes for a rough substrate has an orientation and intensity that allow a more favorable interaction with excitons. This leads to a more efficient exciton radiative decay process, resulting in a nearly twofold difference in excitonic quantum yields. In contrast, for s-polarization, the rate of excitonic light emission is greater in the case of the flat substrate. This is because, in the flat substrate scenario, the local electric field at the exciton position, attributed to the substrate LSPR, exhibits a significant component along the exciton dipole moment direction. On the other hand, for the rough substrate, the excitation of gap plasmon modes leads to an electric field at  $r_{ex}$  with an intensity and orientation that results in a less efficient exciton radiative decay process. Consequently, this leads to a reduced number of emitted photons per elastic tunneling electron.

Finally, Table 5.4 shows that the excitonic quantum yields are strongly greater than the plasmonic one (difference ranging from  $10^6$  to  $10^7$ ). In addition, for p-polarization, an excitonic quantum yield greater than 1 is achieved, which means that more photons are produced than electrons involved in the light emission process. As mentioned before, the significant disparity between the excitonic and plasmonic light emission rates is attributed to the strong assumption made in the excitonic light emission model concerning the number of excitons formed by created hole in the TMD monolayer.

### 5.3.3 Comparison with experimental results

In this chapter, theoretical models have been developed to describe the plasmonic and excitonic light emission processes occurring in a hybrid  $Au/MoSe_2/Au$  tunneling junction. The characteristics of the resultant light emission spectra have been explored, with particular emphasis on their dependency on the main tunneling parameters and substrate roughness.

In this section, the principal results obtained from this theoretical study are compared with the experimental findings obtained in section 3.3 of Chapter 3, where STM-induced luminescence (STM-LE) of a sample comprising a monolayer of  $MoSe_2$  deposited on a granular gold substrate is analyzed. In particular, an investigation into how accurately the theoretical spectra replicate the behavior observed in the experimental spectra with respect to the bias voltage  $V_s$  and tip-surface  $d$  is addressed. It is worthy to note that in the experiments, this variation in  $d$  is achieved by adjusting the user-defined tunneling current for a given bias voltage  $V_s$ . Moreover, the discussion presented below also includes a comparison of the impact of substrate roughness on theoretical and experimental results. During the scanning process, the tip of the STM encounters different regions of the granular sample surface with varying degrees of roughness leading to variations in the experimental STM-LE spectra. In order to account for these variations, theoretical spectra are calculated by considering two types of substrate in the simulated junction: one flat and the other rough. These spectra will be compared to experimental spectra acquired at various locations of the monolayer exhibiting a different degree of surface roughness. Finally, it is worthy to point out that the theoretical spectra presented below are computed using an incident p-polarized electric field impinging on the junction with an incidence angle of  $\theta = 45^\circ$  for the field enhancement calculation. Indeed, in contrast to the s-polarization, gap plasmon modes

within the junction gap are excited for p-polarization for both flat and rough substrates and thus, it is believed that the results obtained for this polarization align better with the experimental observations. Furthermore, the incidence angle has been deliberately chosen to closely align with the conditions of the experimental setup. In fact, the experimental STM-LE spectra are acquired using an optical fiber situated at the same angle ( $45^\circ$ ) with respect to the normal of the sample surface (see Fig. 2.1). This alignment facilitates a more accurate comparison between theoretical and experimental results. The theoretical-experimental comparison presented below is divided into three distinct parts: the first focuses on plasmonic emission, the second addresses the excitonic counterpart, and the final part is devoted to hybrid spectra.

### a) Plasmonic emission

To assess whether the theoretical plasmonic emission spectra exhibit similar trends as the experimental spectra when varying the bias voltage  $V_s$ , two spectra are calculated for two different bias voltages:  $V_s = -1.8$  V and  $-2$  V. The resulting spectra are depicted in Fig. 5.15-A, alongside the experimental plasmonic STM-LE spectra acquired at these bias voltages (Fig. 5.15-B). Additionally, a comparative analysis of the influence of the sample surface roughness on both theoretical and experimental light emission spectra is carried out. Indeed, the theoretical spectra of Fig. 5.15-A have been computed considering a flat (red line) and a rough (green line) sample surface. Then, on the other side, the experimental spectra of Fig. 5.15-B were acquired at different locations of the TMD monolayer surface. Theoretical and experimental spectra are depicted as a function of the wavelength (ranging from 500 to 1100 nm) and energy of the emitted photons.

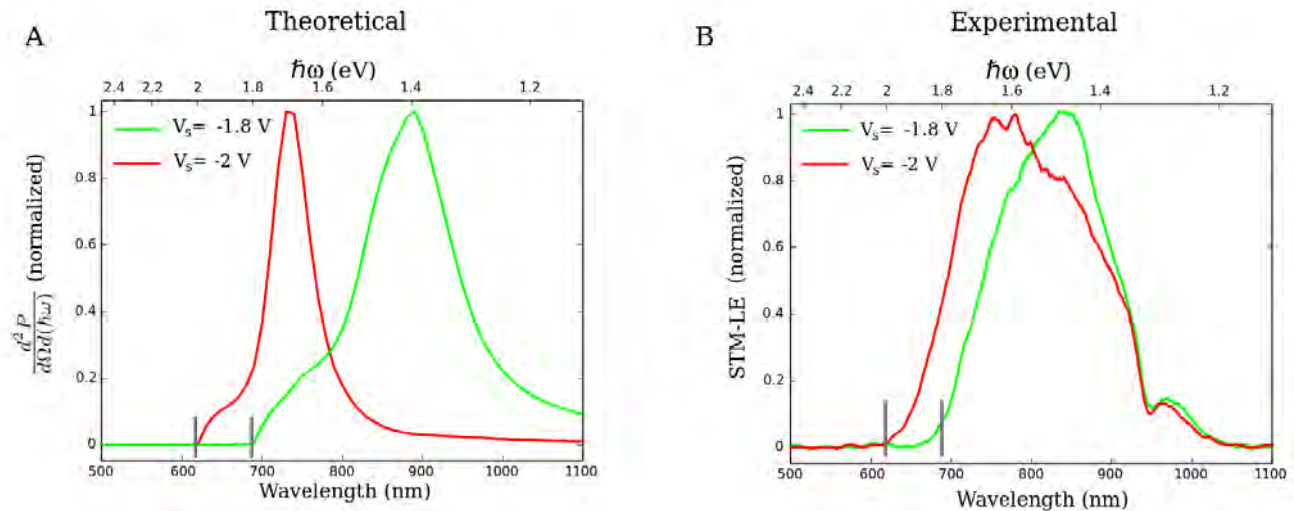


**Figure 5.15:** Comparison of theoretical (A) and experimental (B) plasmonic light emission spectra. Theoretical spectra are computed for a rough substrate with a bias voltage of  $V_s = -1.8$  V (green line) and for a flat substrate with a bias voltage of  $V_s = -2$  V (red line). A tip-surface distance of  $d = 0.2$  nm is considered. Experimental spectra are acquired at two different locations of the  $MoSe_2$  surface with a bias voltage of  $V_s = -1.8$  V (green line) and  $-2$  V (red line), a tunneling current of  $I_t = 10$  nA and an acquisition time of 60 s. Each spectrum is normalized by its maximum.

The theoretical light emission spectra exhibit a quantum cutoff at the wavelength corresponding to  $\hbar\omega = e|V_s|$ , as the experimental spectra. This threshold is indicated in each spectrum by a gray bar. The influence of the bias voltage on the plasmonic experimental STM-LE is primarily given by this quantum cutoff, which limits the maximum energy of the emitted photons. This particular feature is effectively considered in the theoretical spectra.

Beyond the quantum cutoff, a shared characteristic among these spectra is the variation of the energy of some emission peaks when varying the sample roughness. As discussed earlier, the surface roughness has a notable impact on the electromagnetic properties of the gap. Indeed, changes in the sample topography cause alterations in the interaction between the tip and the sample, resulting in different localized electromagnetic modes within the gap. Each contributes to the plasmonic light emission process. Consequently, a distinct spectral lineshape of the light emission spectra is obtained. This is observed for the experimental spectra where different localized surface plasmon modes are excited during the acquisition of each spectrum. Similarly, for the theoretical spectra, the main peak emission is attributed to gap plasmon modes whose properties vary when a rough substrate is considered, leading to the different lineshapes observed between both spectra of Fig. 5.15-A. Nevertheless, experimental spectra feature a greater number of peaks, and these peaks are also broader compared to the calculated spectra. In fact, by comparing the theoretical and experimental spectra obtained for  $V_s = -2$  V (red line) depicted in Fig. 5.15, the theoretical spectrum exhibits a peak and a shoulder, while for the experimental one, at least four peaks are clearly discernible.

The theoretical models developed in this chapter possess inherent limitations in their ability to accurately simulate the complex experimental hybrid junction. In addition, certain features of the description of the plasmonic light emission process have been simplified, as discussed in the first section of this chapter. As a consequence, these limitations and simplifications can lead to theoretical spectra that may not accurately align with experimental spectra in specific aspects. However, it is worthy to note that these observed differences, particularly in the number of peaks and their width, are also influenced by the fact that the experimental spectra are not acquired at precise locations. Indeed, due to thermal drift, the tip and the sample surface constantly shift with respect to each other even in the no-scanning mode (position of the tip “fixed”) of the STM. Thus, not only the electromagnetic modes of the gap for a specific junction configuration are excited but instead, a multitude of electromagnetic modes, corresponding to all the junction configurations that take place while the tip and sample are moving with respect to each other, contribute to the acquired spectrum. Thus, because so many different modes are excited during a spectrum acquisition, experimental spectra exhibit a high number of peaks, and these peaks have a broader profile. On the other side, the electromagnetic modes excited for the theoretical spectra correspond to a unique junction configuration leading thus, to a lower number of peaks. Hence, to better mimic the experimental spectra, it would be necessary to calculate the plasmonic light emission spectrum of several hybrid junctions with different substrate roughness and tip-surface gap and then, sum the results. This approach would yield a theoretical spectrum with different peaks corresponding to the distinct electromagnetic properties of each considered junction.

Another noteworthy aspect, not emphasized in the spectra of Figure 5.15, is that for both experimental and theoretical light emission spectra, a decrease in the tip-surface distance  $d$ , which is equivalent to an increase in the tunneling current used in experimental STM-LE measurements, results in an increment of the light emission intensity. This trend is illustrated in Figure 5.6-A for the theoretical spectra. For the experimental plasmonic emission, this behavior has been analyzed for a purely metallic  $Au/Au$  junction as depicted in Figure 3.3-B. A similar behavior is observed when analyzing the plasmonic STM-LE obtained from a sample consisting of a  $MoSe_2$  monolayer deposited on a granular gold substrate.

After comparing the spectral characteristics of the theoretical and experimental spectra, the next step is to compare the plasmonic quantum yields obtained for each case. For the theoretical one, the approach described in section 5.3.1 to determine the light emission rate is used by considering the theoretical light emission spectrum of Figure 5.15-A calculated for  $V_s = -1.8$  V and a rough substrate. The resulting value of  $\eta_{plas}$  is given in Table 5.5. For the experimental quantum yield, a similar approach is adopted by integrating the experimental spectrum of Fig. 5.15-B acquired for  $V_s = -1.8$  V and taking into account the acquisition time, the solid angle of the optical fiber used for photon collection and the quantum efficiency of the CCD detector of the spectrometer. The values of  $\eta_{plas}$  obtained are given in the following Table.

	Theoretical	Experimental
Quantum yield $\eta_{plas}$	$2 \times 10^{-6}$	$6 \times 10^{-7}$

**Table 5.5:** Theoretical and experimental plasmonic quantum yields

By examining the data presented in Table 5.5, it is observed that the theoretical quantum yield surpasses the experimental counterpart by approximately threefold. The experimental quantum yield measures the number of emitted photons per tunneling electron, not per elastic tunneling electron as in the theoretical quantum yield. However, this comparison remains valid since less than 1% of the electrons contributing to the tunneling current are inelastic [9]. Indeed, the plasmonic emission model presented in section 5.1. leads to a slight overestimation of the plasmonic emission rate. It is important to highlight that several factors present during the acquisition of experimental STM-LE spectra, including the presence of contaminants, humidity, and the previously mentioned thermal drift, are not considered within the theoretical model. These unaccounted factors could potentially explain the slight difference in the quantum yield.

In the mathematical formalism (presented in section 5.1.2), several simplifications were incorporated, including the straightforward description of the electron states wavefunction to model electron tunneling. Additionally, in the plasmonic emission model (explained in section 5.1), various assumptions were made, such as the consideration of only three initial states for electron tunneling. Nevertheless, despite these simplifications and assumptions, it can be observed that the characteristics of the theoretical spectra regarding the main tunneling parameters and the surface roughness closely align with those in

the experimental spectra. Although there is a slight overestimation of the plasmonic quantum yield, it can be deduced that there is qualitative agreement between theoretical predictions and experimental results.

### b) Excitonic emission

The same comparison between theoretical and experimental results carried out above for the plasmonic emission is here addressed for the excitonic process. In Figure 5.16, theoretical and experimental excitonic light emission spectra are displayed. For the theoretical ones, two different substrates, one flat and one rough, are considered along with a tip-surface distance of  $d=0.2$  nm and a bias voltage of  $V_s=-1.7$  V. On the other hand, the experimental spectra are acquired at different locations of the  $MoSe_2$  monolayer surface, using a bias voltage of  $V_s=-1.7$  V and a tunneling current of  $I_t=10$  nA.

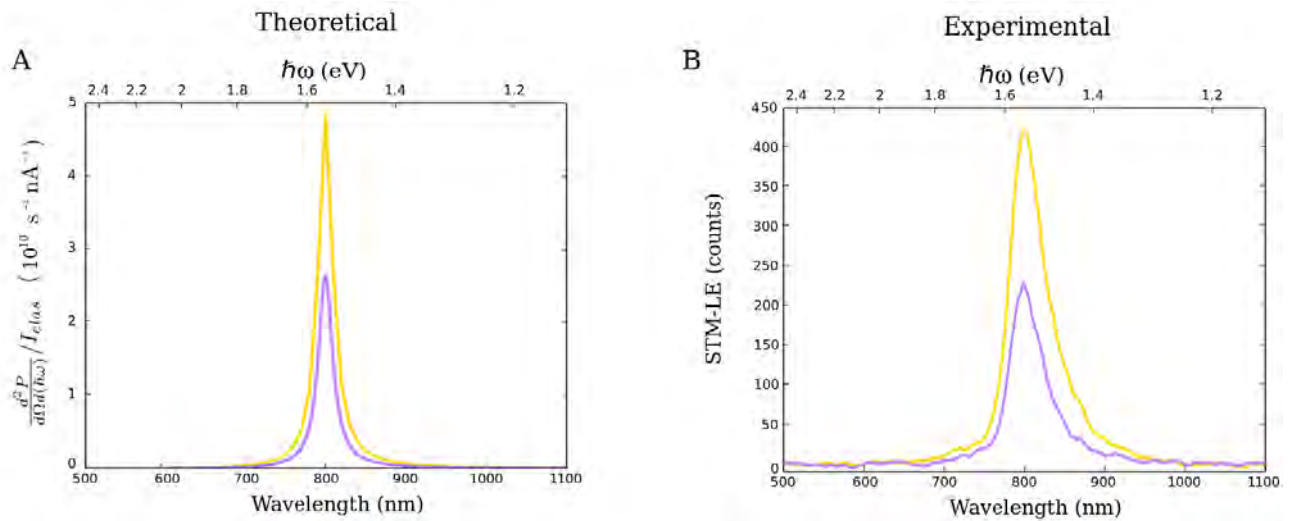


**Figure 5.16:** Comparison of theoretical (A) and experimental (B) excitonic light emission spectra. Theoretical spectra are calculated for a flat substrate (purple line) and a rough substrate (yellow line) using a bias voltage of  $V_s=-1.7$  V and a tip-surface distance of  $d=0.2$  nm. Experimental spectra are acquired at two different locations of the  $MoSe_2$  surface with a bias voltage of  $V_s=-1.7$  V, a tunneling current of  $I_t=10$  nA and an acquisition time of 60 s.

Both theoretical and experimental spectra exhibit a single peak emission at the A-exciton energy ( $\lambda=800$  nm), with the experimental spectra having a broader peak. This is due to the underestimation of the A-exciton damping rate in the theoretical model. Indeed, the damping rates used to compute the theoretical light emission spectra are derived from photoluminescence measurements. However, as discussed in Chapter 3 (see Fig. 3.18), the peak emission observed in photoluminescence measurements is narrower than the one obtained in STM-LE spectra when characterizing the same sample. This accounts for the observed difference in the peak emission width.

A common characteristic observed in both experimental and theoretical spectra is the variation of the peak emission intensity as a function of the sample surface roughness. As highlighted in Chapter 3, the interaction between excitons confined within the TMD monolayer, and localized surface plasmon modes

within the tip-surface gap region can lead to a significant enhancement of the excitonic light emission. Depending on the surface roughness, the characteristics of these plasmon modes differ, affecting the plasmon-exciton coupling and, consequently, the efficiency of the excitonic light emission process. This explains the difference in intensity of the experimental spectra of Figure 5.16-B. In fact, the substrate morphology plays a crucial role in the excitonic light emission efficiency, providing a powerful tool for optimization by tuning it. The interaction between plasmon modes and excitons has been taken into account in the theoretical excitonic model. Indeed, the intensity of the theoretical light emission spectra is proportional to the electric field enhancement, associated mainly with the gap plasmon modes of the junction, at the exciton position along the exciton dipole moment. When the substrate considered goes from flat to rough, the properties of gap plasmon modes change along with their interaction with the excitons, leading to an increment of the excitonic light emission, as shown in Fig. 5.16-A.

The focus will now be shifted towards the examination of the dependence of excitonic light emission spectra on the bias voltage  $V_s$  and the tip-surface distance  $d$ , or on the tunneling current  $I_t$  in the experimental case. In the analysis of the excitonic experimental spectra presented in Chapter 3 (see Fig. 3.17), it has been shown that neither  $V_s$  nor  $I_t$  have a remarkable impact on the emission peak energy. Moreover, the experimental findings indicate that an increment in the tunneling current leads to a more intense STM-LE spectrum. Some random variations in the intensity have also been observed as  $V_s$  changed, but these were attributed mainly to the thermal drift. For the theoretical spectra, it has been observed that variations in the bias voltage  $V_s$  and the tip-surface distance  $d$  have a discernible impact on the intensity of the emission peak, while its energy remains unaffected. Specifically, a reduction in the tip-surface distance  $d$  results in a more pronounced light emission spectrum, as shown in Figure 5.10. This trend aligns with the experimental results. Conversely, an increased bias voltage  $|V_s|$  also results in a more intense light emission, as depicted in Figure 5.9. However, this behavior deviates from what was observed in the experimental case. Indeed, the theoretical excitonic model appears to overestimate the influence of the bias voltage on the light emission intensity in comparison to the experimental findings.

In previous sections, it was discussed that the theoretical excitonic model relies on a strong assumption, assuming that each hole created in the valence band gives rise to an exciton. To determine the overestimation in the number of excitons generated by created hole, a comparison is made between the theoretical and experimental excitonic quantum yields. The excitonic quantum yields are calculated following the same approach as done for the plasmonic emission. For the theoretical quantum yield, the light emission spectrum of Fig. 5.16-A obtained for a rough substrate is considered whereas the experimental quantum yield  $\eta_{exc\ exp}$  is derived by integrating the more intense spectrum from Figure 5.16-B. The resulting excitonic quantum yields are provided in the following table.

	Theoretical	Experimental
Quantum yield $\eta_{exc}$	2	$10^{-6}$

**Table 5.6:** Theoretical and experimental excitonic quantum yields

The calculation of the overestimation in the number of excitons per created hole is then given by:

$$\frac{\eta_{exc\ theo}}{\eta_{exc\ exp}} \sim 10^6 \quad (5.55)$$

Following this approach, the excitonic model presented in this chapter significantly overestimates the quantity of excitons generated within the TMD monolayer per created hole, by approximately an order of magnitude of  $10^6$ . Then, this suggests that in a real hybrid junction, the formation of an exciton occurs for only one out of every  $10^6$  created hole. No estimate of the exciton formation rate per created hole in TMD monolayers has been found in the literature. This study is therefore, to the best of our knowledge, the first effort to evaluate this fundamental quantity.

### c) Hybrid spectra

By introducing the ratio of  $10^{-6}$  excitons per created hole in the excitonic light emission model, a theoretical excitonic quantum yield of the same order of magnitude as the plasmonic one (about  $10^{-6}$  as indicated in Table 5.5) is obtained. Since the rates of excitonic and plasmonic light emission are similar, it is now possible to investigate their combined effect. This analysis aims to generate hybrid theoretical spectra, which encompass both excitonic and plasmonic emission features. Studying this combination provides valuable insights into how these distinct emission characteristics (excitonic and plasmonic) interact and influence the overall spectrum. The resulting spectra are compared with experimental hybrid spectra obtained from STM-LE measurements conducted on an *Au/MoSe<sub>2</sub>/Au* junction (see Fig. 3.19-B).

The excitonic radiated power is computed by considering in the calculations that one out of every  $10^6$  created hole leads to the formation of one exciton, and is then added to the plasmonic one. The combined light emission resulting from both plasmonic and excitonic processes is computed for both flat and rough substrates, with a bias voltage of  $V_s = -1.8$  V and a tip-surface distance of  $d = 0.2$  nm. The resulting spectra are plotted in Figure 5.17-A. These theoretical spectra are compared to experimental hybrid spectra acquired at different locations of the *MoSe<sub>2</sub>* monolayer surface using a bias voltage of  $V_s = -1.8$  V and a tunneling current of  $I_t = 10$  nA.

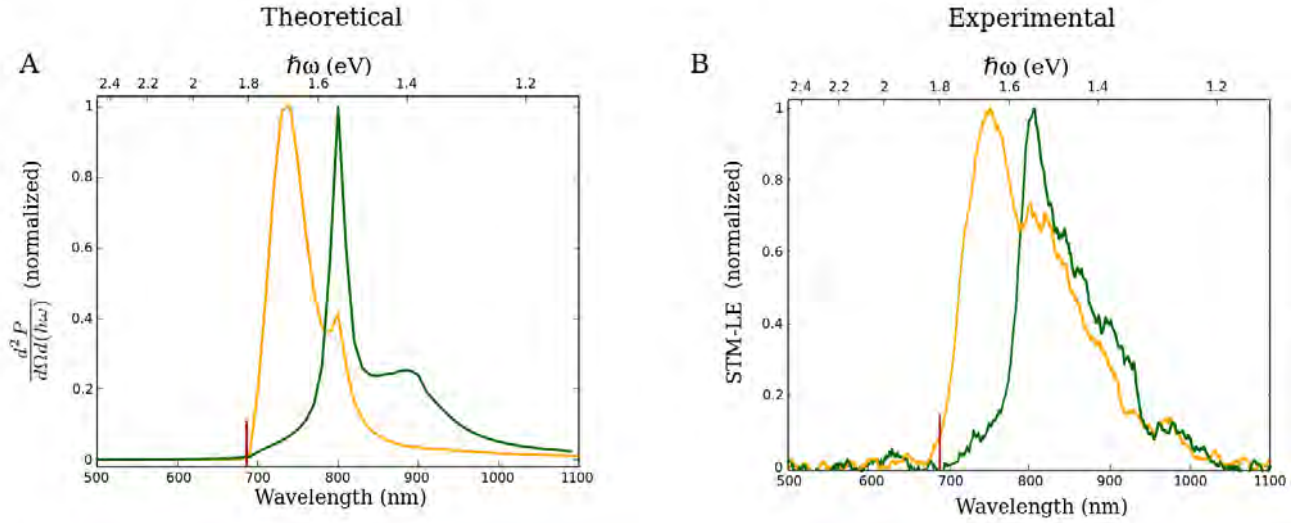


**Figure 5.17:** Comparison of theoretical (A) and experimental (B) hybrid light emission spectra. Theoretical spectra are calculated for a flat substrate (orange line) and a rough substrate (dark green line) using a bias voltage of  $V_s = -1.8$  V and a tip-surface distance of  $d = 0.2$  nm. Experimental spectra are acquired at two different locations of the  $MoSe_2$  surface with a bias voltage of  $V_s = -1.8$  V, a tunneling current of  $I_t = 10$  nA, and an acquisition time of 60 s. Each spectrum is normalized by its maximum.

The theoretical spectra (Figure 5.17-A) display either a broad peak emission or a peak emission with a wide base. In addition, they are characterized by a high-energy threshold following the quantum low  $\hbar\omega = e|V_s|$ , marked by a red bar in the spectra. These characteristics indicate the presence of the plasmonic component in the hybrid spectra. On the other hand, these theoretical spectra display an excitonic component represented by a narrow peak at the wavelength of the A-exciton ( $\lambda = 800$  nm). The same features observed in the theoretical spectra (both the broad plasmonic peak and the narrow excitonic peak) are also found in the experimental hybrid spectra shown in Figure 5.17-B. Moreover, depending on the substrate roughness, either the plasmonic or the excitonic component becomes more prominent in shaping the overall hybrid spectrum. Indeed, for the flat substrate (orange line), the narrow peak associated with the excitonic component is very weak compared to the broader and more intense plasmonic peak. In this case, the plasmonic contribution dominates the theoretical hybrid spectrum. Conversely, when a rough substrate is considered (dark green line), the excitonic component becomes much stronger in the overall spectrum. Indeed, this latter exhibits an intense excitonic peak, while the plasmonic contribution, which is discernible through the broad base of the emission peak, especially at higher wavelengths, is less prominent. When the substrate roughness is introduced, the properties of the plasmon modes within the gap change, altering their interaction with the TMD monolayer excitons. These changes in the plasmonic properties of the junction result in variations in the spectral features and intensity of both plasmonic and excitonic emission processes. Therefore, the contributions of plasmonic and excitonic emissions in the hybrid spectrum are different. This phenomenon has been as well observed experimentally. In the experimental hybrid junction studied, excitonic light emission is generally obtained, enhanced by the plasmon-exciton coupling. However, due to substrate roughness, this coupling can be greatly reduced or absent at certain points of the  $MoSe_2$

surface. Consequently, plasmonic light emission occurs instead. Hence, the substrate roughness plays a crucial role in favoring either excitonic or plasmonic processes.

The theoretical hybrid spectra exhibit the same features as the experimental ones. Additionally, the way these theoretical spectra respond to changes in substrate roughness closely resembles the behavior observed in the actual experiments. When integrating the theoretical and experimental hybrid spectra, as done above for the plasmonic and excitonic emission, the number of photons per tunneling electron obtained is of the same order of magnitude. In Table 5.7, the quantum yields obtained by integrating the theoretical and experimental green spectra of Figure 5.17 are listed.

	Theoretical	Experimental
Quantum yield $\eta_{hybrid}$	$3 \times 10^{-6}$	$9 \times 10^{-7}$

**Table 5.7:** Theoretical and experimental hybrid quantum yields

The theoretical hybrid quantum yield is only three times higher than the experimental one. Thus, the theoretical predictions of the hybrid spectra agree qualitatively with the experimental results. This agreement allows us to validate the ratio of  $10^{-6}$  excitons per created hole incorporated in the excitonic model.

## 5.4 Conclusion

In this chapter, theoretical models describing the plasmonic and excitonic light emission processes taking place in a hybrid  $Au/MoSe_2/Au$  were presented. These processes significantly rely on two key factors: electron tunneling and local electromagnetic environment. The calculations for electron tunneling are based on the models of Johansson *et al.* [1, 2] and Aizpurua *et al.* [3], which, in turn, have their origins in Fermi golden rule. This latter is also employed to describe the radiative recombination of excitons. To account for the influence of the electromagnetic environment on photon emission, the excitonic and plasmonic models include the electromagnetic properties of the hybrid junction, investigated in detail in Chapter 4.

The characteristics of the resulting theoretical spectra and their response to variations in bias voltage  $V_s$ , tip-surface distance  $d$ , and substrate roughness have been examined and compared to the experimental results obtained in Chapter 3 for an equivalent hybrid  $Au/MoSe_2/Au$  STM junction. For the plasmonic emission, the behavior of the theoretical spectra in response to these parameters closely mimics that observed for experimental spectra. In addition, the theoretical model leads to a slight overestimation of the plasmonic quantum yield. Therefore, despite the simplifications and assumptions considered in the plasmonic emission model, such as considering only three initial states for electron tunneling and employing a simplified description of the electron states wavefunctions, there is a good qualitative agreement between the theoretical and experimental findings. On the other hand, in the case of the excitonic process, the theoretical spectra behave similarly to the experimental ones when evaluating the influence of the tip-surface distance  $d$  and the substrate roughness. However, when it comes to the bias

voltage  $V_s$ , it appears that the theoretical model tends to overestimate its impact on the intensity of light emission. Concerning the quantum yield, the excitonic model presented in this chapter significantly overestimates the number of excitons per injected carrier within the TMD monolayer. By comparing the experimental and theoretical quantum yields, this overestimation has been determined leading to the conclusion that, in a real hybrid junction, approximately one out of  $10^6$  created holes gives rise to an exciton. When incorporating this ratio of exciton per created hole in the excitonic model, hybrid spectra can be generated by combining excitonic and plasmonic light emissions. The characteristics of these hybrid spectra closely match those observed experimentally. This alignment confirms that the formation of an exciton occurs for only one out of every  $10^6$  created holes.

The models introduced in this chapter provide valuable insights into the light emission processes occurring in the studied hybrid junction. These models are particularly novel since they provide an unprecedented theoretical description of the light emission from an STM junction involving a semiconductor. Their applicability can be extended to other semiconductor-metal junctions. It is worth mentioning that certain aspects of these models have still room for improvement to enhance their precision and reliability, such as refining the description of electronic states wavefunctions or conducting a more in-depth examination of the role of the substrate roughness. The latter would consist of considering several different rough substrates by playing with the size of the spheres representing the granular surface and their position with respect to the tip. This study is being considered for future work.

## Bibliography

- [1] P. Johansson, R. Monreal, and P. Apell. Theory for light emission from a scanning tunneling microscope. *Phys. Rev. B*, 42(14):9210–9213, 1990.
- [2] P. Johansson and R. Monreal. Theory for photon emission from a scanning tunneling microscope. *Zeitschrift für Physik B Condensed Matter*, 84(2):269–275, 1991.
- [3] J. Aizpurua, S. P. Apell, and R. Berndt. Role of tip shape in light emission from the scanning tunneling microscope. *Phys. Rev. B*, 62(3):2065–2073, 2000.
- [4] Y.-H. Chang, W. Zhang, Y. Zhu, Y. Han, J. Pu, J.-K. Chang, W.-T. Hsu, J.-K. Huang, C.-L. Hsu, M.-H. Chiu, T. Takenobu, H. Li, C.-I. Wu, W.-H. Chang, A. T. S. Wee, and L.-J. Li. Monolayer MoSe<sub>2</sub> grown by chemical vapor deposition for fast photodetection. *ACS Nano*, 8(8):8582–8590, 2014.
- [5] G. L. Nealon, B. Donnio, R. Greget, J.-P. Kappler, E. Terazzi, and J.-L. Gallani. Magnetism in gold nanoparticles. *Nanoscale*, 4(17):5244–5258, 2012.
- [6] V. Iberi, L. Liang, A. V. Ievlev, M. G. Stanford, M.-W. Lin, X. Li, M. Mahjouri-Samani, S. Jesse, B. G. Sumpter, S. V. Kalinin, D. C. Joy, K. Xiao, A. Belianinov, and O. S. Ovchinnikova. Nanoforging single layer MoSe<sub>2</sub> through defect engineering with focused helium ion beams. *Sci. Rep.*, 6(1):30481, 2016.
- [7] R. Péchou, S. Jia, J. Rigor, O. Guillermet, G. Seine, J. Lou, N. Large, A. Mlayah, and R. Coratger. Plasmonic-Induced Luminescence of MoSe<sub>2</sub> Monolayers in a Scanning Tunneling Microscope. *ACS Photonics*, 7(11):3061–3070, 2020.
- [8] J. M. Blatt and V. F. Weisskopf. *Theoretical nuclear physics*. Courier Corporation, 1991.
- [9] P. Johansson. Light emission from a scanning tunneling microscope: Fully retarded calculation. *Phys. Rev. B*, 58(16):10823–10834, 1998.
- [10] L. D. Landau, E. M. Lifshitz, and L. P. Pitaevskii. *Electrodynamics of Continuous Media*. Pergamon Press, 1984.
- [11] J. Bardeen. Tunnelling from a many-particle point of view. *Phys. Rev. Lett.*, 6(2):57–59, 1961.
- [12] H.-L. Dai and W. Ho. *Laser Spectroscopy and Photochemistry on Metal Surfaces*. World Scientific Publishing Company, 1995.
- [13] L. D. Landau and E. M. Lifshitz. *Quantum mechanics: non-relativistic theory*, volume 3. Elsevier, 2013.

- [14] S. Larentis, H. C. P. Movva, B. Fallahazad, K. Kim, A. Behroozi, T. Taniguchi, K. Watanabe, S. K. Banerjee, and E. Tutuc. Large effective mass and interaction-enhanced Zeeman splitting of K-valley electrons in MoSe<sub>2</sub>. *Phys. Rev. B*, 97(20):201407, 2018.
- [15] A. Kormányos, G. Burkard, M. Gmitra, J. Fabian, V. Zólyomi, N. D. Drummond, and V. Fal'ko.  $k \cdot p$  theory for two-dimensional transition metal dichalcogenide semiconductors. *2D Mater.*, 2(2):022001, 2015.
- [16] S. Wang, J. Wang, W. Zhao, F. Giustiniano, L. Chu, I. Verzhbitskiy, J. Zhou Yong, and G. Eda. Efficient carrier-to-exciton conversion in field emission tunnel diodes based on MIS-type van der Waals heterostack. *Nano Lett.*, 17(8):5156–5162, 2017.
- [17] J. Wang, I. Verzhbitskiy, and G. Eda. Electroluminescent devices based on 2D semiconducting transition metal dichalcogenides. *Adv. Mater.*, 30(47):1802687, 2018.
- [18] M. Fox. *Quantum optics: an introduction*, volume 15. Oxford University Press, 2006.
- [19] J. J. Sakurai. *Advanced quantum mechanics*. Pearson Education India, 1967.
- [20] L. C. Andreani, G. Panzarini, and J.-M. Gérard. Strong-coupling regime for quantum boxes in pillar microcavities: Theory. *Phys. Rev. B*, 60(19):13276–13279, 1999.
- [21] I. Abid, W. Chen, J. Yuan, A. Bohloul, S. Najmaei, C. Avendano, R. Péchou, A. Mlayah, and J. Lou. Temperature-dependent plasmon–exciton interactions in hybrid Au/MoSe<sub>2</sub> nanostructures. *ACS Photonics*, 4(7):1653–1660, 2017.
- [22] M. Palummo, M. Bernardi, and J. C. Grossman. Exciton radiative lifetimes in two-dimensional transition metal dichalcogenides. *Nano Lett.*, 15(5):2794–2800, 2015.
- [23] S. Hao, M. Z. Bellus, D. He, Y. Wang, and H. Zhao. Controlling exciton transport in monolayer MoSe<sub>2</sub> by dielectric screening. *Nanoscale Horiz.*, 5(1):139–143, 2020.
- [24] P. Rivera, J. R. Schaibley, A. M. Jones, J. S. Ross, S. Wu, G. Aivazian, P. Klement, K. Seyler, G. Clark, N. J. Ghimire, J. Yan, D. G. Mandrus, W. Yao, and X. Xu. Observation of long-lived interlayer excitons in monolayer MoSe<sub>2</sub>–WSe<sub>2</sub> heterostructures. *Nat. Commun.*, 6(1):6242, 2015.
- [25] C. T. Le, D. J. Clark, F. Ullah, V. Senthilkumar, J. I. Jang, Y. Sim, M.-J. Seong, K.-H. Chung, H. Park, and Y. S. Kim. Nonlinear optical characteristics of monolayer MoSe<sub>2</sub>. *Annalen der Physik*, 528(7-8):551–559, 2016.
- [26] I. Abid, A. Bohloul, S. Najmaei, C. Avendano, H.-L. Liu, R. Péchou, A. Mlayah, and J. Lou. Resonant surface plasmon–exciton interaction in hybrid MoSe<sub>2</sub>@Au nanostructures. *Nanoscale*, 8(15):8151–8159, 2016.

- 
- [27] G. Wang, A. Chernikov, M. M. Glazov, T. F. Heinz, X. Marie, T. Amand, and B. Urbaszek. Colloquium: Excitons in atomically thin transition metal dichalcogenides. *Rev. Mod. Phys.*, 90(2):021001, 2018.

# Conclusion

A thorough investigation of the luminescence of TMD monolayers induced by local low-energy electrical excitation using a Scanning Tunneling Microscope is presented in this thesis. The study focuses on the light emission from a hybrid TMD/plasmonic-metal ( $Au/MoSe_2/Au$ ) STM junction, with particular attention to the intricate interplay between plasmon modes supported by the tip-sample nanocavity, and the excitons confined within the TMD monolayer. The role of these elements in the light emission phenomenon has been analyzed through both experimental and theoretical approaches.

Indeed, by using an STM coupled to a light detection system, light emission induced by STM (STM-LE) from different tunnel junctions is experimentally studied. Significant differences in terms of photon intensity, spectral distribution, and the tunneling conditions necessary for photon emission are observed between the luminescence obtained from a purely plasmonic junction and from a junction comprising a  $MoSe_2$  monolayer where no plasmon modes are involved. The disparities arise from distinct underlying mechanisms behind light emission: on one hand, the radiative decay of tip-induced surface plasmon modes excited by inelastic electron tunneling in the case of the purely plasmonic junction, and on the other hand, the radiative decay of bright excitons for the junction with the TMD monolayer. For a hybrid junction formed by a  $MoSe_2$  monolayer supported by a gold substrate and a gold tip, the photon emission process is governed by the electromagnetic coupling between plasmon modes and excitons. This interaction enhances the intensity of the luminescence originating from exciton decay. The morphology of the plasmonic substrate, on which the monolayer is deposited, significantly influences the light emission process. The specific plasmonic resonances hosted by the tunneling junction when the substrate is nanostructured, exhibit a more favorable spectral and spatial overlap with excitons compared to when a flat substrate is considered. This results in a more efficient plasmon-exciton electromagnetic coupling and thus, in an increment by an order of magnitude of the STM-LE signal. These results represent a promising approach for optimizing light emission efficiency by engineering the morphology of the substrate.

The experimental light emission process from hybrid STM junctions is significantly influenced by the plasmon-exciton electromagnetic coupling. To gain insight into this interaction, the electromagnetic properties of a hybrid  $Au/MoSe_2/Au$  tunneling junction have been studied by means of numerical simulations using DDA (Discrete Dipole Approximation) method. The Quantum-Corrected Model (QCM) has also been employed to account for the effects of electron tunneling at tip-sample distances  $d$

below 0.5 nm. However, these effects appeared to be negligible due to the weak tunneling conductivity considered. By simulating the optical response of the junction to an incident excitation wave, the electromagnetic modes sustained by the junction have been investigated. A Fano-type plasmon-exciton coupling involving the substrate plasmonic mode, the excitons confined within the TMD monolayer, and the tip-surface gap plasmon modes, has been identified. This coupling results in a hybrid gap plasmon-exciton mode localized within the monolayer and at the  $MoSe_2/Au$  substrate interface. The dependence of the spectral characteristics and spatial distribution of these modes on the main tunneling parameters (tip-surface distance  $d$  and bias voltage  $V_s$ ) and on the incident electric field has been addressed. As the tip-surface distance decreases, the gap plasmon modes get more localized, resulting in a reduction of the gap plasmon-exciton coupling. Moreover, when the incident electric field component along the tip axis increases, the hybrid gap plasmon-exciton mode gets “undressed” of its excitonic character to gradually become a pure gap plasmon mode. Incorporating a rough substrate into the simulations yields a distinct tip-surface gap (different size and geometry), reducing the extent to which the optical response of the hybrid junction depends on the incident electric field polarization. Moreover, the interaction between protrusions on the rough substrate surface gives rise to local surface plasmon modes. The electromagnetic properties of a hybrid junction similar to the experimental one have been determined by these simulations. These properties constitute a crucial element in the development of a theoretical model explaining the STM-LE phenomenon.

For the purpose of computing theoretical light emission spectra for a hybrid  $Au/MoSe_2/Au$  STM junction, two theoretical models have been developed: the first one describes the light emission process originating from the excitation of plasmon modes within the gap by inelastic tunneling, while the second one describes the photon emission resulting from the radiative decay of excitons. These models consider the tunneling current as the excitation source and take into account the electromagnetic properties of the junction, including the plasmon-exciton coupling. The resulting theoretical spectra, along with their responses to changes in the main tunneling parameters and substrate roughness, have been analyzed and then compared to experimental findings. For the plasmonic emission, the theoretical study reproduces the main experimental trends, with only a minor overestimation of the light emission quantum yield. Thus, despite simplifications and assumptions in the plasmonic emission model, a strong qualitative agreement between theoretical and experimental results has been achieved. In the case of the excitonic process, the theoretical spectra align with experimental results regarding the tip-surface distance and substrate roughness but exaggerate the impact of the bias voltage on the light emission intensity. In this model, the number of excitons per injected carrier within the TMD monolayer has been indeed deliberately overestimated. By comparing experimental and theoretical excitonic quantum yields, this overestimation has been identified, suggesting that in a real hybrid junction, approximately one out of  $10^6$  created holes results in an exciton. Incorporating this ratio in the excitonic model enables the generation of hybrid spectra, combining excitonic and plasmonic light emissions. These hybrid spectra closely resemble experimental observations, offering strong validation for the estimated ratio of excitons per created hole.

The results presented in this thesis demonstrate that STM-LE serves as a valuable technique to locally probe the opto-electrical properties of two-dimensional semiconductors. This opens an interesting avenue for studying TMD heterostructures such as TMD superlattices by using this technique. Moreover, the local character of the STM-LE technique makes it particularly original and interesting for studying the properties of other quantum emitters, such as molecules or quantum dots. Furthermore, the strain induced by the tip and the temperature effects resulting from the tunneling current are other aspects of the STM-LE technique that, although not addressed here, could offer valuable insights into the fundamental mechanisms governing light-matter interactions and other sample properties. Our findings provide an interesting starting point for the design of plasmonic nanostructured substrates aiming to achieve an enhanced and controlled light emission induced by STM, in particular when excitonic quantum emitters are also involved in the junction. Additionally, the theoretical model developed here exhibits the potential to extend its application to STM junctions involving other semiconductors or quantum emitters. It can also serve as a predictive tool for light emission from various junctions, aiding in the design of plasmonic nanostructured substrates. Therefore, our study of STM-LE from hybrid junctions holds promise for the development of future nanosources of light and their integration into opto-electronic devices.

# Abstract - English

Transition-metal dichalcogenides (TMDs) are a family of semiconductors that exhibit a direct bandgap when their thickness is reduced to a monolayer, giving them remarkable optical and electronic properties, including high-efficiency luminescence. Photon emission from these monolayers is investigated using the STM-LE (Light Emission induced by Scanning Tunneling Microscopy) technique. This innovative method involves the localized injection of charge carriers into TMD monolayers through the tunneling current. This process results in the formation of excitons, electron-hole pairs bound by Coulomb forces, within the TMD monolayer. These excitons decay radiatively emitting photons whose energy corresponds to the direct bandgap of the semiconductor. This light emission process is experimentally studied using an STM microscope combined with a light detection system, enabling spectral and spatial analysis of the photon emission with nanometer-scale resolution.

The electromagnetic interaction between TMD layers and their metallic substrates leads to the formation of hybrid metal-semiconductor structures, the optical and electronic properties of which are under investigation. The nature of the substrate (plasmonic or non-plasmonic) and its morphology (uniform or nanostructured) play a crucial role in both the intensity and spectral distribution of the emitted photons. Indeed, for plasmonic substrates, the photon emission process involves the electromagnetic coupling between plasmon modes excited by electron tunneling and excitons confined within the TMD monolayer. This interaction leads to an enhancement of the photon emission. Moreover, by tuning the morphology of the substrate, it becomes possible to modify this coupling and thus, the photon emission rate.

Considering the significant role of the electromagnetic interaction between plasmon modes and excitons in the luminescence from TMD monolayers within a hybrid TMD/plasmonic-metal STM junction, electromagnetic numerical simulations are carried out using the DDA (Discrete Dipole Approximation) method. These simulations account for electron tunneling using the Quantum Corrected Model. By simulating the optical response of the junction to an incident excitation wave, the electromagnetic modes within the junction and their dependence on the tunneling parameters, such as tip-surface distance and bias voltage, are investigated. In particular, gap plasmon modes and the Fano-type plasmon-exciton coupling at the interface between the monolayer and the plasmon substrate are pointed out. Furthermore, the role of substrate morphology on the properties of these modes is also addressed. Based on theoretical models describing the light emission taking place in purely metallic STM junctions proposed in the literature, a model is developed to compute theoretical light emission spectra for a

---

hybrid TMD/plasmonic-metal STM junction. This model takes into account the optical and electronic properties of the TMD monolayer, and the electron tunneling as the excitation source at the origin of the light emission phenomenon. In addition, using the results obtained from the numerical simulations, the electromagnetic coupling between the excitons confined in the TMD monolayer and the plasmons excited in the nanocavity formed by the tip-surface configuration of the STM is also considered. Finally, the effect of the substrate morphology on the light emission is studied theoretically. These results are compared with the experimental findings in order to validate the model presented.

# Abstract - Français

Les dichalcogénures de métaux de transition (TMD) sont une famille de semi-conducteurs qui présentent un gap direct lorsque leur épaisseur est réduite jusqu'à la monocouche, ce qui leur confère des propriétés optiques et électroniques exceptionnelles, notamment une luminescence avec un rendement élevé. La technique d'émission de lumière dans un microscope à effet tunnel (STM-LE) est utilisée pour étudier l'émission de photons de ces monocouches. Cette technique originale consiste à injecter grâce au courant tunnel des porteurs de charges de manière très locale dans des monocouches de TMD. Cela conduit à la création d'excitons, paires électrons-trous liées par des forces coulombiennes, au sein de la monocouche. Ces excitons vont se désexciter en émettant des photons dont l'énergie correspond au gap direct du semi-conducteur. Ce phénomène de luminescence est mis en évidence expérimentalement en utilisant un microscope STM couplé à un dispositif de détection optique, ce qui permet une analyse de l'émission de photons à la fois sur le plan spectral et spatial avec une résolution nanométrique.

Le couplage électromagnétique des monocouches de TMD avec leurs substrats métalliques donne naissance à des structures hybrides métal/semi-conducteur dont les propriétés optiques et électroniques sont étudiées. La nature du substrat (plasmonique ou non) et sa morphologie (uniforme ou nanostructurée) jouent un rôle essentiel tant sur l'intensité que sur la distribution spectrale de la luminescence émise. En effet, lorsque des substrats plasmoniques sont utilisés, le mécanisme d'émission lumineuse implique le couplage électromagnétique entre des modes plasmoniques excités par le courant tunnel et les excitons confinés au sein de la monocouche de TMD. Cette interaction donne lieu à une émission de photons plus efficace. En jouant avec la morphologie de ces substrats, il est possible d'ajuster ce couplage afin d'obtenir une amplification ou une atténuation de l'émission de lumière.

Sachant que l'interaction électromagnétique entre plasmons et excitons joue un rôle important dans la luminescence émise par les monocouches au sein d'une jonction STM hybride TMD/métal plasmonique, des simulations numériques électromagnétiques sont réalisées via la méthode DDA (Discrete Dipole Approximation). Dans ces simulations, les effets quantiques du courant tunnel sont pris en compte en utilisant le modèle Quantum Corrected Model. Les modes électromagnétiques présents dans la jonction et leur dépendance vis-à-vis des paramètres tunnel (distance pointe-surface et tension de polarisation) sont mis en évidence à partir de la simulation de la réponse optique de la jonction à une onde excitatrice incidente. En particulier, les modes "gap plasmon" et le couplage plasmon-exciton de type Fano se produisant à l'interface entre la monocouche et le substrat plasmonique sont mis en évidence. L'influence de la morphologie du substrat sur les propriétés de ces modes est également analysée.

En s'inspirant des modèles théoriques de l'émission de lumière dans des jonctions STM purement métalliques proposés dans la littérature, un modèle est développé afin d'obtenir des spectres théoriques de luminescence d'une jonction STM hybride TMD/métal plasmonique. Ce modèle prend en compte les propriétés optiques et électroniques de la monocouche, ainsi que le courant tunnel, source d'excitation à l'origine du phénomène de luminescence. De plus, en utilisant les résultats obtenus à partir des simulations numériques, le couplage électromagnétique entre les excitons confinés dans la monocouche de TMD et les plasmons excités dans la nanocavité formée par la configuration pointe-surface du STM est également considéré. Pour finir, l'effet de la morphologie du substrat sur l'émission de lumière est étudié de manière théorique. Ces résultats sont comparés aux résultats expérimentaux afin de valider le modèle présenté.

# Résumé en Français

Le microscope à effet tunnel (STM: Scanning Tunneling Microscope) [1] est un instrument très polyvalent. Traditionnellement utilisé pour imager la topographie de surfaces conductrices telles que des métaux et des semi-conducteurs, il s'est révélé être un outil expérimental intéressant pour induire l'émission de lumière et explorer les propriétés optiques locales d'échantillons à l'échelle atomique. Le mécanisme à la base de l'émission de lumière induite par STM (STM-LE) repose sur le courant tunnel fortement localisé, agissant comme source d'excitation.

Si une faible tension de polarisation est appliquée entre la pointe et la surface ( $V_s < 4$  V), les électrons ont une probabilité non nulle de traverser la barrière tunnel, et un courant tunnel s'établit. Cette probabilité dépend de manière exponentielle de la distance pointe-surface  $d$ , qui est de quelques angströms. Une petite fraction des électrons tunnel vont transiter de manière inélastique d'une électrode à l'autre [2], perdant ainsi une partie ou la totalité de leur énergie. Dans le cas de jonctions STM formées par des métaux plasmoniques, la proximité entre la pointe et la surface de l'échantillon à une distance tunnel conduit à la formation d'une nanocavité plasmonique. L'énergie perdue par les électrons inélastiques entraîne l'excitation de modes plasmoniques de surface localisés (LSP) dans le gap de la jonction. La désexcitation radiative de ces modes donne lieu à l'émission de photons. Ce mécanisme est représenté dans la figure ci-dessous:

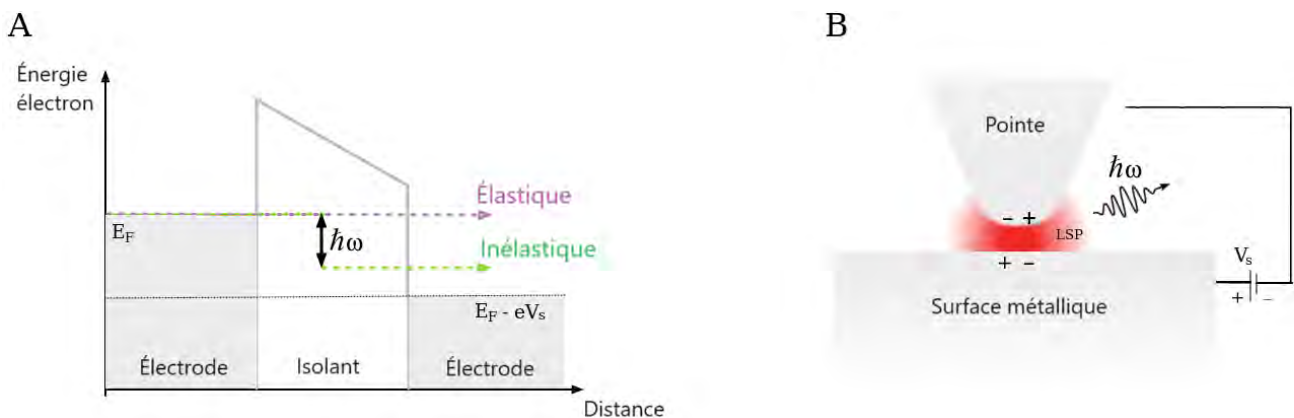


**Fig. 1:** (A) Diagramme de bande illustrant des électrons traversant la barrière de potentiel par effet tunnel de manière élastique (violet) et inélastique (vert). Les électrons inélastiques perdent une partie ou la totalité de leur énergie ( $\hbar\omega$ ) en excitant (B) des modes plasmoniques de surface localisés dans le gap, dont leur désexcitation entraîne l'émission de photons.

La distribution spectrale des photons émis présente un seuil en haute énergie, lié à la différence de potentiel appliquée entre les deux électrodes  $V_s$  selon la loi quantique  $\hbar\omega = e|V_s|$  [3]. En effet, l'énergie perdue par les électrons inélastiques varie de zéro à  $e|V_s|$ , et par conséquent, aucune radiation n'est détectée à une énergie supérieure à  $e|V_s|$ . Le processus d'émission de lumière y compris sa distribution spectrale et son rendement (nombre de photon émis par électron tunnel) dépendent donc des paramètres tunnel tels que la tension de polarisation appliquée à la jonction  $V_s$  et la distance pointe-surface  $d$ . Les caractéristiques de la lumière émise sont également étroitement liées aux propriétés électromagnétiques des matériaux impliqués dans la jonction ainsi qu'à leur géométrie. En fait, l'influence de la géométrie de la pointe et de la surface de l'échantillon sur l'émission de photons a fait l'objet de plusieurs études expérimentales [4]. Les spectres obtenus à partir de jonctions plasmoniques se caractérisent, en dehors du seuil à haute énergie, par la présence de plusieurs pics, dont l'intensité, l'énergie et la largeur varient en fonction de la géométrie de la jonction. Ces variations spectrales sont attribuées aux propriétés des modes LSP, qui évoluent également lorsque la géométrie de la pointe et/ou de la surface de l'échantillon change. En outre, des modèles théoriques ont été élaborés pour comprendre ce processus d'émission et anticiper l'intensité ainsi que la distribution spectrale de la lumière émise par ces jonctions plasmoniques en fonction des paramètres mentionnés [5–10].

Outre les jonctions métalliques, la luminescence induite par STM a été observée dans des jonctions où des molécules sont placées entre des électrodes conductrices et dans des jonctions où l'une des électrodes est un semi-conducteur. Dans le dernier cas, le processus d'émission de lumière est attribué à des transitions électroniques interbandes ou excitoniques se produisant au sein de l'échantillon. Ces transitions électroniques sont provoquées par l'injection de porteurs de charges de manière très locale dans l'échantillon par le biais du courant tunnel, comme le montre la Fig. 2. Ceci rend la technique STM-LE un outil de spectroscopie précieux pour étudier les transitions électroniques et l'énergie des excitons, dans le cas d'échantillons excitoniques, à l'échelle atomique.

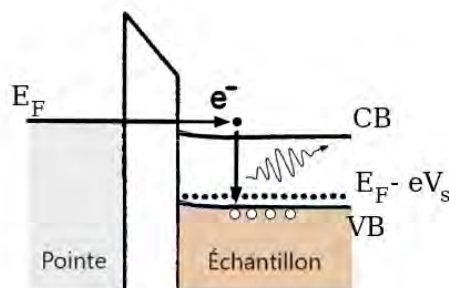


**Fig. 2:** Diagramme de bande illustrant l'émission de photons induite par l'injection de charges (par le biais du courant tunnel) dans un semi-conducteur dopé p et polarisé positivement [11].

Pour les jonctions impliquant un semi-conducteur, en plus des paramètres tunnel, il est nécessaire de prendre en compte le niveau de dopage du semi-conducteur et la polarité de la tension appliquée afin

que le processus d'émission de photons puisse avoir lieu [12, 13]. La luminescence induite par STM a été observée pour divers semi-conducteurs, allant des surfaces aux puits quantiques, en passant par les fils quantiques, et même les points quantiques. Cette thèse se concentre sur l'émission de lumière induite par STM de part de monocouches de dichalcogénures de métaux de transition (TMD), une famille de semi-conducteurs. Les électrons tunnel dans une jonction STM ont une énergie très faible ( $< 4$  eV) et par conséquent, une faible profondeur de pénétration. Cette caractéristique favorise une interaction efficace entre les électrons tunnel et les échantillons ultra-minces, faisant du STM une technique idéale pour étudier les propriétés des matériaux bidimensionnels tels que les monocouches de TMD à l'échelle nanométrique.

La découverte des propriétés extraordinaires des matériaux bidimensionnels a révolutionné la recherche fondamentale et ouvert de nouvelles perspectives d'applications industrielles [14]. Parmi les matériaux 2D, les monocouches de TMD ont suscité beaucoup d'attention. Les TMD présentent la particularité de pouvoir ajuster leur bande interdite et leurs propriétés optiques en fonction du nombre de couches. Les TMD présentant la formule chimique générale  $MX_2$  avec M un métal de transition (*Mo*, *W*) et X un chalcogène (*S*, *Se*, *Te*), se distinguent en tant que semi-conducteurs fortement anisotropes. Ils sont constitués de feuillets liés les uns aux autres par des interactions de type van der Waals. Une seule couche de  $MX_2$  est composée de trois plans atomiques covalents, comprenant un plan d'atomes métalliques (M) pris en sandwich entre deux plans d'atomes de chalcogène (X). La combinaison d'atomes de métaux de transition *Mo* ou *W* avec des atomes de chalcogènes *S* ou *Se* a donné naissance à une large gamme de semi-conducteurs dont la structure de bande, y compris la bande interdite, peut être ajustée par le nombre de couches.

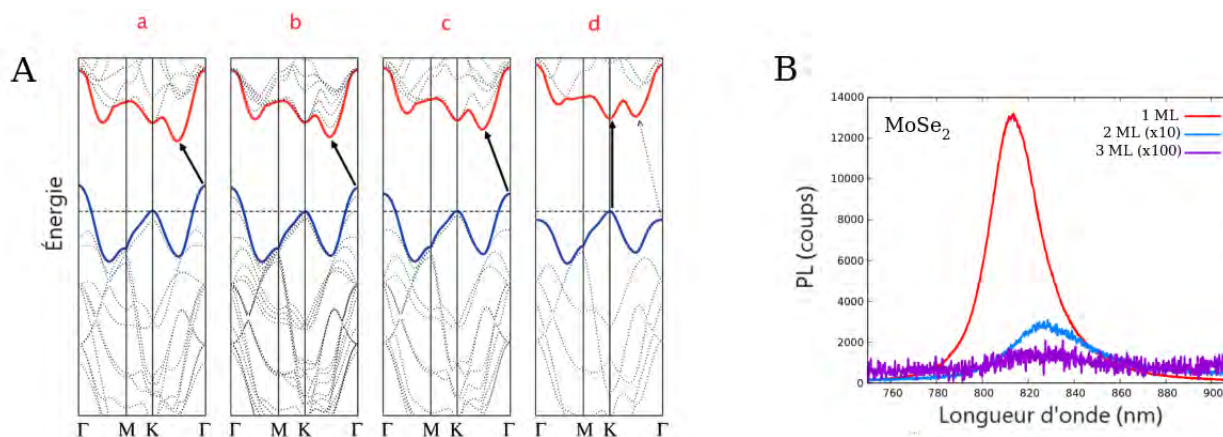


**Fig. 3:** (A) Structure de bande électronique du  $MoS_2$  sous forme massive (a), quadricouche (b), bicouche (c) et monocouche (d) [15]. (B) Spectre de photoluminescence d'une monocouche (rouge), d'une bicouche (bleue) et d'une tricouche (violet) de  $MoSe_2$ . L'augmentation du nombre de couches entraîne une réduction significative de l'intensité du signal de photoluminescence [16].

En effet, les cristaux de TMD présentent une bande interdite indirecte dans leur forme massive, tandis que sous forme de monocouche, ils possèdent une bande interdite directe située aux points *K* de la première zone de Brillouin (Fig. 3-A) [17, 18]. Ceci rend les monocouches de TMD idéales pour

étudier l'interaction lumière-matière. En comparaison avec leur forme massive, elles présentent un signal de photoluminescence plus important et une absorption de lumière plus efficace [16, 19, 20]. En effet, la transition de bande interdite indirecte à bande interdite directe lors du passage de la forme massive à la forme de monocouche, facilite les processus optiques tels que l'émission de lumière, comme le montre Fig. 3-B.

En raison de l'absence de symétrie d'inversion dans les monocouches de TMD, leur structure de bande électronique présente six points  $K$  divisés en deux groupes non équivalents: les points  $K^+$  et  $K^-$ . De plus, un couplage spin-orbite fort est induit par la manque de symétrie d'inversion et les atomes métalliques relativement lourds composant la monocouche. Ce couplage entraîne une levée de dégénérescence des états électroniques aux points non équivalents  $K^+$  et  $K^-$  de la bande valence (BV) et de la bande de conduction (BC) [21]. Pour la monocouche de  $MoSe_2$ , cette séparation entre états de spin up et down dans la bande de valence atteint environ 200 meV, tandis que dans la bande de conduction, elle est de seulement quelques meV. Les propriétés optiques des monocouches de TMD sont gouvernées par des excitons, des paires électron-trou fortement liées par des forces de Coulomb, avec des énergies de liaison pouvant atteindre plusieurs centaines de meV. La levée de dégénérescence conduit à la formation de deux sous-bandes de valence, engendrant deux types d'excitons: l'exciton A et l'exciton B, avec une énergie de 1.55 eV et 1.77 eV respectivement dans le cas du  $MoSe_2$  [22]. Ces excitons sont représentés dans la Fig. 4.

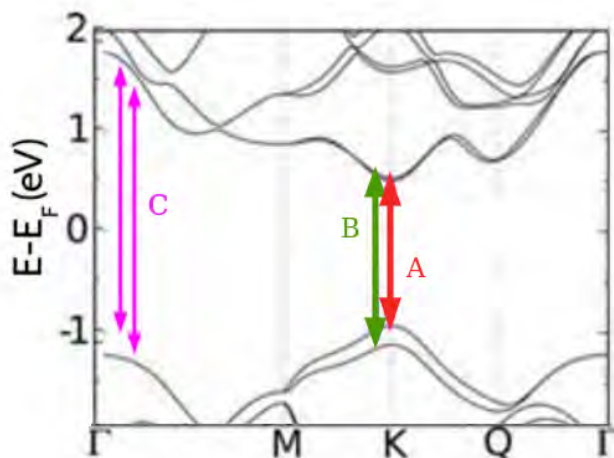


**Fig. 4:** Structure de bande d'une monocouche de  $MoSe_2$  où les excitons A, B et C sont représentés [23].

En outre, du fait de la séparation des spins dans la BC et la BV, les excitons A et B peuvent se présenter sous la forme d'excitons autorisés par spin (électron et trou partageant le même spin) ou d'excitons interdits par spin (électron et trou avec des spins différents). Les excitons autorisés par spin peuvent être optiquement actifs, c'est-à-dire qu'ils peuvent être excités par absorption photonique résonante et peuvent se désexciter de manière radiative. Ils sont ainsi qualifiés d'excitons "bright" (excitons lumineux), tandis que les excitons interdits par spin, optiquement inactifs, sont désignés comme excitons "dark" (excitons sombres). Les excitons "bright", qui participent au processus d'émission de lumière, présentent un moment dipolaire électrique dans le plan de la monocouche. La structure de bande

des monocouches de TMD révèle une BC et une BV parallèles le long de la direction  $\Gamma$ -M donnant naissance aux excitons de type C avec une énergie d'environ 2.6 eV dans le cas du  $MoSe_2$  [24](Fig. 4). Ces excitons, ainsi que leur énergie associée, sont discernés à travers des mesures optiques telles que la photoluminescence. L'interaction lumière-matière au sein de ces monocouches obéit aux règles optiques chirales établies par la conservation de l'énergie, de la quantité de mouvement et du spin. Il est possible d'exciter les excitons "bright" au sein des vallées  $K^+$  ou  $K^-$  en utilisant une lumière polarisée circulairement  $\sigma^+$  ou  $\sigma^-$ , respectivement. Les monocouches de TMD présentent des propriétés optiques, électroniques, "valleytroniques" et spintroniques exceptionnelles qui sont très sensibles à l'environnement diélectrique qui entoure la monocouche. Les monocouches de TMD sont produites soit par exfoliation micromécanique, soit par des méthodes de synthèse. Les feuillets de  $MoSe_2$  étudiés au cours de ma thèse ont été synthétisés par dépôt chimique en phase vapeur (CVD) [25], une technique permettant la croissance contrôlée de monocouches de haute qualité et de grande taille.

En général, les excitons au sein des monocouches de TMD sont excités optiquement, mais ils peuvent également être excités électriquement. En utilisant le courant tunnel du microscope à effet tunnel, des porteurs de charges peuvent être injectés de manière très locale dans les monocouches de TMD, conduisant à la formation d'excitons qui vont se désexciter en émettant des photons dont l'énergie correspond à la bande interdite directe (optique) du semi-conducteur.

Ce phénomène de luminescence est expérimentalement mis en évidence en utilisant un microscope STM (Bruker Veeco Dimension D3100) [16] fonctionnant dans des conditions ambiantes en mode d'utilisation courant constant, c'est-à-dire en mesurant le déplacement en hauteur de la pointe pendant le balayage de la surface de l'échantillon, tout en maintenant un courant tunnel constant. La tête du STM, illustrée en Fig. 5-A, est constituée d'un porte-pointe personnalisé placé à l'extrémité d'un tube piézoélectrique cylindrique. Ce dernier permet un déplacement nanométrique vertical et horizontal de la pointe. La variation de la position  $z$  de la pointe est enregistrée à chaque position latérale ( $x, y$ ). Cette variation est codée en couleur formant des images topographiques avec une résolution de l'ordre du nanomètre (Fig. 5-C). L'utilisation d'un STM dans des conditions ambiantes facilite la préparation de l'échantillon et de la pointe. Cependant, la résolution des images STM peut être dégradée par plusieurs facteurs, notamment par des variations de température provoquant la dilatation ou la contraction des composants du microscope. En effet, la pointe et la surface de l'échantillon se déplacent constamment l'une par rapport à l'autre à cause de la dérive thermique, ce qui se traduit par des mesures de moindre qualité et des images topographiques avec une résolution réduite. Le STM est placé dans une chambre qui bloque tout courant d'air et agit également comme une cage de Faraday pour le protéger de tout rayonnement électromagnétique.

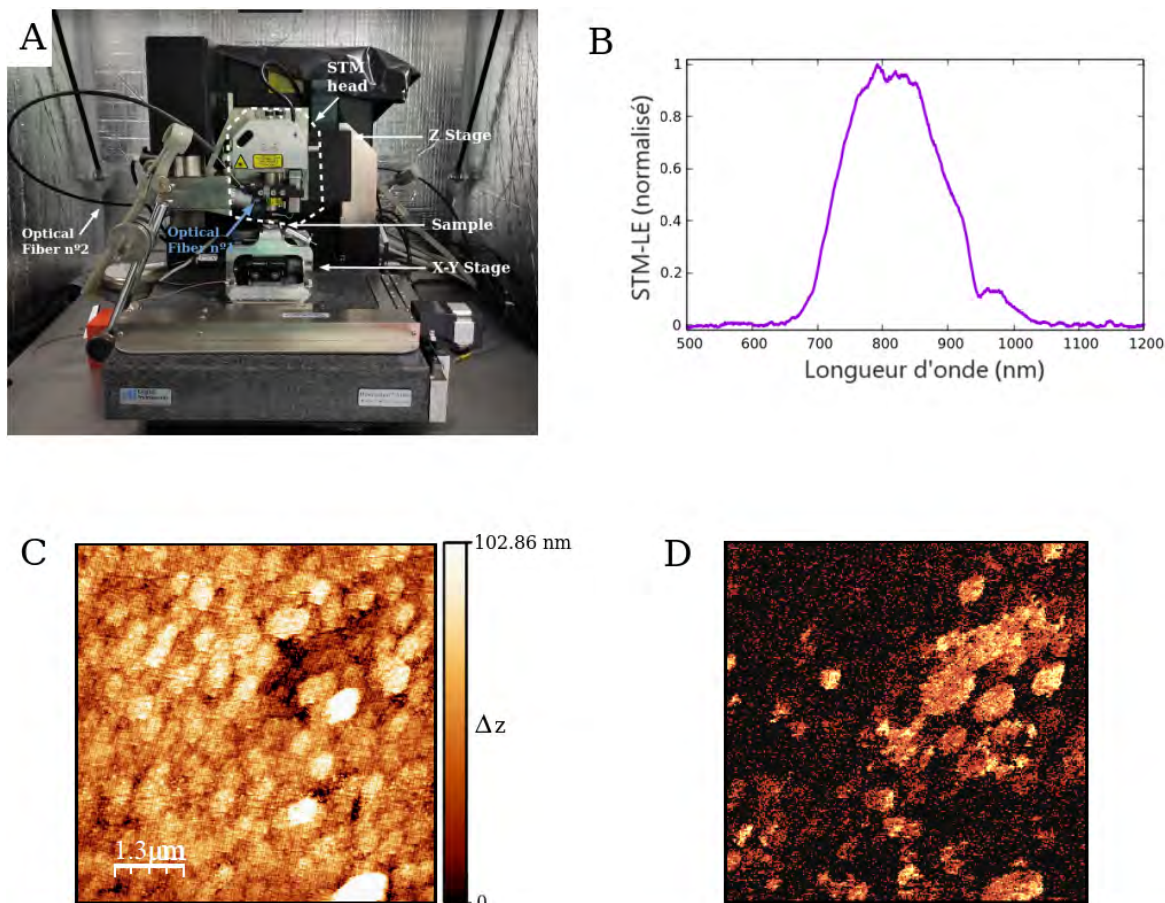


**Fig. 5:** (A) Photographie du microscope à effet tunnel. (B) Spectre STM-LE typique (normalisé) obtenu à partir d'une jonction tunnel  $Au/MoSe_2/Au$  ( $V_s = -1.8$  V;  $I_t = 20$  nA et temps d'acquisition de 90 s). (C) Image topographique STM et (D) cartographie photonique correspondante enregistrées simultanément sur une zone de  $6.5 \mu\text{m} \times 6.5 \mu\text{m}$ . L'échantillon consiste en une monocouche de  $MoSe_2$  déposée sur un substrat d'or polycristallin ( $V_s = +1.8$  V;  $I_t = 15$  nA).

Ce microscope est couplé à un dispositif de détection optique. La collection de photons est réalisée par une fibre optique placée à environ 1 mm de l'apex de la pointe qui permet de transmettre la lumière collectée aux systèmes d'analyse optique: un spectromètre et un tube photomultiplicateur. Ce dispositif expérimental permet d'obtenir trois informations: la topographie de la surface de l'échantillon (Fig. 5-C), la cartographie de photons (Fig. 5-D) et la répartition spectrale des photons émis (Fig. 5-B). Le photomultiplicateur est synchronisé avec le microscope STM de sorte à permettre l'acquisition simultanée du nombre de photons émis et de l'image topographique de la surface de l'échantillon. Ceci permet de corréler les propriétés optiques avec la topographie de la surface étudiée avec une résolution exceptionnelle.

Le rôle de la nature des matériaux impliqués dans la jonction tunnel sur la luminescence induite par STM et ses caractéristiques a été étudié expérimentalement. Le signal STM-LE obtenu à partir d'une jonction purement plasmonique composée d'une pointe en or (fabriquée par attaque chimique) et d'un échantillon d'or polycristallin a été examiné. La rugosité granulaire de cet échantillon a été

identifiée sur les cartographies photoniques obtenues. En effet, sur la cartographie de Fig. 6-B, la surface granulaire de l'échantillon (Fig. 6-A) est discernable. Cela suggère que la rugosité de la surface a une influence sur l'intensité de la luminescence induite par STM. Les spectres obtenus se caractérisent par un seuil en énergie [3] et la présence de plusieurs pics dont l'intensité, énergie et largeur varient en fonction de la géométrie de la jonction (Fig. 6-C). En effet, en raison de la rugosité granulaire de la surface, selon la localisation de l'échantillon où le spectre est acquis, la géométrie de la jonction diffère considérablement. Ceci donne lieu à des spectres avec des pics d'émission différents. Comme mentionné précédemment, la luminescence observée pour ce type de jonction est attribuée à l'excitation par des électrons tunnel inélastiques de modes plasmoniques localisés dans le gap entre la pointe et la surface de l'échantillon. La résonance de ces modes électromagnétiques est étroitement liée à la géométrie de la jonction, ce qui explique les différences observées entre les spectres acquis à différents points de la surface de l'échantillon.

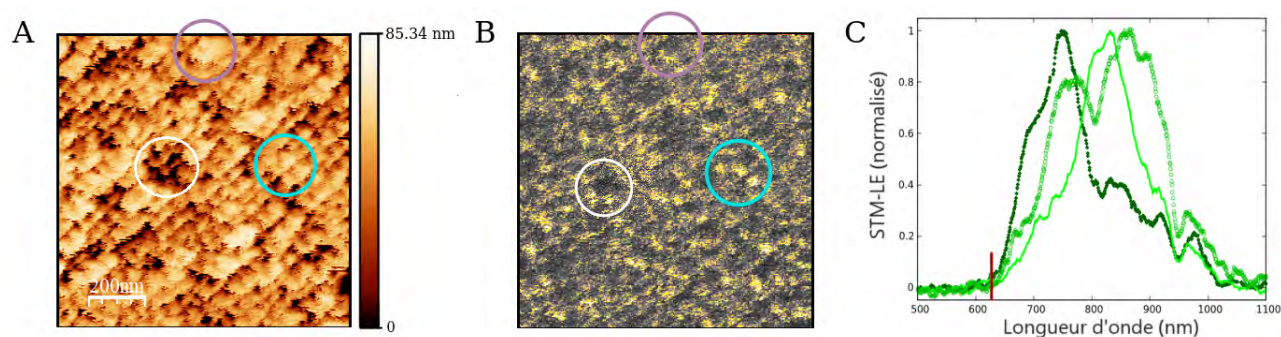


**Fig. 6:** (A) Image topographique STM et (B) cartographie photonique correspondante enregistrées simultanément sur une zone de  $1 \mu\text{m} \times 1 \mu\text{m}$  ( $V_s = +1.8 \text{ V}$ ;  $I_t = 10 \text{ nA}$ ). (C) Spectres STM-LE acquis à différentes localisations de la surface de l'échantillon en utilisant les mêmes paramètres tunnel:  $V_s = +2 \text{ V}$ ;  $I_t = 15 \text{ nA}$  et temps d'acquisition de 60 s. La trait rouge indique le seuil à haute énergie.

L'émission de photons a été observée pour ces jonctions plasmoniques quel que soit le signe de la tension, c'est-à-dire pour les deux directions du courant tunnel. De plus, une augmentation de l'intensité du signal a été observée avec l'augmentation du courant tunnel, suggérant ainsi que le nombre de photons émis est proportionnel au nombre d'électrons tunnel.

Après avoir examiné la luminescence induite par STM issue des jonctions plasmoniques, l'attention se tourne désormais vers un processus d'émission de lumière différent: STM-LE de part de monocouches de  $\text{MoSe}_2$ . Afin d'éviter que des modes plasmoniques ne soient impliqués dans l'émission de lumière provenant des feuillets de  $\text{MoSe}_2$ , ces derniers ont été transférés dans des substrats non plasmoniques comme l'oxyde d'indium-étain (ITO) présentant aussi une surface granulaire [26]. De l'émission de photons a été détectée pour plusieurs monofeuillets de  $\text{MoSe}_2$ , nous permettant ainsi de réaliser des cartographies photoniques et des mesures spectrales. L'émission de lumière est détectée exclusivement lorsqu'une tension de polarisation négative  $V_s$  est appliquée à l'échantillon, c'est-à-dire lorsqu'il y a création de trous dans la monocouche par le courant tunnel. En effet, les monocouches étudiées sont dopées n [27], permettant ainsi aux électrons en excès de former des excitons avec les trous créés par

le courant tunnel. À partir des cartographies photoniques enregistrées aux bords des monofeuillets (voir Fig. 7-A), la luminescence associée à la désexcitation radiative des excitons de la monocouche est observée, en contraste avec l'ITO nu où aucune émission de photons n'a lieu. Un rendement radiatif d'environ  $3 \times 10^{-8}$  photons par électron tunnel est obtenu pour ce type de jonction.

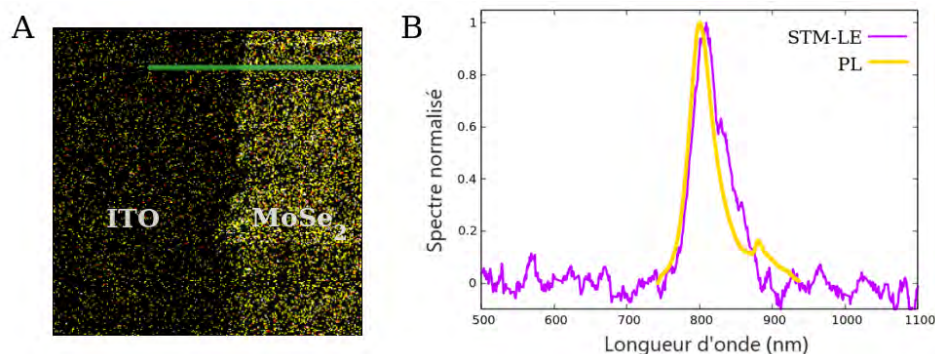


**Fig. 7:** (A) Cartographie photonique acquise au bord d'un monofeuillet de  $MoSe_2$ . La zone d'acquisition est de  $10 \mu\text{m} \times 10 \mu\text{m}$  ( $V_s = -1.8 \text{ V}$  ;  $I_t = 15 \text{ nA}$ ). (B) Spectre normalisé de photoluminescence (jaune) et de STM-LE (violet) obtenus pour une monocouche de  $MoSe_2$  sur ITO. Le spectre STM-LE a été acquis en utilisant les paramètres tunnel:  $V_s = -1.8 \text{ V}$  ;  $I_t = 22 \text{ nA}$  et un temps d'acquisition de 600 s.

Les spectres obtenus à partir de la jonction  $Au/MoSe_2/ITO$  présentent des différences significatives par rapport à ceux observés pour des jonctions purement plasmoniques. Un pic d'émission asymétrique entre environ 740 et 910 nm est observé, avec une intensité maximale autour de 805 nm (1.54 eV). Cette émission correspond à la désintégration radiative des excitons A, formés par injection de charges via le courant de tunnel. Aucune tendance spécifique n'est observée dans l'évolution de l'intensité du pic à mesure que  $|V_s|$  augmente. Cependant, une intensité plus prononcée est constatée lorsque le courant de tunnel est plus élevé. Cela s'explique par l'augmentation du nombre d'électrons participant au courant de tunnel, entraînant ainsi l'injection d'une plus grande quantité de charges dans la monocouche et conduisant à la formation d'un plus grand nombre d'excitons. Par conséquent, une émission de lumière plus efficace est obtenue. Ce pic d'émission est également obtenu quelle que soit la localisation sur la surface de  $MoSe_2$  où le spectre est acquis; seule son intensité varie. En comparant le spectre de STM-LE et le spectre de photoluminescence présentés dans la Fig. 7-B, les deux processus d'émission peuvent clairement être attribués au même mécanisme: la désexcitation radiative des excitons A au sein de la monocouche de  $MoSe_2$ . Néanmoins, quelques différences peuvent être observées entre les deux spectres, telles qu'un léger décalage vers le rouge et une plus grande largeur du pic pour le spectre STM-LE par rapport à celui obtenu par photoluminescence. Ces différences spectrales peuvent être attribuées à plusieurs facteurs, notamment la présence de la pointe, qui peut modifier l'environnement diélectrique entourant la monocouche de  $MoSe_2$  et ainsi altérer ses propriétés optiques intrinsèques, l'augmentation de la température de l'échantillon due à l'injection locale de charges, et/ou la création d'excitons chargés par le courant tunnel.

L'émission de lumière n'est détectée que lorsque la tension appliquée au substrat  $V_s$  est inférieure ou égale à -1.7 V. En effet, lorsque la tension de polarisation  $V_s$  dépasse un certain seuil, des électrons de

la bande de valence de la monocouche peuvent traverser la barrière tunnel vers la pointe. Ce processus entraîne la création de trous dans la bande de valence. Ces trous sont susceptibles d'attirer des électrons de la bande de conduction, entraînant la formation d'excitons. Par la suite, ces excitons peuvent se recombiner de manière radiative, générant ainsi l'émission lumineuse observée. En utilisant une tension positive  $V_s$ , comme la monocouche est dopée n, la formation d'excitons est très peu probable à cause de l'absence de trous dans la bande de valence. Ceci explique l'absence de photons pour  $V_s > 0$ .

Le troisième type de jonction, dont l'émission de lumière a été analysée, est la jonction hybride  $Au/MoSe_2/Au$  où des monofeuillets de  $MoSe_2$  ont été déposés sur un substrat d'or polycrystalline [16]. Dans une configuration hybride, les deux processus radiatifs analysés avant peuvent se produire: la désexcitation radiative des modes plasmoniques excités par les électrons inélastiques, et la recombinaison radiative des excitons au sein de la monocouche de TMD créés par injection de charge. En comparant les résultats de STM-LE obtenus pour ce type de jonction hybride avec ceux obtenus pour la jonction précédente, nous pouvons analyser l'impact de la nature plasmonique du substrat sur la luminescence des monocouches. Selon le signe de la tension  $V_s$ , les cartographies photoniques acquises aux bords de monofeuillets de  $MoSe_2$  sont très différentes (Fig. 8-(B,C)). Pour  $V_s > 0$ , une différence significative de l'intensité du signal STM-LE est observée entre le substrat d'or nu, qui présente une moyenne de 600 coups par seconde, et la couche de  $MoSe_2$  avec que 5 coups par seconde. En revanche, pour  $V_s < 0$ , cette différence d'intensité est significativement plus faible avec une moyenne de 500 et 150 coups par seconde pour le substrat d'or nu et la monocouche de TMD, respectivement.

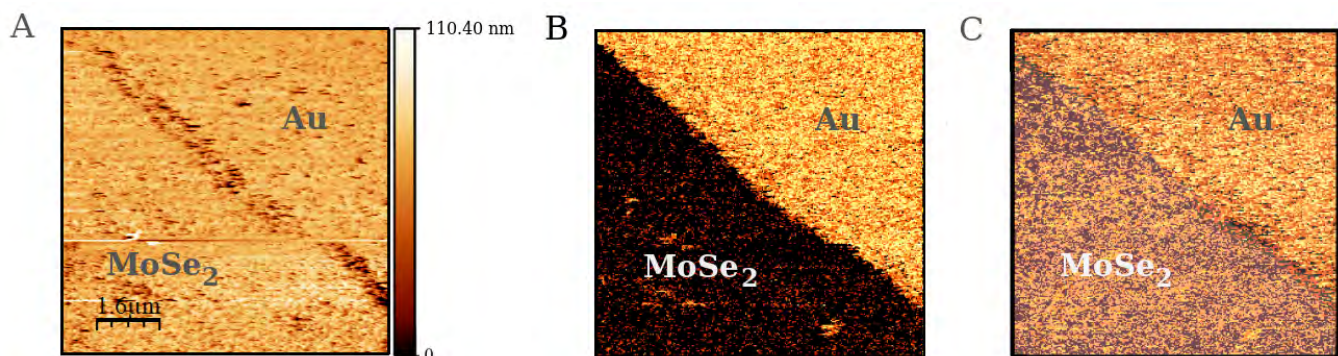


**Fig. 8:** (A) Image topographique STM et (B-C) cartographies photoniques correspondantes enregistrées sur une zone de  $8 \mu\text{m} \times 8 \mu\text{m}$  avec (B) une tension de polarisation positive  $V_s = +1.7 \text{ V}$  et (C) une tension de polarisation négative  $V_s = -1.7 \text{ V}$ . Le courant tunnel utilisé est  $I_t = 5 \text{ nA}$ .

Comme indiqué plus haut, le substrat d'or émet de la lumière indépendamment de la polarité de la tension appliquée à la jonction, car les modes plasmoniques dans la cavité pointe-surface sont excités indépendamment de la direction du courant tunnel. En revanche, la monocouche de  $MoSe_2$  présente un taux d'émission STM-LE significativement supérieur (environ 30 fois plus) lorsque le substrat est polarisé négativement. Ce résultat rappelle la luminescence observée pour la jonction  $Au/MoSe_2/ITO$ , qui se produit exclusivement lorsque  $V_s < 0$ . Un rendement radiatif d'environ  $1 \times 10^{-6}$  photons par électron

(en tenant compte de l'angle solide de la fibre et du rendement quantique du photomultiplicateur) est obtenue pour la jonction hybride (pour  $V_s < 0$ ), soit deux ordres de grandeur supérieurs à celui obtenu avec le substrat d'ITO ( $\sim 3 \times 10^{-8}$  photons par électron). Cette augmentation du taux d'émission lumineuse est attribuée au caractère plasmonique du substrat. En effet, les modes plasmoniques jouent un rôle important dans l'émission de photons provenant de la monocouche. D'autre part, la luminescence de part de la monocouche détectée lorsque  $V_s > 0$  est principalement localisée à des endroits spécifiques de la surface. Cette luminescence peut être attribuée à différents facteurs, tels que l'émission de lumière provenant du substrat causée par des fissures de la monocouche ou d'autres défauts. Ce point sera abordé plus tard. La différence de taux d'émission lumineuse observée entre le substrat d'or nu et la monocouche pour  $V_s < 0$  est attribuée à des mécanismes d'excitation distincts derrière le processus radiatif.

Une analyse spectrale a été réalisée sur l'émission lumineuse induite par STM provenant des monocouches de  $MoSe_2$  déposées sur le substrat d'or, en utilisant une tension de polarisation  $V_s$  négative, tout en faisant varier  $V_s$  et le courant tunnel  $I_t$ . Un seul pic d'émission, avec un maximum autour de l'énergie de l'exciton A (800 nm correspondant à 1.55 eV), est observé dans tous les spectres, indépendamment de la tension de polarisation (négative) et du courant tunnel. Les caractéristiques spectrales, telles que l'absence d'un seuil à haute énergie et la présence d'un seul pic d'émission étroit, confirment que l'émission lumineuse provient de la désexcitation radiative des excitons A confinés dans la monocouche et non des modes plasmoniques. D'autre part, lorsque le courant tunnel  $I_t$  augmente, l'intensité du signal STM-LE augmente ce qui indique qu'un grand nombre de charges injectées dans la monocouche entraîne une augmentation de l'émission de lumière. Le mécanisme à l'origine de l'émission lumineuse de la jonction  $Au/MoSe_2/Au$  est supposé être très similaire à celui proposé pour la jonction  $Au/MoSe_2/ITO$  car les deux émissions présentent la même signature spectrale et un comportement similaire en fonction des paramètres tunnel. Lorsque le substrat est polarisé négativement et qu'un seuil de tension est atteint, des électrons peuvent par effet tunnel, passer de la bande de valence de la monocouche vers la pointe, entraînant la création de trous. Ces trous vont attirer des électrons de la bande de conduction du TMD ou du substrat et former des excitons, qui se désexcitent de manière radiative donnant lieu à l'émission de lumière observée. Tout comme dans le cas de la jonction avec l'ITO, la source de luminescence dans la jonction  $Au/MoSe_2/Au$  est la désexcitation des excitons générés par injection de charges dans la monocouche. Cependant, dans le cas de la jonction hybride  $Au/MoSe_2/Au$ , due au substrat plasmonique, l'excitation des modes plasmoniques par électrons tunnel inélastiques peut se produire également. Un couplage électromagnétique en champ proche se manifeste entre les modes plasmoniques et les excitons en raison de leur chevauchement spatial et spectral. Ce couplage engendre un transfert d'énergie particulièrement efficace, entraînant une augmentation des excitons dans la monocouche et, par conséquent, une augmentation du rendement radiatif.

La Figure 9-A présente les spectres d'émission STM-LE et photoluminescence (normalisés) de la monocouche de  $MoSe_2$  sur un substrat d'or. L'interaction entre les modes plasmon et les excitons augmente l'émission de lumière excitonique, donnant lieu à un spectre STM-LE avec un rapport

signal/bruit très élevé, comparable à celui obtenu par photoluminescence. Ceci est un résultat remarquable, étant donné que le courant tunnel est une source d'excitation plus localisée que l'excitation optique de la technique de photoluminescence. Les deux spectres présentent le même pic d'émission à l'énergie de l'exciton A à 797 nm (1.56 eV) avec une largeur plus importante dans le cas du STM-LE. En appliquant une échelle semi-logarithmique, un deuxième pic d'émission autour de 720 nm (1.72 eV) est mis en évidence. Ce pic est attribué à la désexcitation radiative des excitons B qui est décalé vers le rouge (d'environ 50 meV) par rapport au pic de l'exciton B de monocouches de  $MoSe_2$  suspendues, rapporté par Iberi *et al.* [22]. Ce décalage vers le rouge peut être attribué à l'utilisation d'un substrat différent, entraînant un environnement diélectrique différent autour de la monocouche.

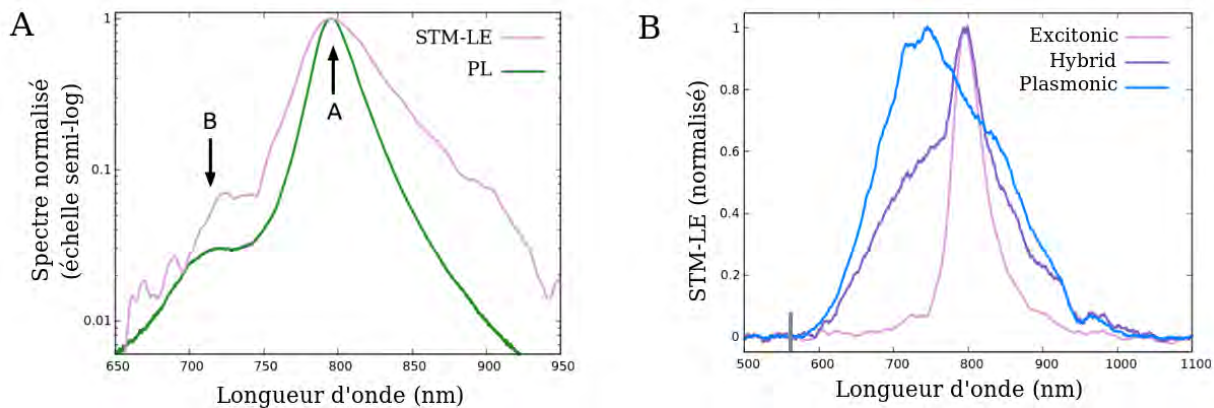


**Fig. 9:** (A) Spectres de photoluminescence (vert) et de STM-LE (rose) normalisés de la monocouche de  $MoSe_2$  sur un substrat d'or. Une échelle semi-logarithmique est appliquée. Le spectre STM-LE a été acquis avec les paramètres tunnel suivants:  $V_s = -2$  V ;  $I_t = 20$  nA et un temps d'acquisition de 90 s. (B) Types de spectres STM-LE obtenus lorsque la pointe balaye des monofeuillets de  $MoSe_2$ : excitonique, hybride et plasmonique ( $V_s = -2.2$  V ;  $I_t = 20$  nA et un temps d'acquisition de 90 s).

Les spectres acquis lors du balayage de certains monofeuillets de  $MoSe_2$  peuvent être classés en trois catégories, comme illustré dans la Figure 9-B. Des spectres d'émission de type excitonique, se caractérisant par un pic d'émission étroit à la longueur d'onde de l'exciton A, sont généralement obtenus. D'autre part, il est également possible d'obtenir des spectres présentant une signature typiquement plasmonique, se caractérisant par la présence de plusieurs pics et un seuil à haute énergie suivant la loi quantique  $\hbar\omega = e|V_s|$ . De plus, un troisième type de spectre, appelé hybride, présentant des caractéristiques distinctives des deux processus radiatifs, excitonique et plasmonique, est obtenu. Les spectres hybrides possèdent une composante plasmonique, caractérisée par des pics avec une largeur importante et un seuil à haute énergie, ainsi qu'une composante excitonique représentée par un pic étroit à la longueur d'onde de l'exciton A.

Des spectres plasmoniques et hybrides ont été souvent obtenus lors du balayage de zones de la monocouche de  $MoSe_2$  présentant des déchirures/fissures provoquées par la pointe. Cependant, parfois, ces spectres STM-LE ont été acquis dans des régions de la monocouche qui semblent exemptes de défauts. Dans ce cas, ces spectres sont attribués à une réduction ou à l'absence du couplage entre les modes plasmoniques et les excitons en raison de défauts atomiques ou de la rugosité de la surface du substrat. Ainsi, au lieu de transférer de l'énergie aux excitons, les modes plasmoniques se désexcitent de manière radiative,

entraînant une luminescence plasmonique.

Le rôle de la morphologie du substrat dans l'émission STM-LE de la monocouche est étudié en utilisant deux substrats d'or nanostructurés différents. En effet, une forte émission de lumière excitonique provenant de la monocouche de  $MoSe_2$  peut être obtenue en utilisant un substrat plasmonique en raison du couplage plasmon-exciton. Ce couplage peut être ajusté en jouant avec la morphologie de la surface du substrat métallique pour accorder/décorder les résonances excitoniques et plasmoniques. Ainsi, en choisissant une morphologie du substrat appropriée, le processus d'émission peut être encore optimisé (plus de rendement). Pour explorer ce point, des monocouches de  $MoSe_2$  ont été transférées sur deux substrats d'or nanostructurés différents, chacun constitué d'un réseau géométrique de cavités. Les cavités de chaque substrat présentent une géométrie distincte, l'une étant pyramidale [16] (Fig. 10-A) et l'autre circulaire.

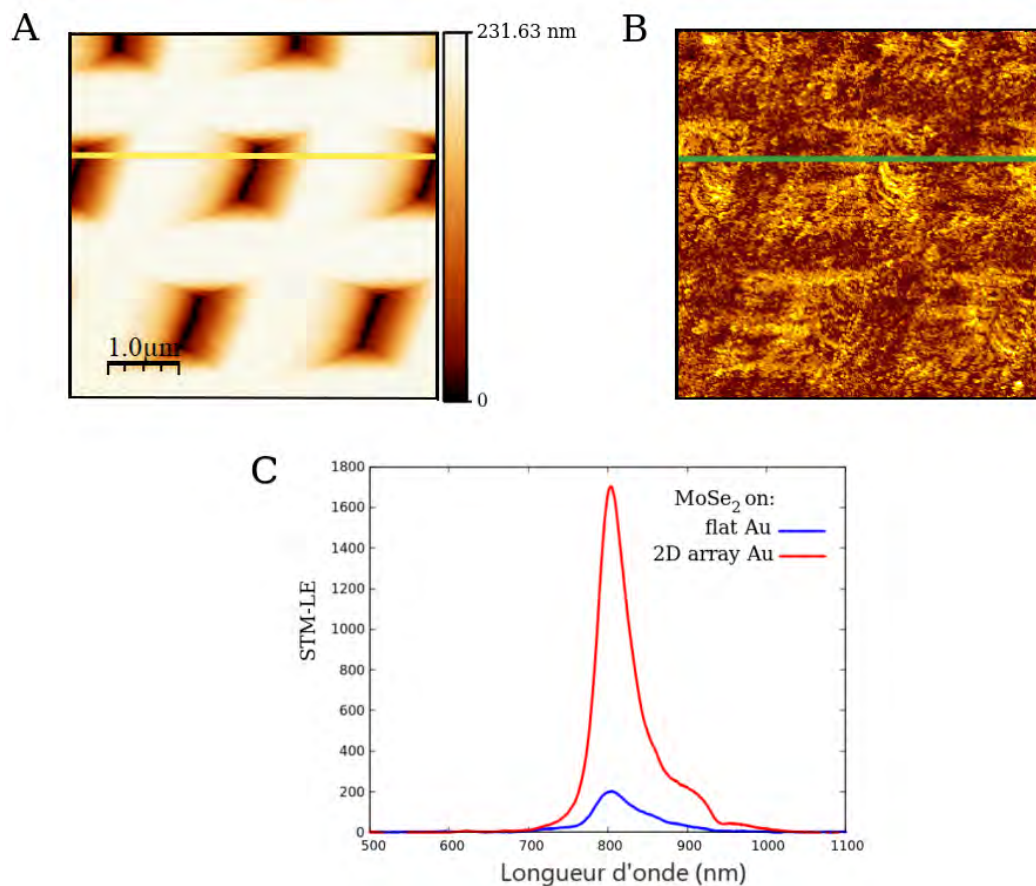


**Fig. 10:** (A) Image topographique STM et (B) cartographie photonique correspondante d'une monocouche de  $MoSe_2$  sur un substrat d'or nanostructuré avec des cavités pyramidales. Les deux images ont été enregistrées simultanément sur une zone de  $5 \mu\text{m} \times 5 \mu\text{m}$  ( $V_s = -1.7 \text{ V}$ ;  $I_t = 2 \text{ nA}$ ). La pointe STM ne peut pas atteindre le fond des cavités en raison de sa géométrie asymétrique. (C) Spectres STM-LE d'une monocouche de  $MoSe_2$  déposée sur la région plate à l'extérieur de la zone nanostructurée (bleu) et sur la zone nanostructurée (rouge) du substrat d'or nanostructuré avec des cavités pyramidales. Les deux spectres ont été acquis avec les paramètres tunnel suivants:  $V_s = -1.8 \text{ V}$ ;  $I_t = 10 \text{ nA}$  et un temps d'acquisition de 120 s.

Des mesures STM-LE ont été effectuées sur des monocouches déposées sur les deux substrats nanostructurés.

En général, un spectre STM-LE plus intense est obtenu pour les monocouches déposées sur une zone nanostructurée par rapport au signal STM-LE obtenu pour les feuillets se trouvant sur une région plate (à l'extérieur de la zone nanostructurée) du substrat. Dans la Fig. 10-C, des spectres STM-LE acquis avec les mêmes conditions tunnel sur une monocouche placée à la fois sur une zone nanostructurée avec des cavités pyramidales et sur une région plate à l'extérieur de la zone nanostructurée du substrat, sont représentés. Une augmentation notable de la luminescence provenant de la partie de la monocouche déposée sur la zone nanostructurée est observée. En particulier, l'intensité maximale à 800 nm montre une augmentation d'environ un ordre de grandeur. Cette amélioration du rendement d'émission dans le cas du substrat nanostructuré est attribuée à un couplage plasmon-exciton plus efficace. Ce couplage est amélioré dû à un chevauchement spectral plus favorable entre les transitions excitoniques et les modes plasmoniques de la surface du substrat nanostructuré excités par les électrons inélastiques. Des cartographies photoniques réalisées sur une monocouche déposée sur une zone nanostructurée (voir Fig. 10-(A,B)) montrent une émission de lumière plus intense aux emplacements correspondant à la monocouche suspendue au-dessus de cavités qu'aux endroits où elle repose sur les bandes plates entre les cavités.

Sachant que l'interaction électromagnétique entre plasmons et excitons joue un rôle important dans la luminescence des monocouches de  $MoSe_2$  dans le cas d'une jonction STM hybride TMD/métal plasmonique, des simulations numériques électromagnétiques ont été réalisées via la méthode DDA (Discrete Dipole Approximation). Ces simulations visent à mettre en évidence les modes électromagnétiques propres à ce type de jonction hybride et à analyser leurs caractéristiques et leur comportement en fonction des paramètres tunnel [28] et de la rugosité de la surface du substrat. L'analyse porte sur la réponse optique d'une jonction tunnel  $Au/MoSe_2/Au$ , où chaque composante est modélisée par un réseau 3D de points dipolaires, soumise à un champ électrique incident. Fig. 11-A présente la jonction modélisée avec une pointe STM en or approximée par un hyperboloïde de révolution avec une longueur de 15 nm et un rayon de courbure à l'apex d'environ 0.15 nm. Cette pointe est positionnée au-dessus d'un substrat en or de dimensions 20 nm  $\times$  20 nm  $\times$  2.2 nm. Une monocouche de  $MoSe_2$ , simulée par un parallélépipède rectangle avec une épaisseur de 0.8 nm [27], est supportée par le substrat d'or. Pour la monocouche de  $MoSe_2$ , nous avons utilisé des indices de réfraction optiques isotropes et anisotropes afin de mettre en évidence le caractère anisotrope de la monocouche dans la réponse optique de la jonction [29, 30]. La distance entre l'apex de la pointe et la couche de  $MoSe_2$  varie entre 0.2 nm et 2 nm. Cette jonction est excitée par un champ électrique incident dont le vecteur d'onde fait un angle de  $\theta = 45^\circ$  par rapport à l'axe de la pointe. Ce champ est linéairement polarisé (polarisation p et s). Ainsi, le champ incident polarisé p a deux composantes: l'une orthogonale et l'autre parallèle à l'axe de la pointe. En revanche, la direction de la polarisation s est orthogonale au plan d'incidence et donc parallèle à la surface de la monocouche de  $MoSe_2$ .

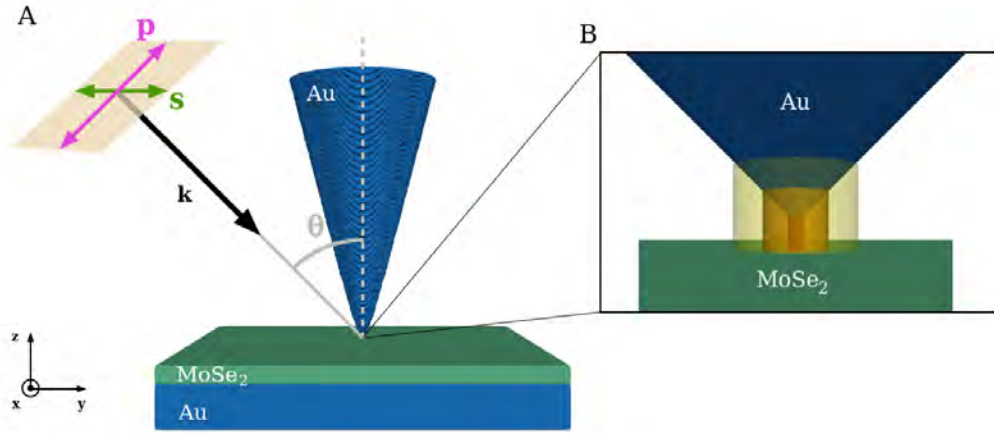


**Fig. 11:** (A) Représentation schématique de la jonction hybride  $Au/MoSe_2/Au$  composée d'une pointe sous forme d'hyperboloïde de révolution et d'une monocouche de  $MoSe_2$  déposée sur un substrat en or avec une surface plane. Elle est excitée par un champ électrique incident polarisé linéairement p ou s (flèche rose et verte respectivement). (B) Dans le régime tunnel ( $d < 0.5$  nm), le modèle Quantum-Corrected Model (QCM) est utilisé et un milieu effectif conducteur est modélisé entre la pointe et la monocouche pour tenir compte des effets quantiques du courant tunnel. Le milieu effectif est composé d'un ensemble de coques cylindriques avec une conductivité dépendante de la distance pointe-surface  $d$ .

Dans ces simulations, les effets quantiques du courant tunnel sont pris en compte en utilisant le modèle Quantum-Corrected Model [31, 32]. En effet, pour des distances pointe-surface inférieures à 0.5 nm (régime tunnel), des phénomènes quantiques tels que le courant tunnel se manifestent, et leur impact sur la réponse optique ne peut plus être considéré comme négligeable. Ils doivent être pris en compte pour une description précise de la physique régissant la jonction. Dans les simulations QCM-DDA, un milieu effectif est introduit entre la pointe et la monocouche, consistant en un ensemble de coques cylindriques homogènes (voir Fig. 11-B). Ce milieu représente le courant tunnel entre la pointe et la surface de la monocouche de TMD. Chaque coque est caractérisée par une permittivité  $\epsilon_g(\omega, d, V_s)$  qui dépend de la distance  $d$  et de la tension de polarisation  $V_s$  donnée par:

$$\epsilon_g(\omega, d, V_s) = 1 + i \frac{\sigma_g(d, V_s)}{\epsilon_0 \omega} \quad (1)$$

où  $\sigma_g(d, V_s)$  est la conductivité statique du courant tunnel, exprimée comme:

$$\sigma_g(d, V_s) = \sigma_0(V_s) \exp\left(-\frac{2d}{l_c}\right) \quad (2)$$

avec  $l_c$  la profondeur de pénétration de la fonction d'onde des électrons dans le vide qui est donnée par  $l_c = \frac{\hbar}{\sqrt{2m\Phi_B}} \sim 0.25$  nm.  $\sigma_0(V_s)$  est la conductivité de la jonction empilée  $Au/MoSe_2/Au$ . En l'absence de données expérimentales concernant cette grandeur physique, nous avons utilisé la conductivité d'une jonction empilée  $Au/MoS_2/Au$  mesurée par Ge *et al.* [33], étant donné que les interfaces  $MoSe_2/Au$  et  $MoS_2/Au$  présentent des hauteurs de barrière Schottky  $\Phi_B$  similaires [34, 35]. Pour une tension de polarisation  $V_s$  variant de 1.5 V à 2.25 V,  $\sigma_0(V_s)$  augmente de  $0.842 \text{ S.m}^{-1}$

à  $20.1 \text{ S.m}^{-1}$ . Comparée à  $\omega\epsilon_0$ , qui est de l'ordre de  $10^4 \text{ S.m}^{-1}$  dans la gamme spectrale étudiée,  $\sigma_g(d, V_s)$  est très faible. Par conséquent, on peut s'attendre à ce que les corrections quantiques aux calculs électrodynamiques classiques aient un impact modéré sur les propriétés optiques de la jonction. Néanmoins, il est intéressant d'évaluer leur effet.

Tout d'abord, la réponse optique de la jonction  $\text{Au}/\text{MoSe}_2/\text{Au}$  à une onde électromagnétique incidente est étudiée dans le régime non-tunnel ( $d = 0.5 \text{ nm}$ ). Les résonances des modes électromagnétiques, en termes de fréquence et d'intensité, sont analysées à partir de la réponse optique en champ lointain et en champ proche. Les propriétés optiques d'une jonction purement métallique  $\text{Au}/\text{Au}$ , avec une distance identique entre la pointe et la surface, sont également examinées afin d'évaluer le rôle de la monocouche dans la réponse optique. Le caractère anisotrope de la monocouche est également pris en compte et soumis à une analyse approfondie. En particulier, des modes gap plasmon sont excités dans le gap par la composante verticale du champ incident lorsqu'il est polarisé p. Leur résonance correspond au pic principal de la Fig. 12-A.

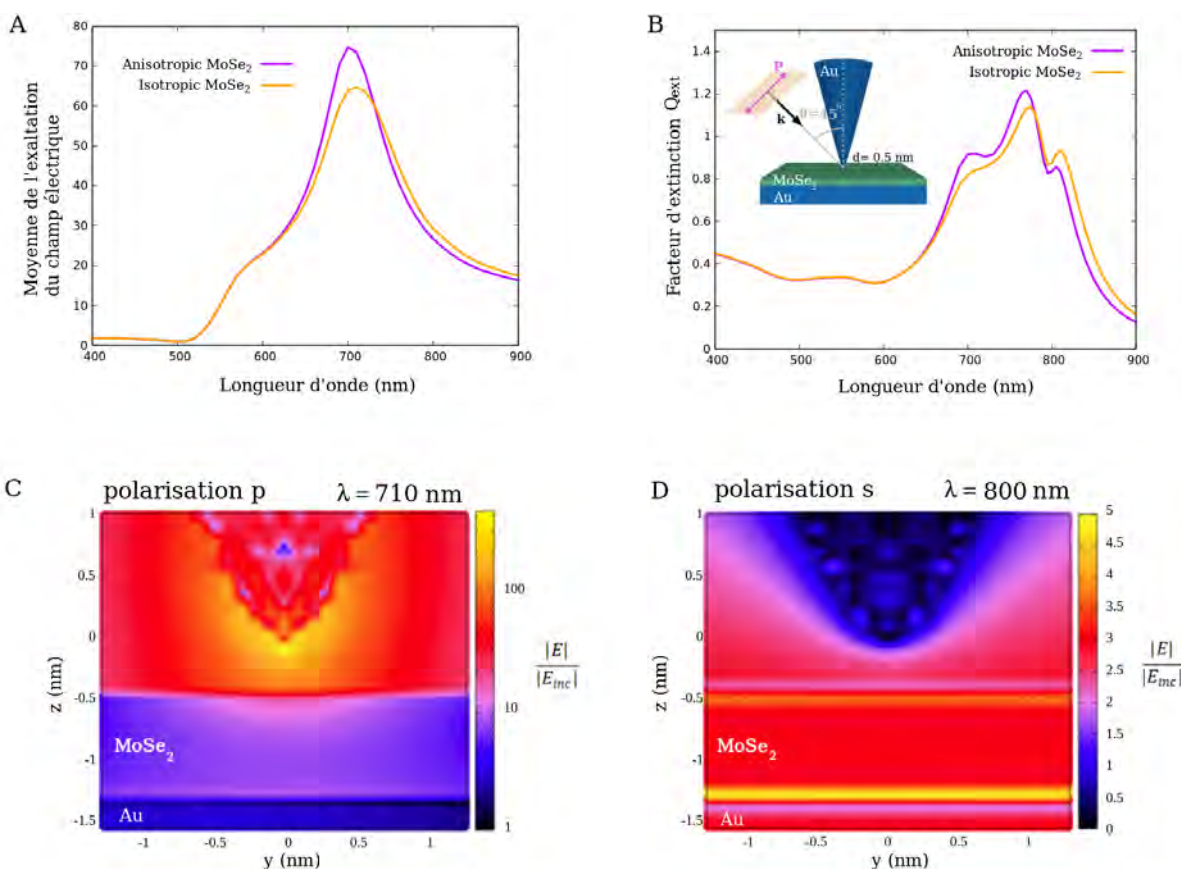


**Fig. 12:** (A-B) Spectres représentant (A) la moyenne de l'exaltation du champ électrique (champ proche) et (B) le facteur d'extinction  $Q_{ext}$  (champ lointain) obtenus pour une polarisation p du champ électrique incident. La couche de  $\text{MoSe}_2$  est décrite en utilisant un indice de réfraction anisotrope (violet) et isotrope (orange). La moyenne de l'exaltation du champ électrique est calculée sur un volume qui inclut le gap, l'apex de la pointe, et une partie de la monocouche. (C-D) Cartes d'exaltation du champ électrique calculées pour un champ incident polarisé p (C) à  $\lambda = 710 \text{ nm}$  (échelle logarithmique) et polarisé s (D) à  $\lambda = 800 \text{ nm}$ .

La résonance gap plasmon est amortie lorsque la monocouche de  $MoSe_2$  est introduite dans la jonction modélisée, car elle constitue un milieu absorbant. Cet amortissement est encore plus marqué lorsque la monocouche est modélisée comme étant isotrope. Les modes gap plasmon se manifestent par un champ électrique très intense dans le gap (voir Fig. 12-C). Puis, une exaltation du champ est également observée à l'intérieur de la monocouche et à l'interface entre la couche  $MoSe_2$  et le substrat d'or. Ce champ induit correspond au mode hybride "gap plasmon-exciton" impliquant les excitons confinés dans la monocouche, les modes gap plasmon, et le mode plasmon de surface transverse du substrat.

La réponse optique obtenue en champ lointain pour les deux polarisations du champ incident présente des interférences avec des minima locaux aux énergies des excitons A et B [22] (Fig. 12-B). Ces interférences résultent d'un couplage de type Fano entre les modes plasmon et les excitons confinés au sein de la monocouche. Pour un champ incident polarisé s, ce couplage se produit entre les excitons et le mode plasmon transverse du substrat, comme le montre le champ électrique exalté à l'interface entre la couche de TMD et le substrat (voir Fig. 12-D) tandis que pour un champ incident polarisé p, les modes gap plasmon sont aussi impliqués. En analysant les spectres obtenus en champ lointain à l'aide du modèle analytique de deux oscillateurs couplés [36], la force du couplage entre les modes plasmoniques et les excitons A, qui donne naissance aux interférences, est déterminée.

La distribution spectrale et spatiale des modes mentionnés est examinée en fonction de la tension de polarisation  $V_s$  et de la distance pointe-surface  $d$ . Cette analyse est réalisée en utilisant le modèle Quantum-Corrected Model, tel que décrit précédemment, pour des distances  $d$  se situant dans le régime tunnel. En raison de la faible conductivité tunnel considérée pour le milieu effectif entre la pointe et la monocouche, les effets du courant tunnel sur la réponse optique de la jonction hybride sont négligeables. De plus, aucune variation n'a été observée en modifiant la tension de polarisation  $V_s$  dans les simulations QCM-DDA. Lorsque la distance  $d$  entre la pointe et la surface diminue, les modes gap plasmon (excités uniquement lorsque le champ électrique incident est polarisé p) deviennent plus localisés, entraînant une diminution du couplage plasmon-exciton qui donne naissance au mode hybride "gap plasmon-exciton".

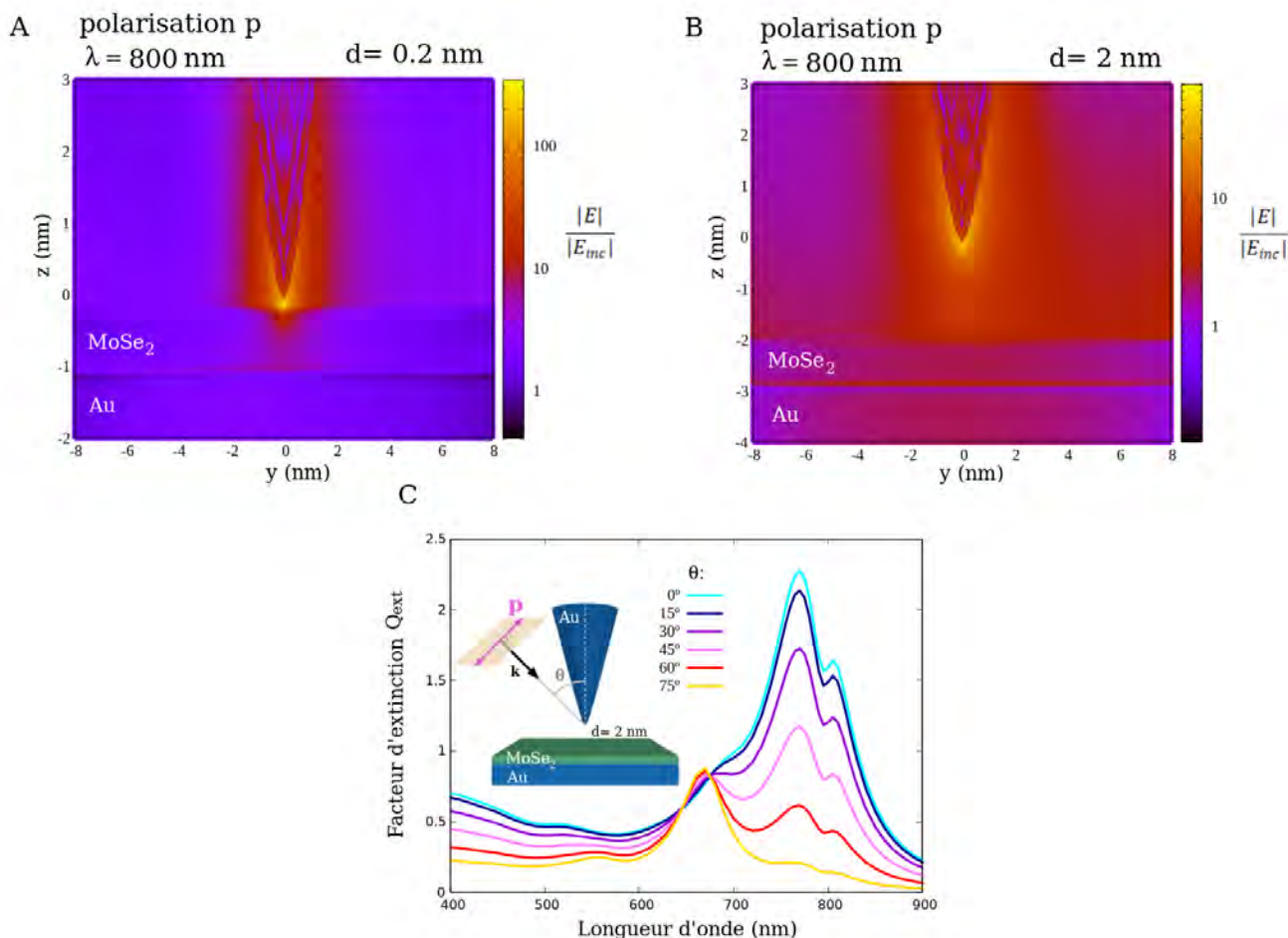


**Fig. 13:** (A-B) Cartes d'exaltation du champ électrique calculées pour un champ incident polarisé p (échelle logarithmique) pour une distance pointe-surface (A)  $d = 0.2$  nm et (B)  $d = 2$  nm à  $\lambda = 800$  nm et pour un angle d'incidence  $\theta = 45^\circ$  par rapport à l'axe  $z$ . Pour  $d = 0.2$  nm, QCM est appliquée avec une tension de polarisation  $V_s = 2$  V. (C) Spectres du facteur d'extinction  $Q_{ext}$  (champ lointain) obtenus pour un champ électrique incident polarisé p avec un angle d'incidence  $\theta$  variant de  $\theta = 0^\circ$  à  $\theta = 75^\circ$  et une distance pointe-surface  $d = 2$  nm.

En effet, comme illustré dans la Fig. 13-(A,B), lorsque  $d$  varie de  $d = 0.2$  nm à  $d = 2$  nm, le champ du mode hybride “gap plasmon-exciton” devient moins localisé et son chevauchement spatial avec la monocouche de  $MoSe_2$  augmente. Ce phénomène entraîne une augmentation de la force du couplage plasmon-exciton. Les caractéristiques de ce mode ont été également étudiées en fonction de la direction de la polarisation du champ incident. À mesure que la composante du champ électrique le long de l'axe de la pointe augmente, ce mode hybride perd progressivement son caractère excitonique pour devenir graduellement un mode gap plasmon pur (voir Fig. 13-C). Pour un champ électrique incident polarisé s, le mode plasmon transverse du substrat est le seul mode plasmonique impliqué dans le couplage plasmon-exciton, et par conséquent, aucune variation de ce couplage n'est observée en modifiant la distance pointe-surface.

Finalement, l'influence de la morphologie du substrat sur les propriétés de ces modes a également été analysée. Pour ce faire, un substrat rugueux a été introduit dans les simulations DDA, et la réponse

optique de cette jonction a été étudiée pour deux positions différentes de la pointe sur la surface granulaire de l'échantillon. Fig. 14-A montre la jonction hybride avec le substrat rugueux pour une position donnée de la pointe.

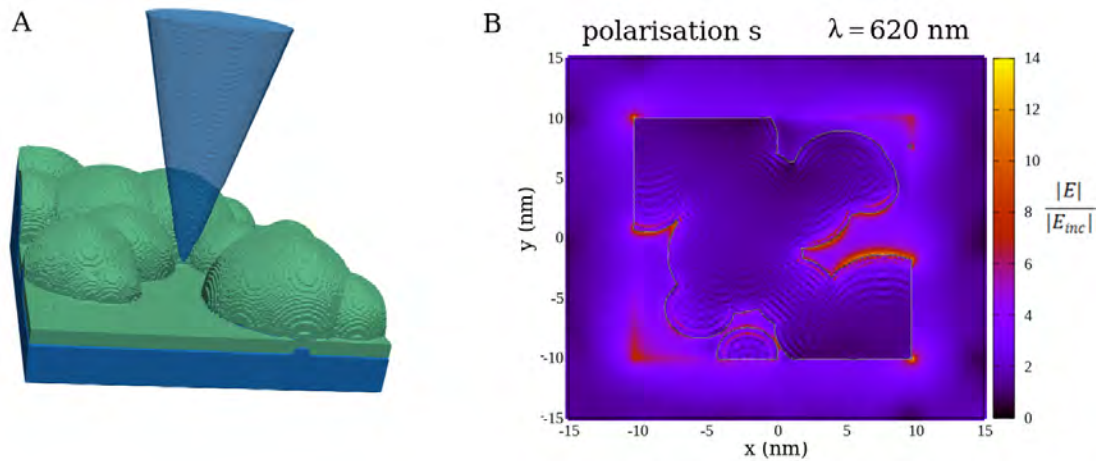


**Fig. 14:** (A) Représentation schématique de la jonction hybride  $Au/MoSe_2/Au$  avec un substrat rugueux. (B) Carte d'exaltation du champ électrique calculée dans le plan xy (orthogonal à l'axe de la pointe) pour un champ électrique incident polarisé s.

Par rapport au cas d'un substrat plat, l'introduction d'un substrat rugueux donne lieu à un gap pointe-surface de taille et de géométrie différente. En analysant la réponse optique (en champ lointain et champ proche), nous avons observé que les spectres obtenus pour les polarisations p et s sont plus similaires entre eux que lorsque le substrat considéré a une surface plane. Ainsi, en considérant un substrat rugueux, la dépendance de la réponse optique de la jonction hybride par rapport à la polarisation incidente est réduite. De plus, des modes plasmoniques de surface locaux résultant de l'interaction électromagnétique entre les protubérances de la surface rugueuse ont été mis en évidence (voir Fig. 14-B).

En s'inspirant des modèles décrivant l'émission de lumière dans des jonctions STM purement métalliques proposés dans la littérature [7, 8, 10], un modèle est développé pour décrire l'émission de lumière induite par STM d'une jonction hybride composée d'une pointe en or et d'une monocouche de  $MoSe_2$  déposée sur un substrat en or. Pour une telle jonction, l'émission de lumière provenant de l'excitation de modes électromagnétiques localisés dans le gap par des électrons tunnel inélastiques peut se produire, tout comme dans une jonction purement plasmonique. Cependant, en raison de la présence de la couche de  $MoSe_2$ , ce sont plutôt des modes hybrides avec un caractère plasmonique prononcé qui sont excités [28]. D'autre part, la luminescence généralement observée pour cette jonction hybride est celle qui résulte de la recombinaison radiative des excitons, déclenchée par la création de trous au sein de la monocouche par le biais du courant tunnel. Ce processus excitonique, est fortement influencé par le couplage électromagnétique plasmon-exciton [16]. Le modèle présenté ici décrit les deux processus radiatifs, plasmonique et excitonique, se produisant dans une jonction hybride avec un substrat présentant soit une surface plane soit une surface rugueuse. Des électrons traversant la barrière tunnel d'un point

spécifique sur la surface de la monocouche de  $MoSe_2$  à un point spécifique sur l'apex de la pointe sont envisagés, avec  $d$ , la distance minimale pointe-surface correspondant à la distance entre ces points.

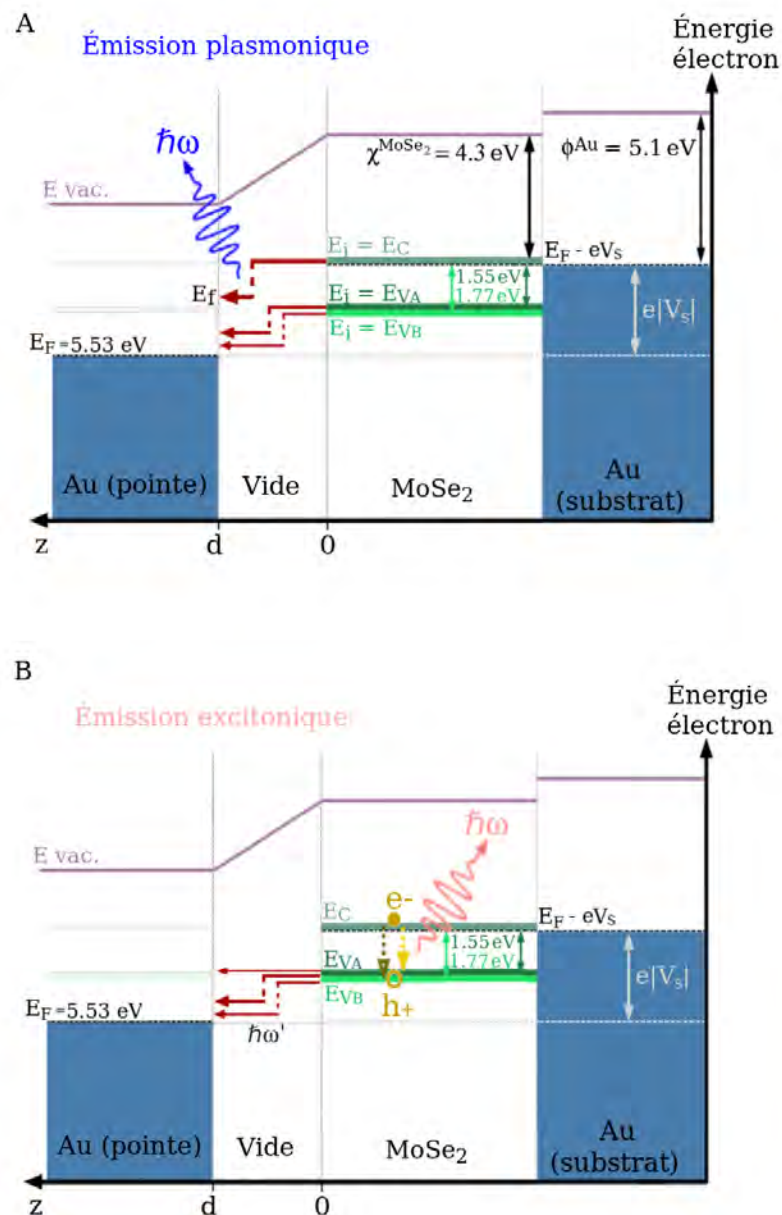


**Fig. 15:** (A) Diagramme de bande montrant le processus radiatif plasmonique: des électrons inélastiques traversent le gap de  $z = 0$  (surface de la monocouche de  $MoSe_2$ ) à  $z = d$  (surface de la pointe en or), donnant lieu à l'émission de photons avec une énergie  $\hbar\omega$  se produisant dans le gap de la jonction. Trois niveaux d'énergie initiaux sont considérés: le minimum de la bande de conduction ( $E_C$ ) et le maximum de chaque sous-bande de valence ( $E_{VA}$  et  $E_{VB}$ ). (B) Diagramme de bande illustrant le processus radiatif excitonique: les excitons A et B se recombinent (représentés par une flèche jaune et une flèche marron), en émettant des photons avec une énergie  $\hbar\omega$ . La désexcitation des excitons est déclenchée par la création de trous dans les sous-bandes de valence par le biais du courant tunnel élastique et inélastique. Ce dernier implique une perte d'énergie  $\hbar\omega'$  dans le gap.

Tout comme les modèles développés pour décrire STM-LE de jonctions purement plasmoniques, les électrodes sont considérées comme des objets tridimensionnels où le courant tunnel se produit entre

elles le long de la direction  $z$  (la barrière de potentiel dans le gap est supposée varier uniquement le long de  $z$ ), tout en conservant la quantité de mouvement transverse. Les propriétés électromagnétiques de la jonction sont introduites dans notre modèle à partir des résultats obtenus des simulations électrodynamiques DDA réalisées pour une jonction hybride  $Au/MoSe_2/Au$ . En effet, l'exaltation du champ électrique dans le gap pointe-surface et au sein de la monocouche, calculée à partir de ces simulations, est incorporée dans le modèle pour tenir compte du couplage plasmon-exciton et de leurs modes hybrides résultants.

Pour l'émission plasmonique, des transitions tunnel inélastiques d'un état initial de la monocouche (avec une énergie  $E_i$ ) à un état final de la pointe (avec une énergie  $E_f$ ) sont considérées, chacune donnant lieu à l'émission d'un photon  $\hbar\omega$ . Trois états initiaux avec des énergie spécifiques sont considérés: le minimum de la bande de conduction (qui est supposé être aligné avec le niveau de Fermi de l'échantillon) et le maximum de chaque sous-bande de valence (voir Fig. 15-A). Pour simplifier le modèle, l'état fondamental des excitons A et B, est supposé être le minimum de la bande de conduction, en négligeant l'énergie de liaison des excitons. En utilisant le théorème de réciprocité de l'électrodynamisme [37], une expression de la puissance rayonnée résultant de toutes les transitions inélastiques peut être obtenue. Cette expression, qui est calculée pour chaque état initial, est issue du modèle d'Aizpurua (équation (8) dans la référence [10]) et est adaptée pour inclure les facteurs d'occupation  $f(E)$  et la tension de polarisation  $V_s$  appliquée à la jonction STM. De plus, la somme discrète sur les états finaux est approximée par un continuum en considérant la densité d'états de la pointe  $\rho_t(E)$ . L'équation suivante est utilisée pour le calcul de la puissance rayonnée pour chaque état initial considéré, puis elles sont additionnées.

$$\frac{d^2P}{d\Omega d(\hbar\omega)} = \frac{\alpha}{h} \left(\frac{\omega}{c}\right)^2 \rho_t(E_i - \hbar\omega) [f(E_i + eV_s) - f(E_i - \hbar\omega)] \left| \int_0^d dz G(z, \omega) M_{if}(z, V_s, \omega) \right|^2 \quad (3)$$

où  $\alpha$  est la constante de structure fine.  $G(z, \omega)$  représente l'exaltation du champ électrique local dans le gap le long de la direction  $z$ , calculée à partir des simulations DDA. Ce terme permet d'introduire dans le modèle les modes électromagnétiques du gap dont leur désexcitation conduit à l'émission de photons. L'élément de matrice de transition tunnel  $M_{if}(z, V_s, \omega)$  est défini dans [10] comme l'intégrale de la densité de courant dans la direction transverse. En décrivant les états initiaux et finaux par des fonctions d'onde d'électrons libres dans le plan  $xy$  et par des fonctions d'onde WKB dans la direction  $z$  [7, 8], l'élément de matrice de transition tunnel peut être écrit comme suit:

$$M_{if}(z, V_s, \omega) = \frac{\mathcal{C}_i \mathcal{C}_f A}{\sqrt{V_{MoSe_2} V_{tip}}} T_{if}(z, V_s, \omega) \delta_{\mathbf{k}_{\parallel i}, \mathbf{k}_{\parallel f}} \quad (4)$$

$V_{MoSe_2}$  et  $V_{tip}$  représentent respectivement le volume de la monocouche de  $MoSe_2$  et de la pointe,  $\mathcal{C}_i$  et  $\mathcal{C}_f$  sont des constantes de normalisation, et  $A$  est la section efficace du courant tunnel. La quantité de

mouvement transverse des électrons tunnel est conservée. Le terme  $T_{if}(z, V_s, \omega)$  est exprimé en fonction de  $\kappa_{i,f}^*(z)$ , l'inverse de la longueur de décroissance des fonctions d'onde des états initiaux et finaux le long de  $z$ .

$$T_{if}(z, V_s, \omega) = \frac{\hbar^2}{2m_e} \frac{\sqrt{\kappa_i^*(0)}}{\sqrt{\kappa_i^*(z)}} e^{-\int_0^z \kappa_i^*(z') dz'} \frac{\sqrt{\kappa_f^*(d)}}{\sqrt{\kappa_f^*(z)}} e^{-\int_z^d \kappa_f^*(z') dz'} \left( -\frac{\kappa_f^*(z)'}{2\kappa_f^*(z)} + \kappa_f^*(z) + \frac{\kappa_i^*(z)'}{2\kappa_i^*(z)} + \kappa_i^*(z) \right) - \hbar\omega \int_0^z dz_o \frac{\sqrt{\kappa_i^*(0)\kappa_f^*(d)}}{\sqrt{\kappa_i^*(z_o)\kappa_f^*(z_o)}} e^{-\int_0^{z_o} \kappa_i^*(z') dz'} e^{-\int_{z_o}^d \kappa_f^*(z') dz'}$$
(5)

avec  $\kappa_{i,f}^*(z) = \sqrt{\kappa_{i,f}(z)^2 + k_{\parallel i,f}^2}$  et

$$\kappa_{i,f}(z) = \frac{\sqrt{2m_e}}{\hbar} \times \sqrt{E_F + \phi^{Au} + (\chi^{MoSe_2} - \phi^{Au} - eV_s) \left( \frac{d-z}{d} \right) - E_{i,f}}$$
(6)

avec  $E_f = E_i - \hbar\omega$ ,  $E_F$  l'énergie de Fermi,  $\phi^{Au}$  le travail de sortie de la pointe en or, et  $\chi^{MoSe_2}$  l'affinité électronique de  $MoSe_2$  (voir Fig. 15-A). Des expressions similaires pour  $T_{if}(z, V_s, \omega)$  et  $\kappa_{i,f}(z)$  sont fournies dans le modèle d'Aizpurua [10], et elles ont été adaptées ici pour la jonction hybride  $Au/MoSe_2/Au$ .

L'expression de la puissance rayonnée pour le processus d'émission de lumière excitonique est liée au taux de recombinaison radiative des excitons  $\Gamma_{rad}$ . Étant donné que la présence d'un trou dans l'un des deux sous-bandes de valence est nécessaire pour former des excitons, comme illustré dans la Fig. 15-B, la probabilité qu'un trou soit présent dans la bande de valence généré par le courant tunnel est prise en compte. Soit  $W_{tunnel}$   $\tau$  le nombre de transitions tunnel qui se produiraient pendant la durée de vie de l'exciton notée  $\tau$ . Cette dernière peut être écrite en fonction de la durée de vie non radiative  $\tau_{nr}$  et la durée de vie radiative  $\tau_r$  par  $\frac{1}{\tau} = \frac{1}{\tau_{nr}} + \frac{1}{\tau_r}$ . Pour les excitons A et B de la monocouche de  $MoSe_2$ ,  $\tau \sim \tau_{nr} = 114$  ps [38] puisque  $\tau_r$  dépasse significativement  $\tau_{nr}$  (voir Tableau 1). De plus, il est supposé que chaque trou créé donne lieu de manière directe à un exciton, une hypothèse forte qui sera discutée plus tard. La puissance rayonnée par unité d'angle solide pour l'émission excitonique s'exprime comme suit:

$$\frac{dP(\omega)}{d\Omega} = \hbar\omega \Gamma_{rad}(\omega) W_{tunnel} \tau_{nr}$$
(7)

Le taux de recombinaison radiative des excitons est exprimée en utilisant la règle d'or de Fermi:

$$\Gamma_{rad}(\omega) = \frac{2\pi}{\hbar} |H_{vc}|^2 \delta(E_C - E_V - \hbar\omega) g(\hbar\omega)$$
(8)

L'Hamiltonien  $H_{vc}$  qui décrit le couplage entre l'exciton avec un moment dipolaire dans le plan [21]

$\mathbf{d}_{ex} = d_{ex} \mathbf{e}_d$ , et le champ électrique local  $\mathbf{E}$ , est exprimé en utilisant l'approximation du dipôle électrique:  $H_{vc} = -\mathbf{d}_{ex} \cdot \mathbf{E} = -\sqrt{\frac{\hbar\omega n}{2\epsilon_0 V}} \mathbf{d}_{ex} \cdot \mathbf{G}(\mathbf{r}, \omega)$ . Le champ vectoriel  $\mathbf{G}(\mathbf{r}, \omega)$  est une quantité sans dimension représentant l'exaltation du champ en  $\mathbf{r}$ . Cette quantité, calculée à partir de simulations DDA, est évaluée à la position de l'exciton  $\mathbf{r}_{ex}$ , considérée au milieu de la monocouche. Ensuite,  $g(\hbar\omega)$  est la densité d'états photoniques à l'énergie du photon  $\hbar\omega$ . La différence d'énergie entre la bande de conduction et la bande de valence  $E_C - E_V$  est égale à l'énergie de l'exciton  $\hbar\omega_{ex}$ . Ainsi, en considérant la densité d'états photoniques par unité d'angle solide, l'équation (8) devient [39]:

$$\begin{aligned} \Gamma_{rad}(\omega) &= \frac{2\pi \hbar\omega n_{MoSe_2} d_{ex}^2}{\hbar 2\epsilon_0 V} |\mathbf{e}_d \cdot \mathbf{G}(\mathbf{r}_{ex}, \omega)|^2 \delta(\hbar\omega_{ex} - \hbar\omega) \frac{2V(\hbar\omega)^2}{\hbar^3 c^3 \pi^3} \\ &= \frac{6}{\pi \tau_r} |\mathbf{e}_d \cdot \mathbf{G}(\mathbf{r}_{ex}, \omega_{ex})|^2 \end{aligned} \quad (9)$$

Dans le cas d'un courant tunnel élastique,  $W_{tunnel}$  correspond au nombre d'électrons tunnel par unité de temps et peut être exprimée comme suit:

$$W_{tunnel} = \frac{I_{elas}}{e} = \frac{4\pi}{\hbar} \rho_t(E_i) [f(E_i + eV_s) - f(E_i)] \left| M_{if} \left( \frac{d}{2}, V_s \right) \right|^2 \quad (10)$$

où l'élément de matrice de transition tunnel  $M_{if}$  est évalué au milieu du gap, c'est-à-dire à  $\frac{d}{2}$ . Dans le cas inélastique, la probabilité d'avoir un trou dans la bande de valence est calculée en intégrant la probabilité d'avoir une transition inélastique sur l'énergie perdue par l'électron pendant le processus, notée  $\hbar\omega'$  (voir Fig. 15-B). Cette énergie varie de 0 (correspondant à la transition tunnel élastique) jusqu'au maximum d'énergie qu'un électron, traversant le gap de manière inélastique depuis la bande de valence de la monocouche jusqu'à la pointe, peut perdre:  $E_i - E_F$ . La perte d'énergie dans le gap,  $\hbar\omega'$ , n'est pas incluse dans la quantité d'énergie émise par la désexcitation radiative des excitons calculée ici. Enfin, la puissance rayonnée par unité d'angle solide et par unité d'énergie photonique de l'équation (7) devient:

$$\begin{aligned} \frac{d^2 P}{d\Omega d(\hbar\omega)} &= \frac{24 \tau_{nr}}{\hbar \tau_r} |\mathbf{e}_d \cdot \mathbf{G}(\mathbf{r}_{ex}, \omega_{ex})|^2 L(\hbar\omega - \hbar\omega_{ex}) \times \\ &\int_0^{E_i - E_F} d(\hbar\omega') \left[ \rho_t(E_i - \hbar\omega') [f(E_i + eV_s) - f(E_i - \hbar\omega')] \left| M_{if} \left( \frac{d}{2}, V_s, \hbar\omega' \right) \right|^2 \right] \end{aligned} \quad (11)$$

L'expression de la puissance rayonnée est modulée par une fonction lorentzienne [40] afin de prendre en compte la distribution en énergie observée dans les résultats expérimentaux:

$L(\hbar\omega - \hbar\omega_{ex}) = \frac{1}{\pi} \frac{\frac{\hbar\gamma}{2}}{(\hbar\omega - \hbar\omega_{ex})^2 + (\frac{\hbar\gamma}{2})^2}$  avec  $\hbar\gamma$  le taux d'amortissement de l'exciton. L'équation (11) est calculée à la fois pour l'exciton A et B en utilisant les valeurs du Tableau 1.

	Exciton A	Exciton B
$\tau_r$	380 ps [41]	187 ns [41]
$\hbar\omega_{ex}$	1.55 eV [22]	1.77 eV [22]
$\hbar\gamma$	42 meV [39]	112 meV [42]

**Tableau 1:** Valeurs de certains paramètres de l'équation (11)

Des spectres STM-LE plasmoniques et excitoniques sont calculés avec ce modèle pour une jonction hybride  $Au/MoSe_2/Au$  avec un substrat présentant une surface plane et une surface rugueuse afin d'évaluer l'influence de la rugosité de l'échantillon sur l'émission de lumière théorique. Avant d'approfondir sur cette étude, le comportement des spectres théoriques en fonction des paramètres tunnel, c'est-à-dire de la distance pointe-surface  $d$  et de la tension de polarisation  $V_s$ , est analysé pour la jonction présentant la surface plane. En ce qui concerne l'émission plasmonique, les spectres théoriques présentent un comportement étroitement similaire à celui des spectres expérimentaux, se caractérisant principalement par un seuil à haute énergie qui suit la loi quantique  $\hbar\omega = e|V_s|$ . Cependant, dans le cas du processus excitonique, le modèle surestime l'impact de la tension  $V_s$  sur l'intensité de l'émission par rapport aux résultats expérimentaux. De plus, l'intensité de la puissance rayonnée plasmonique et excitonique diminue lorsque  $d$  augmente. Cette réduction est due à une diminution de la probabilité de courant tunnel à mesure que  $d$  augmente. Ceci est en accord avec les observations expérimentales.

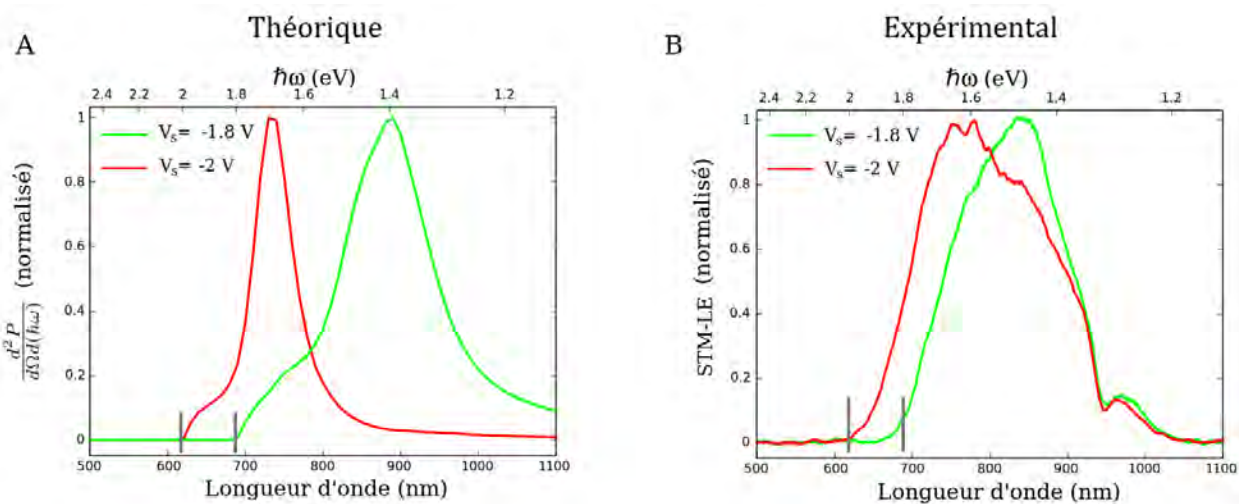


**Fig. 16:** (A) Spectres STM-LE théoriques plasmoniques calculés pour un substrat rugueux avec une tension de polarisation  $V_s = -1.8$  V (vert) et pour un substrat plat avec une tension de polarisation  $V_s = -2$  V (rouge) et  $d = 0.2$  nm. (B) Spectres STM-LE expérimentaux acquis à deux localisations différentes de la surface de  $MoSe_2$  avec une tension de polarisation  $V_s = -1.8$  V (vert) et  $-2$  V (rouge), un courant tunnel  $I_t = 10$  nA et un temps d'acquisition de 60 s. Chaque spectre est normalisé par son maximum.

La Figure 16-A montre les spectres STM-LE plasmoniques calculés pour un substrat plat (en rouge) et un substrat rugueux (en vert) pour deux tensions  $V_s$  différentes et  $d = 0.2$  nm. Leur allure spectrale est dominé par les résonances des modes électromagnétiques du gap, avec la résonance des modes gap plasmon à 1.67 eV (740 nm) pour le substrat plat et à environ 1.42 eV (870 nm) pour le substrat rugueux. En raison de la rugosité de la surface, les deux configurations de la jonction hybride présentent

un gap pointe-surface avec une taille et une géométrie différentes, donnant ainsi naissance à des modes électromagnétiques confinés dans le gap avec des propriétés distinctes. Par conséquent, bien que les deux spectres d'émission présentent le seuil à haute énergie suivant  $\hbar\omega = e|V_s|$ , ils présentent différents pics correspondant aux résonances des modes électromagnétiques excités dans le gap spécifiques pour chaque configuration. Cela concorde avec les résultats expérimentaux de la Fig. 16-B. Il est important de noter que les spectres STM-LE expérimentaux présentent un plus grand nombre de pics avec un profil plus large par rapport aux spectres calculés. Cette différence résulte de la dérive thermique qui provoque le déplacement constant de la pointe par rapport à la surface de l'échantillon, même quand le STM est en mode non-balayage (pointe "fixe"). En effet, les spectres expérimentaux acquies reflètent la contribution de divers modes électromagnétiques du gap excités pendant le mouvement constant de la pointe et de l'échantillon, conduisant à une multitude de pics larges. Le modèle d'émission STM-LE plasmonique présenté ici donne lieu à un rendement de  $\eta_{\text{plas, theo}} \sim 2 \times 10^{-6}$  photons par électron tunnel, légèrement supérieur à l'expérimental ( $\eta_{\text{plas, exp}} \sim 6 \times 10^{-7}$  photons par électron tunnel).

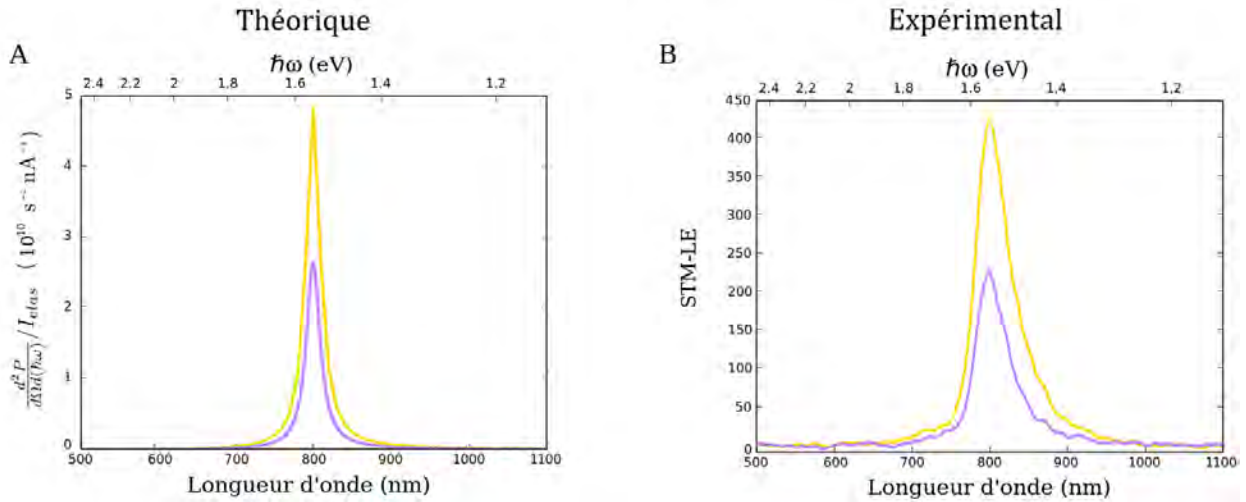


**Fig. 17:** (A) Spectres STM-LE théoriques excitoniques calculés pour un substrat plat (violet) et un substrat rugueux (jaune) en utilisant  $V_s = -1.7$  V et  $d = 0.2$ . (B) Spectres STM-LE expérimentaux acquis à deux localisations différentes de la surface de la couche de  $MoSe_2$  ( $V_s = -1.7$  V,  $I_t = 10$  nA et temps d'acquisition de 60 s.)

Les spectres STM-LE excitoniques théoriques et expérimentaux, présentés dans la Fig. 17, possèdent un seul pic d'émission à l'énergie de l'exciton A, avec les pics expérimentaux étant plus larges. Cette différence de largeur résulte d'un taux d'amortissement de l'exciton A sous-estimé dans le modèle théorique. L'intensité du pic d'émission varie en fonction de la rugosité de la surface. Cette variation est attribuée à une interaction plasmon-exciton différente au sein de la monocouche selon la morphologie de la surface du substrat (rugueux ou plat). Dans le modèle excitonique, le couplage plasmon-exciton est décrit par le terme  $|\mathbf{e}_d \cdot \mathbf{G}(\mathbf{r}_{ex}, \omega_{ex})|^2$ , représentant l'exaltation du champ électrique  $\mathbf{G}$  à la position de l'exciton  $\mathbf{r}_{ex}$  le long de la direction du moment dipolaire de l'exciton  $\mathbf{e}_d$ . Ce dernier se trouve dans le plan de la monocouche [21], c'est-à-dire qu'il est parallèle à la surface de la monocouche. Ainsi, en fonction de la rugosité de la monocouche, la composante du champ vectoriel  $\mathbf{G}$  dans le plan parallèle à la surface

locale de la monocouche à la position de l'exciton change. Donc, en fonction de la rugosité, l'efficacité du couplage plasmon-exciton peut varier, entraînant une émission de lumière excitonique d'intensité variable. Le rendement d'émission excitonique calculé à partir de notre modèle est  $\eta_{exc, theo} \sim 2$  photons par électron tunnel, significativement plus élevé que la valeur expérimentale de  $\eta_{exc, exp} \sim 10^{-6}$  photons par électron tunnel. En effet, le modèle excitonique repose sur une très forte hypothèse, selon laquelle chaque trou créé dans la bande de valence génère un exciton. En comparant ces rendements, le modèle excitonique présenté surestime le ratio d'excitons par trou créé d'un ordre de grandeur de  $10^6$ . Cela suggère que dans une jonction hybride réelle, la formation d'exciton ne se produit que pour un trou créé sur  $10^6$ .

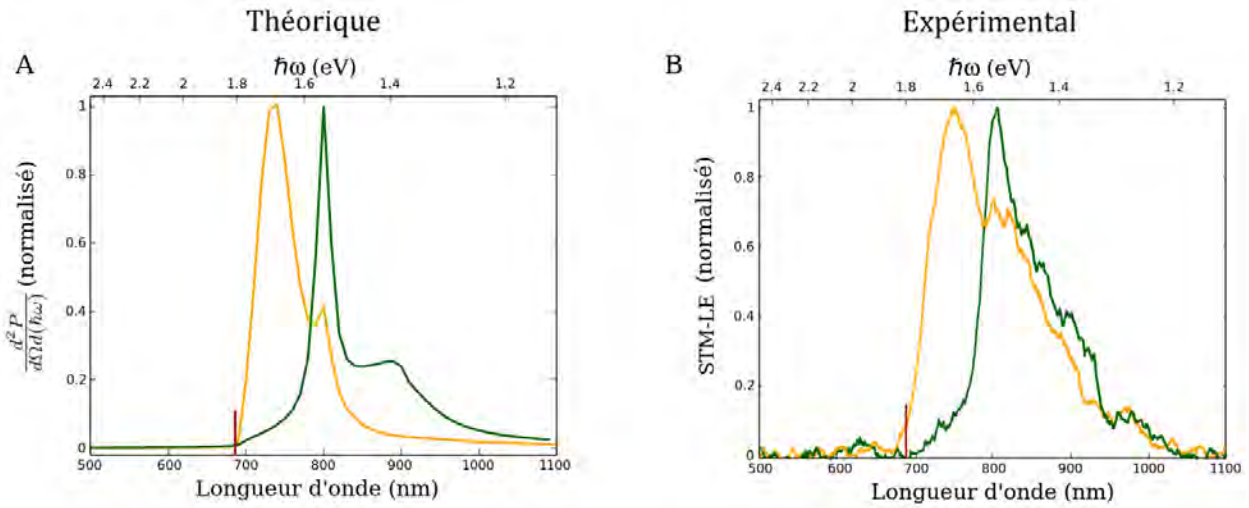


**Fig. 18:** (A) Spectres STM-LE théoriques hybrides calculés pour un substrat plat (orange) et un substrat rugueux (vert) en utilisant  $V_s = -1.8$  V et  $d = 0.2$  nm. (B) Spectres STM-LE expérimentaux acquis à deux localisations différentes de la surface de la monocouche de TMD ( $V_s = -1.8$  V,  $I_t = 10$  nA et temps d'acquisition de 60 s.). Chaque spectre est normalisé par son maximum.

Des spectres STM-LE théoriques hybrides combinant les deux processus radiatifs ont été calculés (voir Fig. 18), en incluant le ratio de  $10^{-6}$  excitons par trou créé dans le modèle excitonique. Selon la rugosité du substrat, soit la composante plasmonique, soit la composante excitonique devient plus prédominante dans la formation du spectre hybride global. Cela est en accord avec les spectres hybrides expérimentaux, où une composante plasmonique ou excitonique plus prononcée est obtenue selon la localisation sur la surface de  $MoSe_2$  où le spectre a été acquis (Fig. 18-B). Le rendement hybride théorique est du même ordre de grandeur que celui expérimental ( $\eta_{hyb, theo} \sim 3 \times 10^{-6}$  photons par électron tunnel et  $\eta_{hyb, exp} \sim 9 \times 10^{-7}$  photons par électron tunnel). L'accord entre les résultats théoriques et expérimentaux valide le ratio de  $10^{-6}$  excitons par trou créé incorporé dans le modèle excitonique.

Au cours de cette thèse, divers processus d'émission STM-LE ont été identifiés, et leurs caractéristiques ont été examinées en détail. L'émission d'une jonction hybride métal/semiconducteur, tant du point

de vue expérimental que théorique, a été étudié en mettant particulièrement l'accent sur le couplage plasmon-exciton et leur influence sur l'émission de lumière. Parallèlement, nous avons exploré le rôle de la morphologie de l'échantillon, analysant comment elle peut ajuster les caractéristiques et le rendement du processus d'émission. De plus, un modèle original a été développé qui, malgré présentant une marge d'amélioration, aboutit à des spectres en très bon accord avec ceux obtenus expérimentalement. En comparant nos résultats issus de la modélisation avec ceux expérimentaux, le rapport entre les excitons formés et les porteurs de charge induit par le courant tunnel dans des matériaux TMD a été déterminé. La technique d'émission STM-LE s'est révélée être un outil précieux pour étudier les propriétés optoélectroniques de monocouches de  $MoSe_2$ . Son application sur d'autres matériaux 2D, tels que d'autres monocouches de TMD ou même des TMD superréseaux semble constituer une piste pertinente à explorer. D'autre part, le modèle présenté ici pourrait être généralisé pour décrire le processus d'émission d'une jonction STM impliquant d'autres types de semiconducteurs ou d'autres émetteurs quantiques. Finalement, l'étude du rôle de la morphologie dans l'émission STM-LE ouvre la voie à la conception de substrats dont la morphologie est optimisée pour favoriser le couplage plasmon-exciton, permettant ainsi d'atteindre un rendement émissif maximal.

## Bibliographie

- [1] G. Binnig, H. Rohrer, Ch. Gerber, and E. Weibel. Tunneling through a controllable vacuum gap. *Appl. Phys. Lett.*, 40(2):178–180, 1982.
- [2] P. Johansson. Light emission from a scanning tunneling microscope: Fully retarded calculation. *Phys. Rev. B*, 58(16):10823–10834, 1998.
- [3] J. H. Coombs, J. K. Gimzewski, B. Reihl, J. K. Sass, and R. R. Schlittler. Photon emission experiments with the scanning tunnelling microscope. *J. Microsc.*, 152(2):325–336, 1988.
- [4] G. Hoffmann, J. Aizpurua, P. Apell, and R. Berndt. Influence of tip geometry in light emission from the scanning tunnelling microscope. *Surf. Sci.*, 482–485:1159–1162, 2001.
- [5] R. W. Rendell, D. J. Scalapino, and B. Mühlshlegel. Role of local plasmon modes in light emission from small-particle tunnel junctions. *Phys. Rev. Lett.*, 41(25):1746–1750, 1978.
- [6] J. Tersoff and D. R. Hamann. Theory and application for the scanning tunneling microscope. *Phys. Rev. Lett.*, 50(25):1998–2001, 1983.
- [7] P. Johansson, R. Monreal, and P. Apell. Theory for light emission from a scanning tunneling microscope. *Phys. Rev. B*, 42(14):9210–9213, 1990.
- [8] P. Johansson and R. Monreal. Theory for photon emission from a scanning tunneling microscope. *Zeitschrift für Physik B Condensed Matter*, 84(2):269–275, 1991.
- [9] B. N. J. Persson and A. Baratoff. Theory of photon emission in electron tunneling to metallic particles. *Phys. Rev. Lett.*, 68(21):3224–3227, 1992.
- [10] J. Aizpurua, S. P. Apell, and R. Berndt. Role of tip shape in light emission from the scanning tunneling microscope. *Phys. Rev. B*, 62(3):2065–2073, Jul 2000.
- [11] Ph. Renaud and S. F. Alvarado. Mapping quantum-well energy profiles of III-V heterostructures by scanning-tunneling-microscope-excited luminescence. *Phys. Rev. B*, 44(12):6340–6343, 1991.
- [12] S. F. Alvarado, Ph. Renaud, D. L. Abraham, Ch. Schönenberger, D. J. Arent, and H. P. Meier. Luminescence in scanning tunneling microscopy on III–V nanostructures. *J. Vac. Sci. Technol. B: Microelectron. Nanometer Struct. Process. Meas. Phenom.*, 9(2):409–413, 1991.
- [13] R. Berndt and J. K. Gimzewski. Injection luminescence from CdS (112<sup>-</sup> 0) studied with scanning tunneling microscopy. *Phys. Rev. B*, 45(24):14095–14099, 1992.
- [14] K. S. Novoselov, A. K. Geim, S. V. Morozov, D. Jiang, Y. Zhang, S. V. Dubonos, I. V. Grigorieva, and A. A. Firsov. Electric field effect in atomically thin carbon films. *Science*, 306(5696):666–669, 2004.

- [15] A. Splendiani, L. Sun, Y. Zhang, T. Li, J. Kim, C.-Y. Chim, G. Galli, and F. Wang. Emerging photoluminescence in monolayer MoS<sub>2</sub>. *Nano Lett.*, 10(4):1271–1275, 2010.
- [16] R. Péchou, S. Jia, J. Rigor, O. Guillermet, G. Seine, J. Lou, N. Large, A. Mlayah, and R. Coratger. Plasmonic-Induced Luminescence of MoSe<sub>2</sub> Monolayers in a Scanning Tunneling Microscope. *ACS Photonics*, 7(11):3061–3070, 2020.
- [17] Y. Zhang, T.-R. Chang, B. Zhou, Y.-T. Cui, H. Yan, Z. Liu, F. Schmitt, J. Lee, R. Moore, Y. Chen, H. Lin, H.-T. Jeng, S.-K. Mo, Z. Hussain, A. Bansil, and Z.-X. Shen. Direct observation of the transition from indirect to direct bandgap in atomically thin epitaxial MoSe<sub>2</sub>. *Nat. Nanotechnol.*, 9(2):111–115, 2014.
- [18] J. Kang, L. Zhang, and S.-H. Wei. A unified understanding of the thickness-dependent bandgap transition in hexagonal two-dimensional semiconductors. *J. Phys. Chem. Lett.*, 7(4):597–602, 2016.
- [19] K. F. Mak, C. Lee, J. Hone, J. Shan, and T. F. Heinz. Atomically thin MoS<sub>2</sub>: a new direct-gap semiconductor. *Phys. Rev. Lett.*, 105(13):136805, 2010.
- [20] A. Splendiani, L. Sun, Y. Zhang, T. Li, J. Kim, C.-Y. Chim, G. Galli, and F. Wang. Emerging photoluminescence in monolayer MoS<sub>2</sub>. *Nano Lett.*, 10(4):1271–1275, 2010.
- [21] G. Wang, A. Chernikov, M. M. Glazov, T. F. Heinz, X. Marie, T. Amand, and B. Urbaszek. Colloquium: Excitons in atomically thin transition metal dichalcogenides. *Rev. Mod. Phys.*, 90(2):021001, 2018.
- [22] V. Iberi, L. Liang, A. V. Ievlev, M. G. Stanford, M.-W. Lin, X. Li, M. Mahjouri-Samani, S. Jesse, B. G. Sumpter, S. V. Kalinin, D. C. Joy, K. Xiao, A. Belianinov, and O. S. Ovchinnikova. Nanoforging single layer MoSe<sub>2</sub> through defect engineering with focused helium ion beams. *Sci. Rep.*, 6(1):30481, 2016.
- [23] Ines Abid. *Plasmonique hybride: Propriétés optiques de nanostructures Au-TMD, couplage plasmon-exciton*. PhD thesis, Université Paul Sabatier, 2017.
- [24] D. Kozawa, R. Kumar, A. Carvalho, K. Kumar Amara, W. Zhao, S. Wang, M. Toh, R. M. Ribeiro, A. H. Castro Neto, K. Matsuda, and G. Eda. Photocarrier relaxation pathway in two-dimensional semiconducting transition metal dichalcogenides. *Nat. Commun.*, 5(1):4543, 2014.
- [25] S. Najmaei, Z. Liu, W. Zhou, X. Zou, G. Shi, S. Lei, B. I. Yakobson, J.-C. Idrobo, P. M. Ajayan, and J. Lou. Vapour phase growth and grain boundary structure of molybdenum disulphide atomic layers. *Nat. Mater.*, 12(8):754–759, 2013.
- [26] D. Pommier, R. Bretel, L. E. Parra López, F. Fabre, A. Mayne, E. Boer-Duchemin, G. Dujardin, G. Schull, S. Berciaud, and E. Le Moal. Scanning Tunneling Microscope-Induced Excitonic Luminescence of a Two-Dimensional Semiconductor. *Phys. Rev. Lett.*, 123(2):027402, 2019.

- [27] X. Wang, Y. Gong, G. Shi, W. L. Chow, K. Keyshar, G. Ye, R. Vajtai, J. Lou, Z. Liu, E. Ringe, B. K. Tay, and P. M. Ajayan. Chemical vapor deposition growth of crystalline monolayer MoSe<sub>2</sub>. *ACS Nano*, 8(5):5125–5131, 2014.
- [28] E. Alves, R. Péchou, R. Coratger, and A. Mlayah. Gap plasmon modes and plasmon-exciton coupling in a hybrid Au/MoSe<sub>2</sub>/Au tunneling junction. *Opt. Express*, 31(8):12549–12561, 2023.
- [29] H.-L. Liu, C.-C. Shen, S.-H. Su, C.-L. Hsu, M.-Y. Li, and L.-J. Li. Optical properties of monolayer transition metal dichalcogenides probed by spectroscopic ellipsometry. *Appl. Phys. Lett.*, 105(20):201905, 2014.
- [30] R. Beiranvand. Theoretical investigation of electronic and optical properties of 2D transition metal dichalcogenides MoX<sub>2</sub> (X= S, Se, Te) from first-principles. *Physica E Low Dimens. Syst. Nanostruct.*, 126:114416, 2021.
- [31] R. Esteban, A. G. Borisov, P. Nordlander, and J. Aizpurua. Bridging quantum and classical plasmonics with a quantum-corrected model. *Nat. Commun.*, 3(1):825, 2012.
- [32] R. Esteban, A. Zugarramurdi, P. Zhang, P. Nordlander, F. J. García-Vidal, A. G. Borisov, and J. Aizpurua. A classical treatment of optical tunneling in plasmonic gaps: extending the quantum corrected model to practical situations. *Faraday Discuss.*, 178:151–183, 2015.
- [33] R. Ge, X. Wu, L. Liang, S. M. Hus, Y. Gu, E. Okogbue, H. Chou, J. Shi, Y. Zhang, S. K. Banerjee, Y. Jung, J. C. Lee, and D. Akinwande. A library of atomically thin 2D materials featuring the conductive-point resistive switching phenomenon. *Adv. Mater.*, 33(7):2007792, 2021.
- [34] L. Huang, B. Li, M. Zhong, Z. Wei, and J. Li. Tunable Schottky barrier at MoSe<sub>2</sub>/Metal interfaces with a buffer layer. *J. Phys. Chem. C*, 121(17):9305–9311, 2017.
- [35] W. Mönch. Valence-band offsets and Schottky barrier heights of layered semiconductors explained by interface-induced gap states. *Appl. Phys. Lett.*, 72(15):1899–1901, 1998.
- [36] I. Abid, A. Bohloul, S. Najmaei, C. Avendano, H.-L. Liu, R. Péchou, A. Mlayah, and J. Lou. Resonant surface plasmon–exciton interaction in hybrid MoSe<sub>2</sub>@Au nanostructures. *Nanoscale*, 8(15):8151–8159, 2016.
- [37] L. D. Landau, E. M. Lifshitz, and L. P. Pitaevskii. *Electrodynamics of Continuous Media*. Pergamon Press, 1984.
- [38] S. Hao, M. Z. Bellus, D. He, Y. Wang, and H. Zhao. Controlling exciton transport in monolayer MoSe<sub>2</sub> by dielectric screening. *Nanoscale Horiz.*, 5(1):139–143, 2020.
- [39] I. Abid, W. Chen, J. Yuan, A. Bohloul, S. Najmaei, C. Avendano, R. Péchou, A. Mlayah, and J. Lou. Temperature-dependent plasmon–exciton interactions in hybrid Au/MoSe<sub>2</sub> nanostructures. *ACS Photonics*, 4(7):1653–1660, 2017.

- 
- [40] P. Rivera, J. R. Schaibley, A. M. Jones, J. S. Ross, S. Wu, G. Aivazian, P. Klement, K. Seyler, G. Clark, N. J. Ghimire, J. Yan, D. G. Mandrus, W. Yao, and X. Xu. Observation of long-lived interlayer excitons in monolayer MoSe<sub>2</sub>–WSe<sub>2</sub> heterostructures. *Nat. Commun.*, 6(1):6242, 2015.
- [41] M. Palummo, M. Bernardi, and J. C. Grossman. Exciton radiative lifetimes in two-dimensional transition metal dichalcogenides. *Nano Lett.*, 15(5):2794–2800, 2015.
- [42] C. T. Le, D. J. Clark, F. Ullah, V. Senthilkumar, J. I. Jang, Y. Sim, M.-J. Seong, K.-H. Chung, H. Park, and Y. S. Kim. Nonlinear optical characteristics of monolayer MoSe<sub>2</sub>. *Annalen der Physik*, 528(7-8):551–559, 2016.

**Titre :** Émission de photons dans un microscope à effet tunnel: Application à l'étude des propriétés optiques et électroniques de systèmes hybrides métal/semi-conducteur

**Mots clés :** couches 2D, effet tunnel, dispositifs opto-électroniques, DDA modélisation, système hybride, exciton

**Résumé :** Les dichalcogénures de métaux de transition (TMD) sont une famille de semi-conducteurs qui présentent un gap direct lorsque leur épaisseur est réduite jusqu'à la monocouche, ce qui leur confère des propriétés optiques et électroniques exceptionnelles, notamment une luminescence avec un rendement élevé. La technique d'émission de lumière dans un microscope à effet tunnel (STM-LE) est utilisée pour étudier l'émission de photons de ces monocouches. Cette technique originale consiste à injecter grâce au courant tunnel des porteurs de charges de manière très locale dans des monocouches de TMD. Cela conduit à la création d'excitons, paires électrons-trous liées par des forces de Coulomb, au sein de la monocouche. Ces excitons vont se désexciter en émettant des photons dont l'énergie correspond au gap direct du semi-conducteur. Ce phénomène de luminescence est mis en évidence expérimentalement en utilisant un microscope STM couplé à un dispositif de détection optique, ce qui permet une analyse de l'émission de photons à la fois sur le plan spectral et spatial avec une résolution nanométrique. Le couplage électromagnétique des monocouches de TMD avec leurs substrats métalliques donne naissance à des structures hybrides métal/semi-conducteur dont les propriétés optiques et électroniques sont étudiées. La nature du substrat (plasmonique ou non) et sa morphologie (uniforme ou nanostructurée) jouent un rôle essentiel tant sur l'intensité que sur la distribution spectrale de la luminescence émise. En effet, lorsque des substrats plasmoniques sont utilisés, le mécanisme d'émission lumineuse implique le couplage électromagnétique entre des modes plasmoniques excités par le courant tunnel et les excitons confinés au sein de la monocouche de TMD. Cette interaction donne lieu à une émission de photons plus efficace. En jouant avec la morphologie de ces substrats, il est possible d'ajuster ce couplage afin d'obtenir une amplification ou une atténuation de l'émission de lumière. Sachant que l'interaction électromagnétique entre plasmons et excitons joue un rôle important dans la luminescence des monocouches dans le cas d'une jonction STM hybride TMD/métal plasmonique, des simulations numériques électromagnétiques sont réalisées via la méthode DDA (Discrete Dipole Approximation). Dans ces simulations, les effets quantiques du courant tunnel sont pris en compte en utilisant le modèle Quantum Corrected Model. Les modes électromagnétiques présents dans la jonction et leur dépendance vis-à-vis des paramètres tunnel (distance pointe-surface et tension de polarisation) sont mis en évidence à partir de la simulation de la réponse optique de la jonction à une onde excitatrice incidente. En particulier, les modes "gap plasmon" et le couplage plasmon-exciton de type Fano se produisant à l'interface entre la monocouche et le substrat plasmonique sont mis en évidence. L'influence de la morphologie du substrat sur les propriétés de ces modes a également été analysée. En s'inspirant des modèles théoriques de l'émission de lumière dans des jonctions STM purement métalliques proposés dans la littérature, un modèle est développé afin d'obtenir des spectres théoriques de luminescence d'une jonction STM hybride TMD/métal plasmonique. Ce modèle prend en compte les propriétés optiques et électroniques de la monocouche, ainsi que le courant tunnel, source d'excitation à l'origine du phénomène de luminescence. De plus, en utilisant les résultats obtenus à partir des simulations numériques, le couplage électromagnétique entre les excitons confinés dans la monocouche de TMD et les plasmons excités dans la nanocavité formée par la configuration pointe-surface du STM est également considéré. Pour finir, l'effet de la morphologie du substrat sur l'émission de lumière est étudié de manière théorique. Ces résultats sont comparés aux résultats expérimentaux afin de valider le modèle présenté.

**Title:** Light emission from a Scanning Tunneling Microscope: Study of the electronic and optical properties of a hybrid metal/TMD system

**Key words:** opto-electronical devices, scanning tunneling microscope, bidimensional systems, exciton, hybrid system, DDA simulation

**Abstract:** Transition metal dichalcogenides (TMDs) are a family of semiconductors that exhibit a direct bandgap when their thickness is reduced to a monolayer, giving them remarkable optical and electronic properties, including high-efficiency luminescence. Photon emission from these monolayers is investigated using the STM-LE (Light Emission induced by Scanning Tunneling Microscopy) technique. This innovative method involves the localized injection of charge carriers into TMD monolayers through the tunneling current. This process results in the formation of excitons, electron-hole pairs bound by Coulomb forces, within the TMD monolayer. These excitons decay radiatively emitting photons whose energy corresponds to the direct bandgap of the semiconductor. This light emission process is experimentally studied using an STM microscope combined with a light detection system, enabling spectral and spatial analysis of the photon emission with nanometer-scale resolution. The electromagnetic interaction between TMD layers and their metallic substrates leads to the formation of hybrid metal-semiconductor structures, the optical and electronic properties of which are under investigation. The nature of the substrate (plasmonic or non-plasmonic) and its morphology (uniform or nanostructured) play a crucial role in both the intensity and spectral distribution of the emitted photons. Indeed, for plasmonic substrates, the photon emission process involves the electromagnetic coupling between plasmon modes excited by electron tunneling and excitons confined within the TMD monolayer. This interaction leads to an enhancement of the photon emission. Moreover, by tuning the morphology of the substrate, it becomes possible to modify this coupling and thus, the photon emission rate. Considering the significant role of the electromagnetic interaction between plasmon modes and excitons in the luminescence from TMD monolayers within a hybrid TMD/metal-plasmonic STM junction, electromagnetic numerical simulations are carried out using the DDA (Discrete Dipole Approximation) method. These simulations account for electron tunneling using the Quantum Corrected Model. By simulating the optical response of the junction to an incident excitation wave, the electromagnetic modes within the junction and their dependence on the tunneling parameters, such as tip-surface distance and bias voltage, are investigated. In particular, gap plasmon modes and the Fano-type plasmon-exciton coupling at the interface between the monolayer and the plasmon substrate are pointed out. Furthermore, the role of substrate morphology on the properties of these modes is also addressed. Based on theoretical models describing the light emission taking place in purely metallic STM junctions proposed in the literature, a model is developed to compute theoretical light emission spectra for a hybrid TMD/plasmonic-metal STM junction. This model takes into account the optical and electronic properties of the TMD monolayer, and the electron tunneling as the excitation source at the origin of the light emission phenomenon. In addition, using the results obtained from the numerical simulations, the electromagnetic coupling between the excitons confined in the TMD monolayer and the plasmons excited in the nanocavity formed by the tip-surface configuration of the STM is also considered. Finally, the effect of the substrate morphology on the light emission is studied theoretically. These results are compared with the experimental findings in order to validate the model presented.